Collective effects in living matter : from cytokinetic rings to epithelial monolayers

Raghavan Thiagarajan

UNIVERSITÉ DE STRASBOURG

ÉCOLE DOCTORALE des sciences chimiques

UMR 7006 – Institut de Science et d'Ingénierie Supramoléculaires (ISIS)

THÈSE présentée par :

Raghavan THIAGARAJAN

soutenue le : **26 Septembre 2016**

pour obtenir le grade de : **Docteur de l'université de Strasbourg**

Discipline / Spécialité : **Physique Cellulaire**

Effets collectifs dans la matière vivante: des anneaux de cytokinèse aux monocouches épithéliales

THÈSE dirigée par :

Dr RIVELINE Daniel	Directeur de Recherche, Université de Strasbourg, ISIS/IGBMC

RAPPORTEURS :

Dr RAO Madan	Professeur, Tata Institute of Fundamental Research, NCBS
Dr SILBERZAN Pascal	Directeur de Recherche, Institut Curie – Centre de Recherche

---

AUTRES MEMBRES DU JURY :

Dr GARDEL Margaret	Professeur, University of Chicago, The James Franck Institute
Dr GIANGRANDE Angela	Directeur de Recherche, Université de Strasbourg, IGBMC
Dr LE GOFF Xavier	Chargé de Recherche, Université de Rennes 1, IGDR

UNIVERSITÉ DE STRASBOURG

ÉCOLE DOCTORALE des sciences chimiques

UMR 7006 – Institut de Science et d'Ingénierie Supramoléculaires (ISIS)

THÈSE présentée par :

Raghavan THIAGARAJAN

soutenue le : **26 Septembre 2016**

pour obtenir le grade de : **Docteur de l'université de Strasbourg**

Discipline / Spécialité : **Cell Physics**

Collective effects in living matter: from cytokinetic rings to epithelial monolayers

THÈSE dirigée par :

Dr RIVELINE Daniel	Directeur de Recherche, Université de Strasbourg, ISIS/IGBMC

RAPPORTEURS :

Dr RAO Madan	Professeur, Tata Institute of Fundamental Research, NCBS
Dr SILBERZAN Pascal	Directeur de Recherche, Institut Curie – Centre de Recherche

---

AUTRES MEMBRES DU JURY :

Dr GARDEL Margaret	Professeur, University of Chicago, The James Franck Institute
Dr GIANGRANDE Angela	Directeur de Recherche, Université de Strasbourg, IGBMC
Dr LE GOFF Xavier	Chargé de Recherche, Université de Rennes 1, IGDR

Acknowledgements

This PhD would not be possible without the unconditional support from many people both in professional and personal walk of my life.

First I would like to start by thanking my advisor, Daniel Riveline for his constant motivation and support throughout my PhD. It was a huge learning experience with him in terms of scientific quality, through the process of scientific debates and training on presentation and writing skills. I can recall a lot of stimulating and fascinating discussions that we had during our meetings which kept my aspirations high. His passion towards research would never fail to inspire me. On the personal level, I enjoyed a strong moral support from him through his motivations and tolerance, in tuning my scientific and personal abilities. It was a great pleasure and rich experience in doing my PhD with him.

I would like to thank Mandar Inamdar for all his patient and dedicated efforts in his guidance, in making me understand the theoretical concepts in spite of me being a novice. All the conversations that we had through plenty of skype sessions were indispensable for my progress in the project.

I would like to thank Karsten Kruse for all the very pleasant and intellectual interactions that we had throughout the long-standing project. His association was always inspiring and enjoyable.

I would like to thank Guillaume Salbreux for all his thought-provoking ideas that significantly helped in progressing and improving our project.

My time during PhD life would not have been happy and complete without my labmates. After joining the lab, it was David Caballero who patiently trained me and helped me to troubleshoot through several of the techniques that I went on to use throughout my PhD. His diligence in achieving a task and hard-working nature are unforgettable. My association with Viktoria Wollrab was a very pleasant experience with lot of learning and fun. I cannot forget those times when she would patiently teach me through different things, sparing her time. I really enjoyed my time in both scientific and non-scientific debates with Amélie Godeau, my peer mate during the PhD. I would like to thank Jordi Comelles for his smart advices in discussions involving science and troubleshooting. I would like to thank Emilie Le Maout, Alka Bhat and David Rodriguez for their support and interesting discussions in the lab. In addition to these, it was a great learning and fun experience in supervising Cedric Fuchs and Simon Lo Vecchio during their Master internships.

I would like to thank Claire Menouna-Ekani for her support through all the administrative support after my arrival in Strasbourg and during my PhD.

I would like to thank the members of the IGBMC Imaging facility - Marcel Boeglin, Pascal Kessler, Basile Gurchenkov, Elvire Guiot, Marc Koch and Yves Lutz for always being around to help and in patient troubleshooting.

I would like to thank Daniel Riveline, Viktoria Wollrab, David Caballero and Mandar Inamdar for critical reading of my manuscript.

I would like to thank Daniel Riveline, Emilie Le Maout, Simon Lo Vecchio and David Rodriguez for the French translations of summary and abstract.

I would like to thank my PhD jury members Angela Giangrande, Madan Rao, Margaret Gardel, Pascal Silberzan and Xavier Le Goff for accepting to travel to Strasbourg and for their critical comments on the manuscript.

I would like to thank the IGBMC HR department and administrative staffs for their help with all the formal procedures during my PhD.

This PhD would not have been possible if it were my parents, Chellammal Thiagarajan and Thiagarajan Venkataraman, and my sister, Lalitha Sree who gave me the warmth and comfort all through my life. My career in scientific life started with inspiration from my father, who happened to be my first science teacher. It would not be an exaggeration to say that I have come this far by standing on his shoulders.

Last but not the least, it was my wife Swathi's support that carried me through all the difficult and turbulent phases of my PhD. This PhD would have been a really difficult task if it was not her motivation and selfless attitude. I am indebted to her for all her support which was a crucial factor in my achievements during the PhD.

Résumé de la thèse

Effets collectifs dans la matière vivante: des anneaux de cytokinèse aux monocouches épithéliales

Les systèmes biologiques sont soumis à plusieurs processus actifs tels que le transport interne des molécules, la division cellulaire, la migration cellulaire et la contraction musculaire pendant la morphogenèse et le développement. Ces phénomènes utilisent l'Adénosine TriPhosphate (ATP) pour générer stress et mouvement d'une manière auto-organisée - fonctionnant ainsi dans un état de non équilibre. Ce cycle travail-énergie dans les systèmes biologiques est maintenu par un réseau de protéines appelé le *cytosquelette*. Fait intéressant, la complexité du mécanisme derrière ces procédés augmente avec l'échelle du système, des événements moléculaires simples de molécules aux effets collectifs complexes, et des dynamiques en cellules uniques aux mouvements collectifs de cellules. Pour comprendre ces phénomènes à des échelles différentes, une description détaillée des propriétés mécaniques du cytosquelette est nécessaire, en tenant compte de la taille et de l'organisation du système. Cependant, une telle description nécessite des expériences novatrices soutenues par un cadre théorique rigoureux.

Dans cette thèse, à travers différents projets, nous visons une approche interdisciplinaire pour comprendre les aspects physiques du cytosquelette, sur une gamme d'échelles mésoscopiques au-delà des descriptions moléculaires: micromètres (anneau cytokinétique et mouvement de la cellule unique) et des centaines de micromètres (collecte de cellules).

1. Agrégats de myosine statiques et rotatifs comme acteurs de la fermeture de l'anneau cytokinétique

Introduction: La fermeture de l'anneau de cytokinèse facilite la séparation physique des cellules filles lors de la division cellulaire [Pollard and Wu, 2010, Nat Rev Mol Cell Biol]. Fait intéressant, ce processus est conservé entre les métazoaires et les champignons dont les organisations cellulaires sont pourtant différentes: les cellules métazoaires possèdent une membrane cellulaire qui est directement liée au cortex alors que les cellules de champignons ne disposent pas de cortex mais possèdent une paroi cellulaire. Dans les deux systèmes, le réseau d'acto-myosine et les protéines de réticulation correspondantes apparaissent comme étant les principaux acteurs [Carvalho et al., 2009 Cell; Mishra et al., 2013, Nat Cell Biol]. Cependant, le mécanisme par lequel l'organisation collective de milliers de filaments et moteurs conduisent à la génération de

stress pendant la fermeture de l'anneau cytokinétique n'est pas clair à ce jour. Dans ce projet, nous abordons cette question en utilisant *Schizosaccharomyces pombe* (fission yeast) et HeLa (cellules de mammifères) comme systèmes modèles [Wollrab et al., 2016, Nat Commun].

Idée et résultats: L'orientation classique de l'anneau - perpendiculaire au plan focal, empêche l'observation complète de l'anneau en une seule acquisition, limitant ainsi un aperçu dynamique de son organisation. Pour remédier à ce problème, nous avons orienté les levures et les cellules de mammifère à la verticale à l'aide d'un nouveau dispositif microfabriqué [Patents: Riveline and Buguin, 2009; Riveline, 2012; Riveline and Wollrab, 2012]. Cette orientation a permis l'observation complète des anneaux avec des résolutions spatiales et temporelles élevées. Étonnamment, nous avons constaté que l'actine et la myosine sont organisées de manière non homogène en zones de haute intensité: les agrégats sont statiques dans l'anneau des cellules de mammifère et tournent chez la levure. Nous avons mesuré les propriétés globales de l'anneau telles que les vitesses de fermeture et la densité d'acto-myosine. Nous avons constaté que les vitesses des deux anneaux chez la levure et les cellules de mammifère augmentent immédiatement après le début de la constriction. Cependant, les densités d'actine et de myosine - mesurées comme intensités des marqueurs de fluorescence correspondants – n'augmentent que de 20%, ce qui indique que la génération de stress pendant la fermeture de l'anneau n'est pas seulement due à la densité d'acto-myosine.

Pour mieux comprendre ce qui déclenche la constriction, nous avons analysé l'organisation spatiale des agrégats: les zones statiques dans les anneaux de cellules de mammifères sont séparés par une distance de ~ 0,8 μm et conservent une trajectoire rectiligne tout au long de la fermeture (dans le référentiel du laboratoire). Chez la levure, les agrégats ont une vitesse de rotation de l'ordre du μm / min avec une durée de vie moyenne de ~ 20 s. Les rotations sont dans les deux directions et sont confirmées par des structures radiales provenant de l'anneau vers la fin de la fermeture. Nous avons également trouvé des agrégats statiques et rotatifs de formine dans les deux systèmes avec les mêmes dynamiques distinctes. Nous avons constaté que les rotations d'acto-myosine ne sont pas perturbées lorsque la synthèse de la paroi cellulaire est inhibée, ce qui suggère que les rotations sont une propriété intrinsèque des gels actifs d'acto-myosine. Par ailleurs, la présence d'inhibiteurs d'acto-myosine perturbe l'organisation des agrégats ainsi que la fermeture des anneaux dans les deux systèmes, ce qui indique l'importance de l'organisation des agrégats dans la constriction. Fait intéressant, la rotation des agrégats chez la levure existe avant l'apparition de la constriction. Au contraire, l'anneau de mammifère passe d'un état homogène en myosine à celui

d'agrégats de myosines exactement au début de la fermeture. Cette transition d'un état homogène à celui d'agrégats, confirmée par les mêmes observations pendant la constriction, souligne le rôle des agrégats dans la production de stress lors de l'apparition de constriction.

Nous avons développé un modèle théorique basé sur [Kruse et Julicher, 2003, Phys Rev E] pour vérifier cette hypothèse. Le modèle décrit l'anneau comme une combinaison de filaments d'actine parallèles et anti-parallèles interagissant avec la myosine. La dynamique résultante des interactions entre les filaments et les moteurs moléculaires sont régis par le taux d'assemblage (ω_c) et de désassemblage (ω_d) des filaments bipolaires, la polarité des filaments interagissant et la vitesse résultante (parallèle α, antiparallèle-β). Les équations microscopiques obtenues à partir de ces règles d'interaction filament-moteur étaient écrites pour obtenir les propriétés mésoscopiques de l'anneau de constriction. Nous avons constaté qu'une valeur critique (α_c) existait pour la vitesse résultante de l'interaction de filaments parallèles qui régissait la nature mésoscopique de l'anneau avec ω_d. L'augmentation de α au-delà d'une valeur critique α_c déclenchait l'apparition des agrégats statiques, et par ailleurs un état dynamique lorsque ω_d était plus grand. Nous avons confirmé expérimentalement l'existence de trois états (homogène, agrégats fixes et agrégats dynamiques) en utilisant des inhibiteurs d'acto-myosine. L'inhibition de la myosine déclenche l'homogénéisation de l'anneau, alors que la «réactivation» de la myosine entraîne la formation d'agrégats dans les cellules de mammifères. Chez la levure, l'inhibition de la polymérisation d'actine conduit à des agrégats immobiles et la restauration de la polymérisation entraîne la rotation. Cela montre que notre modèle rend compte des propriétés mésoscopiques et de leurs transformations au sein de l'anneau cytokinétique.

En outre, nous avons constaté que le stress généré autour de l'anneau augmente non linéairement quand $\alpha > \alpha_c$ dans les cellules de mammifère. Cela suggère que la transition de l'état homogène à l'état d'agrégats qui coïncide avec le début de la fermeture, introduit une augmentation du stress conduisant à la fermeture de l'anneau. Le changement de stress dû à la rotation des agrégats était mineur chez la levure. Cette contrainte variable portée par les agrégats fixes ou rotatifs pourrait avoir comme fonctions la contractilité pour les cellules de mammifère et le transport pour la levure. Ces fonctions distinctes ont été confirmées par des expériences d'ablation au laser où l'ablation conduit à l'ouverture des anneaux cytokinétiques de mammifère, suivie par sa constriction, et la fermeture du point d'ablation due à la rotation des agrégats chez la levure.

Conclusions: Nous avons mis en place un nouveau dispositif pour analyser l'anneau cytokinétique et fait état de nouvelles fonctions associées à l'auto-organisation des gels

actifs. Ce projet met en évidence les transitions dynamiques dans les gels actifs en montrant comment deux organisations spatiales distinctes de gels actifs pourraient réguler deux fonctions distinctes dans des systèmes différents [Wollrab et al., 2016, Nat Commun].

Contributions: Supervision du projet, idée et développement du montage - Daniel Riveline (ISIS/IGBMC, Strasbourg); Théorie: Karsten Kruse (Universität des Saarlandes, Saarbrücken); expériences sur les cellules de mammifères - Viktoria Wollrab (ISIS/IGBMC); expériences sur la levure à fission- Raghavan Thiagarajan et Daniel Riveline (ISIS/IGBMC); élaboration d'un modèle théorique - Anne Wald et Karsten Kruse (Universität des Saarlandes, Saarbrücken).

2. Polyamines synthétiques: de nouveaux composés spécifiques à la dynamique de l'actine pour les cellules de mammifères et la levure à fission

Introduction: Les polyamines macrocycliques sont connues pour induire la polymérisation d'actine [Oriol-Audit et al, 1985, Eur. J. Biochem.]. Un travail précédent de notre laboratoire a étudié les effets inédits de la polyamine cyclique C7 (C_7N_6) et de la polyamine ramifiée C8 (C_8N_6) qui favorisent la croissance des lamellipodes riches en actine [Nedeva et al., 2013, Nat Commun]. Cette étude a montré que les polyamines stabilisent et facilitent la nucléation des filaments d'actine en se liant aux extrémités barbées. Cependant, l'organisation des structures d'actine dans les lamellipodes est tout à fait distincte (organisation en réseau) des autres structures de gels actifs comme le cortex, l'anneau de cytokinèse, le filopode etc. Afin d'explorer l'importance de la dynamique de la polymérisation de l'actine dans une autre structure de gel actif, nous avons étudié la constriction de l'anneau d'acto-myosine lors de la cytokinèse chez la levure en présence de polyamines synthétiques.

Résultats: En continuité de nos résultats sur les cellules de mammifères où C7 et C8 avaient déclenché des lamellipodes en quelques minutes [Nedeva et al., 2013, Nat Commun], nous avons étudié les effets de C7 et C8 pendant la constriction de l'anneau de cytokinèse chez la levure. Les polyamines synthétiques diminuent la vitesse de constriction, C7 de 50%, et C8 de 40%, respectivement. Nous proposons que la stabilisation des filaments d'actine et l'inhibition de la dépolymérisation conduisent à cette diminution. En outre, la nucléation et la stabilisation des filaments d'actine dans

l'anneau pourrait avoir une incidence sur l'efficacité du transport, conduisant ainsi à un taux de fermeture diminué.

Conclusion: Les polyamines synthétiques se sont révélés être des outils puissants pour étudier la dynamique de l'actine [Riveline et al., 2014, Bioarchitecture]. Alors que la dynamique de l'actine a été étudiée surtout grâce à des molécules qui permettent sa dépolymérisation comme la latrunculine A et la cytochalasine D, les polyamines synthétiques ouvrent une autre perspective où la *polymérisation* de l'actine pourrait être utilisée dans des phénomènes biologiques. Ces perspectives pourraient également améliorer notre compréhension des protéines comme la formine, Arp2/3 et l'α-actinine par exemple.

Contributions: Supervision du projet - Daniel Riveline (ISIS/IGBMC, Strasbourg), Expériences et analyse - Raghavan Thiagarajan et Marcia TOGUCHI (ISIS/IGBMC, Strasbourg); Synthèse de polyamines C7 et C8 - Girish Koripelly et Jean-Marie Lehn (ISIS, Strasbourg), et collaborateurs pour les études *in vitro*: Marie-France Carlier (LEBS, Paris).

3. Motilité cellulaire : Ratchetaxie et inversions de sens

Introduction: La migration dirigée est une étape importante en biologie du développement et en médecine. En général, la polarisation (relocalisation des protéines) et l'activité des protrusions, influencée par des facteurs tels que les gradients chimiques [Dona et al., 2013, Nature] ou les substrats géométriques [Jiang et al., 2005, Proc Natl Acad Sci U S A], jouent un rôle clé dans la direction de la migration. Basées sur le modèle du *ratchet* de Feynman, des études récentes ont montré que la rectification de la migration pouvait avoir lieu en utilisant seulement une série de substrats microfabriqués asymétriques (comme des *ratchets*) [Mahmud et al., 2009, Nature Phys.]. En allant plus loin, les travaux précédents de notre laboratoire ont mis en évidence le rôle des fluctuations de protrusions *efficaces* dans ce processus [Caballero et al., 2014, Biophys J] et ont montré que la migration basée sur les *ratchets* peut entrer en compétition avec des gradients biochimiques [Comelles et al., 2014, Biophys J]. Nous avons proposé le terme de *ratchetaxie* pour ce type nouveau de migration [Caballero et al., 2015, Trends Cell Biol]. Cependant, à ce jour, les rôles de la *séparation entre* les motifs du ratchet ne sont pas encore considérés. Dans ce projet, nous essayons de comprendre les effets de la variation de distances entre les micro-motifs sur la directionnalité de la migration cellulaire.

Idée et résultats: Les théories fondées sur le modèle du ratchet thermique de Feynman proposent la rectification de particules browniennes [Chauwin et al., 1994 Europhys Lett.; Chauwin et al., 1995, Europhys Lett.]. Un système de particules browniennes piégées dans un système à deux potentiels a une probabilité égale de se dissiper dans les deux directions. Cependant, l'introduction d'une asymétrie spatiale permet de modifier la durée de vie des particules dans chaque potentiel et le temps de dérive afin de piéger les particules et entraîner un biais élevé vers une direction.

Dans ce projet, nous essayons de reproduire expérimentalement ce cadre théorique qui provoquerait une inversion dans le sens de la migration lorsque la distance entre les motifs varie. Les cellules sont ensemencées sur des substrats - micro-motifs de fibronectine avec une structure asymétrique (triangle). Le reste est passivé avec du PEG. Les structures de fibronectine asymétriques sont périodiquement séparées par une distance de séparation, sur laquelle les cellules adhérentes peuvent se déplacer dans les deux sens. Cela créé un système unidimensionnel formellement équivalent à la particule / système à potentiels décrit précédemment. Le choix de l'orientation est influencé par la fluctuation des protrusions et la distance d'écartement entre les triangles de fibronectine. Dans ce scénario, en changeant les distances séparant les triangles de fibronectine dans différentes expériences, nous cherchons à trouver la distance critique qui déclencherait une inversion dans le sens moyen de la migration.

Nous avons choisi des distances d'espacement (13 μm, 16 μm, 19 μm, 22 μm, 45 μm) autour de la longueur moyenne des protrusions (20,5 μm) des cellules utilisées. Les résultats actuels montrent un biais dans la migration vers le bord fin du triangle, pour toutes ces distances de séparation - résultant dans la ratchetaxie. De plus, nous avons constaté que les distances d'écart négatif / triangles qui se chevauchent avec 25% de chevauchement présentaient également de la ratchetaxie. Afin de trouver le point d'inversion exacte, nous avons modifié le modèle mésoscopique de notre travail précédent pour inclure la distance de séparation - par des arguments simples qui prédisent une inversion de direction à 50% de chevauchement. À l'heure actuelle, nous effectuons des expériences sur cette condition de recouvrement de 50% pour confirmer la prédiction du modèle. En utilisant ce modèle mésoscopique, nous montrons que le comportement en ratchetaxie prédominant dans toutes les conditions est dû à la disponibilité d'une plus grande zone de fixation de ces protrusions efficaces émergeant du bord fin du triangle. En appui de cette affirmation, les expériences sur les 75% condition de chevauchement (où la disponibilité de la zone de fixation pour des protrusions efficaces est similaire dans les deux directions) ne présentaient aucun biais net dans un sens de migration. Nos

expériences dans un avenir proche sur 50% de chevauchement exploreront la prédiction du modèle sur l'inversion du sens.

Conclusion: Ce projet explore les mécanismes de migration directionnelle en reproduisant des déplacements sur des substrats discontinus aux symétries brisées. D'autre part, l'étude met en évidence l'importance de mieux comprendre les signaux responsables de l'inversion, qui, dans un état pathologique typique, pourrait conduire à la migration dirigée des cellules cancéreuses vers des organes cibles, même en l'absence de gradients chimiques à longue portée.

Contribution: La supervision du projet et l'idée - Daniel Riveline (ISIS/IGBMC, Strasbourg), expériences et analyses - Raghavan Thiagarajan (ISIS/IGBMC, Strasbourg), Cedric Fuchs (Faculté de médecine de Strasbourg - DFGSM2) et Simon Lo Vecchio (Cell Physique Master II programme). Conception du modèle: Raphaël Voituriez (UPMC, Paris), et extrapolations avec les séparations : Simon Lo Vecchio.

4. Domaines pulsatiles spontanés dans une monocouche épithéliale

Introduction: Les dynamiques collectives de cellules sont importantes pour la morphogenèse [Solon et al., 2009, Cell; Kruse and Riveline, 2011, 1st ed. Elsevier Inc.]. Ces dynamiques résultent du cytosquelette (gel actif) qui est capable de générer un stress, comme pour la contractilité acto-myosine [Martin et al., 2009, Nature]. La coordination entre les éléments du cytosquelette de plusieurs cellules se manifeste par un effet collectif qui couvre des centaines de micromètres [Angelini et al., 2010, Phys Rev Lett.; Deforet et al., 2014, Nat. Commun.]. Bien que le cytosquelette soit connu pour en être la source, le mécanisme et les facteurs responsables de la mise en place des échelles de longueur et de temps ne sont pas connus. Dans ce projet, nous rapportons un effet collectif inédit des cellules MDCK en monocouche: des pulsations émergent spontanément. Ces pulsations peuvent être utilisées comme un outil pour étudier les facteurs impliqués dans la mise en place des échelles de longueur et de temps dans des tissus.

Résultats: Les cellules MDCK, une fois à confluence, exposent aléatoirement des pulsations collectives spontanées impliquant plusieurs cellules. Nous avons caractérisé les pulsations en calculant la divergence du champ de vitesse qui montre des cycles de contraction et des extensions. En traçant la fonction de corrélation de la divergence, nous avons constaté que les pulsations ont une longueur de corrélation caractéristique de ~ 230 μm, et une période typique de 7 h. L'émergence de ces échelles de longueur et de temps caractéristiques dans la monocouche, nous ont amenés à étudier davantage les facteurs et

les mécanismes qui en sont responsables. Dans un premier temps, nous avons vérifié le rôle de l'interaction cellule-substrat dans la fixation des échelles de longueur sous-jacentes de pulsations.

Substrat interaction / frottement: L'interaction de la monocouche avec le substrat peut être augmentée par revêtement du substrat avec des protéines de la matrice extracellulaire telles que la fibronectine. L'augmentation résultante de l'interaction peut être déduite par une diminution des vitesses de cellules dans la monocouche. Avec cette approche, nous avons comparé les vitesses collectives de cellules dans la monocouche entre l'état normal et le substrat couvert de manière homogène avec de la fibronectine (FN). Comme on s'y attendait, les vitesses collectives de la monocouche diminuent sur le substrat FN homogène, par rapport à la condition contrôle. Cela confirme le rôle du frottement dans cette dynamique collective de monocouche.

En outre, pour vérifier les effets du frottement spécifiquement sur les caractéristiques de pulsation, nous avons conçu un substrat où les régions du FN et non-FN coexistent – les grilles FN imprimées par micro-impression. Afin de maximiser l'effet de la contrainte spatiale, la taille des grilles a été conçue pour correspondre à la taille des pulsations spontanées. Sur ces substrats, les pulsations étaient présentes dans la plupart des réseaux, ce qui indique l'influence de la friction dans l'organisation spatiale. Cet effet a été encore amplifié lorsque les régions non-FN ont été couvertes avec un agent de passivation (PEG). L'introduction de passivation a augmenté l'ampleur de l'interaction du substrat entre le FN et les régions non-FN. Ces résultats, associés aux mesures des cycles et de ses changements, confirment la forte influence du frottement avec la surface dans les caractéristiques des pulsations.

Modèle théorique: Suite à ces résultats, nous avons voulu comprendre l'émergence d'échelles de longueur caractéristiques en condition contrôle. Nous avons pris une approche hydrodynamique; un système de pulsation de cellules peut être décrit par le couplage de la contractilité et de l'interaction cellule-substrat avec les changements correspondants dans la zone de chaque cellule. Dans ce cadre, les pulsations pourraient spontanément survenir en raison de la contractilité inhérente du système dont les changements sont couplés par une rétroaction avec la variation de la hauteur des cellules. Nous avons constaté que les spectres de corrélation de ce modèle théorique présentaient des caractéristiques similaires aux pulsations observées dans notre monocouche. En outre, nous avons validé les résultats du modèle en confirmant les variations de hauteur de la monocouche lors des pulsations. L'expression obtenue pour l'échelle de longueur caractéristique a confirmé l'implication du frottement des cellules avec le substrat, ainsi

que la contractilité. Inspirés par la théorie, nous avons ensuite voulu confirmer expérimentalement le rôle de la contractilité.

Contractilité: L'effet de la contractilité est généré et transmis à travers la monocouche par l'intermédiaire d'activités du cytosquelette. Nous avons utilisé des inhibiteurs du cytosquelette pour étudier le rôle de la contractilité dans la détermination des caractéristiques des pulsations.

L'inhibition de la myosine par la blebbistatine, arrête complètement les pulsations dans la monocouche. Étonnamment, lorsque la myosine est réactivée par lavage de la blebbistatine, la monocouche présente d'importants flux de cellules. Nous attribuons la non-récupération des échelles de longueur de pulsation après lavage avec la destruction de l'ordre spontané dans l'organisation mésoscopique de la myosine qui aurait pu exister avant l'addition de la drogue. L'effet est identique avec l'administration de l'inhibiteur de l'actine, la latrunculine A. Ces résultats confirment le rôle critique des complexes acto-myosine dans les caractéristiques des pulsations.

Les résultats expérimentaux sur substrat, sur la friction et les variations de hauteur, et sur le cytosquelette et sa contractilité, sont en accord avec le modèle pour leur rôle central sur les échelles des pulsations.

Conclusion: Ainsi, nous avons identifié une dynamique collective nouvelle pour étudier déterminer comment les échelles de longueur et de temps sont organisées spontanément dans les tissus biologiques. En utilisant un modèle continu, nous identifions les facteurs conduisant à des pulsations et confirmons expérimentalement ces phénomènes. Avec une analyse plus approfondie et l'interprétation de ces facteurs, nous serons en mesure de déchiffrer les mécanismes impliqués, et d'établir un paradigme pour décrire l'émergence spontanée d'échelles de longueur et de temps dans les systèmes collectifs cellulaires.

Contributions: Supervision du projet et idée: Daniel Riveline (ISIS/IGBMC, Strasbourg); Expériences - Raghavan Thiagarajan (ISIS/IGBMC, Strasbourg); Conception de la théorie - Guillaume Salbreux (l'Institut Francis Crick, Londres); Modélisation théorique et développement - Mandar M. Inamdar (IIT Bombay, Mumbai).

En résumé, mon travail de thèse a visé à comprendre le rôle de phénomènes physiques impliqués dans les systèmes biologiques à travers une gamme large d'échelles mésoscopiques.

Thesis summary

Collective effects in living matter: from cytokinetic rings to epithelial monolayers

Biological systems undergo several active processes like internal transport of molecules, cell division, cell migration and muscle contraction during morphogenesis and development. These phenomena utilize Adenosine TriPhosphate (ATP) to generate stress and displacement in a self-organized manner – thus functioning in a state of non-equilibrium. This work-energy cycle in biological systems is maintained by a network of proteins called *cytoskeleton*. Interestingly, the complexity of the mechanism behind these processes increases with the scale of system, from single molecular events to collection of molecules and from single cell to collection of cells. To understand these phenomena at different scales, a thorough description of the mechanical properties of the cytoskeleton is needed, taking into account the size and organization of the system. However, such a description requires innovative experiments supported by rigorous theoretical framework.

In this PhD thesis, through different projects, we aim at such a combinational approach for understanding physical aspects of the cytoskeleton, over a range of mesoscopic scales beyond molecular descriptions: micrometers (cytokinetic ring and single cell motion) and hundreds of micrometers (collection of cells).

1. Still and rotating myosin clusters as determinants for the cytokinetic ring constriction

Introduction: The constriction of cytokinetic ring facilitates the physical separation of daughter cells during cell division [Pollard and Wu, 2010, Nat Rev Mol Cell Biol]. Interestingly, this process is conserved between metazoan and fungi whose cellular organizations are different: Metazoans possess a cell membrane that is directly linked to cortex, whereas fungi lack cortex and possess a cell wall. In both systems, acto-myosin and related cross-linking proteins are identified to be the major actors [Carvalho et al., 2009 Cell; Mishra et al., 2013, Nat Cell Biol]. However, the mechanism by which collective organization of thousands of filaments and motors lead to stress generation during ring constriction is not clear. In this project, we address this question using *Schizosaccharomyces pombe* (fission yeast) and HeLa (mammalian cell) as model systems [Wollrab et al., 2016, Nat Commun].

Idea and results: The conventional orientation of the ring - perpendicular to the focal plane, prevents its complete observation in single acquisitions, thus limiting insights into its organization. To overcome this issue, we oriented mammalian and fission yeast cells in vertical fashion using a novel microfabricated device [Patents: Riveline and Buguin, 2009; Riveline, 2012; Riveline and Wollrab, 2012]. This orientation allowed complete observation of rings with high spatial and temporal resolutions. Surprisingly, we found that actin and myosin were organized into inhomogeneities of high intensity spots: *clusters*. The clusters were static / still in the mammalian ring and rotating in fission yeast. We measured the global properties of the ring such as closure rate and acto-myosin density. We found that velocities of both mammalian and fission yeast rings increased immediately after the onset of constriction. However, the actin and myosin densities, measured as intensities of the corresponding fluorescence markers increased only by 20%, indicating that stress generation for constriction was not only due to acto-myosin density.

To further understand the onset of constriction, we analysed the spatial organization of clusters. The static clusters in mammalian rings were separated by a distance of ~ 0.8 μm and kept straight trajectories throughout constriction in the laboratory framework. In fission yeast, the clusters rotated in the μm/min speed range with an average lifetime of ~ 20 s. Rotations were in both directions and were further confirmed by structures emanating from the ring towards the end of closure. We also found similar static and rotating clusters of formin, in fission yeast and in mammalian rings respectively. We found that the myosin rotations were not disrupted when cell wall synthesis was prevented, confirming that rotations were inherent property of active gels. However, addition of acto-myosin inhibitors disrupted the cluster organization along with constriction in both systems, indicating the significance of cluster organization in constriction. Interestingly, the cluster rotations in fission yeast ring existed before the onset of constriction. But the mammalian ring transitioned from an homogeneous state to a clustered state exactly at the onset. This transition from homogeneous to clustered state further indicated the role of clusters in stress generation during the onset of constriction.

We developed a theoretical model based on [Kruse and Julicher, 2003, Phys Rev E] to test this hypothesis. The model describes the ring as a combination of parallel and anti-parallel actin filaments interacting through myosin. The dynamics due to the filament-motor interactions are governed by assembly (ω_c) and disassembly (ω_d) rates of bipolar filaments, polarity of interacting filaments and the resultant velocity (parallel-α; anti-parallel-β) and the filament treadmilling velocity (v). The equations from based on these filament-motor interaction rules were coarse-grained to obtain the mesoscopic property of

the constricting ring. We found that a critical value (α_c) existed for the velocity due to interaction of parallel filaments that governed the mesoscopic nature of the ring along with ω_d. The increase of α beyond α_c triggered the stationary clustered state, and a dynamic clustered state when ω_d was also larger. We experimentally confirmed the existence of three states (homogeneous, stationary clustered and dynamic clustered) using acto-myosin inhibitors. Myosin inhibition triggered homogenization of the ring, and 'reactivation' of myosin led to clustered state in mammalian cells for example. In fission yeast, inhibition of actin polymerization led to immobilized clusters and restoration of actin polymerization leds to cluster rotation. This shows that our model captures key mesoscopic properties of myosin and transformations of the ring.

In addition, we found that, the point stress generated along the ring over-linearly increased when $\alpha > \alpha_c$ in the mammalian ring. This shows that transition from homogeneous to clustered state which coincides with the onset of closure, introduces a large increase in stress leading to ring constriction. The change in stress due to cluster rotation was minor in fission yeast. This variable stress in stationary and rotating clusters can be related to biological functions, *i.e.* contractility and transport in mammalian and fission yeast rings respectively. These distinct functions were confirmed by laser ablation experiments where ablation lead to opening of mammalian rings followed by constriction, and healing of the ablation spot due to cluster rotation in fission yeast rings.

Conclusions: We established a new device for investigating the cytokinetic ring, and reported new functions associated to self-organization of active gels. This project highlights the dynamic transitions in active gels by showing how two distinct spatial organizations of active gels regulate two distinct functions in completely different systems [Wollrab et al., 2016, Nat Commmun].

Contributions: Project supervision, idea and device development – Daniel Riveline (ISIS/IGBMC, Strasbourg); Conceived the theory: Karsten Kruse (Universität des Saarlandes, Saarbrücken); Mammalian cell experiments – Viktoria Wollrab (ISIS/IGBMC); Fission yeast experiments - Raghavan Thiagarajan and Daniel Riveline (ISIS/IGBMC); Theoretical model development – Anne Wald and Karsten Kruse (Universität des Saarlandes, Saarbrücken).

2. Synthetic polyamines: new compounds specific to actin dynamics for mammalian cell and fission yeast

Introduction: Macrocyclic polyamines have been shown to induce actin polymerization [Oriol-Audit et al, 1985, Eur. J. Biochem.]. *In vitro*, they are capable of promoting G-actin nucleation, elongation of monomeric actin into helical strands and lateral binding of actin filaments to form bundles. A previous work from our lab. explored the effects of macrocyclic polyamine C7 (C_7N_6) and branched polyamine C8 (C_8N_6) that promoted the growth of actin rich lamellipodia [Nedeva et al., 2013, Nat Commun]. This work showed that synthetic polyamines stabilized and facilitated nucleation of actin filaments by binding to the barbed ends. However, the organization of actin structures in lamellipodia is quite distinct (mesh-like arrangement) from other active gel structures like cortex, cytokinetic ring, filopodia etc. In order to explore the significance of actin polymerization dynamics in another structure, we studied the acto-myosin ring constriction during fission yeast cytokinesis in the presence of synthetic polyamines.

Results: In line with our results in mammalian cells where C7 and C8 had triggered growth of lamellipodia in minutes [Nedeva et al., 2013, Nat Commun], we investigated the effects of C7 and C8 during cytokinetic ring constriction in fission yeast. The polyamines decreased the constriction rate: C7 by 50%; and C8 by 40% respectively. We propose that stabilization of actin filaments and prevention from depolymerization lead to the decreased constriction rate. Also, further nucleation and stabilization of actin filaments in the ring might affect transport efficiency of cell wall machinery, thus leading to decreased rate of closure.

Conclusion: We established polyamines as a powerful tool for investigating actin dynamics [Riveline et al., 2014, Bioarchitecture]. While actin dynamics has been studied only through tools that enable depolymerization like Latrunculin A and Cytochalasin D, synthetic polyamines with their new types of activity on actin open novel perspective where actin polymerization could be used. These insights might also improve our understanding of actin-associated proteins like formin, Arp2/3 and α-actinin.

Contributions: Project supervision – Daniel Riveline (ISIS/IGBMC, Strasbourg), Experiments and analysis – Raghavan Thiagarajan and Marcia Toguchi (ISIS/IGBMC, Strasbourg); Synthesis of Polyamines C7 and C8 – Girish Koripelly and Jean-Marie Lehn (ISIS, Strasbourg), and Collaborator for *in vitro* studies: Marie-France Carlier (LEBS, Paris).

3. Directed cell migration by adhesive ratchets and predicting direction reversal

Introduction: Directional migration is an important step in development and pathological conditions. In general, polarization through relocalisation of proteins, and protrusion activity, influenced by factors such as chemical gradients [Dona et al., 2013, Nature] and substrate geometry [Jiang et al., 2005, Proc Natl Acad Sci U S A], play key roles in the cell directions. Interestingly, based on Feynman's ratchet model, recent studies have shown rectification in migration, only by using a series of asymmetric microfabricated substrates (as ratchets) [Mahmud et al., 2009, Nature Phys.]. Going a step further, previous works from our lab. explained the phenomenon by proving the central role of *efficient* protrusions through probing and adhering [Caballero et al., 2014, Biophys J], and showed that ratchet based migration can compete against biochemical gradients [Comelles et al., 2014, Biophys J]. We coined *ratchetaxis* this new type of migration, where cells combine probabilities to probe and probabilities to adhere [Caballero et al., 2015, Trends Cell Biol]. However in all these cases, the effect of separation between the ratchets / gap distances, are not considered. In this project, we try to understand the effects of variation in gap distances between micro-patterns on the direction of cell migration.

Idea and results: Theories based on Feynman's thermal ratchet model propose rectification of brownian particles [Chauwin et al., 1994 Europhys Lett.; Chauwin et al., 1995, Europhys Lett.]. A system of brownian particle trapped in a tilted two-state potential system, has an equal probability to dissipate in either directions. However with the introduction of spatial asymmetry, the lifetime of particles in each potential and the drifting-time can be tuned to trap the particles with an increased bias to one direction.

In this project, we attempt to experimentally reproduce this theoretical framework which would cause a reversal in migration direction when the gap distance is varied. Cells are seeded on substrates – micro-patterned with asymmetric structures (triangles) of fibronectin, and passivation elsewhere. The asymmetric fibronectin structures are periodically separated by a gap distance. Cells can move in either direction. This creates a one-dimensional system, formally equivalent to the particle/potential system described before. The selection of direction is influenced by the fluctuations in protrusions and the gap distance between fibronectin triangles. In this scenario, by changing the gap distances between the fibronectin triangles in different experiments, we aim at finding the critical gap distance that would trigger a reversal in the direction of migration.

We chose a distribution of gap distances (13 μm, 16 μm, 19 μm, 22 μm, 45 μm) around the mean protrusion length (20.5 μm) of the cells under study. The current results show a bias in migration towards the direction of triangle funneling edge, in all these gap distances – resulting in *ratchetaxis*. In addition, we found that negative gap distances / overlapping triangles with 25% overlap also exhibited ratchetaxis. In order to find the exact reversal point, we modified the mesoscopic model from our previous work to include gap distance – by simple scaling arguments, which predicted direction reversal at 50% overlap. Currently, we are performing experiments on this 50% overlap condition to confirm the model prediction. Using this mesoscopic model, we show that predominant ratchetaxis behavior in all conditions is due to availability of larger attachment area for those efficient protrusions emerging from the triangle funneling edge. In support of this claim, experiments on 75% overlap condition (where the availability of attachment area for efficient protrusions is similar on both directions) showed no net bias in the migration direction. Our near future experiments on 50% overlap will probe the model prediction on direction reversal.

Conclusion: This project probes the mechanism of directional migration through efficient protrusion and ratchetaxis. In addition, the study highlights the importance of understanding the substrate cues responsible for direction reversal, which, in a typical pathological condition might lead to directed migration of cancerous cells towards specifically targeted organs.

Contribution: Project supervision and idea – Daniel Riveline (ISIS/IGBMC, Strasbourg), Experiments and analysis – Raghavan Thiagarajan (ISIS/IGBMC, Strasbourg), Cedric Fuchs (Faculté de médecine de Strasbourg - DFGSM2) and Simon Lo Vecchio (Cell Physics Master II programme). Conceived the model: Raphaël Voituriez (UPMC, Paris), Expanded the model to gap distance: Simon Lo Vecchio.

4. Spontaneous pulsatile domains in epithelial monolayer

Introduction: Collective dynamics of cells are important for morphogenesis in development [Solon et al., 2009, Cell; Kruse and Riveline, 2011, CTDB]. These dynamics result from the cytoskeleton which is capable of generating stress through the acto-myosin contractility [Martin et al., 2009, Nature]. The coordination between the cytoskeletal elements of several cells manifests as a collective effect that spans hundreds of micrometers [Angelini et al., 2010, Phys Rev Lett.; Deforet et al., 2014, Nat. Commun.]. While the cytoskeleton is known to be the source, the mechanism and factors responsible for setting length and time scales are not known. In this project, we report a

new collective effect in MDCK monolayer: spontaneously emerging pulsations, and explain these pulsations as determinants involved in setting length- and time- scales of tissues.

Results: MDCK cells when grown to confluency, exhibited randomly occurring spontaneous collective pulsations involving several cells. We characterized these pulsations by computing divergence of the velocity field which showed cycles of contraction and extensions. By plotting the correlation function of divergence, we found that pulsations had a characteristic correlation length of ~ 230 μm with a typical period of ~ 7 h. The emergence of these characteristic length- and time- scales in the monolayer, motivated to further investigate the responsible factors and the mechanisms. As a first step, we checked the role of cell-substrate interaction in setting the underlying length scales of pulsations.

Substrate interaction/Friction: Interactions of the monolayer with the substrate can be increased by coating the substrate with extracellular matrix proteins like fibronectin. The resulting increase in interaction can be deduced by the decrease in cells velocities in the monolayer. With this approach, we compared the collective velocities of cells in the monolayer between the normal condition and the substrate homogeneously coated with fibronectin (FN). As expected, the collective velocities of the monolayer was decreased on the homogeneous FN substrate, compared to control conditions. This confirmed the role of substrate interaction/friction in the collective dynamics of monolayer.

In addition, to check the effects of friction specifically on pulsation characteristics, we designed a substrate where regions of FN and non-FN co-existed through micro-contact printing – *FN Grids*. To maximize the effect of spatial regulation, the size of the grids were designed to match the size of pulsations. On these substrates, pulsations were present in most of the grids, indicating the influence of friction in spatial organization. This effect was further amplified, when the non-FN regions were coated with a passivating agent (PEG). The introduction of passivation increased the ratio of – magnitude of substrate interaction between the FN and non-FN regions and changed pulsations length- and time- scales. These results support the key influence of substrate friction in spatially regulating the pulsation characteristics.

Theoretical model: Following these results, we wanted to understand the emergence of characteristic length scales in control condition. We took a theoretical hydrodynamic approach; a pulsating system of cells can be described by coupling the contractility and cell-substrate interaction with the corresponding changes in cell area. In this framework, pulsations would spontaneously arise due to the inherent contractility of the system

whose changes are coupled by a feedback through variation in cells height. We found that the correlation spectra of this theoretical model exhibited characteristics similar to the pulsations observed in our monolayer. In addition, we validated the findings of the model by confirming the variations in height of the monolayer during pulsations. The expression for the characteristic length scale confirmed the involvement of substrate friction and contractility. Inspired by the theory, we next wanted to experimentally confirm the role of contractility.

Contractility: The effect of contractility is generated and transduced across the monolayer through the cytoskeletal activities. We used cytoskeletal inhibitor drugs to study the role of contractility in determining the pulsation characteristics.

The inhibition of myosin through blebbistatin, arrested pulsations in the monolayer. Surprisingly, when myosin was reactivated by washing out blebbistatin, the monolayer exhibited large scale flows. We attribute the failure in recovery of pulsation length scales after wash out to the destruction of spontaneous order in the mesoscopic organization of myosin that might have existed before the addition of drug. The effect was identical on administering the actin inhibitor Latrunculin A. These results confirm the critical role of acto-myosin in setting pulsation characteristics.

The experimental results on substrate friction, height variations and cytoskeletal contractility were in agreement with the model in their role on setting length scale of pulsations.

Conclusion: In this project, we utilize a specific collective effect observed in MDCK monolayers to study how length- and time- scales are organized spontaneously. Using a continuum model, we identify the factors leading to pulsations and experimentally confirm the same. With further analysis and interpretation of these factors, we will be able to decipher the involved mechanisms, and establish a paradigm for describing the spontaneous emergence of length and time scales in collective systems.

Contributions: Project supervision and idea: Daniel Riveline (ISIS/IGBMC, Strasbourg); Experiments – Raghavan Thiagarajan (ISIS/IGBMC, Strasbourg); Conceived the theory – Guillaume Salbreux (The Francis Crick institute, London); Theoretical modeling and development – Mandar M. Inamdar (IIT Bombay, Mumbai).

In summary, my PhD work aims at understanding collective phenomena in biological systems across a range of mesoscopic scales.

List of movies and legends

Movie 4.1. Four rings in focus. Several fission yeast cells imaged simultaneously. Rings are visualized by myosin (Rlc1-mCherry) labelling. Time in hh:mm:ss. Temperature 18 °C.

Movie 4.2. Cytokinetic ring constriction of mammalian (HeLa) cell. Full constriction of mammalian cytokinetic ring in both actin (Lifeact-mCherry) and myosin (MHC-GFP). Time in mm:ss.

Movie 4.3. Cytokinetic ring constriction of fission yeast cell. Full constriction of fission yeast cytokinetic ring in both actin (CHD-GFP) and myosin (Rlc1-mCherry). Actin and myosin clusters are visible. Time in mm:ss. Temperature 27 °C.

Movie 4.4. Cluster and arm buckling in fission yeast. Myosin (RLC1-mCherry) cluster present at the point of attachment of the ring. The arm buckles on reaching cell periphery. Time in mm:ss. Temperature 27 °C.

Movie 4.5. Arm buckling in fission yeast cell. Two arms (Myosin, RLC1-mCherry) buckling on reaching cell periphery. Time in mm:ss. Temperature 27 °C.

Movie 4.6. Arm rotations in the cytokinetic ring of fission yeast. Myosin (Rlc1-mCherry) arms emerging from the ring of two different fission yeast cells, rotate in clockwise (CW) and counter-clockwise (CCW) directions. Time in mm:ss. Temperature 27 °C.

Movie 4.7. Rotating clusters in the cytokinetic ring of fission yeast. Clusters in actin (CHD-GFP) and myosin (Rlc1-mCherry) of different cells. Time in mm:ss. Temperature 27 °C.

Movie 4.8. Cluster rotation in CPS1 mutant fission yeast. Myosin (Rlc1-mCherry) cluster rotation after inhibiting cell wall synthesis. Time in mm:ss. Temperature 36 °C.

Movie 4.9. Cytokinetic ring formation from clusters in fission yeast. Myosin (Rlc1-mCherry) clusters rotate and eventually lead to formation of the cytokinetic ring. Time in mm:ss. Temperature 27 °C.

Movie 4.10. Cytokinetic ring formation of mammalian (HeLa) cell. Formation phase of the mammalian cytokinetic ring followed by constriction in both actin (Lifeact-mCherry) and myosin (MHC-GFP). Overlay of 5 z-planes, Time in mm:ss.

Movie 4.11. Constriction after blebbistatin washout in mammalian (HeLa) cell. Myosin pattern of mammalian ring in constriction phase is rescued after blebbistatin is washed out. The ring proceeds to constrict. The ring is visualized by myosin (MHC-GFP) labelling. Overlay of 5 z-planes, Time in mm:ss.

Movie 4.12. Latrunculin A (10μM) treated fission yeast rings. Motion of actin clusters (CHD-GFP) is still visible, while myosin (Rlc1-tdTomato) clusters are still. Time in mm:ss. Temperature 27 °C.

Movie 4.13. Ablation in fission yeast. Ablation of fission yeast (large) ring (CHD-GFP) followed by healing. Time in s. Temperature 27 °C.

Movie 4.14. Ablation in fission yeast. Ablation of fission yeast (small) ring (CHD-GFP) followed by healing. Time in s. Temperature 27 °C.

Movie 4.15. Local fluctuations of detached parts of the cytokinetic ring in fission yeast. A portion of the ring is spontaneously detached and severed (see arrowhead): the two new free ends fluctuate while constriction proceeds elsewhere. Myosin is visualized with Rlc1-mCherry. Time in mm:ss. Temperature 36 °C.

Movie 4.16. Healing of defects observed during cytokinetic ring constriction in fission yeast. Filaments of myosin (bound to actin) detach from the ring, followed by reintegration into the ring. Myosin is visualized with Rlc1-mCherry. Time in mm:ss. Temperature 36 °C.

Movie 5.1. Growth of lamellipodia promoted by C_7N_6 MPA in a NIH3T3 cell transfected with actin-GFP. Time in mm:ss, scale bar 5 μm.

Movie 5.2. Closure of the cytokinetic ring in fission yeast visualized with Rlc1-tdTomato. Comparison between control (left), and in the presence of C_7N_6 MPA (right). The frames were equalized in their contrast. Time in mm:ss, scale bar 2 μm.

Movie 6.1. NIH3T3 cell moving on fibronectin ratchets separated by a gap distance of 19 μm. The cell exhibits an unbiased motion without any rectification throughout the experimental time. Time in hh:mm.

Movie 6.2. NIH3T3 cells moving on overlapped fibronectin triangles (25 % overlap /'–53 μm overlap') - top panel; and on triangles separated by a gap distance of 19 μm - bottom panel. The cells exhibit ratchetaxis, i.e. cell migration direction is rectified in the direction of funneling edge of triangle. Time in hh:mm.

Movie 6.3. NIH3T3 cell moving on fibronectin ratchets separated by a gap distance of 45 μm. The cell moves one step in the funneling edge direction in 48 h. Time in hh:mm.

Movie 7.1. An isolated domain of pulsating cells from the MDCK monolayer. Time in hh:mm.

Movie 7.2. Waves of higher velocities propagating through the monolayer- an example of collective effect. Time in hh:mm.

Movie 7.3. An isolated pulsatile domain with the center focused 'between' the FN lines. The condition corresponds to FN line (W-60 μm + G-150 μm). Time in hh:mm.

Movie 7.4. An isolated pulsatile domain with the center focused 'on' the FN line. The condition corresponds to FN line (W-60 μm + G-150 μm). Time in hh:mm.

Movie 7.5. Cells on FN grid (W-120 μm + G-75 μm) without PEG. The cells on this grid condition do not exhibit pulsations. Time in hh:mm.

Movie 7.6. Cells on FN grid (W-120 μm + G-150 μm) without PEG. Movie shows several cycles of pulsations on this grid. Time in hh:mm.

Movie 7.7. Cells on FN grid (W-120 μm + G-300 μm) without PEG. Movie shows pulsation of cells on this grid. Time in hh:mm.

Movie 7.8. Cells on FN grid (W-120 μm + G-150 μm) with PEG. The white square shows the PEG region. The region outside the white boundary corresponds to FN region. The overlay of FN grid is not shown since the PEG region already distinguishable. Cells in the PEG region exhibit random behavior with higher velocities. Time in hh:mm.

Movie 7.9. Movie showing fluctuations in cell height during the extension and contraction phases. The top panel shows cells (labelled with E-cadherin-GFP) on FN grid (W-120 μm + G-150 μm) with PEG. Left and right sides of the top panel correspond to z-section at 5 μm and 10 μm respectively. Bottom panel shows the 3D view of full z-stack corresponding to the images in the top panel. The height of cells is color coded as indicated by the calibration bar. Time in hh:mm.

Movie 7.10. Movie showing a region of monolayer treated with blebbistatin [100 μM]. The movie shows pulsation before the addition of drug, followed by blebbistatin addition and pulsation arrest and finally flows after wash out of blebbistatin. The last two column of time corresponds to hours and minutes. The first column is incremented to '1' when 60 h is complete.

Movie 7.11. Movie showing a region of monolayer treated with Lat A [1 μM]. The movie shows pulsation before the addition of drug, followed by Lat A addition and pulsation arrest, and finally flows after wash out of Lat A. The last two column of time corresponds to hours and minutes. The first column is incremented to '1' when 60 h is complete.

Movie 7.12. Movie showing a region of monolayer treated with Y-27632 [50 μM]. The movie shows pulsation before the addition of drug, followed by Y-27632 addition and pulsation arrest, and finally flows after wash out of Y-27632. The last two column of time corresponds to hours and minutes. The first column is incremented to '1' when 60 h is complete.

Movie 7.13. Movie showing a region of monolayer treated with mitomycin C [32 μM]. The movie shows a cycle of extension and contraction during incubation with mitomycin C. Time in hh:mm.

Movie 7.14. Movie showing the formation of monolayer in serum free condition and the subsequent pulsations. Time in hh:mm.

Movie 7.15. Movie showing directional flow of cells (indicated by PIV arrows in green) on substrate with fibronectin triangles. The fibronectin triangles are in red. The Time in hh:mm. See appendix section 10.2.2.

Movie 7.16. Movie showing the formation of monolayer on a substrate patterned with fibronectin triangles and rest of the region passivated with PEG. Time in hh:mm. See appendix section 10.2.2.

Movie 7.17. Movie showing a region with pulsatile domain on a substrate patterned with fibronectin triangles and rest of the region passivated with PEG. Time in hh:mm. See appendix section 10.2.2.

Table of Contents

Collective effects at different scales

1 nm – 10 µm | **10 µm – 100 µm** | **100 µm – 1 mm**

Acto-myosin

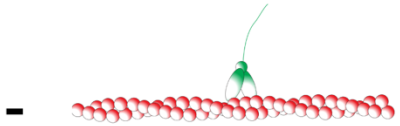

Sarcomere

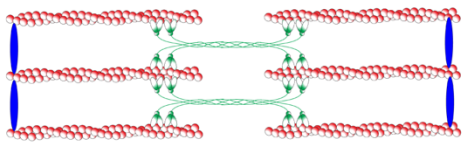

Ensemble

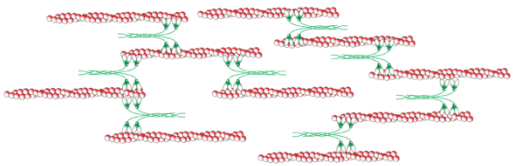

Single cell

Stress fibers

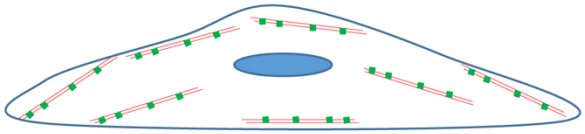

Cortex

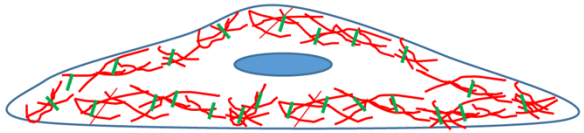

Tissue

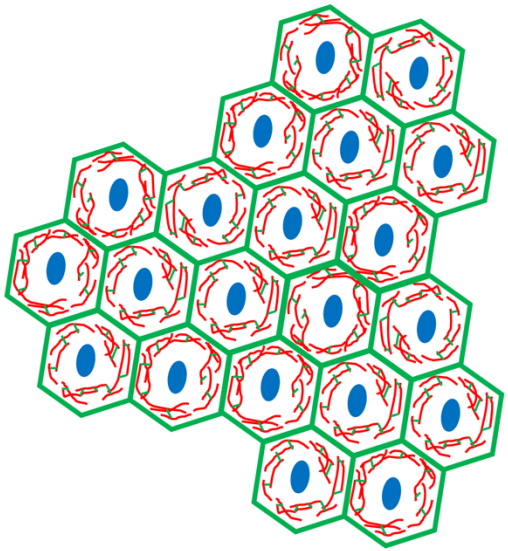

1. PhD motivation: Collective effects at different scales

Any system can be described as an ensemble of individual units, where the arrangement of these units give rise to a systemic pattern, or function of each individual unit together gives rise to a system level function. Often in this scenario, our knowledge of these individual units provides little information for the understanding of a system level behavior. To appreciate this, let us take an example – acto-myosin, as shown in the scheme. We know that actin and myosin are the cytoskeletal components that play a critical role in the architecture and several processes of the cell. The current advancement in the fields of biology, theoretical physics and structural biology gives a good understanding of the interaction between actin and myosin, although not complete. We know that actin is a biopolymer with well-defined polarity. This polarity combined with other factors (local asymmetries / structure) allows myosin to interact in a specific manner: directed movement (in the presence of ATP). This is an easy explanation of the interaction between an actin filament and a myosin motor. However, this is not the case *in vivo*, where thousands or tens-of-thousands of acto-myosin molecules work in ensemble for a particular function. So, let us take a basic functional unit of acto-myosin ensemble – sarcomere. In a sarcomere, the actin filaments are arranged in a defined manner (in terms of polarity) with myosin motors in-between the filaments. In this case, we can extrapolate our understanding of a single acto-myosin interaction and claim that movement of actin filaments towards each other leads to contraction, and away from each other leads to extension. However, if we take a scenario where ensemble of actin filaments are arranged (in terms of polarity) in a random manner with myosin motors in-between (cytokinetic ring for example), it is not intuitive to say what kind of movement leads to contraction and extension. This complexity in understanding increases as we move across scales from nanometers to hundreds of micrometers.

Scheme – Collective effects at different scales: The scheme represents increase in organizational and functional complexity across a range of scales from nanometer to micrometers, with respect to actin and myosin. The first column in 1 nm – 10 μm range highlights single acto-myosin interaction, interaction in sarcomere with defined order (in terms of polarity), and a randomly oriented ensemble of acto-myosin filaments. The second column in 10 μm – 100 μm range highlights acto-myosin organization at the single cell level with examples of stress fibers and cortex. The last column in 100 μm – 1 mm range highlights the acto-myosin organization in a tissue.

In our description above and as shown in the scheme, we moved from interactions at nanometer scale (single acto-myosin) to interactions at tens of micrometer scale (randomly oriented acto-myosin bundle). Now if we go further in scales from single cell level (10 μm to 100 μm) to tissue level (100 μm to 1 mm), the complexity of acto-myosin interaction increases. For example, single cell migration and division to collective migration of cells. In these cases, our understanding of single acto-myosin interaction cannot immediately explain the mechanism of many acto-myosin interactions at this scale in these processes.

In order to understand this 'one to many' transition, we need to find generic interaction rules that can give the averaged effect of collections of acto-myosin or collections of any individual units. This PhD thesis aims at understanding this collective effects at different scales: from collection of acto-myosin (cytokinetic rings) to collection of cells (epithelial monolayer).

We study two main topics on cytokinetic ring and epithelial monolayer, to understand how interactions of randomly oriented actin filaments (through myosin) lead to constriction of cytokinetic ring, and how collection of cells in an epithelial monolayer display a pulsating phenomenon (collective contraction and extension). We address these questions in two different systems: fission yeast and HeLa cells for cytokinetic ring constriction and MDCK monolayer for collective pulsations. Using experiments and theory, we give generic interaction rules, going from nanometer-scale interactions to micrometer-scale interaction during cytokinetic ring constriction, and try to identify those factors that lead to correlated dynamics across several cells in epithelial monolayers.

In addition to these main topics, we also study two other topics that focus on the effect of a new compound on actin polymerization during cytokinetic ring constriction and on directing single cell migration using adhesive ratchets.

1.1 Thesis plan

This thesis is separated into six sections. Each section starts with a summary of the contents highlighting the major points and the organization of the section before going into details. The figures, movies and equations are numbered based on the numbering of the corresponding sections. The thesis starts with a general introduction section where a broad overview of collective effects and cytoskeleton are given. Owing to the well-established literature on the specific topics addressed in this thesis (cytokinetic ring constriction, single cell migration and MDCK monolayer), we restrict to brief introduction in the corresponding chapters, without giving explicit details on the topics themselves in the introduction section. Next, we explain in detail all the materials and protocols used in this thesis in the following section. After this, four separate sections discuss in detail the results obtained in those individual topics. This is followed by a short concluding note and appendix that gives additional details on results and analysis (from results section) and details on products and abbreviations. Finally, the thesis ends with published copies of articles that are discussed in more detail in the results sections.

2. Introduction

In this chapter, I will briefly explain the phenomena of collective behavior. I will start with a general introduction on collective behavior followed by different studies that explain the phenomena. First, I will establish the principles of Vicsek based models with examples at different scales. Then I will explain the differences in collective behavior on changing scales from macroscopic to mesoscopic levels. Following this, I will indicate the need for hydrodynamic description, specifically for acto-myosin systems and explain the active gel theory. Having given an introduction on collective behavior, I will then briefly explain the components of cytoskeleton and sub-cellular structures made of acto-myosin assembly, since dynamics of acto-myosin networks is one of the main focus of this thesis.

2.1 Collective behavior

Collective behavior is a phenomenon where a group of individual units give rise to an ordered motion with specific pattern (1). Colony of ants (Fig. 2.1 a), school of fish (Fig. 2.1 b), flock of birds (Fig. 2.1 c) and pack of animals (Fig. 2.1 d) are some common observations, where individual entities present themselves in a group or community (2). In addition to living systems, inanimate matter (rods and disks) can also be driven into self-propelled state by supplying external energy (on vibrating tables), to exhibit collective behavior (3, 4).

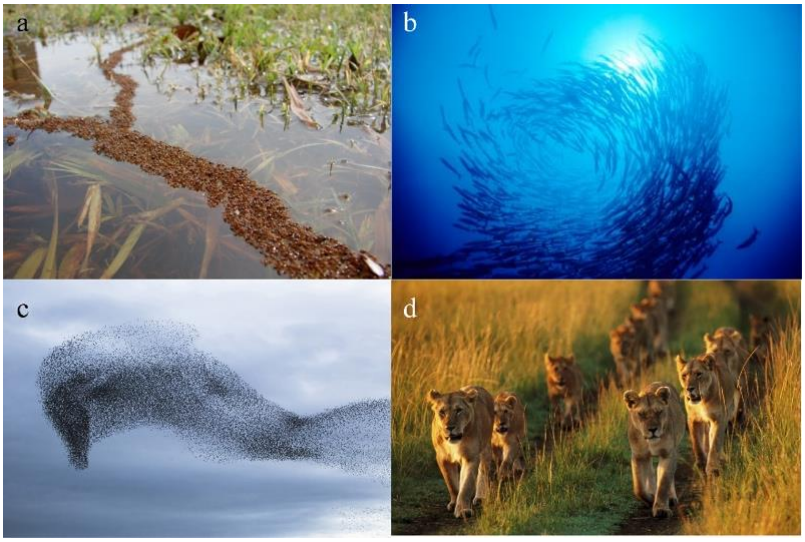

Figure 2.1. A gallery of images showing collective behavior. (a) Two trails of fire ants merging to form a bridge on the water. (b) School of fishes showing a vortex pattern. (c) Flock of starling birds displaying a specific flight pattern. (d) Pride of lions marching in an ordered fashion. Images were obtained online.

These emergent system level behaviors are a result of self-organization process. Where, self-organization results from the adaption in behavior of individual units through local interactions, to exhibit a global pattern. The striking feature of emergent collective behavior is the coherence and synchrony within these groups that is spontaneously emerging due to these local interactions (5). For example, in a flock of birds, each bird follows / stays close to another bird with similar direction and speed. This trend of dependency of each bird on its neighbor, spans the whole group and manifests as a global behavior of the flock. Any changes in this dependency between the individual birds is reflected in the group behavior (change of flocking pattern). This dependency / interaction with neighbor can arise on a simple basis like attraction / repulsion, or in a more complex manner like combination of attraction and repulsion (collisions) (6).

Thus, collective systems can be defined as a group of several entities that undergo interactions with each other based on specific rules in a decentralized manner. The resulting collective behavior depends on the constant feedback within the individual units, and can be several orders of magnitude larger than the individual unit itself. This behavior is different from how the individual units behave when they are not in a group. In this scenario, "how the behavior changes on transition from 'one to many'?", "how the local interactions are translated into collective behavior?" and "if there is a generic principle that underlies the collective behavior of all systems?" are interesting questions addressed in this field. In the following sections, I will give brief descriptions of studies on collective behavior along this line.

2.1.1 Non-equilibrium nature of collective behavior

The action of individual units in a group maintains a constant flux of energy. For example, the flock of birds can be treated as a system of individual units where the change in flocking pattern corresponds to a phase transition in the system (5). The phase transition is triggered by constant dissipation of energy by individual units. This maintains collective behaviors away from equilibrium states – where there is no net flow of energy. Thus systems exhibiting collective behavior are made of active materials in a non-equilibrium state (5). The principles leading to an ordered phase transition or collective behavior from these individual units of active matter is not clear yet.

In the past, several studies using theoretical and experimental approaches have been published to understand the emerging properties of collective behavior (5–7). In the following paragraphs, I will give a brief overview of these studies on collective behavior in general, and then studies specific to *active gels* (acto-myosin and cells for example).

2.2 Flocking models

The simplest of models that describe collective motion are based on the ordering of individual units within the group (5, 8). To understand this, let us go back to our example of bird flock in our previous paragraphs, and ask the question: how a disorderedly moving group of birds can transform to exhibit a coherent behavior?

2.2.1 Grouping from alignment tendency

First of all, the motion of birds depends on visual perception and does not depend on the surrounding medium. Hence we can assume the system to have an inert medium. In this case, the group behavior depends mainly on the speed (magnitude) and direction (vector) of the birds. The disorder within the group is due to the difference in speed and direction. Now, if the birds start to move with an average speed, and the variation in direction between the birds start to decrease – for example the variation is within a tolerance limit 'η', then order starts to emerge within the group. The direction of each bird will be updated to keep up with the average direction of the group at each instant of time. As the difference in speed and 'η' (direction) starts to decrease across the group, the coherence across the group increases leading to a synchronized flocking behavior (8). For example, the direction given by the angle θ_i of birds moving with a fixed velocity in the group is given by:

$$\theta_i^{t+1} = arg\left[\sum_{j\sim i} \vec{v}_j^t\right] + \eta\xi_i^t \qquad (2.1)$$

where t denotes time, i and j represent the particles with current and previous directions respectively, $\vec{v}_i^t$ is the velocity vector of magnitude v_0 along direction θ_i, and ξ_i^t is the noise representing perturbations where η is the noise strength (6). This is a very simple way to achieve a well-defined phase transition from a disordered group to a coherent flock. This model proposed by Vicsek et al. (8), is commonly referred as the "Vicsek model" and has been further developed and used to describe systems with self-propelled particles (5).

2.2.2 Interaction between individual units of the group

While this model gives a simple way to generate order during collective motion, it does not describe the nature of interaction between the individual units / birds in the flock. This model was further improved by Gregoire et al. (9). They showed the dependency of coherence on the number density of the group similar to Vicsek et al. In addition, they introduce a two-body short range interaction force that defines the cohesion between the units / birds of the group, in addition to the alignment tendency. In this scenario, the direction given by the angle θ_i is given by:

$$\theta_i^{t+1} = arg\left[\alpha \sum_{j\sim i} \vec{v}_j^t + \beta \sum_{j\sim i} \vec{f}_{ij}^t\right] + \eta\xi_i^t \qquad (2.2)$$

The expression (2.2) is similar to (2.1) except for the inclusion of interactive forces of amplitude $\vec{f}_{ij}^t$. Here α and β represent the strength of alignment and cohesion. The introduction of these interactive forces, gives another parameter that improves the model precision in understanding the collective behavior.

2.2.3 Interaction with the surrounding medium

The models described above define the emergence of collective behavior in systems without the influence of surrounding medium. Along this line, Szabo et al. (10) experimentally demonstrated ordered phase transition in a group of keratocytes when they reached a critical density. The cells were adhered to a substrate and are capable of reorienting themselves. Based on this observation, they modified the Vicsek model to describe the cohesive movements of adhesive cells. In this model, only the interactive forces between the cells (as used in expression (2.2)) are shown to play a role in the emergence of coherent groups of cells. Instead of using a general alignment tendency with respect to the group (as used in expression (2.1) and (2.2)), the direction of each cell is influenced by the net force acting on the cell, due to the interaction with the substrate and with the neighbor. The motion of cell i under this circumstance will be given by:

$$\frac{d\vec{r}_i(t)}{dt} = v_0\vec{n}(t) + \mu \sum_{j=1}^{N} \vec{F}(\vec{r}_i, \vec{r}_j) \qquad (2.3)$$

where, $\vec{r_i}(t)$ is the position of the cell at that instant of time, v_0 is the velocity of cell with mobility μ, in the direction of the unit vector $\vec{n}(t)$ and $\vec{F}(\vec{r_i}, \vec{r_j})$ is the intercellular force between cells i and j that contributes to motion in addition to v_0.

These models are some examples of vastly available variants of flocking models (5). They describe the transition to an ordered phase by reducing noise strength (deviation in alignment) (9), or by increase in density of the system (10). Hence in general, flocking models can be applied over a range of scales from flock of birds to group of cells. While they give an explanation in-principle for emergence of collective behavior, they do not exactly reflect the global properties of the system.

2.3 Global properties of collective behaviors

In general, the global properties of active matter exhibiting collective behavior can be different based on the system (11). For example, flocking phenomena is observed in group of birds (2) and group of keratocytes (10), whereas contractile stresses are observed in sub-cellular cytoskeleton and cells (12, 13). The differences in these global properties arise due to the differences in specific dynamics arising from the interaction between individual units: flocking due to alignment tendency in birds and keratocytes; and contractile stresses in cytoskeleton and cells, due to polarity based interaction and changes in protein conformations depending on ATP binding. It is also important to take into account these global properties (flocking; contractile stresses) while explaining the collective behavior. At the same time, we need to realize that the interaction between units is different as we move from macroscopic to mesoscopic scales (14). In the following sections, I will first briefly describe how the interactions at the mesoscopic scale are different (mainly acto-myosin based), followed by explanations on active gel theory and other hydrodynamic approaches for describing collective effect at these scales.

2.4 Collective behavior at the mesoscopic scale

The type of interaction during the collective behavior between the units of active system depends on the scale of system. For example, organisms like birds use visual and acoustic perceptions for collective motion. But, entities like bacterial suspension (15), acto-myosin gels (16) and group of cells can interact only through the surrounding medium or by mechanical contact, for maintaining coherence in a group (5). At this scale, the system is in low Reynolds number regime ($Re = \rho a v/\eta$; $inertial\ forces/viscous\ forces$),

where the viscous forces dominate and the inertial forces are negligible (17). Here, ρ and η are the density and viscosity of the fluid, and a and v are the size and velocity of the particle respectively.

2.4.1 Need for hydrodynamic description

For example, in the case of acto-myosin interaction, surrounding medium influences the interactions between the units (actin and myosin). Given this situation, if one has to understand the specific task performed by a collection of actin and myosin motors, the surrounding medium cannot be neglected. Hence in order to model the collective behavior of such a system, one has to use hydrodynamic descriptions.

In this context, Toner and Tu proposed the hydrodynamic equations for macroscopic scales (18) (taking into account velocity and particle density in the system), assuming an inert medium based on the Vicsek model (8). This was further improved by Simha et al. (19) and Hatwalne et al. (20), for self-propelled particles suspended in a medium (taking into account the interactions with the medium – total momentum conservation). These descriptions gave a generalized formulation for active particles interacting with the surrounding medium, but without considering the source required for non-equilibrium transition (11, 21). For example, in the case of actin and myosin networks, the system is driven out of equilibrium by the consumption of Adenosine TriPhosphate (ATP) from the surrounding. The inclusion of source (ATP) that drives the system out-of-equilibrium assures the existence of non-equilibrium state whose emerging global properties (while functioning as collections) can be obtained. These works performed by Kruse et al. (22, 23), lead to the conception of *active gel theory* that specifically explain the collective behavior of acto-myosin systems.

2.4.2 Active gel theory

Actin filaments and myosin motors are the major constituents of actin cytoskeleton (24). Actin filament is a polar structure with defined '+' and '–' ends, where monomeric units are added to one end and removed from another end. These processes at the filament ends occur by the hydrolysis of ATP (~ $10K_BT$; K_B-Boltzmann constant and T-Temperature), thereby controlling the polymerization and depolymerization of actin filaments. The polarity of actin filaments allows the myosin motors to move in a directional manner (for example, MyosinII moves towards the '+' end). The directional movement is facilitated

by the hydrolysis of ATP which otherwise remains bound to actin filament without any activity. Thus ATP hydrolysis triggers activity of actin and myosin. The resulting interaction leads to the formation of acto-myosin network which are dynamic in nature and can lead to various structures like cortex, stress fibers, cytokinetic ring etc. This property of acto-myosin network to self-organize earned the name "active gel or acto-myosin gel" (Fig. 2.2).

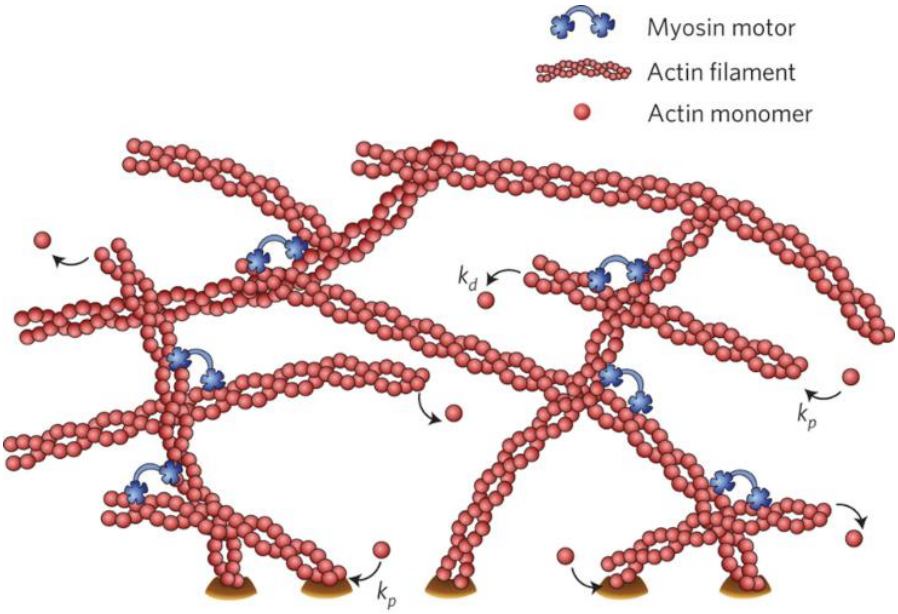

Figure 2.2. Schematic of active gel. Adapted from Prost et al (21). The schematic shows actin filaments assembled from monomeric actin. Myosin motors cross-link the actin filaments. Polymerization and depolymerization processes of the filaments are indicated by k_p and k_d respectively.

The dynamic nature of acto-myosin gel leads to temporary and permanent cross links. This allows the gel to behave like an elastic material at short timescales (<< 100 s) and as a viscous material at longer timescales (100 s – 1000 s) (25). The elastic modulus of the gel is in the range of 10^3 – 10^4 Pa (25), with a characteristic viscoelastic relaxation time 'τ'. In this case, Maxwell relation describes the viscosity (η) of the active gel as a function of elastic modulus (E) and viscoelastic relaxation time: $\eta = E\tau$ (26). Based on these material properties, the behavior of acto-myosin gel at larger length and timescales was obtained using hydrodynamic theory by Kruse et al. (22, 23). In general, the stress generated by a simple fluid can be given by: $\sigma = 2\eta\mu$, where σ and μ are the stress and velocity gradients obtained as derivatives of velocity. However, the stress generated in acto-myosin also depends on the polarity of actin filaments. The rate of change of polarization of filaments can be introduced as orientational field 'h', and the corresponding coefficient ν obtained from the linear hydrodynamic theory and symmetry

arguments. In addition, in the case of acto-myosin gel, the dynamics (actin poly/depolymerization and myosin interaction) are triggered by ATP hydrolysis. Hence one can introduce this energy (ATP) consumption as the difference between hydrolyzed (ADP) and non-hydrolyzed (ATP) states: $\Delta\mu = \mu_{ATP} - \mu_{ADP} - \mu_{P_i}$, where $\Delta\mu$ is the driving force (ATP) that increases with the ATP concentration and decreases with the ADP and P_i (inorganic phosphate) concentration. Thus the obtained hydrodynamic description of active gel behavior will be given by:

$$\sigma = 2\eta\mu + \nu h - \zeta\Delta\mu \qquad (2.4)$$

where the active stress 'σ' is proportional to '$\Delta\mu$' and ζ is the activity coefficient, corresponding to material property of active gel.

2.4.3 Coarse-graining of microscopic equations

The above described models reflect the macroscopic characteristics of the system, without considering the microscopic level interactions of individual units. The microscopic interactions can be included by writing equations describing the interaction of individual actin filament and myosin motors. The obtained equations can then be coarse-grained (averaged) to describe the properties at the macroscopic scale. The advantage of this method is the inclusion of microscopic description of the properties of actin and myosin in the equations. This method of describing acto-myosin gels were demonstrated by Kruse et al. (27, 28) and Liverpool et al. (29). In this PhD thesis, we use this method to understand the self-organization of acto-myosin in cytokinetic ring (section 4).

Until now, I explained various studies that explain the emergence of collective behavior in macroscopic and mesoscopic systems. This thesis will deal similar concepts of collective effects due to self-organization of actin and myosin during cytokinetic ring constriction and during the pulsation of cell collection in epithelial monolayers. In order to understand the collective effects on these systems, first I introduced the concepts of collective behavior. In the following sections, I will briefly explain the components of cytoskeleton that is essential for understanding the main conclusions of this thesis.

2.5 Cytoskeleton

The cytoskeleton is a polymeric network of proteins that forms the scaffold for mammalian cells (24). It is highly dynamic and is involved in some of the vital processes of cell like: migration (30), division (31), structure maintenance (32), organelle transport (33) and signal transduction (34, 35). Most of these processes require local stress generation by cytoskeletal proteins. In addition, the cytoskeleton acts as a mechanical feedback system, giving rise to appropriate cellular response (36). These characteristics of cytoskeleton arise from its mechanical properties which are maintained by three major polymers: actin, microtubule and intermediate filaments, and their corresponding class of motor proteins: myosin for actin, kinesin and dynein for microtubules respectively (24). The physical characteristics of these components like *persistence length* of the polymers, *duty ratio*, *processivity*, *power stroke*, velocity and directionality of the motor proteins contribute to the mechanical properties of cytoskeleton (37). The physical characteristics of motor proteins are due to their interactions with corresponding polymers. The polar nature of actin and microtubule allows directional movement of motor proteins where the polymers act as tracks. In addition, the polymerization / depolymerization process of the filaments themselves, renders them dynamic. These dynamics are achieved by the consumption of ATP which makes these dynamics an energy consuming, non-equilibrium process. The resulting activities leads to self-organization of the cytoskeletal networks corresponding to specific functions: cytokinetic ring, stress fibers, lamellipodia and filopodia (32). In order to understand these activities/functions of cytoskeleton, we need to know the individual characteristics of the respective cytoskeletal proteins. In the following sub-sections, I will briefly explain the characteristics of these proteins.

2.5.1 Actin cytoskeleton

2.5.1.1 Actin

Actin in cytoplasm exists in two forms: monomeric or globular (G) actin and polymeric or filamentous (F) actin, also called as G-actin and F-actin respectively. The F-actin is a two-stranded helical arrangement of G-actin with ~ 7 nm in diameter and a persistence length of ~ 17 μm (Fig. 2.3 a) (38). The helical arrangement (right-handed) and the difference in ends of actin filaments based on assembly and disassembly of G-actin gives polarity to the filaments. The binding of ATP to G-actin leads to a conformational change that allows binding with other G-actin or F-actin. By increased binding of G-actin, a

nucleation center is established which increases the local concentration of G-actin (Fig. 2.3 b) (24).

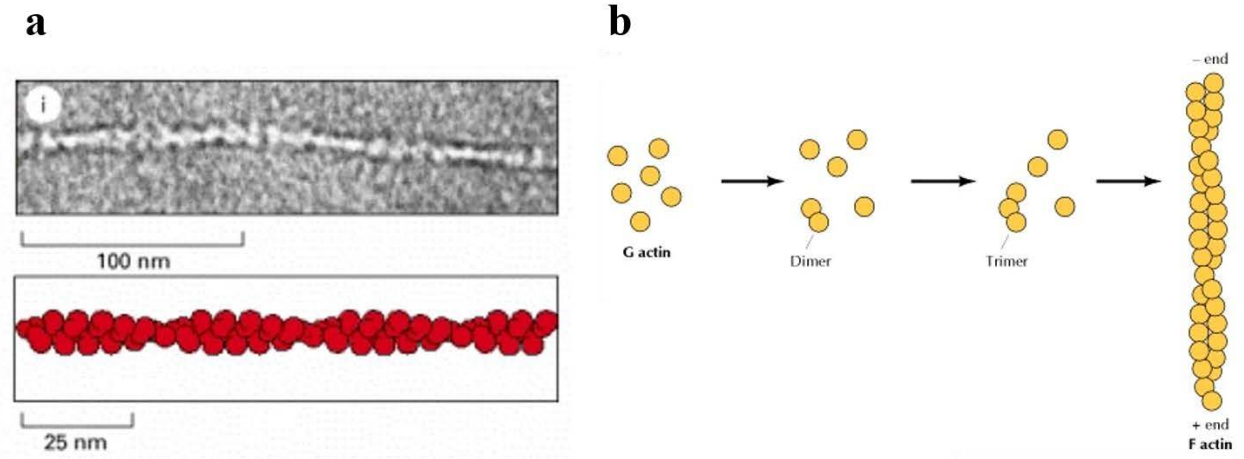

Figure 2.3. Actin filaments, adapted from (24). (a) Electron microscopic (EM) image and schematic of actin filament. (b) Nucleation of monomeric (G) actin leading to the formation of actin filament (F-actin).

The polymerization and depolymerization processes depend on the available concentration of monomeric pool of G-actin close to the filament ends. The end with a concentration of monomeric pool that is higher than the critical concentration, leads to polymerization. This end is called the 'plus'/'+'/'barbed' end. On the other hand, depolymerization occurs when a filament end is exposed to lower concentrations of (G-actin) monomeric pool. This end is called the 'minus'/'–'/'pointed' end (24). The critical concentrations of the monomeric pool at '+' and '–' ends of actin filaments are reported to be 0.1 μM and 0.6 μM, respectively (39). The asymmetry in the binding rate of G-actin to the filament ends leads to growth or disassembly of filaments. Similarly, a balanced polymerization and depolymerization rate between the ends leads to a steady-state. At this state, the filament length stays constant, while leading to momentum transfer. This process is called treadmilling.

2.5.1.2 Actin binding proteins

The formation of actin filament network requires specific growth dynamics, which are controlled by the accessory proteins. Formin and Arp2/3 are nucleators of actin filament, where formin binding to the '+' end facilitates elongation, and Arp2/3 binding leads to filament branching (40). The activation of these nucleators are controlled by factors like Wiskott - Aldrich syndrome (WASP) protein. The filament elongation is also controlled

by Cofilin (Actin Depolymerizing Factor-ADF), which on binding to '–' ends leads to depolymerization (40). On the other hand, cofilin also severs actin filaments which leads to formation of new '+' ends. Similar severing of actin filaments is also achieved by severing proteins: gelsolin and severin (41). Polymerization in these newly severed filaments (with '+' ends) is promoted by the profilin, which recycles ADP bound actin monomers with ATP bound monomers (41). This activates polymerization in the '+' ends. The filament length is also regulated by capping proteins (for example, CapZ) which on binding to filament ends prevent polymerization (41). All these proteins work in a coordinated fashion in regulating the filament length and thereby the actin filament network characteristics. The actin filaments in these networks are cross-linked and bundled by proteins like α-actinin, filamin, fascin and fimbrin (42).

2.5.1.3 Myosin – motor protein associated to actin

Myosin are motor proteins which hydrolyses ATP and convert the energy into directional motion (24). Thus myosin proteins can spontaneously introduce dynamics in actin networks. Several myosin proteins have been identified under the super-family of actin motor proteins, each with a distinct structure, function and characteristic (24, 37). The most commonly studied myosin is myosin II (MyosinII) which moves along the actin filament with a directionality towards '+' end. MyosinII is made of two heavy chains and four light chains (Fig. 2.4 a). Each heavy chain can be split into a head domain and a tail domain, where the tail domains are coiled to form a rod domain (43). The uncoiled portion of tails connecting the head of heavy chain is called the neck region. In this neck region, each heavy chain is associated to a pair of light chains: Essential Light Chain (ELC) and a Regulatory Light Chain (RLC). The phosphorylation of RLC triggers myosin activity which leads to directional motion. The portion of MyosinII including the two heads of heavy chain, four light chains and an extension of the coiled domain (for dimerization) forms the functional part (due to binding of ATP in this site). This portion is called Heavy MeroMyosin (HMM) (Fig. 2.4 a). The rest of MyosinII with coiled domains of heavy chain forms the rod domain (43). From a structural biology perspective, the directional movement of myosin on actin filament occurs in five steps (24) - the steps are explained for single headed myosin (Fig. 2.4 b):

1. The myosin is in rigor conformation: myosin head firmly bound to the actin filament.

2. Binding of ATP to myosin cleft (site at the back of myosin head) leads to slight change in conformation which reduces the affinity of actin binding site.

3. A strong conformational change leads to closing of cleft around the ATP molecule. This allows the myosin head to displace along the actin filament. At this stage, the hydrolysis of ATP is complete but the ADP and inorganic phosphate (P_i) are still bound to myosin.

4. After being displaced from the previous position, the myosin advances (~ 5 nm) towards plus end and makes a weak binding on actin filament. The binding leads to release of P_i. The release triggers a power stroke – myosin head reverts to its original conformation and makes a strong binding with actin filament leading to force generation.

5. At this stage, the myosin head is tightly locked to the actin filament in the rigor configuration. A fresh cycle starts again.

These steps allow myosin movement on actin filament (Fig. 2.4 b). Assembly of myosin filaments are processive (at any instant, one myosin head is bound to actin filament). When these assembly of myosin filaments cross-link actin filaments, the directional movement of myosin leads to stress generation.

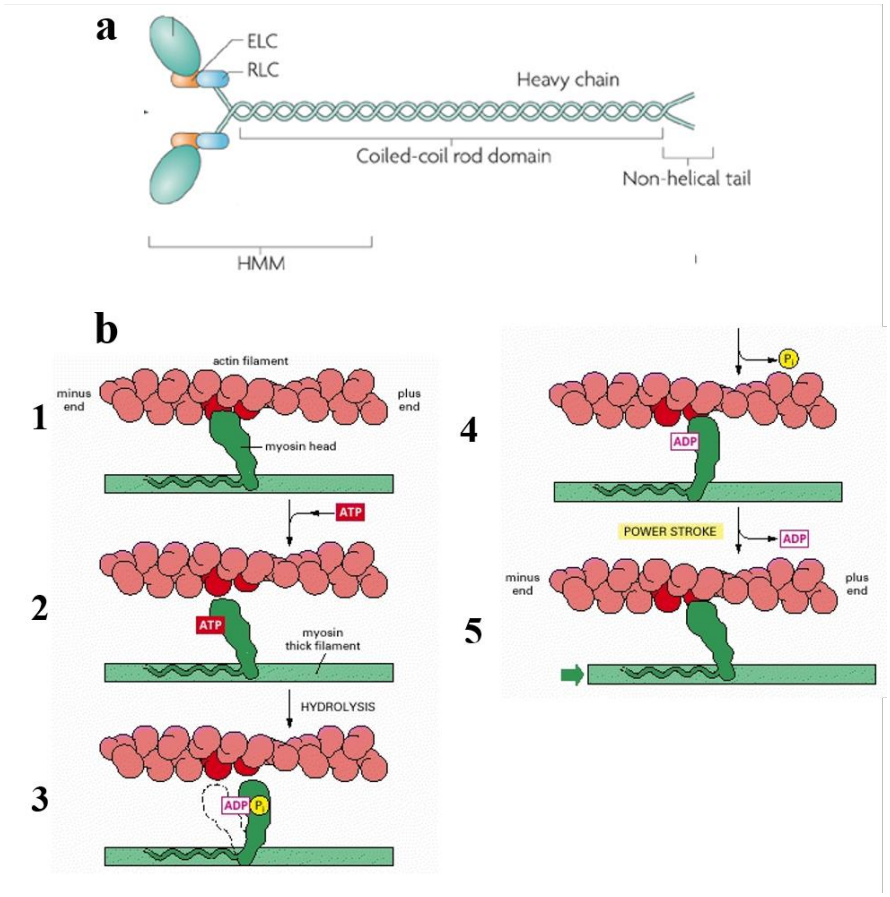

Figure 2.4. Myosin motor protein. (a) Schematic labelled for different domains of MyosinII protein. Adapted from (43). (b) Schematic showing the five steps of (single headed) myosin while walking on actin filament. The steps are explained in the text. Adapted from (24).

2.5.2 Microtubule cytoskeleton

Microtubules (MT) are hollow cylindrical structures with an outer diameter of 25 nm (24) (Fig. 2.5 a). The assembly of microtubules is different from actin – where the monomeric units directly assemble to form a helical structure. Two types of tubulin sub-units exist: α-tubulin and β-tubulin (Fig. 2.5 a). These tubulin sub-units initially polymerize to form protofilaments. Approximately 13 of these protofilaments, then assemble to form a microtubule where α- and β-tubulin are alternatively aligned. The alternative arrangement of tubulin sub-units leads to a situation where each tubulin sub-unit is present at either ends, i.e. α-tubulin at one end and β-tubulin at another end. This naturally gives rise to polarity in microtubule where β-tubulin end forms the '+' end leading to fast growth (44). The binding of tubulin sub-units is facilitated by the consumption of Guanosine Triphosphate (GTP). Similar to actin filaments, microtubules can also treadmill and transfer momentum through polymerization. As long as the GTP-bound tubulin cap is present at the end of microtubule, disassembly of filament is prevented (Fig. 2.5 b). However, when this GTP-bound tubulin cap is hydrolyzed, the filament undergoes a rapid depolymerization leading to disassembly of the filament. This event is called dynamic instability (44) (Fig. 2.5 b).

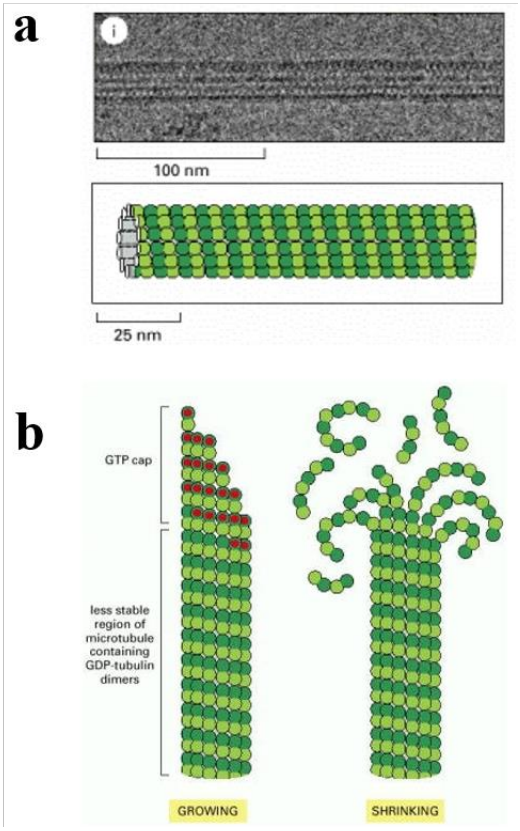

Figure 2.5. Microtubule, adapted from (24). (a) EM image and schematic of microtubule filament. The alternating light and dark green dots on microtubule represent the α- and β-tubulin sub-units. (b) Schematic of catastrophe event. The scheme shows growing microtubule filament due to the presence of GTP cap on the left, and shrinking microtubule filament due to depolymerization in the absence of GTP cap on the right.

The persistence length of microtubule can be between 100 nm to 5 mm, making them the stiffest polymer in the cytoskeletal family (24). The polarity of microtubule allows directional movement of motor proteins kinesin and dynein towards the '+' and '–' ends respectively. Microtubule along with kinesin and dynein are involved in various cellular functions, notably during polarization for (cell) migration and mitotic spindle formation for chromosome segregation (24).

2.5.3 Intermediate filaments

Intermediate filaments are polymers with an average diameter of ~ 12 nm and a persistence length < 1 μm (24). As opposed to actin filaments and microtubules, these intermediate filaments do not exhibit polarity and treadmilling. Some examples of intermediate filaments include keratin, vimentin, desmin and lamin, where lamin is a nuclear protein involved in transcriptional regulation (45).

Having given these details on cytoskeletal components, in the following sections I will explain the sub-cellular structures assembled from and associated to actin and myosin proteins.

2.6 Sub-cellular structures

2.6.1 Cortex

Cortex is a cellular structure predominantly made of actin and myosin that lies immediately below the plasma membrane with an average thickness of ~ 190 nm (Fig. 2.6 a) (46, 47). The cortex resembles a mesh like structure made of actin filaments that are mainly aligned parallel to the membrane (although parallel alignments can be found). This network is a result of nucleation and cross-linking of actin filaments (Fig. 2.6 a) by proteins like Arp2/3, formin, α-actinin, filamin and fimbrin respectively. The resulting network has a mesh size of 20- 250 nm (48). Other linker proteins of ERM family: Ezrin-radixin-moesin are also found which cross-link actin filaments with the plasma membrane (49).

The major interest in cortex lies in its mechanical properties that allows (cell) shape change during various processes. For example, cell rounding (with uniform cortical tension) during mitosis facilitates proper spindle orientation (50). Whereas cell spreading leads to gradients in contractility in the cortex that leads to retraction of cell rear and extension of protrusion, facilitating cell migration. These kind of flows and gradients within the cortex affects the cortical tension and thereby the internal hydrostatic pressure of the cell (Fig. 2.6 a and b). Through (*Atomic-Force Microscopy*) AFM and *micropipette aspiration* experiments, the cortical tension has been estimated to vary between 30 pN/μm to ~ 4000 pN/μm in different systems (46). This variation in cortical tension can be a result of protein (mainly actin) turnover in the cortex. The turnover half-time measured (from different systems) using Fluorescence Recovery and Photobleaching experiments (FRAP) is in the range of tens of seconds. And, the complete turnover of

entire cortical actin occurs in ~ 1 min (46). Hence on timescales less than this turnover time, the cortex behaves like an elastic material and on longer timescales it behaves like a viscous material. While these information help in understanding the cortex characteristics, precise information on dynamics and assembly of cortical actin network is lacking which is necessary for relating the role of cortex in different cellular functions.

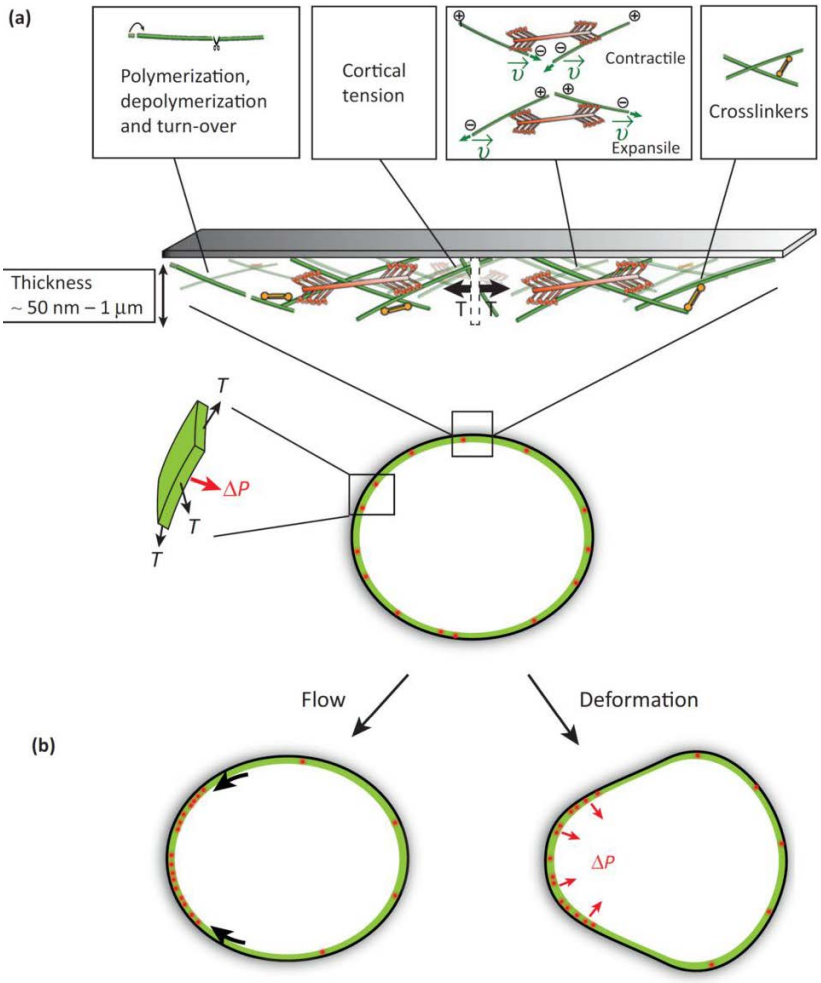

Figure 2.6. Schematic or cell cortex. Adapted from (46). (a) Schematic of cortex (zoomed in portion of the cell curvature). It shows the presence of actin filaments linked by myosin motors and cross-linkers, where polymerization and motor activity leads to dynamics (velocity) (highlighted in boxes). Force (tension-T) is exerted locally by these filament-motor networks that leads to hydrostatic pressure in the cytoplasm (zoomed in portion on the left). Cortex thickness can vary between 50 nm – 1 µm, though recent precise measurements place the average around ~ 190 µm. (b) Gradients in contractility due to acto-myosin interaction can lead to flows in the cortex (left) or lead to cell deformation that results in net displacement of the cytoplasm (right).

2.6.2 Stress fibers

Stress fibers are assembly of acto-myosin structures which are contractile in nature, similar to cytokinetic ring (51). Typically stress fibers are bundles of actin filaments cross-linked by α-actinin. The filaments are arranged in a bi-polar manner where the presence of myosin (MyosinII) leads to contractile stress. In general, stress fibers are associated to focal adhesions, although they can be differently organized.

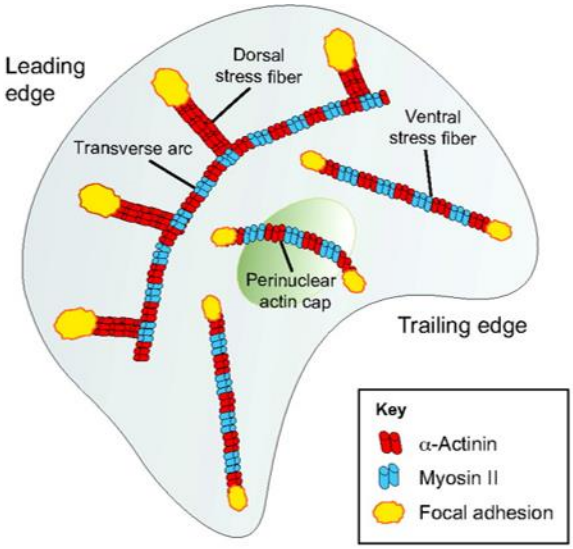

Figure 2.7. Schematic of different types of stress fibers in a migrating cell, adapted from (51). The actin bundles are represented by alternating red and blue colors indicating α-actinin and myosin respectively. Yellow color represents focal adhesion. The scheme shows all types of stress fibers described in the text: dorsal stress fibers, transverse arc, ventral stress fiber and perinuclear actin cap.

Based on the shape of stress fibers, they can be categorized into four types (Fig. 2.7) (51): (i) Dorsal stress fibers – These stress fibers are anchored to focal adhesions close to the cell periphery and generally do not contain myosin (52). Hence they cannot contract. However, these stress fibers are connected to other stress fibers (mentioned below) that are capable of contracting through which force can be transferred to focal adhesions (53) (Fig. 2.7). (ii) The second type of stress fibers are transverse arcs that are composed of alternating α-actinin and myosin, which makes them contractile (54). Transverse arcs are linked to focal adhesions through dorsal stress fibers (Fig. 2.7) and are involved in generating retrograde flow in migrating cells (55). (iii) Ventral stress fibers are those which connect focal adhesions (at both ends) (Fig. 2.7). The contraction of these stress fibers lead to rear retraction during cell migration (56). (iv) The last and most recent of stress fibers are the perinuclear actin cap which are positioned above the nucleus (57) (Fig. 2.7). They regulate the position of nucleus and act as mechanotransducers to the nucleus by transducing forces from microenvironment (58). Stress fibers are more commonly observed in highly spreading cell types in culture like NIH3T3 and MDCK (Madin-Darby Canine Kidney) cells. But analogues of stress fibers can also be found *in vivo*: for example, actin cable leading to dorsal closure during *drosophila* development (59).

2.6.3 Protrusions

Protrusions are actin rich structures that are extended by cells during the process of migration in order to probe the cell environment (60, 61). These actin rich structures were reported as early as 1980's (62). Cells send protrusions to form attachments with the substrate (explained in the next section) that facilitate cell movement (Fig. 2.8). Two main categories of these protrusions are *lamellipodia* and *filopodia* which are actin rich structures (Fig. 2.8). Other protrusions include: (i) Blebs – which are extension of plasma membrane with cortex driven by hydrostatic pressure inside the cell (63), and (ii)

Microspikes – small extensions of lamellipodia that are made of actin bundles (60). Here I will mainly discuss lamellipodia and filopodia which are more relevant for the topics of the thesis.

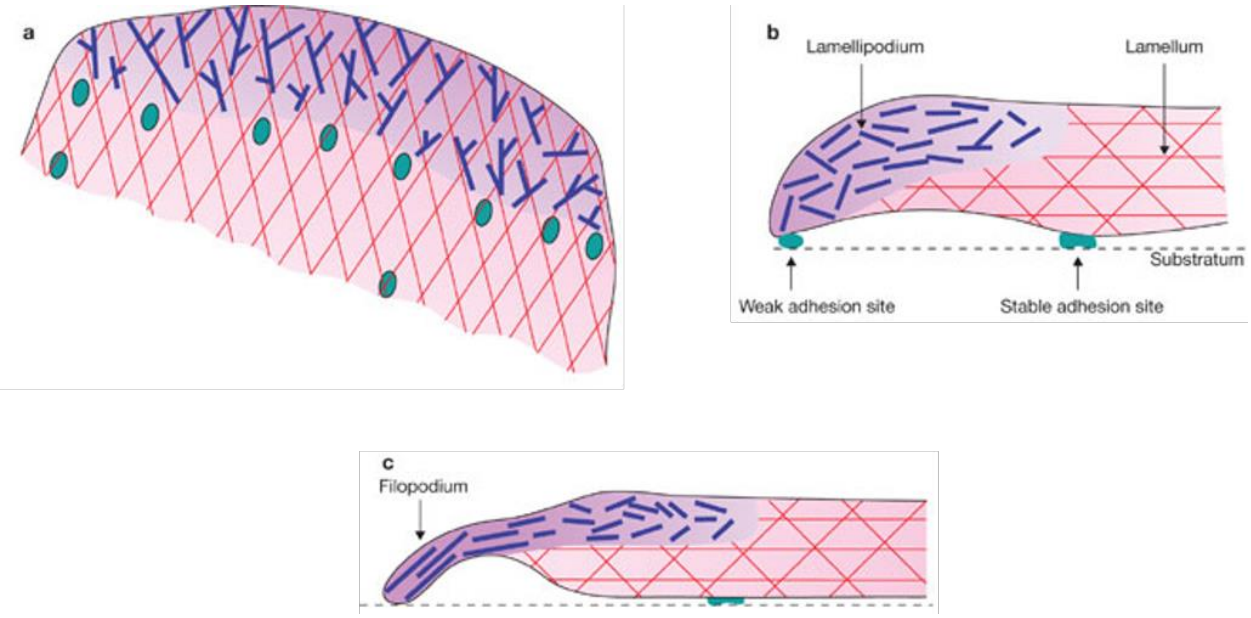

Figure 2.8. Schematic of lamellipodium and filopodium, adapted from (64). (a) and (b) Top and side views of lamellipodia respectively. The blue region corresponds to short actin filaments in the lamellipodium, shown in red are actin filaments from the lamella and the green regions are the adhesion sites on the substrate. The difference between lamella and lamellipodium is shown in (b). (c) Filopodium growing from the lamellipodium.

2.6.3.1 Lamellipodia

Lamellipodia are sheet-like protrusions that vary in width from ~ 1 μm to 5 μm based on cell type, and are made of short actin filaments (65). The actin filaments are branched and arranged in a mesh-like fashion. This branching and network formation (Fig. 2.8 a and b) are triggered by actin polymerization mainly regulated by Arp2/3, whose regulation is in turn controlled by WASP family of proteins (40). Observation of these proteins in lamellipodia, in addition to actin cross-linking and bundling proteins were confirmed by different studies (65). The presence of Arp2/3 close to the cell membrane promotes the growth of branched meshwork while formins trigger barbed-end assembly in actin filaments. In combination with other actin regulating proteins (like capping proteins), this results in treadmilling of array of actin filaments which applies force on the cell membrane to push the cell extension forward (39). This mechanism is critical for lamellipodial growth. The continuous polymerization of actin at the leading edge leads to

retrograde flow (towards the cell body) of actin aided by myosin motors (66). In general, lamellipodia is only rich in actin and actin related proteins. Myosin is typically not observed. Behind the lamellipodia is an acto-myosin rich network called *lamella* which is the merging point of upper and lower portions of cell cortex (67).

2.6.3.2 Filopodia

Filopodia are protrusions that arise from lamellipodia (Fig. 2.8 c) and are thin structures of ~ 0.1 μm to 0.3 μm in diameter (60). These finger-like protrusions are made of tightly bundled actin filaments which are arranged in parallel orientation. The bundles usually contain 10-30 actin filaments which prevents the filopodia from buckling (68). This efficient bundling is the result of fascin which bundles the filaments while filaments are polymerized (69). The exact mechanism of filopodial formation is not understood yet (60). The most accepted mechanism is the assumption of local bundling of actin filaments in lamellipodia that undergoes polymerization due to Arp2/3 (70). This polymerization activity is mainly supported by the observation of Vasodilator-Stimulated Phosphoprotein (VASP) protein in filopodial regions, which prevents the capping of actin bundles. The combined effect of uninhibited polymerization by VASP and bundling by fascin are proposed to overcome the local membrane resistance for growing filopodia (68).

In terms of function, lamellipodia and filopodia together may cooperate in sensing the environment during migration. Specifically, filopodia have been shown to influence navigation of nerve growth cones (71) and lamellipodia in the case of fish keratocytes (72).

2.6.4 Focal adhesion

During cell migration, cells establish contact with the substrate / surrounding matrix to form cell-substrate adhesions (73). These adhesion regions are called focal adhesions which are rich in integrins and integrin associated molecules involved in signaling pathways (Fig. 2.9). Integrins are trans-membrane receptor proteins that connect the sub-cellular cytoskeleton to the external matrix (74).

Focal adhesions play a key role in sensing the surrounding matrix characteristics. They were one of the first cellular organelles whose mechanosensing abilities were experimentally demonstrated (36, 75) and are capable of sensing substrate stiffness (76) and substrate bound molecules (77). Structurally, integrins (on the membrane) connect

ECM with the actin cytoskeleton inside the cell, directly through talin (a cytoskeletal protein inside the cell) (74). Talin also binds to vinculin, which in turn binds to α-actinin and actin (Fig. 2.9). Talin plays a significant role in linking integrins and actin in many ways, which facilitates traction forces that are observed in migrating cells like fibroblasts. It has been shown that disruption of talin leads to immature formation of focal adhesion and differences in traction forces experienced by cells (78). In total, ~ 150 proteins have been identified in association with focal adhesions. In addition to integrin and actin related proteins, these proteins included signaling proteins like Focal Adhesion Kinase (FAK), Src tyrosine kinase and other members of Rho family of GTPases (Fig. 2.9) (74). Together, these structural and signaling complexes perform the environment sensing process.

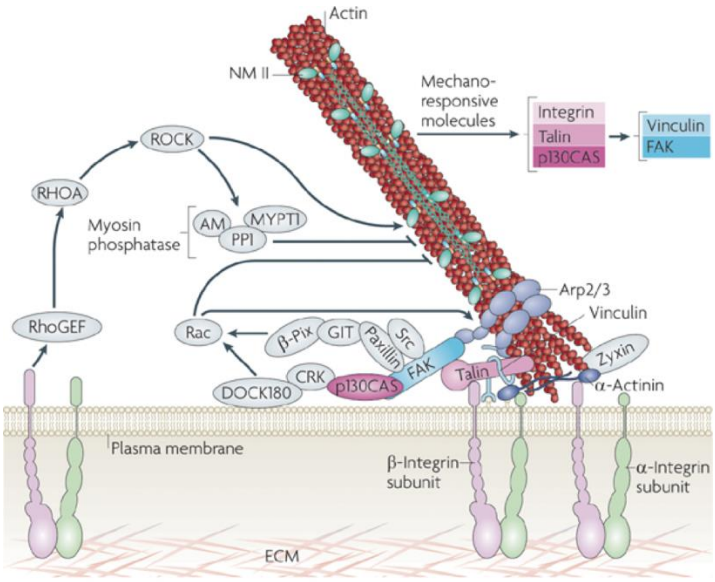

Figure 2.9. Schematic of focal adhesion assembly, adapted from (43). The scheme shows the integrin binding of ECM and actin cytoskeleton across the plasma membrane. The signaling proteins that control the assembly and regulation of focal adhesion are also shown.

In general, focal adhesions are elongated structures and can be found in both central and peripheral regions of the cell-substrate attachments in migrating cells. However, the morphology, size and location of cell-substrate adhesion structure can vary depending on the cell type. Based on these parameters, adhesion structures can be roughly categorized into nascent adhesions and focal complexes, in addition to focal adhesion (79, 80). As opposed to focal adhesion, nascent adhesion and focal complexes are small, dot-like and dynamic in nature. However, their protein compositions are partially similar to focal adhesions. The nascent adhesion and focal complexes are mainly present under protrusive structures (specifically lamellipodia) during cell migration and are found to regulate actin polymerization in the protrusions. In addition to the adhesion types mentioned above, other adhesion structures have also been identified: podosmoes and invadapodia which are significantly different from focal adhesions in terms of organization and composition (81).

2.6.5 Cell-cell junctions

Similar to cell-substrate adhesions, cell-cell adhesion structures are found in cell types forming epithelium or endothelium (82). In these cell types apical and basal sides of plasma membrane are distinguished by a clear lateral membrane. This is a hallmark characteristic of epithelial and endothelial cells which establishes apico-basal polarity (83). This lateral membrane separating the apical and basal sides of the cell are connected to the nearby cells for different purposes: signaling, transport and mechanical connectivity. The connections are established by membrane microdomains whose distribution along the lateral membrane varies based on organism (vertebrates/insects). These microdomains can be distinguished into four categories based on their protein components, which mainly connect the cytoskeleton and signaling components on either cells (Fig. 2.10). The four different microdomains forming the lateral cell-cell junctions are briefly described below:

2.6.5.1 Tight junctions

Tight junction microdomains (Fig. 2.10 a) are found close to the apical (mammalian cells) or basal (insect cells) side depending on the organism (82). Tight junctions are rich in transmembrane proteins: claudins and the integral membrane proteins: occludin and Junction Adhesion Molecules (JAMs). On the cytoplasmic side, the tight junctions are rich in three variants of proteins called Zona Occludens (ZO): ZO-1, ZO-2, ZO-3. The ZO-proteins are responsible for junction formation and in establishing connection between the cytoskeleton of either cells through α-actinin (84). Recently, the protein ZO-1 was shown to play a key role in transcription regulation (85).

2.6.5.2 Adherens Junctions

With respect to tight junctions, adherens junctions are found to the basal side in mammalian cells and to the apical side in insect cells. Adherens junction (Fig. 2.10 e) provides the adhesion strength for the cell-cell junction. This adhesion strength is maintained by E-cadherin which is the most abundant integral membrane protein of this (adherens junction) membrane microdomain. On the cytoplasmic side, the adherens junction contain alpha-catenin, beta-catenin, adenomatosis polyposis coli (APC), plakogoblin and ZO-proteins. All these proteins are connected to both actin and microtubule cytoskeleton to maintain the cell adhesion (86).

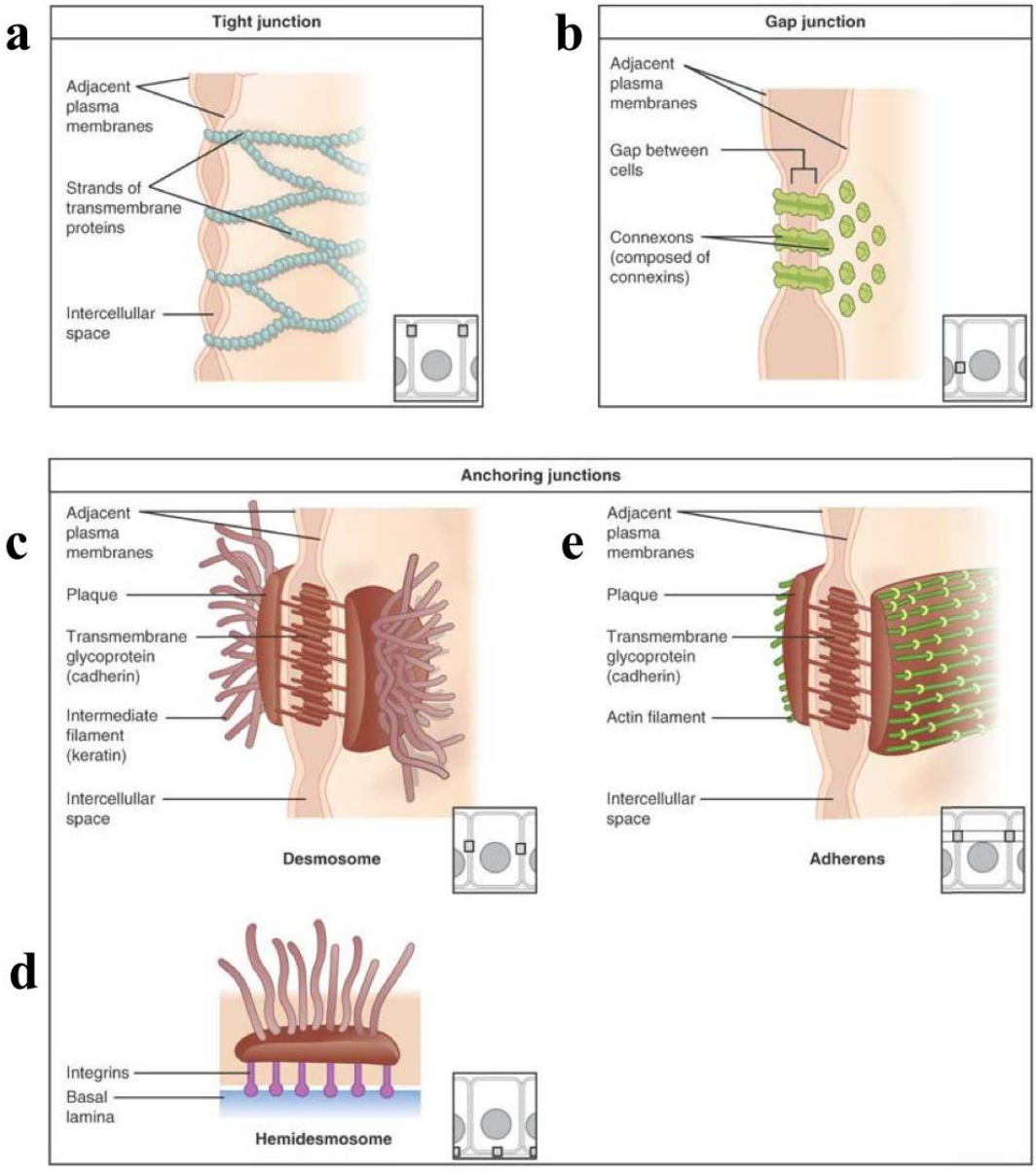

Figure 2.10. Schematic of different microdomains of cell-cell junctions with their respective component proteins. (a) Tight junction, (b) Gap junction, (c) Desmosome, (d) Hemidesmosome and (e) Adherens junction. Image source: OpenStax, Anatomy & Physiology. OpenStax. 25 April 2013. <http://cnx.org/content/col11496/latest/>.

2.6.5.3 Gap junctions

Gap junction microdomains (Fig. 2.10 b) form cell-cell channels that allows diffusion of ions and other molecules between the cells. The opening and closing of gap junctions are necessary for maintaining the electrical polarization of cells (by ion transport) (86). The integral membrane proteins that establish the cell-cell channel are connexins, of which

connexin43 is the most abundant protein. The ZO-protein on the cytoplasmic side links the cytoskeleton and is involved in regulating the size of gap junctions (87).

2.6.5.4 Desmosomes

Desmosomes are microdomains (Fig. 2.10 c) that provide mechanical integrity to the cell-cell junctions in addition to adherens junction, and prevent shearing of cells (88). The integral membrane proteins desmocollin and desmoglein in the desmosome microdomain are linked to the intermediate filaments of cells through desmoplakin on the cytoplasmic side. Desmosomes are critical for tissue integrity and can resist calcium-depletion, as opposed to adherens junctions. Mutations in desmosomes lead to skin diseases (89). A similar structure to desmosome is the hemidesmosome (Fig. 2.10 d) that links epithelial cells to the basal lamina through integrins.

2.6.6 Rho GTPases mediated signaling

The collective behavior section at the beginning of introduction and in general, this thesis explores the physics behind self-organization phenomena at the level of acto-myosin interaction and cells. However, the precise activation of each of these proteins is governed by complex biochemical pathways that drive all the processes of cell in an uninterrupted manner. Along this line, the major pathway that regulates the dynamics of actin cytoskeleton is that of Rho GTPases family of proteins (Fig. 2.11) (35). Signals from the extracellular environment are perceived by ligand-receptor interactions at the membrane surface. Following the received signal, appropriate Guanine-nucleotide Exchange Factors (GEFs) or GTPase Activating Proteins (GAPs) trigger upregulation or downregulation of corresponding Rho proteins. The Rho GTPases then bind to protein kinases or actin related proteins that control the dynamics of actin filaments (F-actin). Among these Rho GTPases, Rho, Rac and Cdc42 are involved in regulating major functions like focal adhesion assembly, lamellipodial formation and filopodial protrusions respectively (90). In addition to regulating actin cytoskeleton, Rho GTPases are also involved in controlling process regulating gene transcription, enzyme activation, vesicle transport and cell division cycle (35).

Of the Rho GTPases, Rho and Rac are expressed as their isoforms: RhoA, RhoB and RhoC and Rac1, Rac2 and Rac3 respectively. These proteins together with Cdc42 are active in the GTP bound state whose binding and unbinding are controlled by GEFs. In

the following sub-sections, I will briefly describe these individual protein transduction pathways with respect to actin cytoskeleton.

2.6.6.1 Rho signaling

Rho proteins have been shown to induce stress fibers when they are overexpressed in cultured fibroblasts (91). Rho kinase 1 (ROCK1) and ROCK2 are the major proteins that are involved in binding several actin cytoskeleton substrates (Fig. 2.11). One of the main targets of ROCK1 and ROCK2 is myosin-binding subunit (MBS) of myosin phosphatase. The regulation of MBS is coupled with the regulation of cofilin phosphorylation which affects actin filament turnover (92). These processes regulate myosin phosphorylation and actin filament dynamics respectively, and indirectly affect the stress generation in acto-myosin filaments. ROCK are also involved in regulating the phosphorylation of Ezrin-Radixin-Moesin (ERM) family proteins thereby controlling the links between actin cytoskeleton and plasma membrane. This phosphorylation activity of ERM proteins is achieved by the binding of ROCK to phosphotidylinsositol-4-phosphate 5-kinase (PIP5K) (92).

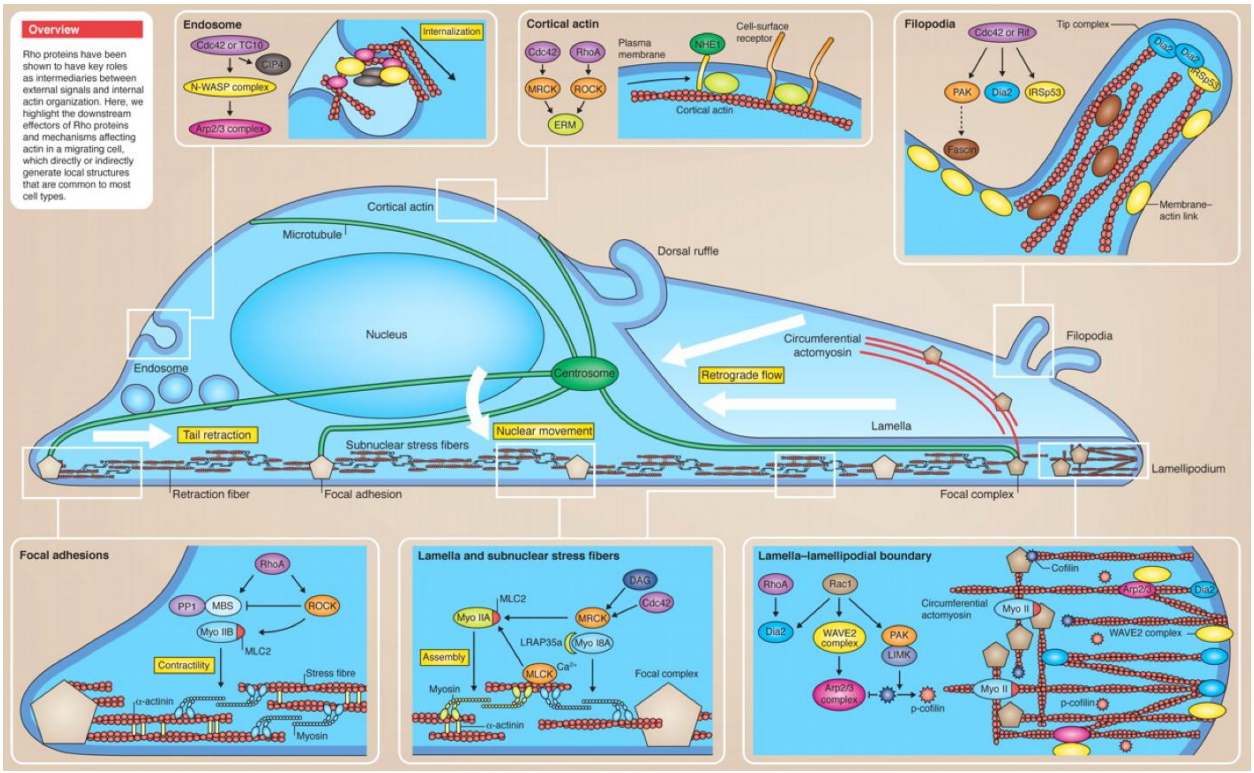

Figure 2.11. Schematic of Rho GTPases signaling associated to actin cytoskeleton. At the center of image is a migrating cell. The white boxes corresponding to cytoskeletal portions of this migrating cell, which are zoomed to explain the related Rho GTPase signaling pathways. Scheme adapted from the poster of Sit et al (90).

2.6.6.2 Rac signaling

The three isoforms of Rac (Rac1, Rac2 and Rac3) are genetically homologous but are responsible for individual functions (35). In general, Rac proteins regulate the processes of lamellipodial formation, membrane ruffles and phagocytosis (Fig. 2.11) (93). Specifically, inhibition of Rac1 in several cell types inhibits lamellipodial formation. In addition, Rac1 is also required for cell polarization during migration triggered by chemotaxis (94). This feature is shared by Rac2 whose high levels have been hypothesized to compensate Rac1 inhibition (95). This regulation of actin related structures is due to direct control of Rac proteins on actin dynamics. Rac regulates nucleation of actin by Arp2/3 and mDia formins through WASP family of proteins. Rac also regulates the severing of actin filaments by gelsolin and severin and the availability of free actin monomers by regulating cofilin that cap the barbed ends. In addition, inhibition of Rac1 and Rac2 have been shown to introduce defects in actin and spectrin meshwork in erythrocytes that may lead to disease states (96).

2.6.6.3 Cdc42 signaling

Cdc42 has been shown to regulate cell polarity and actin cytoskeleton in different eukaryotic organisms (Fig. 2.11) (97). For example, Cdc42 is important for budding in yeast (98), polarity establishment for epithelial cells and during *Drosophila* (99) and *C. elegans* (100) development. In addition to this, Cdc42 mainly regulates the filopodium formation (Fig. 2.11). The role of Cdc42 on actin nucleation is similar to Rac proteins in activating mDia formin through WASP. Actin nucleation by Arp2/3 is regulated by Cdc42 through insulin-receptor substrate p53 Tyr kinase (35). Cdc42 also mediates the actin-filament turnover by regulating cofilin through activation of p21-activated kinase and LIM kinase. The dramatic effect of Cdc42 inhibition has been shown in disruption of directed migration of neuronal growth cones. While these characteristics are parallel to Rac proteins, Cdc42 also regulates cell polarity. For example, Cdc42 in combination with PAR complex is responsible for positioning of microtubules in the migrating front and in the orientation of golgi and microtubule-organizing center (MTOC) (101).

3. Materials, Methods and Instrumentation

This Chapter discusses the products and instruments used in the protocols for the experiments investigating the ring constriction, direction reversal and pulsations in monolayers. The contents include: preparation of microcavities and micropatterns through microfabrication, culture conditions for cell lines, fluorescent markers, details on inhibitor/effector drug conditions, microscopes and optical combinations and softwares used for acquisition and analysis. In the following sub-sections, explanations and the science behind the procedures are first described followed by a detailed description of each step in the protocol. Some tricks and suggestions are given as *italicized* comments. The list of products and corresponding details are provided in the appendix.

3.1 Microfabrication

The process of making micrometer scale structures and patterns involves series of steps from creating a computer based design, fabricating structures through photo-lithography, to molding / replica-molding with soft lithography and/or microcontact printing on the surface (102, 103). It is preferred to perform the fabrication steps in the cleanroom although preparing in the normal lab bench can yield good results for some structures.

3.1.1 Design of photo-mask

The 2D layouts of structures (the top view) that are to be fabricated are drawn with required dimensions using the CleWin 4 layout editing software. The design is sent to a company (SELBA), for printing either on chromium or on acetate sheet.

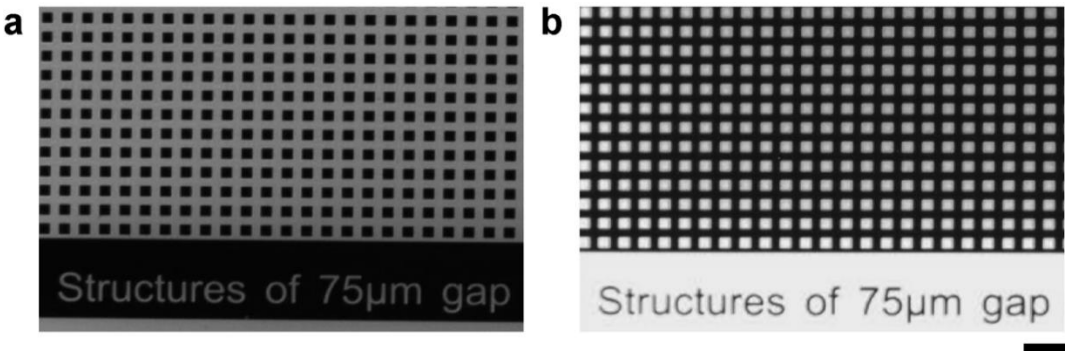

Figure 3.1. Plastic masks for making grids. (a) Mask with positive polarity where the structures are printed on a transparent background. (b) Mask with negative polarity where the transparent structures are printed on a dark background. Scale bar 400 µm.

Masks made of chromium are preferred for high precision (≤1µm) structures. The printed design is used as a mask for photolithography. These generated masks can be positive or negative (Fig. 3.1) based on whether the structures are directly molded, or replica-molded on PDMS during soft lithography.

3.1.2 Photolithography

Photolithography is the process by which designs on the photo-mask are fabricated on a silicon wafer - coated with appropriate photoresist. The fabricated structures are replica of the desired structures. For example, if cavities are the desired structures (on PolyDiMethylSiloxane (PDMS)), then pillars are fabricated on the silicon wafer. The aspect ratio of the structures is carefully selected ($l/h \geq 0.2$ and $d < 20h$; Fig. 3.2) to prevent damage due to line-pairing, buckling or sagging (104, 105), during the soft lithography step.

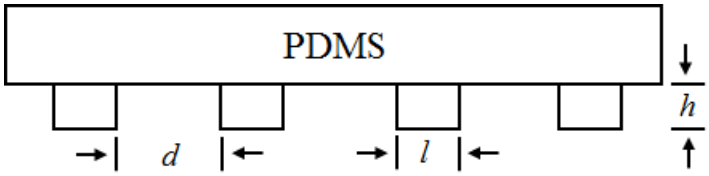

Figure 3.2. Scheme showing a PDMS stamp with microstructures, where *h* is the height of the structure, *d* is the distance between the structures and *l* is the width of the structures (105).

In this process, an appropriately chosen photo-resist/resin based on the thickness of the structures (Microchem SU-8 data sheet), is spin coated on a "clean" silicon wafer. The spin coater speed is critical for the desired thickness. The resin is temperature treated for proper adherence to the wafer, before and after exposure to UV with a mask aligner. After pre-baking, the resin is exposed to UV for cross-linking. The mask-aligner with the help of photo-mask controls the region of cross-linking to reflect the design of printed structures. The intensity and time of exposure are selected based on the thickness and type of resin used (Table 1). Post-baking, the resin coated on the wafer is treated with a developing solution which removes the non-cross-linked resin to reveal the structures.

These fabricated wafers are called "masters" which can be used several times for further soft lithography procedures. The exact protocol for preparing a master with structures in the thickness range of 20-30µm and lateral dimensions of 100-500 µm is detailed below (Fig. 3.3).

Photoresist	Desired thickness [μm]	Spin-coating speed [rpm]	Prebake time for 65 ºC / 95 ºC [min]	Exposure energy [mJ / cm^2] ~	Postbake time for 65 ºC / 95 ºC [min]
SU-8 2007	7	3000	1 / 2	110	1 / 2
SU-8 2007	10	1400	1 / 2	125	1 / 2
SU-8 2007	12.5	1000	1 / 2	130	1 / 2
SU-8 2015	15	3000	1 / 2	140	1 / 2
SU-8 2015	20	2200	1 / 3	145	1 / 2
SU-8 2015	30	1500	1.5 / 4	152	1 / 3
SU-8 2025	30	2800	1 / 3	152	1 / 3
SU-8 2025	40	2100	2 / 5	160	1 / 3
SU-8 2025	50	1700	2.5 / 7	160	1 / 4
SU-8 2025	75	1000	3 / 9	215	1 / 7

Table 3.1. List of SU-8 photoresist with corresponding parameters for desired thickness range. The data were taken from the SU-8 data sheet available at the MicroChem website (http://www.microchem.com/Prod-SU8.htm).

3.1.2.1 Procedure for master fabrication

1. The silicon wafer is washed with ethanol, acetone and isopropanol (in this order) to remove the organic impurities on the surface (Fig 3.3).
2. Then the wafer is placed on a 200 ºC hot plate to remove moisture. *Longer times (~ 1 h) of this step may help proper adherence of SU-8 to the wafer.*
3. After this step, the wafer is ready for spin coating with resin. *At this stage, surface activation in plasma cleaner might yield better adherence of resin to the wafer.*
4. The resin (SU-8 2025 – for 30 μm thickness) is spin coated at 1500 rpm for 45 seconds.
5. The spin coated resin is pre-baked at 65 ºC and 95 ºC for 1 and 3 minutes respectively.
6. After pre-baking, the photo-mask is placed on the resin with the printed side (side with the ink) facing the resin. Using a mask aligner, the resin is exposed to ultra-violet (UV) radiation through the mask for 42 s.
7. The exposed resin is post-baked at 65 ºC and 95 ºC – *the structures are slightly visible at this stage already!*

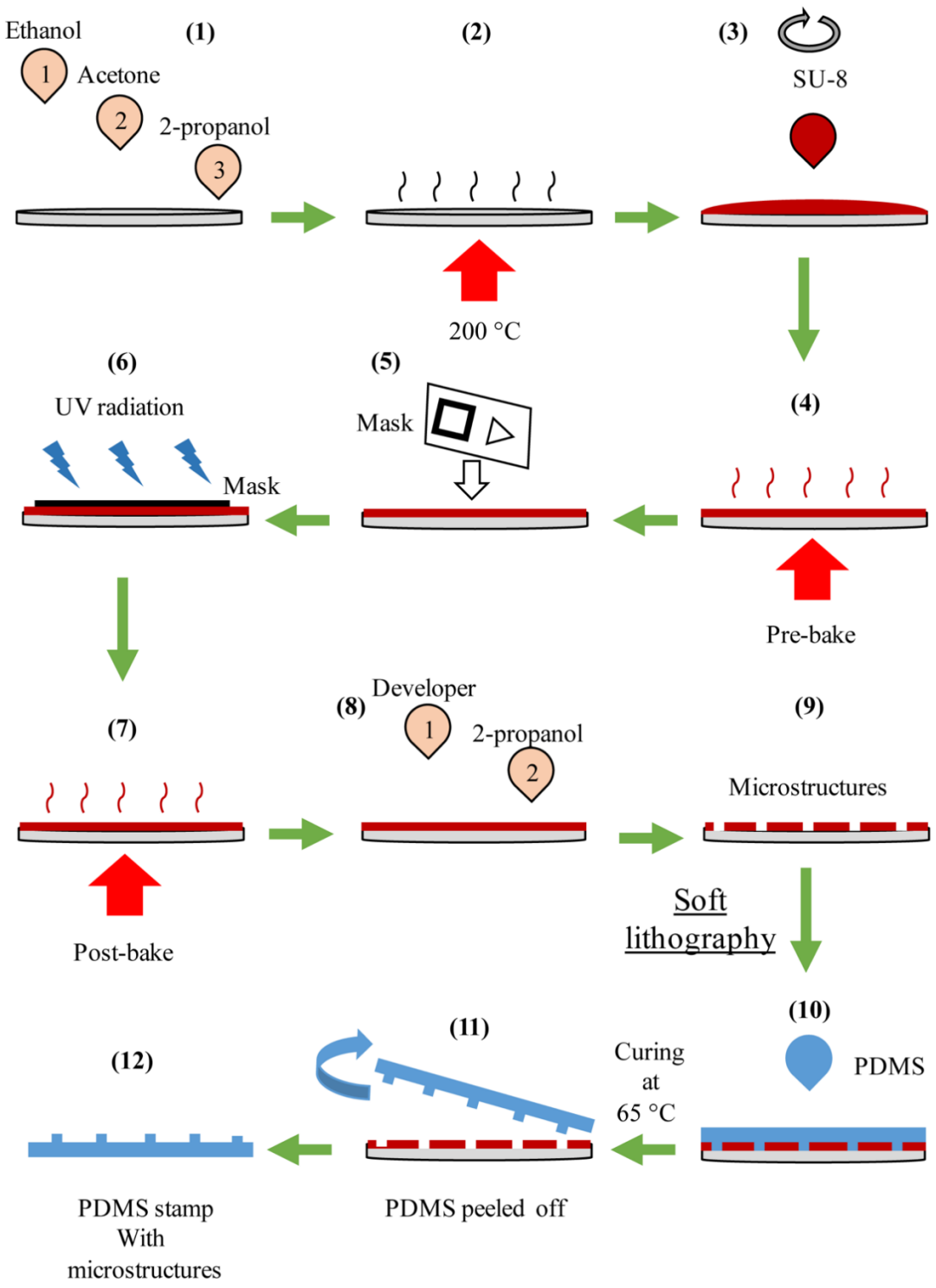

Figure 3.3. The schematic shows different steps of microfabrication: (1) Hierarchical cleaning of the wafer with different solvents, (2) heating at 200 ºC, (3) spin coating with SU-8, (4) Pre-baking, (5 and 6) Exposure with mask, (7) Post-bake, (8) Treating with developer followed by iso-propanol, (9) Confirming micro-structures on the master. (10 – 12) Soft lithography procedures: (10) Pouring PDMS on the master, (11) Peeling off after curing at 65 ºC and (12) Confirming microstructures on the PDMS stamp.

8. Finally, the resin is rinsed in developing solution for 3 minutes and washed with isopropanol. After observation under the microscope, if the structures are not fully developed, then the resin is rinsed for subsequent short time periods of 30 s until the structures are fully developed. *Care should be taken not to overuse the developer solution after appearance of structures. This might start eroding the developed structures.*
9. The developed master can be placed in 200 ºC hot plate for 30 minutes to reinforce the structures (optional).
10. The masters are stored in a plastic Petri dish and can be subjected for prolonged use if they are covered with PDMS and not exposed to environment.

Problems with adhesion can be solved by plasma activation or by making a first coating of 5-10 µm with another SU-8 (see Table 1). The first layer should be pre-baked and exposed without any mask followed by post-baking on which the second layer (with required thickness) should be done.

3.1.3 Soft lithography

Structures of the fabricated wafer are molded on PDMS for further usage like loading cells or micropatterning. PDMS (Sylgard 184) is prepared by mixing silicone elastomer with the cross-linker in a 9:1 (volume/volume) ratio. The mixture is centrifuged at 3000 rpm for 10 minutes to remove the air bubbles formed during mixing. The addition of cross-linker initiates reticulation between the elastomer and hardens over time. *This process of hardening/curing, can be accelerated by curing the PDMS at higher temperatures (1 h at 100 ºC and < 30 min at 150 ºC). By storing the PDMS at -20 ºC (maximum 20-30 days), the curing can be efficiently postponed.*

This PDMS is poured on the fabricated wafer until the wafer is fully covered. Air bubbles are created during the pouring. Also, the high viscosity of PDMS might prevent entry into the micrometer scale spaces between the fabricated structures on the wafer. This will lead to the air being trapped in these micro-spaces and improper molding of the structures on the PDMS. Hence, the Petri dish with the wafer and PDMS is desiccated with a vacuum pump for ~1 h. This process will remove the trapped air bubbles between the micro-spaces, forcing the entry of PDMS into these spaces. *This can be seen by appearance of air bubbles during the desiccation.* Once the air bubbles completely disappear, the Petri dish is stored overnight at 65 ºC for the PDMS to be cured. After curing, the PDMS can

be cut out for further usage. This process of replicating the structures on PDMS can be repeated several times with the same master (Fig. 3.3).

3.1.3.1 Microcavities

Daniel Riveline during his sabbatical stay at Rockefeller University, developed microcavities specifically for visualizing whole cytokinetic rings in proper geometry for fission yeast, and later adapted them for mammalian cells in collaboration with Viktoria Wollrab and Fanny Evenou, and for high-content in collaboration with David Caballero (106–108). Microcavities prepared from PDMS can be used for trapping and loading cells in vertical fashion to observe organelles parallel to the focal plane like the cytokinetic ring (109). In addition, this orientation can impose a quasi-3D environment and allows imaging of cellular organelles in 3D orientation (110). By adapting the diameter and height of the cavities, they can be used for studying multicellular organisms like C. *elegans* (110). Large arrays of these microcavities would allow simultaneous imaging of several samples opening doors for high-content screening with regularized read-outs and unprecedented signal-to-noise ratios.

3.1.3.1.1 Fabrication of microcavities

Microcavities were prepared by first fabricating the microstructures during the photolithography step, followed by molding and replica-molding steps with PDMS (Fig. 3.4). A normal microfabrication procedure is adapted (section 1.1.2.1) for preparing a wafer with cylindrical cavities, which after soft lithography procedure will be used for loading mammalian cells (107). However, cylindrical cavities do not ensure proper trapping of fission yeast – due to their ellipsoidal shape and non-adherent nature. Daniel Riveline and Antonin Hoël perfected the cavities by specially fabricating with a "V" shaped bottom using deep ion etching method (106, 108). The diameter and height of these microcavities are chosen based on the type of cells used: fission yeast (~ 5 µm diameter and ~ 15 µm height) and mammalian cells (~ 22 µm diameter and ~ 40 µm height). Viktoria Wollrab screened diameters for mammalian cell microcavities in the range of 17.5 – 30 µm for heights 30 and 40 µm. The optimal diameter in this range was found to be 22 – 25 µm.

During the soft lithography step, the microcavities are molded as columnar structures / pillars onto PDMS. On replica molding, these pillars can be again transferred as

microcavities on another thin layer of PDMS. To achieve this, the PDMS stamps with pillars are activated and silanized with TriMethylChloroSilane (TMCS) and further spin coated with PDMS. Silanization prevents the PDMS stamp and the replica molded layer from binding irreversibly. The speed of the spin coater sets the PDMS thickness that will contain the replica-molded cavities. The layer with cavities is then peeled off and plasma bonded to #0 glass CS which has a diameter and thickness of 25 mm and 100 µm respectively. This allows better imaging with fluorescent markers, using high numerical aperture objectives. Alternatively, instead of spin coating on the stamps, the PDMS can be spin coated on the coverslips and the stamp is placed on the spin coated coverslip (with pillars facing the CS). The PDMS is further cured and the stamp is peeled off, leaving the cavities on the coverslip. A detailed step-by-step protocol has been published in the Journal of Visualized Experiments (110) (see appendix 10.6).

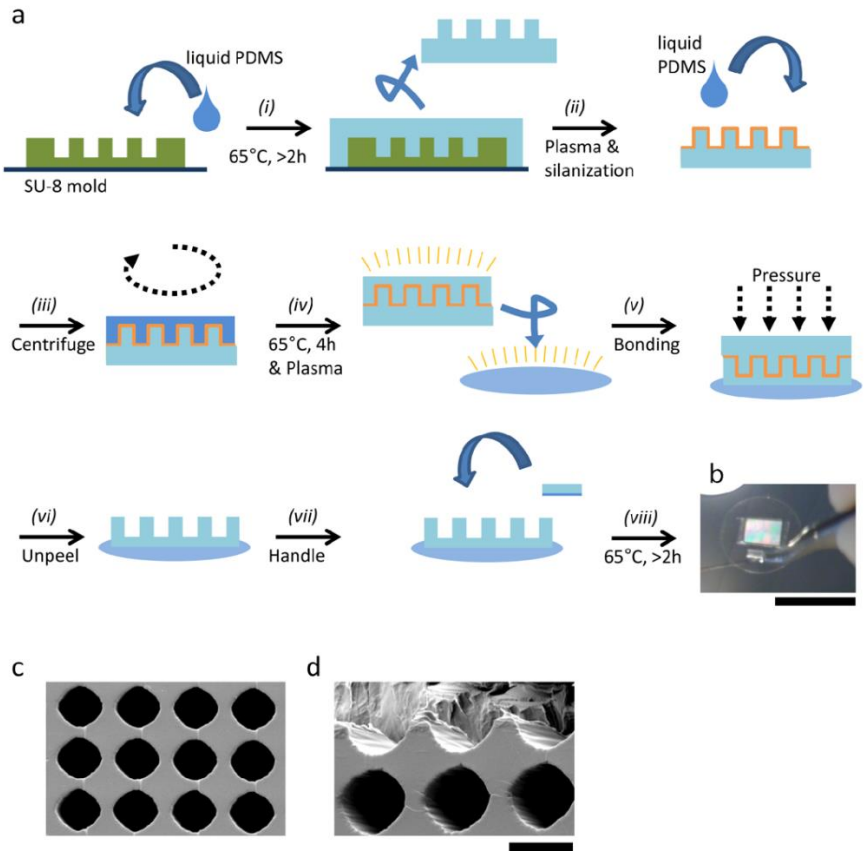

Figure 3.4. (a) Schematic showing the preparation of microcavities: (i) PDMS is poured on the master and cured, (ii) Liquid PDMS is poured on the silanized stamp, (iii and iv) The liquid PDMS is spin coated on the stamp and cured, (v) The stamp with spin coated and glass coverslips are plasma bonded after activation, (vi) The PDMS stamp is unpeeled, leaving the thin PDMS microcavities on the coverslip, (vi and viii) A small piece of PDMS is placed on the glass coverslip to use it as handle after curing. (b) Coverslip with microcavities and handle. Scale bar 2.5 cm. (c and d) Electron microscopy pictures of the microcavities showing lateral and axial dimensions. Scale bar 3.5 µm. Adapted from (110).

3.1.3.1.2 Optimization of microcavities

The above procedures leave a thin layer of PDMS (~ 100 – 200 µm) between the coverslip and the bottom of microcavities (Fig. 3.5 a). This results in loss of fluorescence signal due to scattering. We collaborated with the lab of Jian-Qiu Wu, Ohio State University, United States, and attempted to solve this discrepancy by spin coating the PDMS at higher speeds (~ 8000 rpm) for fission yeast microcavities. But the speed-thickness curve of PDMS remains a plateau after 8000 rpm (10 µm). Due to this saturation of thickness-speed curve, we were unable to design a stencil like setup where the cells would directly rest on the coverslip. However, we succeeded in reducing the base PDMS thickness from 80 – 100 µm to ~ 10 µm, which resulted in gaining ~ 30% more signal than the normal coverslips (Fig. 3.5 b). In this process, we also found that preparing microcavities by spin coating on the stamp and plasma bonding was more efficient in reducing the base PDMS thickness. The height measurements were done by coating fluorescent beads at different levels: bottom of coverslip, bottom of the cavities and outside the cavities (Fig. 3.5 a).

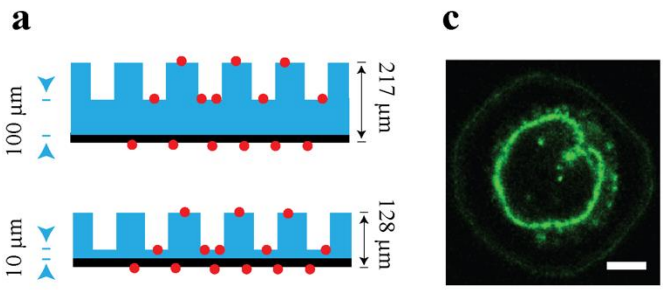

b

	Plain CS	Micro-cavities (1500 rpm)	Micro-cavities (8000 rpm)
Total thick--ness	100 µm	217 µm	128 µm
Rlc1 (raw) intensity [a.u]	8725	5308	7305

Figure 3.5. Optimization of microcavities for fission yeast. (a) Scheme showing microcavities prepared by spin coating at 1500 rpm (top) and 8000 rpm (bottom). The measurements are made with fluorescent beads (red dots) as reference at different positions. Average thickness of base PDMS (between the coverslip and bottom of microcavities) is 100 µm (top) and 10 µm (bottom). (b) Table summarizing the difference in integrated intensity of the ring after reducing the base PDMS thickness. (c) Image of HeLa cell at interphase stage, labelled with NUP-107-EGFP, loaded in microcavity.

We also prepared microcavities for visualizing Nuclear Pore Complexes (NPC). In collaboration with Jan Ellenberg and Vilma Jimenez Sabinina from EMBL, Heidelberg we prepared microcavities to study the assembly and organization of nuclear pore complexes (NPC) during cell cycle. Microcavities of diameter range 17.5 µm to 22 µm were tested for loading HeLa cells tagged for NPC protein – NUP 107 with EGFP (Fig. 3.5 c). Nucleoporin (NUP) 107 is an important component of NPC (111). We found that 20 µm cavities were better suited for studying NPC. Jan Ellenberg team already showed the ring

like organization of NPC (111), which we are together trying to further resolve by loading the cells in microcavities. The orientation of cells in the microcavities would allow complete visualization of the NPC rings during cell cycle, thereby giving insights into the organization.

In future, we are also planning to use a material (MyPolymer) with less refractive index than PDMS for the microcavities (112). This would further increase the signal quality of the labelled structures.

3.2 Micropatterning

Micropatterning is the process of printing proteins of desired shape/geometry onto a substrate which can be further used for specific adhesion of cells. This also gives freedom to change the magnitude of adhesion, and impose spatial control on the cells. Micropatterning can be done either by microcontact printing (113) or UV based micropatterning (114). For the projects used in this thesis, we use microcontact printing for patterning fibronectin on glass coverslips (CS). This allows both selective (with passivation) and non-selective (without passivation) seeding of cells in the presence of fibronectin.

3.2.1 Microcontact printing

In this process, fibronectin is allowed to settle on the PDMS molded microstructures (Fig. 3.6) and they are further transferred on the coverslip by bringing them in contact with each other while applying pressure (115, 116).

To start with, the glass coverslip (CS) on which the patterns are to be transferred should be hydrophilized, which otherwise are highly hydrophobic and cannot bond with proteins. Hydrophilization is achieved by cleaning the CS surface either by physical treatment (plasma cleaning) or chemical treatment (Piranha). In the case of plasma cleaning/activation, the CS is placed in a vacuum chamber where ions are allowed to "bombard" on the surface of CS, thus cleaning the surface and allowing extensions for hydroxyl groups / –OH bonding. On the other hand, "Piranha": a mixture of sulphuric acid (H_2SO_4) and hydrogen peroxide (H_2O_2) in the ratio of 7:3 can be used to act on the CS surface by which all organic and inorganic impurities are removed. Both processes render the CS hydrophilic. *However, we found that the micropatterns were more stable (> 48 h) when Piranha activation was used and hence we always hydrophilized the CS*

only by Piranha treatment. In addition, to promote covalent bonding with fibronectin, the hydrophilized surface is immediately silanized. During silanization, the hydroxyl groups on the hydrophilized surface, attack the alkoxy group of the silane to form stable hydroxyl [-OH] or sulfhydryl [-SH] bonding thus enhancing the stability of fibronectin on the surface (117, 118).

Meanwhile, the PDMS portion containing the suitable motif is cut from the already cured PDMS on the master. This piece of PDMS with motifs on one side is called "stamp". Similar to the CS, the PDMS is also highly hydrophobic and requires plasma activation to hydrophilize the surface. This hydrophilized surface with motifs is incubated with fibronectin solution to allow the binding of fibronectin. After incubation, the surface is carefully dried to remove only the solution, and stamped (brought in contact with pressure) on the silanized surface of the CS. This allows the transfer of fibronectin on the PDMS motifs to the CS with the same geometry while leaving the other regions empty. Thus, selective patterning of fibronectin with required geometry is achieved. The typical protocol followed for microcontact printing is detailed below (Fig. 3.6).

3.2.1.1 Procedure for Microcontact printing

1. The glasswares to be used for this procedure were cleaned with soap and dried with compressed air/oven: two 10 ml Petri dishes and 5 ml bottle for Piranha activation and silanization respectively and 100 ml and 500 ml beakers for rinsing and sonication.

2. The coverslips are immersed into the Piranha added to the glass Petri dish for 10 min. At least 20 ml (14 ml (H_2SO_4) + 6 ml (H_2O_2) – 7:3) is poured to ensure the complete immersion of coverslips. *The reaction of Piranha with the surface generates bubbles which raise the coverslips to float and will lead to improper activation. Hence the coverslips should be "pushed" from time to time into the Piranha.*

3. After 10 min treatment, the coverslips are extensively rinsed with MilliQ water to wash down the Piranha and then sonicated in MilliQ water for five minutes. This ensures the complete removal Piranha solution from the coverslip surface. *During the rinsing step, smooth interaction of water with the coverslip can be observed. This is a good sign of hydrophilicity induced by Piranha.* The sonication ensures complete removal of Piranha which otherwise can affect the patterned proteins and the cells. Only one beaker should be used for sonicating one coverslip. *More than*

one coverslip in a beaker can lead to accumulation of coverslips (due to the activation), which in turn can affect the surface properties.

4. Following sonication, the coverslips are dried with compressed air to remove the water completely and placed in a clean, dry Petri dish. The Petri with the coverslips is further placed in the oven (~ 65ºC) for 10 min to get rid of the moisture and humidity. *Coverslips sliding freely on the Petri is a good signature of perfect drying!*

5. This Petri dish without the lid is then placed with a bottle of 100 µl (3-Mercaptopropyl)trimethoxysilane in a desiccating chamber, connected to a vacuum pump. After 5 min, the chamber is closed and left undisturbed for 1 h. The vacuum created by the pump vaporizes the silane. When the chamber is closed, the alkoxy groups settle down on the coverslips thus forming a self-assembled monolayer of -Si-O-Si- in reaction with already existing hydroxyl groups.

6. After 1 h, the Petri dish with the coverslips is transferred to an oven (~ 65ºC) and stored for at least 1.5–2 h. The high temperature vaporizes and removes the unreacted alkoxy groups from the surface rendering it suitable for patterning proteins and cell seeding.

7. Meanwhile, the desired motif is cut out from the PDMS on the master. The stamp should be further trimmed on the sides to only have a surface with motifs and without any extra space. 1 cm^2 is the preferred area of the stamp for a volume of 100 µl fibronectin. *This is important since the concentration of fibronectin depositing on the motifs can change if too much of extra space is left alongside the motifs. For a precise trimming, the motif boundaries can be indicated by a marker and washed with 70 % ethanol, followed by sonication.*

8. Finally, the stamp is dried with compressed air and placed in oven (~ 65ºC) for 10 min before proceeding to plasma activation. The stamp is plasma activated for 20 s at 0.3 mbar pressure.

9. The stamp is placed in a 3 ml Petri dish. Now, 100 µl of 10 µg/ml rhodamine-fibronectin in Phosphate Buffered Saline (PBS) is added on top of the motifs. *A favorable flow of the fibronectin drop (without large contact angle) on the stamp indicates good activation of the stamp.* The Petri dish is closed and protected by an opaque and humid cover. The rhodamine tagged fibronectin (Cytoskeleton, Inc.) in the solution is allowed to deposit on the motifs for 1 h.

10. After 1 h, the solution is carefully removed with pipette and the wet motif surface is let dry in a clean-ventilated surface. *The drying time depends on the humidity of the environment, gap between the motifs and their height. The drying time needs to be optimized for perfect results based on the motifs. Too much of drying can cause increased adhesion of fibronectin to PDMS leading to improper transfer during the stamping process and similarly, less drying will lead to smeared patterns.*

11. The fibronectin deposited surface of the stamp is carefully placed in contact with the activated side of the CS. For this procedure, a small piece of Parafilm is flattened on to the bench with a water droplet. This gives a convenient flat surface for the coverslip to be placed for stamping. Then the stamp is manually pressed to facilitate the proper transfer of fibronectin. *The amount of pressure to be applied also needs to be optimized based on the type of structures. Application of high pressure can lead to buckling and less pressure will not lead to perfect patterns. Structures with very high l/h and very low d/h ratio (see Fig. 3.2) can withstand high pressures.* After manual pressure, a minimal weight (~ 10 mg) is placed on the stamp for five minutes. *Usage of a paper interface while applying pressures can avoid the sticking of stamp to the surface applying pressure.* However, Simon Lo Vecchio – a rotation Master student in the lab, perfected this step by placing a 50 mg weight for 30 min, which also yielded quality patterns.

12. After the stamping procedure, the stamp is carefully peeled off from the CS. *Before starting the peel-off, one can check if the CS is firmly attached to the stamp by just lifting the stamp. The firm attachment is a good signature of proper patterning.*

13. The quality of the patterns can be checked under a fluorescence microscope following the peel off and stored in a 3 ml Petri dish with PBS. The fluorescence intensity of the fibronectin should be homogeneous on all patterns throughout the stamped surface. This coverslip can be stored in 4 ºC, away from light for further cell seeding after 3-4 h and maximally before 12 h.

14. If the area other than the patterns are to be passivated, before cell seeding, the CS is placed upside down (with the patterns facing the PEG drop) on 100 µl of 100 µg/ml pLL-g-PEG dropped on a flat Parafilm sheet flattened on to the bench, as described in the previous step. The CS should be protected by an opaque and humid cover and left undisturbed for 20 min. After 20 min, the CS is stored in the Petri dish with PBS until cell seeding.

Coverslip activation

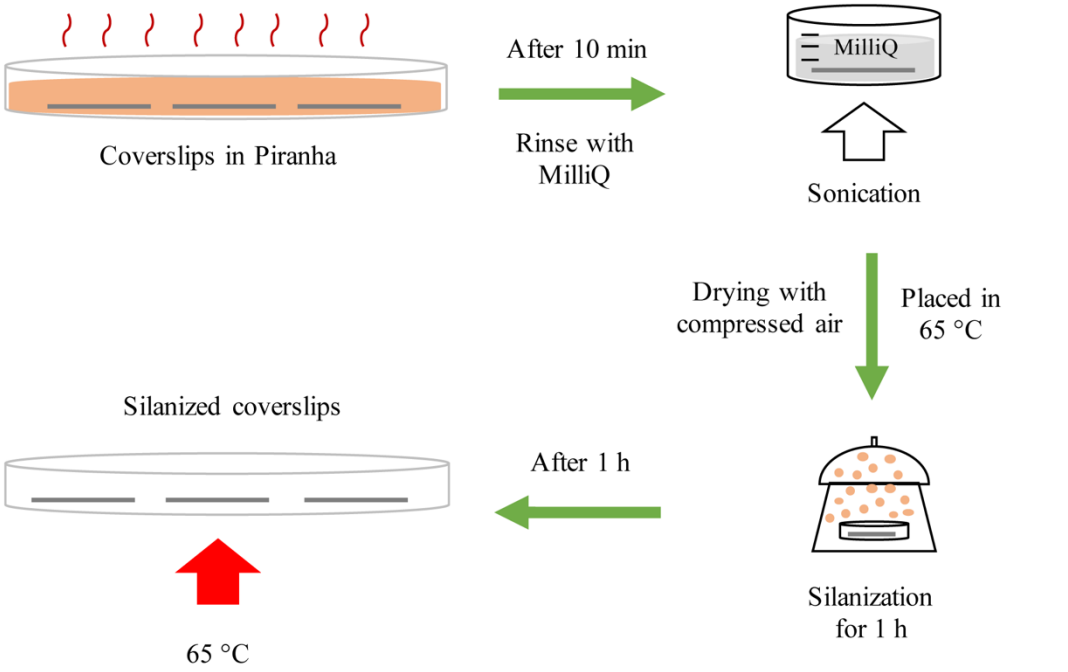

PDMS stamp preparation

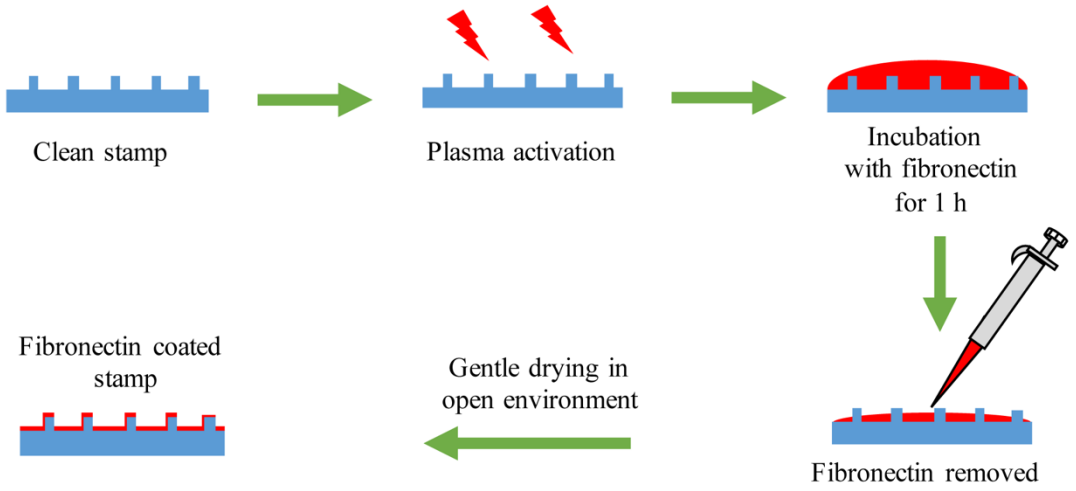

Fibronectin stamping

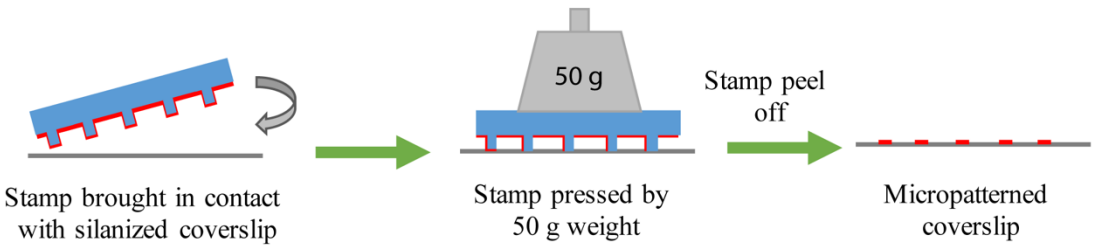

Figure 3.6. Schematic of microcontact printing protocol in three steps: **Coverslip activation** – The coverslip is Piranha treated followed by washing and sonication in milliQ water. The coverslip is then dried and silanized for 1 h. The silanized coverslips are stored in 65 ºC. **PDMS stamp preparation** – A clean PDMS stamp is plasma activated and incubated with fibronectin. After 1 h of incubation, the fibronectin is aspirated and dried to remove the excessive PBS, leaving a thin coating of fibronectin on the stamp surface. **Fibronectin stamping** – The fibronectin coated stamp is brought in contact with the activated coverslip and pressed with a 50 mg weight. After peeling of the stamp, the micropatterns can be visualized under the microscope.

After completion of the procedure, stamps can be heated (~ 60 ºC) in water for 20 min and stored for recycling. Before reusing for next microcontact printing, the stamp should be sonicated in ethanol. In this way the stamps can be reused for several times unless difference in pattern quality is observed. Once the technique is mastered, this procedure can be tried with non-fluorescent fibronectin while using passivation – the settlement of cells on the selected areas (patterns) would be an indicator of the pattern quality.

3.3 Fission Yeast culture

Schizosaccharomyces pombe, commonly referred as fission yeast, is a rod-shaped unicellular fungus. The replating and dilution procedures for fission yeast can be performed on a normal lab bench, close to a bunsen burner flame. The culture is grown on agar plates or in suspension in media, usually at 27 ºC or 32 ºC (119, 120). The agar plates with cells are covered with plastic sheet and always stored upside down to prevent the water (expelled from agar) from contaminating the monoclonal colonies. After thawing, the cells are grown in a series of suspension conditions before loading them into microcavities or on plain CS for experiments. For the suspension conditions, cells are grown on 10ml flasks covered with aluminum foil. Some strains might require specific time/media conditions. The details of different strains and corresponding protein-fluorescent markers are given in Table 3. In general, we follow the protocols as instructed in the Nurse Lab manual (120).

3.3.1 Yeast media

Yeast extract (YE) medium and Edinburgh minimal medium (EMM) were used for growing fission yeast cultures (119, 120). In addition, five amino acids (histidine, glycine) were supplemented to these media (YE+5S and EMM+5S) to ensure nutrient enrichment. The culture is always initiated on YE5S agar plate and is eventually transferred to suspension in liquid media before experiments. However, due to the auto-

fluorescence of YE5S media, experiments were performed only in EMM5S. Further during experiments, instead of autoclaving, *we use filtered (0.2 µm) EMM5S, since the transparency allowed better fluorescence detection – autoclaving leads to "caramelization" giving yellow color to the media.*

3.3.2 Thawing and freezing

Thawing: The frozen stock is scrapped (using a large 5 mm loop) and streaked on a fresh YES agar plate. Initially, the streaking is done on one side of the plate and after some time (~ 30 s), extended into lines which are further broken into segments. The short time delay will allow the cells to lose the effect of glycerol and the broken lines will allow the growth of monoclonal colonies. This plate is stored in 32 ºC until well defined monoclonal colonies appear (usually within 3 days), which will be further used for expanding the culture. If the strain has to be expanded from Whatman paper, the strip is brought in contact on a YE5S agar plate and few drops of autoclaved water are added. The paper strip is then dragged throughout and retained within the plate before storing in 32 ºC, for the colonies to appear.

Freezing: Once the cells are maintained for at least two passages - to have a properly synchronized cell division cycle, a monoclonal colony is scrapped and streaked (continuously / without breaking) on a fresh YES agar plate, which is stored in 32 ºC. After reaching confluency (usually within 2 days), all cells are scrapped and released into Cryovials filled with 1.5 ml of freezing mixture (YE5S+glutamic acid + 30% glycerol). Cells with the media are well agitated to prevent formation of "clumps" and can be directly stored in -80 ºC. These stocks can be used for expanding the culture even after several years.

3.3.3 Culture conditions

While preparing culture for experiments, cells are grown in three steps (Fig. 3.7): (i) Initially on YE5S agar plates, (ii) in liquid phase in YE5S media (starter) (iii) and finally in suspension in YE5S and/or EMM5S depending on the strain. The transfer of cells from Agar plate to starter allows the cells to adapt for liquid media. When grown in suspension, the culture is placed in a shaker incubator to prevent the cells from settling and to receive a constant supply of nutrients. The incubator also ensures proper

temperature maintenance – fission yeast cells are highly sensitive to temperature fluctuations.

In order to study cytokinetic rings, exponentially growing cells were used. The growth curve of fission yeast shows three different phases: (i) lag phase (ii) exponential phase and (iii) stationary phase (120). During the exponential phase, 10 % the cells are undergoing division. The growth of fission yeast in suspension can be monitored by a non-dimensional quantity: optical density (OD) which in this case is the logarithm of ratio of radiant flux/power of incident light (φ_e^i) to scattered light (φ_e^t) [OD = log [φ_e^i/-φ_e^t]]. The change in density (cells per unit volume of media) of the culture depends on whether cells are growing at a higher (exponential phase) or slower (lag/stationary phase) rate. Hence cells for experiments are always selected from the culture/flask which is between an OD of 0.2 and 0.8 to have more cells that would exhibit cytokinetic rings. In this OD range ~ 10 – 30 % of the cells are undergoing division.

3.3.3.1 Procedure for yeast culture

1. When yeast colonies appear on the unfrozen plate, a monoclonal colony is carefully isolated and streaked on a fresh YE5S agar plate (mother plate) and incubated in 32 ºC until isolated colonies appear (2 days maximum). The first YE5S plate ensures proper revival of the culture from frozen state and the mother plate ensures synchronization of cell division cycle. Unfrozen and mother plates with well grown colonies can be stored in 4 ºC for 7-10 days for further usage.

2. A well-defined colony is scrapped from this plate and released into 5 ml of YE5S media in a starter tube (10 ml tube with a movable cap). The starter tube is stored in room temperature for 3 days. Cells multiply by division and settle at the bottom of the tube forming a white precipitate. Media with cells from this tube can be used maximally for 4 days for making further dilutions. *The lid of the starter tube should be loose enough to allow gas exchange.*

3. The first dilution is made in YE5S. *The starter tube is agitated gently to re-suspend the cells in the media*, from which a small quantity is used for making the dilution. By adding 10 µl of media from the starter, a flask containing 10 ml of YE5S will be in the OD range of 0.2-0.8 after 24 h of incubation in a 32 ºC shaker-incubator. The time point at which the culture will reach the proper OD range can be precisely controlled by varying the (30 µl max) quantity of starter media. Since the starter serves to be an intermediate stage for Agar plate and

suspension culture, lots of dead cells are usually present, and contain cells that are not synchronized in cell division cycle. Hence a volume not more than 30 µl is used for making the YE5S dilution to reduce the concentration of dead cells in the following dilutions. In our case, we systematically made 5 µl, 10 µl, 20 µl and 30 µl dilutions in individual 10ml flasks to ensure proper OD range at ~ 28 h, 24 h, 20 h and 18 h respectively. To ensure proper behavior of cells during experiments, the dilution and temperature before the experiments are maintained with the same media (EMM5S) and temperature (27 ºC) as in experiments. Hence the second dilution is made in EMM5S at 27 ºC.

4. For making the second dilution, first the OD is checked in the previous YE5S flasks. *The turbidity of the flask is indicative of the density of the culture – more turbid, higher in OD*. For measuring the OD, *the flask is shaken well* before taking 1 ml of culture, which is loaded into a cuvette. The OD is measured with a spectrophotometer that is pre-calibrated with plain media. We always chose the flask with the OD range of 0.4-0.7 for making the next dilution, to maximize the number of dividing cells per volume of media. After adding 300 µl of culture from this flask, a flask containing 10 ml of EMM5S will be in the OD range of 0.2-0.8 after 20 h of incubation in a 27 ºC shaker-incubator. The increase in volume of culture that is transferred (300 µl), enables to have enough cells in the proper OD range within 24 h with media switch and reduction in temperature. Since cells are taken from a "healthy" flask (OD = 0.4-0.7), the concentration of dead cells will be considerable low, thus justifying the increase in transfer volume (300 µl). *In order to isolate cells from YE5S, to reduce the shock from change in media and to reduce the amount of YE5S being transferred to the EMM5S flask, the culture is centrifuged to collect cells at the bottom and re-suspended in EMM5S.* This re-suspended culture is used for adding into individual 10 ml EMM5S flasks for the second dilution. We systematically made 100 µl, 300 µl, 500 µl and 700 µl dilutions to ensure proper OD range for experiments at different time points: ~ 23 h, 20 h, 18 h and 15 h respectively. After reaching the proper OD range, the cells from these flasks are used for studying the cytokinetic ring closure.

In general, cells can be directly transferred from the YE5S starter tube to EMM5S flasks and subsequently used for experiments thus reducing the protocol to only one dilution. However, this might lead to delay in reaching the proper OD range (for example: > 30h) at the end of first dilution, due to switch in medium and temperature. This cannot be compensated by increasing the transfer volume from the starter, since it will lead to accumulation of dead cells. However, by making a first dilution step with YE5S, the cells

can be grown to proper OD range in ~ 24 h and then a higher transfer volume of these healthy cells can be used for making the second dilution in EMM5S. This also prevents cells from being in the same media for more than 24 h. Hence in our case, we consistently followed the two-step dilution process - first in YE5S and then in EMM5S.

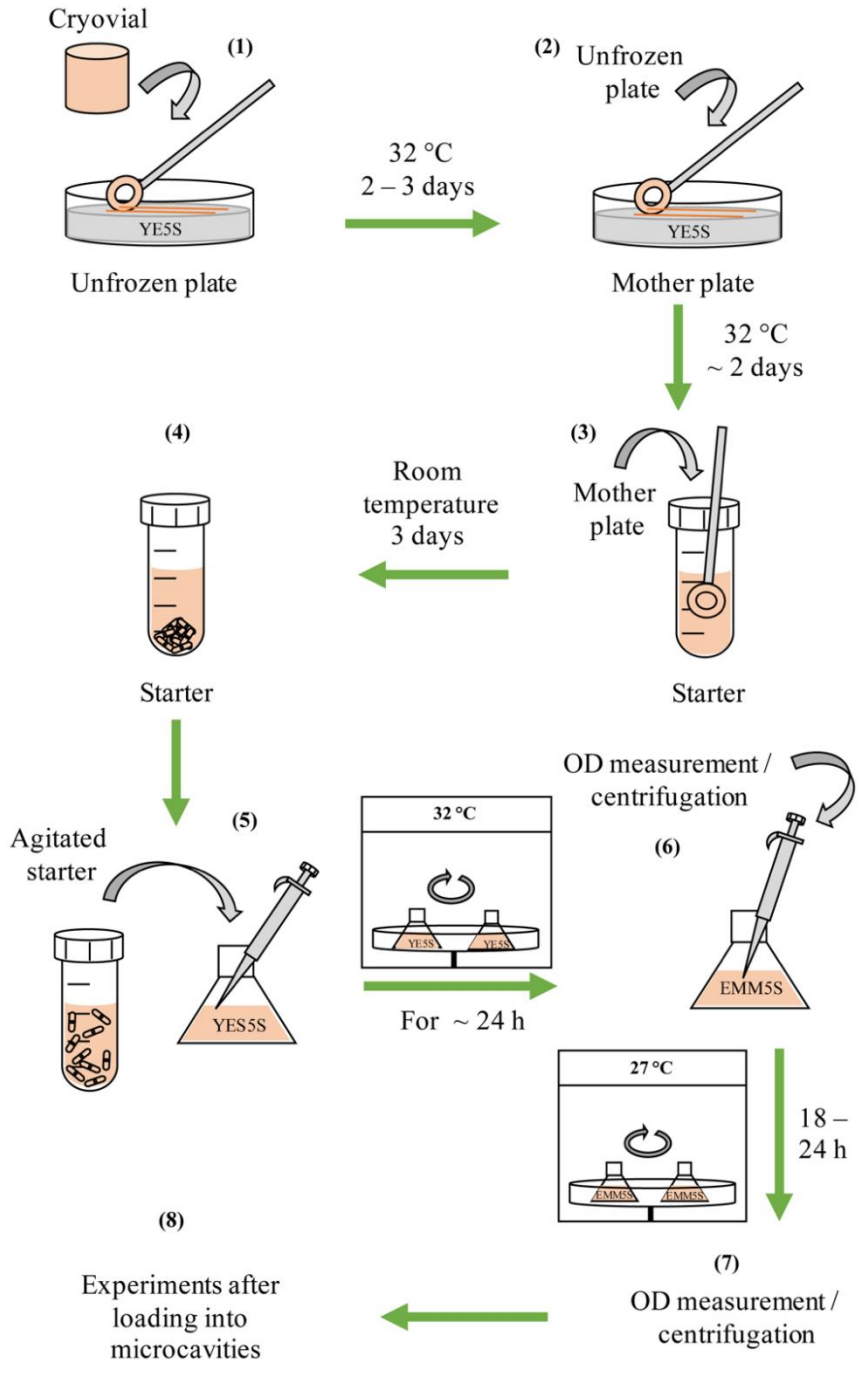

Figure 3.7. Schematic of fission yeast culture: (1) Cells transferred from Cryovial to the YE5S plate and incubated in 32 ºC. (2) Monoclonal colony transferred from unfrozen plate to mother plate and incubated in 32 ºC. (3) Monoclonal colony transferred from mother plate to starter and retained in room temperature. (5) Cells transferred from starter to YE5S flask and placed in shaker-incubator at 32 ºC. (6) Cells transferred from YE5S to EMM5S flask after OD measurement and placed in shaker-incubator at 32 ºC. (7) Cells from the flask with the proper OD are loaded into microcavities for experiments.

In addition, certain strains require special media conditions for example: JW1348 and JW1349, where the Calponin Homology Domain (CHD) is tagged with green fluorescent protein (GFP) and the regulatory light chain (RLC) of myosin is tagged with mCherry and tdTomato respectively (121). These strains were a kind gift from Jian-Qiu Wu, where the CHD-GFP is expressed only after switching the strains to from YE5S to EMM5S. After starting the

incubation with EMM5S, J-Qiu. Wu found that the fluorescence expression levels of CHD-GFP were maximum after 18 h and the dynamics of actin in the cytokinetic ring were normal only before 24 h of incubation (after 24 h, CHD-GFP interferes with actin dynamics). Hence the experiments with these strains were always performed within a time window of 18-24 h.

3.3.4 Preparation of samples for experiments

For the acquisition under microscope, we use custom designed metal holders for 25 mm coverslip. The metal holder is made of two pieces between which the coverslip is sandwiched and can hold a volume of ~ 2 ml of culture (Fig. 3.8, (3)). After receiving from workshop, these holders are cleaned with soap and immersed for two weeks in ethanol, media (that will be used during acquisition) and again in ethanol to completely remove the metal dust deposited during fabrication.

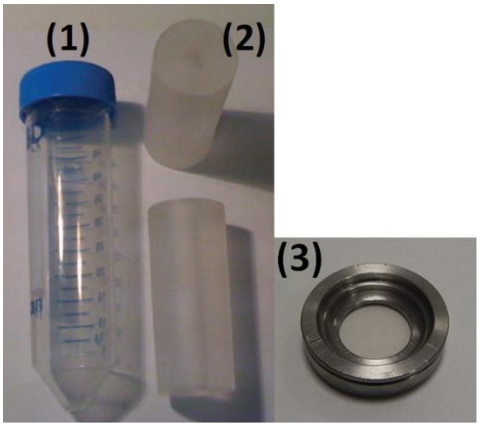

These holders can be repeatedly used and after completion of each experiment, the holders were sonicated twice in ethanol and stored immersed in ethanol for further use.

Figure 3.8. Materials used for sample preparation for acquisition under the microscope. (1) 50 ml Falcon tube into which the cylindrical Poly (Methyl Methacrylate) PMMA piece will be placed – the coverslip with microcavities will rest on this cylindrical piece (2). (3) Metal holder with a coverslip filled with media.

3.3.4.1 Cytokinetic rings perpendicular to the focal plane

To study the rate of ring constriction, fission yeast cells were placed horizontally on the coverslip: ring being perpendicular to focal plane. However, when placed in temperature controlled chambers, thermal fluctuations constantly displace the cells, thus limiting the acquisition of same ring. To avoid this problem, we immobilize cells by coating coverslips with concanavalin A (ConA) – a lectin that binds to glycoproteins on the cell wall of fission yeast (122). To coat the coverslip with ConA, 200 µl of 100 µg / ml ConA is dropped on the coverslip and allowed to dry. These coverslips can be stored for 20-30 days in a clean Petri dish at room temperature for further use.

Before experiments, the holder with coverslip was prepared and 200 µl of culture was dropped on ConA – coated region followed by 10 min incubation for the cells to settle and attach. After 10 min, the nonattached cells were removed by carefully rinsing with filtered EMM5S media. The holder is then filled with 2 ml of EMM5S and proceeded for imaging.

3.3.4.2 Cytokinetic rings parallel to the focal plane

To study the molecular organization of the ring, the fission yeast cells were loaded into microcavities: ring being parallel to the focal plane. For vertically alignment, the fission yeast cells were loaded into the microcavities by centrifugation. The detailed procedure for loading cells is described below (Fig. 3.9):

1. A 50 ml Falcon tube is loaded with a cylindrical piece (123) made of PMMA with an inner radius of 7 mm, outer radius of 26 mm and a height of 26 mm, acting as a resting platform for the coverslip (see Fig. 3.8 (1) and (2)).
2. The Falcon tube is then filled with 13 ml of EMM5S and ensured bubble free by gentle tapping.
3. The coverslip with microcavities is placed into the Falcon tube – *and should properly rest on the cylindrical piece. At this point, the level of media should be a bit above the coverslip. This will ensure that the further addition of media stays above the coverslip.*
4. 4 – 5 ml of culture from a flask of proper OD range is added into the Falcon tube. *The culture should be added carefully by placing the pipette at the center of the Falcon tube and not at the edges. Adding the culture close to edges can disturb the position of coverslip, which might allow the culture to go beneath the coverslip. Reduction in the volume of culture by any means can tremendously affect the filling percentage.*
5. The Falcon tube loaded with coverslip and culture is centrifuged at 2000 rpm for 5 min. The centrifugation is repeated at least 3 times where, after every centrifugation, the Falcon tube is removed and shaken gently. While cells enter the microcavities, large number of cells sediment on top of the microcavities. This will prevent cells from entering into the cavities in the subsequent centrifugation steps. *By gently shaking the Falcon tube, these sedimented cells can be disturbed and re-suspended in the media.*

6. After centrifugation, around 5 ml of media is removed from the Falcon tube. This allows easy removal of the coverslip from the Falcon tube. The coverslip on removal is observed under the microscope to check the filling percentage. If the filling percentage is too low, the centrifugation steps are repeated.
7. After removing the coverslip with microcavities from the Falcon tube, it is carefully loaded into the metal holder and rinsed with filtered EMM5S until all the cells lying on top of the microcavities are washed out.
8. The loaded cells can be further taken for studying the cytokinetic ring dynamics.
9. After completion of the experiment, the coverslips are removed from the metal holder and sonicated thrice in 70% ethanol. After drying, they can be stored in a clean Petri dish at room temperature for future experiments.

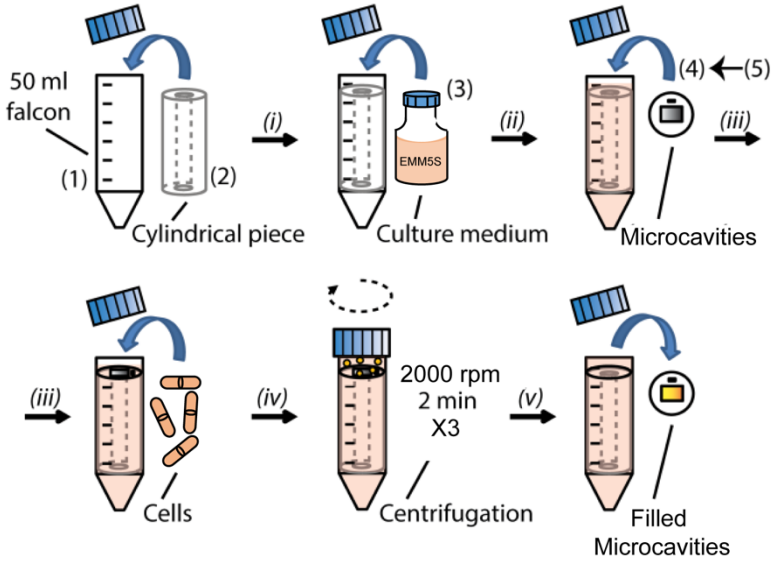

Figure 3.9. Schematic showing the steps for loading fission yeast into microcavities – adapted from (110): (i) A 50 ml Falcon tube loaded with the cylindrical piece is filled with EMM5S media, (ii and iii) The coverslip with microcavities in introduced into the Falcon tube and rested on the cylindrical piece, followed by addition of culture containing cells, (iv and v) The cells are forced to enter into the microcavities by centrifugation after which the coverslip is carefully removed.

3.3.5 Experiments with drugs and mutants

In order to probe the role of cytoskeletal proteins in the cytokinetic ring, their dynamics were observed on administering recommended doses of inhibitor and effector drugs or by studying specific mutants. For the drugs: acquisition was made either during incubation only, or acquired before and during incubation, followed by acquisition after washout. For adding drugs, proper concentrations of the drug were premixed in EMM5S and this premixed media was added to the holder after removing the currently existing media. This allowed for proper mixing of the drug which otherwise might lead to distributions of

varying local concentrations. For washout, the media with the drug was carefully removed and the sample was rinsed at least twice with fresh media before starting the acquisition. This step ensured complete removal of the drug from the sample. The list of drugs used, their target proteins and function, incubation time and their references are given in Table 2.

Drug	**Target protein**	**Function**	**Concentration [μM]**	**Incubation time**
Latrunculin A (124)	Actin	Sequestration of actin monomers and promotion of actin deployerization	1, 2 and 10	20 minutes before washout / acquisition up to 4 h in experiments without wash out
SMIFH2 (125)	Formin	Inhibition of formin Cdc12p	10	up to 3 h [no wash out]
CK 636 (126)	Arp2/3	Inhibition of Arp2/3	24	up to 3 h [no wash out]
C_7N_6 (MPA macrocyclic polyamines) (127)	Actin	Promotion of actin polymerization	300	up to 2 h [no wash out]
C_8N_6 (BPA – branched polyamines) (127)	Actin	Promotion of actin polymerization	100	up to 2 h [no wash out]

Table 3.2. List of cytoskeletal drugs and corresponding concentrations used for fission yeast.

We used a cps1 mutant strain: PN4461 (128), where the mutation was activated by switching the temperature to 36 ºC. The strain was grown as described in section 1.3.3.1 and was switched to 36 ºC two hours before the experiment. The mutation prevented the synthesis of 1,3 – β glucan synthase unit, a cell wall machinery which promotes septum formation during ring closure.

Strain	Genotype	Fluorescent markers	Source / Reference
DR 2	pxl1::kanMX6 leu1+::GFPpxl1+ rlc1-mCherry::natR	Rlc1-mCherry myosin II regulatory light chain GFP-Pxl1 paxillin-like protein	(109)
PPG 5054	h^+ pxl1::kanMX6 leu1+::GFPpxl1+ leu1-32 ura4-D18	GFP-Pxl1 paxillin-like protein Pxl1	(129)
519	h^- bgs1D::ura4+ P_{bgs1}+::GFP-bgs1+:leu1+ leu1-32 ura4-D18 his3-Δ1	GFP-Bgs1 1,3-beta-glucan synthase catalytic subunit Bgs1	(130)
561	h^- bgs4D::ura4+ P_{bgs4}+::GFP-bgs4+:leu1+ leu1-32 ura4-D18 his3-Δ1	GFP-Bgs4 1,3-beta-glucan synthase catalytic subunit Bgs4	Pilar Pérez
JW1348	h^+ nmt41-GFP-CHD (rng2)-leu1$^+$ rlc1-mCherry-natMX6 ade6-M210 leu1-32 ura4-D18	Rlc1-mCherry myosin II regulatory light chain CHD-GFP calponin homology domain	(121)
JW1349	h^+ nmt41-GFP-CHD (rng2)-leu1+ rlc1-tdTomato natMX6 ade6-M210 leu1-32 ura4-D18	Rlc1-tdTomato myosin II regulatory light chain CHD-GFP calponin homology domain	(121)
JM207	h^+ rlc1-mCherry::natR ade- leu- ura-	Rlc1-mCherry myosin II regulatory light chain	James B. Moseley
PN 4461	h^- cps1-191 rlc1-GFP::KanR	Rlc1-mCherry myosin II regulatory light chain	Nurse lab. Collection
DR 7	h leu1-32 his7-366 ura4D18 ade6-M216 myo2-E1 rlc1-mcherry::natR	Rlc1-mCherry myosin II regulatory light chain	This study

Table 3.3. List of fission yeast strains used in this study, their genotype and fluorescent markers (109).

3.4 Mammalian cell culture

In order to study the reversal in the direction of single cell migration and collective effects in monolayer, we used NIH3T3 fibroblast and MDCK (Madin-Darby Canine Kidney) epithelial cells from mouse and dog respectively. The NIH3T3 fibroblasts were acquired from ATCC and the different MDCK strains were kind gifts from different labs as mentioned in Table 4. These strongly adherent cell lines were grown on plastic Petri dishes in a humidified 37 ºC incubator with 5% CO_2. The experiments were performed by growing cells in glass coverslips which were maintained under similar temperature and humidity, but with Leibovitz's L-15 media that does not require buffering by CO_2. The percentage of serum in the media was varied depending on the requirements of the experiments. In general, the protocol for maintaining these cell lines are similar while differences exist in the types of media used and timings involved in the protocol, which are described below.

3.4.1 Media conditions

Both NIH3T3 and MDCK cell lines were grown in DMEM (Dulbecco's Modified Eagle Medium) media containing 5% and 1% glucose, 10% Bovine calf serum (BCS) and Fetal bovine serum (FBS), respectively. The NIH3T3 cells were replated on reaching ~ 50% confluency to prevent abnormal behavior in experiments due to activation of contact inhibition coming from confluent states. However, the MDCK were replated only on reaching ~ 80% confluency to maintain their collective behaviors. During replating, cells were detached from the "old" Petri dish using trypsin + 0.25% EDTA (Ethylenediaminetetraacetic acid) mixture and transferred to new Petri dishes. The incubation time with trypsin was strictly restricted to 3 min for NIH3T3 cells and 8 – 12 min for MDCK cells. Beyond these incubation times, the cells were either exhibiting abnormal behaviors like forming clumps or not viable. All experiments were performed with L-15 media. General storage conditions for the cell culture related substances were: DMEM and L-15 at 4 ºC, trypsin at -20 ºC and serum at -20 ºC.

3.4.2 Thawing and Freezing

***Thawing*:** The procedure for unfreezing is similar for both NIH3T3 and MDCK cells. The frozen stock is thawed by placing the Cryovial in 37 ºC water bath for few minutes.

Without delaying, the cells from the Cryovial were transferred to different Petri dishes with culture to new media ratio of 1:10. The higher percentage of new media dilutes the DMSO (Dimethyl Sulfoxide) coming from the frozen vial. In addition, plating them in different Petri dishes allows better spreading of the cells during the recovery from frozen state, and reduces the concentration of dead cells (if there are any). These plates are stored in 37 ºC for at least three hours. When the cells are settled and attached after three hours, the media is aspirated and rinsed and filled with new media. This step completely removes the DMSO and dead/unhealthy cells from Petri dish. This culture is grown over at least three passages before using for experiments.

***Freezing*:** For freezing 3T3 cells, different plates were grown until 50% confluency. The cells from these plates were trypsinized for three minutes and centrifuged after adding new media in the ratio of 1:2 (trypsinized cells to new DMEM). The supernatant is removed and cells are resuspended in new DMEM with approximately $10^4 – 10^6$ cells in 1.5 ml of freezing mixture (DMEM + 10% DMSO). This media with cells is aliquoted into Cryovials and stored in "Mr. Frosty" freezing container at -80 ºC. The iso-propanol in the freezing container reduces the rate of temperature decrease and prevents cell from from sudden freezing. After three days, the Cryovials are transferred to liquid nitrogen tank for storage. The same procedure is followed for freezing MDCK cells, except that the freezing mixture contains FBS instead of DMEM.

3.4.3 Culture conditions

The procedure for maintenance and replating of NIH3T3 and MDCK cells are described below. All substances required for replating are pre – heated to 37 ºC.

1. After reaching confluency (NIH3T3 ~ 50% and MDCK ~ 80%), the DMEM from the Petri dish is aspirated and rinsed with 1.5 ml of trypsin to remove unhealthy / unattached cells from the culture. This step prevents the dead and unhealthy cells being transferred to the next passage.
2. After quickly rinsing with trypsin, the plates were filled with trypsin and incubated (NIH3T3 – 3 min and MDCK – 8 to 12 min) at 37 ºC.
3. When cells are completely detached, cells with trypsin solution is mixed with new DMEM in a ratio of 1:2 and centrifuged at 1500 rpm for 4 min.
4. After centrifugation, the supernatant was removed and the cells were resuspended in appropriate volumes of DMEM. The volume used for resuspension corresponds

to the plate from which the cells were trypsinized. *After resuspension, the cells were extensively pipetted up and down to have separated single cells. These steps are critical for cell counting.*

5. Cell counting was done at this stage using Neubauer chamber (Celeromics) for using precise number of cells for experiments.
6. After removing corresponding volume of culture for experiments, the remaining culture is transferred to new Petri dishes at different dilutions. For NIH3T3, dilutions (culture to new DMEM) of: 1:20 and 1:40 were confluent in approximately 1 – 3 days. For MDCK, dilutions of: 1:20 and 1:40 were confluent in approximately 2 – 4 days. We systematically chose these dilution ranges since lesser dilutions were leading to abnormal behaviors.
7. The replated Petri dishes were stored in 37 ºC for further usage.

For MDCK strains with fluorescent markers, corresponding antibiotics were systematically added to the DMEM while making dilutions in step 6. See Table 4.

MDCK Strain	Antibiotic	Concentration	Source
E-cadherin – GFP	Geneticin	250 µg / ml	Nelson group
Actin – GFP	Geneticin	250 µg / ml	Nelson group
H2b – mCherry and E-cad – GFP	Hygromycin and Geneticin	200 µg / ml and 400 µg / ml	Silberzan group
Lifeact – mCherry and myosin heavy chain A (mhcA) - GFP	Hygromycin and Puromycin	600 µg / ml and 200 µg / ml	Roland group

Table 3.4. List of MDCK strains based on fluorescent markers, and corresponding antibiotics.

3.4.4 Preparation of samples for experiments

The experiments were done on 25 mm #1 glass coverslip, either plain or micropatterned. The plain coverslips were UV sterilized for 5 min before seeding cells. After cell seeding,

the coverslips were sandwiched in metal holders (described in section 1.3.4) or by PDMS holders (Fig. 3.10) in 3 ml Petri dishes for microscopy. The experiments were always done with L-15 media without antibiotics. A detailed procedure of sample preparation is given below:

1. At first, the coverslips were sandwiched into the sample holders (metal holder or 3 ml Petri dish): While mounting micropatterned coverslips, care should be taken to prevent the drying of fibronectin patterns on the coverslip. *This can be achieved by adding serum free L-15 to the mounted coverslip until cells are seeded. The usage of serum free L-15 prevents the saturation of passivated (pLL-g-PEG) surface which otherwise will happen if the serum is present. For mounting coverslips in the 3 ml Petri dish: First, a 15 – 20 µl drop of L-15 is placed on the Petri dish followed by the coverlip on the drop.* This will prevent the coverslip from moving due to capillarity. Then a PDMS holder is carefully placed on top of the coverslip which will additionally immobilize the coverslip.

2. Meanwhile, appropriate volume of media with specific concentration of cells is prepared (section 1.4.3, step 6). Throughout the thesis, the same initial seeding density was used for all the experiments: NIH3T3 cells: 2000 – 3000 cells; MDCK: 10^6 cells in 2 ml of media.

3. The corresponding volume of media with cells is added into the holder with the coverslip. *Then the media is pipetted up and down to prevent accumulation of cells within the coverslip.*

4. The sample is incubated at 37 ºC for the cells to settle and attach. Typically, 25 min incubation time was used for NIH3T3 cells and 1 h for MDCK cells.

5. After incubation time, the samples were rinsed thrice with L-15 to completely remove DMEM and filled with at least 2 ml of L-15. For experiments with NIH3T3 cells, the L-15 was supplemented with 1% BCS to reduce cell division rate, while for MDCK, the 10% FBS was used.

6. The sample is then taken for image acquisition.

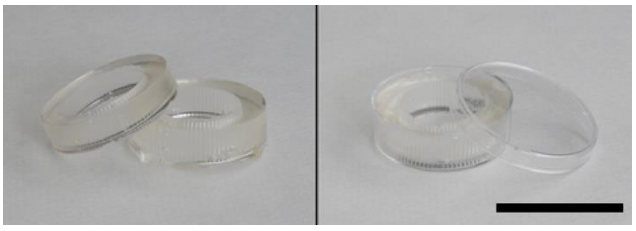

Figure 3.10. Images of PDMS holder (left) used for holding the coverslip in 3 ml Petri dishes (right). Scale bar 3 cm.

3.4.5 Immunostaining

Immunostaining is a classical technique that allows studying a sample (any cell line) in the frozen state with the help of fluorescence imaging. This technique is particularly helpful in studying assemblies of protein localization within cells like stress fibers and focal adhesion for example. In this procedure, the sample is fixed by ParaFormAldehyde (PFA) and antibodies (primary) are targeted to proteins of interest by permeabilization. Then another set of antibodies (secondary) tagged with fluorophores are targeted against the primary antibodies. By this method, an architecture of protein-antibody-fluorophore is built which allows to study the corresponding protein localization several times. The steps involved in immunostaining can be performed at room temperature on lab bench. In the protocol described below, after each step, the sample is washed thrice in 1x PBS with 5 min interval between each washing.

1. First, the DMEM from the sample holder is aspirated and the sample is treated with 2 ml of 3% PFA solution pre-heated at 37 ºC, for 17 min, followed by washing. *PFA can be prepared in large quantities and stored in -20 ºC up to two months.*

2. At this step, the sample can be stored in 1x PBS at 4 ºC up to 12 h, although immediate staining gives better results.

3. The sample is then permeabilized with 2 ml of 0.5% Triton for 3 min, followed by washing. The treatment should not exceed 3 min, which otherwise can damage the sample.

4. Then the sample is treated with 2 ml of 50 mM NH_4Cl for 10 min, followed by washing. This step quenches the auto-fluorescence (green emission) of PFA and is needed only if the sample contains cells transfected with GFP or if the secondary antibody is tagged to GFP.

5. Before immunostaining, the permeabilized sample needs to be passivated for regions other than the targeted proteins to increase the targeted binding of antibodies. Hence, the sample is treated with 2 ml of 5% BSA for 1 h, followed by washing.

6. For antibody staining: a clean Parafilm sheet is flattened on to the bench by few drops of water. 100 µl of BSA mixed with appropriate concentration of primary antibody is dropped on the Parafilm after removing the protective paper. The sample coverslip is now placed on the antibody solution with the cells facing the drop. The coverslip is left undisturbed for 1 h followed by washing.

7. As described in the previous step, the sample coverslip is placed on a 100 µl drop of BSA mixed with appropriate concentration of secondary antibody. The coverslip is thoroughly washed after 1 h of incubation.
8. At this point, the sample can be stained for nucleus by treating the coverslip with 2 ml of 1 µg / ml DAPI (4',6-diamidino-2-phenylindole) for 5 min, followed by washing.
9. The coverslip is then mounted on a labelled microscope slide with 15 µl of 50:50 glycerol – PBS solution. After careful mounting, the edges of the coverslip are sealed with nail polish and dried before storing it in 4 ºC for imaging.

3.4.6 Serum free condition

To study the dynamics of MDCK monolayer in serum free condition (for reduced proliferation rate), the following steps were followed:

1. After trypsinization (step 2 of section 1.4.3), the cells in trypsin were mixed with serum free L-15 and proceeded to centrifugation.
2. After centrifugation, the collected pellet of cells is resuspended in serum free L-15 and the cell counting is done.
3. Appropriate volume of the serum free L-15 (for 10^6 cells) is mixed with fresh serum free L-15 to make a volume of 2 ml. *These three steps should be performed without delays, since cells suspended in serum free media can easily form clumps, severely affecting the seeding cell density and the formation of monolayer.*
4. This 2 ml of media is then added to the coverslip mounted on Petri dish or metal holder, and the sample is left undisturbed for 1 h at 37 ºC.
5. After 1 h, the sample is checked for attached cells and proceeded to imaging, *without any rinsing. If the majority of cells are not attached in 2 h, a fresh sample should be prepared starting from step 1.*

3.4.7 Experiments with inhibitor drugs

To probe the role of cytoskeletal proteins in the pulsations of monolayer, we used recommended doses of inhibitor drugs specifically targeted for these proteins. The

acquisition, addition and washout procedures were done exactly as previously described in section 1.3.5, except that L-15 (supplemented with 10% FBS) was used for dilution of drugs and for washing out drugs. The list of drugs used, their target proteins and function, incubation time and their references are given in Table 5.

Drug	**Target**	**Function**	**Concentration [µM]**	**Incubation time**
Latrunculin A	Actin	Sequestration of actin monomers and promotion of actin deploymerization	1	12 – 14 h before washout
Blebbistatin	Myosin II	Inhibition of ATPase activity	100	12 – 14 h before washout
C3 transferrase	Rho proteins (A, B, C)	Inhibition of Rho proteins	0.04	12 – 14 h before washout
Y - 27632	Rho-associated protein kinase (ROCK)	Inhibition of ROCK	50	12 – 14 h before washout
SMIFH2	Formin	Inhibition of Formin	40	12 – 14 h before washout
CK 666	Arp2/3	Inhibition of Arp2/3	100	12 – 14 h before washout
Nocodazole	Microtubules	Depolymerization of microtubules	10	12 – 14 h before washout
Mitomycin C	DNA (Deoxy ribonucleic acid)	Replication arrest	32	12 h before washout

Table 3.5: List of cytoskeletal drugs used on MDCK monolayer and their corresponding concentrations (131–133).

3.5 Optical setups and Imaging conditions

The different optical setups and configurations that we used for observation and imaging of microfabricated structures on wafers to the dynamics of molecules, to cells, and collection of cells is detailed below.

3.5.1 Microscopes for observation

We used an Olympus SZX7 stereomicroscope equipped with a combination of 10x eyepiece and a DF PL 1.5x objective, for checking the quality of microstructures on the master and on PDMS stamps. The reflected LED illumination and the high magnification range 8x – 56x of the microscope enables easy inspection of the quality of microstructures.

A Nikon eclipse TS100 inverted microscope equipped with Nikon 4x (0.13 NA), 10x (0.25 NA), 20x (0.4 NA), 40x (0.55 NA) phase contrast objectives were used to inspect the quality and confluency of the cell culture in Petri dishes before using for experiments.

3.5.2 Epifluorescence microscopes

For phase contrast and fluorescence imaging, three different custom mounted epifluorescence setups were used. The setups were mounted on an optical table (Newport RG bread board or Kinetic systems- vibra plane) with an inverted Olympus CKX41 microscope. The microscopes were enclosed within a temperature controlled chamber either custom designed and regulated by Airtherm ATX or using the "The Cube & The Box" from Life Imaging Services. The samples were mounted either on a manual stage or on a Marzhauser Wetzler stage with a stepper motor (MW Tango), enabling multi-point acquisitions. To prevent phototoxicity during time-lapse acquisitions, the optical path to the samples from white light and fluorescence lamp (Xcite Metal-halide lamp or OSRAM mercury arc lamp) were controlled by shutters (Uniblitz VCM-D1 / VMM-D1 or ThorLabs SC10) in synchrony with a cooled charge-coupled device (CCD) (Hamamatsu C4742-95 / C8484-03G02 or Scion corporation CFW1612M). The devices were controlled by custom made scripts using either Hamamatsu Wasabi or Micromanager interfaces. The objectives were selected based on the size of features studied (molecular / cellular / supra-cellular) and the required field of view. Studies on cytokinetic rings and focal adhesions were done using: 60x (1.45 Numerical Aperture (NA), oil) Plan Apo or

40x (0.55 NA, air) Olympus objectives. Direction reversal in single cell migration and monolayer dynamics were studied mainly using 4x (0.13 NA) phase contrast objective and occasionally by 10x (0.25 NA) or 20x (0.4 NA) phase contrast objectives. A wide range of acquisition rates from 30 s to 30 min were chosen based on the requirement of the study.

To prevent evaporation of the media, the samples were covered with a clean glass Petri dish or by adding 2 ml of mineral oil (Sigma Aldrich). In addition, the chamber was humidified with constant storage of water.

3.5.3 Sanyo incubator

We used an incubator microscope – SANYO MCOK-5M, integrated with a 10x phase contrast objective, and a Sentech XGA color CCD to scan multiple samples illuminated by LED. The unit is controlled by an MTR-4000 software which automatically regulates the temperature (37 ºC), CO_2 (5%) and humidity (95%) to corresponding set values. The motorized stage can accept up to 12 samples of 3 ml Petri dishes and can run time-lapse acquisitions with multi-points on each sample.

3.5.4 Confocal microscopes

A variety of confocal systems were used in this thesis depending on the sample and nature of acquisition like intensity of sample and corresponding bleaching, type of mounting (on PDMS / glass coverslip), rate of acquisition and two – dimensional (2D) imaging or three- dimensional (3D) reconstruction. Also some setups were specifically chosen for performing operations like ablation and FRAP.

3.5.4.1 Spinning disk confocal

High resolution acquisition of cytokinetic rings to capture the cluster rotation was done exclusively on spinning disk confocal system. This allowed acquiring quality images of rings from cells in the PDMS microcavities, with an exposure time of 100 – 500 ms and a high acquisition rate (500 – 700 ms) with two fluorescence channels. The setup consists of a Yokogawa CSU22 spinning disk unit mounted on a Leica DMI6000 inverted microscope equipped with Andor iQ 1.9.1 acquisition system and a cooled CCD camera

(Andor iXon 897 BI). The spinning disk rotates at a chosen speed between 1500 – 5000 rpm. The sample was mounted on x – y motorized and axial (z) piezo driven stage, and imaged with excitation lasers of range 405 nm, 488 nm, 560 nm and 635 nm. The objectives used were: 100x HCX PL APO CS oil objective (1.4 – 0.7 NA, Leica) and 63x HCX PL APO CS oil objective (1.4 – 0.6 NA, Leica). Experiments were performed with a temperature control unit (Tokai Hit Co, Ltd Stage Top Incubator).

3.5.4.2 Line scanning confocal systems

3.5.4.2.1 Leica SP5-MP and SP8-MP

The cytokinetic rings of mammalian (HeLa) cells loaded in egg cups were imaged by Viktoria Wollrab using the upright SP5 and SP8 systems. The upright alignment and the digital zoom feature in these systems allowed visualization of the clusters which was otherwise difficult due to the PDMS layer. The SP5-MP and the SP8-MP setups were based on Leica DMI6000 CFS upright microscope equipped with a Leica Application Suite Advanced Fluorescence (LAS AF) 2.6.3.8173/LAS AF 3.1.2.8785 acquisition system with photo-multiplier tube (PMT) and hybrid (HyD) detectors. The scanning was done at 400 Hz with either unidirectional or phase corrected bidirectional mode. A water immersion HCX APO L 63x (0.90 NA) W U-V-I Leica objective was used for imaging.

The laser ablations on mammalian and fission yeast were done with the same setups with a special FRAP module. To achieve point ablation, a 25X HCX IRAPO L water objective (0.95 NA, Leica) and an InfraRed (IR) (Coherent Chameleon) 80MHz pulsed femtosecond laser with pre-compensation (Coherent Inc, Santa Clara, California, USA) were used.

The fluorescence recovery after photobleaching (FRAP) experiments on HeLa cells were done by Viktoria Wollrab using the Leica TCS SP2 AOBS MP setup based on a Leica DMIRE2 microscope, equipped with a PMT detector and a 63x HCX PL APO oil (1.4 NA, Leica) objective.

The FRAP experiments on fission yeast were performed by Daniel Riveline at the Rockefeller University using a DeltaVision acquisition system (Applied precision) with a temperature control unit (WeatherStation), and with a cooled CCD camera (CoolSNAP HQ / ICX285) and a 100 x, UPLS Apo (1.4 NA, Olympus) oil objective.

All experiments were performed in a temperature controlled environment (Life Imaging Services “The Cube & The Box”).

3.5.4.2.2 Leica SP8 X

A very precise z-stack acquisition system was needed for studying the variation in height of the cells during pulsations in MDCK monolayer. In order to avoid aberrations due to defocusing which might lead to error in the height calculation, we used the Leica SP8 X confocal system equipped with a Super Z galvanometric stage, with a minimal z step size of 0.3 µm on using a 63x (1.4 NA, oil) objective. In addition, the stage is controlled by an auto-focus algorithm called Leica Adaptive Focus Control (AFC) which prevents defocusing in long term experiments on multiple positions. This further allowed "crisp" 3D reconstructions of monolayer sheets. The SP8 X setup is mounted with an inverted Leica DMI6000 microscope equipped with a Leica Application Suite X acquisition system with PMT and HyD detectors. The scanning was done at 400 Hz with unidirectional mode. The Leica objectives used were: HC PL APO CS2 20x (0.75 NA) air, HC PL APO CS 40x (1.3 NA) oil and HC PL APO CS2 63x (1.4 NA) oil. All experiments were performed under temperature controlled environment using an Oko lab stage top incubator.

3.6 Software packages

The extraction of the acquired images was done with ImageJ/Fiji (frequently updated) or with Wasabi software (Hamamatsu) or with Leica Application Suite (Advanced Fluorescence Lite, 2.6.0 build 7266 or LAS X.

For Image processing and analysis, a variety of ImageJ/Fiji plugins and functionalities were utilized. The list of non-default plugins utilized for different purposes are listed in Table 6, while the rationale and methods are described in the appropriate "Results sections".

The computation of velocity field and corresponding derivatives like divergence and shear were done using the Particle Image Velocimetry (PIV) technique utilizing PIVlab open source software (134). The correlation analysis and the structure factor based spectral analysis were done using a custom-made code developed by Mandar M. Inamdar, IIT Mumbai. A detailed description on the choice of parameters for PIV is discussed in the appropriate results section.

The numerical data analysis and plots were generated by Origin Lab, Microsoft office Excel and MATLAB R2014b.

ImageJ / Fiji plugin	Source
ITCN nuclei counter	http://rsb.info.nih.gov/ij/plugins/itcn.html
Manual tracking	http://rsbweb.nih.gov/ij/plugins/track/track.html
Polar stack auto 2	Developed by Daniel Riveline
Stack register	http://bigwww.epfl.ch/thevenaz/stackreg/
Stack reverser	http://rsb.info.nih.gov/ij/plugins/reverser.html
Hyperstack topography	Developed by Marcel Boeglin, IGBMC Imaging facility
Untilt stacks	*https://imagej.nih.gov/ij/plugins/untilt-stack/index.html*
Z color coded stack	Cookbook functionality, Fiji

Table 6: List of non-default ImageJ plug-ins used for image analysis.

4. Still and rotating myosin clusters as determinants for cytokinetic ring constriction

4.1 Introduction

In this chapter, I will discuss in detail about how the self-organizations of actin and myosin drives cytokinetic ring constriction in two different systems: fission yeast and mammalian cells. Using a novel device, we reveal distinct and unknown organizations of acto-myosin during the ring constriction process. We describe the dynamics of acto-myosin within the ring and its role in stress generation leading to constriction. In addition, we propose a mean-field description of the microscopic equations – based on filament polarity and filament-motor interactions rules, to capture the mesoscopic properties of the ring. Consequently, we highlight the specific parameters leading to distinct organizations of acto-myosin and corresponding functions in fission yeast and in mammalian rings.

This work is published in the Nature Communications journal: Wollrab, V., R. Thiagarajan, A. Wald, K. Kruse, and D. Riveline. 2016. Still and rotating myosin clusters determine cytokinetic ring constriction. Nat. Commun. 11860: 1-9, and the article is attached in the appendix. This chapter will be complementary to the published article and will include detailed descriptions of the results in addition to other interesting results that were not included in the publication. This chapter contains references to the supplementary figures of the paper which are also attached in the appendix.

In this chapter, the results of fission yeast and mammalian rings are explained in parallel. The chapter is organized as follows: I will begin with the problem statement, followed by description of strategies used for complete visualization of cytokinetic rings in a single acquisition. First, I will describe the global properties of the ring. This will include the general constriction behavior and material balance in the ring measured by changes in intensity. The material balance results will be followed by description of structures that lead to material extrusion from the ring, specifically in fission yeast. Then I will explain the distinct clustered organization of acto-myosin in both systems from the measurements of cluster characteristics. Then, I will explain the significance of acto-myosin organization in regulating the cluster characteristics and its relationship with the ring constriction. This will be followed by Fluorescence Recovery by Photobleaching (FRAP) experiments that will highlight the rapid turnover of myosin between the ring and cytoplasm in both systems. Then, I will proceed with the explanation of our theoretical model from which the dynamic equations and force balance are obtained for the filament-

motor interactions. This will also include the details of parameters leading to instability and phase transition. The phase transition and the stress profiles obtained from the model are then experimentally verified in fission yeast and mammalian rings using inhibitor drugs and ablation. Finally, I will finish this chapter with discussion of the results and major conclusions.

This project is a result of team effort. Daniel Riveline designed the device and initiated this study on fission yeast cytokinetic ring, during his sabbatical stay at the Rockefeller University. I continued this project on fission yeast on my arrival in the lab and collaborated with Viktoria Wollrab (former PhD student in the lab), who had meanwhile extended the study in mammalian cells also (135). All the experiments and analysis on mammalian cells were performed by Viktoria Wollrab. The fission yeast experiments were done by myself and by Daniel Riveline. The laser ablation experiments in fission yeast were performed together by myself and Viktoria Wollrab. The theoretical framework was developed by Karsten Kruse from Saarland University, who further improved it with Anne Wald, a master student in his group.

4.2 Cytokinetic ring – a complex acto-myosin structure

The Cytokinetic ring is an assembly of acto-myosin proteins that undergoes constriction for physical separation of cells. In general, biochemical pathways that regulate the cytokinesis process have been identified and described (136, 137). These pathways regulate protein activity to ensure precise spatio-temporal coordination during the ring constriction process (136). But, they do not explain or specify an interaction rule between actin filaments and myosin motors that leads to constriction. In other words, it is easy to describe the contraction and extension mechanism of a well-organized structure like sarcomere, where the polarity of actin filaments is known. Whereas in the case of cytokinetic ring, the scenario is far too complex to comprehend the mechanism leading to ring constriction: the ring involves thousands of actin filaments that are randomly oriented and interacting with myosin motors. In this complex scenario, it is not clear how the interaction between all these randomly oriented filament collections is coordinated to generate constriction. Similarly, the mechanism that breaks the symmetry towards constriction is also not clear. In order to answer these questions, we investigated the spatio-temporal dynamics of acto-myosin in the cytokinetic ring of two systems: fission yeast and mammalian (HeLa) cell, where fission yeast has a rigid cell wall and the mammalian cell has a well-defined cortex. We coupled these experimental results with

our theoretical model to establish a common interaction mechanism that drives the cytokinetic ring constriction in both systems.

4.3 Complete visualization of cytokinetic ring

We used fission yeast and mammalian (HeLa) cells, labelled with fluorescent markers for different proteins that allowed us to visualize their organization and dynamics during the cytokinetic ring constriction process. The ring constriction in these fluorescently labelled strains were imaged after loading the cells into microcavities that allowed complete visualization of the ring (106–108).

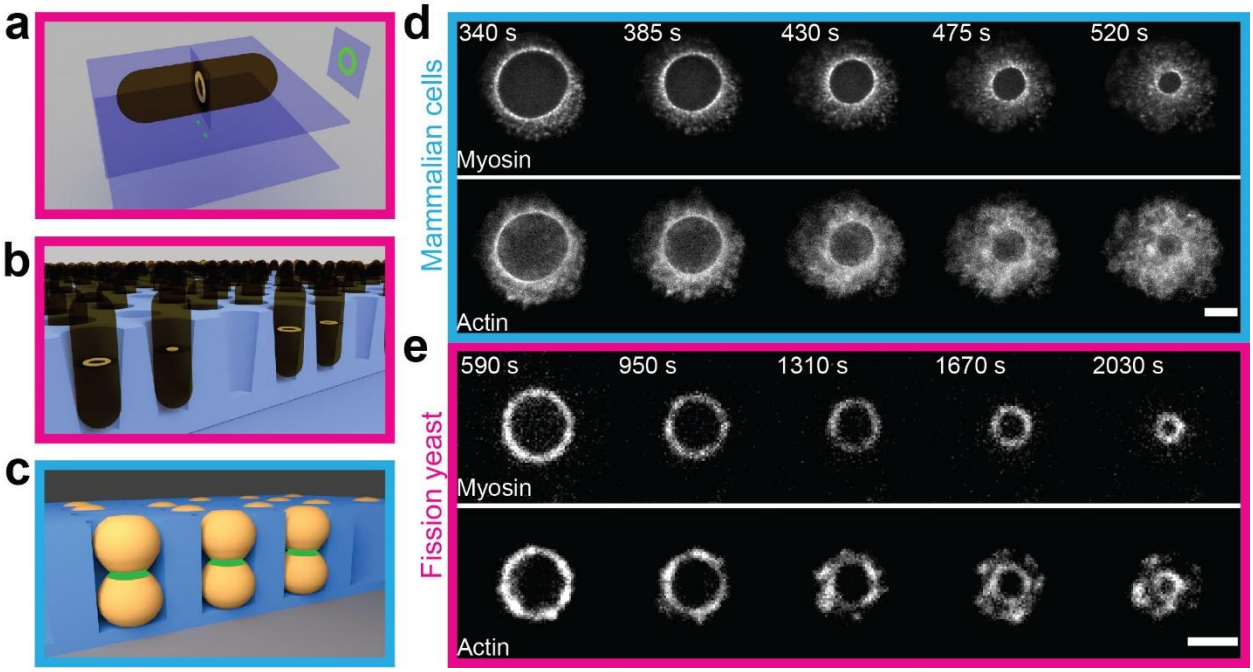

Figure 4.1. Visualizing cytokinetic rings in microcavities. (a) Fission yeast ring oriented perpendicular to the focal plane – ring appears as two dots. (b) Fission yeast and (c) mammalian cells loaded into microcavities in vertical fashion – rings are parallel to the focal plane. Time-lapse of mammalian (d) and fission yeast (e) ring constriction shown in myosin and actin: RLC1-GFP / Lifeact-mCherry and RLC1-tdTomato / CHD-GFP respectively. Scale bar (d) 5 μm and (e) 2 μm (109).

4.3.1 Fluorescent labels for visualizing cytokinetic ring constriction

We used fission yeast strains in which the Calponin Homology Domain (CHD) was tagged with GFP and the Regulatory Light Chain (RLC1) of myosin was tagged with mCherry or tdTomato (121). For mammalian rings, we used a HeLa cell line stably

transfected with Lifeact-mCherry and Myosin Heavy Chain (MHC) tagged with GFP. These fluorescent markers, allowed us to observe and quantify the dynamics of acto-myosin throughout the constriction process (Fig. 4.1 d and e, Movies 4.2 and 4.3). We also observed cells labelled for other proteins (S.Fig 3 and 8). To simplify the comparison of acto-myosin organization and dynamics between the two systems, we will use the terms actin (instead of CHD-GFP and Lifeact-mCherry) and myosin (instead of RLC1-mCherry/tdTomato and RLC1-GFP) throughout the text. Similarly, pink and cyan boundaries will be used to indicate data from fission yeast and mammalian rings respectively, in all the figures.

4.3.2 Loading cells in microcavities

The conventional orientation of the cytokinetic ring - perpendicular to the focal plane, prevents complete observation of the ring, thus limiting insights into its organization (Fig. 4.1 a). By orienting cells in vertical fashion, we visualized complete cytokinetic rings (Fig. 4.1 b and c) (106).

The device is ~ 1 cm^2 in dimension and contains ~ 10^4 of microcavities. The diameter and height of the cavities were adjusted to ensure proper trapping of cells (see methods section 3.1.3.1). The spherical shape of mammalian cells ensured firm trapping in the cylindrical cavities (107). However, in the case of fission yeast cells, the cylindrical cavities were not firmly holding the cells due to their oblong shape. In some conditions, this leads to potential movements of the cells within the microcavities which made the analysis of acto-myosin dynamics difficult. Hence we modified the microcavities with a "V" shaped bottom that allowed firm trapping of fission yeast without any movements (108). In addition, we optimized the protocol for maximal filling percentage in the microcavities, to observe ring constrictions in several cells simultaneously (Movie 4.1). This allowed us to increase statistics on the global properties of the ring like constriction speeds and fluorescence intensities (see methods section 3.1.3.1).

After loading the cells in microcavities, as a first step, we checked if the cells were behaving "normally" in the microcavities – by plotting the ring diameter as a function of time, to compare ring constriction in microcavities and on flat surfaces. We found that constriction behavior was not affected by vertical orientation and the rate of constriction was conserved on flat coverslips and microcavities, for both fission yeast and mammalian cells (S.Fig. 2). In addition, the cell cycle times remained unchanged in this condition.

4.4 Global properties of the cytokinetic ring

After checking the proper constriction behaviors of the ring in microcavities, we first measured the general global properties of the ring in both fission yeast and mammalian cells. We measured the rate of constriction to compare the size and time required for constriction between the two systems. Then to understand the change in material (actin and myosin) density in fission yeast and mammalian rings during constriction, we measured the intensities of the actin and myosin in the ring. Along this line, specific to fission yeast, we also studied the radial extrusions emanating from the ring, which we found to play a role in material extrusion during constriction.

4.4.1 Rate of Constriction

4.4.1.1 Fission yeast ring constriction

During constriction, the fission yeast ring is reduced from a diameter of ~ 3.5 µm to 0.5 µm in ~ 40 min at 27 °C (Fig. 4.2 a). The measurements were made only until 0.5 µm since the ring was not resolvable below this diameter. After formation and before initiation of constriction, the ring diameter remains constant at ~ 3.5 µm for ~ 15 min. After the initiation of constriction, the speed increases linearly until reaching ~ 1 µm diameter before decreasing again. The speed during this linear phase (~ 70 nm/min) was consistent with the previous literature (124).

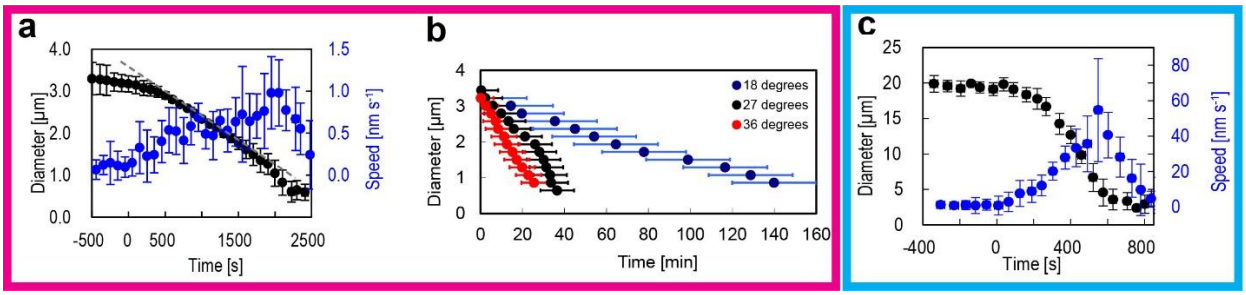

Figure 4.2. Plots showing ring constriction for fission yeast (a and b) and mammalian cell (c). (a) Ring diameter (black) and constriction speed (blue) as a function of time at 27 °C (n = 20). The dashed grey line indicates linear regime of constriction (109). (b) Ring diameter as a function of time at 18 °C (blue), 27 °C (black) and 36 °C (red). (c) Ring diameter (black) and speed (blue) as a function of time at 37 °C (n = 14) (109). Error bars indicate standard deviation.

The constriction rate of fission yeast rings is strictly dependent on temperature: ~ 20 nm/min at 18 °C, ~ 70 nm/min at 27 °C and ~ 100 nm/min at 36 °C as previously reported (Fig. 4.2 b). The constriction rates increased at higher temperatures and decreased at

lower temperatures. In this study, all the fission yeast experiments were done at 27 °C unless mentioned otherwise.

4.4.1.2 Mammalian ring constriction

In the case of mammalian rings, the process of constriction reduced the ring from ~ 20 μm to 2 μm in ~ 500 s while at 37 °C. The speed increases linearly until reaching a diameter of 5 μm followed by a decreasing trend before the diameter stalls at 2 μm (Fig. 4.2 c). All the mammalian ring experiments were done at 36 °C.

Both fission yeast and mammalian rings show an increase in velocity after the initiation of constriction. However, the velocity of constriction in mammalian rings is several folds higher than fission yeast. This leads to the constriction of larger diameter in a much shorter time i.e. 20 μm to 2 μm in 500 s in mammalian cells as opposed to 3.5 μm to 0.5 μm in 40 min in fission yeast. (Fig 4.3 a and c). For the analysis, the outer diameter was taken for measuring the constriction process in both systems.

4.4.2 Material balance in the ring: measured by fluorescent intensities of actin and myosin

The reduction in diameter questions the fate of material within the ring and, in turn the magnitude of stress generation. To check the variation in acto-myosin density during constriction, we measured the fluorescent intensities of actin and myosin in fission yeast and mammalian rings. From the fluorescent intensity measurements, the total intensity gives the estimate for the total amount of molecules and the mean intensity gives the concentration of molecules in the ring.

4.4.2.1 Fission yeast ring intensity

In fission yeast, we measured the intensity of the "doughnut" area by subtracting the inner diameter from the outer. We found that total amount of acto-myosin molecules decreased after the onset of constriction (Fig. 4.3 a). However, while the myosin concentration increased, the concentration of actin stayed almost constant throughout the constriction (Fig. 4.3 b).

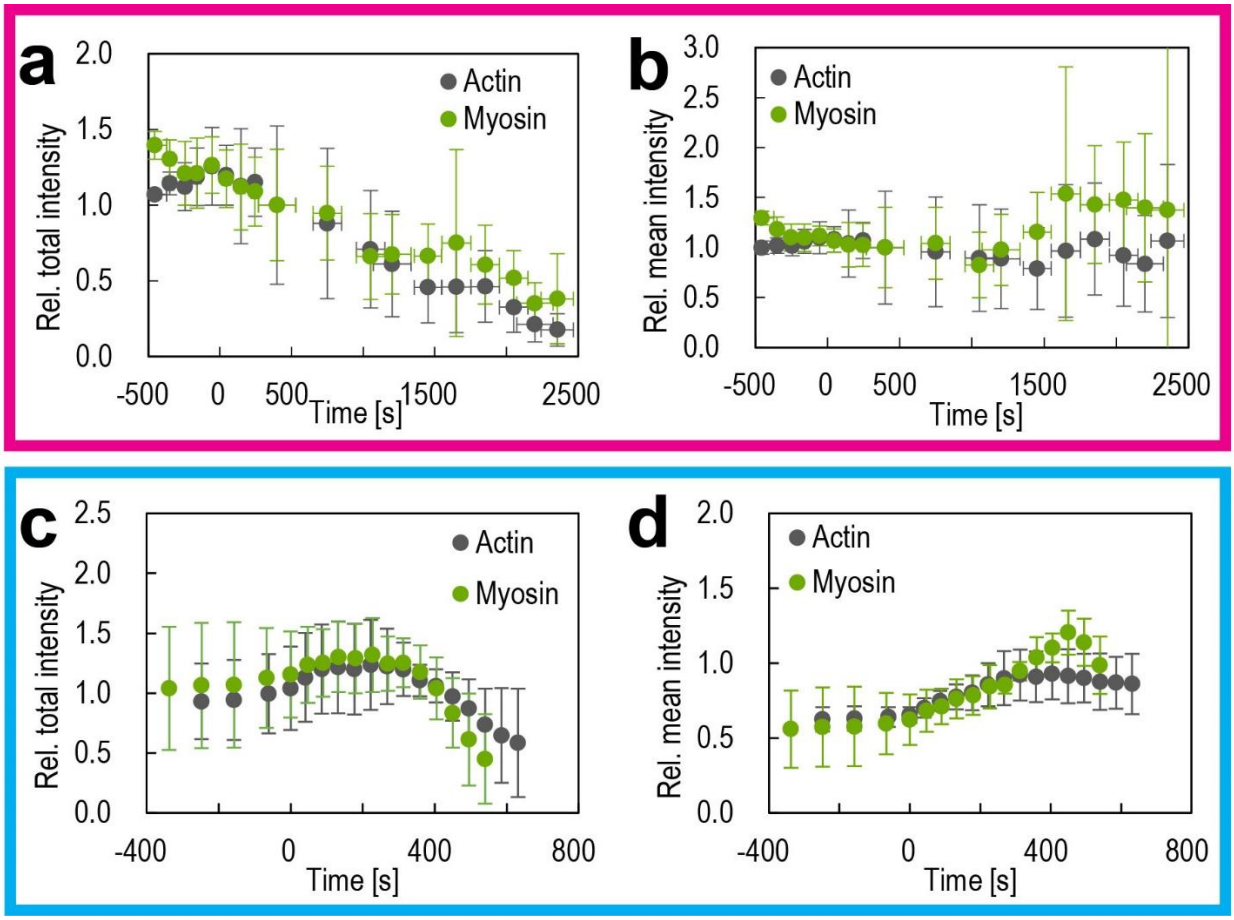

Figure 4.3. Relative mean (a) and total (b) intensity of myosin and actin in fission yeast rings. The intensity is normalized for cells at a diameter of 3.1 μm. The intensity measurements were made from individual snapshots of rings for the time period of 300 s – 2500 s. (n = 241 for both actin and myosin). Relative mean (c) and total (d) intensity of myosin and actin in mammalian rings. The intensity is normalized for cells at a diameter of 10 μm. (n = 10 for myosin and n = 6 for actin). The intensities before constriction were acquired from time-lapse movies of individual rings (n = 3). Error bars indicate standard deviation. Time t_0 in all the plots represents the onset of constriction. Background subtraction was done in both cases (109).

4.4.2.2 Mammalian ring intensity

In the case of mammalian cells, the line intensity was measured by matching the thickness of the line with the ring thickness. We found that total amount of acto-myosin molecules decreased after the onset of constriction (Fig. 4.3 c). However, the concentration of acto-myosin increased during the constriction process (Fig. 4.3 d).

In both fission yeast and mammalian rings, the total amount of acto-myosin molecules decreased, while the myosin concentration increased. But the increase in concentration of myosin in both systems were 20% only. The decrease in total intensity of acto-myosin and a minor increase in mean intensity suggests that acto-myosin is removed from the

ring during constriction process. Usually the intensities of acto-myosin are considered as indirect measure of generated stress (138). However in this case, it is not clear how a minimal increase (20%) in the concentration of myosin, generates enough stress that can be accounted for constriction of the whole acto-myosin network in the fission yeast and mammalian rings.

4.4.3 Material extrusion from the ring in fission yeast

Loss of material (acto-myosin) – inferred from the decreasing total intensity, should be extruded from the ring. Surprisingly in fission yeast, in support of the decrease in total intensity of myosin, we were able to visualize filamentous structures of myosin emanating from the ring towards the end of constriction (Fig. 4.5 a). We coined these structures "*Radial arms"*.

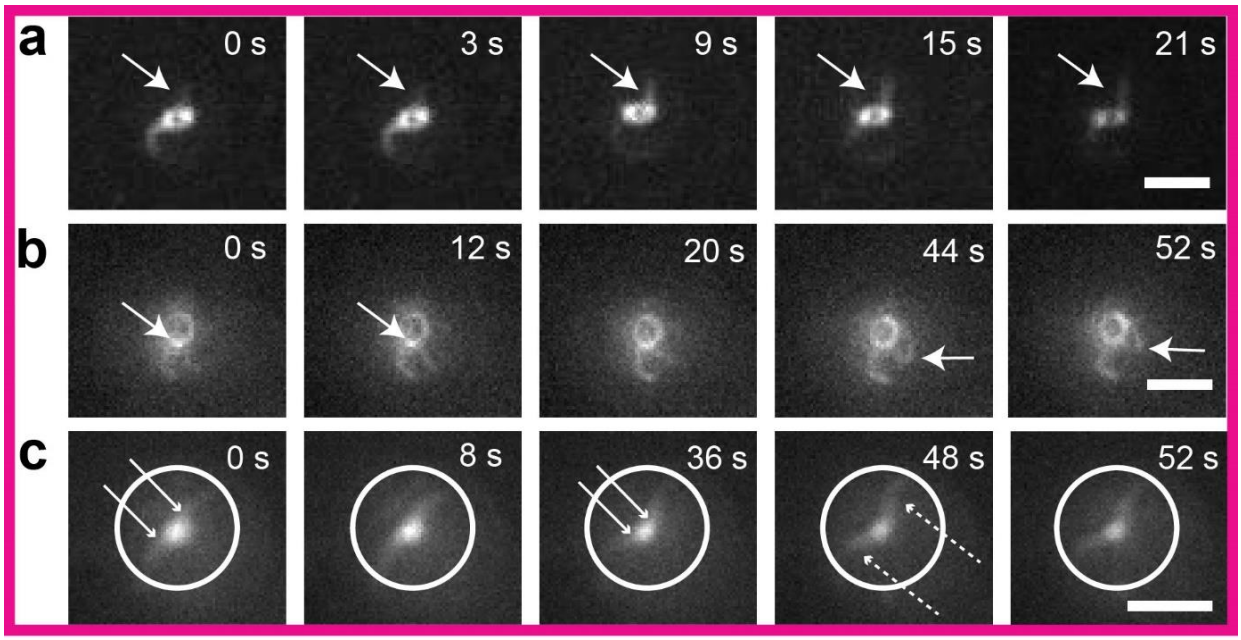

Figure 4.4. Radial arms. (a) Time-lapse images of arm elongation. Arrows indicate the arms. (b) Time-lapse series showing a bright cluster at the point of attachment to the ring (first two images) and buckling of arm (last two images), Arrows indicate the bright cluster and arm buckling. (c) Time-lapse series of a ring with two extending arms buckling when they reach the cell periphery. The white circle indicates the cell periphery. The arrows indicate arms and the dashed arrows indicate buckling. Scale bar 2 μm. The ring is visualized by myosin in all images.

We were able to visualize simultaneously up to four arms in the same ring. After appearance, the arms were elongating radially (Fig. 4.4 a) until they buckled when they reach the periphery / cell wall (Fig. 4.4 c, Movies 4.4 and 4.5). They were dynamic and rotated in both clockwise and counter-clockwise directions (Fig. 4.5 b and c, Movie 4.6).

We extracted the speed of the arms due to rotation and found that it was approximately constant throughout constriction (Fig. 4.5 f). This further emphasizes the dynamic nature of acto-myosin in the ring.

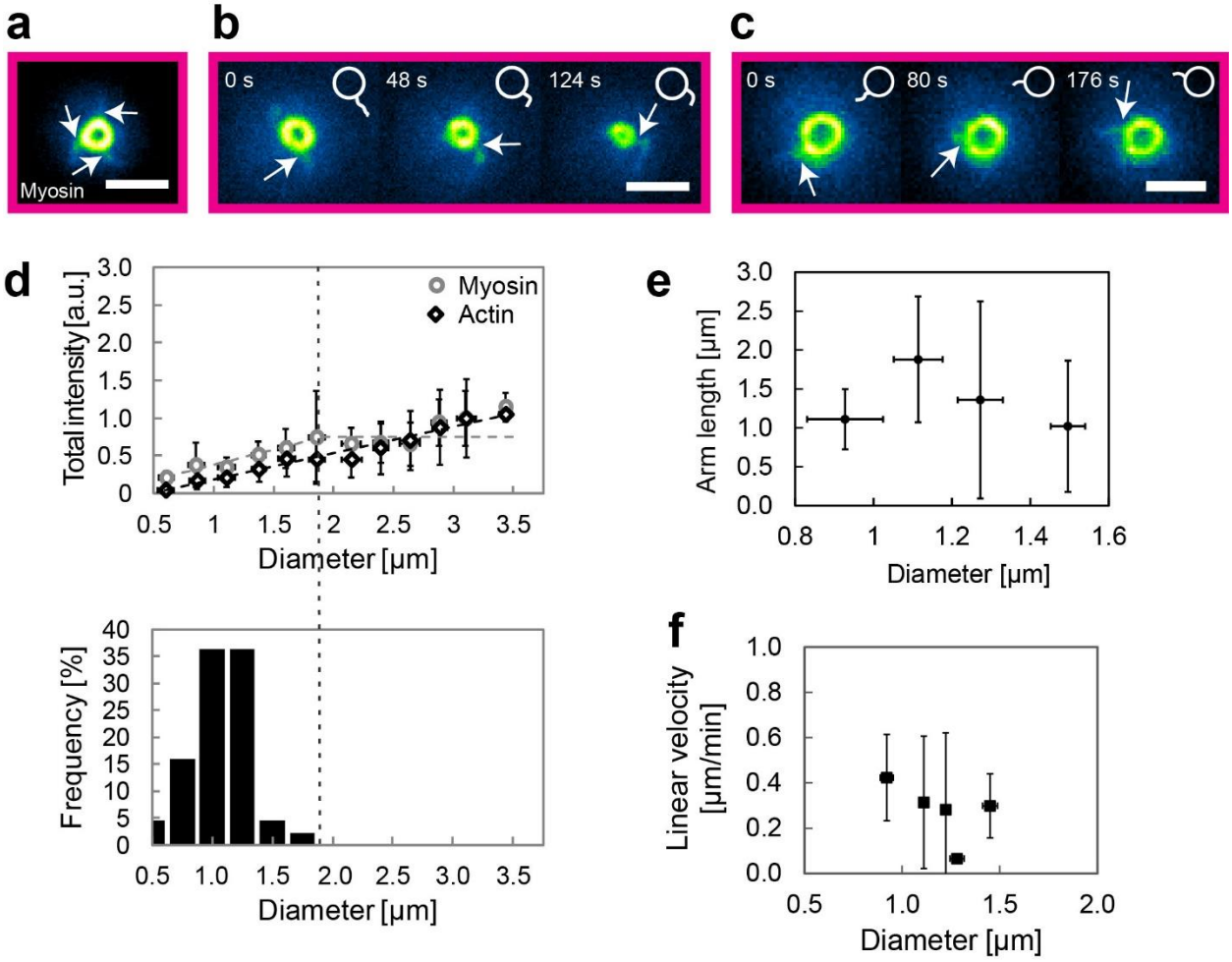

Figure 4.5. Radial arms of myosin. (a) Snapshot of a ring, simultaneously showing three arms. (b) and (c) Time-lapse images showing rotation of arms in counter-clockwise (b) and clockwise directions (c). The inset on the top-right represents the corresponding arm location. Scale bar 2 μm. Arrows indicate the position of arms in (a-c) (109). (d) Correlation between the appearance of arms (bottom) and the intensity of the ring (top). Top – Total intensity of the ring as a function of diameter (n = 241 for both actin and myosin). This plot is similar to the plot in (Fig 4.4 a), except for the parameter in x-axis. Bottom – Frequency (how often a ring at particular diameter exhibits an arm) of arms corresponding to each diameter (n = 44). The arms start appearing at a diameter of 1.5 μm. This regime (diameter < 1.5 μm) at which the arms start to appear correlates with the decrease in total intensity of myosin (indicated by the dotted line). (e) Length of arms as a function of diameter (n = 44). (f) Linear velocity of arms as a function of diameter (n = 5). The dashed lines in (d) are guide for eyes.

The arms start to appear only when the rings reach smaller diameters (~ 1.5 μm) (Fig. 4.5 d - bottom). We found that maximum percentage of cells exhibited arms in the diameter range of ~ 1 μm. Also, cells in the same diameter range (~ 1.2 μm), displayed arms of maximum length (Fig. 4.5 e). This time point also coincides with the decrease in total

intensity of actin and myosin (Fig. 4.5 d). Added to this, most of the rings exhibited a bright cluster at the point of connection of arms (Fig. 4.4 b). The brightness of the cluster indicates high concentration of myosin motors. Hence, at a particular diameter range (~ 1 – 1.2 µm) after which the total intensity of acto-myosin linearly decreases, cells exhibited arms with maximal length that is associated with a bright cluster. Together, these observations suggest that the bright cluster acts as a source for material extrusion and arms act as a medium for material extrusion during constriction.

We did not observe similar structures or any other extrusion mechanism in the case of mammalian rings.

4.5 Clustered organization of actin and myosin in the cytokinetic ring

After analyzing the intensity variations of fission yeast and mammalian rings, we focused on the internal organization of acto-myosin within both systems. To observe the organization of acto-myosin in the rings, we systematically imaged the acto-myosin in the ring using confocal microscopes.

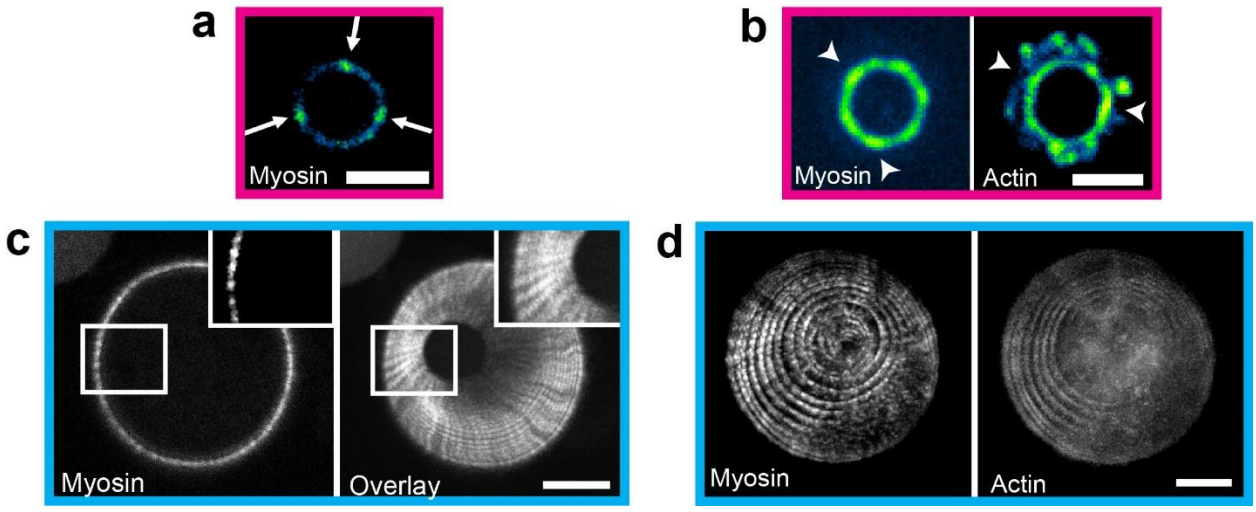

Figure 4.6. Clusters in fission yeast (a) and (b) and mammalian (c) and (d) rings. (a) Snapshot showing three myosin clusters indicated by arrows. (b) Representation of myosin and actin clusters in the same ring indicated by arrows. Actin patches are visible outside the ring similar to (139). (c) Myosin is distributed in regular clusters around the perimeter of the cytokinetic ring. Right: Overlay of 25 frames, starting from the frame shown on the left. The clusters move radially. Time between images 10 s. (d) Overlay of 26 subsequent frames of a closing ring visualized by the fluorescence labeling of myosin and actin. Time between images 45 s, superimpositions of 5 z-planes, plane distance 1.3 µm. Scale bar 2 µm (a, b) and 5 µm (c, d) (109).

The complete and highly resolved visualization of the ring revealed clustered states of actin and myosin in both fission yeast and mammalian rings (Fig. 4.6 a, b and d). Clusters are inhomogeneities in the acto-myosin distribution with high- and low- intensities. Strikingly, in fission yeast and in mammalian rings, the clusters were organized differently. In fission yeast, the clusters exhibited rotation (Movie 4.7) and in mammalian rings they were static in the framework of the ring (Fig. 4.6 c, Movie 4.2). These clusters were easily observable in fission yeast. However, in the case of mammalian cells, the PDMS at the bottom of microcavities makes the observation of clusters more difficult with an inverted setup, due to scattering. Hence the clusters in mammalian ring were systematically imaged with an upright microscope.

4.5.1 Fission yeast ring

In fission yeast, high intensity spots of actin and myosin – clusters – were moving along the ring perimeter. We confirmed the movement to be rotation as opposed to normal diffusion, by kymograph analysis (Fig. 4.7 a and b), and from the observation of arm rotation (Fig. 4.5 b and c). In addition, the high intensity of clusters distinguished them from the low intensity regions of the ring. While clusters were mainly rotating, static clusters of acto-myosin (in the framework of the ring) were also occasionally observed. In addition to actin (CHD) and myosin (RLC1), similar clusters were observed for other proteins also: myosin heavy chain (Myo2), cell division protein - cdc15, wall machinery: β-glucan synthase (Bgs1), and paxillin - Pxl1 (S.Fig. 8). This shows that globally most of the proteins are organized in a clustered fashion, which could be a key necessity for the constriction process.

4.5.1.1 Cluster characteristics in fission yeast ring

To characterize acto-myosin cluster rotations, we transformed rings into lines and made a kymograph of these lines to track cluster movement. In this arrangement, height of the kymograph in pixels is equivalent to the angular denomination (2π) of the ring perimeter. By measuring the slope of clusters in these kymographs, the velocities of clusters were obtained (Fig. 4.7 a and b).

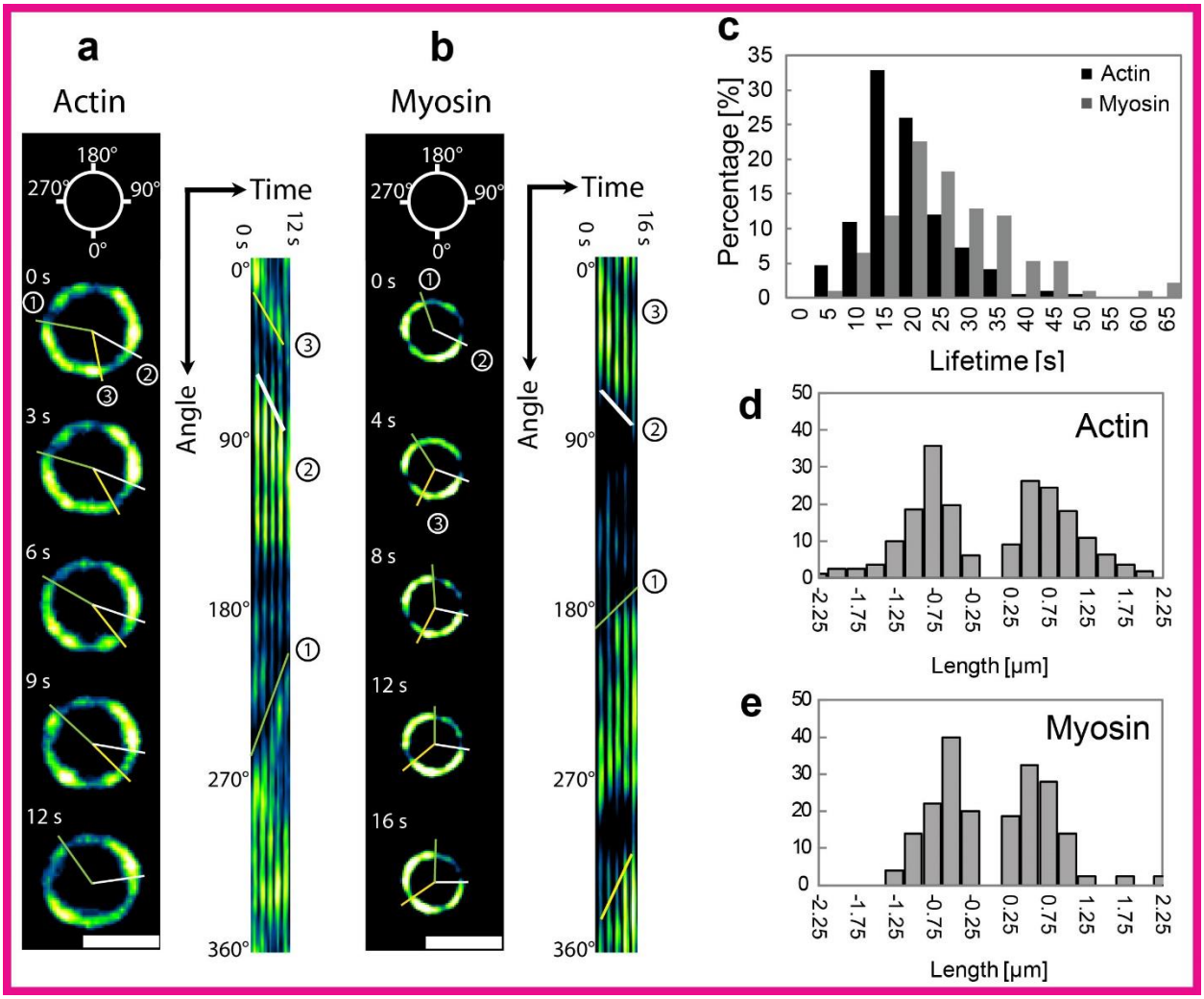

Figure 4.7. Cluster rotation in fission yeast. Rotation of actin (a) and myosin (b) clusters. The analysis is based on a kymograph representation of the ring after polar transformation. Lines highlight the motion of clusters on the ring and in the kymographs. Scale bar 2 µm. (c) Histogram for lifetime of clusters. The mean lifetime is 16.4 s (s.d. = 7.7 s, n = 192) for actin and 24.1 s (s.d. = 11.6 s, n = 93) for myosin. (d) and (e) Distance of cluster movement for clusters rotating clockwise and counterclockwise. The mean distance for actin cluster (d) is 0.72 µm (s.d. = 0.41 µm, n = 192) and 0.52 µm (s.d. = 0.34 µm, n = 93) for myosin cluster (e) (109).

4.5.1.1.1 Rotation of acto-myosin clusters

The clusters moved on average 0.7 µm along the ring perimeter and maximally up to 2 µm (Fig. 4.7 d and e). To achieve this displacement, the clusters exhibited an average life time of 20 s and maximally up to 60 s before diffusing into the low intensity region (Fig. 4.7 c). This persistence length, more or less equivalent to quarter of a perimeter of the largest ring, qualifies the movement as rotation.

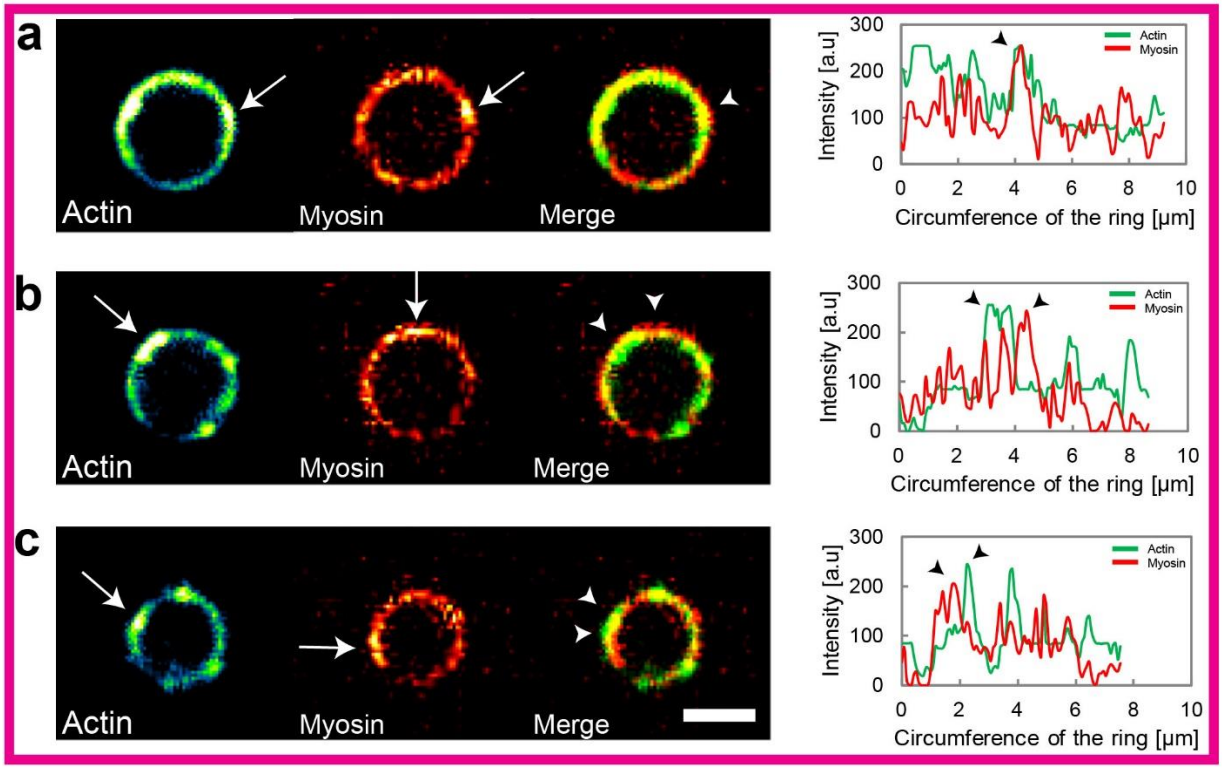

Figure 4.8. Cluster interplay. (a – c) correspond to the same cell at different phases of closure. Each panel is aligned in the order: actin, myosin and the merge with arrows indicating the speckles. The graph in each panel is the intensity plot of actin and myosin against the circumference of the ring and arrows indicate the peaks corresponding to clusters. (a) Cluster co-localization. (b) and (c) Actin and myosin clusters positioned in a sequential manner.

The clusters rotated with equal probability in both directions: clockwise and counter-clockwise, thus preserving the directional symmetry (Fig. 4.7 d and e). Moreover, during rotation the clusters underwent fusion, collision or splitting, followed by movement in same or opposite directions respectively (S.Fig. 9).

Although fusion and collision were observed between clusters for the same proteins, rotations of actin and myosin clusters were independent of each other. We found different scenarios where actin and myosin were co-localizing or sequentially positioned with respect to each other (Fig. 4.8). These scenarios could be the result of difference in velocity characteristics of actin and myosin. During constriction, the speed of actin clusters showed a decreasing trend. But myosin clusters exhibit a constant speed until ~ 2 μm and then show a decreasing trend (Fig. 4.9 a).

By comparing the average speed of clusters, we found that the speed of actin clusters (3 μm/min) was higher than myosin (1.5 μm/min) (Fig. 4.9 b). We associate the increased velocity of actin clusters to the treadmilling of actin filaments, in addition to sliding by

motors. In addition, when we observed constriction at higher temperatures (36 °C) (where the constriction rates are higher, Fig. 4.2 b), the average cluster speeds for myosin were also increased (Fig. 4.9 b). These observations suggested a link between cluster rotations and ring constriction.

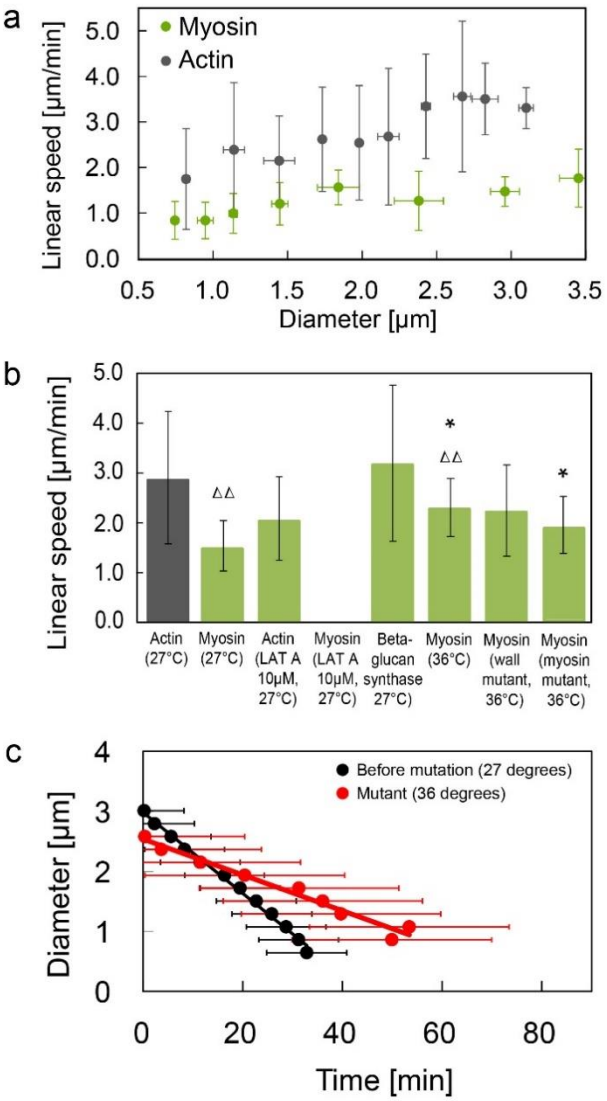

Figure 4.9. (a) The analysis of cluster motion reveals a decrease in actin cluster speed during constriction. Myosin clusters rotate with a constant speed with decreasing tendency towards the end of constriction. Error bars indicate standard deviations. Each point contains 4 to 50 measurements, 202 in total for actin and 77 for myosin. (b) Comparison of the cluster speed in different conditions and for different proteins. Rings with diameters of more than 1.5 µm were used. Each mean value contains 13 to 185 measurements. Error bars indicate standard deviation. One way ANOVA was performed, * $P<0.05$, ΔΔ $P<0.01$ (109). (c) Ring diameter as a function of time before (27 °C) and after (36 °C) activation of mutation in Myo2-E1 strain. The constriction rate decreases on mutant activation.

4.5.1.1.2 Rotation of wall machinery clusters

While acto-myosin are shown to be the main actors of stress generation (140, 141) during ring constriction, alternative hypotheses exist. In fission yeast, the ring constriction is followed by septum formation whose completion results in new cell wall of the separated daughter cells. It has been suggested that insertion of glucan synthase units against the ring leads to a ratcheting effect, thus leading the constriction process (142). This motivated us to look into the organization of wall machinery during ring constriction. We used a strain where the β-glucan synthase unit – Bgs4 was tagged with GFP. Surprisingly, we found rotating clusters of wall machinery (Fig. 4.9 b). The cluster speed was similar to acto-myosin clusters. This motivated our speculations on influence of acto-myosin clusters on wall machinery organization.

4.5.2 Mammalian ring

Contrary to fission yeast clusters, we observed static clusters of myosin during mammalian ring constriction (135). The static nature can be confirmed from the overlay of ring constriction which shows characteristic radial arrangement of clusters (Fig. 4.6 c and d). Similar inhomogeneities were also observed for actin and actin nucleator formin (mDia).

4.5.2.1 Cluster characteristics in mammalian ring

The static clusters in mammalian ring were characteristically separated by ~ 0.8 µm of minimal intensity regions. During the radial movement of the ring throughout constriction, the cluster trajectories were mostly linear. But, occasional curved trajectories were observed, suggesting a potential force imbalance due to irregular myosin distribution. Fusion and splitting of clusters were also observed along the cluster trajectories during constriction (S.Fig. 4).

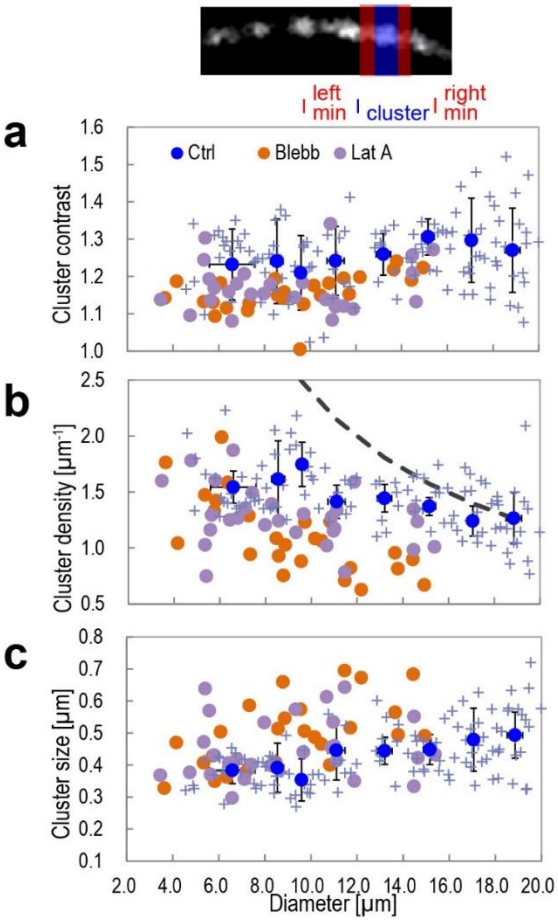

Figure 4.10. Characterization of the myosin pattern in mammalian rings for control (blue) and after incubation with the cytoskeleton drugs blebbistatin (orange) and Lat A (purple). The cluster contrast (a) stays approximately constant. The cluster density (b) is increasing while the ring is constricting, but not as much as expected for a constant number of clusters (dashed line). Cluster density of cells treated with the two drugs is reduced. The cluster size (c) decreases as the ring closes. Blue points represent averages, crosses correspond to single data points, error bars indicate the standard deviation, time-lapses of 11 closing rings were analyzed. Each orange (blebbistatin) or purple (Lat A) point is obtained from averaging the cluster parameters from a fixed ring (blebbistatin: N= 25, Lat A: N=28) (109).

To analyze the patterning of clusters, we quantified the size, contrast and density of clusters. The cluster contrast was estimated as the intensity ratio of bright cluster to the adjacent minimal intensity regions (Fig. 4.10). The cluster size was estimated as the distance between two adjacent minimal intensity regions.

During constriction, all the cluster characteristics (Fig 4.10 a, b and c) stayed about constant. The most interesting parameter was the cluster density which was showing approximately constant trend throughout the constriction. However, the position of the curve, is much below the curve indicating the density trend for a constant density of clusters (Fig. 4.10 b). This indicates loss of individual clusters or fusion events between clusters as mentioned above. Irrespective of the cluster characteristics, a very similar pattern of cluster arrangement is observed throughout the constriction. This strongly suggests active remodeling of clusters to retain the pattern, which might play a role in constriction.

4.6 Role of acto-myosin in regulating constriction and cluster characteristics

Both fission yeast and mammalian rings show self-organization of acto-myosin: rotating and static clusters in fission yeast and mammalian rings respectively (S. Fig. 4 and 9). In addition, the analysis of cluster characteristics hinted links between the cluster organization and constriction. For example in fission yeast, cluster velocity decreases during constriction and in mammalian cells, the cluster pattern is conserved throughout constriction. Hence we were interested in understanding the influence of acto-myosin activity in regulating the cluster characteristics and constriction. To confirm the significance of acto-myosin, we individually targeted these proteins by mutation and specific inhibitor drugs.

4.6.1 Fission yeast ring

4.6.1.1 Role of acto-myosin in cluster rotation

We used Latrunculin A (Lat A) to interfere with the dynamics of actin filaments (143). By adding 10 µM Lat A, we found that myosin clusters were completely stalled along with ring constriction. However, the actin clusters were exhibiting rotation, though with reduced speeds when compared to control condition (Fig. 4.9 b). We attribute this rotation to sequestered actin monomers. By reducing the concentration of Lat A to 2 µM, we observed two behaviors: either the myosin clusters were stalled along with ring

constriction or the myosin clusters were rotating with reduced constriction rate. Actin clusters continued to rotate.

For myosin, we used a myosin mutant strain (myo2-E1) (144, 145), in which the mutation is activated by shifting the strain to 36 °C. By activating mutation in this temperature sensitive strain, we found that the rate of constriction was significantly reduced: 30 nm/min, compared to the constriction rate of control strain at 36 °C: 100 nm/min (Fig. 4.9 c and Fig. 4.2 b). Similarly, the average speed of myosin clusters in the myosin mutant strain were also significantly reduced, compared to the control condition (Fig. 4.9 b). These results strongly indicate the significance of acto-myosin in regulating cluster rotation and the ring constriction process.

4.6.1.2 Rotation: a built-in property of active gels

In addition to acto-myosin, clusters of wall machinery (β-glucan synthase) also exhibited rotation (Fig. 4.9 b). In order to check if the acto-myosin cluster dynamics were independent of the cell wall machinery proteins, we used a wall mutant strain (PN 4461 – cps1) (146), where the synthesis of β-glucan synthase is arrested. Activation of mutation by shifting the strain to 36 °C, we found that the myosin clusters continued to exhibit rotation (Fig. 4.9 b, Movie 4.8). This showed that myosin cluster dynamics were independent of wall machinery and wall growth. In general, rotations in active gels have been shown to be a built-in property of active gels by *in vitro* experiments and theoretical models (28, 147). In line with this, rotation of myosin clusters independent of wall machinery in fission yeast, further emphasizes rotation as a built-in property of active gels *in vivo*.

4.6.2 Mammalian ring

4.6.2.1 Role of acto-myosin in cluster characteristics

In the presence of blebbistatin and Lat A, the rings were stalled and opening respectively (S.Fig. 5 a and d). Added to this severe effect on constriction, the myosin cluster contrast and density were reduced and the size of clusters was increased (Fig. 4.10 b and c and S.Fig. 5 g). These results showed that acto-myosin dynamics were playing a key role in cluster organization, and the ring constriction process.

Thus acto-myosin activity regulates both cluster characteristics and constriction behavior in fission yeast and mammalian cells. In this complex scenario of specific mesoscopic organization during ring constriction, we were curious to check the turnover dynamics of myosin molecules on the ring.

4.7 Myosin turnover in fission yeast and mammalian rings: FRAP measurements

We measured the FRAP of myosin in both systems (Fig. 4.11 a and b). The recovery rate of myosin was ~ 1 s in fission yeast, and ~ 20 s in mammalian ring (Fig. 4.11 c and d). The high turnover indicates constant replenishment of myosin from the cytoplasm. Also in comparison, the timescale of mesoscopic properties like constriction (5 min – fission yeast / 40 min – mammalian ring) and cluster velocity (1.5 µm/min) were much slower. This establishes myosin clusters as structures with rapid inherent dynamics, which however does not affect the mesoscopic characteristics of clusters.

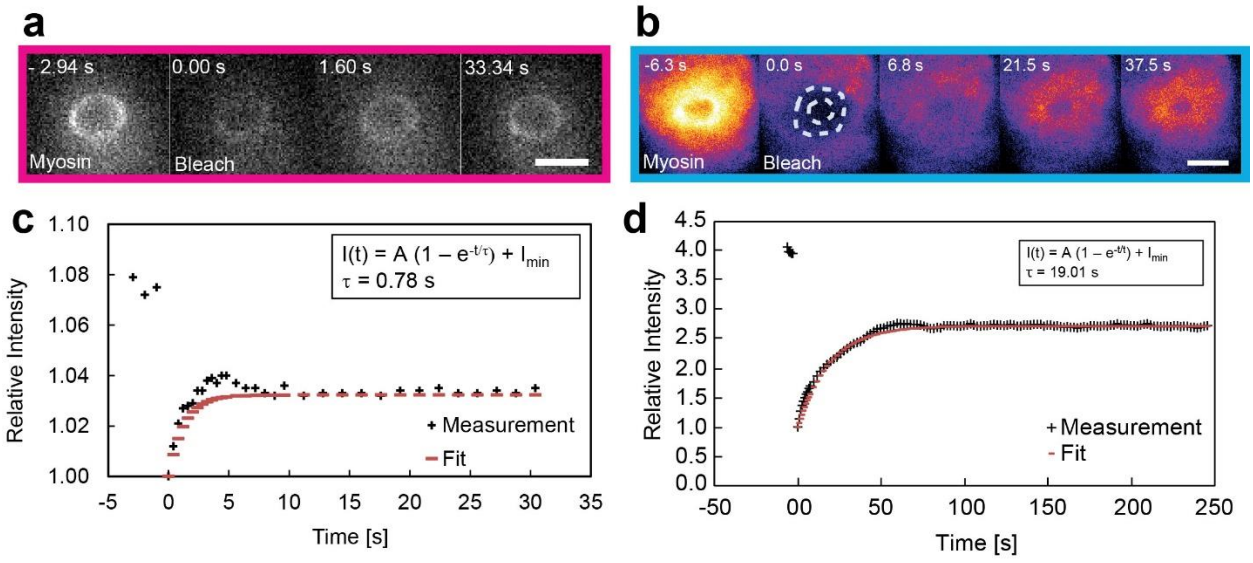

Figure 4.11. FRAP experiments on myosin in the rings of fission yeast (a) and HeLa (b) cells. The entire ring is bleached in both cases and the recovery is partial. Scale bars 2 µm (a) and 5 µm (b). The half time of recovery are ~1s (c) and ~20 s (d) (109).

From these experimental results and analysis, we found that: (i) both fission yeast and mammalian rings exhibit similar auto-organization of acto-myosin – clusters, (ii) while they exhibit clustered state of conserved proteins (acto-myosin) for the same function (ring constriction), they behave differently: rotating and static, (iii) we also found that

acto-myosin strictly regulates the cluster characteristics and constriction behavior in both fission yeast and mammalian rings.

These observations and analyses hinted a link between the clusters and the constriction process itself. Such links between self-organization and mechanical work have been proposed by theoretical models in the literature. Therefore, we turned to theoretical modeling to check if the auto-organized structures of acto-myosin were directly linked to the constriction process.

4.8 Self-organization of filament-motors in cytokinetic ring – theoretical model and experimental verification

4.8.1 Continuum description of the ring

Theoretical frameworks describing the link between self-organization principles and stress generation have been described in the past (27, 28, 148). In this line of thought, we collaborated with Karsten Kruse and Anne Wald, to understand the origin of cluster organization and their function in ring constriction. We developed a minimal filament-motor based model using this framework.

In this model, the dynamics arising from the local interaction of acto-myosin bundles are coarse-grained to understand their roles as ensemble, leading to ring constriction. The dynamics within the ring mainly arise from the velocities generated by filament – motor interaction and filament treadmilling. The specialty of this model lies in the introduction of bipolar filaments in addition to unipolar filaments (Fig. 4.13). The motors are present at the plus ends and coordinate the filament movements. We found that assembly and disassembly rates of bipolar filaments along with filament velocities, significantly contribute to the explanation of the experimentally observed cluster characteristics in both fission yeast and mammalian rings. In the following section, first the construction of the model is described followed by the description on the parameters leading to instability that gives rise to static and oscillatory cluster states.

4.8.1.1 Active filament currents by motor activity

We consider the ring as a circular one dimensional arrangement of filaments, with periodic boundary conditions. The ring has a perimeter of 'L', where the coordinates along the ring perimeter are denoted by 'x'. The bundle is made of filaments of length

'l', whose number densities are denoted by c^+ and c^-, representing their $'+'$ ends aligned in the clockwise and counter-clockwise directions respectively. These filaments undergo displacement due to diffusion from thermal fluctuations and by the action of molecular motors, thus leading to change in density over time across the perimeter. The change in densities obey conservation laws and can be defined as:

$$\partial_t c^+ = D\ \partial_x^2\ c^+ -\ \partial_x J^{++} -\ \partial_x J^{+-} \qquad (4.1)$$

$$\partial_t c^- = D\ \partial_x^2\ c^- -\ \partial_x J^{--} -\ \partial_x J^{-+} \qquad (4.2)$$

where D is the effective diffusion coefficient of the filaments, and J^{++}, J^{--} and J^{+-}, J^{-+} are the active currents resulting from filament sliding by motors in parallel or anti-parallel fashion respectively. The evolution of filament density at any point along the ring perimeter is due to diffusion and relative sliding of filaments due to motor activity. This is given by the equations 4.1 and 4.2: where, first term on the right hand side gives the filament flux due to diffusion. The second and third terms correspond to the fluxes generated by motor based sliding of filaments, oriented in parallel and anti-parallel fashions respectively. This relative movement of filaments strictly depends on the orientation. Assuming that only two-filament interaction dominates, the active currents in the second and third terms of equations (4.1) and (4.2) can be elaborated as:

$$J^{\pm\pm}(x) = \alpha \int_0^l d\xi\ [c^{\pm}(x+\xi) - c^{\pm}(x-\xi)]\ c^{\pm}(x) \qquad (4.3)$$

$$J^{\pm\mp}(x) = \mp\beta \int_0^l d\xi\ c^{\mp}(x+\xi)\ c^{\pm}(x) \qquad (4.4)$$

where: $J^{\pm\pm}$ denote the filament currents between parallel filaments whose $'+'$ ends are oriented in clockwise direction J^{++} or anti-clockwise J^{--} direction respectively, and $J^{\pm\mp}$ denote the filament currents between anti-parallel filaments whose $'+'$ ends are oriented in clockwise $J^{\pm}$ or anti-clockwise $J^{\mp}$ direction respectively. α and β are the velocities due to interaction between parallel and anti-parallel filaments, the reference filaments is positioned at a point along x, ξ is the distance at which the interacting filament is positioned. The right hand side of the equations 4.3 and 4.4 describe the overlap between

filaments with the boundary conditions restricted to $x + l$. Because in our model we consider that the motors are always present at the plus ends of the filaments. In a system described by these parameters, a filament along x will have a relative velocity α or β based on the orientation of another filament located at a distance ξ, where the sign of ξ indicates the direction of movement (Fig. 4.12).

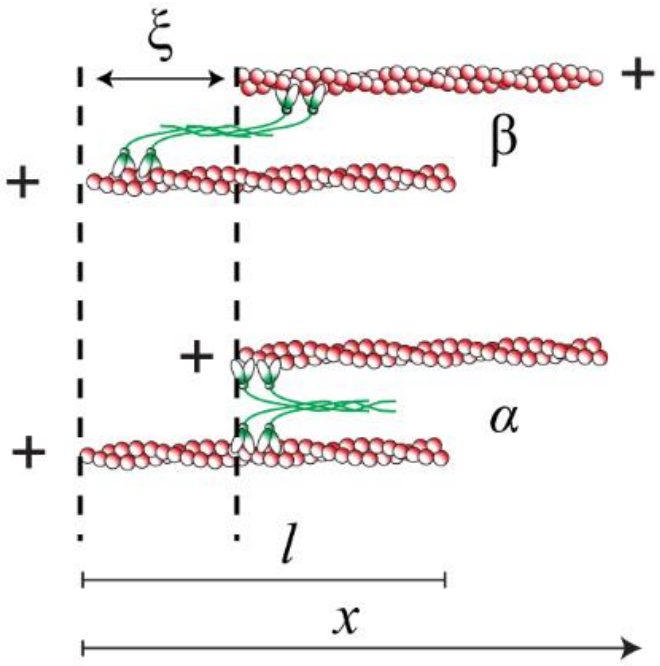

Figure 4.12. Schematic of model construction. The actin filaments are represented as helical structures in red and the myosin motors cross-linking the actin filaments are represented in green. Two filament configurations, based on orientations are shown in the scheme: anti-parallel (β) and parallel (α). The filaments are of length 'l' and the reference filaments (filaments in the bottom of each configuration) are positioned at a point on $'x'$. The reference filaments are cross-linked with another filament positioned at a distance of ξ. The myosin motor moves towards the $'+'$ end in each of these filaments and this motor activity gives rise to filament velocities: (α) from parallel filament interaction and (β) from anti-parallel filament interaction.

Together, equations 4.1 – 4.4 give a simple perspective of changes in filament densities based on the filament displacement due to diffusion and motor driven sliding of filaments.

4.8.1.2 Bipolar filaments

The above mentioned equations (4.1 – 4.4) describe the relative displacement between unipolar filaments. In this scenario, we propose that two unipolar filaments of same orientation can be joined by a nucleator thus giving rise to a bipolar filament. The introduction of bipolar filaments is the major highlight of this model. The presence of bipolar filaments is similar to the search and capture mechanism during fission yeast ring formation, where filaments captured by nodes condense to form a ring (121). The bipolar filaments assemble at the rate of ω_c and disassemble into two unipolar filaments at the rate of ω_d (Fig. 4.13).

Taking into account the assembly and disassembly rates, the change in densities from corresponding active currents for bipolar filaments can be described by:

$$\partial_t c_{bp} = D\ \partial_x^2\ c_{bp} - \ \partial_x J^{bp} - \ \omega_d c_{bp} + \ \omega_c c^+ c^- \qquad (4.5)$$

$$J^{bp}\ (x) = \ \beta \int_0^l d\xi \left[c_{bp}\ (x+\xi) - \ c_{bp}\ (x-\xi)\right] c_{bp}\ (x) \qquad (4.6)$$

Figure 4.13. Schematic of bipolar filaments. Over time (t' > t): Left – the plus ends of two unipolar filaments join to form a bipolar filament with a nucleator in the center (bipolar filament assembly – ω_c). Right – a bipolar filament disassembles into two unipolar filaments (disassembly of bipolar filaments – ω_d) (109).

In the bipolar filament arrangement, monomeric actin units are added to the $'+'$ ends attached to the nucleator, and are removed at the $'-'$ ends away from the nucleator. However, we refrain from giving a detailed description of polymerization / de-polymerization activity and assume that the filaments are in a steady state by exhibiting similar rates of assembly and disassembly at both ends. Thus unipolar and bipolar filaments maintain a constant length of l and $2l$ respectively. This allows to describe the total actin density (c^{tot}) at any point on the ring to be:

$$c^{tot}\ (x) = \int_0^l d\xi \left[c^+\ (x+\xi)\ +\ c_{bp}\ (x+\xi)\ +\ c^-\ (x-\xi)\ +\ c_{bp}\ (x-\xi)\right] \qquad (4.7)$$

Until now, the filament velocities are obtained either from diffusion or active sliding by the motors. But similar rates of assembly and disassembly at the $'+'$ and $'-'$ ends would also lead to filament displacement which needs to be taken into account. In the next step, we include the contribution of this velocity to the evolution of filament flux.

4.8.1.3 Filament treadmilling

In order to describe the equations of motions, we take into account the filament treadmilling in addition to the effect of molecular motors and fluctuations from diffusion (149). The steady state of filaments induces an apparent displacement of the unipolar filaments with a velocity v_{t0}.

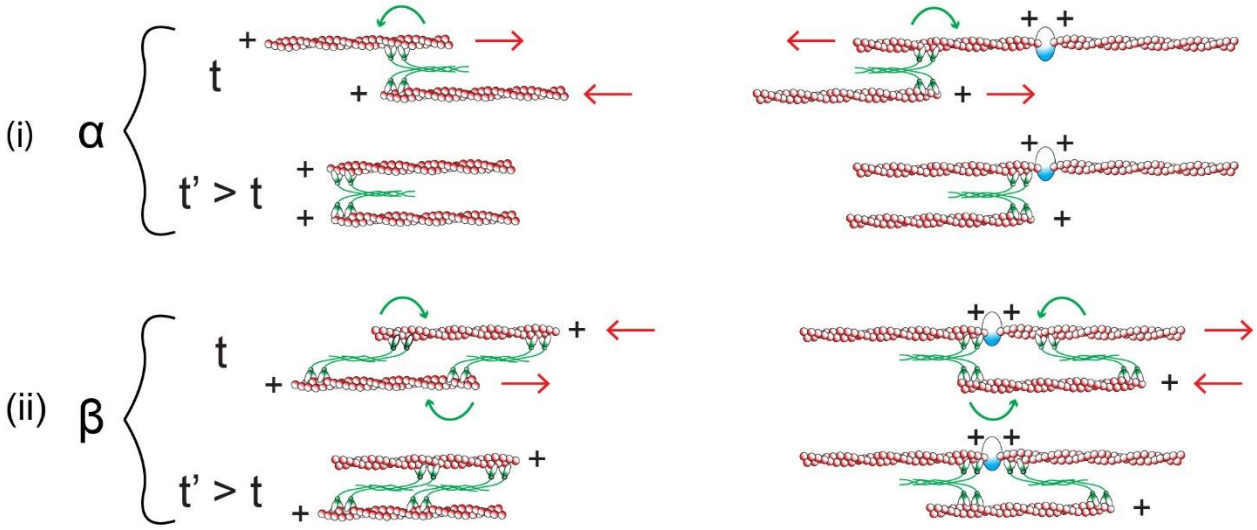

Figure 4.14. Schematic of the model components and their interactions describing the parameters. α and β represent interactions of parallel and anti-parallel filaments respectively. At each plus-end there is a motor, but only motors interacting with another filament are shown. The resultant displacement for each of the orientations α and β after time t' are shown. Green arrows indicate the movement of myosin motors to the $'+'$ ends of the filament. Red arrows indicate the direction of the filament movement (109).

The motors are always present at the plus ends of the filaments and their distribution is given by $c^+ + c^- + c_{bp}$. The presence of motors at the $'+'$ ends is critical for symmetry breaking that would lead to contraction rather than expansion of the filaments. The action of these motors induce filament velocities α and β for filaments of same and opposite orientation (Fig. 4.14). The constant turnover of bipolar filaments (ω_c and ω_d) gives rise to interactions between unipolar-unipolar filaments and unipolar-bipolar filaments (Equation 4.7). These interactions lead to filaments fluxes. The time evolution of actin densities at any point $'x'$ is given by the dynamic equations 4.8, 4.9 and 4.10, which are obtained by substituting active filament currents from equations 4.3, 4.4 and 4.6, and velocity due to treadmilling (v_{t0}).

$$\partial_t c^+(x) = D\partial_x^2 c^+(x) - \partial_x \alpha \int_0^l d\xi [c^+(x+\xi) - c^+(x-\xi)]c^+(x)$$

$$- \partial_x \alpha \int_0^l d\xi \; c_{bp}(x+\xi)c^+(x) + \partial_x \beta \int_0^l d\xi \; (c^-(x-\xi) + c_{bp}(x-\xi)c^+(x)$$

$$-\partial_x v_{t0} c^+(x) - \omega_c c^+(x)c^-(x) + \omega_d c_{bp}(x) \qquad (4.8)$$

$$\partial_t c^-(x) = D\partial_x^2 c^-(x) - \partial_x \alpha \int_0^l d\xi [c^-(x+\xi) - c^-(x-\xi)]c^-(x)$$

$$- \partial_x \alpha \int_0^l d\xi \; c_{bp}(x-\xi)c^-(x) - \partial_x \beta \int_0^l d\xi \; (c^+(x+\xi) + c_{bp}(x+\xi)c^-(x)$$

$$-\partial_x v_{t0} c^-(x) - \omega_c c^+(x)c^-(x) + \omega_d c_{bp}(x) \qquad (4.9)$$

$$\partial_t c_{bp}(x) = D\partial_x^2 c_{bp}(x) - \partial_x \alpha \int_0^l d\xi \big[c_{bp}(x+\xi) - c_{bp}(x-\xi)\big]c_{bp}(x)$$

$$- \partial_x \alpha \int_0^l d\xi \; [c^-(x+\xi) - c^+(x-\xi)]c_{bp}(x)$$

$$- \partial_x \beta \int_0^l d\xi \; [c^+(x+\xi) - c^-(x-\xi)]c_{bp}(x) + \omega_c c^+(x)c^-(x) - \omega_d c_{bp}(x) \qquad (4.10)$$

Equations (4.8) and (4.9) give the flux of unipolar filaments oriented in the clockwise (c^+) and anti-clockwise (c^-) directions respectively. Equation (4.10) gives the flux of bipolar filaments. In the right hand side of above equations (4.8 – 4.10): first term gives the fluctuations due to diffusion with an effective diffusion constant D; the next three terms correspond to the relative sliding velocities of filaments overlapping with each other, based on orientation: parallel (α) and anti-parallel (β). The last three terms in (4.8) and (4.9) correspond to the contribution from the treadmilling velocity (v_{t0}) and assembly and dis-assembly rates of bipolar filaments. Similarly, the last two terms in (4.10) correspond to the assembly and dis assembly rates of bipolar filaments.

Solutions to these differential equations (4.8), (4.9) and (4.10) gives the filament fluxes for a ring in homogeneous condition. These solutions strongly depend on the values of

the parameters involved, i.e. (i) diffusion of filaments (ii) velocities of parallel and anti-parallel filaments, (iii) assembly and dis-assembly of bipolar filaments. If a specific parameter value deviate beyond a critical / threshold value, then the system becomes unstable and the solutions to these equations are different. In the following paragraph the parameters leading to this instability are discussed.

4.8.1.4 Perturbation from homogeneous state

In the current model, the system moved to an unstable state when the velocity of parallel filaments, α increased above a threshold value α_c. This lead to the formation of stationary clusters of motors in the simulation, similar to the clustered state of mammalian rings (Fig. 4.15 a and b).

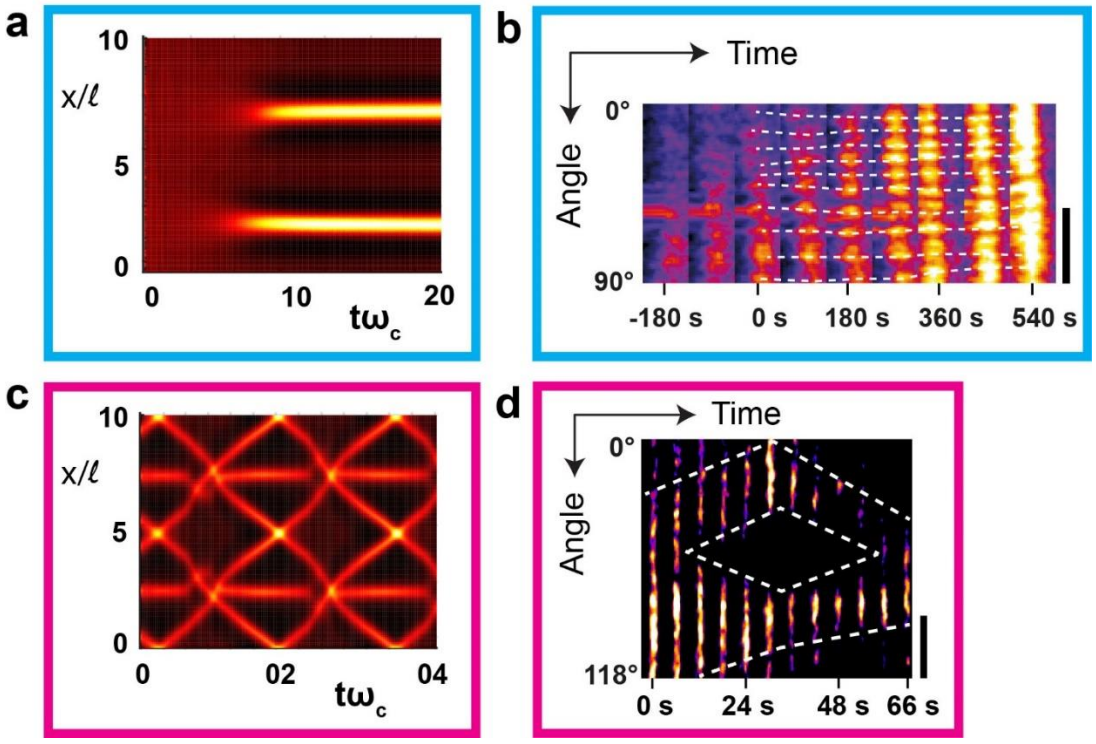

Figure 4.15. Kymographs (perimeter against time) of emerging stationary myosin clusters in the model (a) and in mammalian rings (b). In (a) the parameter α is increased from a sub- to a supercritical value, the initial distribution was homogenous with a random perturbation. Kymographs of rotating myosin clusters in the model (c) and in fission yeast (d). The parameter α is constant in (c). In (b) and (d), dashed white lines serve as guide to the eye. Myosin density is color-coded in all plots. Scale bar 2 μm in (b) and 5 μm in (d) (109).

The clustered phase is due to the presence of bipolar filaments. Motors are present at the center of bipolar filaments and on interaction with other bipolar filaments, tend to align

with their centers, in a homogeneous state. In this case the total force on the filaments is reduced to zero. However, on perturbation due to the increase in α, a local imbalance in force is created by overcoming the homogeneous state maintained by diffusion, leading to clustering of bipolar filaments in the ring.

The separation between the newly formed clusters along the ring distinguishes the clustered state from the homogeneous state. As mentioned above, a bipolar filament of length $2l$ interacts with the motors at the center of another bipolar filament. Hence two clusters of bipolar filaments would be separated by a minimal distance of $4l$ which is in agreement with our simulated measurements during clustered state (Fig. 4.16 a).

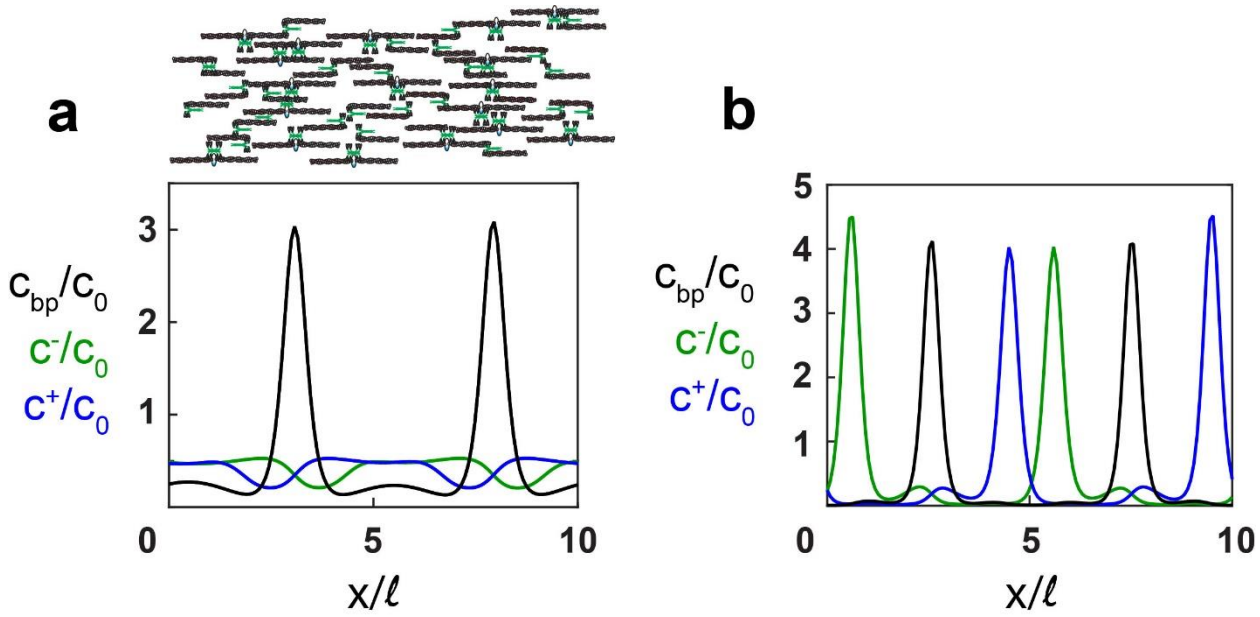

Figure 4.16. Distributions of bipolar filaments (cbp, black) and unipolar filaments (c+, blue, c-, green) corresponding to t=20 ω_c^{-1} of Fig. 4.15 a (a) and to t=0 of Fig. 4.15 c (b). (a – top) In alignment, illustration of the F-actin distributions corresponding to two adjacent myosin clusters (109).

While stationary clusters are a result of bipolar filaments, we found that increase in rate of disassembly of bipolar filaments (ω_d) in addition to $\alpha > \alpha_c$ leads to co-existence of stationary and mobile clusters as in fission yeast ring (Fig. 4.15 c and d). This is due to the fact that residual fluxes of unipolar filaments are always present in the system (Fig. 4.16 b). Hence in the oscillatory state, enhanced unipolar filament fluxes manifest as mobile clusters resulting from the motor distribution around the ring, in addition to the stationary clusters. Whereas in the stationary clustered state, the unipolar filament fluxes are at minimal level, further supporting the evidence of motor confinement to the centers of bipolar filaments (Fig. 4.16 a).

Thus variations in velocities of parallel filaments (α) and disassembly rate of bipolar filaments (ω_d) revealed three phases: homogeneous state, stationary clusters and coexistence of stationary and mobile clusters (Fig. 4.18 a). We also found that variations in filament lengths and velocities added to these phase transitions from static to oscillatory state and other way around.

The model revealed those parameters leading to instability and the corresponding phase transitions. Next we wanted to verify the existence of these transitions: from homogeneous state to clustered and rotating states in experiments.

4.8.2 Transition from homogeneous to clustered state in experiments

4.8.2.1 Homogeneous and clustered states in fission yeast and mammalian ring during the onset of constriction

During the constriction process, there were no transitions between homogeneous to clustered states in both mammalian and fission yeast rings. Hence we decided to image the ring during formation, before the onset of constriction in both fission yeast and mammalian rings.

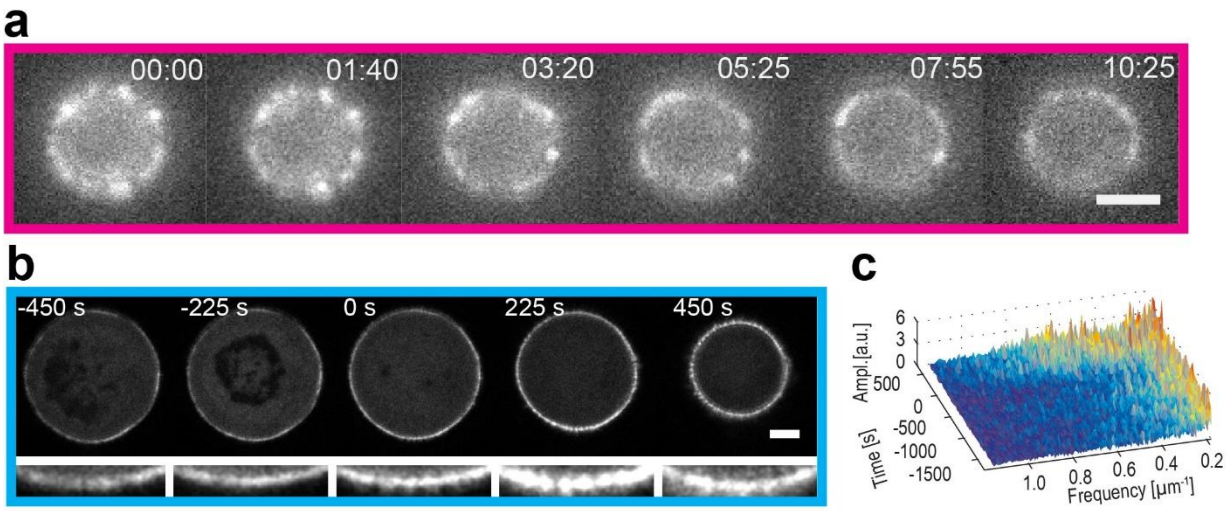

Figure 4.17. Visualizing ring formation in myosin. (a) Formation of fission yeast ring from clusters. Clusters are present prior constriction and eventually form a complete ring. (b) Time-lapse of a cell before, during and after formation of the ring, below a zoomed region (109). Scale bars 2 µm (a) and 5 µm (b). (c) Fourier spectra of the intensity profiles for the ring shown in (b) (109). At t=0 s, which is the onset of constriction, characteristic frequencies appear.

Prior constriction, clusters were already present in fission yeast (Fig. 4.17 a, Movie 4.9). However, mammalian rings exhibited a quasi-homogeneous distribution of acto-myosin, 500 s prior constriction. The clusters with periodic pattern appeared exactly at the onset of constriction (Fig. 4.17 b, Movie 4.10). This was confirmed by Fourier transforming the intensity profile of the ring, which shows appearance of frequency components (corresponding to the periodic clusters) that were absent before the onset of constriction (Fig. 4.17 b). This showed that transition from homogeneous to clustered state occurred during the onset of constriction in mammalian ring.

In addition, we wanted to invoke such a transition using inhibitor drugs where the myosin distribution in mammalian ring will go to a homogeneous state (i.e. $\alpha < \alpha_c$) and the rotating myosin clusters of fission yeast will be stalled ($< \omega_d$). Also, this test would allow us to precisely distinguish the role of clusters, where (i) the constriction would be stalled in the absence of clusters and resume on appearance of clusters in mammalian case, (ii) the constriction would be stalled in the absence of cluster rotation and resume on recovering cluster rotation. These experiments using the drugs would allow us to effectively traverse the phase diagram (Fig. 4.18 a) obtained from the model.

4.8.2.2 Triggering homogeneous to clustered transition in fission yeast and mammalian rings during constriction: cytoskeletal inhibitor drugs

To achieve the observed transition in the model, we incubated mammalian rings (after constriction initiation) with 100 μM blebbistatin for 10 min, followed by washout. The ring was imaged in actin to prevent toxicity of blebbistatin due to excitation at 488 nm.

We found that constriction was stalled and the cluster organization was disturbed. The ring exhibited a quasi-homogeneous state as it appeared during formation. The addition of blebbistatin, inhibits the myosin activity which thereby decreases the force imbalance that is required for the clustering of bipolar filaments. This leads to homogeneous distribution of myosin along the ring. However, when blebbistatin was washed out and replaced with fresh media, the myosin activity was restored. Due to the restoration of myosin activity, the clusters reappeared and the ring underwent constriction (Fig. 4.18 b, Movie 4.11). This is confirmed by the Fourier spectrum of ring intensity, where the characteristic frequency components emerge after washout (Fig. 4.18 c).

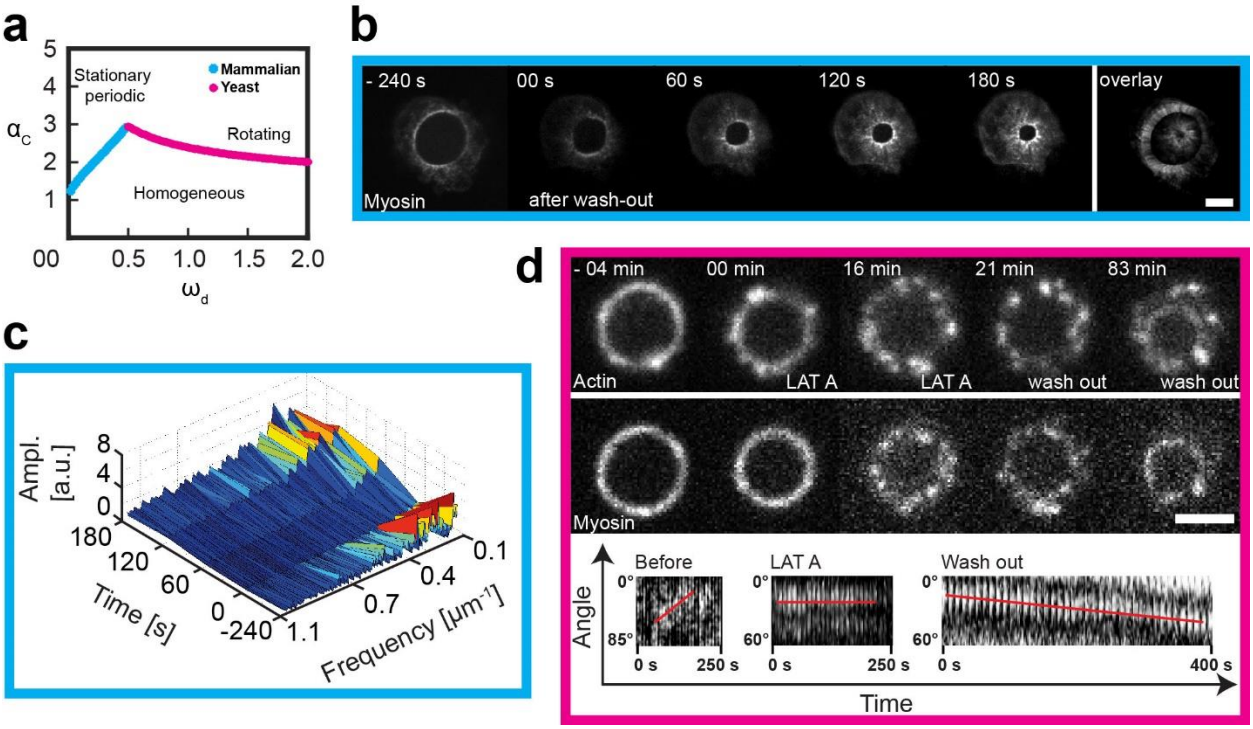

Figure 4.18. (a) Critical value of the parameter α from a linear stability analysis. Blue: stationary instability; pink: oscillatory instability. (b) Mammalian cells before and after 10 min incubation with 100 µM blebbistatin. After drug treatment, the myosin pattern is not present but reappears after washout. Superimposition of 5 z-planes, scale bar, 5 µm. (c) Fourier spectrum of the intensity profiles shown in (b). Characteristic frequencies are seen before blebbistatin addition and starts to reappear after blebbistatin washout at 0 s, which represents the onset of constriction. (d) Fission yeast cell before and after 20 min incubation with 10 µM latrunculin A. The ring disassembles, but actin clusters rotate while myosin clusters are stalled. After washout, the ring re-forms and constricts again. Scale bar, 2 µm. Polar transformed kymographs of the ring in myosin, confirm different behaviors of the clusters before and during the incubation of Lat A and after washout (109).

Similarly, we used Lat A to disrupt cluster organization in fission yeast. The rings were incubated with 10 µM Lat A for 20 min after constriction initiation, followed by washout. Immediately after addition of the drug, the ring broke into clusters of actin. After ~ 20 min the ring exhibited stalled myosin clusters with zero velocity (Movie 4.12). The complete sequestration of actin monomers lead to disassembly of actin filaments thus preventing the mobility of myosin motors. This resulted in stalled myosin clusters. Following this, we wanted to see if the myosin cluster rotation resumed after restoring the activity of monomeric actin – thereby leading to filament nucleation and fluxes. This was confirmed, when myosin clusters resumed rotation and the ring started to constrict after Lat A was washed out (Fig. 4.18 d).

These experiments allowed us to move back and forth between the homogeneous to clustered state in mammalian cells and rotating to static clustered state in fission yeast.

Thus we experimentally reproduced the different phases observed in the phase diagram of simulation (Fig. 4.18 a): homogeneous, stationary clusters and coexistence of stationary and mobile clusters. The fact that constriction is initiated only after the formation of clusters in mammalian ring and rotation of clusters in fission yeast ring, hints an underlying relationship between clustered organization and stress generation for constriction. This motivated us to evaluate the stress profiles first theoretically, followed by experimental confirmation.

4.9 Evaluation of stress generation during ring constriction

We evaluated the stress profiles on the filaments in our model. Kruse et al (27), have previously shown that bundle shortening can lead to effective stress generation for accomplishing mechanical work. We followed a similar approach to evaluate stress profiles in our current model, which involves unipolar and bipolar filament pairs. With this framework, we attempted to test if the clustered organization was linked to the variation in stress profiles during ring constriction.

4.9.1 Mean-field description

We treated the filament as a rigid rod (S.Fig. 11) moving in a viscous medium with friction coefficient $1/\mu$. The interaction with motors generates opposing stress, σ on the filament, to induce a velocity v (equal to α or β). Thus the stress experienced by the filament is given by:

$$\partial_s \sigma = \frac{1}{\mu} v + f_{mot} \qquad (4.11)$$

where the stress along the filament is piecewise linear: the stress profiles of front and rear of the filaments are negative and positive respectively. The point of overlap between the filaments due to motor cross-linking, experiences the highest stress along the interacting filaments (Fig. 4.19 b). Considering only the stress applied by motors connecting two filaments, we integrate the stress contributions of all the filaments ($x - l$ and $x + l$) along the bundle length to obtain total stress profile of the ring.

Since the instability is triggered by α, we plotted the stress profile of the ring as a function of α and found that on reaching α_c, the stress increased dramatically (Fig. 4.19

a). This confirms that the clustered state triggered by critical velocity (α_c) of parallel filaments and disassembly (ω_d) of bipolar filaments, leads to increase in stress due to bundle shortening which otherwise in homogeneous state would be negligible. On the other hand, the regime of rotating clusters exhibited approximately constant stress profile throughout the evolution of α (Fig. 4.19 a).

The increase in stress during the clustered state in mammalian rings combined with appearance of clusters at the onset of constriction, suggested the role of clusters to generate stress. However, such increase in stress is not observed in fission yeast which might be due to the presence of cell wall that follows ring constriction. The synthesis and formation of cell wall might impede a faster constriction resulting from increase in stress. In order to validate this hypothesis on cluster functions in relation to the simulated stress profiles, we attempted to probe the tension in the ring by ablation experiments.

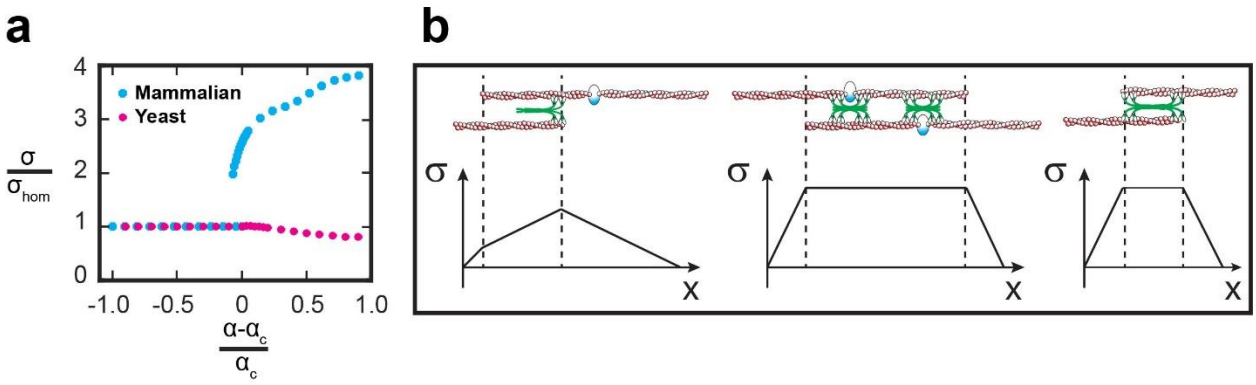

Figure 4.19. (a) Calculated stress σ as a function of myosin activity α undergoing a stationary (blue) or oscillatory (pink) instability. σ_{hom} is the stress in homogeneous state. (b) Illustration of the stress profiles for pairs of a unipolar and a bipolar filament (left), two bipolar filaments (middle), and two unipolar filaments of opposite orientation. (right). Stress is drawn to scale. Only motors cross-linking two filaments are shown (109).

4.9.2 Experimental verification of stress profiles in fission yeast and mammalian cases: Laser ablation of rings

In order to experimentally probe tension in the ring, we performed a point ablation that introduces a cut in the ring and then followed the constriction behavior. In mammalian rings, ablation triggered the opening of ends (Fig. 4.20 a). Immediately after, the ring continued to constrict with higher rate of constriction, while the clusters maintained a radial trajectory (S.Fig. 7). The opening and faster constriction indicate that mammalian ring is under tension. Thus ablation in mammalian ring confirmed the increased stress during ring constriction. This result in addition to cluster appearance and increased stress

simulated from the model at the onset of constriction, clearly establishes the role of clusters to stress increase during mammalian ring constriction process.

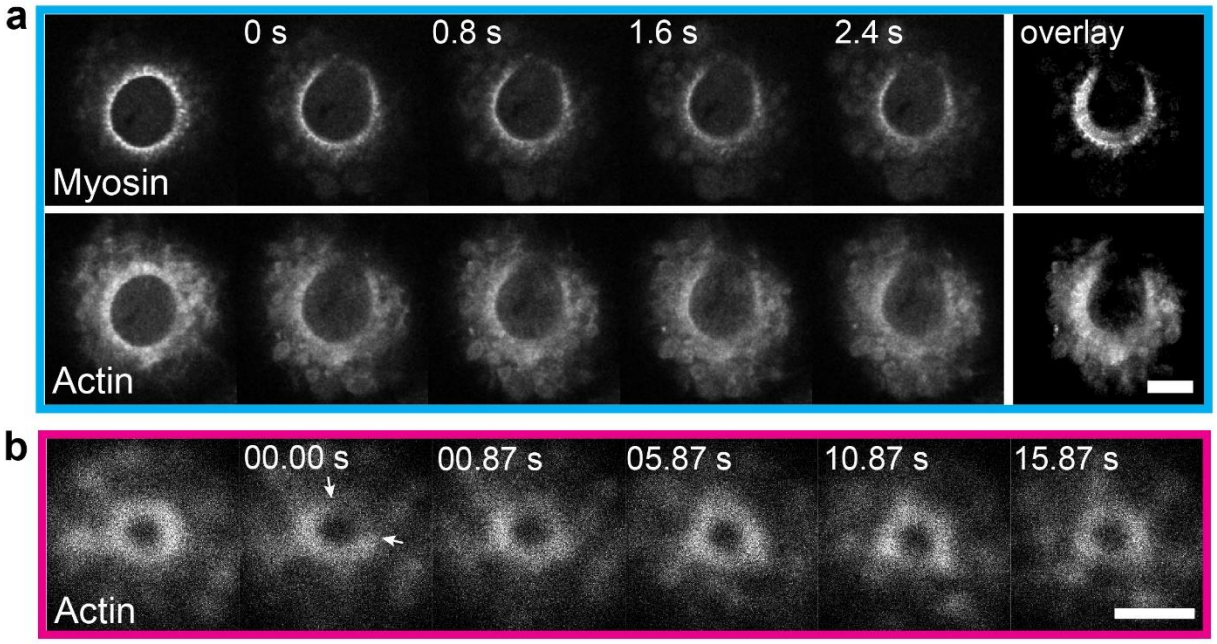

Figure 4.20. Laser ablation of cytokinetic rings. (a) Ablation in mammalian cells and (b) ablation in fission yeast. (a) Ring opens upon cutting. Overlay (9 frames, 0.8s) reveals constriction and radial movement of myosin clusters. Scale bar 5 µm. (b) The ring breaks after cutting (arrows) but is repaired within seconds. Scale bar, 2 µm (109).

Also in fission yeast, ablation triggered opening of the ring. However, the opening healed to reform a complete ring while the clusters continued to rotate (Fig. 4.20 b, Movies 4.13 and 4.14). This shows that fission yeast ring is maintained under a minimal stress when compared to the mammalian case. These experiments substantiate the stress profiles simulated by the model. However, the healing of cytokinetic ring due to acto-myosin cluster rotation was surprising. This shows that cluster rotations homogenize the distribution of acto-myosin in the ring. On the other hand, we know that wall machinery also exhibits rotation. Together, the rotations of acto-myosin and wall machinery suggests transportation of wall machinery proteins by acto-myosin for sequential building of cell wall during the cytokinesis. Thus the minimal stress in the fission yeast ring in addition to longer constriction time (when compared to mammalian ring) can be accounted for constriction with simultaneous transportation of wall machinery for proper building of the cell wall.

4.9.2.1 Healing in fission yeast ring

The constriction rate of fission yeast ring strongly depends on temperature. The constriction rate and the velocity of clusters increase at higher temperatures (Fig. 4.2 b). The most common temperatures used for studying fission yeast cytokinetic ring constriction are 27 °C and 32 °C. However, in order to have a control for comparing the cluster velocities of temperature sensitive mutants (Fig 4.9 b), we visualized the ring constriction at higher temperatures: 36 °C.

Our observations of normal fission yeast ring constriction (non-mutants) in these unconventional temperatures (36 °C) were interesting. We observed defects in myosin where: (i) fracture in the ring leads to loose ends which were fluctuating on time scale of seconds (Fig. 4.21 a, Movie 4.15), and (ii) filaments of myosin (bound to actin) detached from the ring (Fig. 4.21 b, Movie 4.16). Interestingly in all these cases, the defects healed and the ring constriction continued.

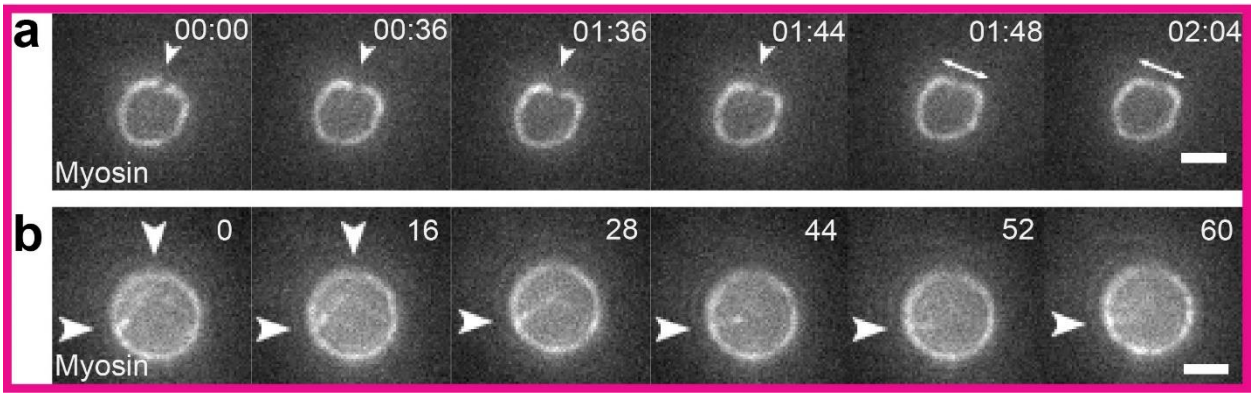

Figure 4.21. Defects in the ring, visualized by myosin. (a) Spontaneous breakage in the ring, which eventually heals to complete the ring (109). (b) Long actin filaments (cables) separating from the ring are integrated back into the ring. All these experiments were done at 36 °C.

These observations further substantiate the homogenization of acto-myosin distribution within the ring, which can be a function of cluster rotation in addition to transport of wall machinery. Also, the fluctuation of fractured ends and constriction after detachment from anchorage suggests a non-contractile ring which is under very minimal stress.

4.10 Discussion

The cytokinetic ring is an interesting case of active gel where an equatorial band of filament-motor assembly cleaves the cell by stress generation. The formation and constriction of this band are extensively studied both from biological and biophysical perspectives. Starting from identification of all the proteins, concentrations during their activity, temporal precision and significance of their contribution, – to main actors of stress generation and estimation of force, the topic has gained huge interest and literature (140, 141, 150–152). In this scenario, we present a new dimension to this topic by emphasizing the role of self-organization of active gels in stress generation. We start by addressing the difficulty in understanding the transition from single filament-motor interaction to many filament-motor interactions. We address this problem by studying two different systems: fission yeast with cell wall and mammalian ring with cortex.

Complete visualization of cytokinetic ring: When cells are placed on flat coverslips, the cytokinetic rings are oriented perpendicular to the focal plane (Fig. 4.1 a). While studies can be made taking advantage of the symmetry, the exact organization of proteins will not be revealed. We established microcavities as a powerful device for studying cytokinetic rings which by vertical orientation of cells allowed visualization of whole cytokinetic rings. This extended the possibility of studying acto-myosin dynamics with precise spatio-temporal resolutions.

Ring constriction: It was interesting that a ring of ~ 3.5 μm diameter closed in ~ 40 min in fission yeast rather a ring of ~ 20 μm took ~ 5 min in mammalian case. The absence of cortex in fission yeast and cell wall in mammalian cells can be cited as generic reasons. This is confirmed by the fast constricting *in vitro* fission yeast spheroplast rings (140). In spheroplast, the cell wall is removed while the acto-myosin ring is intact with most of the actin related proteins. In this case, the cells acquired a spherical shape and the perimeter of cytokinetic ring increased to ~ 15 μm and completed constriction at the rate of 220 nm/s which is several folds faster than the ring constriction in normal (1.16 nm/s) fission yeast cells. This increase in speed clearly shows that interaction of the ring with cell wall in fission yeast plays a major role in the time taken for constriction.

In the case of mammalian ring, the cell wall is absent, but the cell membrane is pulled by the acto-myosin ring during constriction. Turlier et al (153), showed that cortical flows in the furrow lead to active stress during ingression that give rise to the spherical shape of the dividing cells. This cortical activity close to the plasma membrane would be an influencing factor in the plasma membrane ingression during ring constriction in mammalian cells.

Although the presence of cell wall in fission yeast and cortex in mammalian cells, might be a reason for discrepancy in the size – constriction rate relationship, one might also expect a difference in the constriction mechanism between the two systems, although they share the same lot of proteins. This motivated us to study the organization of acto-myosin ring.

What happens to acto-myosin during constriction? Constriction indicates loss of material from the ring. By estimating the fluorescence signal, we found that the total intensity / total amount of acto-myosin in both fission yeast and mammalian rings decreased during constriction. This is consistent with the electron microscopy studies on sea urchin and fission yeast where the volume of filament network was found to decrease and the actin filaments (labelled with heavy meromyosin) shortened during constriction (152, 154) respectively. However, the mean intensity / concentration of myosin increases about 20 % in both rings i.e. the decrease in total amount of myosin is nonlinear with the volumetric change in the ring during constriction. While this increase in concentration has been reported in fission yeast for myosin (Myo2p) (138), a factor of ~ 40 % increase is proposed. In general, constriction requires stress generation and this huge increase in myosin concentration is usually taken as a read out for the stress generation. However, this observation of 40 % increase could be due to the conventional orientation of fission yeast rings. Since we found that the increase was only 20 % on whole (vertically oriented) rings, we reasoned that an additional factor would be required for generating enough stress to initiate constriction.

Clusters of acto-myosin: We found that acto-myosin in both fission yeast and mammalian rings were organized as clusters in distinct manners: rotating in fission yeast and static in mammalian case. Similar clusters of acto-myosin have been observed in fission yeast: nodes consisting of myosin and other proteins have been shown to promote ring formation by search and capture mechanism (121). Similarly, clusters of Myo2 and Myo3 were reported in spheroplast and fission yeast respectively, and they were predicted to play a role in stress generation by pulling actin filaments (141, 155).

Myosin clusters were also observed in *in vitro* reconstituted rings (147). In these *in vitro* rings, actin nucleating regions were micropatterned in a circular geometry. This circular network of actin started to constrict on addition of Myo6. During the constriction process, clusters of myosin were observed, that approximately remained static in the framework of the ring until the end of constriction. Similar clusters of myosin were found to rotate in the presence of α-actinin, an actin cross-linking protein. These scenarios of static clusters leading to full constriction and rotating clusters leading to minimal constrictions are similar to the mammalian and fission yeast rings, respectively in our experiments. Thus

acto-myosin clusters in rings seem to be a generic feature in many systems: mammalian cells, fission yeasts, spheroplasts and *in vitro* reconstitution of rings. Such self-organization of acto-myosin into clusters / puncta / nodes is not restricted to rings but are found in many other systems: *in vitro* reconstitutions of cortex (156, 157), acto-myosin network in mammalian cells (158), during the first division of *C. elegans* zygote (159), both before and during apical constriction in *C. elegans* and *Drosophila* (160, 161).

The cluster characteristics in both fission yeast and mammalian case were affected by inhibiting actin and myosin. This changes in cluster characteristics were associated with stalled ring constriction in both systems. While acto-myosin are the major actors, the cluster characteristics could also be affected by actin cross-linking proteins in fission yeast and mammalian rings. For example in Reymann et al (147), addition of α-actinin leads to rotation of myosin clusters. It would be interesting to check the effect of actin cross linking proteins like α-actinin and fimbrin on cluster characteristics by using specific mutants. In line with actin cross-linking proteins, actin nucleators: Formin and Arp2/3 (See Polyamines section) and depolymerizing factors: Actin depolymerizing factor (ADF) and Cofilin (53, 162) have been shown to play a significant role in ring constriction. Analysis on cluster characteristics after inhibition of these proteins would give better insights into the significance of actin polymerization in regulating cluster characteristics and ring constriction.

What leads to cluster formation and stress generation in the ring? In order to understand the formation of clusters, we need to understand the underlying molecular interactions. In the past, actin dynamics leading to specific organization have been theoretically modelled based on filament orientation and motor activity (148). Similarly, in the work of Reymann et al (147), the constriction of actin networks was mainly attributed to the orientation of actin filaments and myosin motor activity.

With this inspiration, we developed a theoretical model that applies fundamental interaction rules – based on filament polarity, motor density and treadmilling for interaction between two filaments. The resulting displacement was coarse-grained to obtain the collective effect of a continuum of such filaments – cytokinetic ring. In this model, unipolar filaments join to form a bipolar filament, similar to the search and capture mechanism (121) in fission yeast. In mammalian rings, formin is organized as clusters and co-localizes with myosin clusters. These formin clusters would nucleate actin filaments on both sides thus leading to a complete ring with combinations of bipolar and unipolar filament interactions. This provides experimental confirmation for the assumption of bipolar filaments in the model. Moreover, a similar arrangement has been reported by Reymann et al. (147), where dotted nucleating regions lead to growth of actin

filaments on both sides to form complete ring – although the emphasis of Reymann et al. is mainly on the formation of antiparallel bundles and not on bipolar and unipolar filament interactions.

In general during constriction, the ring consists of randomly oriented filaments (152). In such a homogeneous mixture of filaments, the parameter leading to instability and thereby to contraction or extension is a question debated by several theoretical models. One such model (163, 164) explains that in a homogeneous mixture of filaments, bundles of filaments with antiparallel orientation move faster than bundles with parallel filaments. This creates an instability that leads to clustering of filaments with opposite polarity. In this model, where myosin motors are assumed to slide off the filament ends, the instability and the following interactions lead to expansion of the filament network. Note that in our model, motors are positioned in the filament plus ends and do not slide off. This allows the respective movement of other filaments that interact with myosin motor, there by leading to local contractions by interactions of parallel filaments. One important assumption of the above mentioned models is filament rigidity. Other models take into account the elastic behavior of filaments, by assuming differences in force-velocity characteristics of motor populations (165, 166). This difference in force-velocity relationship would buckle/bend the filaments leading to contraction. However, how buckling instability would lead to contraction in a saturating concentration of motors is not clear yet. These models also explain how the symmetry is broken in the acto-myosin network, specifically leading to contraction or extension, and have been experimentally substantiated.

In this scenario, we take into account the formation of bipolar filaments in our model. The introduction of bipolar filaments and treadmilling velocity are unique to this model and gives a holistic perception of the system. Increased velocities of actin clusters in fission yeast (Fig. 4.9 b) can be attributed to this treadmilling velocity. The velocity of parallel filaments play a crucial role by destabilizing the system when they are higher than α_c. In addition, oscillating states are introduced when the number of unipolar filaments increase due to the disassembly of bipolar filaments (ω_d). The simulated static and oscillating patterns were similar to those observed in the experiments (Fig. 4.15).

The phase transitions (static and oscillating cluster states) predicted by our model were confirmed by experiments with specific inhibitors. In these experiments, constriction was stalled in the absence of respective cluster organization, thus highlighting the strong link between cluster organization and constriction. This experimental confirmation shows that our model captures the mesoscopic properties and the respective transformations of the

ring. The drug experiments also highlight the importance of myosin motors for ring constriction in mammalian and fission yeast rings.

Cluster function: The significance of myosin clusters for constriction was evaluated by estimating the stress generated in two systems. The model showed an increase in stress with appearance of clusters for mammalian cells and a constant stress profile for fission yeast. A point ablation was performed to check the tension in the rings. Immediately after ablation, mammalian rings opened and constricted at higher rates, indicating the presence of tension. A circular string under tension would tend to open when the tension is released by introducing a cut. However, if the tension is minimal or absent in the circular string, the cut would lead to loose ends which will not show any opening or constricting behavior. Taken together, this shows the significant role of clusters in increasing stress to constrict the mammalian ring. Moreover, this evidence of tension in the ring questions the extent to which cortex contributes for generating stress during mammalian ring constriction.

The opening of rings in fission yeast also indicated the presence of tension similar to (141). However, it was not followed by increased constriction rate. But surprisingly, the ablated spot healed to form a complete ring. This implies the presence of minimal tension that may not vary during constriction.

The healing of defects after ablation in fission yeast ring can be attributed to cluster rotation. This idea is supported by the formation process in fission yeast, where clusters/nodes of myosin present in the beginning, eventually bridge to form a complete ring (Fig. 4.17 a) (121). In addition, results from FRAP, show a high turn-over rate of myosin from the cytoplasm. These results indicate that cluster rotation is involved in maintaining the integrity of the ring.

In the theoretical model, the filament interactions that lead to cluster characteristics significantly depend on the bipolar filaments and accumulation of myosin motors at the plus ends of the filaments. These assumptions can be experimentally verified by super resolution imaging of end tracking proteins (plus end: Tropomyosin, IQGAP-Rng2, minus end: Formin, capping protein) simultaneously with myosin in both mammalian and fission yeast rings. The accumulation of motors in the $'+'$ ends triggers local contraction due to parallel filament interactions. This allows symmetry breaking which leads to constriction and not expansion of the ring. The assumption of similar force-velocity characteristics of all myosin motors allows simplification of the system and better understanding. However, it would be interesting to see how variations in the force-velocity relationships of motor population affect the ring constriction. Along this line,

introduction of passive cross-linkers may also alter the stress profile along the filament. For example it has been shown that passive cross-linkers are capable of generating stress in overlapping microtubule filaments (167). The introduction of these parameters in the model may provide better insights into the cluster organization and therefore stress generation.

The proposed functions of cluster organization: constriction for mammalian rings and transport of wall machinery for fission yeast, thus explain the discrepancies during constriction: 20 μm in 5 min (mammalian) and 3.5 μm in 40 min (fission yeast). The static clusters of mammalian rings generate higher stress that allows faster constriction, whereas the rotating clusters of fission yeast accommodate septum formation while generating minimal stress for constriction.

Interestingly, concerning the size and time taken for constriction, scaling arguments have been proposed for some systems: Carvalho et al (168), propose a direct scalability of constriction rate with the ring perimeter in *C. elegans* and similar scalability is observed in the filamentous fungus *Neurospora crassa* (169).

In these specific eukaryotic systems (*C. elegans* and *N. crassa*), the concentration of myosin in the ring during constriction has been attributed to higher stress generation. In addition to current proof, it would be interesting to study the independent role of clusters in stress generation without assistance from increased myosin density in mammalian rings. But, specifically affecting the cluster organization without touching acto-myosin activity is extremely tricky. As a first attempt, ablations can be performed specifically by targeting clusters at the onset of constriction. This would hinder stress generation in mammalian cells leading to constriction failure or delayed constriction. On the other hand, ablation can be performed during the formation phase of mammalian ring. Failure to form clusters and constriction onset would then strongly emphasize that constriction onset was only due to the cluster formation in mammalian cells and not due to the increase in myosin density.

Acto-myosin is necessary for septum completion. For proper cell division, fission yeast also requires the completion of septum in addition to ring constriction. We found that wall machinery involved in septum formation were organized into rotating clusters. This observation in addition to previous literature (170, 171), motivated us to propose a link between the cluster rotations of acto-myosin and cell-wall machinery, where the rotations of acto-myosin might transport wall machinery for septum formation. In support of a strong link between the ring and cell wall machinery, the acto-myosin ring tension has been shown to regulate septum circularity during ring constriction (172). In this context,

it is also worth noting that during bacterial cell elongation, wall machinery is shown to be built in a circumferential fashion in coordination with prokaryotic actin homologue – MreB protein (173). The stand-alone characteristics of filament-motor system is further highlighted by *Cps1* mutant experiment, where myosin exhibits rotation in the absence of cell wall synthesis. This establishes rotation to be an in-built characteristic of active gels.

Co-localization analysis of acto-myosin and β-glucan synthase clusters would substantiate the role of acto-myosin cluster rotation in transporting wall machinery. Another confirmation would be to check the BGS1 and BGS4 cluster dynamics in the presence of Latrunculin A. In the presence of Lat A, myosin clusters would be immobilized and should directly affect the cluster rotation of BGS1 and BGS4. On the other hand, it has been shown that the acto-myosin ring slides along the cell axis in paxillin like Pxl1 mutants. By introducing a point mutation that only targets the interaction of Pxl1 with β-glucan synthase, without affecting the positioning of the ring, can give evidence of wall machinery transport by acto-myosin. Finally, an ideal but difficult experiment would be to image in real time the acto-myosin with Pxl1 and BGS1/4 proteins using super resolution microscopy to specifically study the links between them.

Mammalian ring is anchored to the cell membrane. During the constriction of mammalian ring, the cell membrane is also pulled along. Carvalho et al (168), observe a similar trend of increasing concentration for myosin, anillin and septin which they propose to be important for constriction. Along this line, we checked the localization of anillin and septin during ring constriction. Immuno-staining of these proteins simultaneously with myosin confirmed their presence on the ring. This shows that the ring is anchored to the membrane at different points through the interactions of acto-myosin with anillin and septin (S.Fig. 3). This arrangement, where partial co-localization of myosin and formin clusters are observed in the ring in addition to the presence of anillin and septin, may indicate the anchorage of nucleating regions to the membrane. This anchorage through clusters of myosin and formin to the membrane should be necessary for pulling the membrane during constriction, similar to the theoretical simulations proposed previously (121, 141).

In conclusion, we identify a generic link between self-organization and stress generation, which might be the governing principle for ring constriction in all filament-motor based systems. In addition, we highlight the complexity behind the collective effects of active gel organization: the FRAP results indicate that, in spite of such rapid myosin dynamics, the cluster organizations are maintained intact. This serves as an outstanding example of a collective active gel phenomena, where thousands of nanoscale dynamics combine to

model a mesoscopic effect. All the conclusions in this work, from the specific organization of acto-myosin to their corresponding functions, were made purely based on self-organization principles. Self-organization is an inherent characteristic of active gels and has been shown previously with *in vitro* experiments (147, 174–176). But our results on cytokinetic ring constriction in two different *in vivo* systems take this a step further. We show that even *in vivo*, self-organization properties of active gel alone are sufficient to perform a mechanical work independent of the biochemical pathways.

However this work mainly highlights the organization of acto-myosin ring during cytokinesis in single cells. But acto-myosin based rings or contractile structures have been shown to exist in several multicellular systems for different purposes (177) like wound healing (178, 179), cell extrusion (180, 181), apical constriction (182), and vesicle secretion (183). In future, it would be interesting to investigate if such clustered organization is observed in all these contractile structures and to search for a generic organization that would be common between these systems.

5. Synthetic polyamines: new compounds specific to actin dynamics for mammalian and fission yeast cells

In this chapter, I will discuss the effect of synthetic polyamines – a new compound for investigating actin dynamics, on cytokinetic ring constriction in fission yeast. The results are published as a short communication article in BioArchitecture journal: Riveline, D., R. Thiagarajan, J-M. Lehn, M-F. Carlier. 2015. "Synthetic polyamines: new compounds specific to actin dynamics for mammalian cell and fission yeast". BioArchitecture 4: 1-5. The article is attached at the end of the chapter. This chapter will be complementary to the published article, and will include our current line-of-thoughts with new experiments.

I will start by listing the existing methodologies for studying actin dynamics followed by an introduction to natural polyamines, and synthetic polyamine compounds used in this study. This will be followed by a brief description of a previous work from our lab by Nedeva et al (127), to highlight the established effects of synthetic polyamines. Having set the stage for interest in the new drug, I will elaborate on the experiments and results of cytokinetic ring constriction in the presence of polyamines and other inhibitor drugs of actin binding proteins. Finally, I will finish the chapter with a discussion section that will include the perspectives on synthetic polyamines and on the corresponding results on cytokinetic ring constriction.

This project is a result of team effort. The project was conceived by Daniel Riveline in collaboration with Jean-Marie Lehn and Marie-France Carlier. The polyamines were synthesized by Girish Koripelly from Jean-Marie Lehn lab. The experiments on fission yeast cytokinetic rings were performed by myself and Marcia Toguchi – a former post-doctoral fellow in the lab.

5.1 Introduction

The polar nature of actin filaments facilitates polymerization at the barbed-end and depolymerization at pointed end. In steady state, where the polymerization / depolymerization rates are similar at the respective ends, the filament exhibits treadmilling which results in displacement and force generation. In addition, several other actin binding proteins also alter these dynamics: nucleators, capping and severing proteins, polymerization / depolymerization factors etc., (see Introduction section on cytoskeleton proteins 2.5.1) (184, 185). In order to study the role of actin dynamics, either mutations (186), or specific compounds (see list of compounds below) are used to

interfere with the kinetics of actin filaments and other actin related proteins in different manners. Mutations are most reliable, since they specifically target the gene of interest. But, inhibitor drugs provide the advantage of controlling the extent of inhibition, by varying the administered concentration in all cells. In this context, the most commonly used such compounds/drugs are:

1. Latrunculin A and B: sequestration of actin monomers – by binding to monomeric / globular (G) actin and preventing their assembly at the barbed end. Eventually, this leads to depolymerization of (filamentous) F-actin (143).

2. Cytochalasin D: barbed-end capping – by binding to barbed-end of F-actin and preventing both assembly and disassembly of actin monomers. Meanwhile, disassembly at the pointed end will lead to depolymerization of the actin filament (187).

3. Jasplakinolide: stabilizes F-actin and prevents disassembly of actin monomers (188).

While these drugs interfere through direct binding with actin filaments, other drugs control filament dynamics by interfering with actin related proteins:

4. Small molecule inhibitor of formin homology domain 2 (SMIFH2): inhibits formin – by binding to formin and reducing the affinity towards barbed-end. This prevents the formin based nucleation of actin filaments (125).

5. CK-636, CK-666 and CK-548: inhibit Actin Related Proteins 2 and 3 (Arp2/3). CK-636 and CK-666 – by binding to and preventing the conformational change of Arp2/3 complex to promote nucleation of actin monomers. CK-548 – by altering the original conformation of Arp3 (126).

Specific action of these drugs on corresponding proteins, based on concentration were used to highlight the significance of those proteins in actin dynamics. Along this line, synthetic polyamines have been shown to form aggregates *in vitro* (189, 190). Taking advantage of this, a previous study from our lab probed the effects of different polyamines on actin rich structures: the study showed that synthetic polyamines promoted growth of lamellipodia in an unprecedented manner (127).

5.1.1 Natural polyamines

Polyamines are naturally occurring compounds in various tissues and are considered to play an important role in cell proliferation and thereby growth (191–194). The most commonly occurring polyamine compounds in cells are putrescine, spermidine and

spermine (194). In addition to being growth stimulants, they have been shown to exhibit high affinity towards monomeric actin (189). In general, the cationic nature of polyammonium ions promotes a strong electrostatic interaction towards large group of biomolecules which are negatively charged: nucleic acids and lipids. Similarly, the negatively charged globular actin also possess a high affinity towards natural polyamines (ex: spermidine and spermine) in solutions, thus leading to aggregation of monomeric actin (189).

5.1.1.1 Chemical structure of natural polyamines

Polyamines are compounds with functional amine groups that are connected by a chain of methylene group. A simplest example would be ethylenediamine, where two terminal amine groups are separated by a methylene group: [H_2N-CH_2-CH_2-NH_2]. When dissolved in solution, polyamines loose the electron pair present in the amine group by gaining hydrogen and become cationic (polyammonium) in nature. Each of these cationic ammonium ions bind to one monomeric actin by electrostatic interaction, eventually leading to aggregation of actin monomers (189).

The structure of polyamine compounds plays an important role in their interaction with actin monomers. Oriol-Audit experimentally demonstrated that increased separation between the amine groups with increased chain length ($n > 3$ in H_2N-$(CH_2)_n$-NH_2) yielded higher efficiency in actin aggregation *in vitro* (189). For example, Spermine – a naturally occurring polyamine [H_2N-$(CH_2)_3$-NH-$(CH_2)_4$-NH-$(CH_2)_3$-NH_2] has 93 % polymerization yield when compared to ethylenediamine (5 %).

5.1.2 Synthetic polyamines with topological modifications

In addition to natural occurrence, polyamines can also be chemically synthesized in the laboratory. Chemical synthesis, gives the advantage of introducing structural modifications in the polyamine compounds with specific target locations. Along this line, a work from Jean-Marie Lehn lab (190), showed that in addition to increased chain length, topological modifications in polyamine compounds were more efficient in polymerizing monomeric actin. In this work, the polyamines were synthesized as cyclic structures. A cyclic assembly of well separated (amine) macromolecular compounds is called a (polyamine) macrocycle (Fig. 5.1 a). Lehn lab showed that the efficiency of

macrocyclic polyamines in polymerizing monomeric actin *in vitro*, exceeded their natural analogues by at least 30 folds, thus making them *superpolyamines* (190, 195).

5.1.3 Synthetic polyamines: interesting compounds for studying actin dynamics

A general way of studying the significance of a protein, in a particular function *in vivo*, is by inhibiting the protein function: either by mutation or by administering drugs that specifically target these proteins. For example, in the cytokinetic ring section (section 4) we showed that the fission yeast cytokinetic ring constriction was stalled by the addition of Latrunculin A. In this case, the significance of actin during ring constriction was tested by inhibiting (sequestering) its function, where the read-out was halted ring constriction. While this is a common practice for testing the function of proteins using inhibitor drugs (as listed in the introduction, section 5.1), polyamines present a different perspective to study actin dynamics. Instead of inhibiting the activity of actin, the increased affinity of polyamines towards monomeric actin leads to the formation of filaments and aggregates (189, 190). This presents an opportunity to study the actin polymerization dynamics in different cellular processes, by increasing the nucleation of monomeric actin above the natural level. However, in order to use the polyamines *in vivo*, its activity inside the cells should be validated. In this respect, we collaborated with Lehn lab. to test the effect of polyamines *in vivo*.

5.1.3.1 Cyclic and branched polyamines

A previous study from our lab tested the effect of two superpolyamines (C_7N_6 MPA and C_8N_6 BPA) *in vivo*, in collaboration with the Lehn lab (127). These polyamines were topologically different:

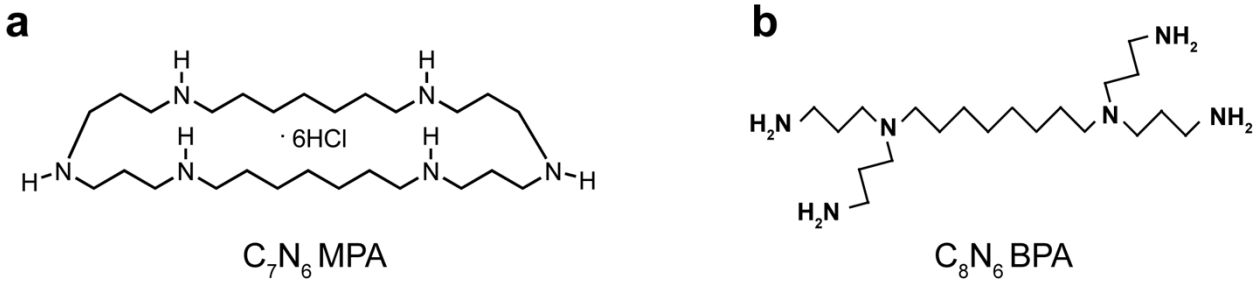

Figure 5.1. Structures of polyamine compounds: (a) C_7N_6 MPA and (b) C_8N_6 BPA, adapted from (196).

C_7N_6 MPA: a macrocyclic polyamine (MPA) where two dipropylene triamine subunits are connected by two seven aliphatic carbon chains to form a closed cyclic structure (Fig. 5.1 a).

C_8N_6 BPA: a branched polyamine (BPA) where two dipropylene triamine subunits are terminally connected by a chain of eight methylene groups in a non-cyclic manner (Fig. 5.1 b). This compound (C_8N_6 BPA) is now commercially available from Calbiochem (508438).

The effect of these polyamines *in vivo* were demonstrated by Nedeva et al. (127), using both *in vivo* and *in vitro* experiments (184, 185). In the following section, I will discuss in detail these results from Nedeva et al., before moving to our current results on cytokinetic ring constriction. To simplify, these polyamines C_7N_6 MPA and C_8N_6 BPA will be called as C7 and C8 respectively, throughout the text.

5.1.4 Synthetic polyamines promote rapid lamellipodial growth in mammalian cells

The work by Nedeva et al (127), demonstrates the effect of polyamines *in vivo*. The conclusions showed that polyamines: (a) lead to bundling of actin filaments, (b) made the filaments stable by direct binding, (c) decreased assembly / disassembly dynamics by specifically binding to barbed end, and (d) promoted nucleation leading to branched meshwork. These conclusions were obtained from a combination of *in vivo* and *in vitro* experiments, where the observed *in vivo* effects were systematically explained by *in vitro* experiments. The results are sequentially described in the following paragraphs. The results obtained were similar for concentrations of 300 µM and 100 µM of C7 and C8 respectively. It was interesting to see that lower concentrations of C8 (100 µM) were able to give similar effects as higher concentrations of C7 (300 µM), indicating a better efficiency of C8.

5.1.4.1 Lamellipodial growth and filament bundling

Both C7 (300 µM) and C8 (100 µM) promoted lamellipodial growth within minutes of addition to the culture medium (Fig. 5.2 a and b; Movie 5.1). The lamellipodial growth was also observed for smaller concentrations (10 µM, 25 µM, 50 µM) of C7 and C8 (see S.Fig 2, Nedeva et al (127)). However, the experiments were carried out with 300 µM C7 and 100 µM C8 to promote a saturating effect of lamellipodial growth.

When the focal contacts in the lamellipodia triggered by C7 and C8 were checked by immunostaining, they were similar to those produced during polarized cell migration (Fig. 5.2 c). In addition to these protrusions, ectopic lamellipodia were also observed. These results reveal that C7 and C8 are capable of entering cells and promoting native lamellipodial growth. The entry of polyamines was further confirmed by the entry of fluorescently labelled C8. Also, these lamellipodia exhibited bundles of actin arranged as microspikes. The bundling of actin filaments was further confirmed by *in vitro* experiments (Fig. 5.2 d).

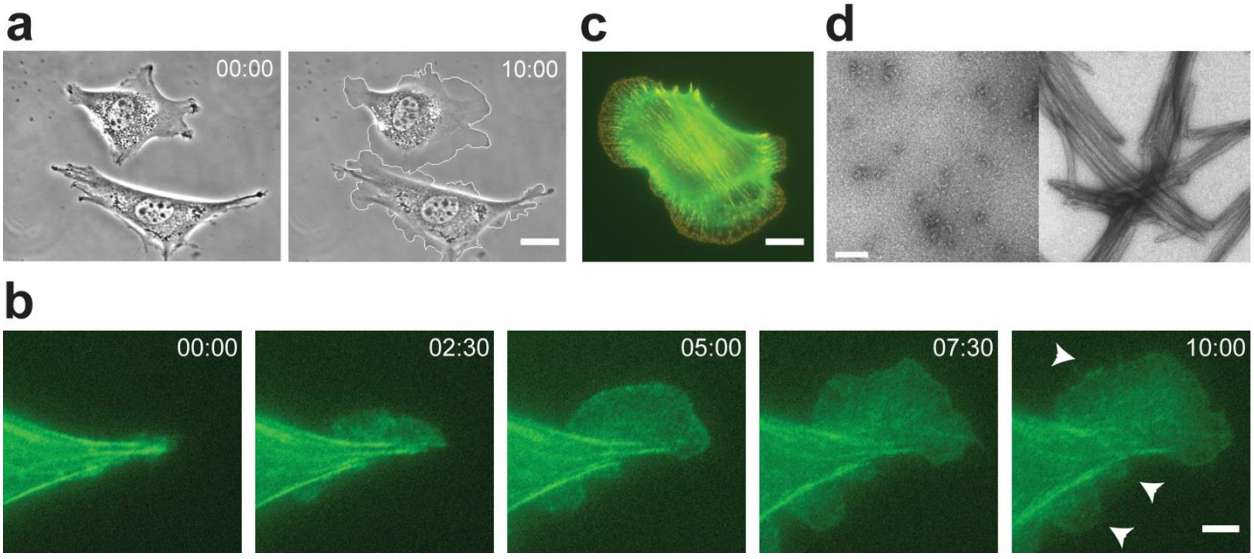

Figure 5.2. (a-c) Synthetic polyamines promote growth of lamellipodia, adapted from (196). (a) Promoted growth of lamellipodia in NIH3T3 cells. Scale bar 30 µm. (b) Dynamics of the growth visualized with actin-GFP in NIH3T3 cells after addition of 300 µM C7 (see Movie 5.1). Time in mm:ss and arrows indicate new lamellipodia. Scale bar 5 µm. (c) Focal contacts are associated with new lamellipodia (actin in green and paxillin in red). Scale bar 20 µm. (d) Bundling of actin filaments, adapted from (127). Electron microscopy observation of actin solutions (2 mM) in low ionic strength in the absence (left panel) or in the presence (right panel) of 300 µM C7. Scale bar 100 nm.

5.1.4.2 Increase in stability of actin filaments

The observed lamellipodia in the presence of synthetic polyamines disassembled after the addition of Cytochalasin D, but remained intact when latrunculin A was added. The inability of monomeric actin sequestration drug to disassemble lamellipodial actin, highlighted that actin filaments were highly stable in the presence of polyamines. The effect of polyamines on actin was due to the direct binding and not by the activation of other pathways. This was shown by the observation of C7 and C8 triggered lamellipodial growth in the presence of cytoskeletal inhibitor drugs: blebbistatin (inhibition of myosin phosphorylation) and Y-27632 (inhibition of Rho associated kinase).

5.1.4.3 Restriction of assembly-disassembly kinetics by barbed-end binding

To understand the precise action of polyamines on actin filaments, Nedeva et al., performed *in vitro* assays with spectrin-actin seeds and gelsolin-actin complexes. These proteins promote barbed end and pointed end growth respectively. When C7 and C8 were added to these seeded filaments, only the barbed end growth was inhibited while pointed-end dynamics showed very minimal effects. To precisely confirm the effect of C7 and C8 on barbed-end, polyamines were added to actin filaments bound to formins. But to achieve half-inhibition of barbed-end assembly, three times higher quantities of C7 and C8 were required, showing that presence of formins at the barbed end prevented the inhibition by polyamines. With these *in vitro* experiments, polyamines were found to bind the barbed end and decrease the assembly-disassembly dynamics, while not affecting the stability of actin filaments – the critical concentration of the monomer pool remained unaffected.

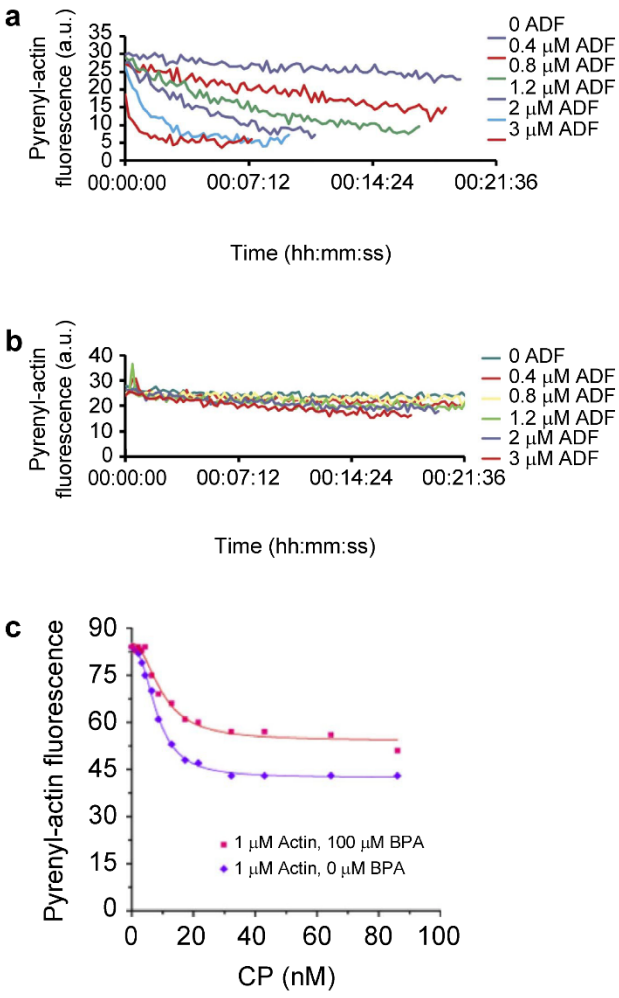

Figure 5.3. Adapted from (127). Polyamines abolish the effect of ADF, leading to lamellipodial growth. Time courses of ADF-induced rapid depolymerization of gelsolin-capped filaments in the absence (a) and presence (b) of 0.15 mM C8. (c) Effect of Capping Protein (CP) on F-actin assembled at steady state (1 μM total actin) in the absence and presence of 100 μM C8. Note that the experimental data points show a sigmoidal dependence on CP concentration owing to the known nonlinear relationship between the critical concentration and the extent of barbed-end capping.

5.1.4.4 Promotion of actin filament nucleation

Coming back to the *in vivo* observation, the branched meshwork of lamellipodia are generated by the action of Arp2/3 complex. In addition, the presence of Capping Proteins (CP) at this site, increases the nucleation of monomeric actin which in combination with Arp2/3 complex would further promote the formation of branched arrays. Meanwhile, the opposing function of Actin

Depolymerizing Factor (ADF) destabilizes actin filaments by severing and increasing pointed-end depolymerization rate. Hence the formation of lamellipodia in normal condition is regulated by the actions of CP and ADF. Irrespective of this balance, C7 and C8 triggered a very fast lamellipodial growth. Hence the effect of ADF and CP in the presence of polyamines was checked by *in vitro* experiments.

In vitro, addition of polyamines decreased the depolymerization rate promoted by ADF, without affecting the actin-ADF binding dynamics (Fig. 5.3 a and b). Further, polyamines lowered the free energy of filament nucleation to a larger extent in the presence of CP. These actions of polyamines lead to increased actin nuclei that will be utilized by Arp2/3 complex for the formation of branched arrays (Fig. 5.3 c). These *in vitro* results show that promotion of actin nucleation was a key factor leading to fast lamellipodial growth in cells. This was further confirmed by (i) the stability of lamellipodia in the presence of latrunculin A and (ii) the retrograde flow observed in lamellipodia (at the cell edge).

This work provided insights into the details of actin-polyamine interactions through several *in vitro* experiments and thereby explained the promoted lamellipodial growth in mammalian cells (127).

5.2 Results

5.2.1 Cytokinetic ring – an active gel *in vivo*

The organization of actin structures in lamellipodia (40, 197, 198) is quite distinct (mesh-like arrangement) from other active gel structures like cortex, cytokinetic ring, filopodia etc (see introduction section). While we established polyamines as powerful compounds by studying actin dynamics in lamellipodia, we wanted to see if their application can be extended to study actin dynamics in a different active gel from a different cellular system.

Along this line, from our results on cytokinetic ring constriction in fission yeast (section 4), we showed that actin dynamics, orientations of actin filaments and their interactions through myosin were key factors in self-organization and stress generation during the ring constriction process. Following this line, we chose to study and further dissect the role of actin dynamics using polyamines, during cytokinetic ring constriction in fission yeast.

5.2.2 Experimental setup and analysis

Fission yeasts were harvested in exponential phase and immobilized on glass coverslip using lectin. The cells were placed horizontally on the coverslip and the rings were visualized as two dots (Fig. 5.4 a). All the experiments were performed in a temperature controlled chamber at 27 °C. For every experiment, the culture was verified by acquiring at least one full ring constriction before adding drugs. After acquisition of one full constriction, media from the holder was replaced with the media premixed with drug. A field-of-view with many rings was chosen, and the acquisition was continued until all the rings completed constriction. Only those rings that were already formed at the time zero (t_0) of acquisition were taken for analysis. Rings that formed after t_0 were not considered for analysis, since cells exposed to polyamines before onset of ring constriction/during formation might exhibit different behaviors than those cells which were exposed during constriction. In the case of Nedeva et al (127) the instantaneous lamellipodial growth after addition of C7 polyamine was taken as cellular read out. In parallel, for ring constriction in fission yeast, the velocity of ring constriction was used as a measure for the action of drug. The acquisitions were made either with RLC1 (Regulatory Light Chain) or CHD (Calponin Homology Domain) for actin and myosin respectively. The fission yeast strains used were: (i) JW1349 labelled for RLC1-tdTomato and CHD-GFP and (ii) DR2 labelled for RLC1-mCherry and Pxl1-GFP (see Table 3.3 in methods section).

5.2.3 Effect of C7 and C8 polyamines on fission yeast cells

The fission yeast cells were exposed to 300 µM of C7. Strikingly, the ring constriction was dramatically delayed in the presence of C7, when compared to control condition (Fig. 5.4 b and Movie 5.2). The mean velocity of constriction in the presence of C7 was reduced two folds than in the control situation: ~ 25 nm/min in the presence of C7 as opposed to ~ 55 nm/min in control (Fig. 5.4 c). These measurements show that C7 polyamine affected the actin dynamics during ring constrictions.

In the case of Nedeva et al., (127) the topological difference between C7 and C8 was shown to play a key role – inferred by the difference in concentration required for triggering lamellipodial growth. Similarly, we wanted to know if addition of C8 affected the ring constriction to the same extent, as observed for lamellipodia. We initially exposed the cells to lower concentration of C8: 100 µM. C8 lead to a significant delay in constriction, when compared to control. The mean velocity of constriction in the presence

of C8 – 100 µM was ~ 40 nm/min, as opposed to ~ 55 nm/min in control (Fig. 5.4 c and Fig. 5.5 a). The difference in mean velocities between control and C8 conditions was significant. This shows that both C7 and C8 affected ring constriction in the same manner: delayed constriction exhibited as lower constriction velocity.

Note that in lamellipodia, smaller concentrations of C8 exhibited similar effects as higher concentrations of C7 (see S.Fig. 2, Nedeva et al). But in cytokinetic ring, the same trend was not observed: the mean velocity of constriction was higher (~ 40 nm/min) in the presence of C8 – 100 µM, when compared to the velocity (~ 25 nm/min) in the presence of C7 – 300 µM (Fig. 5.4 c and Fig. 5.5 c). These differences in dose dependencies between lamellipodia and the ring suggests that interaction of C7 and C8 may depend on the organization of active gel.

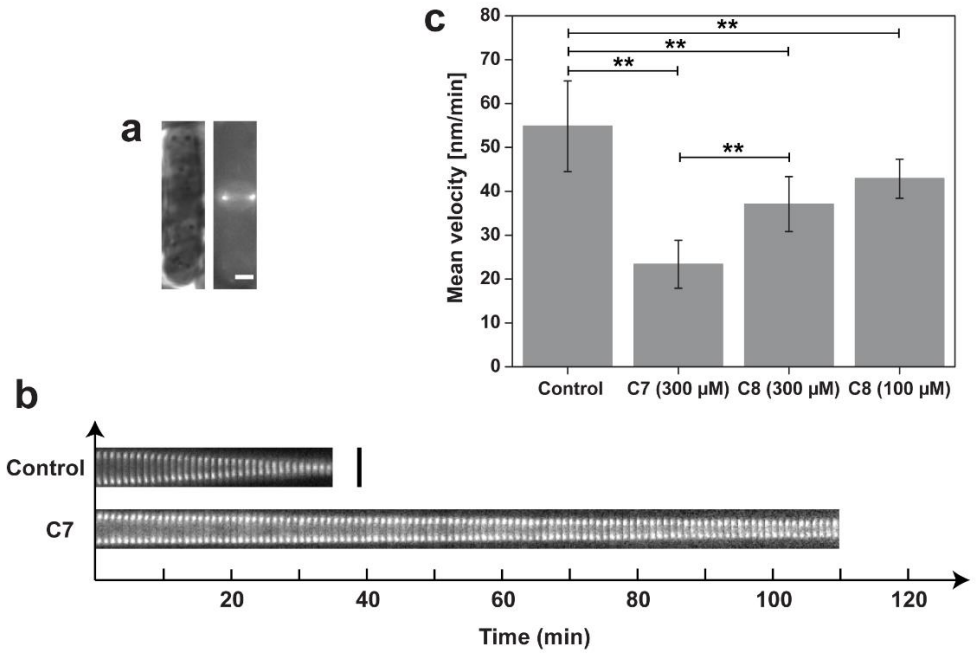

Figure 5.4. (a-b) Synthetic polyamines delay the cytokinetic ring constriction in fission yeast, adapted from Riveline et al. (a) Fission yeast at cytokinesis, (left) phase contrast, (right) the ring visualized with Rlc1-tdTomato, scale bar 2 µm; (b) Montage of dynamics of the ring diameter during constriction for control cells and in the presence of C7; images were equalized in their contrast; scale bar 4 µm. See also Movie 5.2. (c) Mean velocities for control rings and in the presence of 300 µM C7, 300 µM C8 and 100 µM C8. The error bars represent standard deviation of the mean. The biological repeats (N) and number of cells (n) in each condition were: Control (N=15; n=66); C7 (N=7; n=76); C8-300 µM (N=3; n=42); C8-100 µM (N=3; n=35). ** $P < 0.01$ by one-way ANOVA for C7 condition and by Mann-whitney test for 300 µM and 100 µM C8 conditions.

Next, we wanted to test higher concentration of C8: 300 µM, to check if the constriction velocity can then match the effects by 300 µM of C7. The mean velocity in the presence of 300 µM of C8 was ~ 35 nm/min, which was significantly lower than control (~ 55 nm/min) (Fig. 5.4 c and Fig. 5.5 b). But surprisingly, the mean constriction velocity in the presence of C8 – 300 µM (~ 35 nm/min) was still higher than C7 – 300 µM (~ 25 nm/min) (Fig. 5.4 c and Fig. 5.5 d).

These results show that both C7 and C8 had similar effects on the cytokinetic ring constriction – delayed constriction exhibited as lower constriction velocity. However, their interactions seem to depend on the organization of active gel, inferred by the difference in dose dependencies: (i) by triggering lamellipodial growth, the effect of lower concentration of C8 was equivalent to higher concentrations of C7. (ii) by delaying cytokinetic ring constriction, we showed that the effect of C8 was less than the effect of C7 even when similar concentrations were used.

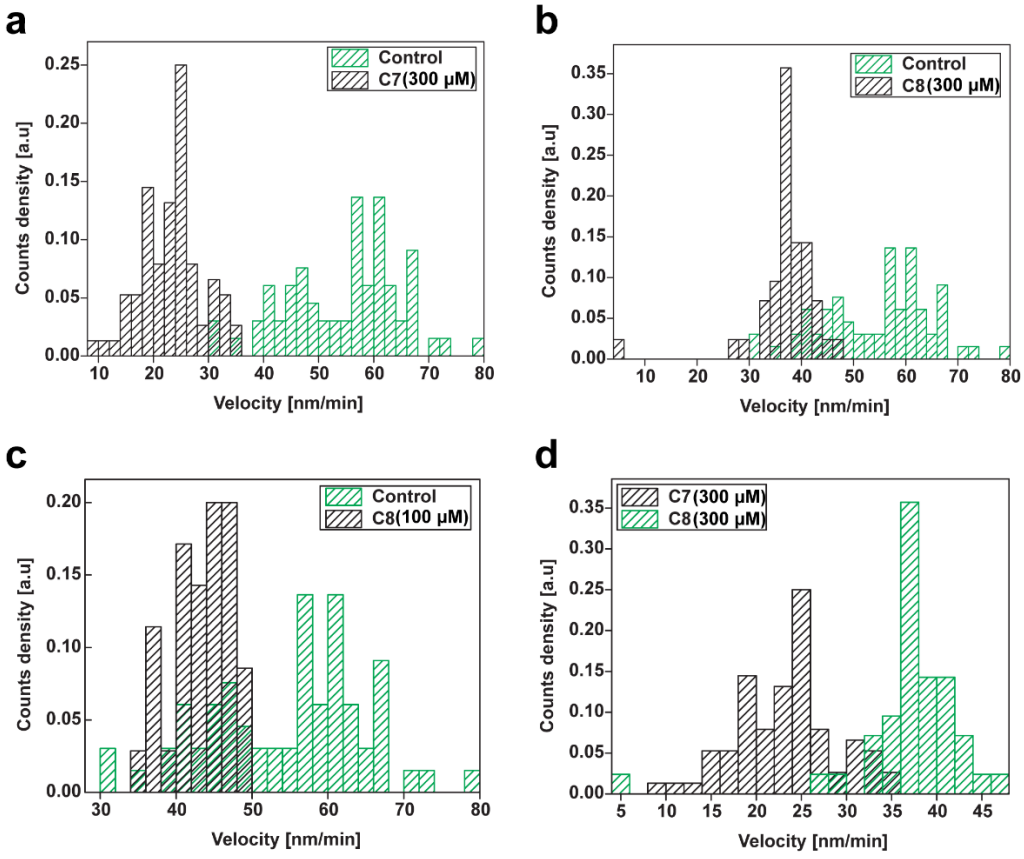

Figure 5.5. Comparison of sample distributions between control and C7-300 µM condition (a), control and C8-300 µM condition (b), control and C8-100 µM condition (c) and 300 µM of C7 and C8 conditions (d). The means were significantly different in all cases. Control (N=15; n=66); C7 (N=7; n=76); C8-300 µM (N=3; n=42); C8-100 µM (N=3; n=35).

5.2.4 Significance of nucleating factors in ring constriction: Formin and Arp2/3

C7 and C8 polyamines bind the barbed end leading to increased stability and nucleation of actin filaments. When these polyamines were added to cytokinetic ring, they led to a delay in constriction, showing that increase in filament stability and nucleation affected ring constriction dynamics. Following this, we wanted to test the role of natural actin nucleators in regulating actin dynamics during ring constriction. In Section 4 on cytokinetic ring constriction, we showed that presence of nucleators allowed the formation of bipolar filaments whose assembly / disassembly (ω_c and ω_d) kinetics played a key role in phase transition between static and rotating clusters. This motivated us to check the role of formin and Arp2/3 nucleators during ring constriction. We used the inhibitors of formin and Arp2/3: SMIFH2 and CK-636 respectively to investigate their significance (125, 126).

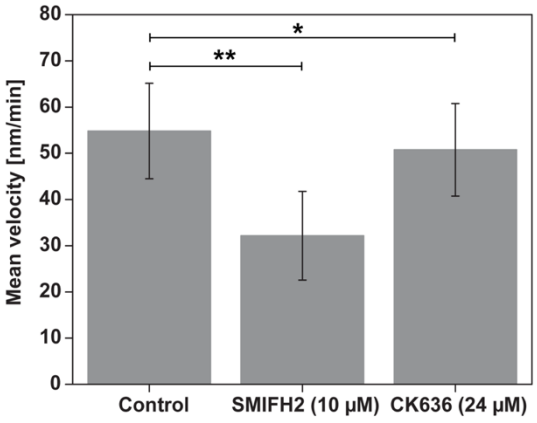

Figure 5.6. Mean velocities for control rings and in the presence of 10 µM and 24 µM SMIFH2 and CK-636 respectively. The error bars represent standard deviation of the mean. Control (N=15; n=66); SMIFH2 (N=7; n=65); CK-636 (N=6; n=54). ** $P < 0.01$ and * $P < 0.05$ by unpaired two-sample t-test for CK-636 condition and by Mann-whitney test for SMIFH2 condition.

First, we inhibited formin cdc12, a formin homolog in fission yeast. We used 10 µM of SMIFH2, the minimal concentration at which the effect is seen on ring constriction (125). The addition of SMIFH2 significantly delayed the ring constriction when compared to control. The mean velocity of constriction in the presence of SMIFH2 was ~ 30 nm/min, as opposed to ~ 55 nm/min in control (Fig 5.6 and Fig 5.7 a). This showed that regulation of actin polymerization / depolymerization dynamics by formin is significant in the ring constriction process as shown with formin mutants (*cdc12-112*) in the literature (124).

Next, we inhibited Arp2/3 complex using 24 µM of CK-636, since CK-636 at this concentration has been shown to inhibit actin polymerization by binding to fission yeast Arp2/3, whereas CK-548 does not (126). The mean velocity of constriction in the presence of CK-636 was ~ 50 nm/min, as opposed to ~ 55 nm/min in control (Fig. 5.6

and Fig. 5.7 b). While the variances of the two population (control and CK-636) were similar ($p > 0.05$, F test), the mean velocity of the conditions were statistically significant ($p < 0.05$ level, unpaired t-test). This confirms that inhibition of Arp2/3 by CK-636 delays ring constriction, although not as dramatically as formin inhibition by SMIFH2.

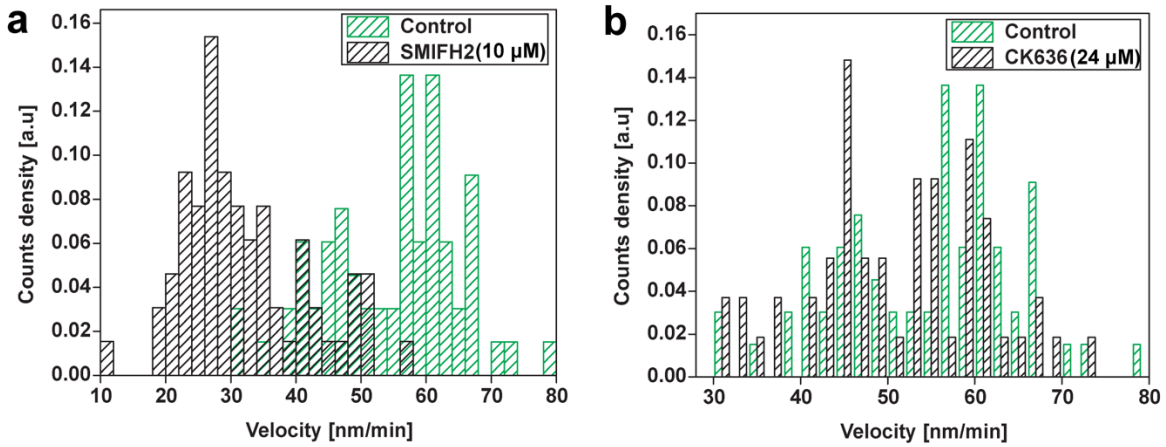

Figure 5.7. Comparison of sample distributions between control and SMIFH2 condition (a), control and CK-636 condition (b). The means were significantly different in all cases. Control (N=15; n=66); SMIFH2 (N=7; n=65); CK-636 (N=6; n=54).

These results show that formin and Arp2/3 are needed for nucleation regulation during the ring constriction process, although role of Arp2/3 is not dramatic (as observed from data and literature (199)). While minimal concentration of CK-636 was used for inhibiting Arp2/3, more information on the significance Arp2/3 on ring constriction can be obtained by scanning the effect at different doses of CK-636.

On the other hand, increase in stability and nucleation of actin filaments by C7 and C8 polyamines also affect the constriction process. It is interesting to note that ring constriction is delayed in both cases: (i) on inhibiting nucleating factors (formin and Arp2/3) and (ii) on introducing nucleation and stability promoting factors (C7 and C8). This suggests a strict regulation of actin nucleation during ring constriction because of which, both increased and decreased nucleation results in a delay in ring constriction. Another reason for delayed constriction in the presence of polyamine could be due to the increased stability of filaments.

To better understand, we are currently trying to measure the constriction velocity in the presence of C7 polyamine together with SMIFH2 and CK-636. To start with, we decided to use the drugs simultaneously: C7+SMIFH2 to test the effect of C7 when formin is inhibited, and C7+CK-636 to test the effect of C7 when Arp2/3 is inhibited. The drug cocktail was premixed with media and added to the sample. The idea of adding the drugs

simultaneously, is to see if the inhibition of natural nucleating factors (formin / Arp2/3) is compensated by the nucleation promotion of polyamines during the ring constriction. In this condition, we expect the mean velocity of ring constriction to be similar to that of the control. This result might indicate the possibilities of considering C7 as a replacement for the natural nucleators (formin /Arp2/3). These results are ongoing and are expected to give insights into the mechanism of interaction between C7 polyamine and actin filaments in cytokinetic rings. Also, this would help in precisely understanding the roles of actin polymerization during ring constriction.

5.3 Discussion

We established polyamines as a new tool for investigating actin dynamics in two *in vivo* active gel structures, from different systems: lamellipodia and cytokinetic ring from mammalian and fission yeast respectively. We show that polyamines enter mammalian cells – inferred by the entry of fluorescently tagged C8 and fast lamellipodial growth, and similarly propose that they enter fission yeast – inferred by delayed ring constriction. From our detailed study on lamellipodia (127), we show that polyamines promote the stability and nucleation of actin filaments by binding to barbed ends with *in vitro* and *in vivo* studies.

When C7 and C8 polyamine were administered to fission yeast cells, both polyamines induced a dramatic delay in the ring constriction. Surprisingly, the relative effects of C7 and C8 in fission yeast cytokinetic ring were not similar to lamellipodia. By triggering lamellipodial growth, lower concentrations of C8 showed similar effects matching the effects of higher concentrations of C7. This indicated a higher efficiency of C8. However, in delaying ring constriction, C8 showed lesser effect / higher velocity of constriction when compared to C7, even at similar concentrations (Fig. 5.4 c). This shows that the efficiency of C8 was lesser than C7 as opposed to its behavior in lamellipodia. At this point, it is also worth noting that smaller concentrations of C7 and C8 were shown to trigger lamellipodial growth in mammalian cells (see S.Fig 2, Nedeva et al). A similar tendency can be expected for ring constriction where smaller concentrations of C7 and C8 may delay ring constriction. This dose dependency in ring constriction will be tested in future.

The delay introduced by polyamines during constriction could be due to their interaction properties with ADF (Actin Depolymerizing Factor) and CP (Capping Proteins) in the cytokinetic ring. In the case of lamellipodia, the inhibitory effect of ADF is abolished by C7 and C8, while increasing the nucleation efficiency in the presence of CP. This leads to

fast lamellipodial growth. In the cytokinetic ring, it has been shown that Adf1 protein is important for the maintenance of ring and inhibition of Adf1 protein leads to delayed growth in culture (200). Similarly, inhibition of actin depolymerization factor (ADF) in other systems have also shown to affect ring constriction (53, 162). This shows that regulation of actin depolymerization is critical during the constriction process and polyamines stabilize the actin filaments against depolymerization. Hence the inhibitory effect of polyamines on Adf1 protein could be a potential factor leading to delayed constriction.

On the other hand, CP (Capping Proteins) are shown to play an important role in ring disassembly during constriction by being antagonistic to formin, in the competition for binding barbed ends (201). This indicates less formin binding to barbed ends, which is a favorable situation for polyamines (127). Thus increased binding of polyamines to the barbed end in addition to CP would lead to increased nucleation promoted by Arp2/3. The increase in number of filaments or filament branching might affect the interaction efficiency of myosin which would directly affect the transport efficiency (Section 4 on cytokinetic ring constriction). This could be another possible explanation for delayed constriction.

The effect of C7 polyamine in triggering lamellipodial growth and delaying ring constriction suggests a strong influence of cyclic topology. On the other hand, the difference in efficiency of C8 polyamine in two systems can be attributed to the difference in organization of actin structures between lamellipodia and cytokinetic ring. Lamellipodia contain meshwork of actin structures whose polymerization and branching are promoted by formin and Arp2/3 respectively (40, 202). Other major proteins present are: actin binding and cross-linking proteins, but the myosin motor proteins are absent (203, 204). Force is generated by the polymerization of actin filaments interacting with the membrane with the help of Arp2/3. This polymerization and branching activity leads to flat protrusive structures which are essential for migration. Whereas cytokinetic ring is a circular assembly of actin filaments and myosin motors, where interaction between actin filaments are dictated mainly by motor proteins (150). The circular arrangement leads to oriented actin filaments along the ring, as opposed to meshwork like structure in lamellipodia. The polymerization and filament-motor interaction leads to an ensemble effect which eventually leads to stress generation and thereby constriction (Section 4 on cytokinetic ring constriction). These strong differences in organization and dynamics, between lamellipodia and the cytokinetic rings can lead to different interactions of actin filaments with polyamines. This difference in interaction might be the factor affecting the efficiency of branched polyamine – C8. In addition to this, note that the topology and

chain length of C7 and C8 are different: The topology of C7 is cyclic, whereas C8 has a branched structure. In terms of chain length, C7 and C8 have 7 and 8 aliphatic carbon chains respectively. It could also mean that sensitivity to organization of actin filaments varies with topology and chain length of the polyamines (189). Further insights into identification of structure based specificity of polyamines to actin organization would make them a more powerful tool for unravelling precise actin organization in different systems. A structural biology based study will address these aspects.

The delay in cytokinetic ring constriction on inhibiting formin is in agreement with the literature (Fig. 5.6): formin cdc12 is important for actin polymerization (124, 141) during constriction. Similarly, arc5p/arc15p the smallest subunit of Arp2/3 is shown to be present in the contractile ring during constriction and promote actin polymerization. Mutation on Wiskot-aldrich syndrome protein (WASP), an activator of Arp2/3 complex delayed constriction (124). Our results on Arp2/3 inhibition also show delayed constriction although they are not as dramatic as formin inhibition (Fig. 5.6). This hints at a possible direct role of Arp2/3 in the ring constriction process which is currently debated (199).

The delay in constriction in both situations: enhancement of nucleation by polyamines and inhibition of nucleation of formin was interesting. These results indicate that actin polymerization activity is tightly regulated during cytokinetic ring constriction.

To further understand the regulation of actin polymerization during ring constriction, we are currently performing experiments with drug cocktails: C7+SMIFH2 and C7+CK-636. In these experiments, we expect a normal constriction rate similar to the control condition, hoping that C7 will be a replacement for the natural nucleators in the ring constriction process. In addition, polyamines also introduce stability to the actin filaments. Hence the resulting readout demands a careful interpretation in order to dissect the effect of increased nucleation and increased stability from the addition of polyamines, in the absence of natural nucleators. With a complete understanding of the effect of C7 on actin dynamics during ring constriction, one can use C7 to study the role of different actin related proteins. For example, the effect of actin cross-linking proteins can be studied when the nucleation and stability of actin filaments are increased (in the presence of polyamine). In addition, polyamines can be used to understand the role of actin dynamics in several scenarios like: filopodia for cell migration, stress fibers for reinforcement, cell-cell adhesion for neighbor interactions and actin patches/nodes in fission yeast endocytic mechanisms.

In conclusion, we established a new tool for studying actin polymerization. Usually drugs are used for studying protein functions through inhibition. In contrast, we present a synthetic compound – polyamine that is capable of promoting actin nucleation and stability. In other words, this compounds builds a cellular structure. It is worth noting that, polyamines are capable of inducing nucleation independent of cytoskeletal pathways. The characteristic of polyamines to enter different systems (mammalian and fission yeast cells) might extend their usage to *in vivo* systems, with possible application in *C. elegans* and *Drosophila*. Note that blebbistatin does not enter fission yeast (122).

This study compares the mean constriction velocities from a distribution of cells as a read-out of polyamine activity. However, on plotting diameter as a function of time, few cells showed non-linear behavior. The source of non-linearity is not clear and remains to be studied. However, we present this study mainly to show that polyamines can be used for studying actin dynamics in fission yeast. The current conclusions from the effect of polyamines on cytokinetic ring will be confirmed in future by: (i) studying ring constriction by complete visualization of the ring using microcavities, (ii) studying fluorescence intensity changes in actin and actin related proteins, and finally (iii) using super resolution techniques to observe the variation in actin dynamics.

6. Directed cell migration by adhesive ratchets and predicting direction reversal

Substrate with asymmetric patterns have been shown to direct and rectify cell migration in the absence of chemical gradients (116). In this chapter, I will discuss our results on reversing cell migration direction, by varying the gap distance (separation) between asymmetric ratchets. In this ongoing project, we scan a range of gap distance and overlap conditions. Based on our results, we report an optimal gap distance, at which the *ratchet* effect is most pronounced – in line with our previous study on *ratchetaxis* (61, 116). In addition, we report a simple mesoscopic model to find a condition at which cell migration direction is expected to be reversed on average.

This chapter will be organized as follows: I will start by giving a brief introduction on how asymmetries in cell and environments surrounding the cell, lead to random and rectified cell migration. I will extend the idea of rectified migration promoted by protrusions that sense local cues from substrate properties. To explain this mechanism of rectified migration – based on asymmetric substrate geometries and protrusions, I will introduce the concept of asymmetric ratchets in physics – borrowed from the ratchet and pawl concept by Feynman. Then, I will explain with examples from literature, on how this thought experiment can be applied for extracting work from random fluctuations. The explanation will be supported by theoretical and experimental examples of particle potential systems in physics. Then, I will explain how these principles of *ratchet effect* can be extended to direct and rectify cell migration, using substrates with asymmetric micropatterns (cell-ratchet system). In addition, I will also detail on the mechanisms that lead to ratcheting cell migration. Having explained in detail the concept of ratchet effect, with examples from physics and similar analogies in cell migration, I will dwell on the parameters giving rise to directionality in cell migration. I will extend justifications on choosing gap distances between the micropatterns as a parameter involved in the choice of directionality in cell-ratchet system. Then, I will explain in detail, our experimental setup with different gap distance conditions, and the associated results. Finally, I will describe our model that highlights the condition leading to reversal of cell migration direction, and will finish with discussion and future perspectives of this on-going project.

This project is a result of team effort. The project was conceived by Daniel Riveline who in collaboration with David Caballero and Jordi Comelles showed ratchetaxis in two separate publications (61, 116, 205). The idea was further extended by Daniel Riveline for direction reversal by changing gap distance. The experiments were performed by myself, and Simon Lo Vecchio and Cedric Fuchs – two Master intern students in the lab.

The actual mesoscopic model was developed by Raphael Voituriez and published in Caballero et al (116). Simon Lo Vecchio further extended this model for predicting direction reversal.

6.1 Introduction

Directional cell migration is an important process in different developmental and pathological phenomena (206). A cell migrating directionally is polarized with a distinct front and rear. The polarized state of a cell is an asymmetric state where the protrusions and protein accumulations are biased to one edge of the cell, which is the migrating front (24) (Fig. 6.1 a). As long as the polarization is maintained, cells exhibit migration. In addition to protrusions and protein accumulations, migrating cells also present an asymmetric shape: for example, in a normal culture, migrating fish keratocytes are crescent shaped (197).

This asymmetric / polarized state of the cell, which is a common characteristic of all migrating cells is often a result of asymmetric environment, although cells can spontaneous polarize in some conditions. For example, gradients of soluble or surface bound compounds and gradients of substrate stiffness lead to directed migration. Migration triggered by these asymmetries / gradients in environment are termed as chemotaxis, haptotaxis and durotaxis respectively (207). In general, cells exhibit stochasticity in the choice of migration, i.e. random change in migration direction. However, the environmental gradients mentioned above, introduce a symmetry breaking thus allowing cells to migrate in a specific direction. In addition, if these environmental gradients span over a larger scale, cells exhibit sustained migration in the same direction. This directional persistence is called *rectification*.

The polarized state of the cell is the first step in directed migration in response to an asymmetric environment. However, a rectified motion requires constant sensing of the environment. The chemical gradients in the environment are sensed by membrane receptors and the mechanical attributes of the environment are sensed by protrusive activities of the cell (207).

6.1.1 Role of protrusions and substrate geometry in rectifying cell migration

In general, *in vitro* in the absence of environmental cues, cells exhibit fluctuations and random motions. These fluctuations are resulting from the protrusive activities like

filopodia which probe the environment for firm attachment (60). Protrusions arise stochastically along the edges of cells. After a protrusion establishes a firm attachment to the substrate, the cell is pulled in the corresponding direction. The point of protrusion attachment that generates migration is random, thus resulting in random motion. Taking into account directed migrations *in vivo* (208), in addition to chemical gradients, protrusive activities may also play a role for directing cell migration. In an environment of long range gradient (where slope of the gradient is smaller), the rate of change in the gradient is very minimal at the scale of a cell. It is not clear how the cell can distinguish the gradients between the front and rear. Hence there needs to be a sensing mechanism in the cells that can probe the local cues in the environment (209). The interaction of protrusions with the substrate during migration steps makes it an ideal candidate for sensing local environmental cues.

Along this line, substrate geometry has been shown to be an important factor in triggering rectified migration. A major interest that has emerged in the recent past is the capability of asymmetric substrates in promoting directional migration of cells, *in vitro* (210–213). In the majority of studies, asymmetric shape is imposed on the cells by seeding cells on usually a teardrop or triangle-like asymmetric micropatterns.

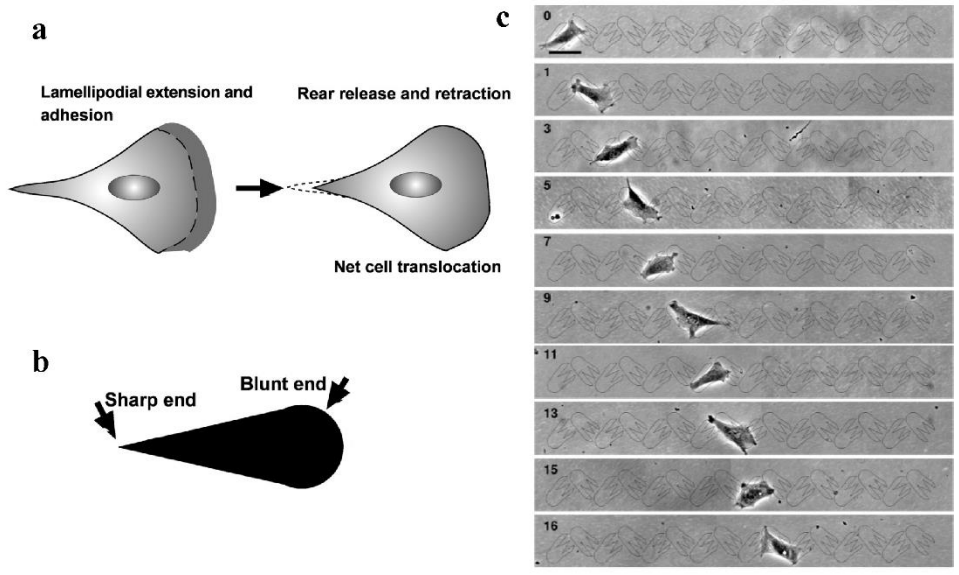

Figure 6.1. (a-b) Adapted from Jiang et al. (210) (a) Representation of cell shape during cell migration. The cell is polarized with preferential extension of lamellipodia in the direction of arrow (left). This leads to cell motion in the same direction (right). (b) The tear drop shaped pattern used for imposing the initial polarization in cells. The sharp and blunt ends are shown by arrows. (c) Adapted from Kumar et al. (211). Micropatterns are arranged in a 'zig-zag' manner. While the micropatterns are not strictly asymmetric, their tilted arrangement allows lamellipodial extension into the successive pattern. This retains the NIH3T3 cell polarization, and leads to rectified migration. Time in hours.

The study by Jiang et al. (210) first proposed the influence of asymmetric substrates in generating directional migration. In this study, cells were confined to teardrop shaped structures to impose an initial polarization or asymmetric shape (Fig. 6.1 b). When the cells were released from the teardrop shaped micropatterns, protrusions always extended

in the direction of blunt end of the tear drop. This induced migration in the same blunt end direction. Jiang et al. (210), proposed that the asymmetric micropatterns forced the cells to take a polarized or asymmetric shape with lamellipodial protrusions extending on the blunt end (Fig. 6.1 b). In addition to lamellipodia, polarization was confirmed by presence of microtubule and centrosome at the blunt end (214). Thus, imposed polarization from the asymmetric patterns, triggered directional motility of cells. This study, as a first, proved the significant role of substrate geometry in imposing the asymmetric shape required for directional migration. However, this study emphasizes the direction of migration due to the asymmetric micropatterns and not persistent migration. Because, the cells would migrate in the direction of blunt end (of the tear drop) only until the polarization is maintained, after which they would exhibit random migration.

Following this work, a study by Kumar et al. (211), showed that directionally persistent migration can be achieved by using a series of micropatterns that are positioned in a "zig zag" manner (Fig. 6.1 c). The patterns were not asymmetric. But, the size of the motifs was adapted so that the cells conform to the size of micropatterns – the tilted placement of successive motifs allowed the attachment of extending lamellipodia. This tilted placement lead to symmetry breaking and the cell motility was rectified to one direction.

In the above mentioned studies, directional migration was achieved by adapting the direction of cell polarization through the asymmetry of the substrate. The polarization here refers to the extension of protrusion and specific localization of proteins on the migrating front. However, rectification can also be achieved only by an asymmetric environment without exciting the cells to the polarized state (212). This process of rectification of any random motion is called ratchetaxis (61).

In the following sections, first I will give the physics behind the ratchet phenomenon, followed by a short description of theoretical and experimental studies on ratchet effects. Then I will explain how ratchet effect can be applied to cell migration, and the mechanism leading to ratchetaxis in cells. After this detailed introduction, I will dwell on the idea of the current project in reversing cell migration, followed by the associated results.

6.1.2 Ratchet – a rectifying device

A ratchet is a device that leads to an irreversible motion or a rectified motion (215). For example, Fig 6.2 shows an example of ratchet device. The device consists of a wheel with asymmetric teeth, i.e. the slope of the teeth on either sides are different. The movement of

the wheel is obstructed by a lever connected to a spring. If fluctuations strong enough to overcome the potential energy of the spring are introduced, the wheel would tend to rotate in one direction, due to the presence of the lever. This rectified rotation of the wheel is due to the periodic positioning of the asymmetrically shaped teeth. This is an example of how periodically positioned asymmetric geometries can be used for rectifying random fluctuations.

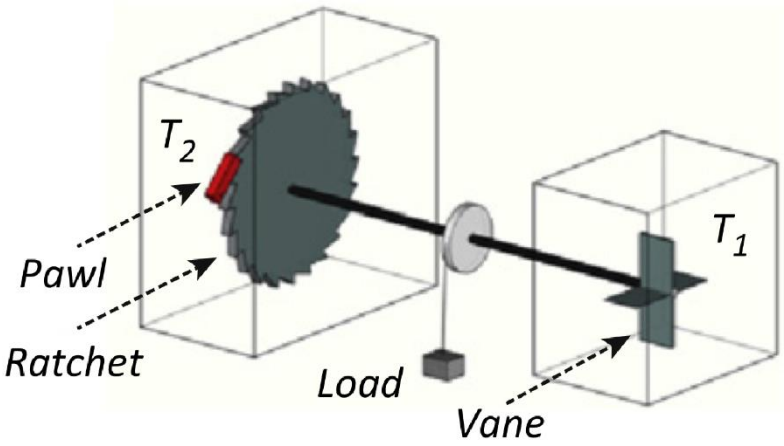

Figure 6.2. Adapted from Caballero et al. (61). Representation of the ratchet and pawl arrangement proposed by Feynman, as part of his thought experiment to explain rectification of random fluctuations. The boxes are in different temperatures (T_1 and T_2). The left box contains a wheel (ratchet) obstructed by a small lever (pawl), connected to a spring. The right box contains a vane, which is connected to the wheel by a shaft. A net rotation of the shaft will lift the load in the center.

If we move to the microscopic world, then particles are exhibiting random movement – Brownian motion, with energy equivalent to k_BT (k_B – Boltzman constant and T – Temperature) (216). Richard Feynman proposed to use the energy of Brownian particles in rectifying the rotation of wheel described in the previous paragraph (215). He proposed that, if the device in Fig. 6.2 is reduced to microscopic scales, then the collision of Brownian particles would introduce enough fluctuations on the wheel. Then, the fluctuations in the wheel will be rectified due to the presence of the lever. Thus, he proposed to extract work (rectified rotation of the wheel) by utilizing thermal fluctuations in the medium. This thought device is called Brownian ratchet. While this was an interesting proposition, he further showed that work cannot be extracted without an external energy source: for example $T_2>T_1$ might lead to rotation since more fluctuations in the wheel can be expected.

But taking this line of thought, several studies that came later, proved the existence of Brownian ratcheting in self-excitable objects (217–219). For example, motor proteins or cells are self-excitable objects that synthesize ATP and extract work from ATP hydrolysis. In the following sections, I will first introduce the theoretical and experimental proofs of ratchet effect in a simplified manner with examples from physics.

These examples will describe how random motion of Brownian particles can be rectified both in diffusive and non-diffusive states, followed by experimental demonstrations. Then I will discuss those studies that have translated the idea of ratcheting for rectifying cell migration.

6.1.3 Ratchets for rectifying particle motions

6.1.3.1 Rectification of diffusing particles

Prost et al. (220), proposed a system where freely diffusive particles are trapped in a two state potential system (Fig. 6.3). This externally applied potential can be switched 'on' and 'off' and has an asymmetric landscape, where b > a. In this situation, if the potential is switched 'on' then the particles are trapped and concentrated in the minima (Fig. 6.3 a). But, when the potential is switched 'off', then particles experience a flat profile and are free to diffuse (Fig. 6.3 b). Although, particles are free to diffuse in all directions, due to the asymmetry of the potential landscape: b > a, the probability of particles to diffuse over the length 'a' is larger than the probability to diffuse over the length 'b'. By repeating this 'on-off' cycles, a macroscopic drift results: effective movement of particles to the right (Fig. 6.3 c). Thus only with an asymmetric potential system, the random motion of diffusive particles can be rectified. This case is very similar to Feynman's ratchet device.

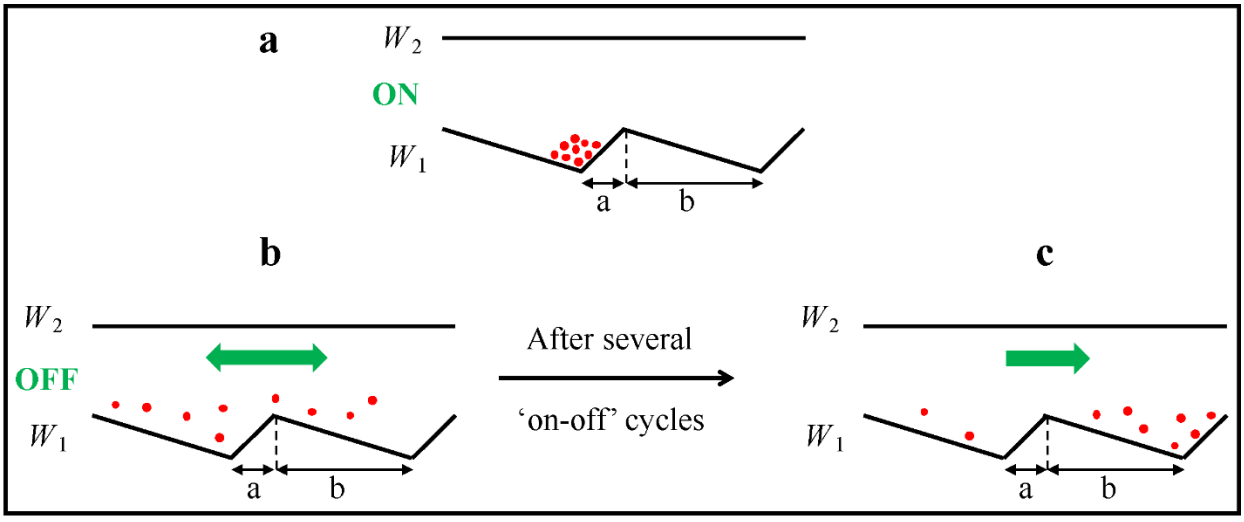

Figure 6.3. Representation of particle-potential system described in Prost et al. (220). The particles can be in two potential states W_1 and W_2. 'a' and 'b' represent the shorter and longer slopes, respectively on either side of the maxima in the potential. The red dots denote particles under study. (a) When W_1 is switched 'on', particles are trapped in the minima due to the asymmetric nature (b > a). (a) But when W_1 is switched 'off', the particles experience a flat profile (W_2), and are free to diffuse (indicated by green arrows). When subjected to several 'on-off'

cycles, the particles are repeatedly trapped in the minima of W_1 or free to diffuse (W_2). (c) During this process, the asymmetry of W_1 ($b > a$), imposes a net macroscopic drift on the particles, directed to the right hand side (indicated by the green arrow).

In the above mentioned case, diffusion is the major force driving the particle motion. However, this setup can be modified to achieve force-free motion or diffusion independent motion. In the following section, explanation of force-free motion by Chauwin et al. (221), is presented.

6.1.3.2 Rectification in the absence of diffusion: Force-free motion

Let us take the same particle-potential system described in the section above. However, in this setup it is assumed that, both potential states have an asymmetrical landscape with the extrema of each other shifted by 'δ' (221) (Fig. 6.4). Where, E_1 and E_2 are the amplitudes of the potentials and, τ_1 and τ_2 are the lifetimes of particles corresponding to potentials W_1 and W_2 respectively (Fig. 6.4). In this setup, by switching on the potentials in an alternating manner, particles will be trapped in the corresponding potential state.

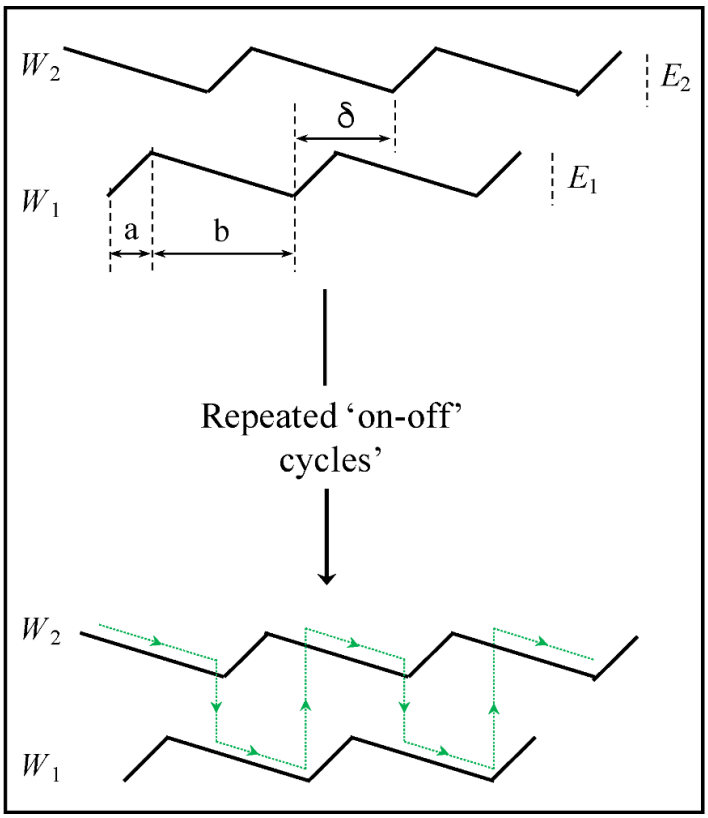

Figure 6.4. Representation of particle-potential system described by Chauwin et al. (221). The system is similar to the one shown in Figure 6.3, except that, the second potential state (W_1) is also asymmetric and the maxima of the potentials are shifted by a distance 'δ' (top). In this system by alternative switching 'on', the particles will be trapped in the corresponding potentials. By repeating the 'on-off' cycles, a macroscopic drift is generated to the right hand side. The mean trajectory of the particles is indicated by green dotted lines and arrows (bottom). Since the particle is always under the influence of potentials, the particle is never subjected to diffusion. Thus the motion is force-free.

Given this scenario, if the lifetime of the particle in each potential state is sufficiently larger ($E_i\tau_i > ab/\mu$; $i = 1, 2$), the particles will move downhill to be trapped in the minima before drifting to the alternative potential. By repeating this process of alternatively switching 'on' the potentials, the particles will be trapped in the

subsequent minima in each potential, thus yielding a rectified motion. Note that in this case the rectification of particle motion is not due to diffusion (k_BT is negligible), and absolutely force-free. This theoretical approach showed the possibility of force-free motion of particles in a two-state asymmetric potential system, spatially shifted with respect to each other (221). Interestingly, two different studies provided experimental proofs for the theoretical approach discussed above (222, 223). These experimental proofs are discussed in the next section.

6.1.3.2.1 Experimental verification of force-free motion

The theory of force-free motion has been experimentally verified by two different studies (222, 223): (i) In the first work (222), colloidal particles were suspended in solution between electrodes of asymmetric shape (Fig. 6.5 (i)). When the suspended particles were subjected to cycles of 'on-off' electric field, the particles were exhibiting directed motion (Fig. 6.5 (ii)). The velocity of the particles was dependent on size, thus allowing applications where size dependent separation of particles is needed.

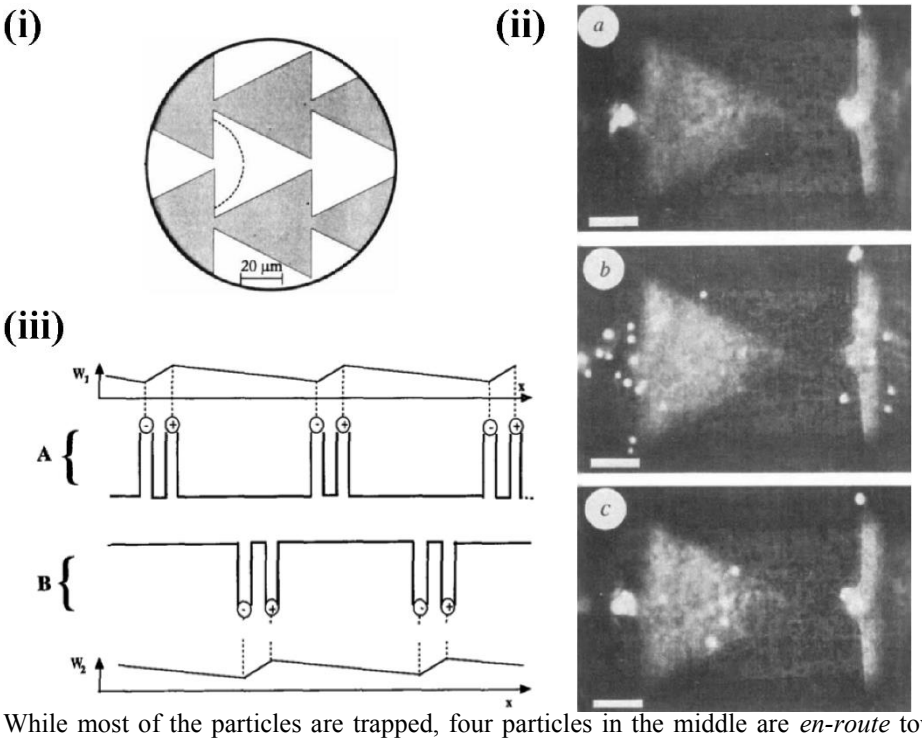

Figure 6.5. (i - ii) Adapted from Rousselet et al. (222). (i) Schematic representation of the electrodes used for trapping particles. The particles can be trapped in one of the electrodes when a potential difference is applied. (ii) Fluorescent particles moving on an electrode similar to (i), by repeated 'on-off' cycles. (i-a) Trapped particles when the voltage is applied. (i-b) Snapshot of dispersing particles due to diffusion when the potential is switched 'off'. (i-c) Snapshot of particles in the late stage of the retrapping process. While most of the particles are trapped, four particles in the middle are *en-route* towards the subsequent trapping site. (iii) Adapted from Gorre-Talini et al. (223). Schematic of the experimental setup used for trapping mercury droplet. Two system of electrodes (A and B) connected to the central canal. A and B are transverse canals connected to electrodes, on either sides to the central canal. The transverse canals of A and B are shifted with respect to each other and correspond to W_1 and W_2 respectively.

(ii) In the second work (223), the influence of electric field on a mercury drop placed in dilute sulphuric acid in a system of canals is studied (Fig. 6.5 (iii)). A central canal, branched with transverse canals on both sides is used. In each side, the canals are periodically placed but their placement is spatially shifted with respect to the transverse canals on the opposite side (Fig. 6.5 (iii)). The canals are filled with sulphuric acid through which a mercury drop is allowed to move. And electrodes are connected to the transverse canals to induce the potential difference. In this spatially shifted asymmetric potential system, by periodically switching the electric fields between the transverse canals on either sides, the mercury drop exhibits a directed motion. Note that, this system is similar to Fig. 6.4, where particles (mercury) move between two potential states (transverse canals on either sides) by switching 'on' and 'off' the potentials (by alternating the electric field between the transverse canals on either sides).

These examples clearly indicated that asymmetric environments can lead to rectification of movements in the presence of an external source of energy. In other words, the asymmetric environments act as ratchets in rectifying the random motions of particles. This ratcheting effect due to asymmetric environments from theoretical and experimental studies, motivated several groups to check, if similar asymmetric environments can be used to rectify / ratchet biological processes like movement of molecular motors and cell migration.

6.1.4 Ratchets for rectifying cell migration

6.1.4.1 Cells are self-propelled particles

Now let's go back to my description of cell migration where the cell goes to a polarized state (asymmetric state) in order to perform migration. In fact, the asymmetric (polarized) state of the cell and the corresponding work done (migration) are the result of ATP hydrolysis that occur within the cell. From a physics point of view, this cycle of ATP production and its utilization for cellular processes like migration, qualifies the cell to be a self-propelled particle moving away from equilibrium (216). By analogy, the cell can be considered as a fluctuating particle which can transit between non-motile state to a polarized-motile state, due to ATP hydrolysis. After being motile, a cell would exhibit a stochastic (random change in direction) motion. In this scenario, it would be interesting to see if a cell would exhibit a rectified motion by placing in an asymmetric environment that is periodically separated.

In the following paragraphs, I will give few examples of ratcheting effect for rectifying cell migration. In addition, I will discuss in detail on a previous study from our lab which gave mechanistic explanation of such ratcheting behavior during cell migration.

6.1.4.2 Rectification of cell migration - ratcheting

The experimental verifications of particle currents motivated similar experimental setups in cell migration. The first demonstration of rectified cell migration by ratcheting was given by Mahmud et al. (212). In this study (212), substrates microetched with asymmetric geometries (triangles) were used. The setup was constructed in such a way that the funneling vertex of a triangle was connected to the next triangle by a small opening (Fig. 6.6 a). The migration of cells on these connected triangles were directed towards the funneling direction, thus showing a ratchet effect. The asymmetric nature of the substrate (triangular geometry), acts as a ratchet by rectifying the random motion of cells towards the funneling edge of the triangles. The explanation for this ratcheting behavior was proposed as follows: cells spreading on the triangles form focal adhesions close to the three vertices of triangles and these focal adhesions are connected by stress fiber bundles (Fig. 6.6 b).

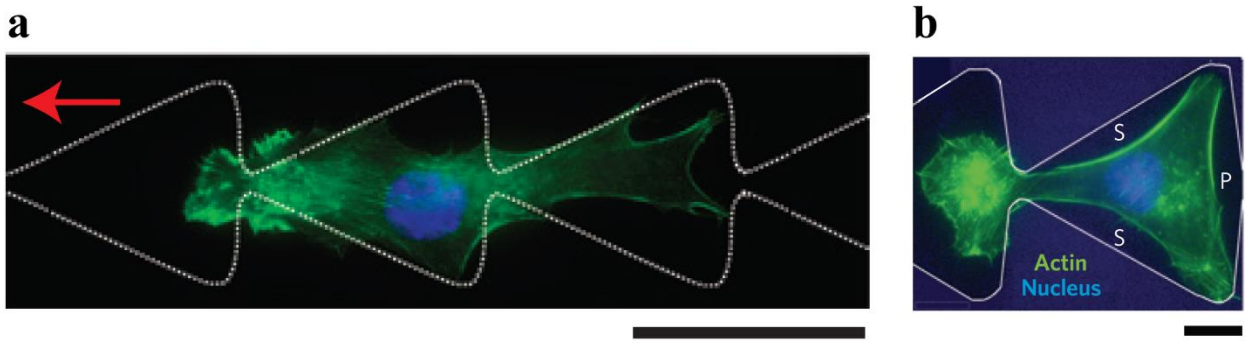

Figure 6.6. Adapted from Mahmud et al. (212). (a) A B16F1 cell moving on ratchet micropattern - ratcheting. The cell extends lamellipodia into the consecutive triangle and moves in the direction of arrow. (b) Snapshot of a cell moving into the next triangle with lamellipodium and actin bundles. 's' and 'p' indicate the side and perpendicular actin bundles of the cell, with respect to the triangle (micropattern). Note that while perpendicular actin bundles are intact, lamellipodium grows from the opposite side without compromising the actin bundles. In both (a) and (b), the dotted lines outline the shape of micropattern, green color indicates actin and blue indicates nucleus. Scale bar 50 μm (a) and 12.5 μm (b).

They propose that sending protrusion from the focal adhesion close to the funneling vertex to the next triangle would be energetically favorable for the cell. Because sending protrusion from the base of the triangle, would require breakage of stress fibers connecting the other two focal adhesions which run parallel to the triangle base. In

addition, they show evidences of cell sorting in different cell types by adapting the ratchet characteristics to the morphology of the cells.

In this study (212), it was proposed that connection between the triangles allowed lamellipodial protrusions to direct cell migration. However, it was a theoretical proposition and experimental measure of energetics can be tedious. As I mentioned in the introduction (section 6.1.1) and as mentioned elsewhere (224), filopodial dynamics also play a key role in directing cell migration. Motivated by this, a previous study from our lab investigated the role of protrusion dynamics (116), which is discussed in detail in the following section.

6.1.4.3 Protrusion fluctuations lead to ratcheting of cell migration

Protrusions randomly arise from the cell edges for probing the environment to eventually result in migration. In order to study the role of fluctuations in protrusions in directing cell migration, Caballero et al. (116) in our lab, used NIH3T3 cells plated on substrates (coverslip) with asymmetric micropatterns (triangles) of fibronectin (Fig. 6.7 a (Configuration (i))). The concentration of fibronectin (10 µg/ml) was chosen appropriately to match the maximum velocity of NIH3T3 cells. The fibronectin triangles were separated by a gap of 20.5 µm, which corresponds to the mean protrusion length in NIH3T3 cells. Similarly, the area of fibronectin triangle was chosen to match the mean area of NIH3T3 cells. Except for the fibronectin triangle, the rest of the substrate was passivated using pLL-g-PEG.

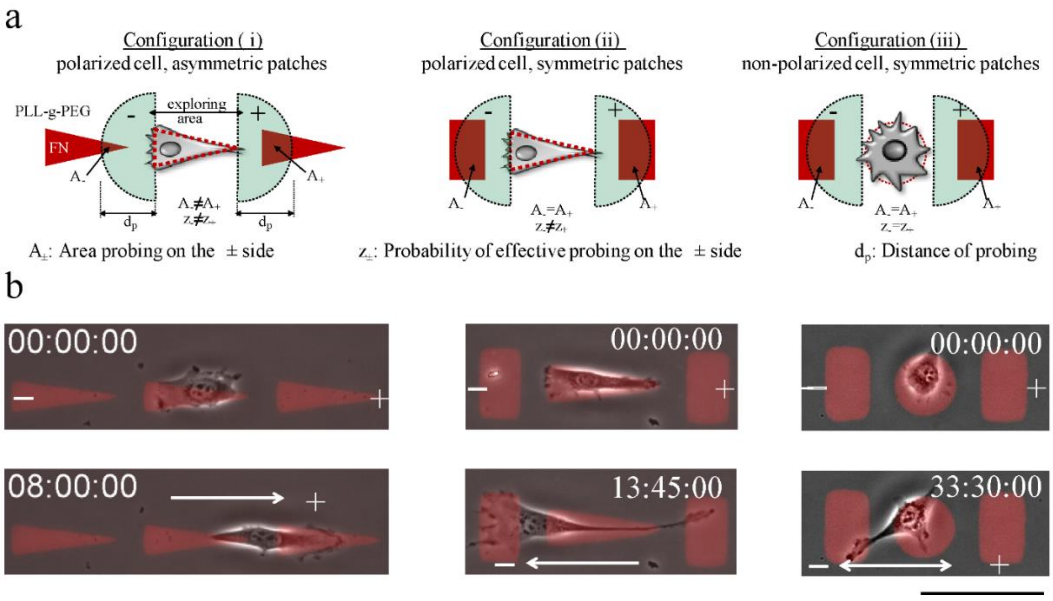

Figure 6.7. Adapted from Caballero et al. (116). Three different configurations of fibronectin micropatterns (in red) to monitor the first step of the cell by placing the cell in the central micropattern. The neighboring micropatterns on either sides of the cell provide attachment area (indicated by semi-circle) for cell protrusions. (b) Initial (t_0) and final ($t_{first\ steo}$) steps of a cell in each configuration. Snap shots correspond to the configuration exactly above. Arrows indicate the direction of movement. In second and third column of (b), '+' and '–' signs indicate cell migration direction to the right and left hand sides of the cell respectively, following the usage of '+' and '–' directions for funneling edge and base of the fibronectin triangle in the first column of (b). Scale bar 100 μm.

In this setup, cells were forced to extend filopodial protrusions in order to establish attachment in the neighboring pattern and to generate motion from one triangle to another. These protrusions which eventually lead to migration of the cell, were called efficient protrusions – 'z' denotes the number of efficient protrusions generated per unit time.

Cells took the shape of fibronectin triangle and polarized on the '–' edge. For simplicity, two ends of the triangle: funneling edge and base, were denoted as '+' and '–' edges respectively. The length of the protrusions arising from either sides of the cell was similar. However, the attachment area for protrusions on the adjacent fibronectin triangles in either sides were different ($A_+ \neq A-$) (Fig. 6.7 a (Configuration (i))). Thus this setup allowed to study in detail the filopodial dynamics.

6.1.4.3.1 Protrusion frequency, stabilization time and attachment area

The difference in accessible area introduced a bias in the activity of efficient protrusions ($z_+ \neq z_-$) (Fig. 6.7 a (Configuration (i))). This bias in activity of efficient protrusions was clear, when the cells placed on triangles migrated on average in the direction of '+' end (Fig. 6.7 b (Configuration (i))). In general, the cell showed a stochastic behavior, i.e. they migrated in both '+' and '–' directions. The rectification is a measure of average motions in '+' and '–' directions. the Note that migration of cells towards the funneling edge is similar to Mahmud et al. (212) (for some of the cell types), but in contrast, the setup of Caballero et al. (116), had separations between the triangles. In order to study the role of protrusion fluctuations leading to migration towards funneling edge, Caballero et al., measured two parameters (Fig. 6.8 a): (i) Frequency of probing (ν) given by the number of protrusions reaching the adjacent triangle, and (ii) Stabilization time (τ) or dwelling time of the protrusion on the adjacent triangle. Interestingly, it was found that the number of protrusions (ν) was larger on the '–' direction but the stabilization time was larger on the '+' direction in the ratchet configuration (Fig. 6.8 a). This showed that the two parameters ($\nu_\pm$ and $\tau_\pm$) competed in inducing cell migration on respective directions. In

other words, efficient protrusion generated per unit time (z_i) depended on probing frequency ($\nu_{\pm}$) and stabilization time ($\tau_{\pm}$).

6.1.4.3.2 Index to predict mean directionality of cell migration

The efficient protrusion generated per unit time (z_i) can be described by $z_i = s_i\nu_i = \beta\nu_i\tau_i$, a dimensionless quantity obtained by scaling arguments. Where s_i denotes the probability of a protrusion attaching efficiently to the direction i and, β is the rate of activation of efficient protrusions which is assumed to be a constant. Since $\nu_{\pm}$ and $\tau_{\pm}$ were obtained experimentally, an index was derived from z_i to predict the direction of migration. This direction index was given by (I_{dir}) (Fig. 6.8 b), where:

$$I_{dir} = \frac{(z_+ - z_-)}{(z_+ + z_-)} \qquad (6.1)$$

The movement of cells from one triangle to another in the ratchet configuration is dictated by the asymmetry in $\nu_{\pm}$ and $\tau_{\pm}$. One can use the direction index (I_{dir}) to predict the direction of elementary step where: $I_{dir} > 0$ indicates a step in the '+' direction, $I_{dir} < 0$ indicates a step in the '–' direction, and $I_{dir} \approx 0$ indicates an unbiased motion. After obtaining the $\nu_{\pm}$ and $\tau_{\pm}$ values experimentally, the I_{dir} was estimated to be 0.33 for the ratchet configuration (Fig. 6.8 b). The positive value of I_{dir} indicated the motion of cell towards the '+' direction, in agreement with the experimental results. This confirmed the role of filopodial protrusions from the '+' edge of the triangle in ratcheting cell migration.

6.1.4.3.3 Non-ratchet geometries and the significance of Rho pathway

The significance of protrusion from the '+' edge, was attributed to the larger accessible area when compared to the area available for protrusions on the '–' edge. In order to test this hypothesis, two other configurations were tested: (i) triangle surrounded by rectangle (Fig. 6.7 a and b (Configuration (ii))) and (ii) circular patch surrounded by rectangles (Fig. 6.7 a and b (Configuration (iii))). In the first case: the area available for protrusion attachment on both sides of the triangle was identical ($A_+ = A-$) (Fig. 6.7 a (Configuration (ii))). But distributions of protrusions arising from the two edges '+' and '–' were different ($\nu_- > \nu_+$) (Fig. 6.8 a). In this configuration, the value of I_{dir} was "– 0.57", indicating migration in the '–' direction, i.e. in the direction of polarization (Fig. 6.8 b).

In the second case: both the accessible area and the distribution of protrusions were similar ($A_+ = A_-; \nu_- > \nu_+$) (Fig. 6.7 a (Configuration (iii)) and Fig. 6.8 a). In this configuration, due to the absence of asymmetry in protrusion parameters $\nu_\pm$ and $\tau_\pm$, the cell migration should result in an unbiased motion. As expected, the value of I_{dir} was close to zero, indicating an unbiased motion (Fig. 6.8 b). The conclusions from the I_{dir} values for both first (-0.57) and second case (0.13) were in agreement with the experiments. These results confirm the role of asymmetry in protrusion fluctuations to be the key mechanism behind rectification of cell migration on asymmetric patterns.

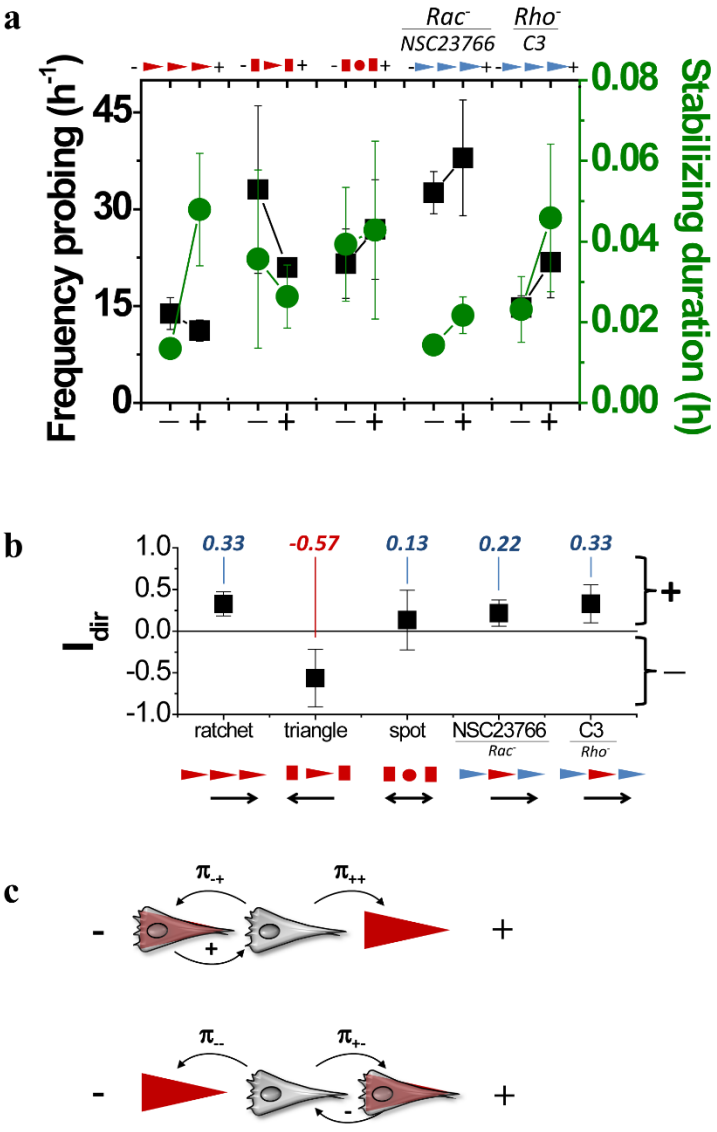

Figure 6.8. Adapted from Caballero et al. (116). (a) Protrusion activity during cell motion. (a) Measurement of the frequency of probing (ν) and the stabilization duration (τ) of filopodia in the + and – sides. The data show an asymmetry in the filopodia dynamics for cases (i), (ii), (iv) and (v). (b) The direction index I_{dir} was calculated using the measured (ν) and (τ). The I_{dir} parameter shows a correlation between the sign and the migration direction. (c) Schematic for π_{ij}; the cell first moves along the dashed lines and then along the solid lines.

The role of asymmetric fibronectin triangles was further substantiated when cells moved on average in the '+' direction after inhibition of Rho and Rac pathways which are shown to regulate cytoskeletal dynamics for distinct reasons (Fig. 6.8 a and b). While these results correspond to the first step, similar ratcheting effect based on protrusions were obtained, when cells were observed on series of triangles for a period of 48 h. The results on longer time scales were further supported by estimating ratios of persistence length and persistence

time: L_p^+/L_p^- and T_p^+/T_p^-. Thus fluctuations in protrusion seem to be the major factor in rectifying cell migration on asymmetric substrates.

6.1.4.3.4 Mesoscopic model for cell trajectories

The ratcheting behavior was consistent at both short and long time scales. But in order to find if the prediction on choice of direction from the first step, can be applied to long term consequences, a mesoscopic model was developed in collaboration with Raphael Voituriez. In contrast to the existing random walk models, this model considered only a one-step memory to capture the behavior of cell trajectories at longer time scales. This was done by introducing a transition probability 'π_{ij}' between two steps (Fig. 6.8 c). π_{ij} gives the probability of a cell moving in direction 'j', based on its previous step in the direction 'i'. By knowing π_{ij}, the probability of a step in '+' direction at each stationary state (Π_+) can be obtained:

$$\Pi_+ = \frac{1 - \pi_{--}}{2 - (\pi_{++} + \pi_{--})} \qquad (6.2)$$

After obtaining the stationary distributions for the probability of a step in '–' direction (Π_+) in similar way, the bias can be expressed as:

$$\frac{\Pi_+}{\Pi_-} = \frac{1 - \pi_{--}}{1 - \pi_{++}} \qquad (6.3)$$

When the measured values of π_{ij} were used for predicting the bias given by expression (6.3), the predictions were found to be quantitatively in agreement with the experimental observations for persistence length and direction bias values. This model specifically considers migration on ratchets as a Markovian process. This allows to take into account the transient changes in cell trajectories during cell migration as opposed to models based only on long range chemical gradients. Note that the transition probability π_{ij}, takes into account both the asymmetry of the triangles and the memory of previous step. The asymmetry of the triangle affects the protrusion activity and the memory corresponds to previous polarity of the cell. This model thus considers both fluctuations in protrusions, and the effect of polarization to predict and capture the long time behaviors of cell trajectories.

In conclusion, this study by Caballero et al. (116), established the role of fluctuations in efficient protrusions to be a key mechanism behind the rectification of cell migration in asymmetric ratchets.

6.1.4.4 Nucleus contributes to ratcheting behavior

In addition to protrusion fluctuations, mechanical interactions of cell body – specifically due to nucleus, has been shown to trigger directed migration under asymmetric ratchet conditions in our lab (205) and elsewhere (225). In contrast to Caballero et al. (116), these studies employed environment with ratchet geometries that involved interaction with cell body: tilted micro pillars (225) and topographical ratchets (205). They studied cell trajectories in these environments both experimentally and theoretically. From these results, the studies conclude that nucleus being a "bulky" organelle in the cell, increases the mechanical interaction of cell body with the ratchet like environment thus contributing to rectified migration.

These works conclusively demonstrate rectification of cell migration using asymmetric ratchets (116, 205, 212, 225). In addition, they identify fluctuations in protrusions and mechanical guidance of nucleus as the prime factors behind the ratcheting effect. With these strong findings, we coined the term *Ratchetaxis* (61) to describe the rectification in cell migration due to asymmetry in local cues of the cell microenvironment.

6.2 Direction reversal of cell migration by adhesive ratchets - Results

Using ratchets as a means for directed cell migration is interesting. However, there are cues by which cells migrating in one direction change their course of migration to a different direction (226–228). We reasoned that such a cue should exist in ratchetaxis. In a system of periodically separated asymmetric triangles, there should be a parameter whose threshold should be critical in changing the effect on cell migration by the ratchets to polarization. In other words, directional bias towards the funneling edge (ratchetaxis) should be reversed by inducing migration towards the base of the triangle (polarization). In order to identify this parameter, we went back to theoretical studies on particle currents that were rectified by asymmetric potentials. In the following paragraph, I will explain the theoretical proposition for direction reversal of particle currents in a system (229) similar to the one described before (section 6.1.3).

6.2.1 Reversal of particle current during asymmetric pumping

Chauwin et al. (229), showed that rectified particle currents can be reversed by changing the lifetime and drift time of the particles in each potential state (Fig. 6.9). Let us consider a particle-potential system where W_i indicates the potential, τ_i indicates the lifetime of the particle in the corresponding potential and τ_{ia}, τ_{ib} indicate the drift time of the particle down the corresponding slopes (a, b); (i = 1, 2), where 'b' is the larger slope. The two states of the potential are aligned in such a way that maxima of W_1 faces the minima of W_2 (Fig. 6.9). In this scenario, let us assume that the particles are subjected to the alternative switching 'on' of the potentials. We take the ratio of: lifetime of the particle (τ_i) in a potential over the drift time of the particle on the larger slope 'b' (τ_{ib}) – τ_i / τ_{ib}. If this ratio is larger than one, then the lifetime of the particle in the corresponding potential is larger than the drift time required to move down the larger slope 'b'. If the ratio is smaller than one, then the lifetime of the particle is smaller than the drift time on the larger slope. This implies the distance travelled while the particle is in a particular potential state. Based on this ratio, we consider two situations: (τ_1 / τ_{1b}) > (τ_2 / τ_{2b}) and (τ_1 / τ_{1b}) < (τ_2 / τ_{2b}).

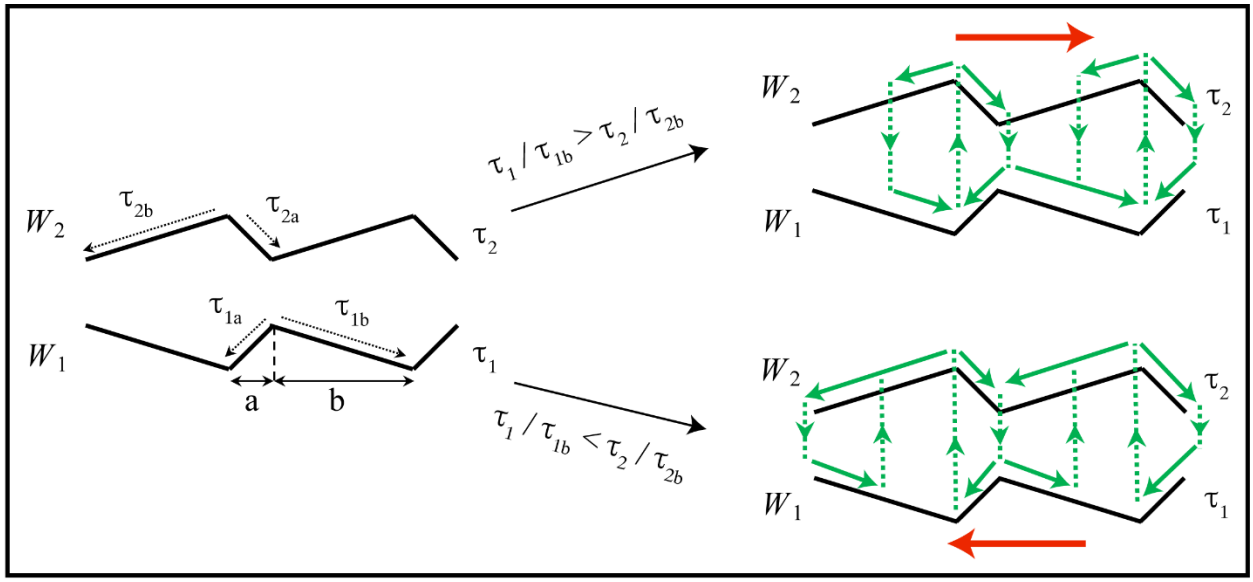

Figure 6.9. Representation of particle-potential system described by Chauwin et al. (229). The particles can exist in two potential states W_1 and W_2. 'a' and 'b' represent the shorter and larger slopes, respectively on either side of the maxima. τ_1 and τ_2 represent particle lifetimes in W_1 and W_2. τ_{1a}, τ_{1b} represent drift times on shorter slope 'a' and τ_{2a}, τ_{2b} represent drift times on larger slope 'b' in W_1 and W_2 respectively. By repeating 'on-off' cycles, the particles exhibit directed motion based on the drift time: (τ_1 / τ_{1b}) > (τ_2 / τ_{2b}) leads to right drift and (τ_1 / τ_{1b}) < (τ_2 / τ_{2b}) leads to left drift, on average.

In the first case: $(\tau_1 / \tau_{1b}) > (\tau_2 / \tau_{2b})$, the ratio of lifetime to drift time on the larger slope 'b' is larger in W_1 than W_2. In other words, the distance travelled downslope by the particles is larger in W_1 than the distance travelled by the particles in W_2. In this case, the net motion of the particle will be to the right (Fig. 6.9).

In the second case: $(\tau_1 / \tau_{1b}) < (\tau_2 / \tau_{2b})$, where the ratio of lifetime to drift time on the larger slope 'b' is smaller in W_1 than W_2. In this case, the distance travelled downslope by the particles is smaller in W_1, than the distance travelled by particles in W_2. Hence the net motion of the particle will be reversed and move towards the left (Fig. 6.9).

From these results, this study identifies the drift time – that dictates the distance travelled by the particles in the corresponding potential, to be a key parameter in setting directionality.

Now let's go back to ratchetaxis, where cell migration is triggered by a system of periodically separated asymmetric fibronectin triangles (116). This is a one-dimensional system where triangles can be treated as asymmetric potentials on which the cells move. Cells are similar to the fluctuating particles where fluctuations arise from protrusions that allow the cells to move from one triangle to another. This cell-ratchet system can be considered formally equivalent to the particle-potential system described before. Although cell-ratchet is a single state system, we tried to identify an equivalent parameter that would correspond to the drift time of the particles in the particle-potential system.

6.2.2 Gap distance: parameter setting mean directionality

Caballero et al. (116) showed that cells send protrusions to the neighboring triangles, whose frequency and stabilization lead to ratchetaxis. In their case (116), the triangles were separated by a gap of 20.5 μm which were bridged by the protrusions for moving the cells to the neighboring triangle. From their results (116), it is clear that cells establish efficient protrusions by attaching to neighboring triangles, to trigger cell migration. In this setup, the gap distance between triangles is the major triggering factor for the cells to send protrusions in order to probe the environment. Once the protrusions attach to the fibronectin triangles on either sides, variations in protrusion parameters $\nu_{\pm}$ and $\tau_{\pm}$ set the directions of migration.

From the understanding of ratchet based migration in this setup (116), one can assume that, the gap distance between the triangles plays a central role in setting the amount of probing and variation in protrusion parameters ($\nu_{\pm}$ and $\tau_{\pm}$). For example, cells placed in a system of connected triangles (Fig. 6.10 b) will not require the probing by filopodia,

since the lamellipodial protrusions can easily extend into the immediately available space (212). Similarly, cells placed in connected environments where the accessible area for protrusions are more or less same on both sides (Fig. 6.10 c), may not exhibit variations in protrusion parameters ($\nu_{\pm}$ and $\tau_{\pm}$).

From these arguments, one can realize that gap distance plays a significant role in the required amount of probing and in the variation of protrusion parameters ($\nu_{\pm}$ and $\tau_{\pm}$). In other words, with reduced gap distance, the need for probing the environment and the corresponding time required for probing will be reduced. Similarly, with increased gap distance, the protrusions from the cells will have to reach the neighboring triangles by bridging the large gap distance, thus increasing the amount of probing (Fig. 6.10 a – last row). In this manner, we can assume gap distance to be a formal equivalent of drift time in the particle-potential system, where drift time corresponds to the distance moved by the particle downslope of the potential. Also by decreasing or increasing the gap distance, the protrusion parameters ($\nu_{\pm}$ and $\tau_{\pm}$) will vary on both sides. Note that, fluctuation in protrusion parameters was the key mechanism for rectified migration in the results of Caballero et al. (116). Thus by changing gap distance and the resulting variation in protrusion parameters, reversal in direction of migration can be expected.

Therefore, we treat gap distance in the cell-ratchet system to be a formal equivalent of drift time in the particle-potential system. By establishing this equivalence between gap distance and drift time, we hypothesized the existence of a critical gap distance at which reversal in the direction of cells will occur.

6.2.3 Ratchets with different gap distances

In order to test this hypothesis, we used a system of microcontact printed triangles, similar to Caballero et al. (116), but with different gap distances (Fig. 6.10). The area of triangle was chosen to be 1590 μm^2, to match the mean area of the triangles. We consider similar notations as Caballero et al., where the funneling edge and the base of the triangles are denoted as '+' edge and '–' edge, and similarly migrations in the direction of funneling edge and triangle base are denoted as migration in '+' and '–' directions respectively. These notations will be used throughout the text hereafter.

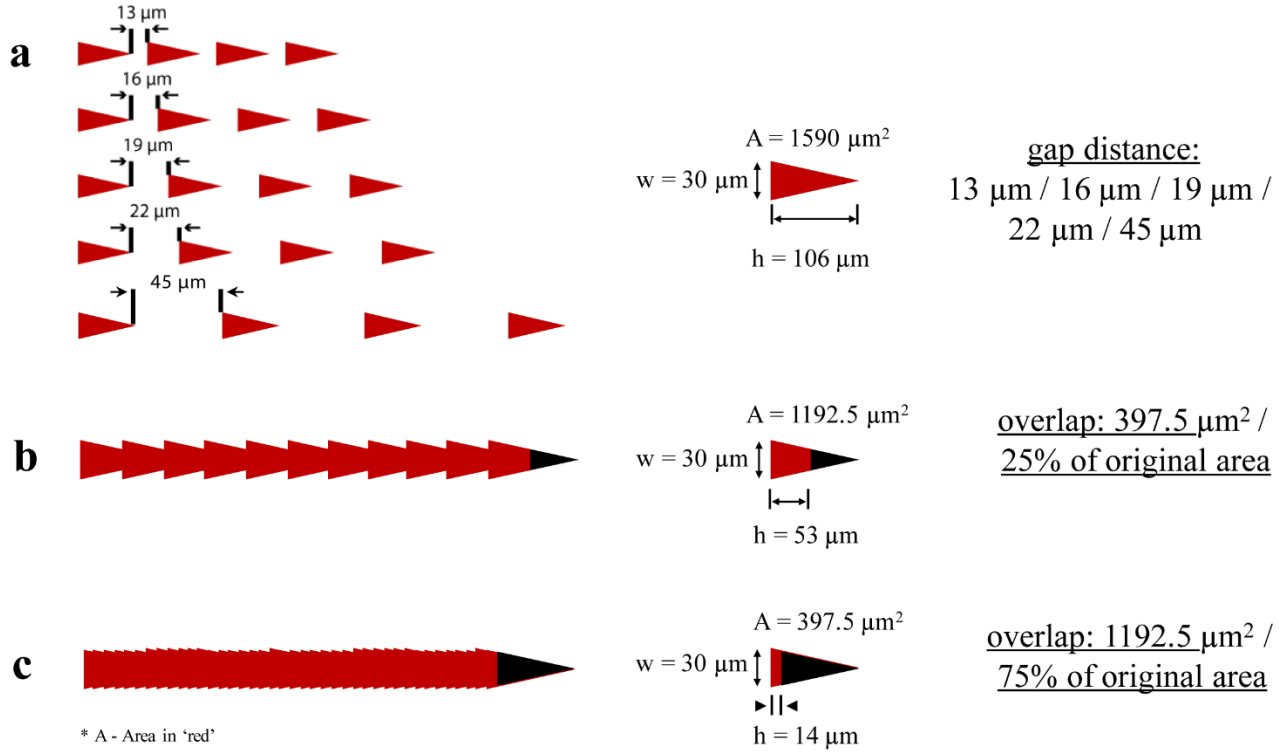

Figure 6.10. Schematic of ratchet configurations used in the current study. Conditions with different gap distances (a), 25 % overlap (b) and 75 % overlap (c).

We chose a large range of gap distances which included negative gap distances or overlapping triangles, and positive gap distances. The chosen conditions were: in overlap condition – 75 % and 25 % overlaps, and in gap distance condition – 13 µm, 16 µm, 19 µm, 22 µm and 45 µm (Fig. 6.10). With this large range of conditions, we were able to scan different scenarios: (i) symmetric 'line' like condition (75 % overlap), (ii) minimal overlapping condition (25 % overlap), (iii) separations with small gap distances (13 µm and 16 µm), (iv) gap distances close to the condition used by Caballero et al. (116), (19 µm and 22 µm) and (v) gap distances far from the condition used by Caballero et al., (45 µm). With this large range of conditions, we hoped to find a critical gap distance at which the cells would reverse their direction by moving towards '–' direction instead of ratcheting in the '+' direction.

6.2.3.1 Setup and acquisition

The triangular patterns of fibronectin with different gap distances were first microfabricated by photolithography and transferred to PDMS by soft lithography processes as in Caballero et al (116). The PDMS stamp was used to create triangular

patterns of fibronectin on the glass coverslip by micro-contact printing (Fig. 6.11 a and b). A specific concentration of 10 µg/ml of rhodamine-fibronectin was used for the patterning, since this concentration corresponds to the maximum velocity of cells (116). 100 µg/ml of pLL-g-PEG was used for passivating rest of the coverslip surface.

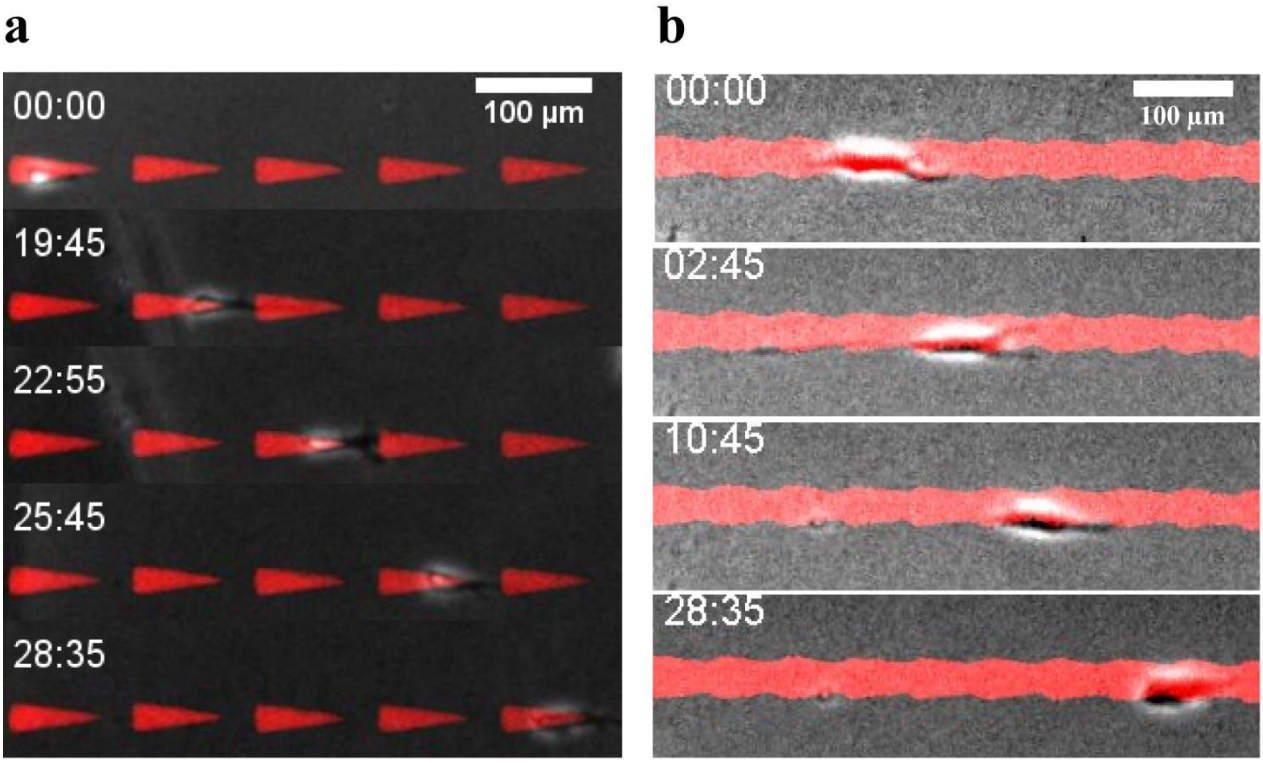

Figure 6.11. Kymographs of cells exhibiting ratchetaxis: cells moving in '+' direction in 22 µm gap distance condition (a) and 25 % overlap condition (b). '+' direction corresponds to the funneling edge of the triangle. In both conditions, cells send protrusions to the neighboring triangles for migration. Time in hh:mm. Scale bar 100 µm.

The NIH3T3 cells, maintained approximately at 50 % confluency were used for seeding on the micropatterned coverslip. For acquisition, cells were maintained in 1 % serum condition to reduce the rate of cell division, similar to Caballero et al (116). Migrations of cells on patterned coverslip were acquired using an inverted microscope, equipped with temperature controller. The migration was acquired for 48 h with an acquisition frequency of 1 frame every 5 minutes. Such a long period (48 h) of acquisition allowed us to capture the effect of ratchets on cell migration (Fig. 6.11 a and b). All these protocols are explained in detail in the methods section (section 3).

6.2.3.2 Analysis

After acquisition of cell motions on fibronectin triangles, the videos were analyzed with the following parameters: from cell trajectories, persistence lengths ($L_p^{\pm}$) and persistence times ($T_p^{\pm}$) were measured. Persistence length and persistence time correspond to the distance travelled by a cell and the corresponding time taken respectively without pausing. We assume the cell to be pausing if the cell was not moving for more than 30 min, similar to Caballero et al (116). The persistence length was measured in lattice units (l.u). One lattice unit is the distance between the centers of two triangles. The persistence time was measured in hours (h). Finally, the direction bias was estimated by comparing the initial and final position of the cells. For example, '+' direction bias would mean that the final position of the cell was at least one lattice unit to the right of the initial position. There is no final bias if the cell returns to its original position.

In order to have an unbiased analysis, cells were selected based on the following criteria: (i) Cells undergoing division and collision were discarded. (ii) Cells following the trail of another cell were discarded. (iii) Cell trajectories where cell body was positioned outside the triangle were discarded.

In the following section, I will discuss the results of experiments by which we probed our hypothesis of direction reversal triggered by gap distance. First, we ascertain the effect of gap distance on cell trajectories. Then we check the direction bias in the cells migrating in '+' and '–' in different gap distances, which will be followed by a simple mesoscopic model.

6.2.4 Cells on ratchets

After seeding cells on micropatterns, the cells start spreading on fibronectin triangles. They exhibit fluctuations, which are short scale movements within the triangle that do not correspond to migration (Movie S1 of Caballero et al. (116)). Eventually, they send protrusions in order to probe the nearby area for establishing an efficient protrusion. When the protrusions attach to the neighboring triangles, the side where the efficient protrusion has been created triggers migration. Following this, the cell performs similar migration steps on the micropatterns giving rise to a persistent motion (Fig. 6.11 a and b). As mentioned earlier, the cells exhibit stochasticity in the direction of migration (Movie 6.1). Hence, rectification is deduced from the average motion exhibited by the cells in each ('+' and '–') direction.

6.2.5 Effect of gap distances on cell migration

To confirm the effect of gap distance on cell migration in the ratchet configuration, we wanted to check the trajectories of cells in maximal overlap and maximal gap distance conditions. So we plated cells on micropatterned ratchets with 75 % overlap and 45 µm gap distance, and acquired the trajectories for 48 h. Cells on overlapped triangles exhibited motion in both '+' and '–' directions, without any pausing during migration (Fig. 6.12 a).

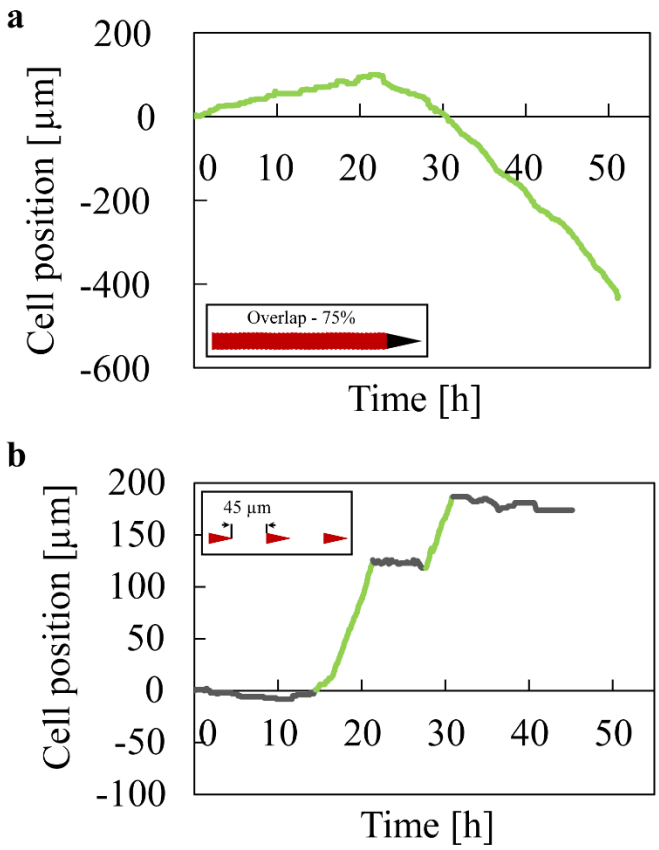

Figure 6.12. Plots of cell trajectories moving in 75 % overlap condition (a) and 45 µm gap distance condition (b). Positive and negative values in y-axis represent migration in '+' and '–' directions respectively. (a) Trajectory of a cell moving in the 75 % overlap condition does not show pausing, even while changing direction. (b) Trajectory of a cell moving in 45 µm condition shows frequent pausing (in grey) during migration (in green). The corresponding overlap and the gap distance schemes are shown within the plot.

In general, one could expect a pause when cells change the polarization while changing direction. Interestingly, there was no pausing even while changing direction in the 75 % overlap condition (Fig. 6.12 a). This shows that absence of gap distance allows easy probing for the cell which leads to continuous motion without any pausing. Note that we consider the cell to have made a pause if it does not move for more than 30 min.

In contrast, cells on fibronectin ratchets separated by 45 µm gap distance exhibited pausing after moving one lattice unit, i.e. from one triangle to next with a gap distance of 45 µm (Fig. 6.12 b). Cells showed a minimal pausing time of 5 h before moving one lattice unit. This pausing behavior shows that the gap distance is increasing the time of probing to make the next step during migration. Also, the gap distance is forcing the cell to extend protrusions for probing and to find the next triangle to establish an efficient protrusion.

These results confirm the effect of gap distance in cell migration, which is confirmed by (i) continuous cell migration without pausing time in the absence of gap distance (Fig. 6.12 a) and (ii) increased pausing time on introduction of gap distance (Fig. 6.12 b).

Next, we checked the direction bias in cell migration on ratchet configurations with different overlap and gap distance conditions.

6.2.6 Direction bias in cell migrating on fibronectin ratchets

We checked the direction bias of cells migrating on various overlap and gap distance conditions: 25 % and 75 % overlap, and 13 μm, 16 μm, 19 μm, 22 μm and 45 μm gap distance. The final position of the cells (right '+' or left '–') at 48 h was used to obtain the final direction bias and, the number of cells with respective direction bias ('+' or '–') was plotted for each condition. In each condition, the bias was observed as follows (Fig. 6.13 a):

6.2.6.1 Overlap conditions

In the maximal overlap condition: 75 % overlap, cells showed no net bias in migration, i.e. the number of cells moving towards '+' and '–' directions were similar (Fig. 6.13 a). From the results of Caballero et al. (116), the absence of net bias is expected in this 'line-like' condition, since the area probed by protrusions on either sides is approximately similar. This eliminates the ratchet effect and allow cells to migrate in both directions.

In the minimal overlap condition: 25 % overlap, cells showed a strong bias towards the '+' direction, i.e. the number of cells migrating towards the '+' direction was two folds higher than the number of cells migrating in '–' direction. Although, the triangles were connected, the difference in area between '+' and '–' directions, lead to ratchet effect (Fig. 6.13 a and Movie 6.2-top panel).

Thus in overlap conditions cells exhibited no directional bias if the accessible area for protrusions on both sides were similar (75 %), and showed strong ratcheting when the accessible area on funneling edge '+' was larger. These results were similar to that of Mahmud et al. (212), where strong bias towards the funneling edge was observed when the opening of triangle (during overlap), was ~ 10-20 μm and no net bias was observed when the opening of triangle was > 30 μm. In our case, triangles with 25 % overlap have an opening of 15 μm and triangles with 75 % overlap have an opening of ~ 30 μm (Fig.

6.13 a). Thus ratchet effect takes over in the overlap condition when an asymmetry in protrusion attachment area is introduced.

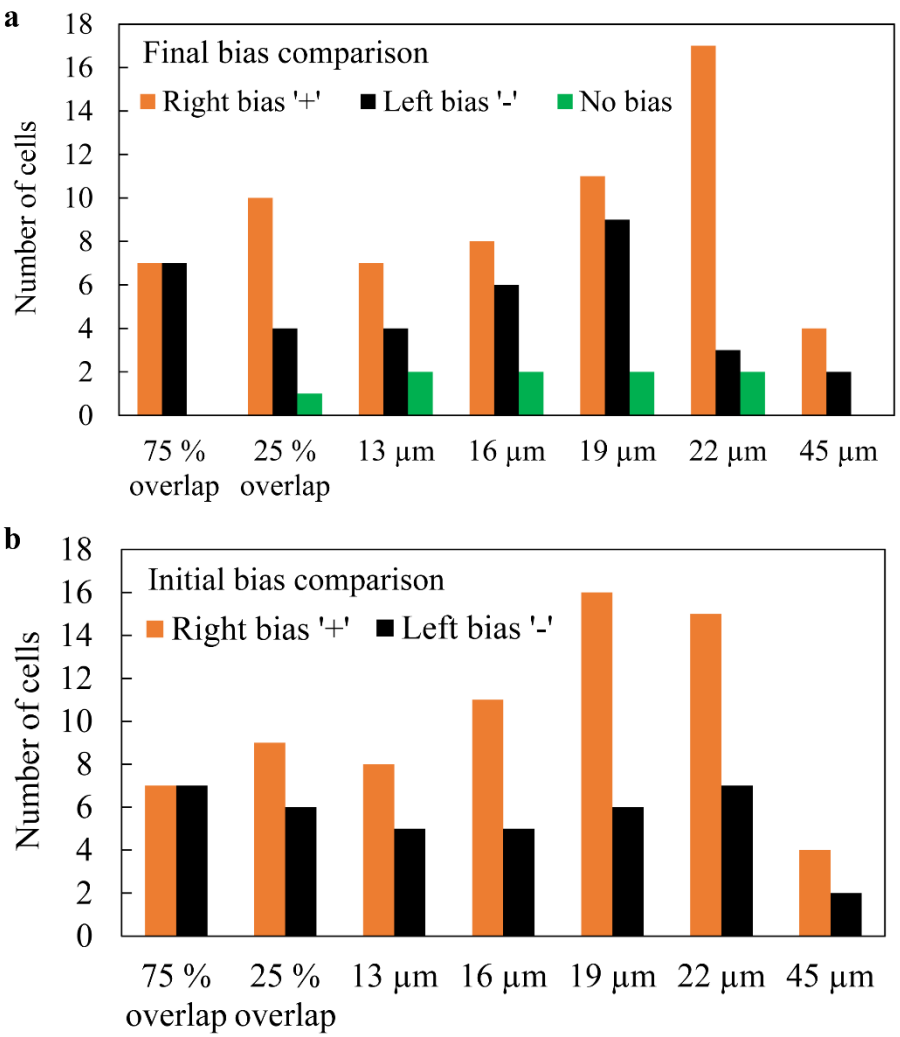

Figure 6.13. Plots showing final direction bias and initial step bias. (a) Plot showing number of cells with a final directional bias towards '+' and '–' directions. Final direction bias is decided by final position of the cell with respect to the initial (t_0) position. (b) Plot showing number of cells with a first/initial step bias towards '+' and '–' directions. Initial step bias is decided by the direction of first step with respect to the initial (t_0) position. '+' / Right direction indicates migration towards the funneling edge of the fibronectin triangle. '–' / Left direction indicates migration towards the base of the fibronectin triangle. In both plots conditions are color coded as follows: irange – right bias '+'; black '+' – left bias and green – no bias. Number of biological repeats (N) and number of cells (n) in each condition: Overlap: 75 % (N-10, n-14); 25 % (N-10, n-15); Gap distance: 13 µm (N-4; n-13); 16 µm (N-10; n-16); 19 µm (N-3; n-22); 22 µm (N-17; n-22); 45 µm (N-4; n-6).

6.2.6.2 Gap distance conditions

In general, all the gap distance conditions: 13 µm, 16 µm, 19 µm, 22 µm and 45 µm exhibited a bias towards '+' direction (Movie 6.2-bottom panel). In the case of gap distances (13 µm, 16 µm, 19 µm) that were less than the condition used by Caballero et al. (116) (20.5 µm), the bias in the '+' direction was not striking, i.e. the number of cells moving to the '+' direction was minimal (Fig. 6.13 a). Whereas in the case of 22 µm gap distance, the bias towards '+' direction was extremely striking, i.e. the number of cells

moving towards the '+' direction was four times larger than the number of cells moving towards '–' direction (Fig. 6.13 a). The striking ratcheting effect (movement in '+' direction) in this gap distance range: 20.5 µm (Caballero et al.) and 22 µm (current study), shows this gap distance to be the optimal condition for ratchetaxis.

The increased ratchet effect in this gap distance range (20.5 µm - 22 µm) was substantiated, after analyzing 45 µm gap distance condition. In general, the number of moving cells in 45 µm gap distance condition was much less, which clearly reflected the difficulty in migration for the cells due to increased gap distance (Movie 6.3). However, the number of cells moving towards '+' direction was very minimal in the 45 µm gap distance, similar to the smaller gap distance conditions mentioned above (Fig. 6.13 a). Thus a gap distance of 22 µm leads to pronounced ratchet effect and gap distances smaller (13 µm, 16 µm, 19 µm) and larger (45 µm) than 22 µm, show minimal ratcheting. Cells with no net directional bias were also observed in all the conditions except 45 µm condition (Fig. 6.13 a and Movie 6.1).

On the other hand, migration of cells on 45 µm gap distance was interesting, since the protrusions were able to cover this large gap distance. Caballero et al. (116), reported a maximum protrusion length of 35 µm in a ratchet configuration with 20.5 µm gap distance. However, in our case, we were able to observe cells extending protrusions and exhibiting migration in the 45 µm gap distance condition. This shows that: (i) filopodial protrusions play an important role in migration and (ii) the length of protrusions is altered based on environmental cues, i.e. when the gap distance is increased. Along this line, it would be interesting to check the maximum protrusion length in the ratchet configuration.

By scanning the above mentioned conditions (overlap and gap distance), we observed only two scenarios of migration: migration without net directional bias (75 % overlap) and ratchetaxis / net directional bias towards '+' direction (25 % overlap, 13 µm, 16 µm, 19 µm, 22 µm and 45 µm). However, direction reversal was not observed. The reason could be that: we are still within the regime of ratcheting, with these overlap and gap distance conditions. Hence, the critical condition leading to direction reversal should be either between 75 % and 25 % overlap.

Meanwhile, we looked at the direction of the initial / first step of the cells in each of these ratchet conditions (overlap / gap distance). After cell seeding, the cells spread on fibronectin triangles, eventually leading to protrusion and migration. Since all conditions except 75 % overlap were showing ratchetaxis, we wanted to check if the tendency of ratcheting was exhibited by the cells from the very first step in these conditions.

Interestingly, the directional bias of the first step was very similar to the final directional bias (Fig. 6.13 b). In all conditions (25 % overlap, Gap distance: 13 µm, 16 µm, 19 µm, 22 µm and 45 µm), except 75 % overlap, the number of cells exhibiting a first step in '+' direction was higher than the number of cells making a first step towards '–' direction. This result further substantiates the ratcheting effect observed from the final direction bias.

Currently, we are performing more experiments in the overlap and gap distance conditions to increase the number of cells per condition. In addition, we are performing new experiments on overlap conditions between 75 % and 25 % and, similarly for gap distance conditions above 45 µm to find the critical gap distance leading to direction reversal. In order to better characterize the observed ratcheting effect, we are analyzing the persistent length ($L_p^{\pm}$) and persistent time ($T_p^{\pm}$) of the cell trajectories in all the above mentioned conditions. For example, by comparing $L_p^{\pm}$ and $T_p^{\pm}$ between each condition, the best condition that leads to rectification and reversal can be identified, i.e. the condition in which the cells migrate in the same direction with minimal or no pausing time.

Thus, the experimental results show a strong ratcheting behavior / ratchetaxis in most of the conditions. From Caballero et al. (116), we know that the area available for protrusion and the protrusion parameters: frequency of probing and stabilization time of protrusions, play a significant role in the choice of directionality. Hence, based on these parameters, we developed a simple mesoscopic model to simulate the conditions (overlap / gap distance) leading to direction reversal for cells migrating on ratchets.

6.2.7 Mesoscopic model for simulating direction reversal

We developed a simple mesoscopic model based on the cell-ratchet system (Fig. 6.14 a and b). The force generated by efficient protrusions leads to cell migration in the corresponding direction. Caballero et al. (116), derived a direction index I_{dir}, based on the efficient protrusion generated per unit time z_i, where $z_i = \beta \nu_i \tau_i$. In this expression for z_i, right hand side gives the frequency of probing (ν_i) by the generated protrusions with a stabilization time (τ_i). After a particular number of protrusions have been attached to the triangle on each side of the cell, migration is initiated. This rate of activation of protrusion (β), i.e. a normal attached protrusion turning out to be an efficient protrusion is assumed constant. However, for a successful migration step, in addition to fluctuations in protrusion parameters ($\nu_{\pm}$ and $\tau_{\pm}$), the asymmetry in protrusion accessible area also

contributes significantly. In the expression of z_i, this asymmetry in accessible area is indirectly incorporated in ν_i, since the frequency of probing depends on the available area for protrusion attachment (Fig. 6.14 a and b).

In our model, to simulate the conditions leading to reversal, we explicitly introduce the variation in accessible area for the protrusion on either sides of the triangle, and simplify the expression of z_i by scaling arguments again. We express z_i as a function of n_i, s and A_{probed}:

$$z_i = n_i . s . \frac{A^i_{probed}}{A_{tot}} \qquad (6.4)$$

where: n_i is the number of protrusions generated during the experimental time and $'n_i'$ can be expressed as $n_i = \nu_i T_{exp}$ (ν_i – frequency of protrusion; T_{exp} – total time of experiment). $'s'$ is the probability of a protrusion getting stabilized. To simplify, we assume the probability of protrusion getting stabilized (s) to be same on either sides of the cell. Finally, A^i_{probed} is the attachment area for the protrusions on the neighboring triangles ($i = '+',\ '-'$) on either sides of the cell. A_{tot} is the total area of the triangle to which A_{probed} belongs. Thus we redefine z_i to explicitly include the variation in accessible area. Importantly, the variation in frequencies of protrusion between the polarized and non-polarized sides of the cell are reflected in n_i, the number of protrusions generated during the experimental time.

Next, we show that A_{probed} depends on the protrusion length (λ) and gap distance (a) by basic geometry (Fig. 6.14 and Fig. 6.15 a and b). After cells spread on triangles, they generate protrusions on both sides. We assume that the point of protrusion generation lies on the triangle tip in '+' edge and at the triangle base in the '–' edge. For a given length of filopodial protrusion, the probing area can be described as a semi-circle with the point of protrusion generation being the center, on either sides (Fig. 6.14 a and b). Now, the area covered by this semi-circle on neighboring triangles, will give the attachment area for the protrusions. The attachment areas on the neighboring triangles in the '+' and '–' direction in different overlap and gap distance conditions, can be obtained by the expressions (6.5 – 6.8).

In these expressions: A^i_{probed} denotes the attachment area of protrusion on the neighboring triangles ($i = '+',\ '-'$), $'\lambda'$ represents the length of protrusion, $'a'$ represents the gap distance between triangles, $'\beta'$ represents the shorter side of the trapezoid, and $'\theta' \; and \; '\alpha'$ represent the vertex and base angles of the triangle. The

expressions for the attachment area in overlap and gap distance conditions are given below, and details are explained in the appendix section 10.1.

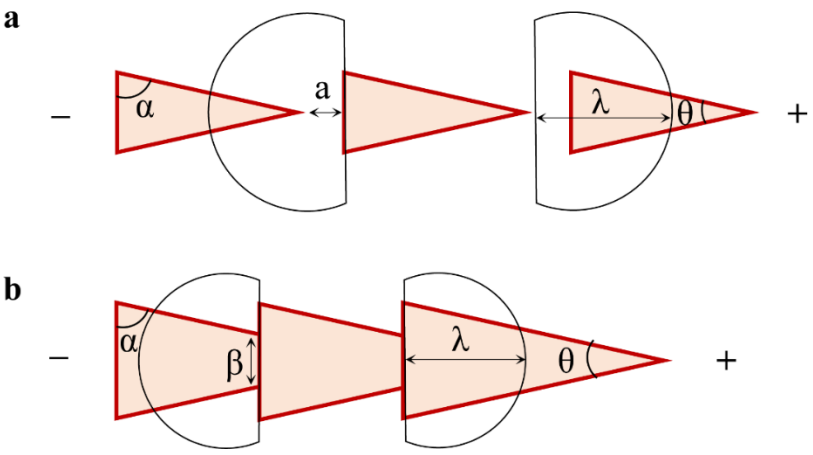

Figure 6.14. Schematic of ratchet configurations with gap distance (a) and overlap (b) conditions. '+' and '–' indicate the direction towards funneling edge and base of the triangle. Semi-circle in black indicates the available attachment area for the protrusions on either side. 'λ' indicates the protrusion length, 'a' indicates gap distance, 'θ' and 'α' indicate vertex angle and base angle of the triangle, 'β' indicates the shorter base of the trapezoid, formed by the semi-circle.

(i) For the 'line-like' condition, i.e. 75 % overlap condition, the attachment area (A_{probed}) in the '+' and '–' directions is given by:

$$A^{i}_{probed} = \begin{cases} 30.\lambda & if\ \lambda > 15\ \mu m \\ \dfrac{\pi.\lambda^2}{2} & if\ \lambda \leq 15\ \mu m \end{cases} \qquad (6.5)$$

(ii) For 'non-line' like or 'ratchet' like overlap, i.e. 25 % overlap condition, the attachment area resembling a trapezoid in both '+' and '–' directions are given by the expression (6.6) for the '+' direction and (6.7) for the '–' direction (Fig. 6.14 b):

$$A^{+}_{probed} = \left(30 - (\lambda - a).\sqrt{\frac{1 - sin^2(\alpha)}{sin^2(\alpha)}}\right).(\lambda - a) \qquad (6.6)$$

$$A^{-}_{probed} = \left(\beta + \lambda . \sqrt{\frac{1 - sin^2(\alpha)}{sin^2(\alpha)}} \right) . \lambda \qquad (6.7)$$

(iii) For the gap distance conditions, the attachment area resembles a trapezoid in the '+' direction and is given by the expression (6.6), while the attachment area resembling a circular sector in the '–' direction is given by (Fig. 6.14 a):

$$A^{-}_{probed} = \frac{1}{2} . (\lambda - a)^2 \theta \qquad (6.8)$$

By substituting A_{probed} in the expression (6.4), the corresponding variation in attachment area based on conditions (overlap or gap distance), can be included. Note that A_{probed} depends on the protrusion length $'\lambda'$ and gap distance $'a'$, which is now included in (z_i) – efficient protrusions generated per unit time. Thus z_i completely captures the dynamics of the cell-ratchet system, especially as a function of protrusion length and overlap/gap distance. Using this, we can find the direction index $(I_{dir} = (z_+ - z_-)/(z_+ + z_-))$ given by (6.1) for any condition, based on protrusion length, gap distance and area available for attachment. The positive and negative values of I_{dir} correspond to migration in '+' and '−' directions respectively.

We plotted I_{dir} as a function of protrusion length and gap distance (Fig. 6.15). In order to capture the critical gap distance leading to direction reversal of cell migration, we scanned a large range of values for protrusion length: (10 μm to 150 μm) against, gap distance and overlap conditions: (30 μm to –110 μm) conditions.

6.2.7.1 Larger attachment area in the '+' direction leads to ratcheting

First, it was clear that the attachment area (A_{probed}) was always larger for the protrusions arising from the '+' edge (Fig. 6.15 c). Hence, for all overlap and gap distance conditions (except the 'line' like 75 % overlap condition), $A^{+}_{probed} > A^{-}_{probed}$. Note that Caballero et al. (116), showed that increased attachment area is a major factor in triggering more efficient protrusions and thereby migration in the corresponding direction. This justifies why ratchetaxis (cell migration towards '+' direction) was observed in the 25 % overlap and all the gap distance conditions (13 μm, 16 μm, 19 μm, 22 μm and 45 μm) (Fig. 6.13 a).

Next, we plotted the direction index (I_{dir}) for different protrusion length as a function of overlap and gap distance (Fig. 6.15 a and b). Note that, in Fig. 6.15 a and b, positive gap

distance indicates 'separation' and negative gap distance indicates 'overlap' between the triangles. In general, the value of I_{dir} increased as the gap distance increased. Specifically, for gap distances from + 22 μm to – 50 μm, the value of I_{dir} was positive for the protrusion lengths close to mean value (20 μm), indicating migration in the '+' direction. The negative gap distance "– 50 μm", corresponds to 25 % overlap between the triangles. This confirms our experimental observation where 25 % overlap condition and all the gap distances show migration in the '+' direction: ratchetaxis. As mentioned in the previous paragraph, the availability of large attachment area in the '+' direction results in migration towards '+' direction, irrespective of the protrusion length.

6.2.7.2 Equal attachment inhibits directional migration

As expected, for larger overlap conditions (≈ "– 100 μm"), the value of I_{dir} was approximately zero – meaning no net directional bias in migration (Fig. 6.15 a). This result is in agreement with our experimental observation where 75 % overlap condition showed no net directional bias (Fig. 6.15 a). The negative gap distance "– 100 μm", approximately corresponds to 75 % overlap between the triangles. The maximal overlap (75%) is close to a 'line' like condition, and hence the area available for attachment on either sides is similar ($A^{+}_{probed} \approx A^{-}_{probed}$). This results in random generation of efficient protrusions on both sides due to the fluctuations in protrusion parameters ($v_{\pm}$ and $\tau_{\pm}$), resulting in migration on both directions without a net directional bias.

6.2.7.3 Direction reversal occurs at 50 % overlap condition

Interestingly at 50 % overlap (≈ "– 75 μm gap distance"), the I_{dir} showed a negative value, indicating migration in the '–' direction (Fig. 6.15 a). Thus at 50 % overlap, the direction of cell migration towards '+' direction should be reversed, to move in '–' direction. The reason for this reversal trend could be due to two reasons: (i) attachment area on the neighboring triangles is approximately same $\left(A^{+}_{probed}/A^{-}_{probed} = 1.06\right)$. Hence the probability of generating efficient protrusions does not depend on area, but only on the number of protrusions (n_i). On the other hand, (ii) unlike the 'line' like 75 % overlap, 50 % overlap should be able to impose an asymmetric shape of the cell (triangular shape). This asymmetry will generate more protrusions on the polarized edge ('–') than the non-polarized edge ('+'). Thus, the asymmetry in number of protrusions ($n_{-} > n_{+}$) combined with similar attachment areas on both sides ('+' and '–') will give

rise to direction reversal, i.e. migration in the '–' direction. We are currently probing this condition in experiments to verify the reversal in directionality.

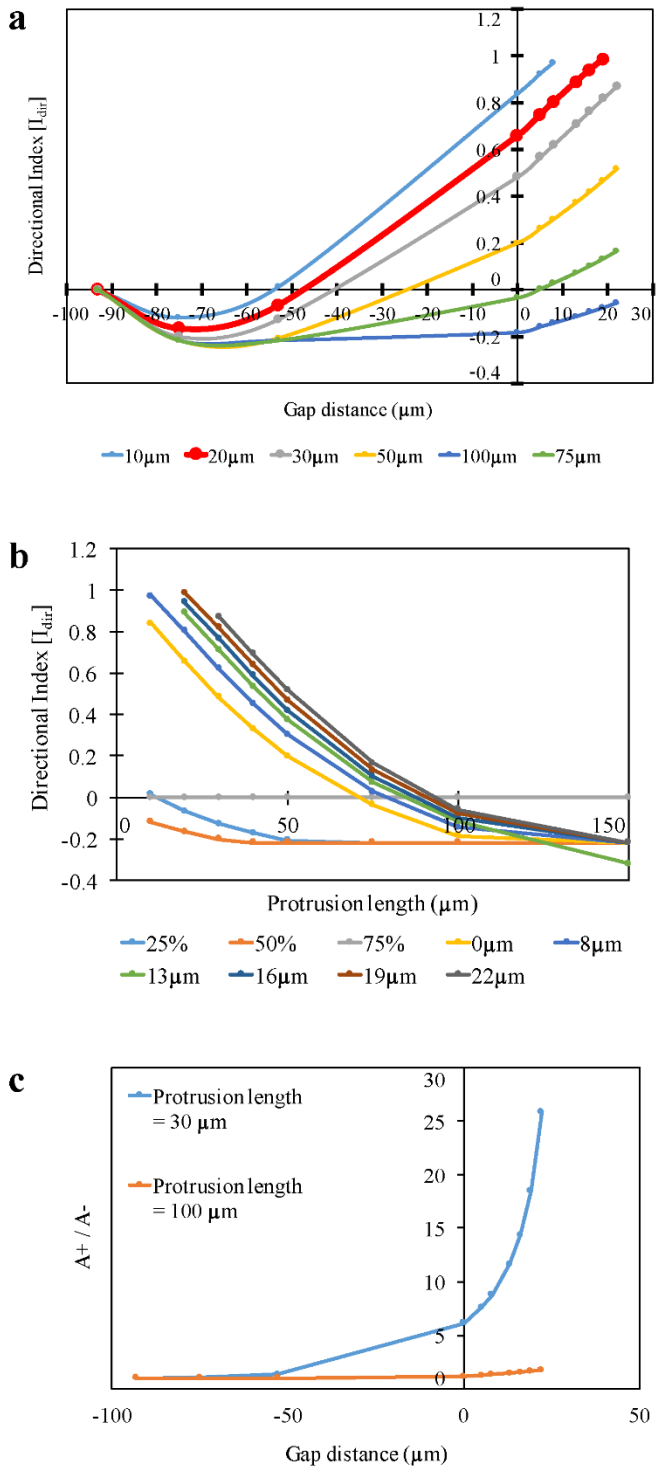

Figure 6.15. (a) Plot showing direction index (I_{dir}) for different protrusion length as a function of gap distance. (b) Plot showing direction index (I_{dir}) for different gap distances as a function of protrusion length. (c) Plot showing ratio of attachment area in '+' direction to attachment area in '–' direction as a function of gap distance for two protrusion lengths (30 µm and 100 µm).

6.2.7.4 Larger protrusion length inhibits directional migration

These simulated results: (i) $I_{dir} > 0$ (ratchetaxis) for gap distances from + 22 µm to – 50 µm (25 % overlap), (ii) $I_{dir} \approx 0$ (absence of directional bias) for 75 % overlap ("– 100 µm gap distance"), and (iii) $I_{dir} < 0$ (reversal in direction of migration) for 50 % overlap (≈ "– 75 µm gap distance") are applicable for protrusion lengths close to the mean value – 20 µm (Fig. 6.15 b). In the case of larger protrusion lengths (~ 100 µm), the variation in area between '+' and '–' directions is negligible, irrespective of the percentage of overlap and gap distance between the triangles. Hence I_{dir} becomes negative, meaning the cells with long protrusions on both sides would tend to migrate in the direction of polarization ('–' direction) (Fig. 6.15 b).

Thus with this simple model, we were able to capture the major parameters leading to direction reversal: asymmetry in area, number of protrusions and gap distance.

6.3 Discussion

Directed cell migration due to long range chemical gradients has been demonstrated *in vivo* (230, 231). But the mechanisms leading to rectification for large scale migration are not clear. Because rate of change of long range gradients with respect to distance is minimal. In such an environment, how cells sense the difference in gradient between the front and rear is difficult to understand (61).

In this scenario, we and others have shown that environmental factors like substrate geometry, sensed by protrusion and mechanical interaction of cell body, play a strong role in directed cell migration (116, 205, 225). From *in vitro* experiments, we show that asymmetries in substrates act as ratchets to rectify the fluctuations in protrusions giving rise to a directed cell migration (116). This was achieved by forcing the cells to migrate on asymmetrically shaped (triangular) fibronectin patterns. In this setup, fibronectin triangles act as ratchets and asymmetry in the available attachment area for protrusions, combined with frequency and stabilization of protrusions lead to ratchetaxis. While the asymmetric geometries / fibronectin triangles can rectify cell migration in one direction, it would be interesting to know if the migration direction can be reversed by using a similar setup of fibronectin triangles / ratchets.

We address this question in the current work, based on studies from particle-potential systems (217). We reason that variation in separation / gap distance between fibronectin triangles should lead to reversal of cell migration direction. We probe this hypothesis by scanning different overlap and gap distance conditions of ratchet configurations. Results from these experiments showed ratcheting in all cases: 25 % overlap and 13 µm, 16 µm, 19 µm, 22 µm, 45 µm gap distances, except for the 'line' like 75 % overlap condition. Of all the conditions, ratcheting effect was most pronounced in 22 µm gap distance, which is closer to the mean protrusion length 20.5 µm. Interestingly, this pronounced ratcheting effect is not seen in 19 µm gap distance which is also closer to the mean protrusion length (20.5 µm). Thus, 22 µm gap distance happens to be a condition where the ratcheting due to protrusion characteristics are dominant. In general, asymmetry in attachment area for protrusions, and the resulting variations in protrusion parameters (frequency of probing and stabilization time) were found to be the major factors for ratchetaxis in all conditions.

However, in addition to these parameters, protrusion length can also play a strong role in ratchetaxis (Fig. 6.15 b). Note that protrusion length distribution changes based on the gap distance: In Caballero et al. (116), where the gap distance was 20.5 µm, the maximum protrusion length was found to be 35 µm. However, in the current study, cells migrate on fibronectin ratchets with gap distance of 45 µm (Fig. 6.12 b). Extension of

protrusions across 45 μm gap distance, resulting in migration emphasizes the role of protrusions in directed migration, and the potential dependency of protrusion length on gap distance (Fig. 6.15 b).

In general, substrate attachments have been shown to strengthen long filopodia (68). Along this line, results showing extension of long protrusions across 45 μm, raises the question of force-length relationship in filopodia. For example, how the length of effective protrusion / filopodia leading to a migration step, varies with different overlap and gap distance conditions? Answering this question might explain the pronounced ratcheting effect at a gap distance close to mean protrusion-length. To start with, we can measure the mean filopodial length in each gap distance condition on both '+' and '–' directions. By plotting the mean protrusion length for each condition against the final directional bias of each condition the relationship between efficient protrusions leading to directional migration and their corresponding length can be explored.

While the 22 μm gap distance condition shows a pronounced ratcheting effect, a net directional bias was absent in the 'line' like 75 % overlap condition. The absence of net bias was due to equal availability of attachment area for the protrusions on either sides of the cell. The transition from no net bias in directionality, to ratchetaxis (migration in the '+' direction) occurs at the 25 % overlap where the asymmetry in attachment area favors ratcheting. In the Figure 6.13 a, the tendency of migration transits from no net bias (zero) to ratcheting behavior at 25 % overlap condition, and reaches a peak at 22 μm gap distance, followed by a fall at 45 μm gap distance. This tendency will eventually reach zero at a gap distance larger than 45 μm, since the gap distance will be larger than the maximal protrusion length.

Therefore, we can expect direction reversal close to the tails of the curve, i.e. between the conditions where no net directionality is observed and the condition where ratcheting starts to appear. This regime of reversal would be between the 'line' like 75 % overlap and 25 % overlap conditions. But a similar reversal in direction may not be expected at the other end (gap distances larger than 45 μm gap distance).

In a condition with maximal gap distance, (for example 100 μm) one might expect two scenarios: (i) The cell will be trapped in the fibronectin triangle and exhibit fluctuations without escaping. Thus net migration from one triangle to another will be absent. (ii) On the other hand, cell might escape into the passivated region with a first step in '–' direction. In general, cells conform to the shape of triangle and hence will be polarized towards the triangle ('–' direction) base. This leads to more number of protrusions arising from the '–' edge. Hence, the probability of cells to escape into the passivated region is

higher in the '–' direction than in the '+' direction. Note that, passivated regions only decrease the attachment of protrusions to the substrate. However, protrusion attachment and thereby migration is not completely absent. In this scenario, the cells will always escape in the '–' direction and perform random walk until they find another fibronectin triangle. After reaching the triangle, the cell will once again polarize and escape in the '–' direction. After several such cycles of random walk and escaping in '–' direction, one might expect a net motion in the '–' direction, assuming that the cell does not find the same triangle after every random walk. This would be an interesting condition where cells would exhibit a persistent random walk, with a net direction.

The above mentioned conditions (conditions between 75 % and 25 % overlap and gap distances larger than 45 μm) are not tested yet and we are currently planning experiments along this line. In addition, we are also currently measuring the persistence length ($L_p^{\pm}$), persistence time ($T_p^{\pm}$) and velocity of cells in different conditions.

Reversal in cell migration direction was not observed in experiments with the current overlap and gap distance conditions (Overlap: 75 % and 25 %; Gap distance: 13 μm, 16 μm, 19 μm, 22 μm, 45 μm). This motivated us to develop a simple mesoscopic model in order to predict a condition that would lead to reversal in direction. We redefined z_i (efficient number of protrusions per unit time) by scaling arguments and explicitly introduced the variation in attachment area 'A_{probed}' (on the fibronectin triangles present on either sides of the cell). The expression of A_{probed}, depends on protrusion length $'\lambda'$ and gap distance $'a'$ between the triangles. Note that, as mentioned in the previous paragraphs of discussion section, protrusion length and the corresponding gap distance play a key role in migration direction. With this redefined z_i, we plot the I_{dir} computed for different protrusion lengths against different overlap and gap distance conditions. We find that: (i) $I_{dir} \approx 0$ in the 'line' like 75 % overlap conditions, indicating no net directional bias, (ii) $I_{dir} > 0$ for conditions from 25 % overlap, 13 μm, 16 μm, 19 μm, 22 μm, until 45 μm gap distance, indicating ratchetaxis, and finally (iii) $I_{dir} < 0$ for 50 % overlap condition, indicating reversal in cell migration direction. The reason for reversal at 50 % overlap condition is proposed as: (i) equal amount of area available for protrusion attachment on both '+' and '–' directions, and (ii) polarized shape of the cell induced by triangles in 50 % overlap condition. Hence, increased number of protrusions arising from the polarized edge would lead to migration in the '–' direction. Thus from the model, we predict the direction reversal to happen in 50 % overlap condition.

In this model, we make two major assumptions: (i) the probability of stabilization on the neighboring fibronectin triangles is assumed equal in both ('+' and '–') directions. In

general, the dynamics of protrusions like attachment to the substrate, is not an independent event. It also depends on the neighboring protrusions (68). The number of protrusions varies between the polarized and non-polarized side of the cell and based on the availability of attachment area (116). Hence, the number of protrusions on either side of the cell will be different. Therefore, based on the number of neighboring protrusions, the probability of stabilization may tend to vary. This variation should be measured experimentally and incorporated into the model. Along this line, another important assumption of the model is: (ii) the value for frequency of protrusions (ν), is borrowed from Caballero et al. (116), where the measure actually corresponds to the frequency of efficient protrusions (that lead to migration). In our model, we assume those values for total number of protrusions arising from each side, which may or may not get stabilized. This is another reason for assuming the probability of stabilization to be same on either sides (assumption (i)). In order to strengthen the model, these values should be experimentally measured for each overlap and gap distance conditions, which we are planning to do in future.

In conclusion, this work can be considered as a first step in identifying and quantifying the parameters that would lead to reversal in cell migration direction. We compare the cell-ratchet system to the particle-potential system of Chauwin et al. (229). We identify gap distance between the fibronectin ratchets to be an equivalent parameter to the particle drift time that leads to reversal in particle motion in Chauwin et al. (229). By scanning various overlap and gap distance conditions through experiments, we show that ratcheting effect varies as a function of gap distance. In addition, with the help of a simple mesoscopic model, we propose a condition (50 % overlap) at which direction reversal will occur.

With these results, we show that directional cell migration (ratchetaxis) and reversal of direction can occur only based on local cues from the substrate geometry. The dependence on local cues from interaction with the environment can complement long range chemical gradients in directing cell migration. However, these results require dedicated *in vivo* experiments. As a first step, projects in our lab are currently exploring directional migration in cells that are exposed to ratchets and chemical gradients in both co-operative and competitive environments. Similarly, it would be interesting to construct 3D ratchets using 3D printers to investigate cell migration condition, closer to *in vivo*. With these experiments one can fully understand the mechanisms behind ratchetaxis, in order to apply and study directional migration *in vivo*.

7. Spontaneous pulsatile domains in epithelial monolayers

In this chapter, I will address how dynamics with spontaneous length and timescales emerge in a system of collection of cells. We report a specific phenomenon – pulsation of collection of cells in confluent Madin-Darby Canine Kidney (MDCK) monolayers. Pulsatile domains are group of cells in the monolayer that span ~ 20 cell length, undergoing cycles of collective contraction and extension. We use these pulsations arising from the monolayer as a phenomenon to address and understand, how length and timescales are spontaneously emerging in a system. We show that friction due to interaction of cells with the substrate plays a significant role in setting the lengthscale of pulsations. We substantiate this by matching the lengthscale of pulsations with fibronectin patterns of various dimensions, patterned on the substrate. Following this, we take a continuum description to show a simple way to generate pulsation by coupling cell area, cell height and contractility. In agreement with the model, we experimentally demonstrate height fluctuations in cells during pulsations and, disruption of pulsation on inhibiting cytoskeletal proteins. Together, these observations reveal collective self-organized dynamics in epithelial monolayer whose length and timescales are controlled by their mechanical environments.

In this ongoing project, we try to characterize and understand the above mentioned factors leading to the spontaneous emergence of pulsatile domains. While most of the experiments are complete, we are currently working to improve our analysis strategies. In this manuscript, I will present a summary of results from our experimental observations and the current analysis.

This chapter is organized as follows: The chapter begins with the question of understanding the factors responsible for spatio-temporal correlation in collective cellular environments. First, I will introduce our experiments through which we observed the pulsation phenomenon in MDCK monolayers. Followed by this, I will describe the analysis strategies that we used for understanding pulsation characteristics like: contraction-extension cycles, pulsation boundary, center of pulsations, correlation length and period of pulsations. Having discussed the methods to characterize pulsations, I will introduce our hypothesis for potential role of substrate friction in regulating the correlation length of pulsations. Then, I will explain in detail our results on the role of substrate friction through different experiments. After this, I will discuss our theoretical model on oscillating tissue that further confirms the role of friction. Using the model, I will show how contractility in pulsations is linked to fluctuations in cell heights by deriving an expression for characteristic lengthscale for pulsations. This will be

substantiated by a section on experimental confirmation of cell height fluctuations during pulsations. Then, I will discuss the significance of cytoskeletal proteins by different experiments involving cytoskeletal inhibitor drugs. Here the results concerning changes in collective behavior of cells during inhibition and after reactivation of cytoskeletal proteins will be discussed in detail. Having shown the experimental and theoretical model based results on the role of friction, cytoskeletal proteins and the need for cell height fluctuations, I will present our experiments on the effect of cell density in pulsations. Finally, I will finish this chapter with a discussion on comparisons to other studies and the future perspectives of this project.

This project is a result of team effort and is ongoing. The project was conceived by Daniel Riveline. All the experiments were performed by myself. The theoretical model was conceived by Guillaume Salbreux, The Francis-Crick institute, London and currently being developed by Mandar M. Inamdar, IIT Bombay, Mumbai. The MATLAB scripts for extracting data from the experiments using winding number analysis and correlation analysis were coded by Mandar M. Inamdar.

7.1 Introduction

In vivo, tissue scale processes during development and pathological conditions involve action of collection of cells (232–238). Interestingly, these processes occur under confluent environments where cells are densely packed. In spite of this spatial constraint, they exhibit interesting dynamics which possess a characteristic length and timescale (239). How these length and timescales emerge and factors responsible for this precise spatio-temporal regulation are not well understood.

In order to understand this spatio-temporal regulation, we decided to study the dynamics of an established *in vitro* system where collection of entities exhibit an ensemble effect. We chose MDCK cell monolayer. MDCK cells are an established paradigm of epithelial cells for studying collective effects like collective migration, wound healing etc. These cells establish cell-cell contacts through E-cadherin junctions thus forming a continuum of cells. The confluent state of MDCK cells presents an *in vitro* scenario analogous to those observed *in vivo*. This motivated us to study the confluent states of MDCK monolayer to understand the factors leading to spontaneous emergence of length and timescales.

7.1.1 Experimental setup

We used MDCK cells labelled with GFP for E-cadherin. The cells were plated on glass coverslips, mounted on metal holder (see methods section 3.4.4). The cells were seeded with an initial density of ~ 10^6 cells / 175 mm^2 in an L-15 medium supplemented with 10 % Fetal Bovine Serum (FBS). The cells were then imaged in phase contrast microscopy with a wide field objective (4 X) to capture the monolayer activity over a large area. The high seeding density and high percentage of serum allowed to reach confluency in ~ 6 h – 8 h on a surface of 175 mm^2 coverslip. The evolution of monolayer was observed for at least 48 h to capture the long term behavior of monolayer, with an acquisition rate of 1 frame every 5 min / 10 min. For simplicity, the MDCK monolayer will be addressed as monolayer throughout the text.

Interestingly, from the acquisitions of monolayers for 48 h, we found spontaneous emergence of pulsatile domains of cells. These domain of cells exhibited collective contraction and extension, which we call as pulsation or pulsatile domain. The pulsatile domains exhibited a specific size and period. This kind of spontaneous collective dynamics in an *in vitro* system (MDCK), motivated us to further explore the phenomena. In the following sections, I will first describe in detail these pulsations and the methods used for analyzing these dynamics.

7.1.2 Spontaneous pulsations in confluent epithelial monolayer

After reaching confluency, domains or collection of cells spontaneously started to exhibit contraction and extension in a collective manner (Fig. 7.1, Movie 7.1).

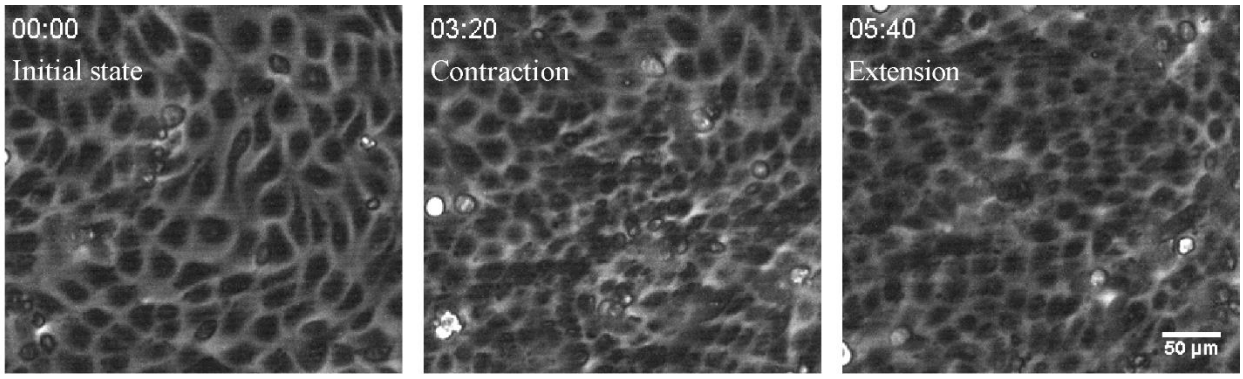

Figure 7.1. An isolated pulsating domain. Three snapshots of pulsating domain at different phases. First snapshot: Initial state of pulsating domain, i.e. before the cells initiated contraction. Second snapshot: Cells in contraction phase. Increased cell density is observed at the center of the pulsating domain, where cells are in compressed state. Third snapshot: Cells in extension phase. Cell density is lower and the cells are in more spread state when compared

to contraction phase. But the cell density is higher than the initial state due to cell division. Time in hh:mm; Scale bar 50 μm.

As a first step in order to confirm the observed phenomenon, we performed preliminary manual analysis. We selected the cells present at the periphery of pulsating domain and manually tracked them (Fig. 7.2 a and b).

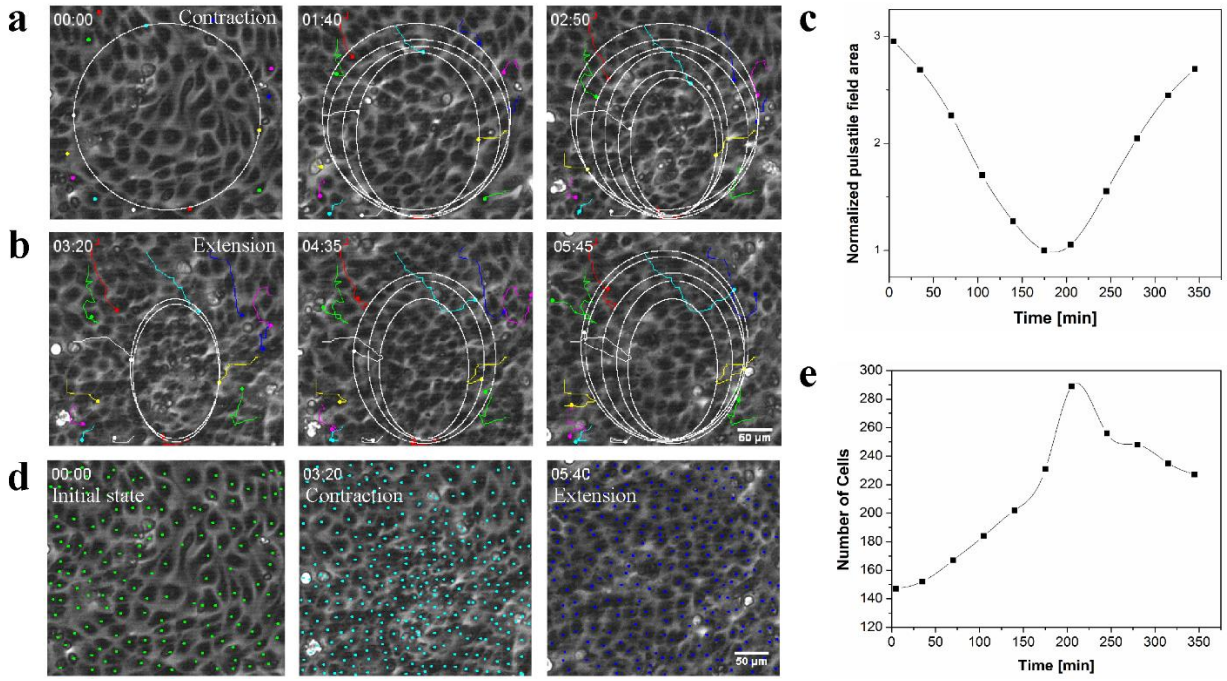

Figure 7.2. An isolated pulsating domain, same as shown in (Fig. 7.1). (a) and (b) Boundaries of pulsatile domain obtained by connecting the trajectories of peripheral cells. (a) Shows cells moving towards a common center of the pulsatile domain. (b) Shows cells moving away from the common center. The trajectories of cells used for marking the boundary are indicated in different colors. (c) Plot showing the decrease in pulsatile domain area followed by rescue during the time of pulsation. The plot corresponds to the domain showed in (a-b). (d) Manual counting of cell density for the domain in (a-b). The snapshots represent different phases of pulsation. Each dot in the snapshots correspond to a cell. (e) Plot (corresponding to (d)) showing an increasing trend in cell density, followed by a decreasing trend. The density does not come back to the initial value due to the cell division in the monolayer.

The trajectory obtained from the manual tracking of the peripheral cells were clearly showing a pulsating behavior: the direction of trajectory first moved towards the center (Fig. 7.2 a) and then move away from the center (Fig. 7.2 b). This behavior confirmed the pulsatile nature of cell collection in the domains. In addition, using these trajectories, we tried to draw a boundary of the cells that are exhibiting pulsation (Fig. 7.2 a and b). For this, we had fit a circle through the trajectory points of the peripheral cells at different time intervals. This fit indicated a clear trend in decrease of pulsatile domain area (contraction), followed by an increase in area (extension) (Fig. 7.2 c).

However, this area obtained from the peripheral cell trajectories could be due to synchronized flow of cells without contraction and extension characteristics. So, we manually counted the number of cells in the region of the pulsating domain (Fig. 7.2 d). In this context, "domain" corresponds to the area formed by collection of cells exhibiting pulsation and the "region" corresponds to a larger area encompassing pulsatile domains. The automated ImageJ plugins for cell counting were not appropriate, since the center of pulsation was extremely crowded that resulted in poor thresholding by plugins. By manual counting, we found a clear increase in cell density up to two folds during the contraction phase followed by a decrease in cell density during extension (Fig. 7.2 e). This tendency of increased cell density during contraction and decreased cell density during extension shows that more number of cells were compressed into the pulsatile domain region during contraction than the extension phase (Fig. 7.2 d). Thus pulsating domains were not just synchronized cell flows but exhibited contraction-extension characteristics.

With these preliminary analysis, we confirmed the characteristics of pulsating domains. By observation, we found that these domains extended over ~ 20 to 30 cells and exhibited pulsation with a period of ~ 6 h (Fig. 7.2 a, b and d).

7.1.3 Pulsations: *in vitro* phenomenon to study spatio-temporal regulation

The confluent monolayer also occasionally presented with other collective effects apart from pulsations: mechanical waves of higher velocities in monolayer (Movie 7.2) and directional flows of cells (see appendix section 10.2.2). However the phenomena of pulsations was more striking as oscillations at the molecular and cellular scale are shown to be inherent *in vivo* (14, 240). More specifically, oscillations have been shown to perform specific functions (shape change) *in vivo* during development with characteristic timescales ranging from seconds to minutes (161, 241, 242). This motivated our study on spontaneous pulsatile domains observed in MDCK monolayers.

The pulsatile domains were spontaneously emerging and possessed a characteristic length and timescale; i.e. only cells extending over a particular distance / lengthscale (~ 20 to 30 cells) were exhibiting the characteristic of contraction and extension. Similarly, the contraction-extension cycle occurred over a particular period / timescale (~ 6 h). This spontaneous regulation of spatio-temporal characteristics of a group of cells is the hall mark of collective effect. Moreover, the existence of this unique collective effect (pulsating domains) in an *in vitro* system, presented an opportunity to study the factors

regulating the length and timescales, since conditions *in vitro* are easy to control and study.

Therefore, we started analyzing the pulsations in a detailed manner to identify the factors involved in setting the length and timescales. Through the identification of these factors *in vitro*, one can find similar analogies in *in vivo* system that would give insights into how length and timescales are regulated in some of the complicated *in vivo* processes (243).

In order to study these pulsations, first we wanted to establish a rigorous method of analysis, as opposed to the manual analysis described before. Manual analysis like extraction of pulsatile domain area by manual tracking of peripheral cells are not concrete. A bias might be introduced by the experimenter while choosing the peripheral cells for estimating the pulsatile domain boundary. For example: only choosing the best cells that correspond to pulsatile behavior. In addition, pulsations result from the action of collection of cells. Estimating pulsation characteristics (like pulsatile domain area) only from the readout of few cells (peripheral cells for estimating boundary) might lead to error. In order to solve these type of issues, we wanted to analyze the domains in an unbiased manner, mainly using Particle Image Velocimetry (PIV) and correlation functions. In the following section, I will describe these methods which we used for extracting the pulsatile domain characteristics like length and timescales.

7.2 Strategies for analyzing pulsatile domains

7.2.1 PIV and divergence estimates

After acquiring MDCK monolayers with pulsations, we used PIV to plot the instantaneous velocity values for defined regions / interrogation windows that contain cells. The velocity plot obtained from the PIV is a result of cross-correlation analysis between the interrogation windows of subsequent time points. To perform PIV, we divided the image frame into interrogation windows of size 64 pixel x 64 pixel, which is slided by a step size of 32 pixels. By plotting the velocity values for such interrogation windows across an acquired frame, the instantaneous velocity field of the cells in that frame / at that time point is obtained. From this velocity field, the velocity components (across x and y axes) can be obtained for each position on the image frame. We used the PIVlab software for plotting the velocity fields in monolayer (134).

We use the obtained velocity field of the monolayer to study pulsation characteristics. Pulsatile domains in monolayer exhibit directional movement of cells towards and away from a common center. Thus the domain area functions as a sink during the contraction phase which leads to collective movement of cells into the domain area; and as a source during the extension phase which leads to collective movement of cells away from the domain area (Fig. 7.3 a). In other words, pulsation exhibits a gradient in velocity field (towards and away from the center of pulsation). This velocity gradient can be given by: $div\, V = \nabla . V = \frac{\partial V_x}{\partial x} + \frac{\partial V_y}{\partial y}$; where $div\, V$ or $\nabla . V$ represents the divergence of the velocity field (V), V_x and V_y represent the velocity components corresponding to x and y axis respectively. Divergence plot quantifies a point on the vector field either as a source or sink. For example, an interrogation area with a positive divergence value qualifies as a source (cells moving away from this area) and with a negative divergence value qualifies as a sink (cells moving into this interrogation area) (Fig. 7.3 a). Thus by estimating divergence across the monolayer, one can find the instantaneous nature (source/sink) of a region or domain of cells and, how the nature of region varies over time. For example, if the divergence values are color coded as blue for contraction (negative divergence values) and as red for extension (positive divergence values), a region with pulsatile domain would alternate between blue and red colors, indicating contraction and extension respectively (Fig. 7.3 c).

7.2.2 Winding number for finding pulsation centers

After plotting the divergence for the whole monolayer (in the acquired frame), we wanted to identify/extract the pulsatile domains from the monolayer. Cells undergoing pulsations move towards and away with respect to a common center. During this back and forth movement, the velocity of cells decrease as they approach the center and their velocity is close to zero when they are in the vicinity of center. Thus the region in and around the pulsating centers do not exhibit a characteristic velocity and can be treated as critical points (regions without a well-defined velocity or near-zero velocity). We wanted to identify these regions with critical points in the monolayer, which together with the divergence information of that region would identify the pulsating regions. In other words, a pulsating region will have a critical point with a surrounding divergence field that exhibits contraction (blue) and extension (red) (Fig. 7.3 c). The nature of the critical point, i.e. association with contraction and extension of pulsation can be deduced by finding the index of the critical point. The index of this critical point is obtained by finding the Winding number for the corresponding region.

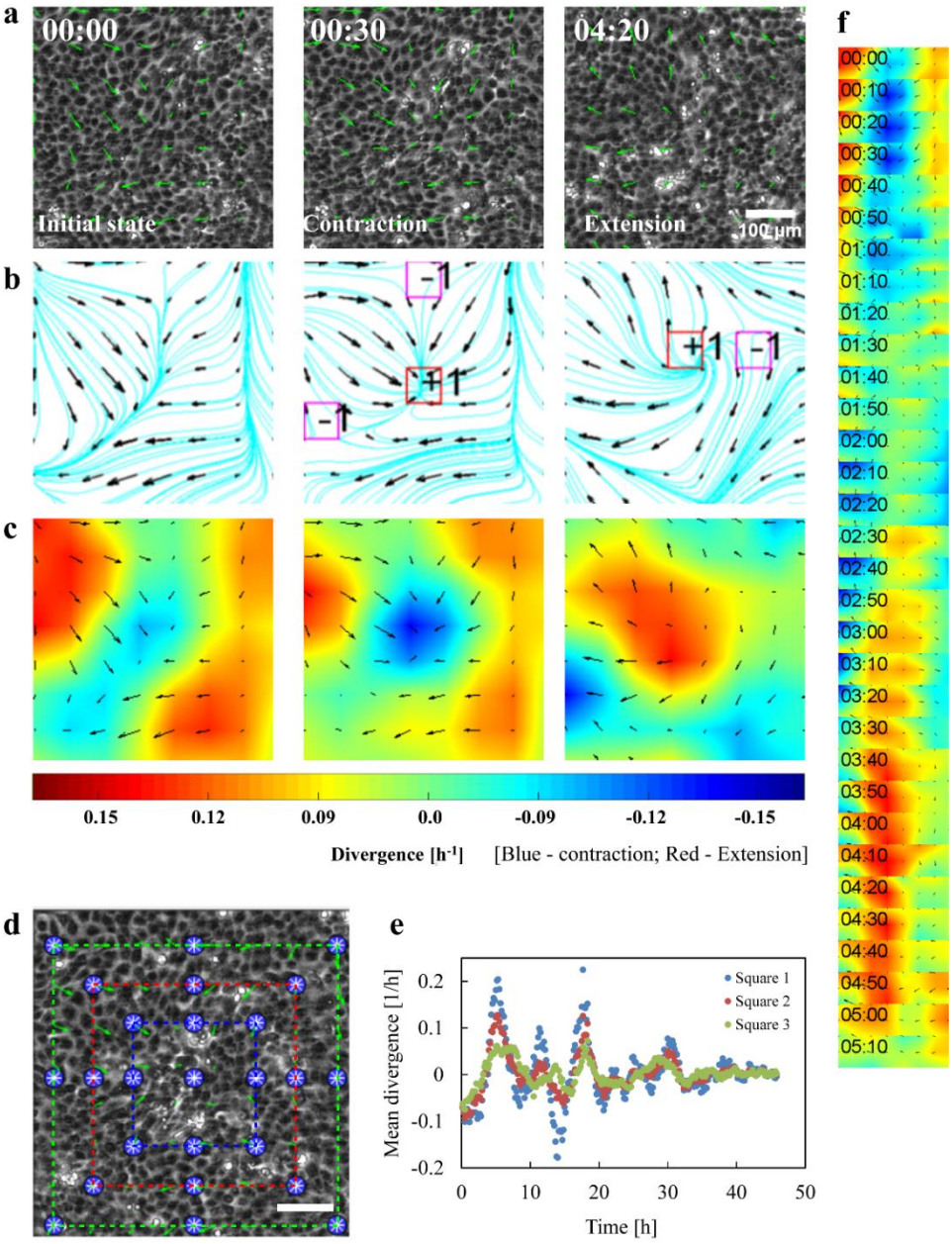

Figure 7.3. Description of isolated pulsatile domain by PIV, winding number analysis, divergence plot and estimation of domain boundary and period. (a) Snapshots with PIV plots for a pulsatile domain undergoing contraction and extension. First image shows the initial state and the subsequent images show the following contraction and extension. The area of each image is chosen as explained in (e) and corresponds to square 3 in (e). (b) Plot with critical points using winding number analysis, corresponding to (a). '+1' with a red square indicates the position of critical point which corresponds to the center point of source or sink characteristic of the pulsatile domain. '-1' corresponds to a non-source/sink characteristic, usually a saddle – see appendix section 10.2.1. (c) Divergence plot corresponding to (a). The plot is color coded with blue and red indicating contraction and extension respectively. (d) Snapshot of the pulsatile domain used for estimating domain boundary, manually. Squares are drawn incrementally away the center. The increments were done in steps of 64 pixels to correlate with the PIV plot. Scale bar, 100 µm. (e) Mean divergence of the pulsatile domain area using different boundaries. Each plot corresponds to a square and is color coded to represent the squares shown in (d). The initial time point (t_0) corresponds to the time when the monolayer reaches confluency. (f) Kymograph of the pulsatile domain center shown in (c). Time in hh:mm.

We made a plot containing index of critical points for every frame (time point) of experiment, where '+1' corresponds to a region containing a critical point (Fig. 7.3 b). A detailed description of Winding number and how the plot with critical points are obtained, is given in appendix section 10.2.1.

Thus, using winding number, we were able to identify the critical points with an index of '+1' in the monolayer. Still, a critical point with an index of '+1' in a velocity field can represent both vorticity and source/sink (divergence) like patterns. Hence, in order to identify the critical points with '+1' that specifically corresponded to source/sink like behavior of pulsations, we correlated the critical points in the plot (of the image frame) with the color coded plots of divergence (of the same image frame). By combining the critical points (pulsatile domain centers) and the divergence of the region (pulsatile behavior), we isolated potential pulsatile domains in the monolayer (Fig. 7.3).

The next step was to identify the distance over which the effect of pulsatile domains dictated /or the boundary of cells, that exhibited contraction and extension behaviors in phase with the region surrounding the center of pulsating domain.

7.2.3 Pulsatile domain area

In order to estimate the pulsatile domain area, closed boundaries (squares) surrounding the identified critical points (pulsating domain center) were drawn incrementally away from the pulsation center (Fig. 7.3 d). We estimated the mean divergence of the area surrounded by each of the closed boundaries. By plotting the obtained mean divergence over time, one could observe oscillations in divergence plot (negative divergence – contraction; positive divergence – extension) (Fig. 7.3 e). In this case, amplitude of the mean divergence corresponding to contraction and extension would decrease while moving away from the center. Hence the boundaries that are farther from the pulsation center, would include cells that are not completely under the influence of pulsation (collective contraction and extension). This can be detected from the decrease in amplitude of mean divergence. Thus we took the boundary that showed reduced amplitude of mean divergence, as the final boundary of pulsatile domain where the effect of pulsation vanishes (Fig. 7.3 e). This allowed us to obtain a tentative size of the pulsatile domains: ~ 200 μm (~ 20 to 30 cells) (Fig 7.3 a, b and c). The next step was to estimate the period of pulsations.

7.2.4 Pulsatile domain period: kymograph

After isolating pulsatile domains using critical points (center) and boundary estimation, we wanted to estimate the time between peak contraction and peak extension of pulsations. For this, we made kymographs of the center of isolated pulsating region that

corresponded to alternating contraction (blue) and extension (red) peaks. The timescale obtained from the kymograph was taken as the period of pulsation: ~ 5 – 6 h (Fig. 7.3 f).

This series of analysis steps: (i) divergence plot of monolayer, (ii) identification of critical points, (iii) estimation of pulsatile domain boundary and (iv) time between the contraction and extension peaks, facilitated the isolation of pulsatile domains. From these analyses, we estimated the size of pulsating domain to be ~ 200 μm (~ 20 to 30 cells) and the time between peak contraction and peak extension to be ~ 5 – 6 h.

While this procedure was unbiased to some extent, manual interpretations were required in some of the steps. For example: selection of critical points, precise estimation of pulsatile domain boundary and precise identification of contraction-extension peaks. These steps were critical in identifying the length (size) and timescale of pulsations. In addition, pulsatile domains emerge randomly across the monolayer. But in the analysis strategies described above, the length and timescales were determined only from those manually isolated pulsatile domains (Fig. 7.3 d and f). Thus manual selection introduces a bias by selectively picking pulsations, without considering all the pulsations occurring in the monolayer. This further motivated us to use a rigorous unbiased approach without requiring any manual interpretation.

In literature, the most commonly used method for extracting collective behavior from a velocity field in a non-invasive manner, is correlation based analysis (244–246). Based on these studies, we decided to extract the pulsation characteristics (length and timescales) using correlation based methods.

7.2.5 Correlation length of pulsations

The pulsatile domain exhibits a characteristic size (lengthscale), because cells within the domain are correlated in their behavior, i.e. all the cells within the domain exhibit same characteristic (contraction or extension) at any instant of time. This contraction and extension behaviors can be deduced by measuring the divergence. From this divergence plot, one can obtain the distance over which a similar divergence characteristic or correlation in divergence characteristic exists (Fig. 7.4 a). Here, divergence characteristic means: negative and positive divergence, representing contraction and extension respectively. This correlation is given by:

$$C_{dd}(r) = \int div\,(x) \times div\,(x + r)\,dx \qquad (7.1)$$

Where: x indicates a point on the monolayer and $div\,(x)$ indicates the divergence at the point 'x', $x + r$ indicates a point at distance 'r' from 'x' and $div\,(x + r)$ indicates the divergence at the point $x + r$. $C_{dd}(r)$ denotes the divergence correlation over the distance 'r'. The correlation coefficient (after normalization) will yield a value of '1' for perfect correlation between points, and values less than '1' as the correlation decays. The correlation coefficient value takes negative values if the points are anti-correlated.

We developed a MATLAB code to find the correlation in divergence across the monolayer. The obtained divergence correlation for every time point decays and reaches a minima after a particular distance 'r' (Fig. 7.4 c). The distance at which the correlation curve reaches minima, indicates the divergence correlation length (of pulsations) existing in the monolayer at that time point. We averaged the correlation length of monolayers obtained every 5 h, over a total duration of 48 h (experimental time) (Fig. 7.4 c). Thus the obtained divergence correlation length corresponds to the mean correlation length of pulsations occurring in the monolayer throughout the time of experiment. For these analyses, the time zero (t_0) was taken as the point where the monolayer becomes confluent.

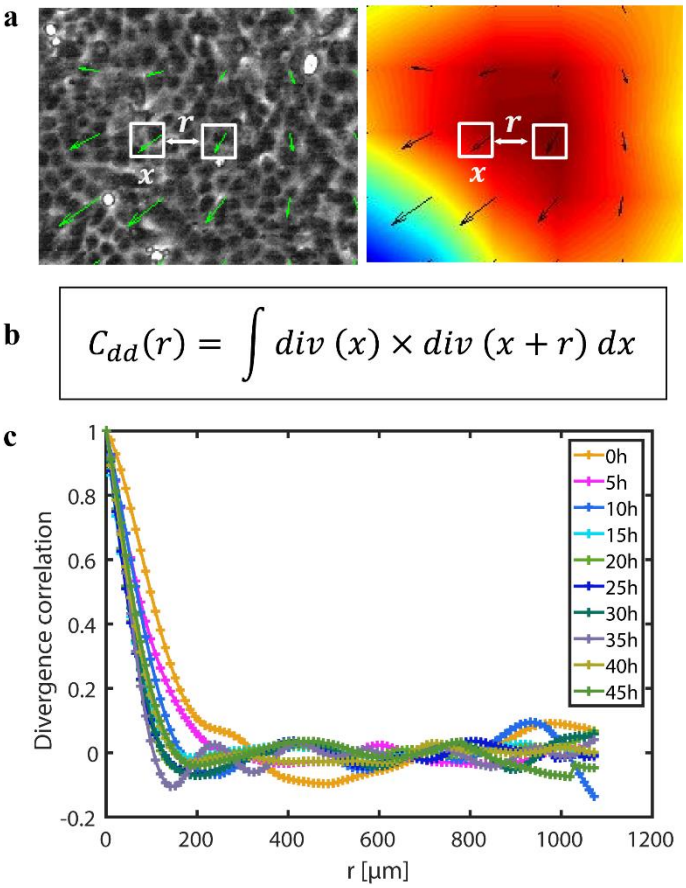

Figure 7.4. Spatial correlation analysis for estimating the distance over which correlation of divergence exists. (a) Snapshots of raw data and divergence plot to show the correlation analysis. Correlation between the chosen point 'x'and '$x + r$' after moving by a distance 'r'. (b) Expression for finding the divergence correlation between two points separated by a distance 'r'. C_{dd} represents the divergence correlation function and $div\,(x)$ and $div\,(x + r)$ represents the divergence of the two points. (c) Decay of divergence correlation function over distance 'r' along the image frame of monolayer. This divergence correlation plot corresponds to a control experiment, where correlation (curves) is plotted every 5 h. Each curve corresponds to the time shown in legend. The 'r' corresponding to the minima of each curve is taken as the correlation length for that time point.

We estimated the mean correlation length of pulsations for experiments where the MDCK cells were grown on normal (without any surface treatment) coverslips. Note that from here on, these

experiments will be addressed as control experiments throughout the text. The obtained mean correlation length of pulsations corresponded to ~ 230 µm (~ 20 to 30 cells). This correlation length was similar to those values obtained from the previous analysis using manual tracking and winding number (~ 20 to 30 cells).

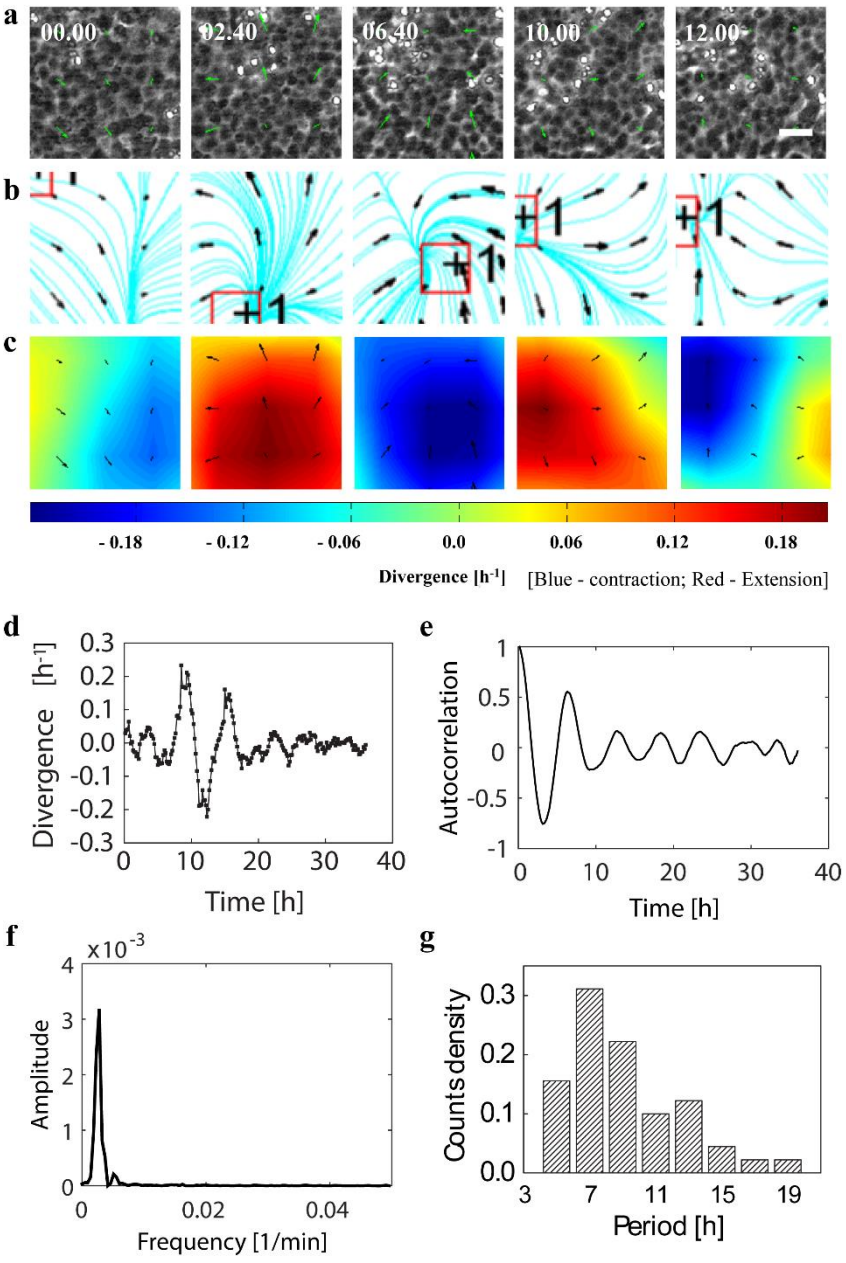

Figure 7.5. Description of a pulsatile domain using correlation analysis. The mean divergence correlation length (230 µm in this case) is used for isolating a pulsatile domain of particular area. (a) Snapshots of a pulsatile domain representing two cycles. Scale bar 100 µm. (b) Plot of critical points corresponding to (a). (c) Divergence plot of the pulsatile domain corresponding to (a). (d) Oscillations in mean divergence of the area corresponding to (a) as a function of time (whole experiment). Positive and negative divergence values correspond to extension and contractions respectively. The initial time point (t_0) corresponds to the time when the monolayer reaches confluency. (e) Autocorrelation of the divergence plot shown in (d). The autocorrelation shows periodic repetitive oscillations. (f) Power spectrum (of the Fourier transform of divergence) corresponding to (a). A clear peak appears and the peak corresponds to 6 h. (g) Distribution of periods obtained from 4 different control experiments (Number of biological repeats, N=4). The peak of the distribution is around 7 h.

Thus in control condition, the correlation length of pulsations was found to be ~ 230 µm. We used this correlation length to define the area of pulsatile domains (230 µm x 230 µm / 230 µm^2) identified by winding number and divergence characteristics (Fig. 7.5 a, b and c). The mean divergence of the isolate pulsatile domain area showed oscillations over the

time of experiment (Fig. 7.5 d). The periodicity of these oscillations were further confirmed by obtaining the autocorrelation of this divergence plot (Fig.7.5 e).

Having quantified the correlation length in an unbiased manner, we wanted to find the factors responsible for setting this lengthscale in pulsations. To identify these factors, we probed different conditions where we used the same correlation analysis for estimating the mean (divergence) correlation length in each condition. I will present the experimental conditions probing these factors (setting the lengthscale of pulsations) in the following sections, mainly based on arguments from variations in correlation length.

While I will discuss mainly the correlation length based arguments in this manuscript, we are currently performing the analysis for deducing the timescale of pulsations in all these conditions. In this process, the analysis of control condition for deducing timescale is complete and is described here – for estimating the pulsation period, we did the following: since we know the correlation length of pulsations (~ 230 μm), we used this lengthscale to define areas of 230 μm^2 throughout the monolayer. The whole monolayer was scanned by sliding windows of 230 μm^2 areas throughout the image frame. From the Fourier transform of the mean divergence of these areas over time, we obtained the power spectrum (Fig. 7.5 f). The power spectrum always showed a clear peak yielding a timescale for the pulsations occurring in the defined areas. We obtained a distribution of timescales for the control experiments, from 4 h to 19 h, where the peak of the distribution was around 7 h (Fig. 7.5 g). The 7 h timescale corresponds to the mean period of pulsations existing in the control experiments and is similar to those values obtained from the previous analysis using manual tracking and winding number (~ 5 h to 6 h). Currently we are working on improving and automating the analysis to find the pulsation period for all other conditions discussed below.

7.3 Factors responsible for setting pulsation lengthscales

The MDCK monolayer on reaching confluency spontaneously exhibits pulsatile domains with a natural lengthscale of ~ 230 μm. This indicates a tight spatial regulation of pulsations. However, it is not clear how this lengthscale is established, i.e. how boundaries of pulsatile domains are established, within which cells are coordinated for contraction and extension cycles, while cells outside the boundaries are not influenced.

In general, dynamics in the monolayer are dictated externally by the interaction of cells with the underlying substrate and internally by the cytoskeletal activities. For example: in MDCK cell monolayer system, frictional forces due to the cell-substrate interaction are

necessary for collective migration (247) and wound closure (248, 249), and cytoskeletal components are vital for different collective effects (132, 178, 250). These examples strongly show the involvement of friction due to cell-substrate interaction and cytoskeletal elements in different dynamics of MDCK monolayer system. With motivation from these studies, we hypothesized these factors (substrate friction and cytoskeleton) should be playing a role in setting the lengthscales of pulsations. To understand the role of these factors in regulating pulsation lengthscale, we measured the correlation length of pulsations on substrates with varying friction and in experiments with inhibited cytoskeletal elements. In the following sections, these experimental conditions are described in detail.

7.4 Friction affects correlation length and positioning of pulsations

Friction is induced by the interaction of cells in monolayer with the underlying substrate. This cell-substrate interaction is promoted by ExtraCellular Matrix (ECM) proteins. It has been shown that by increasing the concentration of ECM proteins on the substrate, the motility/velocity can be tuned for various cell types (116, 249, 251). From a previous study in our lab (116), we know that optimal velocities for NIH3T3 cells can be obtained by micropatterning 10 μg/ml of fibronectin on substrates. We reasoned that, 10 μg/ml of fibronectin – in addition to the ECM proteins depositing from the serum in media, will increase the cell-substrate interaction – leading to higher friction. Since migration velocity is proportional to the substrate friction, the increase in substrate friction can be deduced by decreased velocities of cells in monolayer. Thus velocities of cells in monolayer can be an indirect measure of friction.

7.4.1.1 Experimental setup and analysis

All the experiments requiring micropatterning of rhodamine fibronectin (10 μg/ml) were done by microcontact printing protocol. After microcontact printing, MDCK cells were seeded on these coverslips and allowed to settle for ~ 1 h. The samples were then rinsed to remove non-adherent cells and proceeded for image acquisition. Note that only those micropatterns that were of good quality (based on homogeneity of fluorescent images) were selected for acquisition. For all the experiments, acquisition was continued for at least 48 h after the monolayer reaches confluency. In those experiments requiring passivation (other than the fibronectin coated regions), the coverslips were incubated with

100 µg/ml pLL-g-PEG after microcontact printing and before cell seeding. For more details on the sample preparation protocol, see methods, section - 3.4.4.

For analysis (of all experiments), the time at which monolayer reaches confluency is taken as initial time point (t_0) and the analysis is performed for at least 48 h from t_0. The velocities discussed in the manuscript correspond to the mean collective velocity of cells in the MDCK monolayer, obtained from PIV measurements, unless specifically mentioned otherwise. In the following sections, rhodamine fibronectin will be abbreviated as "FN" and pLL-g-PEG will be abbreviated as "PEG" for convenience.

7.4.1.2 Pulsations on homogeneous fibronectin coating

In order to test the hypothesis of increased friction, we homogeneously coated glass coverslips with rhodamine fibronectin (FN) and cultured MDCK monolayers on these coverslips. Then we compared the mean velocities of cells in the monolayer between control and homogeneous FN condition. As expected, we found that mean velocities were significantly lower in the homogeneous FN condition (~ 6 µm/h) than control experiments (~ 18 µm/h) (Fig. 7.6 a). This reflects a clear increase in magnitude of substrate friction due to homogeneous FN coating. The monolayer on homogeneous FN surface also showed pulsations. In order to compare the pulsation on homogeneous FN condition with the control, we checked the correlation length of pulsations.

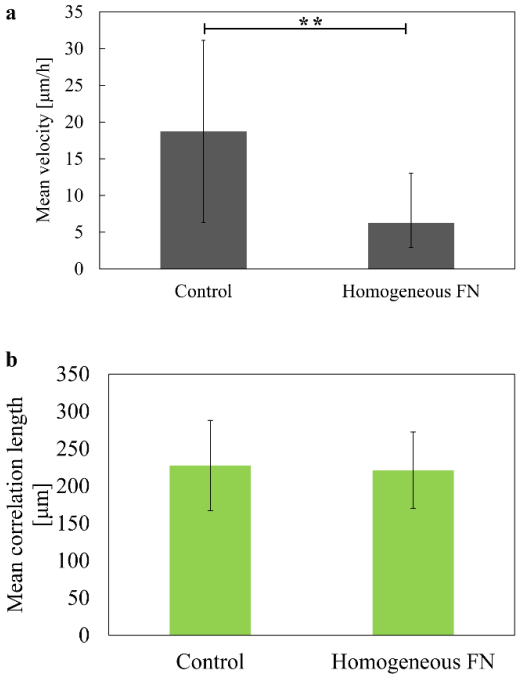

Figure 7.6. Comparison between control and homogeneous FN experiments. (a) Comparison of mean velocity obtained using PIV. The velocities are time averaged for the entire experimental time. Control (N=3); homogeneous FN (N=3). ** $P < 0.01$ by Mann-whitney test. (b) Comparison of mean divergence correlation length obtained using the method described in Fig. 7.4. The conditions are not significantly different from each other. Control (N=4); homogeneous FN (N=6). Error bars indicate standard deviation of mean.

Interestingly, the divergence correlation length (of pulsations) in the homogeneous FN condition was similar to the correlation length of pulsations in control: ~ 230 µm (Fig. 7.6 b). While this

result is surprising, the increase in friction only affects the (decreases) velocity, which in turn affects the divergence (amplitude) values. However, this does not challenge neither the existence of pulsations nor the correlation length of pulsations. In other words, the similarity in correlation length between the homogeneous FN and control conditions is due to the global increase in friction in the homogeneous FN condition, i.e. all the cells in the monolayer on homogeneously coated FN substrate experience a similar friction. Except for an increase in magnitude of friction, this situation is similar to the control condition, where all the cells in monolayer experience similar substrate friction (due to the deposition of ECM proteins from the serum in media). Therefore, we reasoned that as long as all the cells in monolayer experienced similar amount of friction, only the divergence amplitude can be changed but the correlation length will remain unaffected.

This tendency of similar friction across the monolayer can be changed by differential variation of the friction across the substrate. For example, by selectively patterning some regions of the substrate with FN, cells on FN region will experience more friction than the cells on non-FN region. If the ratio of friction between the cells on FN and non-FN region is high enough, the corresponding change in divergence amplitude between these two regions will lead to change in divergence correlation length. In addition, by tuning the selective patterning / design of FN pattern, we can also regulate the positioning of pulsations. I will briefly discuss the positional regulation of pulsations in the following paragraph, so that both positional regulation and correlation length modification of pulsations can be discussed in the later sections

7.4.1.3 Positional regulation of pulsations

The pulsations in control and homogeneous FN conditions were randomly positioned. If the substrate interaction of cells can be precisely controlled by differentially varying the FN patterns, in addition to regulating correlation length, the positioning of pulsation can also be controlled by the proper choice of FN patterns. For example, cells on FN patterns will behave as barriers (due to high friction) in propagating the divergence characteristics of non-FN region. Thus two populations of cells with lower and higher velocities will co-exist in the system, triggering a variation in correlation length.

7.4.1.4 Pulsations on fibronectin line patterns

In order to regulate the correlation length and the position of pulsations, we started by patterning FN lines: glass coverslip with lines of FN separated by non-FN regions in-between (Fig. 7.7). The difference in adhesion between the FN and non-FN regions was expected to vary correlation length and the positioning of pulsations.

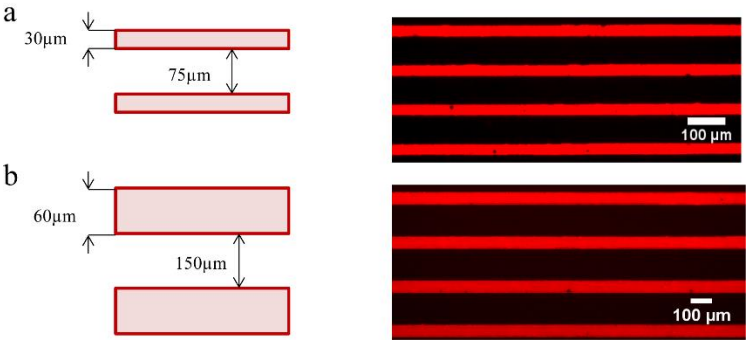

Figure 7.7. Example of FN line conditions, where substrate is patterned with interspaced FN lines. Two examples with schematic and image snapshot are shown for: (a) FN line (W-30 µm + G-75 µm) and (b) (W-60 µm + G-150 µm), where 'W' indicates width of FN line and 'G' indicates the gap in-between.

However, in order to see this correlation, the width of FN and non-FN region should be chosen in such a way that the collective properties of the tissue are not arrested. If the widths are too small, the influence of substrate friction would be comparable only at the scale of single cells and if the widths are too large, the influence of substrate friction would be similar over large lengthscales as in homogeneous FN condition. Hence in order to see a variation in correlation length and pulsation positions, the width of FN and non-FN regions should be optimal to allow collective behavior of MDCK cells. In the past, cells in migrating MDCK monolayers have shown to exhibit a correlation length (in velocity) of ~ 200 µm (246). In addition, variety of collective migration modes were observed in MDCK cells, when they were allowed to migrate on FN strips ranging from 20 µm – 400 µm (252).

Motivated by these studies, we performed experiments with FN lines of width 30 µm and 60 µm separated by gaps/non-FN regions of 75 µm and 150 µm (Fig. 7.7). Note that the FN line width will be hereafter denoted as "W" for width, the non-FN regions will be denoted as "G" for gap and the combination of experiments with these parameters will be denoted as W-30 µm + G-75 µm, for example. From the combination these parameters, we tested four different conditions: W-30 µm + G-75 µm; W-30 µm + G-150 µm; W-60 µm + G-75 µm; W-60 µm + G-150 µm.

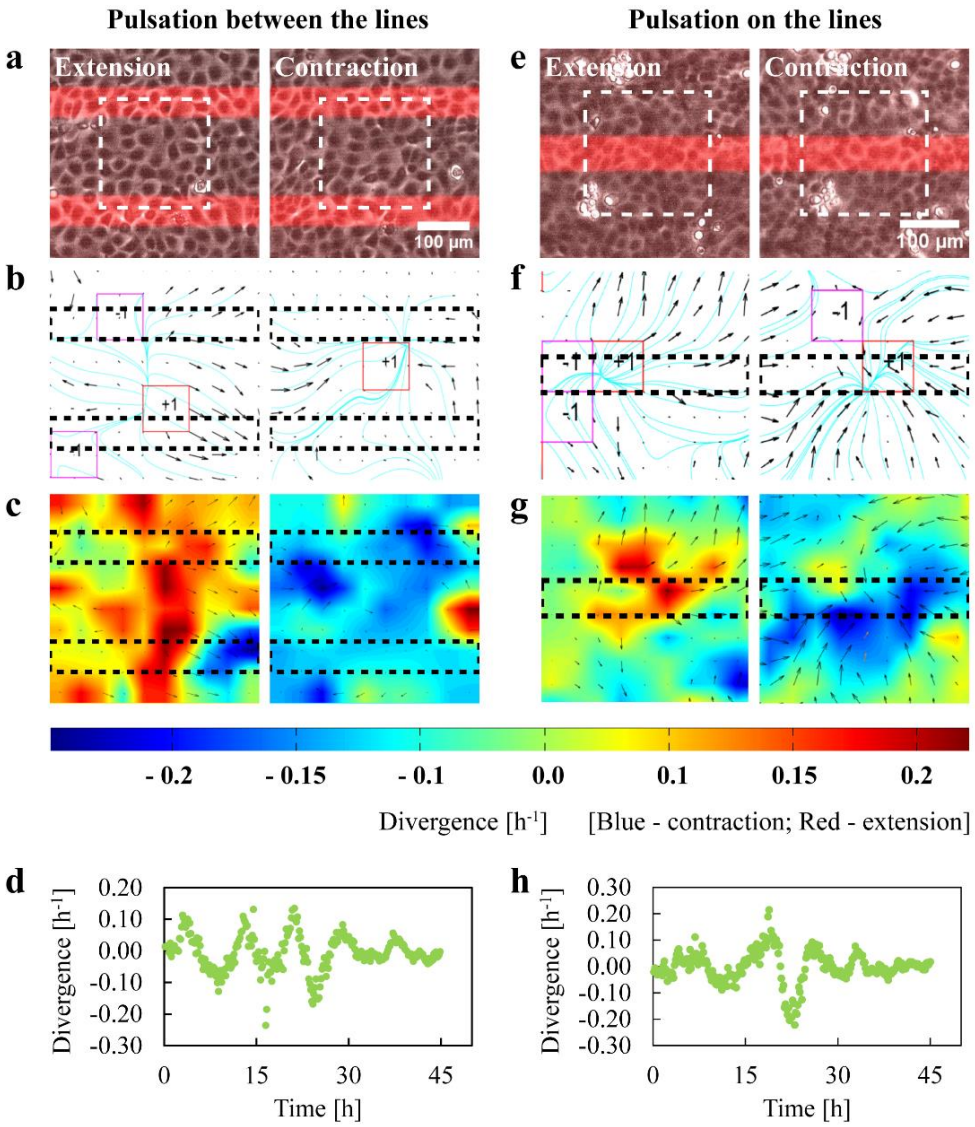

Figure 7.8. Pulsations in FN line experiments. In all the FN line experiments, pulsations were present between and on the lines. In this example, both cases of pulsations 'between' (a, b, c, d) and 'on' (e, f, g, h) the lines are shown from an experiment with FN line (W-60 µm + G-150 µm) condition. (a) and (e) Raw data with cells on substrate patterned with FN lines. The two snapshots in (a) and (e) represent extension and contraction characteristics. White dotted lines represent the pulsatile domain area obtained from the correlation analysis. The area of this dotted lines is 205 µm^2, corresponding to the correlation length of this condition (~ 205 µm). However, the region surrounding the pulsatile domain is also shown to represent the position of pulsatile domains with respect to the lines. (b) and (f) Plots with critical points using winding number analysis, corresponding to (a) and (e) respectively. The critical points (+1) are located 'between' the lines in (b) and 'on' the line in (f). (c) and (g) Divergence plots corresponding to (a) and (e) respectively. Black dotted lines in (b, c, f and g) correspond to the FN lines. (d) and (h) Mean divergence plots for the whole experiment, corresponding to the pulsatile domain (white dotted lines) shown in (a) and (e). In all these experiments, the initial time point (t_0) corresponds to the time when the monolayer reaches confluency.

In all these cases, pulsations were spontaneously emerging after the cells reached confluency (Fig. 7.8 d and h; Movies 7.3 and 7.4). Then we checked the position of pulsations and the correlation length in these conditions. We found that the position of pulsations was distributed both: between the FN lines (Fig. 7.8 a, b and c; Movie 7.3) and on the FN lines (Fig. 7.8 e, f and g; Movie 7.4). This was confirmed by the location of critical point with corresponding divergence characteristics 'between' (Fig. 7.8 b and c) and 'on' (Fig. 7.8 f and g) the lines. On the other hand, the divergence correlation length

of all these FN line conditions were not significantly different from control: ~ 200 µm to 230 µm (Fig. 7.9 a and b). Thus the positioning of pulsations and correlation length were similar to that of control condition.

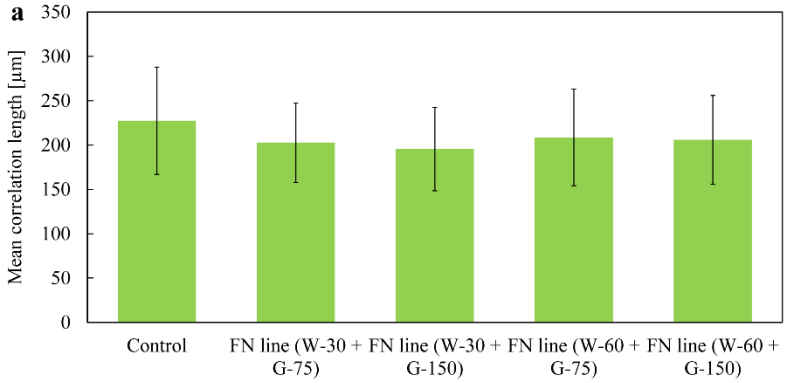

b

Experimental condition	Mean divergence correlation length
Control	227 ± 60 µm
Homogeneous FN	221 ± 51 µm
FN Line (W-30 + G-75)	202 ± 44 µm
FN Line (W-30 + G-150)	195 ± 47 µm
FN Line (W-60 + G-75)	208 ± 54 µm
FN Line (W-60 + G-150)	205 ± 50 µm

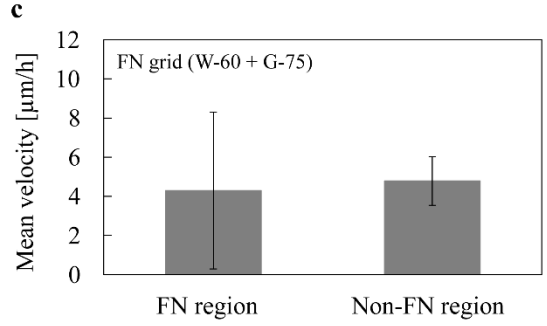

Figure 7.9. Comparison of mean divergence correlation length and velocity of cells in FN line experiments. (a) Mean divergence correlation length for the control and all the FN line conditions. The conditions are not significantly different from each other. Control (N=4); for all other FN line conditions (N=3). (b) Table summarizing the mean divergence correlation length values for control, homogeneous FN condition and for all the FN line conditions. (c) Comparison of collective velocities obtained from PIV. Velocity of cells on FN region, i.e line and non-FN region, i.e. interspace between the lines for the condition FN line (W-60 µm + G-75 µm). This condition was chosen for representation, since the width of FN line and interspace are similar in this condition. The velocities are not significantly different between the FN region and non-FN region.

This result was intriguing, since the introduction of FN lines with varying width and gap distances did not lead to any difference in pulsation characteristics. In order to ascertain the effect of FN lines, we compared the mean velocities of cells on FN lines and non-FN regions. To our surprise, we found that the mean velocities of cells on FN and non-FN regions were similar ~ 4.8 µm/h (Fig. 7.9 c). This similarity in mean velocities, indicated that the FN lines separated by gaps were not efficient in generating two population of cells with different velocities.

Based on these results, we hypothesized two reasons for the absence of difference in correlation length and spatial regulation of pulsations: (i) the FN design "line" was not appropriate in controlling the positioning of pulsations, and (ii) the ratio of magnitude of friction between FN and non-FN regions was not large enough to induce a change in

correlation length. We decided to test these two hypotheses by growing monolayer on FN "grid" like patterns and FN grid with a passivating agent instead of normal regions, respectively.

7.4.1.5 Pulsations on fibronectin grid patterns

First, we decided to change the design of FN pattern to control the positioning of pulsations. We hypothesized that, an array of FN lattices with non-FN regions in the center of each lattice should be able to position/focus the pulsations. In other words, an optimally designed FN lattice – matching the size of pulsations should be able to position/trap the pulsations within each lattice. Along this line, changes in the size of FN lattices should also influence the correlation length of pulsations. This motivated us to design FN stripes surrounding a non-FN region/gap, which together form a FN "grid". The size of FN grids had to be chosen in such a way that cells on FN stripes would act as barrier/boundaries in order to influence the position and correlation length of pulsations.

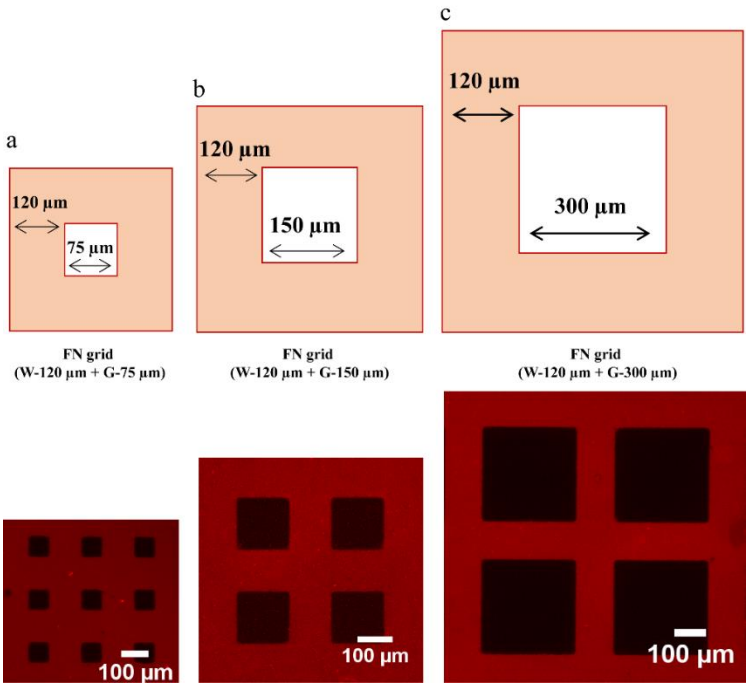

Figure 7.10. Representation of FN grid conditions. For each condition, a schematic with dimensions and a snapshot of FN grid patterns are shown. The red region in the schematic and images correspond to fibronectin coating. (a) FN grid (W-120 µm + G-75 µm), (b) FN grid (W-120 µm + G-150 µm), (c) FN grid (W-120 µm + G-300 µm), where 'W' is the width of FN region/stripe and 'G' is the width of the gap within the FN grid.

Previously in the case of FN lines, we found that a combination of FN widths: 30 µm and 60 µm, separated by gaps of 75 µm and 150 µm did not lead to any change in spatial regulation and correlation length of pulsations (Fig. 7.8 and Fig. 7.9). In addition to the type of pattern: "lines", the absence of any effect in the FN line conditions, is because the FN line is not optimal in influencing the collection of cells. With this reasoning, we designed FN grids where the width of FN stripes was 120 µm: a two-fold increase in width when compared to the FN lines. While keeping a constant width of FN stripes (120 µm), we decided to vary the gap size of non-FN region (75 µm,

150 µm, 300 µm) within the FN grid (Fig. 7.10). This gives a combination of three different FN grid sizes: 315 µm^2 (W-120 µm + G-75 µm); 390 µm^2 (W-120 µm + G-150 µm); and 540 µm^2 (W-120 µm + G-300 µm) (Fig. 7.10). The results from each of these conditions were interesting.

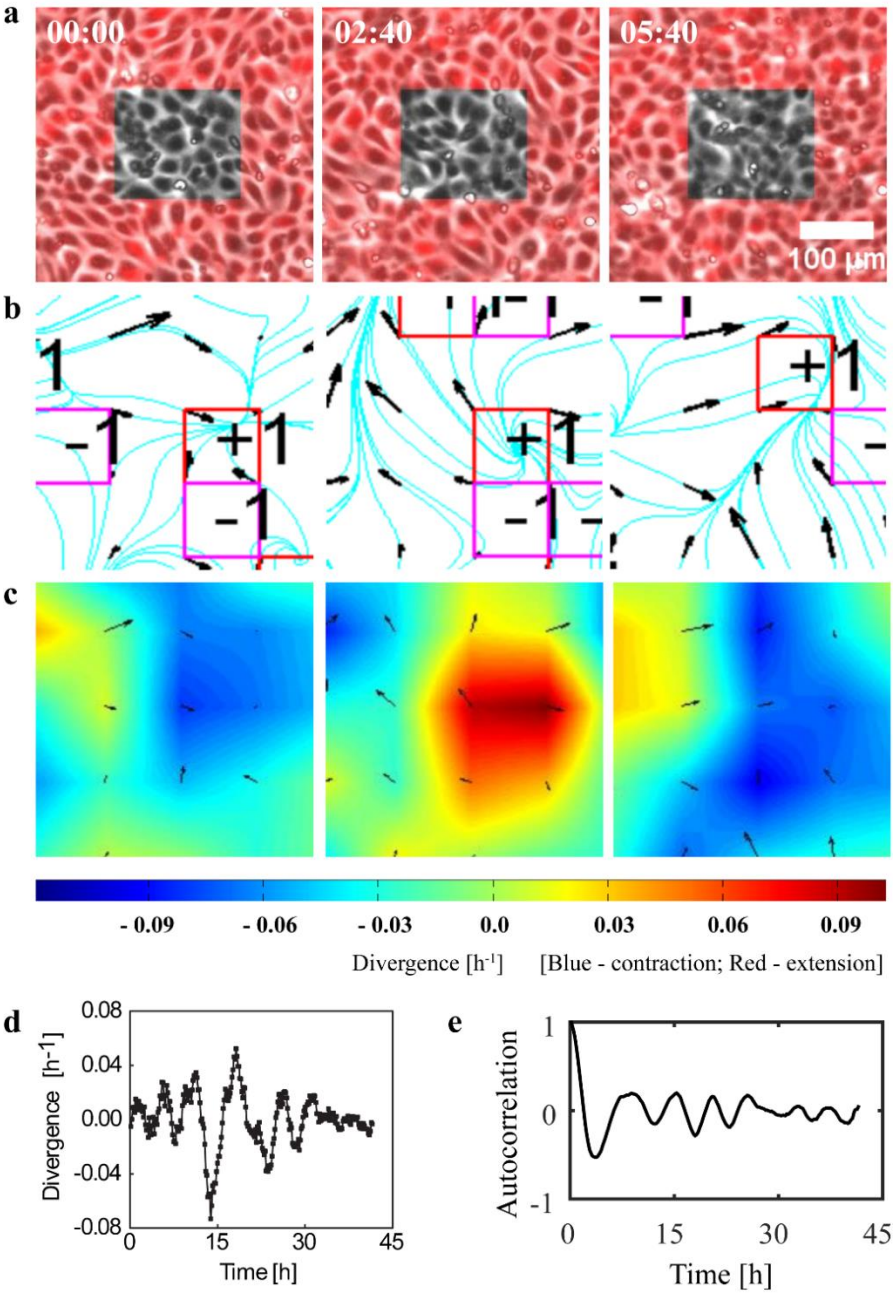

Figure 7.11. Example of a pulsation in FN grid (W-120 µm + G-150 µm) experiment without PEG. (a) Snapshot of raw data of an isolated FN grid. In this condition, the divergence correlation length (~ 385 µm) corresponds to the size of FN grid (390 µm), hence the whole area of FN grid is represented. The first snapshot corresponds to a contracting domain followed by snapshots showing extension and contraction. Time in hh:mm. (b) Plots with critical points (+1) using winding number analysis corresponding to (a), showing the pulsation center with source/sink characteristics. (c) Divergence plot corresponding to (a). (d) Mean divergence plot over the time of experiment for the pulsatile domain shown in (a). The initial time point (t_0) corresponds to the time when the monolayer reaches confluency. (e) Autocorrelation of the divergence plot shown in (d).

7.4.1.5.1 FN grid (W-120 µm + G-75 µm)

In this condition, where the gap within the FN grid was the least (75 µm), no pulsations could be observed in the raw data (Movie 7.5). Then we measured the divergence correlation length in the monolayer and found the mean correlation length to be ~ 200 µm (Fig. 7.12 a and b). While the correlation length is similar to that of control (~ 230 µm), we found that the mean correlation lengths of these to conditions to be statistically different.

7.4.1.5.2 FN grid (W-120 µm + G-150 µm)

Interestingly, in this condition where the width of FN stripe and the gap were more or less equal, pulsations were found to be localized in many of the FN grids (at least 50 % – manual observation) (Fig. 7.11 a, b and c; Movie 7.6). This was confirmed by the location of critical point with corresponding divergence characteristics within the FN grid (Fig. 7.11 b and c). While oscillations existed in the divergence values throughout the experiment (Fig. 7.11 d), periodicity of the oscillations reduced after ~ 25 h (Fig. 7.11 e). Next we measured the mean divergence correlation length of monolayer. The mean correlation length was found to be ~ 385 µm, which was significantly larger than the control condition (~ 230 µm) (Fig. 7.12 a and b). More interestingly, the mean divergence correlation length, corresponding to the size of pulsations (~ 385 µm) matched the size of the FN grid (390 μm^2). Note that one side of FN grid equals 390 µm, since the length of one side is: FN width (120 µm) + gap (150 µm) + FN width (120 µm) (Fig. 7.10). Thus, the FN grid condition: W-120 µm + G-150 µm, triggers positional regulation of pulsations and induced a change in correlation length of pulsations that matched the size of FN grid.

7.4.1.5.3 FN grid (W-120 µm + G-300 µm)

In this FN grid condition where the gap within FN grid was the maximum (300 µm), pulsations were observed in almost all the FN grids (Movie 7.7). However, on measuring the correlation length of pulsations, we found that the mean divergence correlation length was very similar to the control condition: ~ 230 µm (Fig. 7.12 a and b). This FN grid condition imposed positional regulation of pulsations but without any variation in the correlation length.

The results detailed above on three different FN grid conditions suggested the role of friction (from the FN) and type of pattern (grid) in regulating the positioning and size of pulsations. First of all, increasing the width of FN stripe to 120 µm seem to influence a collection of cells, as opposed to the FN line conditions (W-30 µm / 60 µm). However, by changing the pattern from FN line to FN grid, the total area of regions coated with FN regions also change.

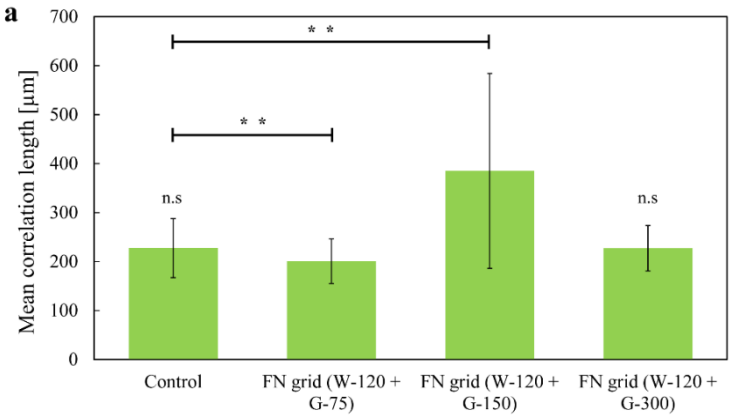

b

Experimental condition	Mean divergence correlation length
Control	227 ± 60 µm
FN grid (W-120 + G-75)	200 ± 45 µm
FN grid (W-120 + G-150)	385 ± 198 µm
FN grid (W-120 + G-300)	227 ± 46 µm

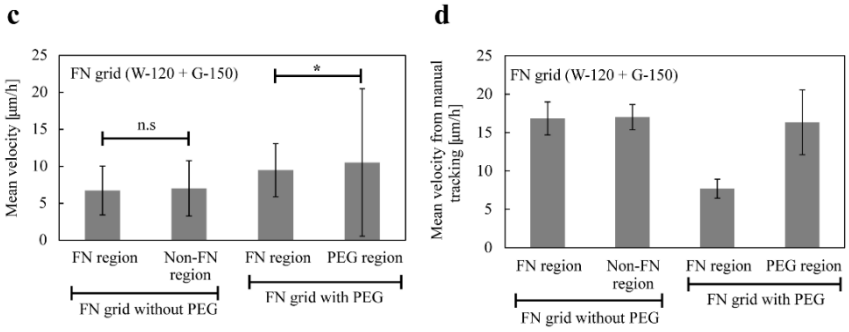

Figure 7.12. Comparison of mean divergence correlation length and velocity of cells in FN grid experiments. (a) Mean divergence correlation length of control and all FN grid conditions. Control (N=4); FN grid (W-120 µm + G-75 µm) (N=3); FN grid (W-120 µm + G-150 µm) (N=4); FN grid (W-120 µm + G-300 µm) (N=3). ** P < 0.01 by Mann-whitney test. n.s – data not significantly different. (b) Table summarizing the mean divergence correlation length values for control and all FN grid conditions. (c) Comparison of collective velocities measured from PIV for the FN grid (W-120 µm + G-150 µm) experiments. Velocities are compared between cells on FN and non-FN regions in FN grids without and with PEG. For all conditions (N=3). * P < 0.05 by Mann-whitney test. n.s – data are not significantly different. (d) Comparison of velocities measured by manual tracking in FN grid (W-120 µm + G-150 µm) experiments, to confirm the results of (c). Manually tracked velocities of cells are compared between cells on FN and non-FN regions in FN grids without and with PEG. The results are shown here are average velocities obtained by tracking 7 cells in each case: FN and non-FN regions in FN grid without and with PEG.

When compared to the FN line experiments, the total area of FN coated regions (in FN grid conditions) increase approximately by: (i) three folds in the FN grid (W-120 µm + G-75 µm), (ii) more than two folds in the FN grid (W-120 µm + G-150 µm), and (iii) a bit less than two folds in the FN grid (W-120 µm + G-300 µm) conditions. With such

larger FN regions, the FN grid conditions should exhibit a correlation length (of pulsations) similar to the control condition, without any change in pulsation positions. Because, in the experiments of homogeneous FN and FN lines, the correlation length of pulsations was similar to the control (Fig. 7.6 b) without any effect on the pulsation positions. But the correlation length measured in the FN grids were significantly different (except W-120 μm + G-300 μm) from control (Fig. 7.12 a and b). Thus, the difference in correlation lengths and pulsation positions are not only due to the variation in friction (due to FN regions), but also due to the design of FN patterns. In contrast to homogeneous FN condition and FN line conditions, the lattices of FN grids match the pulsation size which allows in tuning the position and size of pulsations.

Among the three conditions of FN grids, the condition where the width of FN stripe and the gap are equal (W-120 μm + G-150 μm), seem to allow the best tuning of pulsation characteristics: (i) localized pulsations within FN grids (Fig. 7.11 a, b and c) and (ii) size of pulsations matching the FN grid size (Fig. 7.12 a and b). Thus the effect of this FN grid condition on spatial regulation of pulsations, can be called analogous to a "resonance condition".

However, when the gap within the FN grid is reduced (FN grid: W-120 μm + G-75 μm), pulsations do not occur (Movie 7.5). The decreased divergence correlation length (compared to control) also supports this result, but needs to be confirmed by the dynamic structure factor analysis, in future. The absence or reduced pulsations seem to be a result of imbalance between the width of FN stripe (120 μm) and the gap (75 μm). This difference reduces the correlation required for the collective pulsation of cells. On the other hand, when the gap within the FN grid is increased (FN grid: W-120 μm + G-300 μm), pulsations are localized in the FN grids, with a similar correlation length as in control (Fig. 7.12 a and b). Since the size of gap (300 μm) is much larger than the natural correlation length of pulsations (~ 230 μm), each grid localizes /traps the pulsations, with cells on FN stripes acting as barriers. For the same reason, monolayer on this FN grid condition exhibits a correlation lengthscale (~ 230 μm) very similar to control condition (~ 230 μm), i.e. the system goes back to the natural lengthscale.

While these results strongly emphasize the role of FN grid, we found that the mean velocity of cells on FN region/stripes similar to the mean velocity of cells in non-FN region (Fig. 7.12 c and d). This difference in results was not immediately clear. It was surprising that the mean velocities of cells in homogeneous FN and control conditions were significantly different (Fig. 7.6 a), but a similar tendency was not observed between the coexisting FN and non-FN regions in FN line and FN grid condition (Fig. 7.12 c and

d). Hence we wanted to ascertain the role of fibronectin in increased substrate interaction, by increasing the relative friction between the FN and non-FN regions.

7.4.1.6 Conditions with co-existing passivated and FN coated regions

In order to increase the relative friction between FN and non-FN regions, we passivated the non-FN regions with pLL-g-PEG (PEG). Passivation reduces the adhesion of cells in these regions. Hence by introducing PEG, two regions: highly adhesive (FN stripe) and less adhesive regions (PEG) are co-existing in the same sample. Note that, in the previous case of FN grid, the non-FN region was not passivated and cells can adhere in this region. We tested the effect of passivation in all the three FN grid conditions: (W-120 µm + G-75 µm / 150 µm / 300 µm). We found that in all conditions, monolayer exhibited other dynamics in addition to pulsations. The cells in PEG region collectively moved within the FN grid in an random manner (Movie 7.8) and exhibited significantly higher velocities (Fig. 7.12 c and d) when compared to the cells on FN stripes. The higher velocities of cells in PEG region is indicative of reduced substrate-interaction and lower velocities of cells in FN region indicates high friction. Though pulsations were not the only dynamics in these FN grid conditions with PEG, the observations clearly indicated the existence of two population of cells: with reduced velocity on FN stripes and with higher velocity in PEG regions. With these results, we reasoned that indeed FN regions increase cell-substrate interaction. We propose that increase in friction is manifested in velocity comparisons (Fig. 7.12 c and d) of cells, only if the difference in adhesion was considerably higher as in the FN grid condition with PEG. But if the difference in adhesion is not considerably high as in FN grid (without PEG) condition, then the effect of FN manifests only in the collective behavior (position and size of pulsation) but not in the velocity comparisons.

To better understand this complex behavior, we decided to visualize the focal adhesions of MDCK cells in the monolayer. If the PEG and FN regions lead to reduced and increased cell-substrate interactions respectively, this tendency should be reflected in focal adhesions (179). For example, absence or lesser focal adhesions on PEG region, compared to increased focal adhesion in the FN region. We visualized the focal adhesions by immunostaining for vinculin. Surprisingly, there was no difference in the focal adhesion distribution between the PEG and FN. These experiments did not reveal the cellular mechanism behind the spatial regulation of pulsations observed in FN grid conditions. In other words, it was not clear how the difference in friction between the FN and non-FN regions (with or without passivation) were perceived by cells. To clarify this

point, we are currently planning to measure the fluorescence life-time of focal adhesions (253). Our expectation is to see focal adhesions with longer lifetimes in cells on FN regions and focal adhesion with shorter lifetimes in cells on non-FN regions.

The precise cellular mechanism of how substrate friction influences the cell behavior was not clear from the FN grid experiments. However, the FN grid experiments indicated the role of grid dimension and the resulting friction in setting the lengthscale and positioning of pulsations.

Still, the question of "how a natural lengthscale appears spontaneously?" in control condition, is not answered yet. In order to understand how the natural lengthscale (of pulsations) appears, and to further explore the factors involved in setting the lengthscale of pulsations, we developed a theoretical framework for an oscillating tissue. In the following section, I will describe in detail the theoretical model that highlights the factors required for setting a characteristic lengthscale of the pulsating domains.

Meanwhile, in addition to experiments on FN lines and FN grids, we also performed curiosity based experiments on substrate coated with FN triangles that resulted in pulsations and directional flows of cells. With substrate friction playing an important role in collective behavior of cells, the experiments on FN triangles were motivated by the idea of collective ratchetaxis (see section 6 - ratchetaxis). While flows were observed occasionally, the results were not consistent. For more details, see appendix section 10.2.2. On the other hand, appearance of pulsations in this condition further motivated us to explore the factors involved in the regulation of pulsatile domain characteristics.

7.5 Continuum description of oscillating tissue

In line with the previous works on tissue dynamics (254), we developed a continuum model for an oscillating tissue. In this model, we first express the mass and momentum balance of the oscillating tissue. Then in addition to passive area stress, we include 'ζ', to depict the active stress generated during the dynamics (pulsations) using constitutive equations. The oscillatory dynamics is modeled based on two variables: average cell area (inverse of cell density) 'a' and active stress 'ζ'. After the model is established for the tissue, we perturb the model by including noise terms. The noise terms will excite different modes in the system which respond differently, giving rise to pulsations.

While this is a classical description of a dynamic tissue, our model specifically highlights the need for *height fluctuations* in cells during pulsations. Since we assume the volume of cells to be conserved, the contraction and extension phases of pulsation result in cell

height fluctuations, with a characteristic lengthscale. This confirmed the need for height fluctuations in cell monolayer, which were further substantiated by experiments. Finally, using the model, we derive the characteristic lengthscale of an oscillating tissue which depends on: elastic modulus of cell (which is a function of height fluctuations), substrate friction and turnover time of molecules that generate active stress 'ζ'. In the following section, I will describe in detail the proposed model and how we derive the characteristic lengthscale.

7.5.1 Material and momentum balance in the monolayer

Let us assume a large tissue where the average cell area is given by 'a', and the material turnover is dictated by the rate of cell division and cell death (k_d).

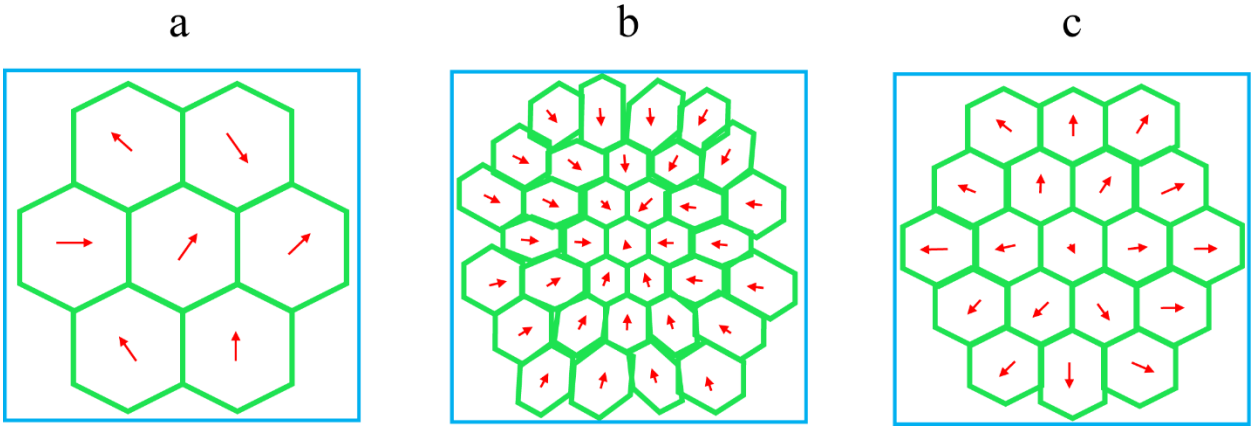

Figure 7.13. Schematic of an isolated region (in cyan) containing a pulsating domain. The domain represents a collection of cells in a region. This domain of cells undergo pulsation which includes a cycle of contraction and extension. (a) Domain of cells with random motility. (b) Domain undergoing contraction. This leads to decrease in average cell area in the pulsating domain and increase in cell density locally – in the region. (c) Domain extending to restore the initial cell area (a_0). Note that the number of cells has increased locally when compared to (a), due to cell division (k_d). The cells are represented by green boundaries and the red arrows give the direction of cells in (a), (b) and (c).

In the experiments, when a domain (collection of cells) starts to pulsate, the following events occur (Fig. 7.5): (i) cells within the pulsating domain move towards a common center and undergo contraction. (ii) Following contraction, the cells move away from the center and will try to resume their original area (which they possessed before contraction). We transfer this scenario of contraction and extension to the model by utilizing those terms which affect cell area, similar to the divergence plot of pulsations in the experiments. In the model, we assume that the cells move with a velocity 'v' during

contraction and extension, which leads to variation in the average cell area 'a' (Fig. 7.13). This variation in velocity and cell area strongly depends on the rate of cell division and cell death (extrusion) 'k_d', with units of 1/time. Thus k_d establishes a material balance during the pulsation process. The velocity gradient and the change in cell area can be linked by:

$$\nabla . V = v_{kk} = \frac{1}{a_0}\frac{da}{dt} + k_d \qquad (7.2)$$

In equation (7.2), $\nabla . V$ and v_{kk} denote the divergence of the pulsating domain which evolves with changes in cell area 'a' – given by the first term, and the source/sink term 'k_d' (cell division/death), on the right hand side.

When this domain of tissue becomes pulsatile, cells exhibit motion in order to move towards the center and extend away from the center, leading to contraction and extension (Fig. 7.13) respectively. This contraction and extension process represented by the change in area induces a stress in the monolayer. The generated stress is in turn balanced by interaction of cells with the substrate. This force balance mechanism is given by:

$$\alpha v_i = \partial_j \sigma_{ji} \qquad (7.3)$$

where, $'\alpha'$ corresponds to friction coefficient, v – velocity of cells and σ – induced stress in the monolayer. i and j correspond to the x and y components. In the next step we define the factors contributing to the induced stress.

7.5.2 Stress generated in the monolayer due to pulsation

The change in cell area during pulsation depends on: (i) elastic modulus and (ii) internal viscosity of the cells. We introduce the active stress term 'ζ' which triggers active contractility. This active stress term is assumed to be the concentration of molecules that causes contraction and extension, and hence will have the units of density (number of molecules / area). In this case, the number of molecules will be proportional to the generated force. This allows the induced stress in the monolayer to be described as a function of contractility 'ζ', elastic modulus and internal viscosity of the cells in the pulsating domain. The obtained expression for stress will therefore be:

$$\sigma_{ij} = \sigma \delta_{ij} = \left(K \left(\frac{a - a_0}{a_0} \right) + \zeta + \mu v_{kk} \right) \delta_{ij} \qquad (7.4)$$

where, 'σ' corresponds to induced stress, 'K' – elastic modulus due to change in area (a_0 – initial area; a – final area) with units of (force / area), 'ζ' – contractility (active stress term), 'μ' – internal viscosity due to the pulsation defined by 'v_{kk}', where 'μ' has units of (force x time / area). The evolution of stress 'σ' over time, depends on the evolution of contractility 'ζ', the change in modulus 'K' and internal viscosity 'μ'. The evolution of ζ over time is described in the following paragraph.

7.5.3 Evolution of contractility

During the contraction phase of pulsation, the cell area and contractility, deviate from the initial values (a_0 and ζ_0) to a different value (a and ζ). However, the system (monolayer) will try to restore both the variables (area and contractility) to the initial values again (Fig. 7.14), as per the model. Thus during pulsation, a cycle of changes in area and the concentration of molecules leading to contractility is ensued, i.e. from 'a_0' and 'ζ_0' to 'a' and 'ζ' and vice versa.

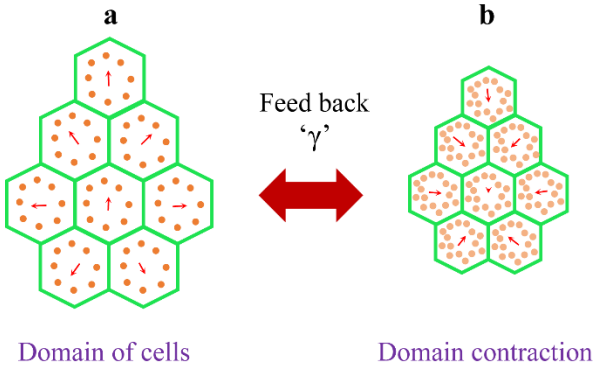

Figure 7.14. Schematic of pulsating domain with the molecules leading to contractility. Domain represents a collection of cells in (a-b), where the green outline indicates cell boundaries. During pulsation, the domain of cells constrict (b) leading to change (increase) in concentration of molecules generating contractility (orange dots). The system tries to restore (a) the concentration of molecules leading to contractility 'ζ' and the area 'a' to the initial values 'ζ_0 and a_0'. This is achieved by a feedback through coupling factor 'γ'. The arrows in both (a) and (b) indicate the direction of cell motility.

We define this restoration of initial values (a_0 and ζ_0) in the model by a feedback factor 'γ'. The feedback factor 'γ', functions as a coupling between the cell area and the concentration of molecules generating contractility. And, has a unit corresponding to ζ/τ, where 'τ' is time. These changes give the evolution of contractility 'ζ' over time, which can be expressed as:

$$\frac{d\zeta}{dt} = -\zeta_0 v_{kk} - \frac{1}{\tau}(\zeta - \zeta_0) - \gamma\left(\frac{a - a_0}{a_0}\right) \qquad (7.5)$$

where: the first term on right hand side corresponds to advection, i.e. change in positional density of the molecules leading to contractility (ζ), during pulsation (v_{kk}). The second term gives the rate of change of 'ζ', and the last term gives the coupling between change in cell area and the corresponding change in 'ζ'.

Note that equations (7.2 – 7.5) are results of linear approximations. For example, in equation (7.2), $a = a_0 + \delta a$, where 'δa' corresponds to intrinsic fluctuations in area 'a'. However we assume that $\delta a \ll a_0$ so that $a = a_0$, to the lowest order. We introduce similar approximations for velocity 'v', stress 'σ' and active stress 'ζ' for the linearization process.

7.5.4 Continuum equations of pulsatile domain

In the above sections, we described the characteristics of pulsatile domain in terms of change in area (equation 7.2), momentum balance within the monolayer (equation 7.3), corresponding factors contributing to stress (equation 7.4), and their evolution over time (equation 7.5). In these equations there are four variables in total: velocity (v), stress (σ) (only isotropic part), area (a) and contractility (ζ). In order to simplify the description of pulsations, we rearranged the equations and substituted equation 7.2 and 7.3 in equations 7.4 and 7.5, to express the pulsations only in terms of area (a) and contractility (ζ), which are the major contributing factors. Therefore we obtain:

$$(\alpha - \mu\Delta)\frac{da}{dt} = K\Delta a + \zeta_0\Delta\zeta \qquad (7.6)$$

$$(\alpha - \mu\Delta)\frac{d\zeta}{dt} = -K\Delta a - 1\Delta\zeta - (\alpha - \mu\Delta)\left(\frac{1}{\tau}\zeta + \bar{\beta}a\right) \qquad (7.7)$$

Where, $\Delta = \nabla^2$, $(a - a_0)/a_0$ has been substituted by 'a', $(\zeta - \zeta_0)/\zeta_0$ has been substituted by 'ζ', and $\bar{\beta} = \gamma/\zeta_0$, where '$\gamma$' is the coupling factor that feedbacks the change in area to the concentration of molecules generating contractility 'ζ'. These two equations (7.6) and (7.7) are the primary equations that give the continuum description of pulsatile domains.

7.5.5 Oscillations in the model

In the current description (equations 7.6 and 7.7), the model incorporates factors needed for pulsations to occur. However, the model does not exhibit oscillations spontaneously. For the model to oscillate, the system should be perturbed from equilibrium state. To introduce perturbations, we increase the strength of intrinsic fluctuations/noise existing in the system. By increasing the strength of noise, 'ζ' is perturbed from a steady value, thus leading to a situation where $\zeta \neq \zeta_0$ triggers dynamics within the system. The triggered

dynamics will in turn contribute to two factors: (i) fluctuations in concentration of molecules leading to contractility (ζ) or force generation, and (ii) fluctuations in cell area (a), due to random cell division and extrusion. Note that the primary equations (7.6) and (7.7) are expressed in terms of area and contractility which are the two main variables leading to pulsations. Therefore, we introduce noise in these equations and obtain equations (7.8) and (7.9) after normalization and rearrangements:

$$(1-\mu\Delta)\frac{da}{dt} = \Delta a + \frac{1}{K}\Delta\zeta + \beta_d\xi_d(t) \tag{7.8}$$

$$(1-\mu\Delta)\frac{d\zeta}{dt} = -\frac{1}{\tau}(1-\mu\Delta)(\zeta - a) - \Delta a - \frac{1}{K}\Delta\zeta + (1-\mu\Delta)\beta_c\xi_c(t) \tag{7.9}$$

In equations (7.8) and (7.9): ξ_c is the unit chemical noise corresponding to the concentration of molecules leading to contractility (force generation) and ξ_d is the unit mechanical noise corresponding to cell division (and the resulting change in cell area). Similarly, β_c and β_d are the strengths of noise levels corresponding to ξ_c and ξ_d.

7.5.6 Mechanism of instability and resulting pulsations

The introduction of additional noise β_c and β_d will excite different modes in the system (monolayer), through the fluctuations in concentration of molecules leading to contractility, and area respectively. This leads to a dynamic system where the area (a) and the concentration (of molecules generating contractility - ζ) are perturbed from their initial values (a_0 and ζ_0). As explained before, the system will try to restore the deviations in 'a' and 'ζ' to their initial values (Fig. 7.14). During this process, the rate at which the 'a' and 'ζ' are restored to their initial values need not be in phase. For example, the restoration to initial values of one of the variables (a and ζ) might be faster than the other. This difference in restoration rates may give rise to pulsations.

In order to check the existence of pulsations in the system, the divergence correlation function $C_{ij}^{d}(q,\omega)$ of the domain is obtained by expressing equations (7.8) and (7.9) in Fourier space. Where, C_{ij}^{d} represents the divergence (d) correlation function (C), in x (i) and y (j) components. 'q' indicates spatial frequency, where $1/q$ corresponds to the lengthscale. 'ω' indicates temporal frequency, where $1/\omega$ corresponds to period. By plotting the power spectrum of this divergence correlation function against wavelength and frequency, a clear peak was not observed, since for large values of 'q' the power

spectrum did not decay to zero. In principle, the existence of peaks in wavelength and frequency confirms the presence of a dominant length and timescales in the system.

7.5.6.1 Significance of cell height fluctuations

The absence of decay in power spectrum for large values of 'q' suggested the existence of pulsations only at the scale of cell and not at the scale of domains (collections of cells). This is because the model incorporated elastic modulus (first term of equation (7.4)) as a function of cell area fluctuations, without explicitly accounting for changes in cell height. As a result, individual cells can exhibit area fluctuations which can be independent of the neighboring cells. This results in oscillations at the scale of cell. In order to overcome this issue, we included an additional modulus term 'K_h' which incorporates the height changes in cells and provides an additional lengthscale. After the inclusion of '$'K_h$' term, normalization and rearrangements were performed in equations (7.8) and (7.9) to obtain:

$$(1-\mu\Delta)\frac{da}{dt} = \Delta a + K_h\Delta\Delta a + \frac{1}{K}\Delta\zeta + \beta_d\xi_d(t) \tag{7.10}$$

$$(1-\mu\Delta)\frac{d\zeta}{dt} = -\frac{1}{\tau}(1-\mu\Delta)(\zeta - a) - \Delta a - K_h\Delta\Delta a - \frac{1}{K}\Delta\zeta + (1-\mu\Delta)\beta_c\xi_c(t) \tag{7.11}$$

Equations (7.10) and (7.11) represent the description of pulsatile domains after including the '$'K_h$' term. Following the inclusion of '$'K_h$' term, the variation in cell area will be compensated by corresponding variations in height of cells in the pulsatile domain. The resulting additional lengthscale will be given by $\sqrt{K_h/K}$. We assume $\mu = 0$ (neglect internal viscosity) and obtain the correlation function by expressing the equations (7.9) and (7.10) in Fourier space. Then we plotted the power spectrum of divergence correlation function $C_{ij}^{d}(q,\omega)$ against 'q' and 'ω' (Fig. 7.15 a and b). This plot showed peaks corresponding to length and timescales, with a decay in correlation function (Fig. 7.15 a and b). We interpolate these decays of correlation function between limits of 'q' ($q \to 0;\ q \longrightarrow \infty$), and obtain an expression for the lengthscale of pulsatile domains:

$$l \sim \left(\frac{K_h\tau^2}{\bar{\beta}\alpha}\right)^{\frac{1}{4}} \tag{7.12}$$

The obtained characteristic lengthscale denoted by 'l' is a function of '$'K_h'$' term, turnover time of the molecules leading to contractility 'τ' and the friction due to interaction of cells with the substrate 'α'. $1/\omega = \tau^2\bar{\beta}$, where '$1/\omega$' gives the timescale at which the

oscillations are maximum. $\bar{\beta} = \gamma/\zeta_0$, where '$\gamma$' is the coupling between cell area and the concentration of molecules generating contractility 'ζ'.

Thus with this continuum description, we identified the factors potentially responsible for the appearance of spontaneous lengthscale of pulsations.

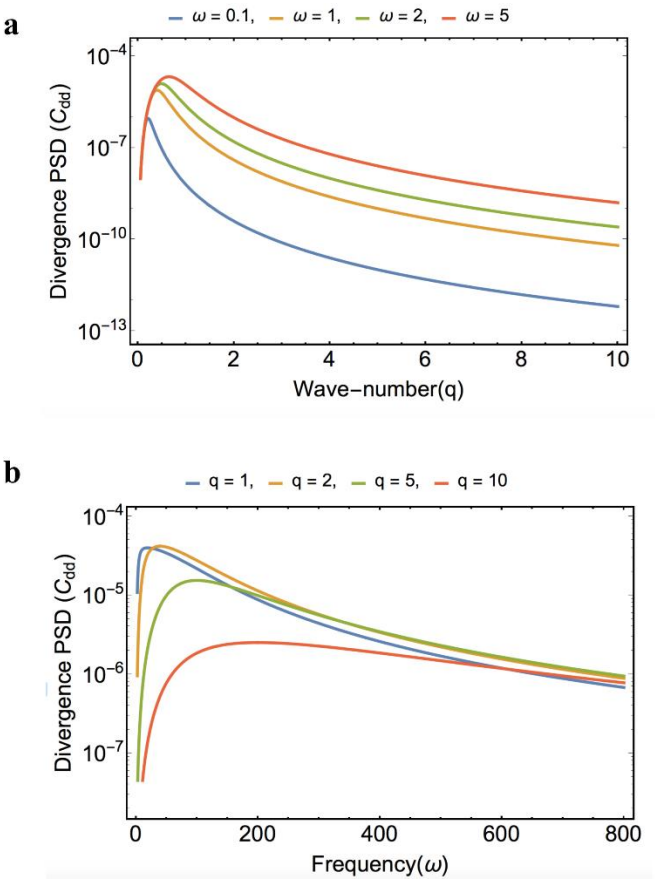

Figure 7.15. Power Spectral Density (PSD) obtained using the expression (7.12) for characteristic lengthscale. (a) Plot showing peak in power spectrum as a function of wave-number (q) for different frequencies (ω). (b) Plot showing peak in power spectrum as a function of frequency (ω) for different wave-numbers (q). $1/q$ and $1/\omega$ correspond to the characteristic length and timescales. The presence of a peak corresponds to pulsations. The values of parameters used for this plot are: $K = 0.1$; $K_h = 50$; $\tau = 0.01$; $\mu = 5$; $\beta_c = 0.4$; $\beta_d = 0$.

The next step is to experimentally verify the role of each of these factors: (K_h, τ, $\bar{\beta}$, and α). The significance of cell-substrate interaction (α) has been already shown by FN grid experiments. The significance of K_h term can be highlighted by checking the fluctuations in cell heights in the monolayer. τ and $\bar{\beta}$ depend on 'ζ' which is the concentration of molecules generating contractility. First, the dependency of characteristic lengthscale on stress generating molecules: actin and myosin, should be substantiated. Once the role of actin and myosin is proven, the turnover time of these proteins by FRAP experiments, and instantaneous change in cell area can be measured by segmentation analysis. These experiments will yield an indirect measure of τ and $\bar{\beta}$. In the current stage of the project, we had already performed experiments showing the: fluctuations in cell height during pulsation, and the importance of actin and myosin for the pulsation phenomena. In the following sections, these experiments will be described in detail.

7.6 Fluctuations in cell height

In order to probe the variations in cell height during pulsations, we had to obtain z-stack of the pulsating region from which the changes in cell height can be extracted. However, finding the precise region with pulsations is difficult, since pulsations appear randomly in the control experiments. Therefore, as a first step we imaged the monolayer in the FN grid condition with PEG (W-120 µm + G-150 µm), where one can expect the pulsations to appear in FN grid. The inclusion of PEG ensures the effect of difference in friction between the FN and non-FN regions. We acquired the z-stack of MDCK cell (labelled with GFP for E-cadherin) dynamics for 48 h on the FN grid with PEG, using confocal microscopy (see methods, section 3.5.4.2.2).

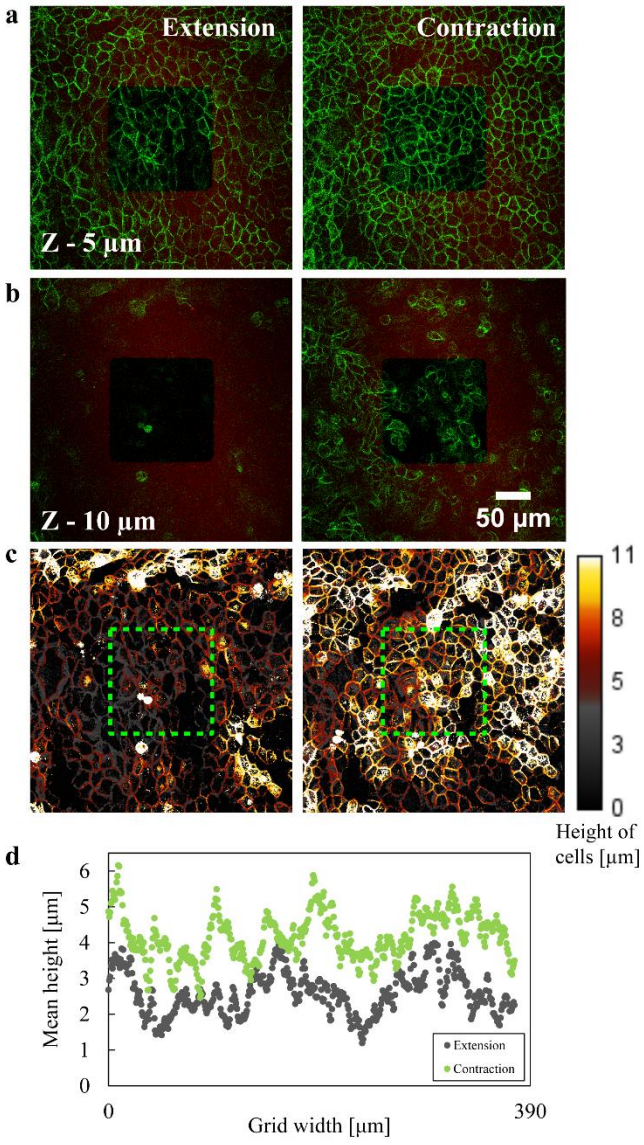

Figure 7.16. Height fluctuations in cells during pulsation. (a) and (b) Confocal sections of the cells at 5 µm and 10 µm planes respectively. Snapshots in (a) and (b) show the same region with extension and contraction phases of the cells at different time points, on a FN grid (W-120 µm + G-150 µm) with PEG. The cells (labelled with E-cadherin-GFP) are shown in green and the FN grid is shown in red. The gap within the FN grid is passivated with PEG. Snapshots in (a) correspond to a lower Z-slice (5 µm) and cells are seen both during extension and contraction. In (b), the apical side of cells are not visible during the extension phase and are visible during the contraction phase. (c) Images color coded for the height of cells during extension and contraction phases corresponding to (a, b). The color coded images were obtained from a custom-made ImageJ plugin to extract cell heights. Green square represents the boundary of FN and PEG regions. (d) Plot showing mean height of cells for the FN grid area shown in (a, b). The mean height of cells are larger during the contraction phase.

After acquisition, we found that cells in the monolayer exhibited a heights of ~ 10 µm – 12 µm. We compared the height of cells at different time points based on the appearance of apical side of cells at larger heights / slices in z axis. We chose two z planes at 5 µm and 10 µm as the middle and highest planes for visualizing the

cells, respectively (Fig. 7.16 a and b). During the contraction phase of pulsation, the apical side of cells were visible in 10 μm plane, i.e. cells exhibited increased height during contraction (Fig. 7.16 b). On the other hand, during extension, the apical side of cells was not completely visible in the 10 μm plane, i.e. cells exhibited shorter heights during extension (Fig. 7.16 a). We confirmed this tendency in height by a custom-made ImageJ plugin, where the cells showed a mean height of ~ 10 μm during the contraction and ~ 5 μm during extension (Fig. 7.16 c and d; Movie 7.9). While these values were specifically obtained for FN grid condition (W-120 μm + G-150 μm) with PEG, we are currently analyzing the data for the same FN grid condition without PEG and increasing statistics.

These results confirmed the fluctuations in heights of cells during pulsations and therefore validates the introduction of 'K_h' term in our oscillating tissue model. Next, we checked the role of actin and myosin molecules in triggering pulsations.

7.7 Role of cytoskeletal proteins in pulsatile domains

In order to validate the introduction of the active stress term 'ζ', we need to confirm the significance of stress generating proteins in the pulsation process. Cytoskeletal proteins in the cell have been shown to generate stress, of which actin, myosin and related proteins in the Rho pathway are major contributors (24). To check the role of these cytoskeletal proteins, we used the corresponding inhibitor drugs. The difference in pulsation characteristics before and after the addition of inhibitor drugs, will reveal the significance of each of these proteins.

The experiments involving cytoskeletal inhibitor drugs were performed in the following manner. MDCK cells were seeded in normal coverslips as in control condition. Then the sample was acquired for ~ 12 h – 20 h, to allow the monolayer to reach confluency and to allow the emergence of pulsations. After the appearance of pulsations, inhibitor drugs were added into the sample and the monolayer was incubated with drugs for ~ 12 h. We know the period of pulsation to be ~ 7 h. Hence, acquisition for ~ 12 h in the presence of drugs allowed us to study the effect of drugs precisely on pulsations. After the incubation period, the media with drugs was washed out and replaced with new media. Thus each drug experiment involved three phases: control check (first 12 h – 20 h), drug incubation (next 12 h) and wash out (last 24 h). Separate experiments were performed for each drug. For the inhibition of cytoskeletal proteins, we used the following inhibitors with corresponding concentrations (131): blebbistatin (100 μM) for myosin inhibition, Lat A (1 μM) for monomeric actin sequestration, Y-27632 (50 μM) for Rho associated kinase

(ROCK) inhibition, SMIFH2 (40 μM) and CK-666 (100 μM) for disrupting actin nucleation by inhibiting formin and Arp2/3 respectively, and nocodazole (10 μM) for inhibiting microtubules. For more precise details, see methods, section 3.4.7.

7.7.1 Inhibition of cytoskeletal proteins prevents pulsations

The pulsations that were present in the monolayer before the addition of blebbistatin and Lat A were completely arrested after the addition of drugs (Movie 7.10 and 7.11). The cells in the presence of blebbistatin showed small range movements and exhibited blebs (Movie 7.10). On the other hand, cells in the presence of Lat A exhibited no activity (Movie 7.11). This is due to the depolymerization of actin filaments present in the cell-cell adhesions. In the same manner, pulsations were arrested on adding other inhibitors: Y-27632, SMIFH2, CK-666 and nocodazole. In the presence of these drugs, cells exhibited only individual movements without any collective activity. Thus, arresting of pulsations in all the above mentioned cases, highlights the importance of: acto-myosin activity, actin polymerization from formin and Arp2/3, and ROCK in the stress generation required for pulsations. These inhibitor drug based experiments validate the introduction of 'ζ' term in our oscillating tissue model. While these experiments were required to confirm the role of cytoskeletal elements in pulsations, the involvement of cytoskeletal elements is not surprising. After the pulsations were arrested by the inhibition of cytoskeletal proteins, we wanted to know if the pulsations can be rescued by washing out the drug from the sample.

7.7.2 Inhibition and reactivation of myosin leads to large scale flows

The results after washout were very interesting. When washout was performed in the experiments of blebbistatin / Lat A / Y-27632, pulsations did not appear; rather the monolayer exhibited large scale flows (Movie 7.10 and 7.12). After washing out blebbistatin, all the experiments consistently showed large scale flows. But in the case of Lat A and Y-27632, washout of drugs showed two different results in the monolayer: (i) large scale flows (Movie 7.11 and 7.12) or (ii) small range individual cell movements without any collective behavior. Similarly, washout in the experiments of SMIFH2 / CK-666 / nocodazole also resulted in small range movements of cells. Neither pulsations nor flows were observed in these (SMIFH2 / CK-666 / nocodazole) cases. Thus by restoring the activity of cytoskeletal proteins after inhibition, pulsations were not rescued.

Alternatively, the monolayer exhibits a different collective effect (flows) or small range movements of cells.

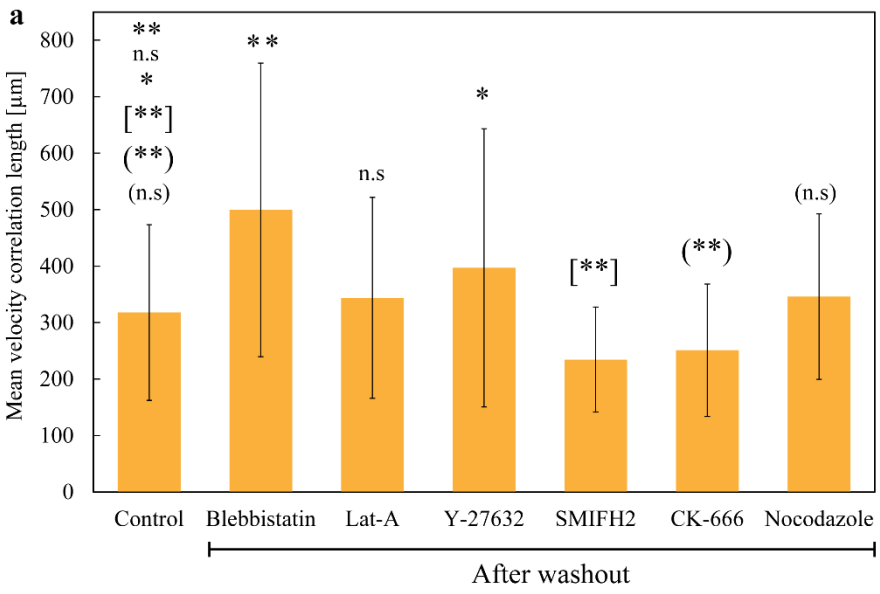

b

Experimental condition	Mean velocity correlation length	Result
Control	317 ± 155 µm	-
Blebbistatin (after washout)	499 ± 260 µm	Flows
Lat A (after washout)	343 ± 177 µm	Flows / local cell movements
Y-27632 (after washout)	396 ± 246 µm	Flows / local cell movements
SMIFH2 (after washout)	234 ± 92 µm	Local cell movements
CK-666 (after washout)	251 ± 117 µm	Local cell movements
Nocodazole (after washout)	346 ± 146 µm	Local cell movements

Figure 7.17. (a) Comparison of velocity correlation length between different cytoskeletal drug inhibitor experiments, after washing out the drug, and the last 24 h in control condition. This shows the distance in monolayer with correlated velocities during flows (of cells) or small range movements. Control (N=4); Blebbistatin (100 µM) (N=4); Lat A (1 µM) (N=3); Y-27632 (50 µM) (N=5); SMIFH2 (40 µM) (N=2); CK-666 (100 µM) (N=2); Nocodazole (10 µM) (N=4). **, [**], (**) $P < 0.01$ by Mann-whitney test. * $P < 0.05$ by Mann-whitney test. n.s and (n.s) – data are not significantly different. (b) Table summarizing the mean velocity correlation length values for control and for all cytoskeletal inhibitor drug conditions, after wash out.

To have an estimate of the new activity in monolayer (flows), we measured the mean velocity correlation length after washout (last 24 h), in all the drug conditions (Fig. 7.17 a and b). These values were compared with the mean (velocity) correlation length of monolayer from the last 24 h in control condition. Note that the correlation in velocity is estimated, as opposed to divergence correlation used for pulsations. After washout, the mean correlation length of monolayer in the experiments of blebbistatin (~ 500 µm) and Y-27632 (~ 400 µm) was significantly larger than the control condition (~ 320 µm) (Fig. 7.17 a and b). This increase in velocity correlation length clearly highlights the presence of large scale flows. In the Lat A experiment, although flows were observed after washout in some cases, the mean correlation length (~ 340 µm) was not significantly larger than control (~ 320 µm) (Fig. 7.17 a and b). Thus small range movements of cells dominate the monolayer in after

washing out Lat A. Similarly, the correlation length in the washout cases of SMIFH2, CK-666 and nocodazole also highlighted small range movements: SMIFH2 (~ 230 μm) and CK-666 (~ 250 μm) – significantly smaller than control; nocodazole (~ 350 μm) – similar to control (Fig. 7.17 a and b).

These results emphasize the role of cytoskeletal proteins in pulsations and collective behavior of cells in general. The variations in washout conditions between different cytoskeletal proteins, suggests unique functions for each of these proteins. For example, blebbistatin and Y-27632 washout always leads to a different collective effect: flows. Whereas, washout in Lat A and other actin related protein inhibitors (SMIFH2, CK-666) leads to destruction of collective behavior (small range movements of cells). To better understand the role of these proteins, we are planning to visualize the organization of these proteins by fluorescence imaging. The organization of these proteins under different collective behaviors (pulsations and flows) might help in understanding their function in each of these processes.

In conclusion, the experiments on FN grid, cell height fluctuations, and cytoskeletal inhibitor drugs suggest the significance of: substrate friction, cell height fluctuations and cytoskeletal proteins in the spatial organization of pulsations. These results support the factors obtained from the oscillating tissue model in defining a characteristic lengthscale for the pulsations. One other important factor that can influence pulsatile domains is the cell density in the monolayer. We address the role of density in the following section.

7.8 Significance of density for pulsations

The emergence of pulsations amidst spatial constraints (in a confluent monolayer) is the highlight of underlying collective behavior, as opposed to other collective effects like collective migration and wound closure. However, during the timescale of experiment (48 h), cell proliferation leads to the densification of monolayer. The densification can be realized from Fig. 7.2 e: the local density in the pulsatile domain region increases due to the domain contraction. However, after extension the local density does not come back to the initial value. This difference in density before and after pulsation corresponds to cell proliferation in the monolayer. The densification of monolayer due to increasing cell density will reduce the spatial freedom of the cells to move, and the pulsating domains will eventually cease to exist. This is clear from the divergence plot of pulsating domains where the divergence oscillations reach a damping point after ~ 35 h (Fig. 7.5 d). Thus pulsations are screened out by increase in density. In this scenario, we wanted to know if by maintaining a constant cell density, the damping point of pulsations can be extended.

7.8.1 Inhibition of cell proliferation

Maintaining a constant cell density over the experimental time is not possible. However, the rate of cell proliferation can be reduced by using drugs like mitomycin C (133). We performed experiments in the same manner as in the cytoskeletal drug inhibition cases: Mitomycin C (5 µg/ml or 32 µM) was added after the monolayer reached confluency and exhibited pulsations (~ 12 h to 20 h). Then the monolayer was observed in the presence of drug for ~ 12 h, since incubation with mitomycin C for more than 12 h was deemed toxic for the cells (133, 255). After 12 h of incubation, the monolayer showed increased extrusion and difference in morphology of cells. Hence, only the first 12 h of incubation was taken for analysis.

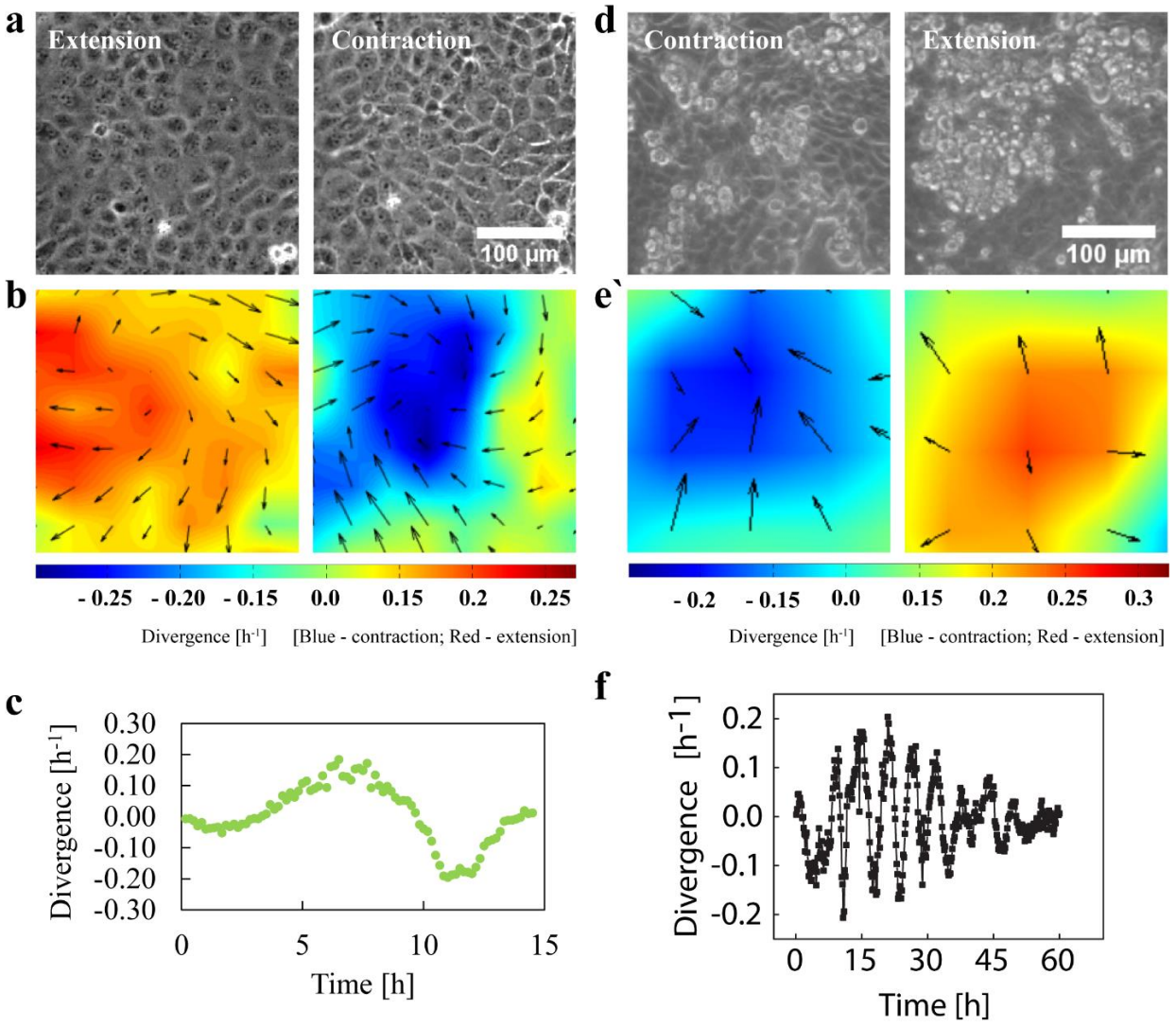

Figure 7.18. Isolated pulsatile domains during incubation with mitomycin C and serum free condition. (a) Snapshots of extension and contraction phases of a pulsatile domain isolated from a monolayer during incubation with mitomycin C. The pulsatile domain area is 250 µm^2, corresponding to the mean divergence correlation length (~ 250

μm) in monolayer during incubation with mitomycin C. (b) Divergence plot corresponding to (a). (c) Plot showing mean divergence of the pulsatile domain shown in (a), over the (mitomycin C) incubation time. The initial time point (t_0) corresponds to the time when mitomycin C is added to the sample. (d) Snapshots of contraction and extension phases of an isolated pulsatile domain in serum free condition. (e) Divergence plot corresponding to (d). (f) Plot showing mean divergence of the pulsatile domain shown in (d), over the time of experiment. The initial time point (t_0) corresponds to the time when the monolayer reaches confluency.

After acquisition, first we estimated the mean divergence correlation length (size of pulsations) in the monolayer in the presence of mitomycin C: ~ 250 μm (Fig. 7.19 a and b). Using this correlation length, we isolated a pulsatile domain in the monolayer and observed the divergence oscillations before and after the addition of mitomycin C. We found that divergence oscillations in the domain were not affected due to reduced proliferation rate after addition of mitomycin C (Fig. 7.18 a, b and c; Movie 7.13). This result is suggestive of an extended damping point of pulsations. However, this result indicates the presence of divergence oscillations only for ~ 12 h (incubation time with the mitomycin C), after the reduction in proliferation rate was triggered by adding the drug. The toxicity of the drug after ~ 12 h prevents from studying the effect on maintaining the reduced proliferation rate for more than 12 h.

7.8.2 Serum free experiments

In order to study the effect of reduced proliferation rate for prolonged times, we performed experiments in the serum free condition. Growth factors present in the serum in cell culture media promote the proliferation of cells. We hypothesized that proliferation rate of cells can be reduced by growing cells in a serum free (growth factors free) media. This would allow us to study the effect of reduced proliferation rate for prolonged times – only if the cells formed a monolayer and exhibited pulsations in this drastic (serum free) condition. We plated cells on normal glass coverslip with serum free media and acquired the evolution of cells. For the precise protocol of serum free experiments, see methods, section 3.4.6.

To our surprise, the cells formed a monolayer in serum free condition. More interestingly, the monolayer exhibited pulsations (Fig. 7.18 d and e; Movie 7.14). We estimated the mean divergence correlation length in the monolayer: ~ 280 μm (Fig. 7.19 a and b), and using this correlation length we isolated a pulsatile domain. Interestingly, the divergence oscillations of the domain extended for more than ~ 35 h (Fig. 7.18 f), when compared to the control condition where divergence oscillations reached a damping point around ~ 35 h (Fig. 7.5 d). This shows that damping point of pulsations can be extended by reducing the proliferation rate of cells and thereby the densification of monolayer.

On the other hand, there are other differences in serum free condition when compared to control condition. In addition to growth factors, serum also contains ECM proteins that promote cell-substrate interaction. Hence in control condition, the deposition of ECM proteins (from serum) on the substrate promotes cell-substrate interaction. This maintains a minimal amount of friction as mentioned. The absence of these ECM proteins in the serum free condition, considerably reduces the friction. Although this difference in friction was not reflected in velocity of cells, it may affect the correlation length.

The obtained mean correlation length in the monolayer, in the presence of mitomycin C (~ 250 µm) was not significantly higher than control (~ 230 µm) (Fig. 7.19 a and b). This suggests that cell density actually does not affect the size of pulsations. However, in the serum free experiments the mean correlation length (~ 280 µm) was significantly higher than control (~ 230 µm) (Fig. 7.19 a and b), indicating an increase in pulsation size. This increase in pulsation size can also be attributed to the reduced friction in the serum free experiments. Another clear difference between mitomycin C and serum free condition is the period of pulsations. From Fig. 7.18 c and f, it is clear that period of pulsation is longer in the presence of mitomycin C, but the period of pulsation is ~ 2 fold smaller in serum free condition. Thus, the readout of serum free condition (extended damping point of pulsations due to reduced proliferation rate) is a function of two variables: friction and reduced proliferation rate. In order to better understand the readout of serum free condition, experiments are required to probe the individual influence of friction and proliferation rate – on extended damping point of pulsations.

a

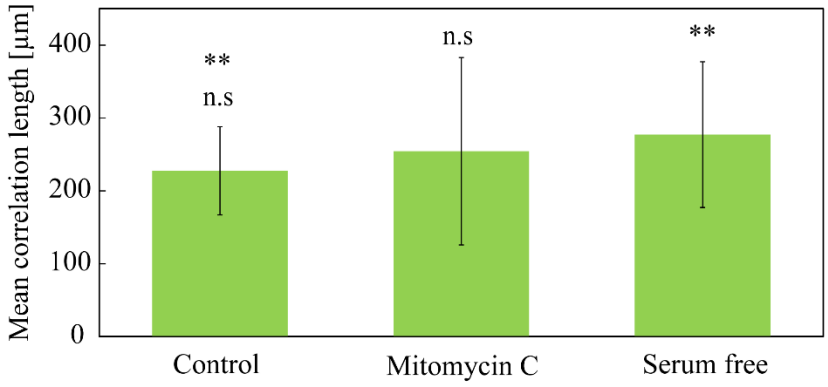

b

Experimental condition	Mean divergence correlation length
Control	227 ± 60 µm
Mitomycin C	254 ± 128 µm
Serum free condition	277 ± 100 µm

Figure 7.19. (a) Comparison of mean divergence correlation length between control, mitomycin C and serum free experiments. Control (N=4); Mitomycin C (N=2); Serum free (N=2). ** P < 0.01 by Mann-whitney test. n.s – data are not significantly different. (b) Table summarizing the mean divergence correlation length values for control, mitomycin C and serum free conditions.

Although these methods for reducing proliferation rate (12 h in mitomycin C and serum free condition) are not robust, they provide a first step understanding on the influence of reduced proliferation rate in pulsations. Meanwhile, we are currently probing other means for maintaining a constant cell density in the monolayer and thereby to study the effect on pulsations.

7.9 Discussion

Collective behaviors in epithelial monolayers have been explored mainly in the context of migration and wound healing (256). In these cases, the monolayer is presented with a free space that triggers symmetry breaking, which eventually results in collective motions. However, several *in vivo* processes require collective behaviors under confluent conditions (232, 233, 238). This necessitates the understanding of collective behaviors (motions) emerging amidst spatial constraints. Following this line, in this study we explore the potential factors responsible for maintaining correlation in the activities of cells, in a confluent monolayer. We study these factors on a specific collective effect where collection of cells exhibit coordinated movements of contraction and extension with respect to a common center. We call these coordinated contraction and extension as pulsatile domains or pulsations. While similar pulsations in monolayer were recently reported by some groups (133, 257–259), our observation of this phenomena was independent of these works.

We show that pulsations spontaneously appear in confluent MDCK monolayers without any external stimulation as opposed to pulsations appearing: (i) in confined environments (133, 259) and (ii) in expanding monolayers (257, 258). In the case of confined environments (i), emergence of pulsations is triggered by confinement itself, which in turn influences the correlation length of pulsations. On the other hand, in a system of expanding monolayer (ii), the influence of migrating periphery on the confluent inner regions is not clear. In this context, note that mechanical (velocity and stress) waves have been shown to traverse the expanding monolayer (260). In our case, the monolayer is confluent over a large area (175 mm^2) and pulsations spontaneously appear within the monolayer. The confinement area (from the coverslip size – 15 mm diameter) is several folds larger than the observed correlation length (~ 230 μm). This completely rules out any influence of confinement / boundary effects in the observed phenomena (pulsations). Thus the measured divergence correlation length (representing the size of pulsations) corresponds to the contractility based natural or inherent correlation length in the monolayer.

We quantitatively represent the contraction and extension cycles of pulsations by divergence oscillations in the monolayer. Using long term experiments (48 h), we show that these divergence oscillations exist for longer timescales (~ 35 h) and confirm the repetitive pattern from the autocorrelation of divergence field. Also, we identify the existence of a common center in the pulsatile domain, leading to collective contractions and extensions. This common center was identified by performing a winding number analysis of the velocity field in the region. These results, specifically highlighting the occurrence of pulsations over longer times (with increased duration of experiments) and the identification of pulsation center, further distinguishes our observation from the previous studies.

In addition to studies mentioned above (133, 257–259), pulsatile domains can also be observed in the data from literature, where pulsations are not the subject of study (179, 261). This shows that pulsation phenomena are inherent to MDCK monolayers. We use this naturally occurring phenomena (pulsations) to study the factors responsible for setting the correlation length in monolayers. Correlation analysis allows the estimation of collective effects in an unbiased manner (244), and has been used widely in studying epithelial systems (245–247, 262, 263). Following this line, we characterized these pulsations by estimating the mean divergence correlation length over the experimental time in monolayer. The estimated correlation length corresponds to the size of pulsations (~ 230 μm). Having obtained the correlation length, we wanted to investigate those factors setting this lengthscale in the monolayer. We hypothesized that cell-substrate interaction (friction) and cytoskeletal proteins should play a significant role in regulating the lengthscale of pulsations. To study the influence of these factors on pulsations, we compared the variation in mean (divergence) correlation length between the experimental conditions. The results obtained from this comparison was used for substantiating the role of each of these factors.

However, in addition to correlation length, comparing the variations in pulsation period will provide more information on the influence of these factors (friction, cytoskeletal proteins and density). In order to obtain the pulsation period, we discretized the monolayer into areas (sliding window method) defined by the correlation length. The distribution of periods obtained from the power spectrum of these individual areas was used to extract a mean period. In this manner we estimated the mean pulsation period in control condition: ~ 7 h.

Dynamic structure factor: While the length and timescales can be obtained by the methods described above, these values correspond to the: (i) averaged correlation length obtained at different time points and (ii) mean period from a distribution of timescales

obtained from different regions in the monolayer. This process of averaging, reduces the precision of the obtained values for correlation length and period of pulsations. In addition, the sliding window process for obtaining the pulsation period was performed manually, i.e. the sliding windows were drawn manually to obtain the corresponding power spectrum. These discrepancies can be resolved by estimating the dynamic structure factor of the divergence characteristics of monolayer (258). Dynamic structure factor is the Fourier transform of the spatio-temporal correlation function. This gives the Fourier components of the spatio-temporal fluctuations of divergence (corresponding to the pulsations), from which the length and timescales can be obtained. The spatio-temporal correlation function of pulsations is given by:

$$C_{dd}(r,\tau) = \iint div\,(x,t) \times div\left(x + r,\ t + \tau\right) dx\, dt \qquad (7.13)$$

$C_{dd}(r,\tau)$ denotes the divergence correlation over space (r) and time (τ). Now, the dynamic structure factor can be obtained by taking the fourier transform of equation (7.13):

$$S\,(q,\omega) = \iint C_{dd}\,(r,\tau).\ e^{-i2\pi qr}.e^{-i2\pi\omega\tau}\, dr\, d\tau \qquad (7.14)$$

Where, $S\,(q,\omega)$ denotes the dynamic structure factor of the spatial and temporal frequencies 'q' and 'ω', respectively. The peaks obtained in the power spectrum of $S\,(q,\omega)$ as a function of wavelength and period will give the time and lengthscales of pulsations, respectively. We are currently performing this analysis for all the experiments in order to compare the obtained length and timescales.

The current analysis only considers the variation in correlation length of pulsations. In addition, the variations in pulsation period under different conditions from the dynamic structure factor will be more informative. For example, when the proliferation rate of cells is reduced using mitomycin C, the correlation length is not affected, but the period of pulsation seems to be increased (Fig. 7.18 c). However, this data is from one pulsatile domain. Whereas, the power spectrum of $S\,(q,\omega)$ as a function of wavelength will reveal the period of pulsations in the monolayer in an unbiased manner.

Number of pulsations in the field of view. As mentioned above (for the estimation of pulsation period), parameters other than correlation length can improve the comparison between different experimental conditions. Another parameter that can be measured is the number of pulsations in the field-of-view. During the course of experiment, monolayer presents with numerous pulsations. The structure factor analysis will only help in finding

the length and timescales of pulsations. However, it would also be interesting to quantify the number of pulsations occurring over a defined area of monolayer, during the experimental time. This value (number of pulsations/area) in combination with the length and timescales of pulsations will make the comparison between different experimental conditions robust. For example, in the FN grid condition (W-120 μm + G-150 μm), the correlation length of pulsations (~ 385 μm) match the FN grid size (~ 390 μm). In this case, one can expect more number of pulsations per area (pertaining to grids) to occur, when compared to control condition. In finding the number of pulsations (per area), one needs to clearly define the boundary of pulsatile domains in the monolayer and correlate the boundary with the associated critical point (center) in the pulsation region – as described in section 7.2. We are currently working on automating this analysis for the extraction of values from different experimental conditions.

Friction affects correlation length of pulsations. The difference in velocities of cells on control and homogeneous FN condition motivated us to explore the role of friction. We found that differential variation of friction by matching the size of pulsations, directly affects the pulsation length. Experiment with FN grid (W-120 μm + G-150 μm) shows that size of pulsation can be adapted if the lattice size matches the pulsation size; by adapting the width of FN stripe and the gap within the FN grid to influence collection of cells. Further the role of friction was confirmed by experiments on FN grid with PEG, where the velocities of cells on the FN stripe was at least two folds smaller than the velocities of cells on PEG region (due to reduced interaction with substrate).

While these experiments confirm the role of friction in regulating the pulsation characteristics, the cellular mechanism could not be deciphered. In general, absence of focal adhesion in passivated regions is taken as a cellular read out for reduced cell-substrate interaction (substrate friction) (179). In our case, focal adhesions were present in both FN and non-FN / passivated regions. Given this situation, we are currently planning to measure the lifetime of focal adhesions on FN and non-FN / passivated regions to see if any variation exists. On the other hand, focal adhesions can be visualized on experiments by increasing the relative concentrations of fibronectin and passivating agent.

In the current design of FN grid, the width of FN stripe/region is maintained constant (120 μm). We know that reduction in the width of FN region to 60 μm and 30 μm (as in FN line condition) does not impose dramatic effect on regulating pulsations. However, experiments by varying the width of FN region in FN grid conditions will help in understanding the effect of patterns (“grid” as opposed to “lines”) on spatial regulation of

pulsations. The corresponding designs have been microfabricated and we are currently testing these conditions.

Another parameter we would like test is the gaps between the FN grids. The currently used array of FN grids are in connected fashion, i.e. gaps are only within the FN grid and not between the FN grid. However, studying pulsations on a lattice of separated FN grids would be more interesting. This situation would allow us to understand how variation in friction only in specific regions of the tissue affects the collective dynamics. In addition, variations in the separation distance between the FN grid and the corresponding effect on pulsation characteristics will give more insights into the correlation length of pulsations with respect to friction. We have already microfabricated these patterns where the separation between the FN grids are varied as 75 μm, 150 μm and 300 μm. These experiments remain to be tested.

All the above mentioned experiments with FN grids help in understanding how the surrounding mechanical environments regulate tissue dynamics. It has been shown that ECM density and organization play a critical role in collective invasion of tissues (264). More specifically, the connections to adjacent tissues by surrounding matrix have been shown to be important during development, *in vivo* ablation of this matrix leads to abnormal shapes during the *drosophila* wing development (254). Along this line, our work on FN grid can increment the understanding of how collective tissue dynamics are altered based on interactions with surrounding tissue.

Continuum modelling of pulsations. To understand the natural emergence of spontaneous length and timescales of pulsations, we developed a continuum model in line with Etournay et al (254). Recently, similar continuum models have been developed for oscillating tissues (259). Also, pulsations have been described by the classical Vicsek/particle-based model (133). In a particle-based model, cells are treated as discrete entities with spontaneous velocities (10). The collective behavior within a group of cells depends on the adaptation of this spontaneous velocity with respect to the neighboring cell. Using this approach, Deforet et al. (133) show that breathing modes/pulsations spontaneously emerge due to the amplification of naturally existing oscillatory modes in a confined environment. In this context, it is worth noting that confinement can also lead to other behaviors depending on factors like polarization of cells and density (265). In our case, the tissue is spread over a vast area that completely neglects the effects due to confinement. But still pulsations spontaneously emerge in the tissue/monolayer. In this scenario, we decided to model the tissue as a continuous entity where the distribution functions of system components like contractility, coupling between contractility and cell area/cell height can be modelled.

In our model, we specifically show that pulsations in monolayer are due to the tight coupling between cell area, cell height and contractility. We show that fluctuations in cell height accompanies collective pulsation of cells in the monolayer (expression (7.12)). This yields a peak in power spectrum corresponding to a characteristic lengthscale. We confirmed the existence of these height fluctuations during pulsations by measurements. We show that cells increase in height during contraction phase when compared to the extension phase. As a first step, these experiments were performed on FN grid with PEG for ease in localization of pulsations and to include the effect of variation in friction (between the PEG and FN regions). In order to further substantiate these results, we are currently performing experiments on FN grid without PEG and in control conditions.

The variation in cell height during pulsations is in contrary to the previous observation of Zehnder et al. (258), where cell height fluctuations were not observed in pulsations. In their case, fluctuations in cell height occurs only when the channels facilitating water transfer were blocked. This allowed them to conclude the significance of osmotic pressure for generating pulsations. This difference in observation could be due to the precision in height measurement during acquisition or during extraction. Note that we extract the values of cell height during pulsation as opposed to observation based inference by Zehnder et al (258). In addition, this difference in results shows that mechanisms other than osmotic pressure (like contractility) might also be involved in generating pulsations.

Contractility due to cytoskeletal proteins is necessary for pulsations. The arrest of pulsations on inhibiting cytoskeletal proteins (myosin, actin, ROCK, formin, Arp2/3, microtubules) using cytoskeletal inhibitors, highlights their role in pulsations. However, the failure in rescuing pulsations after washout was not intuitive. In addition, emergence of a new collective effect (flows) in some cases (blebbistatin, Y-27632 washout) and destruction of collective behavior in other cases (Lat A, SMIFH2, CK-666, nocodazole) makes the understanding difficult. In this scenario, one can assume pulsations and flows to be a result of specific organization of actin and myosin in the cells. In other words, the natural organization of actin and myosin molecules during the growth of monolayer leads to emergence of pulsations. This specific organization of acto-myosin is set at time zero (t_0) which is the time point at which monolayer reaches confluency. However, during the process of inhibition and restoration of their activity, their organization is disturbed. If this change in organization is different from the natural organization (at t_0), then pulsations will not be restored. In addition, if the new organization is polarized (for example, towards one edge in all the cells) then flows can emerge in the monolayer. Examples of such polarized flows with specific organization of proteins can be found in

literature (160, 266, 267). While this hypothesis gives a simple explanation for the role of actin and myosin, it needs to be validated by fluorescence imaging. We are currently planning such experiments to visualize the positional organization of actin and myosin. This can be achieved by imaging the actin and myosin in monolayer: on FN grids for pulsations, during incubation with the inhibitor drugs and after washout. The variations in organization of actin and myosin in these different scenarios (pulsation, cytoskeletal inhibition and after washout) would improve the understanding of actin and myosin in collective behaviors. In addition, we are planning to test the effect of contractility by ablation experiments. For example, ablation of one cell in the monolayer would release the tension in the surrounding tissue. This would trigger pulsations in the regions surrounding the ablation point, confirming the role of stress generated by acto-myosin.

Density affects pulsations. The damping of divergence oscillations over the time of experiment shows that increase in cell proliferation affects the existence of pulsations by increasing the spatial constraints. This suggests the existence of a particular density regime at which the pulsatile domains emerge and sustain in the monolayer. Along this line, it would be interesting to estimate the critical densities at which the pulsations start to appear and disappear. This can be done by measuring the variation in cell density during experiments and the correlation with appearance and damping of pulsations.

What is the origin of pulsations? This work mainly addresses the factors involved in the regulation of pulsation characteristics in monolayer. But the main factor that leads to the origin of pulsations is not clear yet. In this context, Zehnder et al. (257, 258), in their work on similar kind of pulsations, propose osmotic pressure variations as a potential source for the pulsations in monolayer – mainly based on their observations of fluid transfer between the cells. However, an experimental verification on fluid transfer between the cells and the surrounding medium is lacking. Such an exchange between the cells and surrounding medium can compensate the fluid transfer between the cells, which can compensate volume fluctuations. Note that in our work, we observe a strong variation in cell height during pulsations. While observation of height variations does not challenge the fluid transfer observed between the cells by Zehnder et al., the only/dominant role of osmotic pressure in originating pulsations is not clear.

Oscillations have been reported *in vivo* at different developmental stages in different organisms (160, 161, 242, 268–271), with timescales ranging from seconds to minutes. In general, these type of oscillations have been shown to arise from collective effects of molecular motors (272), as substantiated by the *in vivo* studies mentioned previously. But how these microscopic oscillations are transformed into oscillations at the cell level is not well understood (14). The role of cytoskeletal proteins in sustaining pulsations was clear

from the inhibitor drug experiments. But in order to know, how they lead to the origination of pulsations and further translate into cellular and tissue scale pulsations, we need to visualize (by fluorescence microscopy) these proteins in the monolayer.

In conclusion, we establish pulsations to be an inherent phenomenon of the confluent MDCK monolayers with specific length and timescales. The FN grid and inhibitor drug experiments show that pulsation characteristics can be altered by changing friction and cytoskeletal proteins. The generic nature of these factors (interaction with substrate/neighboring tissue and cytoskeletal proteins) in controlling tissue dynamics can be further substantiated by different studies (160, 242, 254, 273, 274). On the other hand, the pulsation characteristics were not altered in other conditions like homogeneous FN and FN line coated substrates. This shows the robustness of the spontaneous lengthscale in the system. This makes pulsations in MDCK monolayers a suitable phenomenon to study the tissue scale dynamics and the associated length and timescales. These type of studies regarding tissue scale processes would increment our understanding of large scale problems like: “how multiple cells cooperate to generate a tissue?”, “how tissues stop growing after reaching a particular size in a definitive timescale?” and “morphogenesis of organs”.

8. Conclusion

The major goal of this thesis is to understand the collective effects that are generated from an ensemble of individual interactions. We address this question in two different studies: (i) cytokinetic ring, where thousands of acto-myosin filaments are involved in generating constriction and (ii) MDCK monolayer, where collection of cells exhibit pulsation in a coordinated manner.

In the case of cytokinetic ring constriction, we study two systems (fission yeast and mammalian cell) and show that myosin exhibits a clustered (self-organized) state in the ring, but in a distinct manner: rotating in fission yeast and static in mammalian cells. Using a theoretical model, we propose a generic interaction rule for both the systems, based on which we identify the critical parameters that lead to difference in organization in the two systems. In addition, using theory and experiments, we show how the distinct self-organized states drive the ring constriction: stress generation in mammalian cells and transport in fission yeast. This study shows how the same set of proteins (acto-myosin) can be organized differently for the same function (ring constriction) in different systems. Moreover, this study illustrates how difference in collective behavior of the same proteins can result in different properties (stress generation and transport).

In the case of MDCK monolayer, we study how groups of cells can exhibit a characteristic dynamic (pulsation) in a coordinated fashion. Using experiments we show that cell-substrate interaction is critical for setting the lengthscales of pulsations. We confirm this by a theoretical model which gives a characteristic lengthscale for an oscillating tissue as a function of substrate friction. In addition, we show that the characteristic length scale is also a function of tightly coupled: cell area, cell height and contractility, which are further confirmed by experiments. This study aims at identifying the generic physical parameters that are involved in setting the spontaneous length scale in collection of cells. In this aspect, this study can be a forerunner in understanding the self-organization and collective dynamics *in vivo* that are essential for morphogenesis during development.

Thus we show how in one case (cytokinetic ring), the different manifestation of collective effects serves different purposes, and in another case (pulsations in monolayer), the physical factors responsible for generating coordinated dynamics.

In addition to these works, we also report two studies where: (i) we explore the application of a new compound (synthetic polyamines) for dissecting actin dynamics and (ii) probe the possibility of direction reversal in single cell migration during ratchetaxis.

In conclusion, this thesis in addition to highlighting the significance of collective phenomena, also emphasizes the need for investigating the physical phenomena in biological systems in addition to the vast expanse of established biochemical and genetic studies.

9. References

1. Vicsek, T. 2001. A question of scale. Nature. 411: 421.
2. 1997. Animal Groups in Three Dimensions. Cambridge University Press.
3. Blair, D.L., T. Neicu, and A. Kudrolli. 2003. Vortices in vibrated granular rods. Phys. Rev. E. 67: 031303.
4. Narayan, V., S. Ramaswamy, and N. Menon. 2007. Long-lived giant number fluctuations in a swarming granular nematic. Science. 317: 105–8.
5. Vicsek, T., and A. Zafeiris. 2012. Collective motion. Phys. Rep. 517: 71–140.
6. Méhes, E., and T. Vicsek. 2014. Collective motion of cells: from experiments to models. Integr. Biol. (Camb). 6: 831–54.
7. Ramaswamy, S. 2010. The mechanics and statistics of active matter. Annu. Rev. Condens. Matter Phys. 1: 323–345.
8. Vicsek, T., A. Czirk, E. Ben-Jacob, I. Cohen, and O. Shochet. 1995. Novel type of phase transition in a system of self-driven particles. Phys. Rev. Lett. 75: 1226–1229.
9. Grégoire, G., and H. Chaté. 2004. Onset of Collective and Cohesive Motion. Phys. Rev. Lett. 92: 025702.
10. Szabó, B., G.J. Szöllösi, B. Gönci, Z. Jurányi, D. Selmeczi, and T. Vicsek. 2006. Phase transition in the collective migration of tissue cells: Experiment and model. Phys. Rev. E. 74: 061908.
11. Marchetti, M.C., J.F. Joanny, S. Ramaswamy, T.B. Liverpool, J. Prost, M. Rao, and R.A. Simha. 2013. Hydrodynamics of soft active matter. Rev. Mod. Phys. 85: 1143–1189.
12. Bendix, P.M., G.H. Koenderink, D. Cuvelier, Z. Dogic, B.N. Koeleman, W.M. Brieher, C.M. Field, L. Mahadevan, and D.A. Weitz. 2008. A Quantitative Analysis of Contractility in Active Cytoskeletal Protein Networks. Biophys. J. 94: 3126–3136.
13. Joanny, J., and J. Prost. 2009. Active gels as a description of the actin- myosin cytoskeleton. HFSP J. 3: 94–104.
14. Kruse, K., and D. Riveline. 2011. Spontaneous Mechanical Oscillations. Implications for Developing Organisms. 1st ed. Elsevier Inc.
15. Drescher, K., J. Dunkel, L.H. Cisneros, S. Ganguly, and R.E. Goldstein. 2011. Fluid dynamics and noise in bacterial cell-cell and cell-surface scattering. Proc. Natl. Acad. Sci. 108: 10940–10945.

16. Jülicher, F., K. Kruse, J. Prost, and J.-F. Joanny. 2007. Active behavior of the Cytoskeleton. Phys. Rep. 449: 3–28.

17. Purcell, E.M. 1977. Life at low Reynolds number. Am. J. Phys. 45.

18. Toner, J., and Y. Tu. 1995. Long-Range Order in a Two-Dimensional Dynamical XY Model: How Birds Fly Together. Phys. Rev. Lett. 75: 4326–4329.

19. Simha, R.A., and S. Ramaswamy. 2002. Hydrodynamic Fluctuations and Instabilities in Ordered Suspensions of Self-Propelled Particles. : 1–4.

20. Hatwalne, Y., S. Ramaswamy, M. Rao, and R.A. Simha. 2004. Rheology of Active-Particle Suspensions. Phys. Rev. Lett. 92: 118101.

21. Prost, J., F. Jülicher, and J.-F. Joanny. 2015. Active gel physics. Nat. Phys. 11: 111–117.

22. Kruse, K., J.F. Joanny, F. Jülicher, J. Prost, and K. Sekimoto. 2004. Asters, Vortices, and Rotating Spirals in Active Gels of Polar Filaments. Phys. Rev. Lett. 92: 078101.

23. Kruse, K., J.F. Joanny, F. Jülicher, J. Prost, and K. Sekimoto. 2005. Generic theory of active polar gels: A paradigm for cytoskeletal dynamics. Eur. Phys. J. E. 16: 5–16.

24. Alberts, B., A. Johnson, J. Lewis, M. Raff, K. Roberts, and P. Walter. 2007. Molecular Biology of the Cell. .

25. Wottawah, F., S. Schinkinger, B. Lincoln, R. Ananthakrishnan, M. Romeyke, J. Guck, and J. K??s. 2005. Optical rheology of biological cells. Phys. Rev. Lett. 94: 1–4.

26. Joanny, J.-F., and J. Prost. 2009. Active gels as a description of the actin-myosin cytoskeleton. HFSP J. 3: 94–104.

27. Kruse, K., and F. Jülicher. 2000. Actively contracting bundles of polar filaments. Phys. Rev. Lett. 85: 1778–1781.

28. Kruse, K., S. Camalet, and F. Jülicher. 2001. Self-propagating patterns in active filament bundles. Phys. Rev. Lett. 87: 138101.

29. Liverpool, T.B., and M.C. Marchetti. 2005. Bridging the microscopic and the hydrodynamic in active filament solutions. EPL (Europhysics Lett. 69: 846.

30. Lauffenburger, D.A., and A.F. Horwitz. 1996. Cell migration: A physically integrated process. Cell. 84: 359–369.

31. Eggert, U.S., T.J. Mitchison, and C.M. Field. 2006. Animal cytokinesis: from parts list to mechanisms. Annu. Rev. Biochem. 75: 543–66.

32. Fletcher, D.A., and R.D. Mullins. 2010. Cell mechanics and the cytoskeleton. Nature. 463: 485–492.

33. Rogers, S.L., and V.I. Gelfand. 2000. Membrane trafficking, organelle transport, and the cytoskeleton. Curr. Opin. Cell Biol. 12: 57–62.

34. Etienne-Manneville, S., and A. Hall. 2002. Rho GTPases in cell biology. Nature. 420: 629–635.

35. Hall, A. 2005. Rho GTPases and the control of cell behaviour. Biochem. Soc. Trans. 33: 891–895.

36. Riveline, D., E. Zamir, N.Q. Balaban, U.S. Schwarz, T. Ishizaki, S. Narumiya, Z. Kam, B. Geiger, and A.D. Bershadsky. 2001. Focal contacts as mechanosensors: externally applied local mechanical force induces growth of focal contacts by an mDia1-dependent and ROCK-independent mechanism. J. Cell Biol. 153: 1175–86.

37. O'Connell, C.B., M.J. Tyska, and M.S. Mooseker. 2007. Myosin at work: Motor adaptations for a variety of cellular functions. Biochim. Biophys. Acta - Mol. Cell Res. 1773: 615–630.

38. Gittes, F., B. Mickey, J. Nettleton, and J. Howard. 1993. Flexural rigidity of microtubules and actin filaments measured from thermal fluctuations in shape. J. Cell Biol. 120: 923–34.

39. Ananthakrishnan, R., and A. Ehrlicher. 2007. The forces behind cell movement. Int. J. Biol. Sci. 3: 303–317.

40. Svitkina, T.M., and G.G. Borisy. 1999. Arp2/3 complex and actin depolymerizing factor/cofilin in dendritic organization and treadmilling of actin filament array in lamellipodia. J. Cell Biol. 145: 1009–1026.

41. Winder, S.J., and K.R. Ayscough. 2005. Actin-binding proteins. J. Cell Sci. 118: 651–4.

42. Otto, J.J. 1994. Actin-bundling proteins. Curr. Opin. Cell Biol. 6: 105–9.

43. Horwitz, A.R. 2009. Non-muscle myosin II takes centre stage in cell adhesion and migration. Nat. Rev. Mol. Cell Biol. 10: 778–790.

44. Valiron, O., N. Caudron, and D. Job. 2001. Microtubule dynamics. Cell. Mol. Life Sci. 58: 2069–84.

45. Herrmann, H., H. Bär, L. Kreplak, S. V. Strelkov, and U. Aebi. 2007. Intermediate filaments: from cell architecture to nanomechanics. Nat. Rev. Mol. Cell Biol. 8: 562–573.

46. Salbreux, G., G. Charras, and E. Paluch. 2012. Actin cortex mechanics and cellular morphogenesis. Trends Cell Biol. 22: 536–545.

47. Clark, A.G., K. Dierkes, and E.K. Paluch. 2013. Monitoring actin cortex thickness in live cells. Biophys. J. 105: 570–80.

48. Morone, N., T. Fujiwara, K. Murase, R.S. Kasai, H. Ike, S. Yuasa, J. Usukura, and A. Kusumi. 2006. Three-dimensional reconstruction of the membrane skeleton at the plasma membrane interface by electron tomography. J. Cell Biol. 174: 851–62.

49. Fehon, R.G., A.I. McClatchey, and A. Bretscher. 2010. Organizing the cell cortex: the role of ERM proteins. Nat. Rev. Mol. Cell Biol. 11: 276–87.

50. Fischer-Friedrich, E., A.A. Hyman, F. Jülicher, D.J. Müller, and J. Helenius. 2014. Quantification of surface tension and internal pressure generated by single mitotic cells. Sci. Rep. 4: 6213.

51. Tojkander, S., G. Gateva, and P. Lappalainen. 2012. Actin stress fibers - assembly, dynamics and biological roles. J. Cell Sci. 125: 1855–64.

52. Tojkander, S., G. Gateva, G. Schevzov, P. Hotulainen, P. Naumanen, C. Martin, P.W. Gunning, and P. Lappalainen. 2011. A molecular pathway for myosin II recruitment to stress fibers. Curr. Biol. 21: 539–50.

53. Hotulainen, P., E. Paunola, M.K. Vartiainen, and P. Lappalainen. 2005. Actin-depolymerizing factor and cofilin-1 play overlapping roles in promoting rapid F-actin depolymerization in mammalian nonmuscle cells. Mol. Biol. Cell. 16: 649–664.

54. Hotulainen, P., and P. Lappalainen. 2006. Stress fibers are generated by two distinct actin assembly mechanisms in motile cells. J. Cell Biol. 173: 383–94.

55. Zhang, X.-F., A.W. Schaefer, D.T. Burnette, V.T. Schoonderwoert, and P. Forscher. 2003. Rho-dependent contractile responses in the neuronal growth cone are independent of classical peripheral retrograde actin flow. Neuron. 40: 931–44.

56. Mitchison, T.J., and L.P. Cramer. 1996. Actin-based cell motility and cell locomotion. Cell. 84: 371–9.

57. Khatau, S.B., C.M. Hale, P.J. Stewart-Hutchinson, M.S. Patel, C.L. Stewart, P.C. Searson, D. Hodzic, and D. Wirtz. 2009. A perinuclear actin cap regulates nuclear shape. Proc. Natl. Acad. Sci. U. S. A. 106: 19017–22.

58. Nagayama, K., Y. Yahiro, and T. Matsumoto. 2011. Stress fibers stabilize the position of intranuclear DNA through mechanical connection with the nucleus in vascular smooth muscle cells. FEBS Lett. 585: 3992–7.

59. Jacinto, A., W. Wood, S. Woolner, C. Hiley, L. Turner, C. Wilson, A. Martinez-Arias, and P. Martin. 2002. Dynamic Analysis of Actin Cable Function during Drosophila Dorsal Closure. Curr. Biol. 12: 1245–1250.

60. Mattila, P.K., and P. Lappalainen. 2008. Filopodia: molecular architecture and

cellular functions. Nat. Rev. Mol. Cell Biol. 9: 446–454.

61. Caballero, D., J. Comelles, M. Piel, R.R. Voituriez, and D. Riveline. 2015. Ratchetaxis: Long-Range Directed Cell Migration by Local Cues. Trends Cell Biol. 25: 815–827.

62. Abercrombie, M. 1980. The Croonian Lecture, 1978: The Crawling Movement of Metazoan Cells. Proc. R. Soc. London B Biol. Sci. 207: 129–147.

63. Charras, G., and E. Paluch. 2008. Blebs lead the way: how to migrate without lamellipodia. Nat. Rev. Mol. Cell Biol. 9: 730–6.

64. Chhabra, E.S., and H.N. Higgs. 2007. The many faces of actin: matching assembly factors with cellular structures. Nat. Cell Biol. 9: 1110–1121.

65. Small, J.V., T. Stradal, E. Vignal, and K. Rottner. 2002. The lamellipodium: Where motility begins. Trends Cell Biol. 12: 112–120.

66. Lin, C.H., E.M. Espreafico, M.S. Mooseker, and P. Forscher. 1996. Myosin drives retrograde F-actin flow in neuronal growth cones. Neuron. 16: 769–82.

67. Marbach, S., A. Luise Godeau, D. Riveline, J.F. Joanny, and J. Prost. 2015. Theoretical study of actin layers attachment and separation. Eur. Phys. J. E. 38: 1–14.

68. Mogilner, A., and B. Rubinstein. 2005. The Physics of Filopodial Protrusion. Biophys. J. 89: 782–795.

69. Kureishy, N., V. Sapountzi, S. Prag, N. Anilkumar, and J.C. Adams. 2002. Fascins, and their roles in cell structure and function. Bioessays. 24: 350–61.

70. Svitkina, T.M., E.A. Bulanova, O.Y. Chaga, D.M. Vignjevic, S. Kojima, J.M. Vasiliev, and G.G. Borisy. 2003. Mechanism of filopodia initiation by reorganization of a dendritic network. J. Cell Biol. 160: 409–21.

71. Bentley, D., and A. Toroian-Raymond. 1986. Disoriented pathfinding by pioneer neurone growth cones deprived of filopodia by cytochalasin treatment. Nature. 323: 712–715.

72. Verkhovsky, A.B., T.M. Svitkina, and G.G. Borisy. 1999. Self-polarization and directional motility of cytoplasm. Curr. Biol. 9: 11–20.

73. Geiger, B., J.P. Spatz, and A.D. Bershadsky. 2009. Environmental sensing through focal adhesions. Nat. Rev. Mol. Cell Biol. 10: 21–33.

74. Huttenlocher, A., and A.R. Horwitz. 2011. Integrins in cell migration. Cold Spring Harb. Perspect. Biol. 3: 1–16.

75. Balaban, N.Q., U.S. Schwarz, D. Riveline, P. Goichberg, G. Tzur, I. Sabanay, D. Mahalu, S. Safran, A. Bershadsky, L. Addadi, and B. Geiger. 2001. Force and focal

adhesion assembly: a close relationship studied using elastic micropatterned substrates. Nat. Cell Biol. 3: 466–72.

76. Engler, A.J., S. Sen, H.L. Sweeney, and D.E. Discher. 2006. Matrix elasticity directs stem cell lineage specification. Cell. 126: 677–89.

77. Hersel, U., C. Dahmen, and H. Kessler. 2003. RGD modified polymers: biomaterials for stimulated cell adhesion and beyond. Biomaterials. 24: 4385–415.

78. Zhang, X., G. Jiang, Y. Cai, S.J. Monkley, D.R. Critchley, and M.P. Sheetz. 2008. Talin depletion reveals independence of initial cell spreading from integrin activation and traction. Nat. Cell Biol. 10: 1062–8.

79. Zaidel-Bar, R., M. Cohen, L. Addadi, and B. Geiger. 2004. Hierarchical assembly of cell-matrix adhesion complexes. Biochem. Soc. Trans. 32: 416–20.

80. Geiger, B., and K.M. Yamada. 2011. Molecular architecture and function of matrix adhesions. Cold Spring Harb. Perspect. Biol. 3.

81. Linder, S. 2007. The matrix corroded: podosomes and invadopodia in extracellular matrix degradation. Trends Cell Biol. 17: 107–17.

82. Giepmans, B.N.G., and S.C.D. van Ijzendoorn. 2009. Epithelial cell-cell junctions and plasma membrane domains. Biochim. Biophys. Acta. 1788: 820–31.

83. Yeaman, C., K.K. Grindstaff, and W.J. Nelson. 1999. New perspectives on mechanisms involved in generating epithelial cell polarity. Physiol. Rev. 79: 73–98.

84. Fanning, A.S., B.J. Jameson, L.A. Jesaitis, and J.M. Anderson. 1998. The tight junction protein ZO-1 establishes a link between the transmembrane protein occludin and the actin cytoskeleton. J. Biol. Chem. 273: 29745–53.

85. Chiba, H., M. Osanai, M. Murata, T. Kojima, and N. Sawada. 2008. Transmembrane proteins of tight junctions. Biochim. Biophys. Acta. 1778: 588–600.

86. Goodenough, D.A., J.A. Goliger, and D.L. Paul. 1996. Connexins, connexons, and intercellular communication. Annu. Rev. Biochem. 65: 475–502.

87. Hunter, A.W., R.J. Barker, C. Zhu, and R.G. Gourdie. 2005. Zonula occludens-1 alters connexin43 gap junction size and organization by influencing channel accretion. Mol. Biol. Cell. 16: 5686–98.

88. Garrod, D., and M. Chidgey. 2008. Desmosome structure, composition and function. Biochim. Biophys. Acta. 1778: 572–87.

89. Green, K.J., and J.C. Jones. 1996. Desmosomes and hemidesmosomes: structure and function of molecular components. FASEB J. 10: 871–81.

90. Sit, S.-T., and E. Manser. 2011. Rho GTPases and their role in organizing the actin cytoskeleton. J. Cell Sci. 124: 679–83.

91. Wheeler, A.P., and A.J. Ridley. 2004. Why three Rho proteins? RhoA, RhoB, RhoC, and cell motility. Exp. Cell Res. 301: 43–9.

92. Ridley, A.J. 2001. Rho family proteins: coordinating cell responses. Trends Cell Biol. 11: 471–7.

93. Jaffe, A.B., and A. Hall. 2005. Rho GTPases: biochemistry and biology. Annu. Rev. Cell Dev. Biol. 21: 247–69.

94. Boureux, A., E. Vignal, S. Faure, and P. Fort. 2007. Evolution of the Rho family of ras-like GTPases in eukaryotes. Mol. Biol. Evol. 24: 203–16.

95. Roberts, A.W., C. Kim, L. Zhen, J.B. Lowe, R. Kapur, B. Petryniak, A. Spaetti, J.D. Pollock, J.B. Borneo, G.B. Bradford, S.J. Atkinson, M.C. Dinauer, and D.A. Williams. 1999. Deficiency of the hematopoietic cell-specific Rho family GTPase Rac2 is characterized by abnormalities in neutrophil function and host defense. Immunity. 10: 183–96.

96. Kalfa, T.A., S. Pushkaran, N. Mohandas, J.H. Hartwig, V.M. Fowler, J.F. Johnson, C.H. Joiner, D.A. Williams, and Y. Zheng. 2006. Rac GTPases regulate the morphology and deformability of the erythrocyte cytoskeleton. Blood. 108: 3637–45.

97. Heasman, S.J., and A.J. Ridley. 2008. Mammalian Rho GTPases: new insights into their functions from in vivo studies. Nat. Rev. Mol. Cell Biol. 9: 690–701.

98. Etienne-Manneville, S. 2004. Cdc42--the centre of polarity. J. Cell Sci. 117: 1291–300.

99. Genova, J.L., S. Jong, J.T. Camp, and R.G. Fehon. 2000. Functional analysis of Cdc42 in actin filament assembly, epithelial morphogenesis, and cell signaling during Drosophila development. Dev. Biol. 221: 181–94.

100. Gotta, M., M.C. Abraham, and J. Ahringer. 2001. CDC-42 controls early cell polarity and spindle orientation in C. elegans. Curr. Biol. 11: 482–8.

101. Gomes, E.R., S. Jani, and G.G. Gundersen. 2005. Nuclear movement regulated by Cdc42, MRCK, myosin, and actin flow establishes MTOC polarization in migrating cells. Cell. 121: 451–63.

102. Franssila, S. 2010. Introduction to Microfabrication. 2nd ed. Chichester, UK: John Wiley & Sons, Ltd.

103. Qin, D., Y. Xia, and G.M. Whitesides. 2010. Soft lithography for micro- and nanoscale patterning. Nat. Protoc. 5: 491–502.

104. Huang, Y.Y., W. Zhou, K.J. Hsia, E. Menard, J.U. Park, J.A. Rogers, and A.G. Alleyne. 2005. Stamp collapse in soft lithography. Langmuir. 21: 8058–8068.

105. Xia, Y., and G.M. Whitesides. 2001. Self-assembled Monolayer Films: Microcontact Printing. Encycl. Mater. Sci. Technol. : 8309–8314.

106. Riveline, D., and A. Buguin. 2009. Devices and methods for observing the cell division. .

107. Wollrab, V., and D. Riveline. 2012. Devices and methods for observing eukaryotic cells without cell wall. .

108. Riveline, D. 2012. Methods for observing cells with cell wall or invertebrate embryos with oblong eggshell. .

109. Wollrab, V., R. Thiagarajan, A. Wald, K. Kruse, and D. Riveline. 2016. Still and rotating myosin clusters determine cytokinetic ring constriction. Nat. Commun. 7: 11860.

110. Wollrab, V., D. Caballero, R. Thiagarajan, and D. Riveline. 2016. Ordering Single Cells and Single Embryos in 3D Confinement: A New Device for High Content Screening. J. Vis. Exp. 115: 1–15.

111. Szymborska, A., A. De Marco, N. Daigle, V.C. Cordes, J.A.G. Briggs, and J. Ellenberg. 2013. Nuclear pore Scaffold Structure Analyzed by Super-Resolution Microscopy and Particle Averaging. Science (80-.). 341: 655–658.

112. Ravasio, A., S. Vaishnavi, B. Ladoux, and V. Viasnoff. 2015. High-resolution imaging of cellular processes across textured surfaces using an indexed-matched elastomer. Acta Biomater. 14: 53–60.

113. Wilbur, J.L., A. Kumar, H.A. Biebuyck, E. Kim, and G.M. Whitesides. 1996. Microcontact printing of self-assembled monolayers: applications in microfabrication. Nanotechnology. 7: 452–457.

114. Azioune, A., M. Storch, M. Bornens, M. Thery, and M. Piel. 2009. Simple and rapid process for single cell micro-patterning. Lab Chip. 9: 1640–1642.

115. Théry, M., and M. Piel. 2009. Adhesive micropatterns for cells: A microcontact printing protocol. Cold Spring Harb. Protoc. 4: 1–12.

116. Caballero, D., R. Voituriez, and D. Riveline. 2014. Protrusion fluctuations direct cell motion. Biophys. J. 107: 34–42.

117. Tang, X., M. Yakut Ali, and M.T.A. Saif. 2012. A novel technique for micro-patterning proteins and cells on polyacrylamide gels. Soft Matter. 8: 7197.

118. Wong, I., and C.M. Ho. 2009. Surface molecular property modifications for poly(dimethylsiloxane) (PDMS) based microfluidic devices. Microfluid.

Nanofluidics. 7: 291–306.

119. Forsburg, S.L., and N. Rhind. 2006. Basic methods for fission yeast. Yeast. 23: 173–183.

120. 2016. Fission Yeast: A Laboratory Manual. Cold Spring Harbor Laboratory Press.

121. Vavylonis, D., J.-Q. Wu, S. Hao, B. O'Shaughnessy, and T.D. Pollard. 2008. Assembly mechanism of the contractile ring for cytokinesis by fission yeast. Science. 319: 97–100.

122. Riveline, D., and P. Nurse. 2009. "Injecting" yeast. Nat Meth. 6: 513–514.

123. Allen, T.D., S.A. Rutherford, S. Murray, H.S. Sanderson, F. Gardiner, E. Kiseleva, M.W. Goldberg, and S.P. Drummond. 2007. Generation of cell-free extracts of Xenopus eggs and demembranated sperm chromatin for the assembly and isolation of in vitro-formed nuclei for Western blotting and scanning electron microscopy (SEM). Nat. Protoc. 2: 1173–9.

124. Pelham, R.J., and F. Chang. 2002. Actin dynamics in the contractile ring during cytokinesis in fission yeast. Nature. 419: 82–86.

125. Rizvi, S.A., E.M. Neidt, J. Cui, Z. Feiger, C.T. Skau, M.L. Gardel, S.A. Kozmin, and D.R. Kovar. 2009. Identification and characterization of a small molecule inhibitor of formin-mediated actin assembly. Chem. Biol. 16: 1158–68.

126. Nolen, B.J., N. Tomasevic, A. Russell, D.W. Pierce, Z. Jia, C.D. McCormick, J. Hartman, R. Sakowicz, and T.D. Pollard. 2009. Characterization of two classes of small molecule inhibitors of Arp2/3 complex. Nature. 460: 1031–4.

127. Nedeva, I., G. Koripelly, D. Caballero, L. Chièze, B. Guichard, B. Romain, E. Pencreach, J.-M. Lehn, M.-F. Carlier, and D. Riveline. 2013. Synthetic polyamines promote rapid lamellipodial growth by regulating actin dynamics. Nat. Commun. 4: 2165 (1–11).

128. Liu, J., H. Wang, and M.K. Balasubramanian. 2000. A checkpoint that monitors cytokinesis in Schizosaccharomyces pombe. J. Cell Sci. 113: 1223–1230.

129. Pinar, M., P.M. Coll, S.A. Rincón, and P. Pérez. 2008. Schizosaccharomyces pombe Pxl1 is a paxillin homologue that modulates Rho1 activity and participates in cytokinesis. Mol. Biol. Cell. 19: 1727–38.

130. Cortés, J.C.G., J. Ishiguro, A. Durán, and J.C. Ribas. 2002. Localization of the (1,3)β-D-glucan synthase catalytic subunit homologue Bgs1p/Cps1p from fission yeast suggests that it is involved in septation, polarized growth, mating, spore wall formation and spore germination. J. Cell Sci. 115: 4081–4096.

131. Harris, A.R., A. Daeden, and G.T. Charras. 2014. Formation of adherens junctions leads to the emergence of a tissue-level tension in epithelial monolayers. J. Cell

Sci. : 2507–2517.

132. Reffay, M., M.C. Parrini, O. Cochet-Escartin, B. Ladoux, A. Buguin, S. Coscoy, F. Amblard, J. Camonis, and P. Silberzan. 2014. Interplay of RhoA and mechanical forces in collective cell migration driven by leader cells. Nat. Cell Biol. 16: 217–23.

133. Deforet, M., V. Hakim, H.G. Yevick, G. Duclos, and P. Silberzan. 2014. Emergence of collective modes and tri-dimensional structures from epithelial confinement. Nat. Commun. 5: 3747.

134. Thielicke, W., and E.J. Stamhuis. 2014. PIVlab – Towards User-friendly, Affordable and Accurate Digital Particle Image Velocimetry in MATLAB. J. Open Res. Softw. 2: e30.

135. Wollrab, V. 2014. Active Gels in vivo: Patterns and dynamics in cytokinetic rings and their functions in cell division. .

136. Wu, J.Q., J.R. Kuhn, D.R. Kovar, and T.D. Pollard. 2003. Spatial and temporal pathway for assembly and constriction of the contractile ring in fission yeast cytokinesis. Dev. Cell. 5: 723–734.

137. Normand, G., and R.W. King. 2010. Understanding cytokinesis failure. In: Advances in Experimental Medicine and Biology. . pp. 27–55.

138. Wu, J.-Q., and T.D. Pollard. 2005. Counting cytokinesis proteins globally and locally in fission yeast. Science. 310: 310–4.

139. Sirotkin, V., J. Berro, K. Macmillan, L. Zhao, and T.D. Pollard. 2010. Quantitative analysis of the mechanism of endocytic actin patch assembly and disassembly in fission yeast. Mol. Biol. Cell. 21: 2894–904.

140. Mishra, M., J. Kashiwazaki, T. Takagi, R. Srinivasan, Y. Huang, M.K. Balasubramanian, and I. Mabuchi. 2013. In vitro contraction of cytokinetic ring depends on myosin II but not on actin dynamics. Nat. Cell Biol. 15: 853–9.

141. Stachowiak, M.R., C. Laplante, H.F. Chin, B. Guirao, E. Karatekin, T.D. Pollard, and B. O'Shaughnessy. 2014. Mechanism of cytokinetic contractile ring constriction in fission yeast. Dev. Cell. 29: 547–561.

142. Proctor, S.A., N. Minc, A. Boudaoud, and F. Chang. 2012. Contributions of turgor pressure, the contractile ring, and septum assembly to forces in cytokinesis in fission yeast. Curr. Biol. 22: 1601–1608.

143. Spector, I., N.R. Shochet, Y. Kashman, and A. Groweiss. 1983. Latrunculins: novel marine toxins that disrupt microfilament organization in cultured cells. Science. 219: 493–5.

144. Wong, K.C., N.I. Naqvi, Y. Lino, M. Yamamoto, M.K.K. Balasubramanian, Y.

Iino, M. Yamamoto, and M.K.K. Balasubramanian. 2000. Fission yeast Rng3p: an UCS-domain protein that mediates myosin II assembly during cytokinesis. J. Cell Sci. 113: 2421–2432.

145. Lord, M., and T.D. Pollard. 2004. UCS protein Rng3p activates actin filament gliding by fission yeast myosin-II. J. Cell Biol. 167: 315–325.

146. Liu, J., H. Wang, D. McCollum, and M.K. Balasubramanian. 1999. Drc1p/Cps1p, a 1,3-β-glucan synthase subunit, is essential for division septum assembly in Schizosaccharomyces pombe. Genetics. 153: 1193–1203.

147. Reymann, a.-C., R. Boujemaa-Paterski, J.-L. Martiel, C. Guerin, W. Cao, H.F. Chin, E.M. De La Cruz, M. Thery, and L. Blanchoin. 2012. Actin Network Architecture Can Determine Myosin Motor Activity. Science (80-.). 336: 1310–1314.

148. Kruse, K., and F. Jülicher. 2003. Self-organization and mechanical properties of active filament bundles. Phys. Rev. E. Stat. Nonlin. Soft Matter Phys. 67: 051913.

149. Erlenkämper, C., and K. Kruse. 2013. Treadmilling and length distributions of active polar filaments. J. Chem. Phys. 139.

150. Pollard, T.D., and J.-Q. Wu. 2010. Understanding cytokinesis: lessons from fission yeast. Nat. Rev. Mol. Cell Biol. 11: 149–55.

151. Huang, J., Y. Huang, H. Yu, D. Subramanian, A. Padmanabhan, R. Thadani, Y. Tao, X. Tang, R. Wedlich-soldner, and M.K. Balasubramanian. 2012. Nonmedially assembled F-actin cables incorporate into the actomyosin ring in fission yeast. J. Cell Biol. 199: 831–847.

152. Kamasaki, T., M. Osumi, and I. Mabuchi. 2007. Three-dimensional arrangement of F-actin in the contractile ring of fission yeast. J. Cell Biol. 178: 765–771.

153. Turlier, H., B. Audoly, J. Prost, and J.-F. Joanny. 2014. Furrow Constriction in Animal Cell Cytokinesis. Biophys. J. 106: 114–123.

154. Schroeder, T.E. 1972. The contractile ring. II. Determining its brief existence, volumetric changes, and vital role in cleaving Arbacia eggs. J. Cell Biol. 53: 419–34.

155. Takaine, M., O. Numata, and K. Nakano. 2015. An actin-myosin-II interaction is involved in maintaining the contractile ring in fission yeast. J. Cell Sci. 128: 2903–18.

156. Gowrishankar, K., S. Ghosh, S. Saha, R. C., S. Mayor, and M. Rao. 2016. Active Remodeling of Cortical Actin Regulates Spatiotemporal Organization of Cell Surface Molecules. Cell. 149: 1353–1367.

157. Köster, D.V., K. Husain, E. Iljazi, A. Bhat, P. Bieling, R.D. Mullins, M. Rao, and

S. Mayor. 2016. Actomyosin dynamics drive local membrane component organization in an in vitro active composite layer. Proc. Natl. Acad. Sci. 113: E1645–E1654.

158. Luo, W., C. Yu, Z.Z. Lieu, J. Allard, A. Mogilner, M.P. Sheetz, and A.D. Bershadsky. 2013. Analysis of the local organization and dynamics of cellular actin networks. J. Cell Biol. 202: 1057–1073.

159. Mayer, M., M. Depken, J.S. Bois, F. Jülicher, and S.W. Grill. 2010. Anisotropies in cortical tension reveal the physical basis of polarizing cortical flows. Nature. 467: 617–621.

160. Rauzi, M., P.-F. Lenne, and T. Lecuit. 2010. Planar polarized actomyosin contractile flows control epithelial junction remodelling. Nature. 468: 1110–1114.

161. Roh-Johnson, M., G. Shemer, C.D. Higgins, J.H. McClellan, A.D. Werts, U.S. Tulu, L. Gao, E. Betzig, D.P. Kiehart, and B. Goldstein. 2012. Triggering a cell shape change by exploiting preexisting actomyosin contractions. Science. 335: 1232–5.

162. Ono, K., M. Parast, C. Alberico, G.M. Benian, and S. Ono. 2003. Specific requirement for two ADF/cofilin isoforms in distinct actin-dependent processes in Caenorhabditis elegans. J. Cell Sci. 116: 2073–85.

163. Zemel, A., and A. Mogilner. 2009. Motor-induced sliding of microtubule and actin bundles. Phys. Chem. Chem. Phys. 11: 4821–33.

164. Craig, E.M., S. Dey, and A. Mogilner. 2011. The emergence of sarcomeric, graded-polarity and spindle-like patterns in bundles of short cytoskeletal polymers and two opposite molecular motors. J. Phys. Condens. Matter. 23: 374102.

165. Lenz, M., T. Thoresen, M.L. Gardel, and A.R. Dinner. 2012. Contractile units in disordered actomyosin bundles arise from F-actin buckling. Phys. Rev. Lett. 108: 238107.

166. Lenz, M., M.L. Gardel, and A.R. Dinner. 2012. Requirements for contractility in disordered cytoskeletal bundles. New J. Phys. 14: 033037.

167. Lansky, Z., M. Braun, A. Lüdecke, M. Schlierf, P.R. Ten Wolde, M.E. Janson, and S. Diez. 2015. Diffusible crosslinkers generate directed forces in microtubule networks. Cell. 160: 1159–1168.

168. Carvalho, A., A. Desai, and K. Oegema. 2009. Structural Memory in the Contractile Ring Makes the Duration of Cytokinesis Independent of Cell Size. Cell. 137: 926–937.

169. Calvert, M.E.K., G.D. Wright, F.Y. Leong, K.-H. Chiam, Y. Chen, G. Jedd, and M.K. Balasubramanian. 2011. Myosin concentration underlies cell size-dependent

scalability of actomyosin ring constriction. J. Cell Biol. 195: 799–813.

170. Muñoz, J., J.C.G. Cortés, M. Sipiczki, M. Ramos, J.A. Clemente-Ramos, M.B. Moreno, I.M. Martins, P. Pérez, and J.C. Ribas. 2013. Extracellular cell wall β(1,3)glucan is required to couple septation to actomyosin ring contraction. J. Cell Biol. 203: 265–82.

171. Cadou, A., A. Couturier, C. Le Goff, L. Xie, J.R. Paulson, and X. Le Goff. 2013. The Kin1 kinase and the calcineurin phosphatase cooperate to link actin ring assembly and septum synthesis in fission yeast. Biol. Cell. 105: 129–48.

172. Thiyagarajan, S., E.L. Munteanu, R. Arasada, T.D. Pollard, and B. O'Shaughnessy. 2015. The fission yeast cytokinetic contractile ring regulates septum shape and closure. J. Cell Sci. 128: 3672–81.

173. Garner, E.C., R. Bernard, W. Wang, X. Zhuang, D.Z. Rudner, and T. Mitchison. 2011. Coupled, circumferential motions of the cell wall synthesis machinery and MreB filaments in B. subtilis. Science (80-.). 333: 222–5.

174. Nédélec, F.J., T. Surrey, A.C. Maggs, and S. Leibler. 1997. Self-organization of microtubules and motors. Nature. 389: 305–8.

175. Riveline, D., A. Ott, F. Jülicher, D.A. Winkelmann, O. Cardoso, J.J. Lacapère, S. Magnúsdóttir, J.L. Viovy, L. Gorre-Talini, and J. Prost. 1998. Acting on actin: the electric motility assay. Eur. Biophys. J. 27: 403–8.

176. Backouche, F., L. Haviv, D. Groswasser, and A. Bernheim-Groswasser. 2006. Active gels: dynamics of patterning and self-organization. Phys. Biol. 3: 264–73.

177. Bement, W.M. 2002. Actomyosin rings: The riddle of the sphincter. Curr. Biol. 12: R12–R14.

178. Brugués, A., E. Anon, V. Conte, J.H. Veldhuis, M. Gupta, J. Colombelli, J.J. Muñoz, G.W. Brodland, B. Ladoux, and X. Trepat. 2014. Forces driving epithelial wound healing. Nat. Phys. 10: 683–690.

179. Nier, V., M. Deforet, G. Duclos, H.G. Yevick, O. Cochet-Escartin, P. Marcq, and P. Silberzan. 2015. Tissue fusion over nonadhering surfaces. Proc. Natl. Acad. Sci. 112: 9546–9551.

180. Eisenhoffer, G.T., P.D. Loftus, M. Yoshigi, H. Otsuna, C.-B. Chien, P.A. Morcos, and J. Rosenblatt. 2013. Crowding induces live cell extrusion to maintain homeostatic cell numbers in epithelia. Nature. 484: 546–549.

181. Marinari, E., a Mehonic, S. Curran, J. Gale, T. Duke, and B. Baum. 2012. Live-cell delamination counterbalances epithelial growth to limit tissue overcrowding. Nature. 484: 542–545.

182. Kiehart, D.P., C.G. Galbraith, K.A. Edwards, W.L. Rickoll, and R.A. Montague.

2000. Multiple forces contribute to cell sheet morphogenesis for dorsal closure in Drosophila. J. Cell Biol. 149: 471–490.

183. Rousso, T., E.D. Schejter, and B.-Z. Shilo. 2016. Orchestrated content release from Drosophila glue-protein vesicles by a contractile actomyosin network. Nat. Cell Biol. 18: 181–90.

184. Loisel, T.P., R. Boujemaa, D. Pantaloni, and M.F. Carlier. 1999. Reconstitution of actin-based motility of Listeria and Shigella using pure proteins. Nature. 401: 613–6.

185. Bernheim-Groswasser, A., S. Wiesner, R.M. Golsteyn, M.-F. Carlier, and C. Sykes. 2002. The dynamics of actin-based motility depend on surface parameters. Nature. 417: 308–311.

186. Subramanian, D., J. Huang, M. Sevugan, R.C. Robinson, M.K. Balasubramanian, and X. Tang. 2013. Insight into actin organization and function in cytokinesis from analysis of fission yeast mutants. Genetics. 194: 435–446.

187. Wessells, N.K., B.S. Spooner, J.F. Ash, M.O. Bradley, M.A. Luduena, E.L. Taylor, J.T. Wrenn, and K. Yamada. 1971. Microfilaments in cellular and developmental processes. Science. 171: 135–43.

188. Bubb, M.R., A.M.J. Senderowicz, E.A. Sausville, K.L.K. Duncan, and E.D. Korn. 1994. Jasplakinolide, a cytotoxic natural product, induces actin polymerization and competitively inhibits the binding of phalloidin to F-actin. J. Biol. Chem. 269: 14869–14871.

189. Oriol-Audit, C. 1978. Polyamine-Induced Actin Polymerization. Eur. J. Biochem. 87: 371–376.

190. Oriol-Audit, C., M.W. Hosseini, and J.M. Lehn. 1985. “Superpolyamines”. Macrocyclic polyamines induce highly efficient actin polymerization. Eur J Biochem. 151: 557–559.

191. Herbst, E.J., and E.E. Snell. 1949. Putrescine and related compounds as growth factors for Hemophilus parainfluenzae 7991. J. Biol. Chem. 181: 47–54.

192. Rosenthal, S.M., and C.W. Tabor. 1956. The pharmacology of spermine and spermidine; distribution and excretion. J. Pharmacol. Exp. Ther. 116: 131–8.

193. Pohjanpelto, P., and A. Raina. 1972. Identification of a Growth Factor produced by Human Fibroblasts in vitro as Putrescine. Nature, Publ. online 23 Febr. 1972; | doi10.1038/10.1038/newbio235247a0. 235: 247–9.

194. Janne, J., L. Alhonen, and P. Leinonen. 1991. Polyamines: from molecular biology to clinical applications. Ann. Med. 23: 241–259.

195. Carlier, M.F., G.K. Koripelly, J.M. Lehn, I. Nedeva, and D. Riveline. 2014.

Branched or macrocyclic polyamines and uses thereof. WO2014029888 A3.

196. Riveline, D., R. Thiagarajan, J.M. Lehn, and M.F. Carlier. 2014. Synthetic polyamines: new compounds specific to actin dynamics for mammalian cell and fission yeast. Bioarchitecture. 4: 144–148.

197. Svitkina, T.M., A.B. Verkhovsky, K.M. McQuade, and G.G. Borisy. 1997. Analysis of the actin-myosin II system in fish epidermal keratocytes: Mechanism of cell body translocation. J. Cell Biol. 139: 397–415.

198. Small, J. V, S. Auinger, M. Nemethova, S. Koestler, K.N. Goldie, A. Hoenger, and G.P. Resch. 2008. Unravelling the structure of the lamellipodium. In: Journal of Microscopy. . pp. 479–485.

199. Wu, J.-Q., V. Sirotkin, D.R. Kovar, M. Lord, C.C. Beltzner, J.R. Kuhn, and T.D. Pollard. 2006. Assembly of the cytokinetic contractile ring from a broad band of nodes in fission yeast. J. Cell Biol. 174: 391–402.

200. Nakano, K., and I. Mabuchi. 2006. Actin-depolymerizing protein Adf1 is required for formation and maintenance of the contractile ring during cytokinesis in fission yeast. Mol. Biol. Cell. 17: 1933–45.

201. Kovar, D.R., J.-Q. Wu, and T.D. Pollard. 2005. Profilin-mediated competition between capping protein and formin Cdc12p during cytokinesis in fission yeast. Mol. Biol. Cell. 16: 2313–24.

202. Yang, C., L. Czech, S. Gerboth, S. Kojima, G. Scita, and T. Svitkina. 2007. Novel Roles of Formin mDia2 in Lamellipodia and Filopodia Formation in Motile Cells. PLoS Biol. 5: e317.

203. Matsudaira, P. 1994. Actin crosslinking proteins at the leading edge. Semin. Cell Biol. 5: 165–174.

204. Ponti, A., M. Machacek, S.L. Gupton, C.M. Waterman-Storer, and G. Danuser. 2004. Two distinct actin networks drive the protrusion of migrating cells. Science. 305: 1782–6.

205. Comelles, J., D. Caballero, R. Voituriez, V. Hortigüela, V. Wollrab, A.L. Godeau, J. Samitier, E. Martínez, and D. Riveline. 2014. Cells as active particles in asymmetric potentials: Motility under external gradients. Biophys. J. 107: 1513–1522.

206. Reig, G., E. Pulgar, and M.L. Concha. 2014. Cell migration: from tissue culture to embryos. Development. 141: 1999–2013.

207. Petrie, R.J., A.D. Doyle, and K.M. Yamada. 2009. Random versus directionally persistent cell migration. Nat. Rev. Mol. Cell Biol. 10: 538–549.

208. Faure-André, G., P. Vargas, M.-I. Yuseff, M. Heuzé, J. Diaz, D. Lankar, V. Steri, J.

Manry, S. Hugues, F. Vascotto, J. Boulanger, G. Raposo, M.-R. Bono, M. Rosemblatt, M. Piel, and A.-M. Lennon-Duménil. 2008. Regulation of dendritic cell migration by CD74, the MHC class II-associated invariant chain. Science (80-.). 322: 1705–10.

209. Vogel, V., and M. Sheetz. 2006. Local force and geometry sensing regulate cell functions. Nat. Rev. Mol. Cell Biol. 7: 265–275.

210. Jiang, X., D.A. Bruzewicz, A.P. Wong, M. Piel, and G.M. Whitesides. 2005. Directing cell migration with asymmetric micropatterns. Proc. Natl. Acad. Sci. U. S. A. 102: 975–8.

211. Kumar, G., C.C. Ho, and C.C. Co. 2007. Guiding cell migration using one-way micropattern arrays. Adv. Mater. 19: 1084–1090.

212. Mahmud, G., C.J. Campbell, K.J.M. Bishop, Y.A. Komarova, O. Chaga, S. Soh, S. Huda, K. Kandere-Grzybowska, and B.A. Grzybowski. 2009. Directing cell motions on micropatterned ratchets. Nat Phys. 5: 606–612.

213. Kumar, G., C.C. Co, and C.C. Ho. 2011. Steering cell migration using microarray amplification of natural directional persistence. Langmuir. 27: 3803–3807.

214. Luxton, G.W.G., and G.G. Gundersen. 2011. Orientation and function of the nuclear-centrosomal axis during cell migration. Curr. Opin. Cell Biol. 23: 579–588.

215. Feynman, R.P., R.B. Leighton, and M. Sands. 1989. The Feynman Lectures on Physics. .

216. Riveline, D. 2013. “Single molecule”: theory and experiments, an introduction. J. Nanobiotechnology. 11 Suppl 1: S1.

217. Bier, M. 1997. Brownian ratchets in physics and biology. Contemp. Phys. 38: 371–379.

218. Jülicher, F., A. Ajdari, J. Prost, and F. Julicher. 1997. Modeling molecular motors. Rev. Mod. Phys. 69: 1269–1282.

219. Hänggi, P., and F. Marchesoni. 2009. Artificial Brownian motors: Controlling transport on the nanoscale. Rev. Mod. Phys. 81: 387–442.

220. Prost, J., J.J.F. Chauwin, L. Peliti, and A. Ajdari. 1994. Asymmetric pumping of particles. Phys. Rev. Lett. 72: 2652–2655.

221. Chauwin, J.-F., A. Ajdari, and J. Prost. 1994. Force-Free Motion in Asymmetric Structures: A Mechanism without Diffusive Steps. EPL (Europhysics Lett. 27: 421–426.

222. Rousselet, J., L. Salome, A. Ajdari, and J. Prost. 1994. Directional motion of brownian particles induced by a periodic asymmetric potential. Nature. 370: 446–

448.

223. Gorre-Talini, L., and P. Silberzan. 1997. Force-free motion of a mercury drop alternatively submitted to shifted asymmetric potentials. J. Phys. I. 7: 1475–1485.

224. Zheng, J.Q., J.J. Wan, and M.M. Poo. 1996. Essential role of filopodia in chemotropic turning of nerve growth cone induced by a glutamate gradient. J. Neurosci. 16: 1140–1149.

225. Le Berre, M., Y.-J. Liu, J. Hu, P. Maiuri, O. Bénichou, R. Voituriez, Y. Chen, and M. Piel. 2013. Geometric friction directs cell migration. Phys. Rev. Lett. 111: 198101 (1–5).

226. Harms, B.D., G.M. Bassi, A.R. Horwitz, and D. Lauffenburger. 2005. Directional persistence of EGF-induced cell migration is associated with stabilization of lamellipodial protrusions. Biophys. J. 88: 1479–88.

227. Weiger, M.C., S. Ahmed, E.S. Welf, and J.M. Haugh. 2010. Directional persistence of cell migration coincides with stability of asymmetric intracellular signaling. Biophys. J. 98: 67–75.

228. Krause, M., and A. Gautreau. 2014. Steering cell migration: lamellipodium dynamics and the regulation of directional persistence. Nat. Rev. Mol. Cell Biol. 15: 577–590.

229. Chauwin, J.-F., A. Ajdari, and J. Prost. 1995. Current Reversal in Asymmetric Pumping. Europhys. Lett. 32: 373–378.

230. Bénazéraf, B., P. Francois, R.E. Baker, N. Denans, C.D. Little, and O. Pourquié. 2010. A random cell motility gradient downstream of FGF controls elongation of an amniote embryo. Nature. 466: 248–252.

231. Donà, E., J.D. Barry, G. Valentin, C. Quirin, A. Khmelinskii, A. Kunze, S. Durdu, L.R. Newton, A. Fernandez-Minan, W. Huber, M. Knop, and D. Gilmour. 2013. Directional tissue migration through a self-generated chemokine gradient. Nature. 503: 285–9.

232. Weijer, C.J. 2009. Collective cell migration in development. J. Cell Sci. 122: 3215–3223.

233. Friedl, P., and D. Gilmour. 2009. Collective cell migration in morphogenesis, regeneration and cancer. Nat. Rev. Mol. Cell Biol. 10: 445–457.

234. Sawyer, J.M., J.R. Harrell, G. Shemer, J. Sullivan-Brown, M. Roh-Johnson, and B. Goldstein. 2010. Apical constriction: A cell shape change that can drive morphogenesis. Dev. Biol. 341: 5–19.

235. Aigouy, B., R. Farhadifar, D.B. Staple, A. Sagner, J.C. Roper, F. Julicher, and S. Eaton. 2010. Cell Flow Reorients the Axis of Planar Polarity in the Wing

Epithelium of Drosophila. Cell. 142: 773–786.

236. Martin, A.C., and B. Goldstein. 2014. Apical constriction: themes and variations on a cellular mechanism driving morphogenesis. Development. 141: 1987–1998.

237. Gupta, T., and A. Giangrande. Collective cell migration: all for one and one for all. J. Neurogenet. 28: 190–8.

238. Scarpa, E., and R. Mayor. 2016. Collective cell migration in development. J. Cell Biol. 212: 143–155.

239. Zhang, H., and M. Labouesse. 2012. Signalling through mechanical inputs: a coordinated process. J. Cell Sci. 125: 3039–49.

240. Kruse, K., and F. Jülicher. 2005. Oscillations in cell biology. Curr. Opin. Cell Biol. 17: 20–26.

241. Martin, A.C., M. Kaschube, and E.F. Wieschaus. 2009. Pulsed contractions of an actin-myosin network drive apical constriction. Nature. 457: 495–9.

242. Solon, J., A. Kaya-Çopur, J. Colombelli, and D. Brunner. 2009. Pulsed Forces Timed by a Ratchet-like Mechanism Drive Directed Tissue Movement during Dorsal Closure. Cell. 137: 1331–1342.

243. Rauzi, M., U. Krzic, T.E. Saunders, M. Krajnc, P. Ziherl, L. Hufnagel, and M. Leptin. 2015. Embryo-scale tissue mechanics during Drosophila gastrulation movements. Nat. Commun. 6: 8677.

244. Segrè, P., E. Herbolzheimer, and P. Chaikin. 1997. Long-Range Correlations in Sedimentation. Phys. Rev. Lett. 79: 2574–2577.

245. Angelini, T.E., E. Hannezo, X. Trepat, J.J. Fredberg, and D.A. Weitz. 2010. Cell migration driven by cooperative substrate deformation patterns. Phys. Rev. Lett. 104: 1–4.

246. Petitjean, L., M. Reffay, E. Grasland-Mongrain, M. Poujade, B. Ladoux, A. Buguin, and P. Silberzan. 2010. Velocity fields in a collectively migrating epithelium. Biophys. J. 98: 1790–1800.

247. Doxzen, K., S.R.K. Vedula, M.C. Leong, H. Hirata, N.S. Gov, A.J. Kabla, B. Ladoux, and C.T. Lim. 2013. Guidance of collective cell migration by substrate geometry. Integr. Biol. 5: 1026.

248. Cochet-Escartin, O., J. Ranft, P. Silberzan, and P. Marcq. 2014. Border forces and friction control epithelial closure dynamics. Biophys. J. 106: 65–73.

249. Ravasio, A., I. Cheddadi, T. Chen, T. Pereira, H.T. Ong, C. Bertocchi, A. Brugues, A. Jacinto, A.J. Kabla, Y. Toyama, X. Trepat, N. Gov, L. Neves de Almeida, and B. Ladoux. 2015. Gap geometry dictates epithelial closure efficiency. Nat.

Commun. 6: 7683.

250. Vedula, S.R.K., H. Hirata, M.H. Nai, A. Brugués, Y. Toyama, X. Trepat, C.T. Lim, and B. Ladoux. 2013. Epithelial bridges maintain tissue integrity during collective cell migration. Nat. Mater. 13: 87–96.

251. Palecek, S.P., J.C. Loftus, M.H. Ginsberg, D.A. Lauffenburger, and A.F. Horwitz. 1997. Integrin-ligand binding properties govern cell migration speed through cell-substratum adhesiveness. Nature. 385: 537–40.

252. Vedula, S.R.K., M.C. Leong, T.L. Lai, P. Hersen, A.J. Kabla, C.T. Lim, and B. Ladoux. 2012. Emerging modes of collective cell migration induced by geometrical constraints. Proc. Natl. Acad. Sci. U. S. A. 109: 12974–9.

253. Lee, H.-H., S.-C. Tien, T.-S. Jou, Y.-C. Chang, J.-G. Jhong, and Z.-F. Chang. 2010. Src-dependent phosphorylation of ROCK participates in regulation of focal adhesion dynamics. J. Cell Sci. 123: 3368–77.

254. Etournay, R., M. Popović, M. Merkel, A. Nandi, C. Blasse, B. Aigouy, H. Brandl, G. Myers, G. Salbreux, F. Jülicher, and S. Eaton. 2015. Interplay of cell dynamics and epithelial tension during morphogenesis of the Drosophila pupal wing. Elife. 4: 1–51.

255. Poujade, M., E. Grasland-Mongrain, A. Hertzog, J. Jouanneau, P. Chavrier, B. Ladoux, A. Buguin, and P. Silberzan. 2007. Collective migration of an epithelial monolayer in response to a model wound. Proc. Natl. Acad. Sci. U. S. A. 104: 15988–93.

256. Saw, T.B., S. Jain, B. Ladoux, and C.T. Lim. 2015. Mechanobiology of Collective Cell Migration. Cell. Mol. Bioeng. 8: 3–13.

257. Zehnder, S.M., M. Suaris, M.M. Bellaire, and T.E. Angelini. 2015. Cell volume fluctuations in MDCK monolayers. Biophys. J. 108: 247–250.

258. Zehnder, S.M., M.K. Wiatt, J.M. Uruena, A.C. Dunn, W.G. Sawyer, and T.E. Angelini. 2015. Multicellular density fluctuations in epithelial monolayers. Phys. Rev. E - Stat. Nonlinear, Soft Matter Phys. 92: 1–8.

259. Notbohm, J., S. Banerjee, K.J.C. Utuje, B. Gweon, H. Jang, Y. Park, J. Shin, J.P. Butler, J.J. Fredberg, and M.C. Marchetti. 2016. Cellular Contraction and Polarization Drive Collective Cellular Motion. Biophys. J. 110: 2729–2738.

260. Serra-Picamal, X., V. Conte, R. Vincent, E. Anon, D.T. Tambe, E. Bazellieres, J.P. Butler, J.J. Fredberg, and X. Trepat. 2012. Mechanical waves during tissue expansion. Nat. Phys. 8: 628–634.

261. Cohen, D.J., W. James Nelson, and M.M. Maharbiz. 2014. Galvanotactic control of collective cell migration in epithelial monolayers. Nat. Mater. 13: 409–417.

262. Murrell, M., R. Kamm, and P. Matsudaira. 2011. Substrate viscosity enhances correlation in epithelial sheet movement. Biophys. J. 101: 297–306.

263. Angelini, T.E., E. Hannezo, X. Trepat, M. Marquez, J.J. Fredberg, and D.A. Weitz. 2011. Glass-like dynamics of collective cell migration. Proc Natl Acad Sci U S A. 108: 4714–4719.

264. Kumar, S., A. Kapoor, S. Desai, M.M. Inamdar, and S. Sen. 2016. Proteolytic and non-proteolytic regulation of collective cell invasion: tuning by ECM density and organization. Sci. Rep. 6: 19905.

265. Soumya, S.S., A. Gupta, A. Cugno, L. Deseri, K. Dayal, D. Das, S. Sen, and M.M. Inamdar. 2015. Coherent Motion of Monolayer Sheets under Confinement and Its Pathological Implications. PLoS Comput. Biol. 11: 1–30.

266. Heisenberg, C.P., and Y. Bellaïche. 2013. Forces in tissue morphogenesis and patterning. Cell. 153.

267. Das, T., K. Safferling, S. Rausch, N. Grabe, H. Boehm, and J.P. Spatz. 2015. A molecular mechanotransduction pathway regulates collective migration of epithelial cells. Nat Cell Biol. 17: 276–287.

268. Blanchard, G.B., S. Murugesu, R.J. Adams, A. Martinez-Arias, and N. Gorfinkiel. 2010. Cytoskeletal dynamics and supracellular organisation of cell shape fluctuations during dorsal closure. Development. 137: 2743–52.

269. Zhang, H., F. Landmann, H. Zahreddine, D. Rodriguez, M. Koch, and M. Labouesse. 2012. A tension-induced mechanotransduction pathway promotes epithelial morphogenesis. Nature. 470: 99–103.

270. Fernandez-Gonzalez, R., and J. a Zallen. 2011. Oscillatory behaviors and hierarchical assembly of contractile structures in intercalating cells. Phys. Biol. 8: 045005.

271. Sawyer, J.K., W. Choi, K.-C. Jung, L. He, N.J. Harris, and M. Peifer. 2011. A contractile actomyosin network linked to adherens junctions by Canoe/afadin helps drive convergent extension. Mol. Biol. Cell. 22: 2491–508.

272. Jülicher, F., and J. Prost. 1997. Spontaneous Oscillations of Collective Molecular Motors. Phys. Rev. Lett. 78: 4510–4513.

273. Kumar, A., T. Gupta, S. Berzsenyi, and A. Giangrande. 2015. N-cadherin negatively regulates collective Drosophila glial migration through actin cytoskeleton remodeling. J. Cell Sci. 128: 900–12.

274. Maître, J.-L., H. Turlier, R. Illukkumbura, B. Eismann, R. Niwayama, F. Nédélec, and T. Hiiragi. 2016. Asymmetric division of contractile domains couples cell positioning and fate specification. Nature. 536: 344–348.

10. Appendix

10.1 Directed cell migration by adhesive ratchets and predicting direction reversal

In this section, the expressions obtained for "attachment area" of protrusions on separated triangles are explained in detail.

(i) In the case of separated triangles, the attachment area for the protrusions is given by a semi-circle overlapping on the neighboring triangle (Fig. 10.1 a). For simplicity, we approximate the curvature of the circle to a straight line, so that the attachment area resembles a trapezoid (Fig. 10.1 a). With this assumption, we obtain the expression for protrusion attachment area as follows:

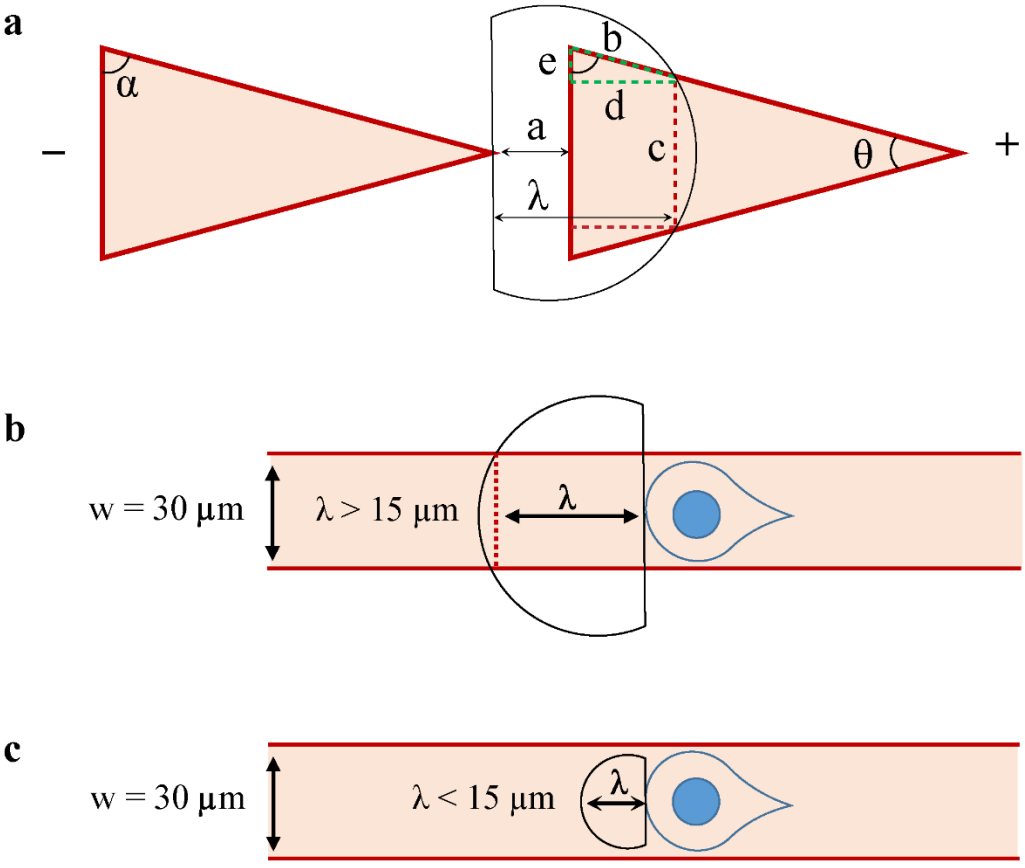

Figure 10.1. Schematic of ratchet configuration with gap distance (a) and 'line' like condition (b) and (c). In (b), the protrusion lengths are assumed to be larger than the line width ($\lambda > 15$), and in (c) the protrusion lengths are assumed to be less than the line width ($\lambda < 15$).

In Figure 10.1, base of the triangle equals 30 μm, θ – the vertex angle equals 16° and α – the base angle equals 82°. These values are obtained from the experimental design of the micropattern. λ – denotes the protrusion length, a – denotes the gap distance, c – denotes the approximated side of the trapezoid (indicated by the red dotted line close to the curvature of the semi-circle). In the triangle within trapezoid (marked by green dotted lines), b – denotes the hypotenuse and other two sides are denoted by 'c' and 'e'.

In the setup described in Fig. 10.1 a:

$$d = \lambda - a \qquad (10.1)$$

$$b = \frac{d}{\sin\theta} \qquad (10.2)$$

$$e = \sqrt{b^2 - d^2} \qquad (10.3)$$

$$c = 30 - 2e \qquad (10.4)$$

By substitutions,

$$c = 30 - 2\left(\sqrt{\left(\frac{\lambda - a}{\sin\theta}\right)^2 - (\lambda - a)^2}\right) \qquad (10.5)$$

The area of the trapezoid in Fig. 10.1 a will be:

$$A_{trapezoid} = \left(\frac{30 + c}{2}\right).(\lambda - a) \qquad (10.6)$$

By substituting (10.5) in (10.6), the attachment area in the '+' direction (A^{+}_{probed} – expression 6.6) can be obtained for triangles with separation.

$$A^{+}_{probed} = \left(30 - (\lambda - a).\sqrt{\frac{1 - sin^2(\alpha)}{sin^2(\alpha)}}\right).(\lambda - a)$$

The same expression applies for A^{+}_{probed}, in overlap triangles. The expression for attachment area in the '–' direction in overlap triangles A^{-}_{probed}, is obtained in a similar manner.

(ii) Next, we define the A^{i}_{probed} obtained in a 'line' like condition, i.e. 75 % overlap condition. In this condition, we assume the setup to be a perfect line, with a width similar to the base of the triangle (30 μm) (Fig. 10.1 b and c). λ – denotes the protrusion length. Assuming that the protrusions arise from a center point on the edge of the cell, A^{i}_{probed} is approximated as: (i) a rectangle $(30.\lambda)$, if the protrusion length is larger than 15 μm (half-width of the line) (Fig. 10.1 b). (ii) a semi-circle $(\pi.\lambda^2/2)$, if the protrusion length is smaller than 15 μm (Fig. 10.1 c).

10.2 Spontaneous pulsatile domains in epithelial monolayers

10.2.1 Winding number for finding centers

In order to find the critical points, we first plotted the streamlines of the velocity fields. Streamlines are curves which trace the tangent of the local velocity vector at any instant of time. Streamlines are tools for visualizing the instantaneous characteristic of the velocity field. For example, vectors corresponding to flows in a particular direction. After plotting streamlines of the velocity field in the monolayer, we use them to find the nature of critical points. The nature of critical point might correspond to two scenarios: (i) vorticity or source/sink like behavior and (ii) saddle (two vectors with opposite direction crossing the critical point). This nature can be identified by finding the index of the critical point.

The index of a critical point is given by Winding number. Winding number refers to the number of revolutions made by a closed curve around a critical point, with a smallest possible radius. The critical point will be the center of revolution and the closed curve can be defined by the streamlines. The winding number of a closed curve will be given by:

$$W = \int \frac{V_1.dV_2/ds - V_2.dV_1/ds}{V_1^2 + V_2^2}\, ds \qquad (10.7)$$

where, W represents Winding number, V_1 and V_2 correspond to the velocity components of x and y, s corresponds to the length of the curve defining the region, within which the critical point is located. With this winding number, the index of critical point can be

identified. Further, we developed a MATLAB code to identify the nature of critical points, where vorticity or source/sink like behaviors are marked as '+1' and saddle like regions are marked as '– 1'. In other words, when the regions defined by the closed curve contains a critical point, the region is denoted by '+1'. In contrary, if the curve passes through a critical point, then the region is denoted by '– 1'.

10.2.2 Directional flows on fibronectin ratchets

Motivated by the effect of friction on pulsation characteristics, we were curious to know if directionality can be introduced into collective dynamics by ratchet mechanism, as described for single cells in the ratchetaxis section (Section 6). In order to test this, we coated the substrate with fibronectin triangle of similar dimensions used in the ratchetaxis section (Section 6). We found that, on reaching confluency the monolayer exhibited two different dynamics: pulsations and directional flows (Movie 7.15). The presence of directional flows in a confluent monolayer was surprising, since we never observed flows in the monolayer except in (cytoskeletal inhibitor) drug washout conditions. These flows were suggestive of a possible "collective ratchetaxis" due to the fibronectin (triangle) ratchets. However, the flows were directed in both directions: funneling edge and the base of triangle. We hypothesize that by optimally configuring the size of triangles to match the correlation length of the system (MDCK monolayer), flow characteristics (direction, coherence) can be altered. In that case, the mechanism by which fibronectin triangles lead to directional flows can be explored. An interesting experiment along this line would be to visualize the localization of planar cell polarity proteins during the flows induced by fibronectin triangles.

In order to dramatically vary the effect of the fibronectin triangles, we passivated the regions other than fibronectin triangles with PEG. After seeding cells on these substrates, we found that cells first grew on triangles making a connected line of MDCK cells (Movie 7.16). Then, the cells started exploring the PEG region with filopodia-like protrusions until they came in contact with the cells from the neighboring triangle line. After making contact, the cells eventually bridge the PEG region to form a monolayer. The observation of filopodia like protrusions was surprising since protrusions in MDCK monolayer resemble more the lamellipodia as usually found in leader cells. This shows that changes in cell-substrate interactions can lead to different morphologies of cells. After reaching confluency the cells also exhibited pulsations (Movie 7.18). These observations further support the role of cell-substrate interaction in deciding tissue dynamics.

10.3 List of Abbreviations

Abbreviation	Corresponding name
PDMS	Polydimethylsiloxane
UV	Ultra violet radiation
TMCS	Trimethylchlorosilane
CS	Coverslip
NPC	Nuclear pore complex
GFP	Green fluorescent protein
EGFP	Enhanced green fluorescent protein
FN	Fibronectin
pLL-g-PEG	Poly-L-Lysine grafted with polyethylene glycol
PBS	Phosphate buffered saline
YE+5S	Yeast Extract + 5 Supplements
EMM	Edinburgh minimal medium
DMSO	Dimethyl Sulfoxide
OD	Optical density
CHD	Calponin homology domain
RLC	Regulatory light chain
MHC	Myosin heavy chain
Lat A	Latrunculin A
Con A	Concanavalin A
SMIFH2	Small molecule inhibitor of formin homology domain 2
MPA	Macrocyclic polyamine

BPA	Branched polyamine
Arp2/3	Actin related protein2/3
NIH3T3 cells	National institute of health 3T3 cells
MDCK cells	Madin-Darby Canine Kidney cells
FBS	Fetal bovine serum
BCS	Bovine albumin serum
DMEM	Dulbecco's modified eagle medium
L-15	Leibovitz-15
Pen-Strep	Penicillin-Streptomycin
EDTA	Ethylenediaminetetraacetic acid
ATCC	American type cell culture
ECM	Extracellular matrix
PFA	Paraformaldehyde
BSA	Bovine Serum Albumin
DAPI	4',6-Diamidino-2-phenylindole dihydrochloride
ROCK	Rho Kinase
RT	Room Temperature
CCD	Charge-coupled device
EM	Electron microscopy
GEF	Guanine nucleotide exchange factor
PMT	Photomultiplier tube

10.4 List of products

Product name	Product reference
Silicon wafer	Si-Mat
SU-8	MicroChem
SU-8 developer	Chimie Tech Services (DevSU8/4)
PDMS - Sylgard 184	Dow Corning (DC184-1.1, 0002-01-000032)
Photomask	SELBA
Mask aligner	SUSS MicroTec (MJB3)
Oxygen Plasma cleaner	Diener Electronic (Zepto B)
Spin coater	Laurell Technologies (WS-400B-6NPP/Lite)
My-134 / Bio-134-1	MyPolymer
(3-Mercaptopropyl)trimethoxysilane	Fluorochem (S10475)
TriMethylChloroSilane (TMCS)	Sigma Aldrich (C72854)
Sulphuric acid	Sigma Aldrich (258105)
Hydrogen peroxide	Sigma Aldrich
pLL-g-PEG	SuSoS AG
Yeast extract media-YES (Agar)	MP Biomedicals (4101-732)
Yeast extract media-YES (Media)	MP Biomedicals (4101-522)
Edinburgh minimal media-EMM	MP Biomedicals (4110-012)
EMM supplements	MP Biomedicals (4104-012)

Dimethyl sulfoxide (DMSO)	Sigma Aldrich (D8418)
DMEM	Invitrogen Gibco (12007559)
BCS	Sigma Aldrich (C8056)
FBS	Thermo Fisher Scientific HyClone (10309433)
Penicillin-Streptomycin antibiotics	Invitrogen-Thermo Fisher Scientific (11548876)
Trypsin-EDTA	Invitrogen-Thermo Fisher Scientific (11570626)
Leibovitz L-15	Invitrogen-Thermo Fisher Scientific (11540556)
Latrunculin A	Sigma Aldrich (L5163)
(-) Blebbistatin	Sigma Aldrich (B0560)
SMIFH2	Sigma Aldrich (S4826)
CK-636	Sigma Aldrich (C7374)
CK-666	Sigma Aldrich (SML0006)
C3-transferrase	Cytoskeleton Inc (CT03)
Y-27632	Sigma Aldrich (Y0503)
Nocodazole	Sigma Aldrich (M1404)
PBS	Invitrogen Gibco (11530486)
TRITC Fibronectin	Cytoskeleton Inc (FNR01)
HiLyte 488 Fibronectin	Cytoskeleton Inc (FNR02)
Geneticin	Invitrogen-Thermo Fisher Scientific (11548616)
Puromycin	Invitrogen-Thermo Fisher Scientific

	(12122530)
Mineral oil	Sigma Aldrich (M8410)
Polystyrene, film (25 μm)	Good Fellow (ST311025)
Parafilm	Bemis (PM-999)

10.5 Products used for immunostaining

Product name	**Product reference**
PFA (Paraformaldehyde)	Sigma Aldrich (P6148)
BSA (Bovine Serum Albumin)	Sigma Aldrich (A2153)
Triton	Sigma Aldrich (93443)
Glycerol	Sigma Aldrich (G2025)
Phalloidin AlexaFluor 488	Invitrogen-Thermo Fisher Scientific (A12379)
Phalloidin AlexaFluor 546	Invitrogen-Thermo Fisher Scientific (A22283)
AlexaFluor 488 (anti-rabbit)	Molecular Probes (A-11034)
AlexaFluor 647 (anti-rabbit)	Molecular Probes-Thermo Fisher Scientific (A-21245)
Cy3 (anti-rabbit)	Jackson ImmunoResearch (111-166-047)
Cy3 (anti-mouse)	Jackson ImmunoResearch (115-165-146)
DAPI (4',6-Diamidino-2-phenylindole dihydrochloride)	Sigma Aldrich (32670)
Hoechst 33342	Thermo Fisher Scientific (10150888)

10.6 Published articles

1. Wollrab, V., D. Caballero, R. Thiagarajan and D. Riveline. Ordering single cells and single embryos in 3D confinement: A new device for high content screening. Journal of Visualized Experiments. In Press.

2. Wollrab, V., R. Thiagarajan, A. Wald, K. Kruse and D. Riveline. 2016. Still and rotating myosin clusters as determinants for cytokinetic ring constriction. Nat. Commun. 7:11860 (1-9).

3. Riveline, D., R. Thiagarajan, J. M. Lehn, and M. F. Carlier. 2014. Synthetic polyamines: new compounds specific to actin dynamics for mammalian cell and fission yeast. Bioarchitecture 4:144-148.

Video Article

Ordering Single Cells and Single Embryos in 3D Confinement: A New Device for High Content Screening

Viktoria Wollrab[1,2], David Caballero[1,2], Raghavan Thiagarajan[1,2], Daniel Riveline[1,2]

[1]Laboratory of Cell Physics, Institut de Science et d'Ingénierie Supramoléculaires (ISIS), CNRS and Université de Strasbourg

[2]Development and Stem Cells Program, Institut de Génétique et de Biologie Moléculaire et Cellulaire (IGBMC), CNRS and Université de Strasbourg

Correspondence to: Daniel Riveline at riveline@unistra.fr

URL: http://www.jove.com/video/51880
DOI: doi:10.3791/51880

Keywords: Bioengineering, Issue 115, Microcavities, Replica Molding, Microfabrication, High-content screening, 3-Dimensions, Single Cells, Nucleus, Golgi, Cytokinetic Ring.

Date Published: 9/18/2016

Citation: Wollrab, V., Caballero, D., Thiagarajan, R., Riveline, D. Ordering Single Cells and Single Embryos in 3D Confinement: A New Device for High Content Screening. *J. Vis. Exp.* (115), e51880, doi:10.3791/51880 (2016).

Abstract

Biological cells are usually observed on flat (2D) surfaces. This condition is not physiological, and phenotypes and shapes are highly variable. Screening based on cells in such environments have therefore serious limitations: cell organelles show extreme phenotypes, cell morphologies and sizes are heterogeneous and/or specific cell organelles cannot be properly visualized. In addition, cells *in vivo* are located in a 3D environment; in this situation, cells show different phenotypes mainly because of their interaction with the surrounding extracellular matrix of the tissue. In order to standardize and generate order of single cells in a physiologically-relevant 3D environment for cell-based assays, we report here the microfabrication and applications of a device for *in vitro* 3D cell culture. This device consists of a 2D array of microcavities (typically 10^5 cavities/cm^2), each filled with single cells or embryos. Cell position, shape, polarity and internal cell organization become then normalized showing a 3D architecture. We used replica molding to pattern an array of microcavities, 'eggcups', onto a thin polydimethylsiloxane (PDMS) layer adhered on a coverslip. Cavities were covered with fibronectin to facilitate adhesion. Cells were inserted by centrifugation. Filling percentage was optimized for each system allowing up to 80%. Cells and embryos viability was confirmed. We applied this methodology for the visualization of cellular organelles, such as nucleus and Golgi apparatus, and to study active processes, such as the closure of the cytokinetic ring during cell mitosis. This device allowed the identification of new features, such as periodic accumulations and inhomogeneities of myosin and actin during the cytokinetic ring closure and compacted phenotypes for Golgi and nucleus alignment. We characterized the method for mammalian cells, fission yeast, budding yeast, *C. elegans* with specific adaptation in each case. Finally, the characteristics of this device make it particularly interesting for drug screening assays and personalized medicine.

Video Link

The video component of this article can be found at http://www.jove.com/video/51880/

Introduction

Current *in vitro* cell-based assays are two-dimensional (2D). This configuration is not natural for mammalian cells and therefore is not physiologically relevant [1]; cells show a diversity of shapes, sizes and heterogeneous phenotypes. They present additional serious limitations when applied to screening applications, such as a disordered distribution within the plane and extreme phenotypes of cellular organelles (stress fibers, in particular). This is particularly important in clinical trials for drug testing, where high budgets are spent each year. Most of these drugs though fail when applied to animal models because of the artificial 2D culture condition in early stages of drug screening. In addition, by using this approach, specific cell organelles cannot be properly visualized, such as the cytokinetic actomyosin ring during cell mitosis, and generally structures that are evolving in the plane perpendicular to the plane of observation. Some new 2D assays have been proposed in order to overcome the above-mentioned drawbacks and important insights on cytoskeleton organization have been observed [2,3]. However, these assays still present one serious limitation: cells show a very spread phenotype in contrast to what is observed *in vivo*, where cells present a 3D architecture. These artifacts associated with the culture method may trigger non-physiological features such as enhanced stress fibers [1,4,5].

Three-dimensional cell culture assays provide multiple advantages when compared to 2D environments [6,7]. They are physiologically more relevant, and results are therefore meaningful. As an example, cells embedded in hydrogels show 3D-like structures but their morphologies differ from one cell to another [8,9] . However, their morphologies differ from one cell to another, which complicates screening applications. An alternative strategy is to embed single cells in microfabricated cavities [10,11]. Cell position, shape, polarity and internal cell organization can then become normalized. Besides providing 3D-like architecture to cells, microcavities also allows for high-content screening studies [10,12-14]; single cells can be ordered into microarrays and cellular organelles and their evolutions can be observed in parallel. This regularity provides good statistics with low number of cells and better temporal/spatial resolutions. Useful compounds are easier to identify reliably.

In this study, we show the fabrication and application of a new 3D-like single cells culture system for high-content-screening applications [10,12,13]. The device consists of an array of elastomeric microcavities (10^5 cavities/cm^2), coined 'eggcups' (EC). Dimensions and total volume of EC in this work are optimized to the typical volume of individual NIH3T3 and HeLa cells during cell division. Morphology of the cavities – cylindrical

– is selected to properly orient cell shape for the visualization of active processes. Replica molding is used to pattern an array of EC onto a thin polydimethylsiloxane (PDMS) layer adhered on a glass coverslip [15,16]. Cells are introduced in the EC by centrifugation. We report here observation and normalization of cellular organelles (actin stress fibers, Golgi apparatus and nucleus) in 3D (EC) in comparison with the same cells on 2D (flat) surfaces. We also report the observation of active dynamical processes such as the closure of the cytokinetic actomyosin ring during cell mitosis [17]. Finally, we show results of this methodology on other systems with rigid walls, such as budding yeast, fission yeast and *C. elegans* embryos which confirms the applicability of our methodology to a wide range of model systems.

We next present a detailed and exhaustive protocol in order to fabricate and apply the 'eggcups' for 3D microfabrication. Our approach is simple and does not need a clean room. We anticipate that this new methodology will be particularly interesting for drug screening assays and personalized medicine, in replacement of Petri dishes. Finally, our device will be useful for studying the distributions of cells responses to external stimuli, for example in cancer [18] or in basic research [19].

Protocol

1. Microfabrication of 'Eggcups'

1. Fabrication of the Master: Microcavities Array
    1. Heat a 3'' silicon wafer up to 200 °C to evaporate any presence of humidity.
    2. Spin-coat a thin layer of SU-8 photoresist. Adjust the volume of resin and spinning speed depending on the desired thickness and photoresist type. This thickness will dictate the depth of the 'eggcups' (EC). For a 30 µm thick layer and SU-8 2025, spin-coat at 2,800 rpm.
    3. Pre-bake the wafer at 65 °C for 1 min (step 1 of 2) for a 30 µm thick SU-8 2025 layer. Adapt the time depending on the photoresist type and thickness desired. Check the manufacturer datasheet for details.
    4. Pre-bake the wafer at 95 °C for 3 min (step 2 of 2) for a 30 µm thick SU-8 2025 layer. Adapt the time depending on the photoresist type and thickness desired. Check the manufacturer datasheet for details.
    5. Load the wafer on the mask aligner for UV exposure. Place the photolithography mask on it. The mask shows a pattern of circular features (disks) of 20 µm in diameter. Ensure a perfect contact between each other.
    NOTE: Different manufacturers offer photolithography masks. The spatial resolution will determine the final cost. Acetate masks provide acceptable resolution (≈10 µm) at low cost. Chromium masks provide better resolution but are more expensive. Adapt the diameters of disks (from the photolithography mask) to the volume of cells. Dimensions of disks on the mask will determine the diameter of cavities in the device. Small diameters will lead to a low filling; too large diameter will not confine the cells. For HeLa and NIH3T3 cells, diameters of 20 µm to 25 µm are suggested.
    6. Check the power of the UV lamp prior exposition and optimize the exposure time accordingly. Irradiate (wavelength = 365 nm) for 41.5 sec (or the optimized exposure time) at 250 mJ/cm^2.
    NOTE: SU-8 2025 is a negative photoresist, which means that exposed regions to UV will be cured. In this case, the circular features were black and the rest transparent. Positive photoresist work in the opposite way: non-exposed regions are cured. Select the photoresist accordingly, depending on the design and photo-mask.
    NOTE: Protect the eyes from UV light with appropriate safety glasses.
    7. Remove gently the mask from the photoresist layer.
    8. Post-bake the wafer at 65 °C for 1 min (step 1 of 2) for a 30 µm thick SU-8 2025 layer. Post-bake the wafer at 95 °C for 3 min (step 2 of 2) for a 30 µm thick SU-8 2025 layer. Adapt the time depending on the photoresist type and thickness desired. Check the manufacturer datasheet for details. After post-baking, cool the wafer to room temperature on the bench for around 1 min.
    9. Place the wafer in the spin-coater and drop few mm of SU-8 developer to cover the whole wafer area. Develop for 2 min and then spin-coat at 1,000 rpm for 30 sec. Repeat the procedure three times.
    10. Rinse with 2-propanol to ensure the complete removal of undeveloped SU-8. Appearance of white regions is an indication of incomplete development. If so, repeat the developing step an additional time.
    11. Hard-bake the wafer at 200 °C to ensure robustness of the fabricated microstructures. This step is optional.
    12. Store the 3'' wafer with microstructures inside a 94 mm x 15 mm polystyrene Petri dish.
    NOTE: There is no need for surface treatment, in particular silanization, for the next steps.

2. Fabrication of the Polydimethylsiloxane (PDMS) Replica: Pillars Array
    1. Thoroughly mix in a 1:10 ratio (w/w) the cross-linker and the pre-polymer for a total of 30 g inside a 50 ml tube.
    NOTE: Using a 1:10 (v/v) ratio is also working.
    2. Centrifuge the tube at 1,800 x g for 5 min to remove air bubbles.
    3. Drop gently the PDMS on top of the microstructures.
    NOTE: If air bubbles appear during this step, degas the sample using a vacuum pump for 15-20 min.
    4. Place the sample in an oven at 65 °C for 4 hr.
    NOTE: The curing time varies between users and, together with the cross-linker:pre-polymer proportion. This time will dictate the rigidity of the PDMS. It is recommended to cure more than 2 hr and to stick to a fixed curing time.
    5. Use a scalpel to gently cut the area of interest (stamp) of about 1 cm^2 which includes around 10^5 microcavities or 'eggcups'.
    NOTE: Cut first the PDMS and then, peel it off gently. Check the quality of the PDMS replica with an optical microscope.

3. Fabrication of 'eggcups' by replica molding. In the following, two alternative strategies for the fabrication of 'eggcups' are described. Both protocols are similar and provide identical results:
    1. Strategy 1
        1. Activate the fabricated PDMS stamp by oxygen plasma treatment for 30 sec. Store temporarily the activated stamps into a closed Petri dish to prevent deposition of dust.
        NOTE: Adjust the exposition time if other gases for the plasma are used.

2. Place the activated PDMS stamp upside up (the side with the structures) in a Petri dish next to a 15 ml tube cap. Fill the cap with 200 µl of Trimethylchlorosilane (TMCS). Close the Petri dish and let the stamp silanize for 7 min.
   NOTE: Some temporary deformation on the stamp and/or change in color (white) may be observed. The stamp will recover its original shape in short time and the structures will not be affected.
   NOTE: TMCS produces acute inhalation and dermal toxicity, and is highly flammable (with ignition flashback able to occur across considerable distances). Consequently, it should be used in a fume cupboard away from sources of ignition.
3. Place the PDMS stamp on the spin-coater with the structures upside up. Put a small drop of few microliters (around 20 µl) of liquid PDMS (1:10 w/w cross-linker:pre-polymer) on top of the structures. Spin-coat at 1,500 rpm for 30 sec to deposit a thin layer of PDMS on top of the structures.
   NOTE: If the stamp does not fit the spin-coater chuck place the stamp on top of a Petri dish lid with a small hole at its center.
4. Place the stamp in the oven at 65 °C for 4 hr to cure the deposited spin-coated PDMS layer.
5. Activate the thin PDMS layer by placing the PDMS stamp upside up, together with a glass coverslip #0 of 25 mm in diameter, using oxygen plasma cleaner for 30 sec. Proceed quickly to the next step.
   NOTE: Coverslips with other thicknesses, shapes, and dimensions can be used as well. However, some cellular structures could be difficult to visualize depending on the selected coverslip thickness and objective magnification and/or NA and/or working distance. Check the objective data sheet.
6. Place in contact the stamp (the side with the thin spin-coated layer) with the glass coverslip. Press gently all around the surface of the stamp with tweezers to make the 'bonding'. Finally, keep a constant pressure on top of the stamp for around 10 sec.
7. After 30 min gently 'peel' the stamp out of the coverslip in order to 'liberate' 'eggcups' (see **Figure 1**). Rinse thoroughly with ethanol and dry. If PDMS 'eggcups' are not well adhered on the glass coverslip (*i.e.* they detach during the 'unpeeling' step), consider adjusting the settings of the plasma cleaner and restart at step 1.3.1.5.
   NOTE: This step is delicate. Pay attention in order to avoid breakage of the coverslip and/or detachment of the thin PDMS layer.
8. Glue a small piece (handle) of cured PDMS of 1 mm x 1 mm x 3 mm in volume at the edge of the coverslip with a small drop of liquid PDMS and cure the PDMS as before. This will facilitate the manipulation of the sample afterwards (see **Figure 1**). This step is optional.

2. Strategy 2
   1. Hydrophilize the fabricated PDMS stamps by oxygen plasma treatment for 30 sec. Store temporarily the activated stamps in a closed Petri dish to prevent deposition of dust.
      NOTE: Adjust the exposition time if other gases for the plasma are used.
   2. Hydrophilize the 25 mm diameter glass coverslips #0 oxygen plasma treatment at 15 W for 30 sec. Proceed quickly to the next step.
      NOTE: Coverslips with other thicknesses, shapes, and dimensions can be used as well. However, cellular structures will be difficult to visualize depending on the selected coverslip thickness and objective characteristics (see note above).
   3. Spin-coat a small drop of PDMS (1:10 w/w cross-linker:pre-polymer) of few microliters onto the glass coverslips. Spin-coat at 1,500 rpm for 30 sec for a final thickness of around 50 µm.
   4. Glue a small piece (handle) of cured PDMS of 1 mm x 1 mm x 3 mm in volume at the edge of the coverslip with a small drop of liquid PDMS and cure the PDMS as before. This will facilitate the manipulation of the sample afterwards (see **Figure 1**). This step is optional.
   5. Store temporarily the PDMS-coated coverslips onto a clean wipe inside a Petri dish to protect from dust deposition.
   6. Put a drop of silanizing reagent on top of each stamp and let it evaporate for 1-2 min. Then, dry them under a stream of N_2.
      NOTE: In this step, a temporary deformation of the stamp can be observed during evaporation. The stamp will recover its original shape after drying with N_2 without any permanent deformation of microstructures.
   7. Drop very gently the silanized stamp on top of the PDMS-spin-coated glass coverslip stored in the Petri dish. Make sure that both sides are completely parallel during the contact. Avoid pressing or moving the stamp after placing it onto the PDMS-coated coverslip.
   8. Place the Petri dish with samples in the vacuum for 1-2 hr to remove air bubbles.
      NOTE: Ensure that samples are totally horizontal to avoid stamp displacement. Avoid also vibration potentially caused by the vacuum pump.
   9. Place the samples in the oven at 65 °C for 4 hr.
   10. Gently, peel off the stamp to reveal 'eggcups'. Rinse thoroughly with ethanol and dry.
       NOTE: Practice at this point is needed. Pay attention in avoiding breakage of the coverslip and/or detachment of the thin PDMS layer.

2. Introducing Cells into the 'Eggcups'

In order to introduce mammalian cells inside 'eggcups', PDMS surface needs to be functionalized with adhesion proteins of the extracellular matrix. This example uses fibronectin but other proteins of interest, such as collagen, could be used.

1. Hydrophilize the 'eggcups' in the oxygen plasma cleaner for 30 sec.
   NOTE: Optimize the parameters if needed.
2. Prepare a solution in PBS 1x of 20 µg ml^{-1} fibronectin from Bovine sources.
3. Sterilize the 'eggcups' with UV for 5 min. Deposit a small drop (around 20-50 µl) of fibronectin solution to cover the entire 'eggcups' area and incubate for 1 hr at RT. Protect the sample from drying.
4. Rinse gently the 'eggcups' with PBS 1x. Repeat 3 times.
   NOTE: The sample is ready to use immediately or stored at 4 °C in the dark for several weeks.
5. Introduce a cylindrical custom-made plastic piece of 63 mm in height, 26 mm of external radius and 7 mm of internal radius dimensions into a 50 ml tube (see **Figure 2**) [20]

CAUTION: Use UV-sterilized items or sterilize them prior use.
NOTE: This piece can be easily fabricated in the lab. or by any available machine shop.

6. Put 13 ml of cell culture medium inside the tube (see **Table 1**). The medium should fill at least 2 cm above the cylindrical piece to ensure complete immersion of the sample.
   NOTE: For details of specific cell types, and other model systems such as yeast or *C. elegans* embryos, and the corresponding medium used, refer to section 5 and **Table 1**. The described protocol was optimized for HeLa, NIH3T3 cells, and other cell lines (see **Table 1**).
7. Introduce very gently the 'eggcups' inside the tube and parallel to the upper side of the plastic piece. Use sharp tweezers to hold the sample using the PDMS handle. Press gently the coverslip until it lies on top of the upper side of the plastic piece, until it is fully immersed (see **Figure 2**).
   NOTE: It is recommended to use sharp and straight tweezers. With curved tweezers, the manipulation of the sample is difficult and may cause breakage.
8. Culture cells until 80-100% confluence in a P60 Petri dish and collect them by trypsinization.
   NOTE: Cells can be wild-type, transfected or treated with any drug of interest.
   NOTE: Avoid the formation of cell aggregates which will avoid single cells to enter the 'eggcups'. To optimize this step, pipette up and down thoroughly after trypsinization.
9. Re-suspend cells into 5 ml culture medium. Pipette 200 µl of cells on top of the 'eggcups'.
   NOTE: Drop cells as centered as possible on top of the 'eggcups' but avoiding physical contact. This will prevent breakage and/or damage of the sample.
10. Centrifuge at 1,800 x g for 2 min.
    NOTE: After the first centrifugation, check in a microscope the filling percentage of the 'eggcups'.
11. Pipette again 200 µl of cells on top of the 'eggcups' and centrifuge at 1,800 x g for 2 min. Repeat for a total of three times in order to optimize the filling percentage.
    NOTE: After the last centrifugation, check with a microscope the filling percentage of 'eggcups'. If necessary, repeat the filling + centrifugation steps until reaching the desired filling percentage.
12. Remove the sample from the tube using the sharp tweezers holding the PDMS handle. Make sure to be careful in not 'disturbing' cells which are held in the 'eggcups' (see **Figure 2**).
13. Place the sample in a Petri dish with medium. Rinse to remove the excess of cells which are not in the 'eggcups' by pipetting up and down three times gently next to each side (total 4 sides) of the microstructure array.
    NOTE: Pipetting too strongly may release some cells out from the 'eggcups'.
14. Replace the medium with fresh medium to remove nonattached cells.
    NOTE: In this step a drug of interest can be added.
15. Fix cells or prepare them for time-lapse imaging.See step 4.1.

3. Observation of Active Cellular Dynamics in 'Eggcups': Cytokinetic Ring Closure

NOTE: This example uses HeLa cells which are transfected with MYH10-GFP and Lifeact-mcherry for myosin and actin, respectively, key active molecules involved in the cytokinetic ring closure during cell mitosis. The device is prepared with microcavities of 25 µm in diameter. For their observation, an epifluorescence inverted microscope was used, equipped with a 60X oil objective (1.40 NA, DIC, Plan Apo) and GFP (myosin) and TxRed (actin) filters. Alternatively an upright confocal microscope was used, equipped with a 25X or 63X HCX IR APO L water objective (0.95 NA). For this example, it is highly recommended to synchronize cells by using the double thymidine block, mitotic block or mitotic shake-off method [21-24].
NOTE: The thickness of the PDMS used for the 'eggcups' allows the usage of a variety of objectives both in inverted and upright positioned microscopes.

1. Place 'eggcups' into a microscope holder and fill it with 1 ml of 10 % FCS L-15 observation medium. To avoid evaporation, place a glass lid on top of the holder or apply a thin layer of mineral oil on top of the medium.Select the 60X oil objective.
   NOTE: L-15 medium is adequate for non-CO_2 atmospheres. Note also that some compounds of DMEM are auto-fluorescent. When using this medium, it is recommended to photobleach the fluorescent compounds by illuminating it with a high intensity lamp for 1-2 hr.
   NOTE: Avoid using plastic lids when working with DIC imaging.
2. Place the holder with 'eggcups' and observation medium in the microscope. Focus carefully using brightfield light until the 'eggcups', and cells are in the same plane of observation.
3. Open the software and adjust the parameters. Select the filters TxRed and GFP for actin and myosin; adjust the exposition time for each channel. A typical acquisition rate is 5 sec for both channels.
   NOTE: The exposition time may have to be adjusted depending on the setup used, dye or other cellular organelles of interest.
4. Select the region of interest and seek for a cytokinetic ring using either the GFP or TxRed channel. Focus accurately.
   NOTE: The ring is sharper in myosin and easier to recognize.
5. Run the automatic acquisition in both channels until the ring is completely closed.
   NOTE: Some photobleaching may be observed. Adjust the microscope parameters in order to reduce it.

4. Observation of Fixed Cellular Organelles into the 'Eggcups'

This step can be performed before or after step #3. Cells can be directly fixed after the centrifugation step and stained for the organelle of interest or after the observation in the microscope. This example shows the staining of the Golgi apparatus, nucleus and actin fibers on NIH3T3 fibroblasts in 'eggcups'.

1. Fixation of Cells in the 'Eggcups'
   1. Prepare 3% paraformaldehyde (PFA) and warm at 37 °C. Remove the 'eggcups' sample from the 50 ml tube (or the microscope holder) and place it inside a P35 Petri dish. Rinse once with PBS 1x.
      NOTE: Protocols for the preparation of 3 % paraformaldehyde are widely available elsewhere.

CAUTION: Use nitrile gloves and eye protection during the preparation of PFA.

2. Remove completely the PBS and drop 1 ml of 3% PFA and incubate for 17 min. Remove the PFA and rinse twice with 1 ml of PBS 1X. Permeabilize cells using 1 ml of 0.5% Triton for 3 min and wash twice with PBS 1x for 5 min.

2. Staining of Cells in 'Eggcups'
    1. Incubate cells for Golgi apparatus staining with the primary antibody rabbit polyclonal anti-Giantin in a 1:500 dilution in PBS. Place a 100 µl drop of antibody solution onto a plastic film sheet and incubate the cells inside the 'eggcups' upside down for 45 min.
    NOTE: Protect the sample with a cover to prevent drying.
    2. Release carefully the 'Eggcups' and place them into a P35 Petri dish. Rinse 3 times, 5 min each, with PBS 1x.
    3. Prepare a cocktail in PBS with the secondary antibody Cy3 goat anti-rabbit (1:1,000) and with Phalloidin Alexa Fluor 488 (1:200) for staining actin stress fibers.
    4. Incubate cells with a 100 µl drop of antibody solution onto a plastic film sheet and incubate cells inside the 'eggcups' upside down for 45 min.
    5. Release carefully the 'eggcups' and place them into a P35 Petri dish. Rinse 3 times, 5 min each, with PBS 1x.
    6. Incubate cells for nucleus staining placing a 100 µl drop of 1 µg ml^{-1} DAPI in PBS onto a plastic film sheet and incubate cells inside the 'eggcups' upside down for 45 min. This step can be performed with step 4.2.3.
    7. Release carefully the 'eggcups' and place them into a P35 Petri dish. Rinse 3 times, 5 min each, with PBS 1x.
    8. Mount cells using a 15 µl Glycerol:PBS (1:1 v/v) on a standard microscope glass slide and seal the sample with nail polish to avoid drying.
    NOTE: Depending on the 'eggcups' thickness, mounting may be difficult. It is recommended to store then the sample into a P35 Petri dish in PBS, protected from drying.

3. Microscope Observation
NOTE: For this example an upright confocal microscope is used, equipped with PMT and Hybrid detectors. A 25X or 63X HCX IR APO L water objective (0.95 NA) was selected to provide a wide field of the sample and show the applicability of the device for high-content-screening applications.
    1. Select the 25X or 63X water objective.
    NOTE: Different objectives can be used depending on the application and signal. But usage of high numerical aperture objectives is recommended.
    2. Place the fixed sample with the 'eggcups' and focus carefully using brightfield light (phase contrast or DIC) until the 'eggcups' and cells are in the plane of observation.
    3. Open the software and adjust the parameters. Select the filters GFP, Cy3 and DAPI for actin, Golgi and nucleus observation, respectively; adjust the exposition time for all channels.
    NOTE: The exposition time may have to be adjusted depending on the setup.
    4. Select and focus the region of interest; start image capture (see **Figure 3**).

5. Adaptation for the Observation of Yeast Cells and *C. elegans* Embryo

1. Fission and Budding Yeast cells
NOTE: This example uses fission yeast cells which are tagged with RLC1-mcherry and CHD-GFP for myosin and actin, respectively. The budding yeast cells are not fluorescently labeled here. For fission yeast observation an inverted spinning disk confocal microscope was used. A 100X HCX PL APO CS oil objective (1.4 NA) was used for all acquisitions. Alternatively, cells were also observed using an inverted phase-contrast microscope equipped with a 20X phase contrast air objective LCPlanFl (0.4 NA). In this example, the protocol is identical for both cell types.
    1. Prepare the 'eggcups' surface as described above. For fission and budding yeast cells, prepare cavities of 5 µm in diameter (see **Table 1**). In this case, the surface does not need to be functionalized with adhesion proteins.
    NOTE: The filling can be optimized by using conical 'eggcups'. This shape captures and retains the cells avoiding releasing during the rinsing step after centrifugation. Filling percentage is optimum at about 80%. These conical 'eggcups' can be fabricated by means of Deep Reactive Ion Etching [13].
    2. Culture yeast cells in the proper culture media (see **Table 1**) until reaching an optical density (OD) in the range of 0.2 and 0.8. Sonicate the culture of yeast cells to remove aggregates.
    3. Insert yeast cells in 'eggcups' by centrifugation. For centrifugation, 4 ml of cultured cells in the appropriate OD is added onto the tube with 'eggcups'. After the first centrifugation, gently shake the tube to re-suspend cells which are not in the 'eggcups', while cells in the 'eggcups' are not disturbed. Without opening the tube, centrifuge again and repeat this step twice. This ensures the deposition of cells from the culture into the empty microcavities and will increase the filling percentage.
    NOTE: When working with yeast, it is recommended to pre-heat the centrifuge to the working temperature during experiments
    NOTE: The protocol can be paused here and continued up to 12 hr later. In this case, store the sample at the working temperature and cover it to prevent evaporation.
    4. Place 'eggcups' in a microscope holder and fill the holder with filter sterilized medium for imaging. Now rinse the cells with the same media until the floating yeast cells are removed efficiently. Take care not to disturb cells in 'eggcups' during the rinsing process.
    5. Select the 100X oil objective and focus carefully. Open the software and adjust the parameters. For fission yeast, select the filters GFP and TxRed for actin and myosin and adjust the exposition time for both channels. A typical acquisition rate is 3 sec.
    NOTE: Depending on the fluorophore, type of tagging and the set-up, exposure time varies for other systems.

2. *C. elegans* Embryo
NOTE: This example uses *C. elegans* embryos 25-30 µm wide and 50-55 µm long. Embryos were cultured as indicated in [25]. A simple visual protocol of how to manipulate *C. elegans* can be found in [26]. The observation was performed using an inverted phase-contrast microscope equipped with a 40X air objective 0.55 NA.

1. Prepare the 'eggcups' surface as described above and 25 µm in diameter (see **Table 1**). In this case, the surface does not need to be functionalized with adhesion proteins.
2. Culture the *C. elegans* embryos in the proper culture media (see **Table 1**).
3. Insert embryos in 'eggcups' by centrifugation as described above (see section 2.6 to 2.12) using ultrapure water as culture medium. NOTE: Embryos were 'behaving' normally in ultrapure water for the duration of the experiment. Alternatively use a physiological M9 buffer for long-term experiments.
4. Rinse the sample as described above (see section 2.14). Place the 'eggcups' into a microscope holder. Select the 40X air objective and focus carefully. Open the software and adjust the parameters. Select an acquisition rate of 3 sec.

Representative Results

The 'eggcups' (EC) are a novel high content-screening methodology which allows the visualization of oriented cells and embryos in a 3D environment. Additionally, some cellular processes, which are difficult to observe in standard 2D (flat) cultures, can be observed by this new method. **Figure 1a** shows a summary of the procedure for the EC microfabrication (see also Section 1 in the above-described protocol). The method is simple, fast, efficient and without any requirement of special equipment. **Figure 1b** and **1c** shows a large-scale picture and a magnified scanning electron microscope image of 'eggcups', respectively. As it can be observed, their shape and size are very regular. This method is very flexible; different shapes and sizes can easily be fabricated and adapted for different model systems. The dimensions of ´eggcups ´ were selected in the following manner: dimensions of cells which undergo division were measured on 2D surfaces: they have a spherical shape and their diameter was taken as a good indication for the EC diameter. Cells in ´eggcups´ elongate and orient along their long axis during cell division for example. This dimension depends on the system – cells and embryos – so this dimension should be evaluated in each case.

Figure 2 shows the material needed (**Figure 2a**) and a step-by-step protocol (**Figure 2b**) about how to use the 'eggcups' (see also Section 2 in the above-described protocol). The filling of the EC with cells of interest (or other model systems) is very simple and fast. Typically, it takes less than 20-30 min, which also includes the time for cell trypsinization. After the filling, samples can be used to study active processes (live imaging) or can be fixed and stained for the visualization of organelles of interest (see also Sections 3 and 4 in the protocol described above).

On flat surfaces, cells show heterogeneous responses and extreme phenotypes of cellular organelles. In fact, it has been suggested that actin stress fibers (and other cellular organelles) are artifacts of the culture conditions [1]. In order to prove this hypothesis, we cultured NIH3T3 cells both on 3D 'eggcups' and on flat surfaces and compared the phenotypes of different cellular organelles, namely actin stress fibers, Golgi apparatus and nuclei. **Figure 3** shows an example of how cells are organized on both configurations. In EC, cells are distributed in an ordered array showing a homogeneous spherical-like phenotype (**Figure 3a**). On flat surfaces, cells show the typical disordered, spread and heterogeneous morphology (**Figure 3b**). There are also significant differences in cytoskeleton structures. In particular, cells on 'eggcups' show a reduction in the number of stress fibers compared to flat surfaces. This is further confirmed in the 3D reconstructed images where no clear stress fibers are visible (see **Figure 3c**-**d**). This confirms that some cellular structures are magnified in 2D cultures. This is also in agreement with observations performed *in vivo* where stress fibers cannot be identified.

The Golgi apparatus also shows significant variation in their phenotype depending on the culture condition (see **Figure 4**). The Golgi apparatus on 2D cultures typically shows an extended phenotype 'embracing' the nucleus periphery whereas in 'eggcups' it shows a more compacted phenotype (see **Figure 4a**-**b**). In order to simulate a drug screening manipulation, we also evaluated the effect of drugs on cells cultured on both environments. We selected Blebbistatin mainly because it disrupts the actin stress fibers and could have an effect on Golgi morphology (see **Figure 3c**-**d**). Since the Golgi is located next to the cell nucleus, this drug could also have an effect on its architecture. We first observed that cells treated with this drug showed a less regular and uniform morphology compared to wild type (WT) cells (see **Figure 3c**-**d**). We then compared and quantified the Golgi phenotype observed on 'eggcups' and on flat surfaces (see **Figure 4c**). We observed that on 2D surfaces cells showed mostly an extended phenotype whereas on 'eggcups' cells showed a more compacted phenotype. We did not observe though a striking difference between WT and Blebbistatin-treated cells.

Finally, on 2D surfaces the cell nucleus is randomly oriented whereas for cells in EC it is orthogonally oriented with respect to the XY plane in both WT and Blebbistatin treated cells (see **Figure 5a**-**c**). This highlights the strength of the device to orient cellular organelles, similar to a former application of the method for orienting the plane of observation of the cytokinetic ring in yeast and mammalian cells [10,12,13]. We finally studied how the nucleus sphericity(defined as $\psi = [\pi^{1/3} 6V_n^{2/3}]/A_n$, where V_n is the volume of the nucleus and A_n its surface area) was affected depending on the culturing condition and upon the treatment of cells with Blebbistatin. **Figure 5d** shows the corresponding distributions of ψ. We did not observe a difference for WT^{flat} *vs* WT^{EC}, which reveals that the EC are not affecting the normal sphericity of cells. However, we observed a difference when comparing WT^{EC} to $Blebb^{EC}$ suggesting that the EC are revealing a real effect of the drug that is masked in 2D.

Live cell studies using 'eggcups' allow also identification of novel active processes which are not visible in standard cultures. We plated cells in EC and visualized cell division. **Figure 6** shows a sequence of images of the cytokinetic ring closure during cell mitosis. The 'eggcups' device allows a complete visualization of the ring, whereas standard 2D cultures only shows two areas which corresponds to one single plane [10]. Reconstruction of the ring from a sequence of z-stack images using 2D cultures can be done [27], but important information is lost. The quality is diminished due to low z resolution and dynamic processes cannot be resolved. Actin and myosin are the key proteins in the force generation of cell division. Their dynamics cannot be imaged and studied in 2D culture (**Figure 6a**), whereas with 'eggcups' it is immediately revealed. We have identified novel structures and processes: in HeLa cells we find periodic accumulations of myosin [17]. These accumulations move radially as the ring is closing (**Figure 6b**). In fission yeast we also find inhomogeneities in myosin and actin (**Figure 6c**, right) [17]. In contrast to what we see in HeLa cells, they rotate on the ring during closure. The speed is in the range of µm min^{-1} and would not be resolvable by z reconstruction with standard microscopes. Finally the cytokinetic ring can be further studied by staining for its components. We find that there is an accumulation of phosphotyrosine in the vicinity of the ring (**Figure 6d**). We can also show that anillin is colocalizing in the ring (**Figure 6e**). By staining the cells in this orientation, we reveal that anillin shows also an inhomogeneous distribution.

The 'eggcups' were also applied to different model systems: we reported mammalian cells, fission yeast, but we also tested budding yeast and *C. elegans* (see **Figure 7a**-**e**). In this case, the protocol was adapted for each specific system in terms of culture media, cavities size and

morphology (see **Table 1**). As an example, conical *V*-shaped 'eggcups' were the optimal morphology for immobilizing fission yeast efficiently [12], instead of completely cylindrical (or U-shaped) shape used for mammalian cells [13]. This allowed testing the effect of different cytoskeleton drugs with potential application in Life Science research. This demonstrates the flexibility and reliability of the developed methodology.

Furthermore, the highly ordered arrangement of cells allows an easy, automated read-out of the fluorescence of single cells. We illustrate this by inserting NIH3T3 cells expressing GFP in 'eggcups' (**Figure 8a**). The cell position can be easily recognized and the corresponding expression level measured. **Figure 8b** shows the distribution of fluorescence signals. This can be applied to any read-out (immunofluorescence, fluorescent reporters in cells for example).

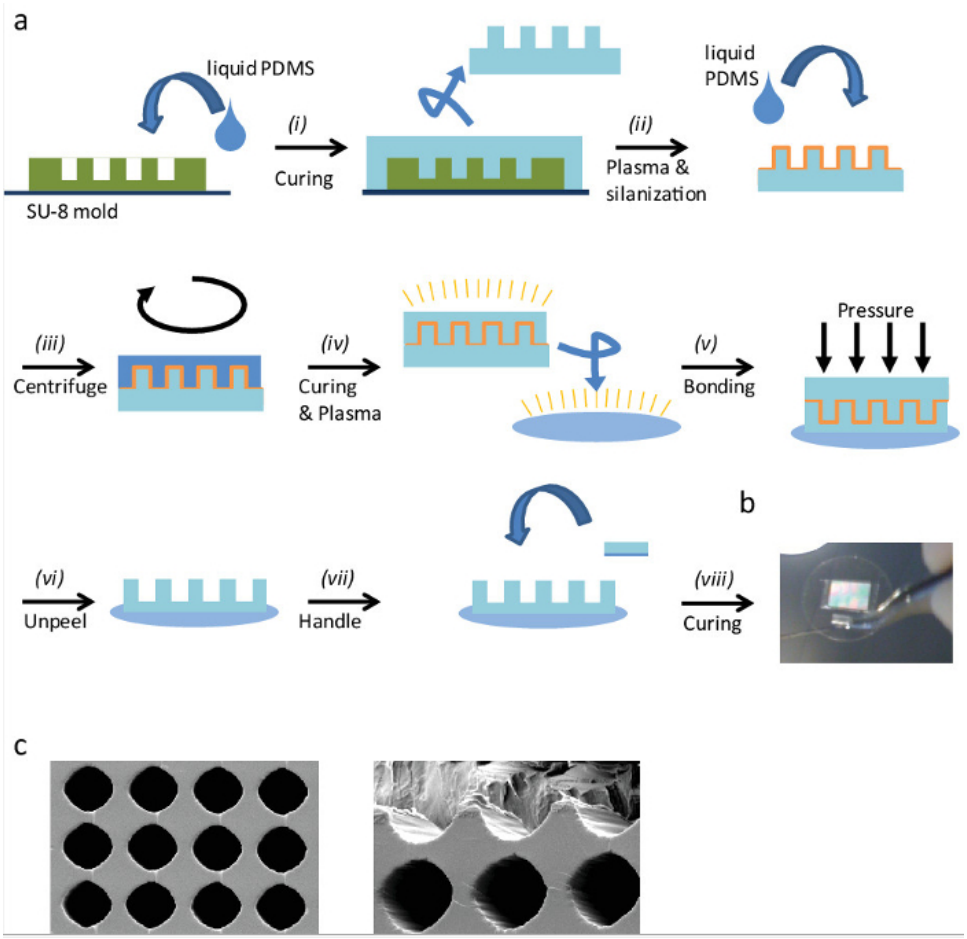

Figure 1: Fabrication of 'eggcups'. (**a**) Schematic description of the fabrication procedure of 'eggcups' by replica molding: (i) Pour liquid PDMS on the SU-8 mold and cure it. (ii) Cut out the stamp and remove it carefully from the surface, then plasma activate it to silanize it. (iii) Pour liquid PDMS on the silanized stamp and centrifuge it to obtain a thin PDMS layer. (iv) After curing the PDMS layer, plasma activate both, the PDMS covered stamp and a glass coverslip. (v) Plasma bind both by applying a gentle, homogeneous pressure. (vi) After plasma bonding, remove carefully the stamp to uncover the 'eggcups' surface. (vii) To simplify the handling in the next steps, add a small PDMS handle piece. Bind the PDMS piece to the coverslip by gluing it with liquid PDMS and (viii) cure it then in the oven. (**b**) Image of a 25 mm coverslip with PDMS 'eggcups' and a handle. (**c**) Scanning electron microscope images of PDMS 'eggcups'. The distance between centers of 'eggcups' is 30 µm, and their diameter about 25 µm. *(Left)* Top view. *(Right)* 'Eggcups' are cut to image the inner part. Please click here to view a larger version of this figure.

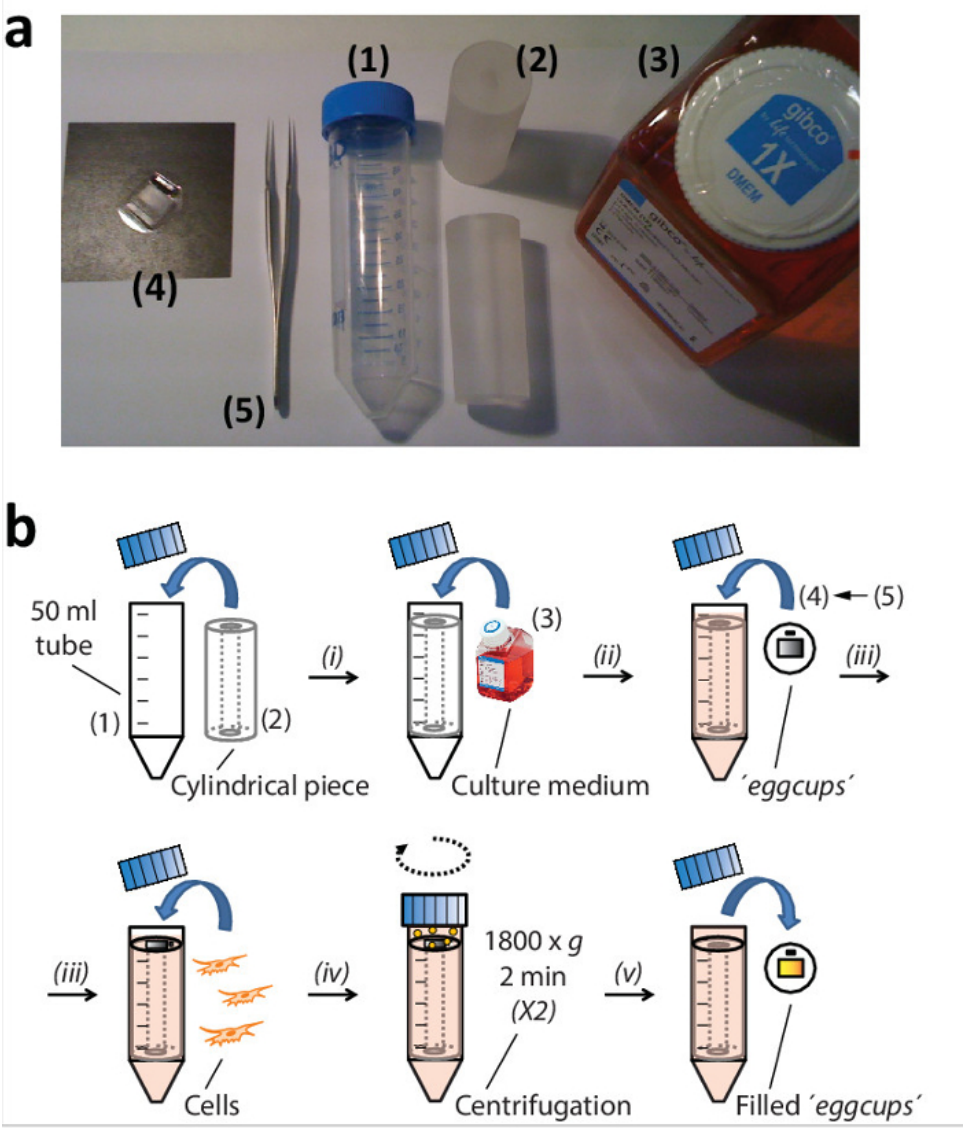

Figure 2: (**a**) Elements needed for the EC filling. (1) 50 ml tube; (2) cylindrical piece (top and side view); (3) cell culture medium; (4) 'eggcups'; (5) sharp tweezers. (**b**) Schematic of the EC filling procedure. (i) A cylindrical piece is first introduced into a 50 ml tube and filled with 13 ml of cell culture medium. Next, (ii) the 'eggcups' are gently deposited on top of the cylindrical piece using sharp tweezers to manipulate the EC using the small PDMS piece. (iii) Cells at the proper density are pipetted on top of the EC. (iv) Cells are introduced in the 'eggcups' by centrifugation. (v) Finally, the sample is gently released out from the tube and it is ready to use. Please click here to view a larger version of this figure.

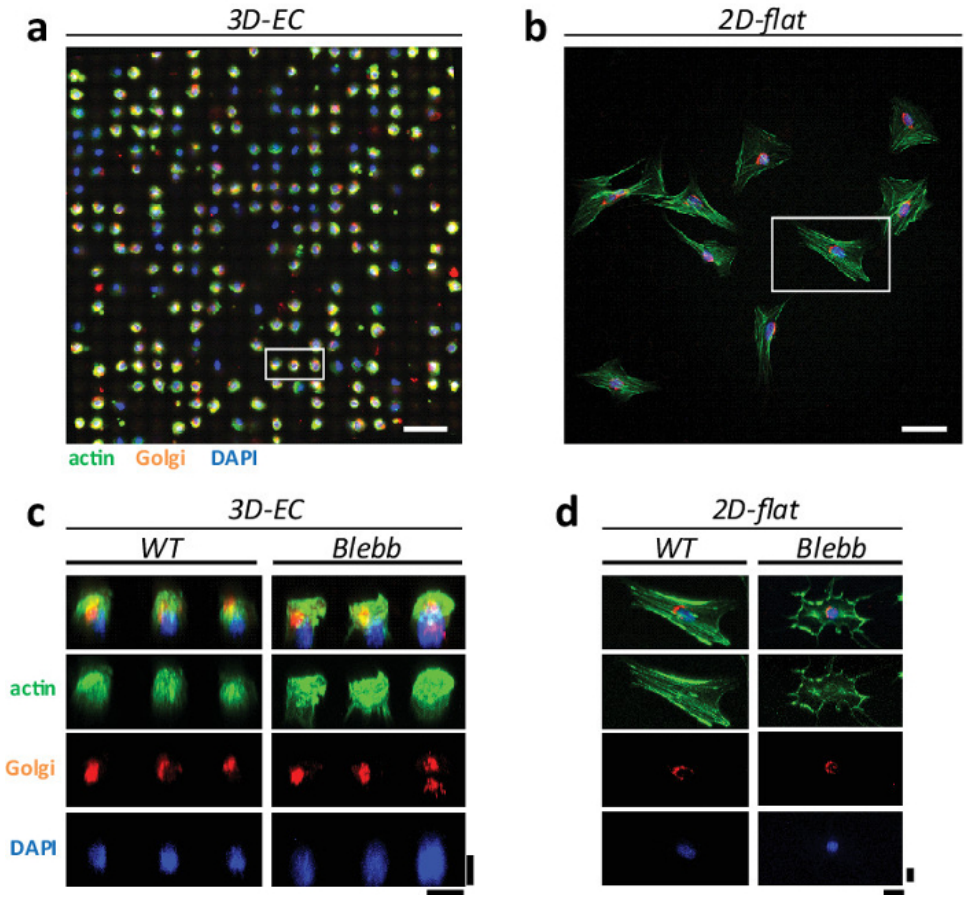

Figure 3: Comparison of cell phenotypes on 3D 'eggcups' and 2D flat surfaces. Confocal microscopy (25X water objective, 0.95 NA, Leica) image of NIH3T3 cells on (**a**) EC forming an ordered array, and showing a homogeneous spherical phenotype, and on (**b**) standard 2D flat culture, randomly distributed with heterogeneous phenotypes. Cells were stained for actin (in green), Golgi (in orange) and nucleus (in blue). Scale bars = 100 µm. (**c**) 3D reconstruction of cells on EC and (**d**) on flat surfaces for WT and Blebbistatin-treated cells. Scale bars = 20 µm. Please click here to view a larger version of this figure.

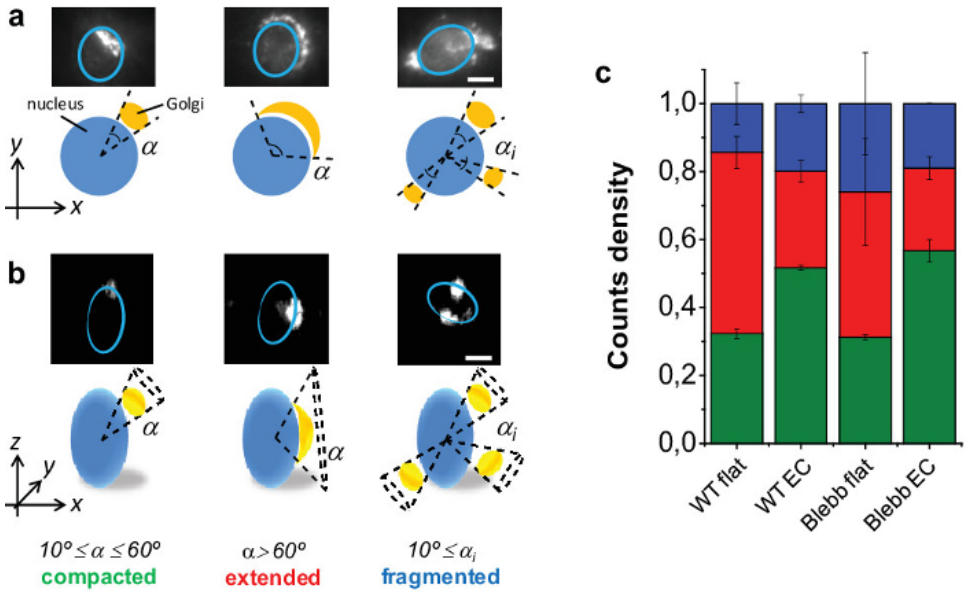

Figure 4: Study of NIH3T3 Golgi apparatus phenotype. Schematic and sample image of Golgi phenotype classification for cells on (**a**) flat and (**b**) EC. Cells were classified as compacted, extended or fragmented depending on the α-value. (**c**) Quantification of Golgi phenotypes. Scale bars = 10 µm. Please click here to view a larger version of this figure.

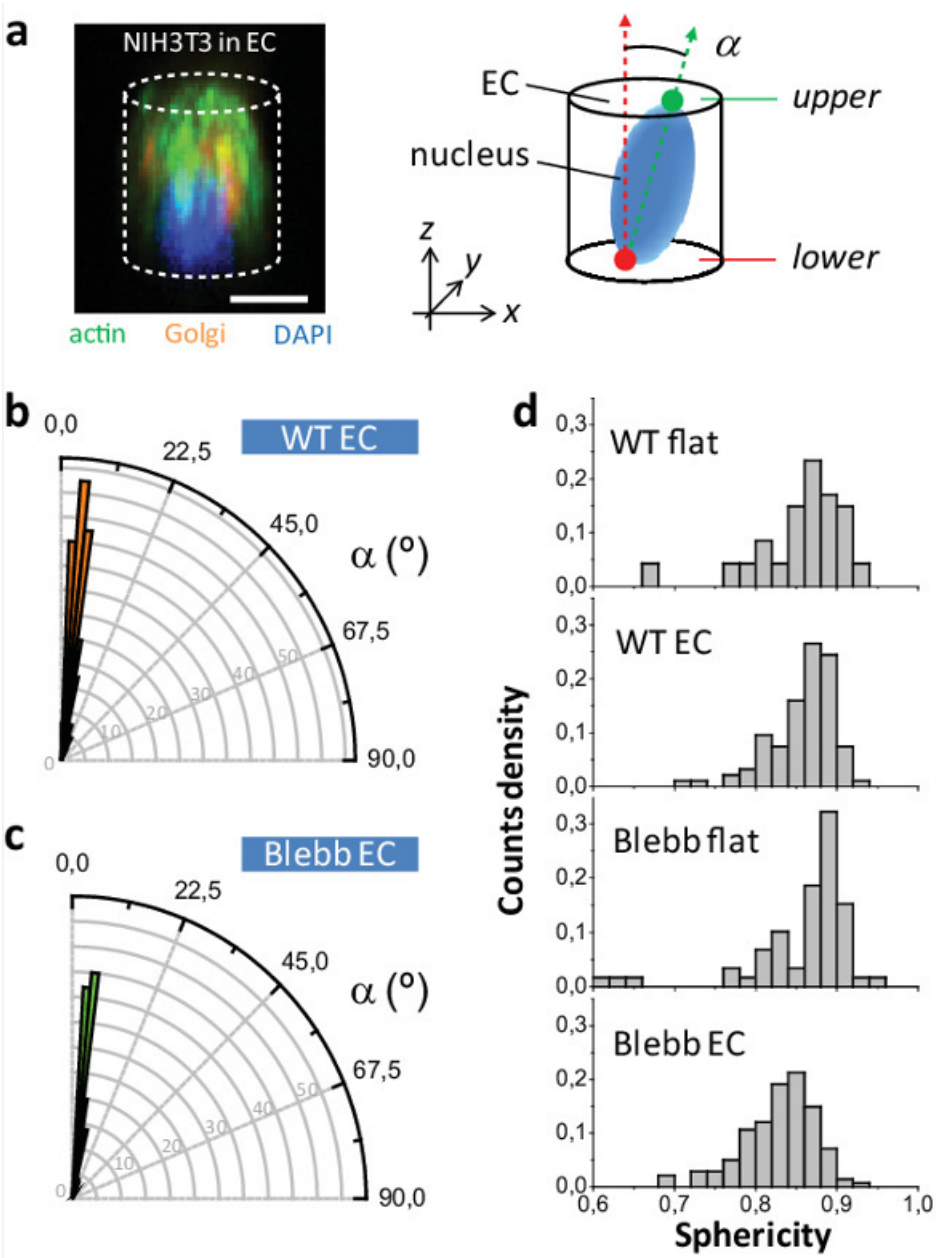

Figure 5: Study of NIH3T3 nucleus phenotype. (**a**) *(Left)* Confocal microscopy image of a NIH3T3 cell inside an EC and stained for actin (in green), Golgi (in orange) and nucleus (in blue). *(Right)* Scheme of nuclei orientation inside EC. (**b**) Angular distribution of nuclei inside EC for WT and (**c**) Blebbistatin-treated cells. (**d**) Nucleus sphericity values for WT and Blebbistatin-treated cells both for EC and flat surfaces ($P[WT^{EC}\text{-}Blebb^{EC}] < 0.001$, $P[Blebb^{flat}\text{-}Blebb^{EC}] < 000.1$; $n_{WT}^{flat}=47$, $n_{WT}^{EC}=94$, $n_{Blebb}^{flat}=59$, $n_{Blebb}^{EC}=141$ cells). Scale bar = 10 µm. Please click here to view a larger version of this figure.

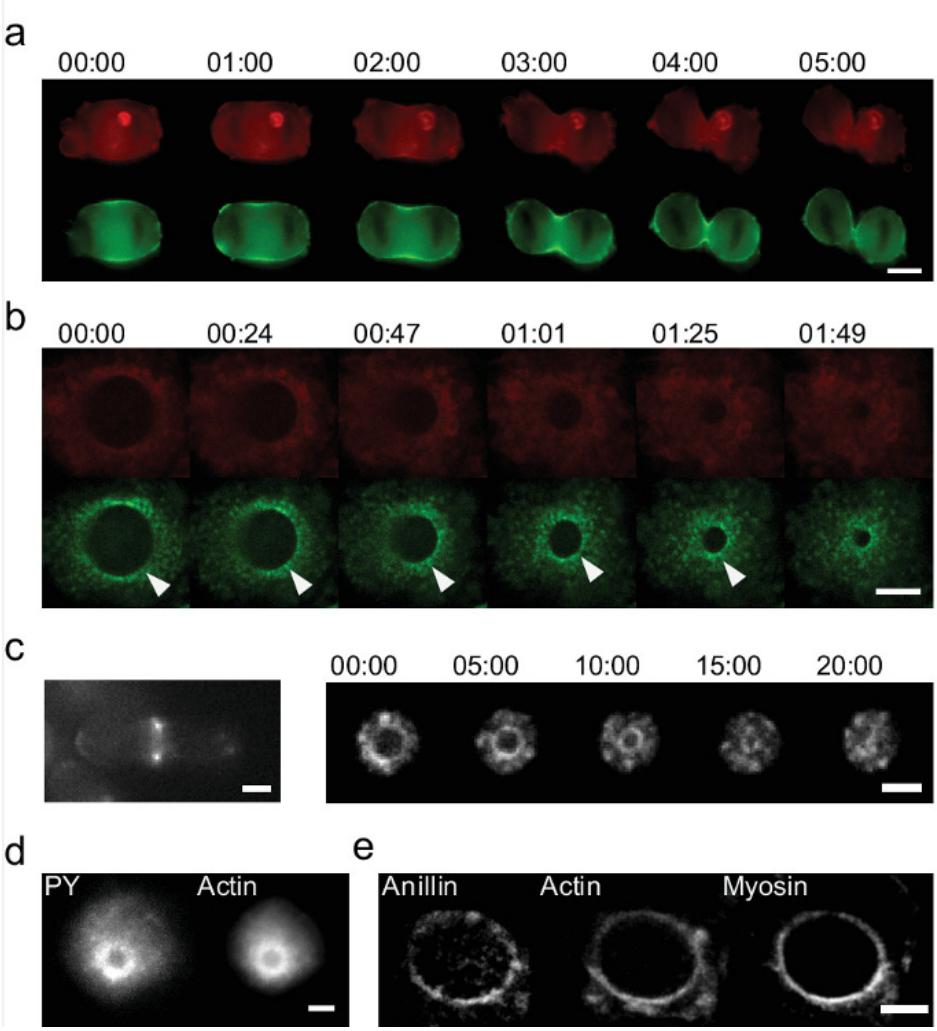

Figure 6: Detailed study of the cytokinetic ring in live and fixed samples and in two systems using 'eggcups'. (**a**) Time sequence of the cytokinetic ring using standard 2D *in vitro* culture. Only two bright spots in actin (Lifeact-mcherry, red) and myosin (GFP tagged, green) are visible in the cleavage furrow of the HeLa cells (Scale bar = 10 µm). (**b**) Time sequence of the closure for the cytokinetic ring in HeLa cells during mitosis using 'eggcups'. The images show actin (in red) and myosin (green). 'Eggcups' allow the identification of still myosin accumulations. One example is highlighted with an arrowhead. (Scale bar = 5 µm). (**c**) The cytokinetic ring can also be visualized in fission yeast. *(Left*) Cells lie on a flat surface, the cytokinetic ring is only visible as two dots. *(Right)* Cells in 'eggcups': the entire closure can be captured. Actin is labeled with CHD-GFP (Scale bars = 2 µm). Time in min:sec. (**d**-**e**) Examples of stained cytokinetic rings. (**d**) Actin-GFP expressing HeLa cells are stained for phosphotyrosine (PY) which also shows signal in the ring (Scale bar = 5 µm). (**e**) HeLa cells expressing GFP tagged myosin and Lifeact-mcherry (actin) are stained for anillin. Anillin is revealed to localize in the cytokinetic ring and less concentrated in the cortex. It shows co-localization with actin and myosin (Scale bar = 5 µm). Please click here to view a larger version of this figure.

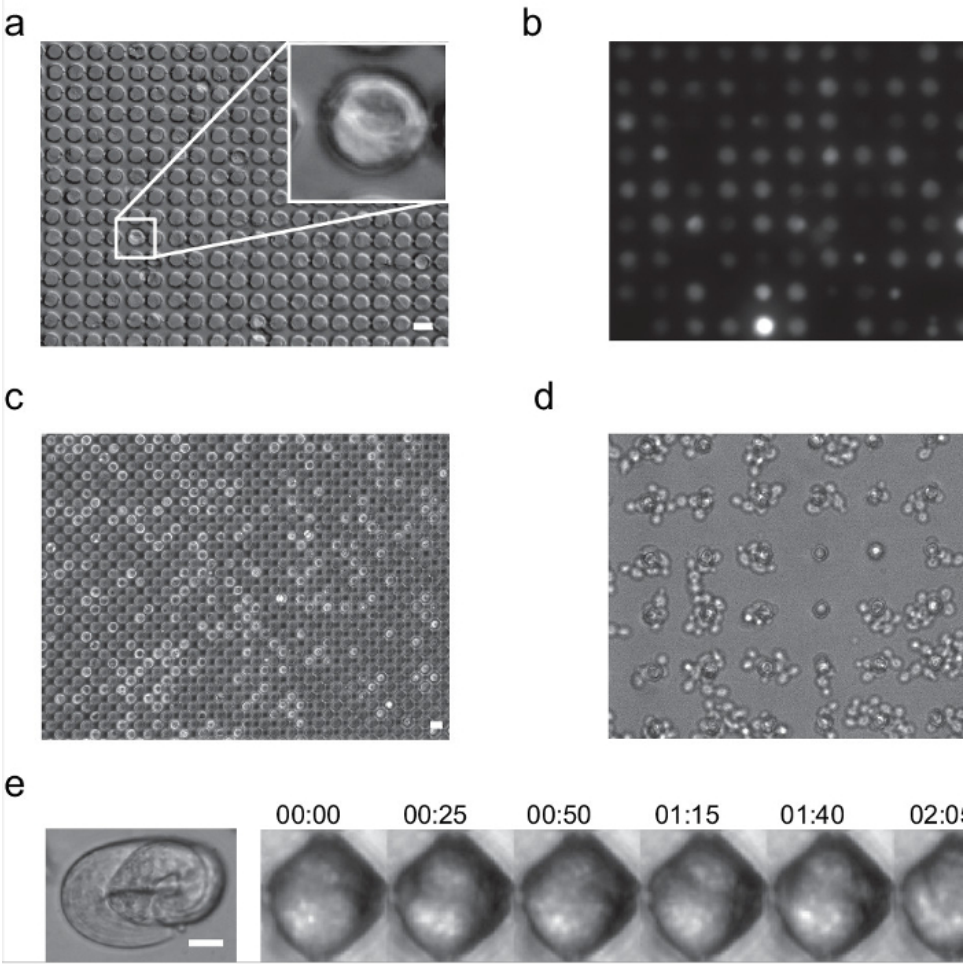

Figure 7: Application of the 'eggcups' to other cell types and model systems. (**a**) U2OS (human osteosarcoma). The inset shows a dividing cell. (Scale bar = 20 µm). (**b**) NIH3T3 cells expressing GFP. Difference in expression levels can be easily read out (Scale bar = 20 µm). (**c**) SW480 cells (Scale bar = 20 µm). (**d**) Budding yeast; their cycle time is unchanged. (Scale bar = 10 µm). (**e**) *C. elegans* worms; *(Left)* on a flat surface. *(Right)* In 'eggcups', embryo is seen from an otherwise hidden perspective. (Scale bars = 10 µm). Time in min:sec. Please click here to view a larger version of this figure.

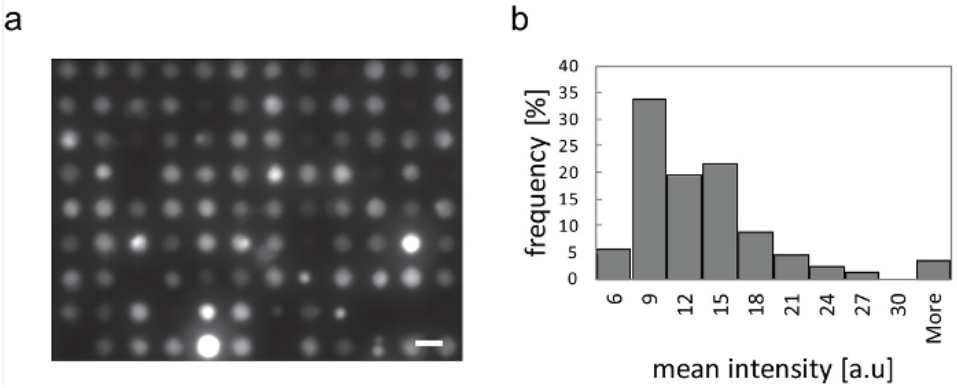

Figure 8: The organization in an array of 'eggcups' allows an automated analysis of cell population. (**a**) NIH3T3 cells in EC (Scale bar = 20 µm). They have different expression levels of GFP. (**b**) Automated recognition of cell position allows an individual analysis of the expression level. It is summarized in the histogram of the GFP expression of the cell population. Please click here to view a larger version of this figure.

Model System	Type	Culture Medium	Observation Medium	'eggcups' diameter (µm)	Comments/ Description
Mammalian cells	NIH3T3	10 % BCS high-glucose DMEM	10 % BCS L-15	20	Other stable cell lines, such as REF52 or MDCK, as well as primary cell lines, cancerous cells and/ or stem cells can also be inserted in the 'eggcups'.
	HeLa	10 % FCS high-glucose DMEM	10 % FCS L-15	25	Available from many different sources.
	U2OS	10 % FCS high-glucose DMEM	10 % FCS L-15	20-25	Available from many different sources.
	SW480	10 % FCS high-glucose DMEM	10 % FCS L-15	17-20	Available from many different sources.
Yeast	Fission Yeast	Agar plate (YE5S) and liquid media (YE5S and EMM5S)	Filter sterilized EMM media (see the list of materials)	5	The surface does not need to be functionalized with adhesive proteins.
	Budding Yeast	Agar plate (YPD) and liquid media (YEPD and SD)	SD media	5	The surface does not need to be functionalized with adhesive proteins.
Embryo	*C. elegans*	NGM plate	ultrapure water	25	Alternatively M9 medium can be used for long-term experiments. The recipe of this salted solution can be found here: http://cshprotocols.cshlp.org/content/2009/5/pdb.rec11798.full?text_only=true

Table 1: Culture conditions in 'eggcups' for different model systems. The above-related protocol can easily be adapted by just replacing the described culture conditions and the size of 'eggcups'.

Discussion

Replica molding was used in order to fabricate the 'eggcups'. The fabrication process does not need a clean room; it is easy and simple, although some practice may be required. In particular, releasing the PDMS stamp is the most critical step in order to produce a large area of high quality 'eggcups'. For this reason, special care has to be taken in this step. If this step is repeatedly failing, consider to optimize the plasma cleaner parameters prior to the silanization and plasma binding. Insufficient silanization will lead to strong sticking of the stamp to the PDMS film. If this is observed, the incubation time with the silanizing reagent can be increased. Note that other techniques and materials can be applied to fabricate the 'eggcups', which can be functionalized with a large range of ligands (fibronectin, gelatin, collagen, *etc.*). In particular, microcavities in polystyrene can be easily fabricated by custom-made hot-embossing technique. This ensures biocompatibility and direct comparison with results obtained in standard culture dishes. Similarly, special care and practice are required in order to optimize the filling percentage. In particular, the rinsing step is critical in order to ensure an appropriate filling with no excess of cells, contributing to noise and background in the signal. If cells are removed easily from cavities, consider to change the size or depth of cavities.

'Eggcups' provide 3D-like architecture to cells and high-content screening assays using a simple protocol. Cellular organelles and active processes unknown using standard culture assays can be easily visualized by means of inserting single cells on individual microcavities ('eggcups'). Depending on the model system, the size, shape and their dimensions can be easily adapted. In this way mammalian cells, fission yeast, budding yeast and *C. elegans* can be manipulated and studied, as well as any embryos such as *Drosophila*, mice or human embryos for *in vitro* fertilization, or stem cells for example.

In this setup single cells are captured. This is in contrast to epithelial tissues encountered *in vivo*. However, this environment could be reproduced in our 'eggcups' by coating the side walls with cadherins to mimic cell-cell contacts using more flexible elastomers. Focal contacts will be promoted by the deposition of fibronectin at the bottom of wells. These respective distributions of adhesion molecules should allow in reproducing the cellular environments encountered *in vivo*. By this method one would approach the physiological conditions.

Medium exchange in our assay is ensured. Cells in EC do not show any degradation when performing both short- and long-term experiments due to lack of medium exchange. Note also that cells in EC can be cultured until confluence although the main interest is when individual cells or embryos are isolated within the cavities.

Orientation of organelles or entire organisms is revealing new information. We show different dynamics of actin and myosin in the cytokinetic ring. Although the cytokinetic ring in fission yeast and mammalian cells is composed of similar key components, we show with this setup, that their specific dynamics is different [17]. This is supporting the result, that the closure mechanism in the two systems is different as well. To develop and investigate such a hypothesis, the orientation of the cell is indispensable. In future studies, this device can be also used to investigate other events related to organelle organization in cells.

Beyond that, this technique can be of great use in developmental biology. Elongated embryos can be easily oriented, observed or further treated in a defined orientation. Probably our assay would not impose polarity of embryos, but the high filling percentage would allow to extract the desired read-out in a reliable manner. Altogether 'eggcups' could be a good device for high-content screenings.

Other culture assays have been proposed. These methods range from multiple cells in 2D dimensions in multiwell plates, to single cells deposited in micropatterned adhesive motifs with identical shape. However, none of them is appropriate to overcome the limitations detailed above on the observation of cellular organelles and dynamical processes [1].

Future improvements to our system will allow the applicability of 'eggcups' to industry-oriented purposes. As an example, drug screening applications in pharmaceutical companies require the use of multiwell plates [14,28]; implementing 'eggcups' into such platforms will potentially improve the reliability of tests and results. As such, high content-screening assays will be performed using the commonly used automatized processes of pharmaceutical companies (and academic research laboratories) using robots. This will ensure repeatability and reliability with low variability. Some commercial products based on 3D-cell cultured assays have already appeared in the market highlighting the importance of this kind of assays. Finally, these devices open new perspectives for personalized medicine: cells from patient could be placed in 'eggcups', and treatment cocktails could be tested in a physiological environment; the biomarker read-out will allow to anticipate an optimal treatment to be given to the patient [29]. Altogether the physical shape of the cells and embryos are guiding the architecture of the cavities, and we hope that the device and this method will be widely spread in the future.

Disclosures

We have nothing to disclose.

Acknowledgements

We acknowledge L. Brino (IGBMC High Content Screening facility, Illkirch, France) for providing us with the anti-Giantin antibody, M. Labouesse Lab. for *C. elegans* (IGBMC) and B. Séraphin Lab. for budding yeast (IGBMC), E. Paluch and A. Hyman for fluorescent HeLa cells (MPI-CBG, Dresden), J. Moseley (Dartmouth Medical School) and J.Q. Wu (Ohio State University) for fission yeast cells; A. Hoël and F. Evenou for experimental help, C. Rick (IBMC, Strasbourg, France) for technical help, and J.C. Jeannot (Femto-st, France) for help in microfabrication. This work was supported by funds from the CNRS, the University of Strasbourg, Conectus, La Fondation pour la Recherche Médicale and the ci-FRC of Strasbourg.

References

1. Cukierman, E., Pankov, R., Stevens, D. R., & Yamada, K. M. Taking Cell-Matrix Adhesions to the Third Dimension. *Science.* **294**, 1708-1712 (2001).
2. Azioune, A., Storch, M., Bornens, M., Thery, M., & Piel, M. Simple and rapid process for single cell micro-patterning. *Lab Chip.* **9**, 1640-1642 (2009).
3. Mandal, K., Balland, M., & Bureau, L. Thermoresponsive Micropatterned Substrates for Single Cell Studies. *PLoS ONE.* **7**, e37548 (2012).
4. Pampaloni, F., Reynaud, E. G., & Stelzer, E. H. K. The third dimension bridges the gap between cell culture and live tissue. *Nat Rev Mol Cell Biol.* **8**, 839-845 (2007).
5. Baker, B. M., & Chen, C. S. Deconstructing the third dimension: how 3D culture microenvironments alter cellular cues. *J Cell Sci.* (2012).
6. Ghibaudo, M., Di Meglio, J.-M., Hersen, P., & Ladoux, B. Mechanics of cell spreading within 3D-micropatterned environments. *Lab Chip.* **11**, 805-812 (2010).
7. Greiner, A. M., Richter, B., & Bastmeyer, M. Micro-Engineered 3D Scaffolds for Cell Culture Studies. *Macromol Biosci.* **12**, 1301-1314 (2012).
8. Khetan, S. *et al.* Degradation-mediated cellular traction directs stem cell fate in covalently crosslinked three-dimensional hydrogels. *Nat Mater.* **12**, 458-465 (2013).
9. Legant, W. R. *et al.* Measurement of mechanical tractions exerted by cells in three-dimensional matrices. *Nat Meth.* **7**, 969-971 (2010).
10. Riveline, D., & Buguin, A. Devices and methods for observing the cell division. *WO/2010/092116.* (2010).
11. Ochsner, M. *et al.* Micro-well arrays for 3D shape control and high resolution analysis of single cells. *Lab Chip.* **7**, 1074-1077 (2007).
12. Riveline, D. Devices and methods for observing cells with cell wall or invertebrate embryos with oblong eggshell *WO 2013144302 A1.* (2012).
13. Riveline, D., & Wollrab, V. Devices and methods for observing eukaryotic cells without cell wall. *WO 2013135809 A1.* (2012).
14. Zanella, F., Lorens, J. B., & Link, W. High content screening: seeing is believing. *Trends Biotech.* **28**, 237-245 (2010).
15. Wolfe, D., Qin, D., & Whitesides, G. in *Microengineering in Biotechnology* Vol. 583 *Methods in Molecular Biology.* eds Michael P. Hughes & Kai F. Hoettges) Ch. 3, 81-107 Humana Press, (2010).
16. Mehling, M., & Tay, S. Microfluidic cell culture. *Curr Op Biotech.* **25**, 95-102 (2014).
17. Wollrab, V., Thiagarajan, R., Wald, A., Kruse, K., & Riveline, D. Still and rotating myosin clusters determine cytokinetic ring constriction. *Nat Commun.* 7, 11860-11869 (2016).

18. Yao, X. *et al.* Functional analysis of single cells identifies a rare subset of circulating tumor cells with malignant traits. *Integr Biol.* **6**, 388-398 (2014).
19. Eberwine, J., Sul, J.-Y., Bartfai, T., & Kim, J. The promise of single-cell sequencing. *Nat Meth.* **11**, 25-27 (2014).
20. Allen, T. D. *et al.* Generation of cell-free extracts of Xenopus eggs and demembranated sperm chromatin for the assembly and isolation of in vitro-formed nuclei for Western blotting and scanning electron microscopy (SEM). *Nat. Protocols.* **2**, 1173-1179 (2007).
21. Robbins, E., & Marcus, P. I. Mitotically Synchronized Mammalian Cells: a Simple Method for Obtaining Large Populations. *Science.* **144** (1964).
22. Whitfield, M. L. *et al.* Stem-loop binding protein, the protein that binds the 3" end of histone mRNA, is cell cycle regulated by both translational and posttranslational mechanisms. *Molecular and Cellular Biology.* **20** (2000).
23. Straight, A. F. *et al.* Dissecting Temporal and Spatial Control of Cytokinesis with a Myosin II Inhibitor. *Science.* **299**, 1743-1747 (2003).
24. Tang, J., Erikson, R. L., & Liu, X. Checkpoint kinase 1 (Chk1) is required for mitotic progression through negative regulation of polo-like kinase 1 (Plk1). *Proc Natl Acad Sci.* **103**, 11964-11969 (2006).
25. Zahreddine, H., Zhang, H., Diogon, M., Nagamatsu, Y., & Labouesse, M. CRT-1/Calreticulin and the E3 Ligase EEL-1/HUWE1 Control Hemidesmosome Maturation in C. elegans Development. *Curr Biol.* **20**, 322-327 (2010).
26. Porta-de-la-Riva, M., Fontrodona, L., Villanueva, A., Cer & n, J. Basic Caenorhabditis elegans Methods: Synchronization and Observation. *JoVE.* e4019 (2012).
27. Saha, S., & Pollard, T. D. Anillin-related protein Mid1p coordinates the assembly of the cytokinetic contractile ring in fission yeast. *Mol Biol Cell.* **23**, 3982-3992 (2012).
28. Prestwich, G. D. Evaluating Drug Efficacy and Toxicology in Three Dimensions: Using Synthetic Extracellular Matrices in Drug Discovery. *Acc Chem Res.* **41**, 139-148 (2007).
29. Futamura, Y. *et al.* Morphobase, an Encyclopedic Cell Morphology Database, and Its Use for Drug Target Identification. *Chem Biol.* **19**, 1620-1630 (2012).

nature COMMUNICATIONS

ARTICLE

Received 2 Sep 2015 | Accepted 6 May 2016 | Published 1 Jul 2016

DOI: 10.1038/ncomms11860 OPEN

Still and rotating myosin clusters determine cytokinetic ring constriction

Viktoria Wollrab[1,2,3,4,5,6,†], Raghavan Thiagarajan[1,2,3,4,5], Anne Wald[6], Karsten Kruse[6] & Daniel Riveline[1,2,3,4,5]

The cytokinetic ring is essential for separating daughter cells during division. It consists of actin filaments and myosin motors that are generally assumed to organize as sarcomeres similar to skeletal muscles. However, direct evidence is lacking. Here we show that the internal organization and dynamics of rings are different from sarcomeres and distinct in different cell types. Using micro-cavities to orient rings in single focal planes, we find in mammalian cells a transition from a homogeneous distribution to a periodic pattern of myosin clusters at the onset of constriction. In contrast, in fission yeast, myosin clusters rotate prior to and during constriction. Theoretical analysis indicates that both patterns result from acto-myosin self-organization and reveals differences in the respective stresses. These findings suggest distinct functional roles for rings: contraction in mammalian cells and transport in fission yeast. Thus self-organization under different conditions may be a generic feature for regulating morphogenesis *in vivo*.

[1] Laboratory of Cell Physics ISIS/IGBMC, ISIS & icFRC, Université de Strasbourg & CNRS, 8 allée Gaspard Monge, Strasbourg 67000, France. [2] Institut de Génétique et de Biologie Moléculaire et Cellulaire, Illkirch, France. [3] Centre National de la Recherche Scientifique, UMR7104, Illkirch, France. [4] Institut National de la Santé et de la Recherche Médicale, U964, Illkirch, France. [5] Université de Strasbourg, Illkirch, France. [6] Theoretical Physics, Saarland University 66123, Saarbrücken, Germany. † Present address: FOM Institute AMOLF, 1098 XG Amsterdam, The Netherlands. Correspondence and requests for materials should be addressed to K.K. (email: k.kruse@physik.uni-saarland.de) or to D.R. (email: riveline@unistra.fr).

Cytokinesis is the final step of the eukaryotic cell cycle, dividing the cell into two and separating the two nuclei generated during mitosis into the newly formed daughter cells[1]. Animal cells and some fungi use a ring of actin and myosin II to constrict a cleavage furrow at the beginning of cytokinesis[2,3] as shown, for example, with fluorescence microscopy and electron microscopy for *Caenorhabditis elegans*[4], sea urchin eggs[5], newts[6,7], mammalian cultured cells[8] and fission yeast[9–14].

Concentrations of actin, myosin and actin-associated proteins such as nucleating and crosslinking proteins have been estimated quantitatively for fission yeast[15] and for *Dictyostelium discoideum*[16]. Understanding cytokinetic ring dynamics has usually been based on muscle acto-myosin with sliding filaments generating forces in a manner analogous to sarcomeres[2,17,18]. In sea urchin[5], it was shown that actin volume decreases during constriction, in agreement with proposed filament shortening during closure in fission yeast[12] where actin and actin-associated proteins decrease in quantity during closure while the total amount of myosin appears to be constant[15]. These results suggest that some ring components, like actin and actin-associated proteins disassemble during constriction, whereas others such as myosins become more concentrated potentially promoting higher forces.

Fission yeast studies suggest that the filament polarities and the distribution of myosin motors are important for mechanical closure[19]. Studies of filament polarity using myosin decoration indicate that actin filaments have a mixed polarity within the cytokinetic ring, although arrays as seen in sarcomeres have not been reported[16]. In addition, the dynamics and the mesoscopic mechanisms of ring closure remain unclear, and this is also true for mammalian cell cytokinetic rings[20–23].

In this study, we orient mammalian and fission yeast cells using micro-cavities to image cytokinetic rings in single focal planes[24–26]. We find that the internal organization and dynamics of rings are different from sarcomeres and distinct in the different cell types. In mammalian cells, the periodic pattern of myosin clusters emerges from a homogeneous distribution at the onset of constriction. In contrast, in fission yeast, myosin clusters appear during ring formation[27]. We report that they rotate prior to and during constriction. We use a continuum theory to study acto-myosin dynamics which indicates that both patterns result from acto-myosin self-organization. Furthermore the theoretical analysis reveals differences in the respective stresses generated by the different myosin organizations. We confirm these results with experimental tests. These findings suggest distinct functional roles for rings: contraction in mammalian cells and transport in fission yeast.

Results

Orienting cytokinetic rings. To increase the spatial and temporal resolution, we oriented mammalian cells and fission yeast cytokinetic rings parallel to their plane of observations. We introduced them into microfabricated wells[24,25] prepared by soft lithography (Fig. 1a,b and Supplementary Fig. 1). This allowed the acto-myosin rings to be positioned in a single focal plane (Fig. 1c,d and Supplementary Movies 1 and 2). The ring was visualized by fusion of fluorescent proteins with myosin and actin markers (Methods). Other proteins of both rings were also observed (Supplementary Figs 3 and 8). This orientation allowed us to investigate the inner dynamics of the ring with a time resolution of seconds. We first established that acto-myosin ring constriction in the vertically oriented cells behaved similarly to cells growing horizontally on a microscope slide, after onset of constriction ($t = 0$ s, Supplementary Fig. 2). Cells underwent division with timing similar to cytokinesis on flat surfaces. We measured the diameter as a function of time (Fig. 1e,h) during the whole process of cytokinesis, which transforms the mammalian ring from 20 µm diameter to 2 µm within 500 s at 37 °C and the fission yeast ring from 3.5 to 0.3 µm within 40 min at 27 °C. The time courses of the constriction process differed: the velocity of mammalian rings increases monotonously until a diameter of ~5 µm and stalls at ~2 µm, whereas the velocity of fission yeast rings increases until ~3 µm, is then constant until ~1.5 µm and increases again until complete constriction. To understand the origin of discrepancies between both cell types, we measured total intensities (Fig. 1f,i), and derived the average protein densities (Fig. 1g,j) as an indicator for the generated stress. Changes in myosin and actin densities alone were within 20% only after time 0 s, and do not readily explain the sudden onset of constriction in neither mammalian nor fission yeast rings. This prompted us to take a closer look at the spatial organization of these proteins within the ring at the onset of constriction.

Still and rotating myosin clusters. We first focused on the localization of proteins during mammalian ring closure. Strikingly, the myosin assembles into clusters (Fig. 2a), which are separated by a typical distance of 0.8 µm. In the reference frame of the ring, these clusters persisted at the same location throughout constriction (Fig. 2a and Supplementary Movie 2). The cluster trajectories were mostly straight, although curved trajectories were also observed (Supplementary Fig. 4b). Occasionally neighbouring clusters fused or split (arrows in Supplementary Fig. 4a). Contrasting with actin that showed a less pronounced pattern (Fig. 2b), we detected clusters of the actin nucleator mDia2 (ref. 28), a member of the formin family, co-localizing with myosin clusters (Fig. 2c). In fission yeast, we observed similar clusters for myosin and actin (Fig. 3a–c). Contrary to mammalian clusters, they exhibited motion, rotating typically 0.7 µm clockwise and counter-clockwise in about 20 s within the same rings (Fig. 3g,h, Supplementary Fig. 10a,b and Supplementary Movies 3 and 4), even prior to the onset of constriction. Rotation was further demonstrated through myosin-rich radial extrusions, which extended to the cell periphery during closure (Fig. 3d–f and Supplementary Movie 5). Velocities were measured by polar transformation of the ring to a line followed by kymograph representation, and they were in the µm per min range (Fig. 3g–i). They were larger for actin than for myosin, but both velocities decreased during closure. Despite different mechanical and molecular conditions, cytokinetic rings thus share common motifs in acto-myosin but with different dynamics.

We next asked whether myosins within clusters in both systems were recycling. We measured the turnover time for myosins using Fluorescence recovery after photobleaching (FRAP), and we obtained ~20 s and ~1 s for mammalian and fission yeast rings, respectively (Supplementary Figs 6a,b and 10c,d). This is fast compared with the total duration of the closure, 500 s and 40 min, showing fast exchange with cytoplasmic myosin. Despite this myosin dynamics, clusters kept constant features in mammalian rings: the average cluster size (distance between two adjacent fluorescence intensity minima), the average cluster density and the cluster contrast (the ratio of the mean fluorescence intensities of the cluster and the two neighbouring regions) (Fig. 2d). Together, these measurements suggest that myosin clusters involve myosin dynamics while keeping constant their mesoscopic read-outs.

Myosin clusters and ring constriction. We next wondered whether clusters could be affected by modulating the activity of acto-myosin. Constrictions of mammalian rings in the presence of the myosin inhibitor blebbistatin or the monomeric actin

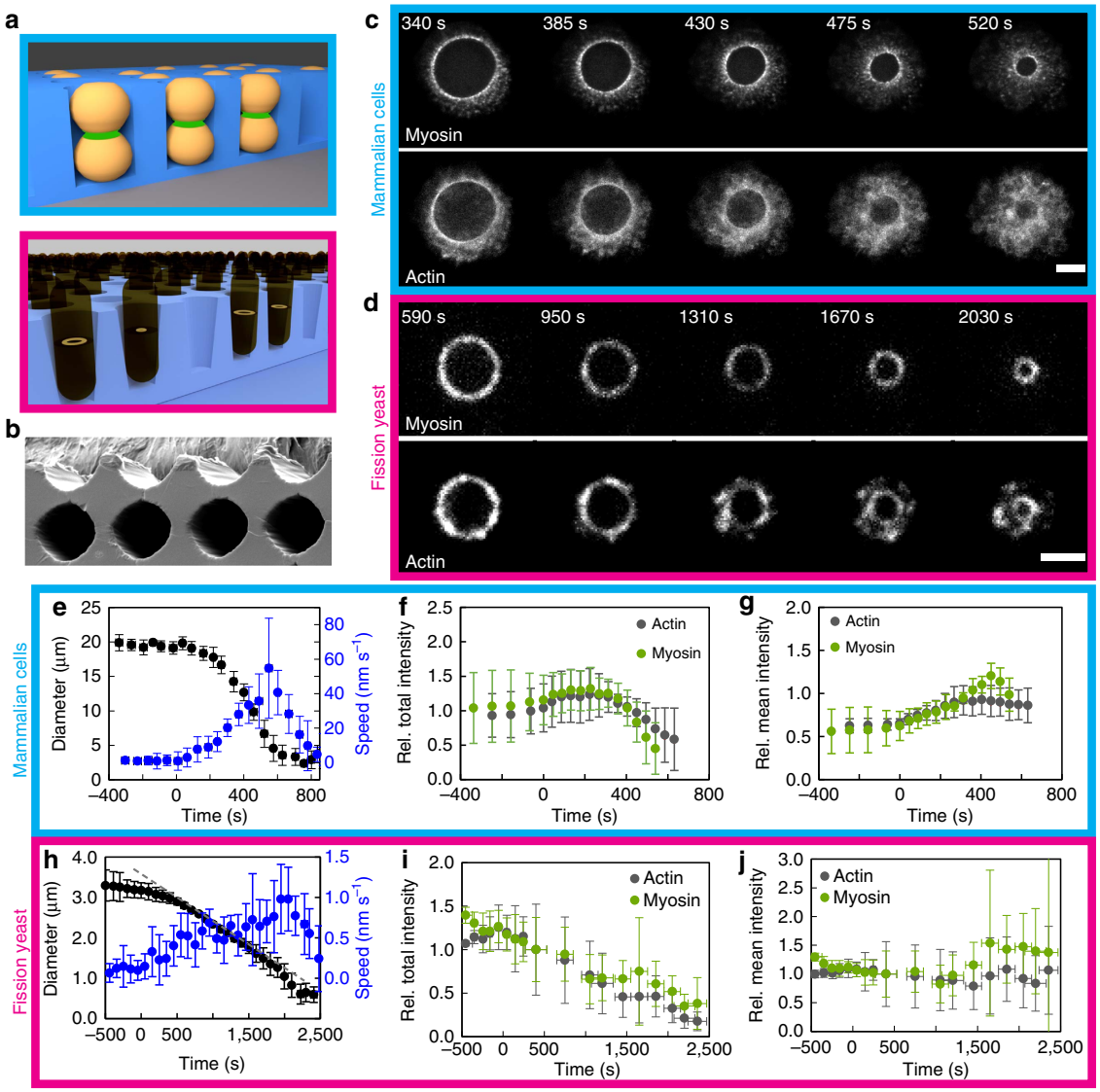

Figure 1 | The cytokinetic ring in one plane of focus. (**a**) Cells are oriented in micro-cavities during cytokinesis along the axis of division. (**b**) Electron microscopy image of an array of PDMS micro-cavities. Cavity diameter = 25 μm. (**c**,**d**) The cytokinetic ring visualized in mammalian cells (**c**, HeLa) and fission yeast (**d**) by myosin (MHC-GFP in **c**; Rlc1-mCherry in **d**) and actin (Lifeact-mCherry in **c**; CHD-GFP in **d**) (**c**) shows superimposition of five *z*-planes. Scale bar, 5 μm in **c**; 2 μm in **d**. Time zero is the onset of constriction. (**e**,**h**) Ring diameter and the corresponding closure speed as a function of time. (**e**) $N = 14$, (**h**) $N = 20$. The velocity is computed from individual constriction curves and then averaged. In **h**, the grey dashed line indicates the linear constriction regime. (**f**,**g**) Relative mean (**g**) and total (**f**) intensity of myosin and actin in the cytokinetic ring of mammalian cells. The intensity is normalized for cells at a diameter of 10 μm. $N = 10$ for myosin, $N = 6$ for actin. (**i**,**j**) Relative mean (**j**) and total (**i**) intensity of myosin and actin in the cytokinetic ring of fission yeast cells. The intensity is normalized for cells at a diameter of 3.1 μm. The intensity measurements were made from individual snapshots of rings for the time period of 300–2,500 s. $N = 241$ for both actin and myosin. The intensities before constriction were acquired from time-lapse movies of individual rings ($N = 3$). (**e**–**j**) Error bars indicate s.d.

sequestering agent latrunculin A were impaired in both cases while actin and myosin densities remained constant (Supplementary Fig. 5). In addition, the cluster density was reduced, but cluster size was increased compared with normal closure; the cluster contrast was slightly reduced (Fig. 2d). This was associated to stalled constriction for blebbistatin, and opening of rings for latrunculin A. Cluster dynamics was also altered in fission yeast (Fig. 3j): in the presence of 10 μM latrunculin A, velocities of ring constriction were reduced and clusters stopped. In addition, a mutant in myosin (*myo-E1*) was also exhibiting correlations in reduced velocities for ring constriction and clusters. Altogether, these experiments show that acto-myosin activity affects clusters. However, when we blocked the addition of the sugar wall with a wall mutant (*cps1-191*), cluster rotation was preserved with velocities similar to wild-type rings (Fig. 3j). This suggested that rotation is a built-in property of the acto-myosin ring in fission yeast, independently of the wall growth.

While clusters were present in fission yeast prior to ring constriction, mammalian rings already formed exhibited a quasi-homogeneous distribution up to 500 s prior to constriction (Fig. 2e and Supplementary Movie 6) with similar myosin density. Concomitantly with the onset of constriction, this distribution was changed into quasi-periodic clusters as reported above. Fourier transformation of the intensity profile supports the appearance of periodic structures (Fig. 2f). The maximum spatial frequency is consistent with the cluster density measurement. The simultaneous appearance of long lasting clusters during the onset

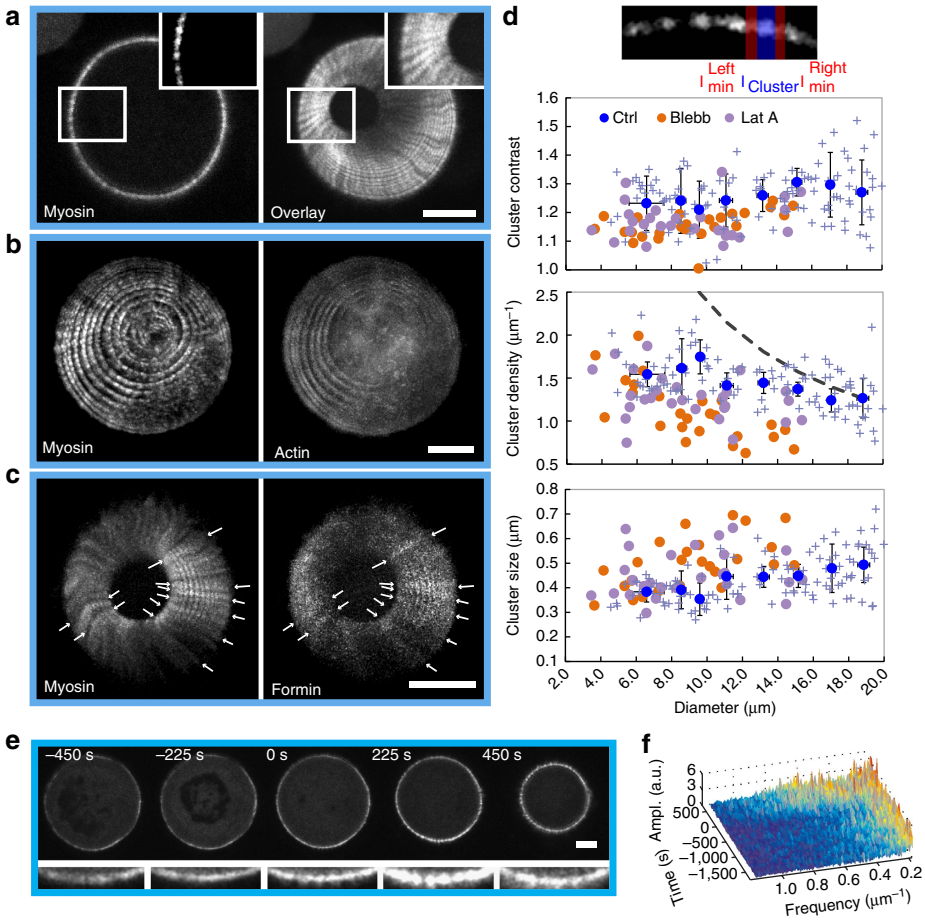

Figure 2 | Cytokinetic rings of mammalian cells exhibit regular patterns. (**a**) Myosin is distributed in regular clusters around the perimeter of the cytokinetic ring. Right: overlay of 25 frames, starting from the frame shown on the left. The clusters move radially, though little and collective rotations are visible for larger diameter. Time between images 10 s. (**b**) Overlay of 26 subsequent frames of a closing ring visualized by the fluorescence labelling of myosin and actin. Time between images 45 s, superimpositions of five *z*-planes, plane distance 1.3 μm. (**c**) The cytokinetic ring visualized by the labelling of myosin and mDia2-formin. Formin colocalizes with myosin (arrows). Overlay of 17 frames, time between frames 10 s. (**d**) Characterization of the myosin pattern in the control (blue) and after incubation with the cytoskeleton drugs blebbistatin (orange) and latrunculin A (purple). The cluster contrast stays about constant. The cluster density is increasing while the ring is constricting, but not as much as expected for a constant number of clusters (dashed line). Cluster density of cells treated with the two drugs is reduced. The cluster size decreases as the ring closes. Blue points represent averages, crosses correspond to single data points, error bars indicate the s.d., time-lapses of 11 closing rings were analysed. Each orange (blebbistatin) or purple (latrunculin A) point is obtained from averaging the cluster parameters from a fixed ring (blebbistatin: $N=25$, latrunculin A: $N=28$). (**e**) Time-lapse of a cell before, during and after formation of the cytokinetic ring visualized for myosin, below a zoomed region. Scale bar, 5 μm. (**f**) Fourier spectrum of the intensity profiles from the ring shown in **e**. At $t=0$ s, higher frequency structures appear. Scale bar, 5 μm in **a**–**c**,**e**; $t=0$ s is the onset of constriction.

of closure, together with the striking observation that none of the observed rings constricted in the absence of clusters, suggest that self-organization *per se* of myosin rather than an increase in motor density triggers a larger stress inducing constriction.

Physical model of acto-myosin organization. To test the possible mechanisms of pattern formation in cytokinetic rings, we used the physical framework of ref. 29 (Supplementary Note 1). We built the model on generic rules of interactions between parallel and anti-parallel actin filaments through myosin motors (Fig. 4a). Motivated by the observation of coarsening of nodes in fission yeast, we extend the previously developed framework and consider in addition to polar filaments also bipolar structures. In the spirit of a minimal description, we assume that polar filaments of fixed lengths can assemble into bipolar structures at rate ω_c and disassemble at rate ω_d. Molecular motors induce sliding between parallel and anti-parallel filaments at effective velocities α and β, respectively. Turnover of actin filaments is taken into account through an effective velocity v_{to}.

Our analysis revealed that there is a critical value α_c, such that the homogeneous state is unstable against perturbations for $\alpha>\alpha_c$, which only weakly depends on the value of β. Then myosin clusters appeared (Fig. 4b) which were stationary in some cases and moving in others, where ω_d was larger (Fig. 4d). Stationary clusters resembled the pattern observed in mammalian cells: after randomly perturbing a homogenous myosin distribution, the system develops clusters in the myosin distribution separated by a typical distance. These states remain essentially unchanged for simulated times longer than hours and would appear stationary during the course of ring constriction in a living cell. Only after these very long periods would two clusters fuse and further fusion events would take even longer time. Mathematically, the stationary state seems to contain only one cluster. In the case of moving clusters, we always observed pairs of clusters moving in opposite directions

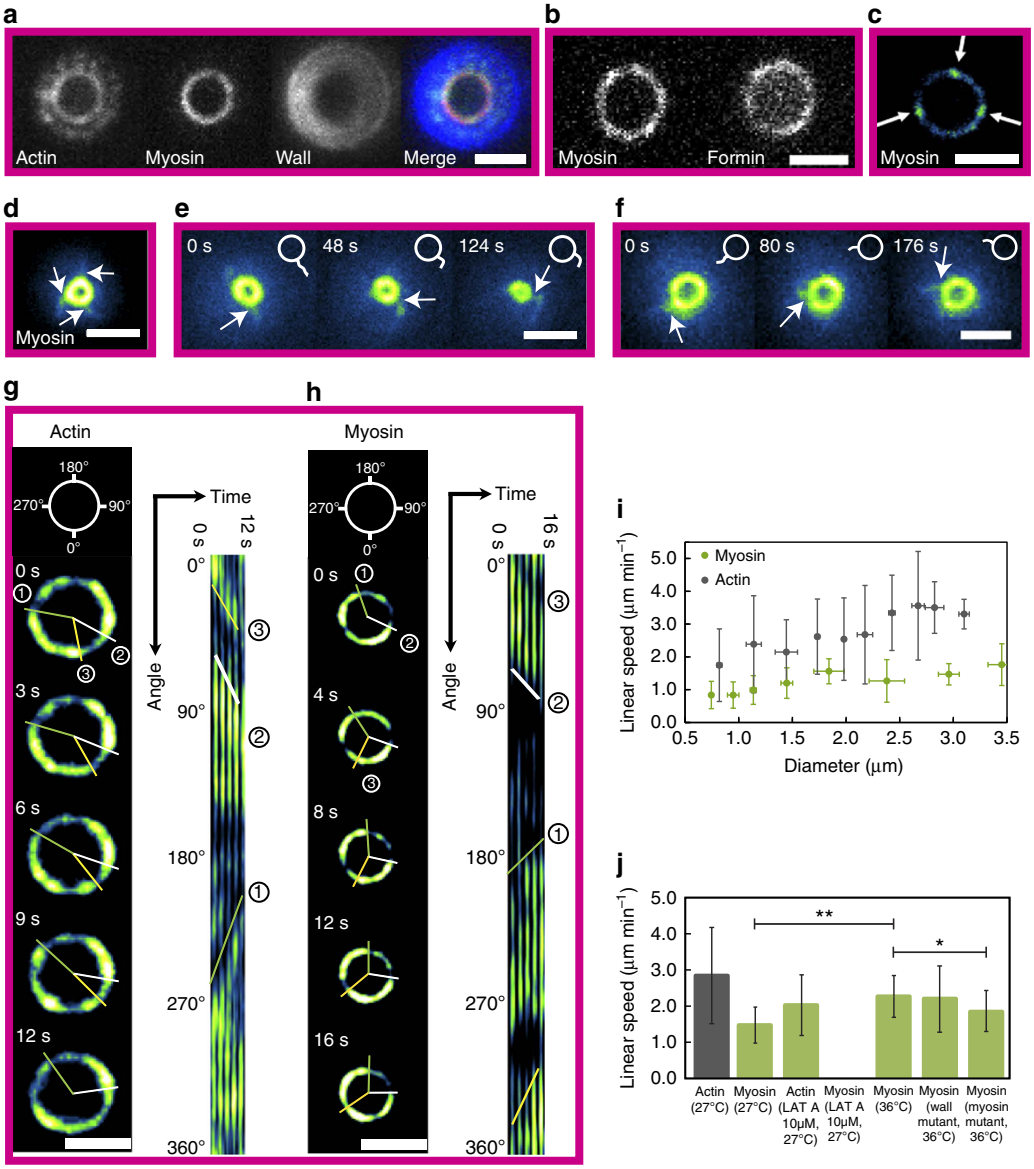

Figure 3 | Actin and myosin cluster rotate in fission yeast rings. (**a**) The fission yeast cytokinetic ring visualized by actin (CHD-GFP) myosin (Rlc1-tdTomato) and cell wall (calcofluor) labelling. (**b**) The ring is visualized by myosin and formin (Cdc12-GFP) labelling. Scale bar, 2 μm. (**d**–**f**) Representation of arms extending out of a ring (**d**). Arms attached to the ring (arrows) rotate counter-clockwise (**e**) and clockwise (**f**). The rings are visualized by myosin labelling (Rlc1-mCherry). Scale bar, 2 μm. (**c**,**g**,**h**) Representation of clusters (arrows) in the cytokinetic ring visualized by myosin (Rlc1-mCherry) (**c**). During ring constriction, clusters of actin (CHD-GFP) (**g**) and myosin (Rlc1-tdTomato) (**h**) rotate clockwise and counter-clockwise. The analysis is based on a kymograph representation of the ring after polar transformation. Lines highlight the motion of clusters on the ring and in the kymographs. Scale bar, 2 μm. (**i**) The analysis of cluster motion reveals a decrease in actin cluster speed during constriction. Myosin clusters rotate with a constant speed with decreasing speed towards the constriction completion. Error bars indicate s.d. Each point contains 4–50 measurements, 202 in total for actin and 77 for myosin. (**j**) Comparison of the cluster speed in different conditions and for different proteins. Rings with diameters of >1.5 μm were used. Each mean value contains 13–185 measurements. Error bars indicate s.d. One-way analysis of variance was performed, $^{*}P<0.05$, $^{**}P<0.01$.

co-existing with stationary clusters. These phenomena were visible in kymographs of rings in mammalian cells and in fission yeast (Fig. 4c,e and Supplementary Fig. 9). The apparent discrepancy between the extension of clusters in Fig. 4d and in Fig. 4e may result from the point spread function of the set-up. In addition, the regular pattern of the simulation is modified by molecular noise. Importantly, the mechanism studied by the simulation reproduces co-existing clusters rotating in opposite directions, which is the key feature of myosin in fission yeast rings.

The instability of the homogenous state results from the presence of bipolar filaments. Motors tend to approach the centres of two overlapping bipolar filaments. In the homogenous state, the total force on a bipolar filament vanishes. If this balance is broken by a perturbation, bipolar filaments will accumulate in clusters if their interaction, which is given by the parameter α, outcompetes the homogenizing effects by the diffusion term. This mechanism yields a typical distance between clusters of four filament lengths (Supplementary Note 1), which we indeed observe in our calculations (Fig. 4f, top). Polar filaments essentially follow the dynamics of the bipolar filaments. Note, that in steady state, there are still non-vanishing filament fluxes: motors drive bipolar filaments into clusters, while filament assembly and disassembly that we capture by treadmilling, lead to

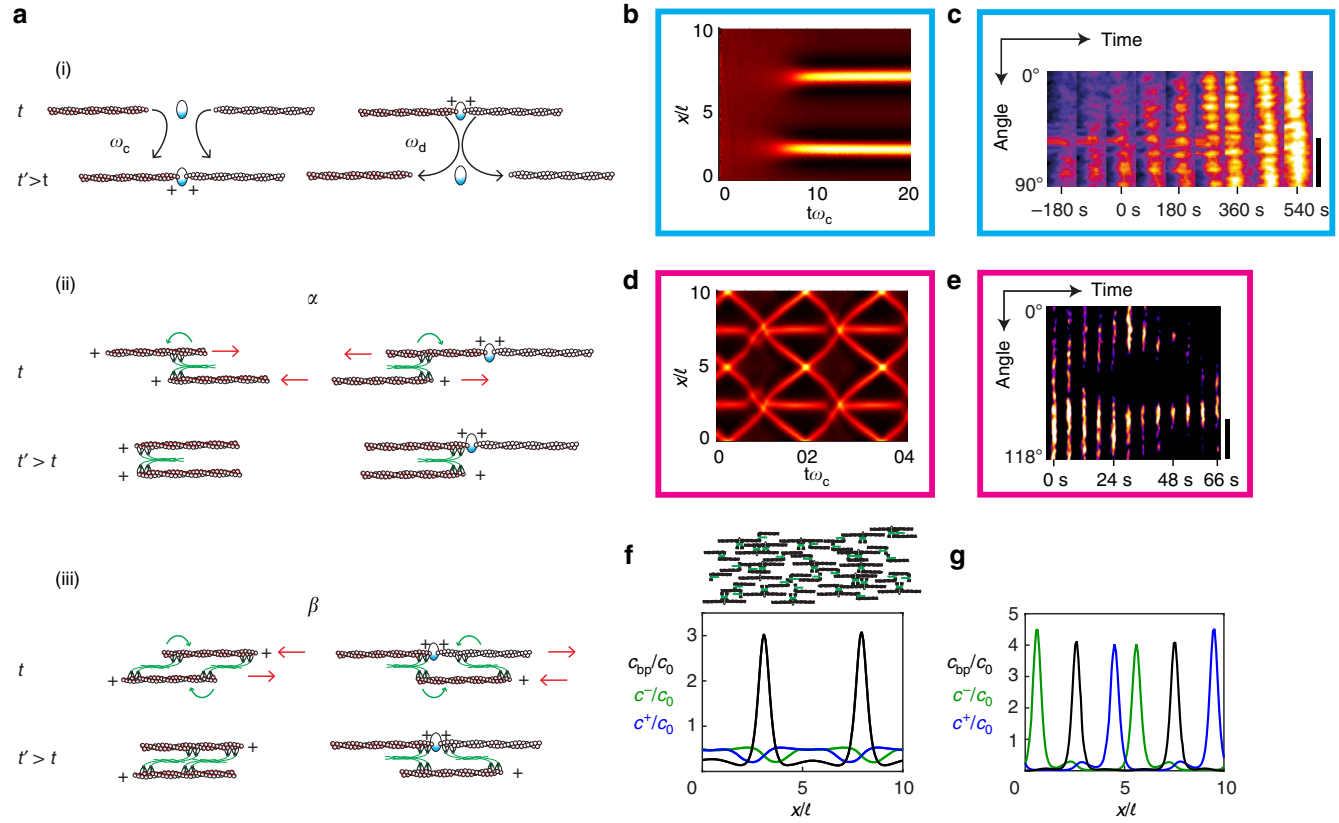

Figure 4 | Model for acto-myosin rings. (**a**) Schematic of the model components and their interactions describing the parameters (see text). At each plus-end there is a motor, but only motors interacting with another filament are shown. (**b**,**c**) Kymographs of emerging stationary myosin clusters in the model (**b**) and in mammalian cells (**c**). Myosin density is colour-coded. In **b**, the parameter α is increased from a sub- to a supercritical value, the initial distribution was homogenous with a random perturbation. (**d**,**e**) Kymographs of rotating myosin clusters in the model (**d**) and in fission yeast (**e**). Myosin density is colour-coded, and the parameter α is constant in **d**. In **c**,**e**, dashed white lines serve as a guide to the eye. (**f**,**g**) Distributions of bipolar filaments (c_{bp}, black) and polar filaments (c^+, blue, c^-, green) corresponding to $t = 20\ \omega_c^{-1}$ of Fig. 4b (**f**) and to $t = 0$ of Fig. 4d (**g**). (**f**, top) In alignment, illustration of the F-actin distributions corresponding to two adjacent myosin clusters.

outflux of polar filaments from clusters. The steady state densities show furthermore that the myosin clusters are associated with the bipolar filaments (Fig. 4f, bottom). For the oscillatory state, the densities reveal that stationary clusters are associated with bipolar filaments, whereas mobile clusters are linked with polar filaments (Fig. 4g).

We then systematically investigated the effect of changes in both parameters α and ω_d (Fig. 5a). Three states were apparent: homogenous distribution, stationary clusters and dynamic clusters co-existing with stationary clusters. Changes of other parameters also affect the system, for example, changes in filament lengths and/or in the velocity can induce transitions from rotating to still clusters and vice versa. Moreover we qualitatively reproduced the changes in cluster contrast and cluster size reported above (Fig. 2d) when changing actin polymerization and myosin activity (Supplementary Note 1).

We wanted to evoke experimentally the transition from homogeneous to patterned states, as well as immobilizing rotating clusters. To effectively move in parameter space, we applied different drugs. For mammalian rings, we reduced myosin activity, which corresponds to a reduction of the parameter α in the model, by incubating with 100 µM blebbistatin and found homogenization of myosin. Strikingly, after washing the compound, constriction was re-initiated together with the formation of myosin clusters (Fig. 5b,c and Supplementary Movie 7). This further supports our conclusion that cluster formation triggers constriction. For fission yeast rings, cells were incubated with 10 µM latrunculin A and myosin clusters were stopping with a stalled ring (Fig. 5d and Supplementary Movie 9). After washing the compound, rotation was re-initiated together with ring constriction. These drug experiments illustrate that the inner dynamics of cytokinetic rings is qualitatively captured by our theory.

Stress and myosin clusters. We next looked for potential functions of such dynamics by calculating the stress associated with still and rotating clusters (Fig. 6a). We evaluated the stress in the ring by summing at each point the stresses in all filaments overlapping with this point[21,30] (Supplementary Note 1 and Fig. 6b). With increasing values of α, the stress also increased monotonically. At the value of α_c for which the homogenous filament distribution becomes unstable and leads to stationary patterns, the sensitivity of the stress to changes in α increased dramatically (Fig. 6a). As a consequence, the spontaneous rearrangement of filaments in the ring is accompanied by an increase in the stress generated by the ring that is significantly larger than the increase expected for a homogenous ring with increasing α (Fig. 6b). In contrast, the stress changes less than expected for the homogeneous state when the clusters were rotating (Fig. 6a). This difference suggests distinct roles for still and rotating clusters, contraction and transport, respectively, and we turned back to experiments to probe this prediction.

We reasoned that a ring under tension would continue to contract after rupture. We therefore locally ruptured rings by

laser ablation (Methods). Indeed, with laser ablation, the mammalian ring opens (Fig. 6c). The remaining bundle further contracted (Supplementary Fig. 7) while myosin clusters moved radially. In contrast, ablated fission yeast rings were healing within seconds without constriction (Fig. 6d). Also, clusters continued to rotate after ablation, suggesting that the remainder

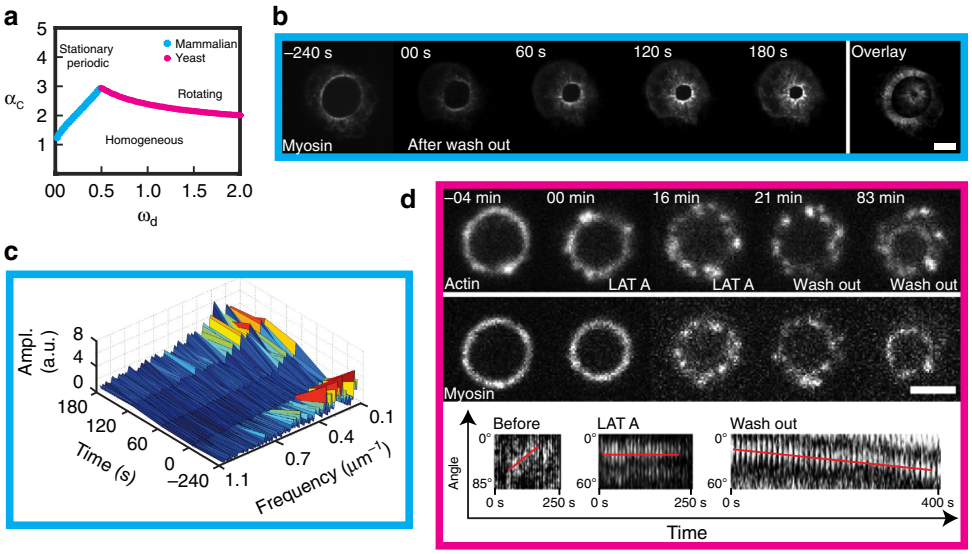

Figure 5 | Myosin clusters form through a dynamic instability. (**a**) Critical value of the parameter α from a linear stability analysis. Blue: stationary instability; pink: oscillatory instability. (**b**) Mammalian cells before and after 10 min incubation with 100 µM blebbistatin. After drug treatment, the myosin pattern is not present but reappears after wash out. Superimposition of five *z*-planes; scale bar, 5 µm. (**c**) Fourier spectrum of the intensity profiles shown in **b**. Characteristic frequencies are seen before blebbistatin addition and starts to reappear after blebbistatin wash out at 0 s. (**d**) Fission yeast cell before and after 20 min incubation with 10 µM latrunculin A. The ring disassembles, but motion of actin clusters (CHD-GFP) is still visible (see Supplementary Movie 9) while myosin (Rlc1-tdTomato) clusters are still. After wash out, the ring re-forms and constricts again. Scale bar, 2 µm. Polar-transformed kymographs of the ring in myosin (Rlc1-tdTomato) confirm different behaviours of the clusters before and during the incubation of latrunculin A and after wash out.

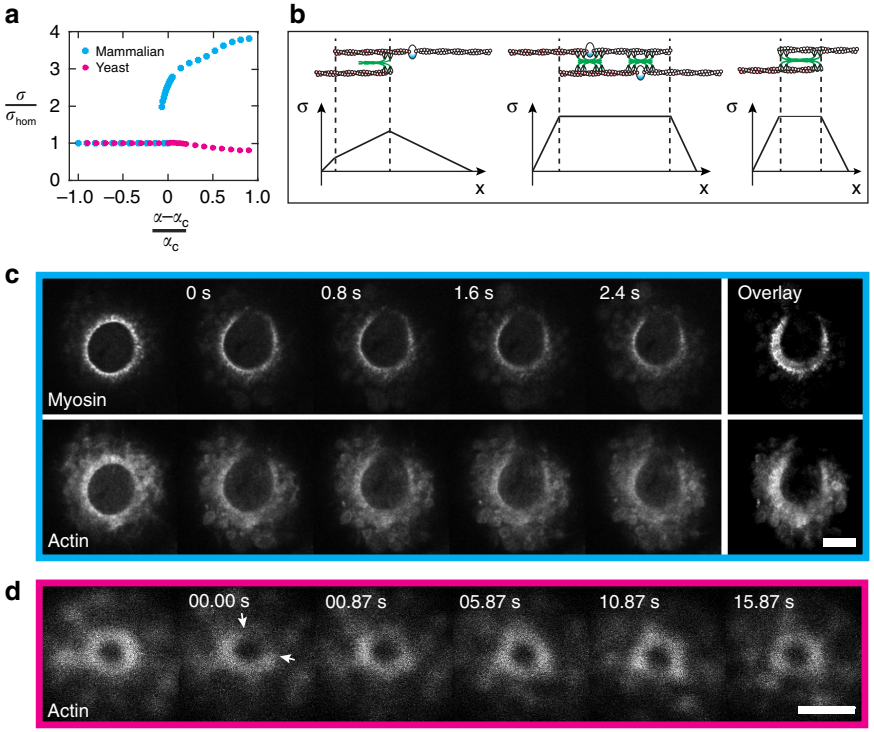

Figure 6 | Motor-induced mechanical stresses in contractile rings. (**a**) Calculated stress σ as a function of myosin activity α undergoing a stationary (blue) or oscillatory (pink) instability. σ_{hom} is the stress in homogeneous state. (**b**) Illustration of the stress profiles for pairs of a polar and a bipolar filament (left), two bipolar filaments (middle) and two polar filaments of opposite orientation (right). Stress is drawn to scale. Only motors crosslinking two filaments are shown. (**c**,**d**) Laser ablation of cytokinetic rings in mammalian cells (**c**) and in fission yeast (**d**). (**c**) Ring opens on cutting. Overlay (9 frames, 0.8 s) reveals constriction and radial movement of myosin clusters. Scale bar, 5 µm. (**d**) The ring breaks after cutting (arrows) but is repaired within seconds. Image smoothed with ImageJ. Scale bar, 2 µm.

of the ring was not affected by ablation. In addition, we acquired a ring with a portion locally detached and ruptured (Supplementary Movie 8). Both new free ends fluctuated over timescales of seconds: this suggests that the ring is not contractile because for a contractile ring the detached parts would retract and straighten. Finally, we also tracked proteins involved in the synthesis of the wall: Bgs4 clusters were also rotating (Supplementary Fig. 9c). These results suggest that the myosin cluster rotation could be related to transport of the wall machinery in fission yeasts rings.

Discussion

The different functions of the myosin clusters reported above are related to distinct network states and emerge from simple interactions rules between actin and myosin. Consequently, they can play an essential role in a variety of situations where signalling pathways may fail to give satisfactory explanations. These situations notably comprise fission yeast ring formation[27], *in vitro* rings[31] and acto-myosin networks[32], stress fibres in mammalian cells[33], cortices in *C. elegans*[34], and cytoplasmic networks in *C. elegans*[35] and in *Drosophila*[36].

Methods

Microfabrication. Micro-cavities were prepared with standard microfabrication methods (see Supplementary Fig. 1 and Supplementary Methods). Briefly, silicon masters prepared with deep reactive ion etching or photolithography and filters were used to prepare molds[24]. Cavities were prepared by pouring liquid polydimethylsiloxane (PDMS) onto these masters; PDMS was allowed to cure at 65 °C for 4 h, before being unpeeled carefully. These stamps were passivated and then pressed on PDMS-coated coverslips to mold the final micro-cavities. Alternatively passivated stamps were coated with PDMS. After curing, the PDMS layer was bound to coverslips and the stamp unpeeled.

Experimental chamber preparation. For experiments with mammalian cells, functionalized cavities were used. Cavities are plasma activated and incubated for at least 1 h at room temperature or overnight in the fridge with 20 μg ml^{-1} fibronectin (Sigma). Cavities for experiments with fission yeast are not coated. Prior to observation, HeLa cells were synchronized by mitotic shake off[37]. Cells were inserted in cavities by centrifuging the cell suspension on the cavities three times with 800*g*, each time 2 min (mammalian cells)/5 min (fission yeast). The coverslip with cavities was supported by a custom-made plastic cylinder in a 50 ml vessel. For fission yeast experiments, the centrifuge was preheated to the temperature of the experiment. The coverslip with cavities was removed from the holder and was inserted in a home-made chamber. Removing cells on top of the cavities by gently rinsing of the sample improved the imaging quality. Fresh medium was immediately added to the formed chamber.

We checked that neither cells were rotating within cavities by following external fiducial markers, that is, stationary motifs in cells visualized by phase contrast microscopy. In an alternative set-up shown in Supplementary Fig. 2, coverslips with cells were oriented vertically with respect to the plane of focus. The coverslip was held by two binder clips[38]. The coverslip was patterned with fibronectin (Cytoskeleton) by standard microcontact printing protocols[39]. Mammalian cells were synchronized with the double thymidine block[40].

Cell culture. HeLa cells expressing mCherry-Lifeact and MHC–GFP or only MHC–GFP were used (gift from Anthony Hyman, MPI-CBG Dresden). They were cultured in DMEM with 10% FCS, 2 mM L-glutamine and 1% penicillin/streptomycin antibiotics (all Invitrogen). For imaging, we used L-15 medium (Invitrogen) supplemented with 10% foetal calf serum and 2 mM L-glutamine. Fission yeast was grown in exponential phase at 32 °C, and then diluted in YE5S medium (MP Biomedicals). The strains JW1348 and JW1349 (see Supplementary Table 1) were cultured in EMM5S (MP Biomedicals) at 27 °C for 18–24 h before acquisition. Cultures which had reached an optical density of 0.2–0.8 were used for experiments. We visualized entire rings in our set-up with a variety of *Schizosaccharomyces pombe* strains reported in Supplementary Table 1. At the restrictive temperature (36 °C), the temperature sensitive strain PN 4461 was observed for 2–5 h after the temperature shift.

The generic terms 'myosin' and 'actin' are used throughout the article for clarity: they refer to MHC and Lifeact for mammalian cells rings, and to Rlc1 and CHD for fission yeast rings, respectively.

Transfection. The mDia2 plasmid was a gift from Watanabe[28]. We transfected cells with Lipofectamin 2000 (Invitrogen).

Cytoskeleton drugs and staining. Blebbistatin was used at a concentration of 100 μM and latrunculin A (Sigma) at a concentration of 1.5 μM (mammalian cells)/ 10 μM (fission yeast). To expose cells immediately with the drugs, the compounds were diluted to the indicated concentration in imaging medium before addition. Medium in which the cells were incubated was removed and the medium with the drug was added. At the end of the incubation time, the drug containing medium was removed and replaced by fresh medium. To characterize the pattern in mammalian cells, cells were incubated for 15 min with blebbistatin (100 μM) or 1.5–3 min with latrunculin A (1.5 μM) and then fixed with 3% paraformaldehyde (PFA, Sigma). For staining, HeLa cells were fixed with 3% PFA (Sigma) and permeabilized with Triton (Sigma). Immunostaining was performed using anti-anillin (gift from M. Glotzer, 1:500) and anti-septin7 (Proteintech, 13818-1-AP, 1:500) primary antibodies.

Optical set-ups. To acquire cytokinesis in HeLa cells, we used the Leica TCS SP-5-MP or SP-8-MP confocal, upright microscopes equipped with a Leica Application Suite Advanced Fluorescence LAS AF 2.6.3.8173/LAS AF 3.1.2.8785 acquisition system with photomultiplier tube (PMT) and hybrid detectors. We used a ×25 or ×63 HCX IR APO L water objective (0.95 numerical aperture (NA), Leica). Cytokinetic rings in fission yeast cells were acquired with a ×100 HCX PL APO CS oil objective (1.4 NA, Leica) mounted on a spinning disk microscope based on a Leica DMI6000 inverted microscope, equipped with a Yokogawa CSU22 spinning disk unit and Andor iQ 1.9.1 acquisition system. For laser ablation experiment, we used the TCS SP-5-MP (HeLa cells) or SP-8-MP (fission yeast) upright microscopes with an infrared femtosecond pulsed lasers (SP-5: Coherent Ultra, SP-8: Coherent Vision II with precompensation). Rupture in contrast to bleaching was checked by measuring changes in the ring curvature right after ablation. Experiments to measure the constriction were also performed on epifluorescent microscopes (Nikon Eclipse Ti inverted microscope (×60, oil, 1.40 NA, DIC, Nikon) and Olympus CKX41 inverted microscope (×100 UPlanFl, oil, 1.30 NA, Olympus, ×100 UPlanSApo, oil, 1.40 NA, Olympus and ×60 PlanApo, oil, 1.45 NA, Olympus). For FRAP experiments on HeLa cells, we used the Leica TCS SP2 AOBS MP based on a Leica DMIRE2 microscope, equipped with a PMT detector and a ×63 HCX PL APO oil (1.4 NA, Leica) objective. Experiments with HeLa cells were performed at 37 °C and with fission yeast at 27 °C if not indicated differently.

Analysis. We measured the ring diameters with ImageJ. The onset of constriction was set at $t=0$ s. Individual diameter–time plots were aligned at diameter 10 μm for mammalian rings and averaged. The speeds were computed through the changes in diameters over time steps of 100 s for yeast and 45–60 s for mammalian cells. The intensities and intensity profiles were measured with ImageJ.
To determine the intensity during closure, we used single images and time-lapse movies (see Supplementary Methods). The time-lapse movies were needed to extract a time information in regimes where the radius does not change over time. The cluster contrast was determined by dividing the intensity of a cluster by the mean intensity of the two neighbouring minima. The cluster density corresponds to the numbers of clusters per perimeter. To analyse the formation of the pattern in the cytokinetic ring in mammalian cells, the intensity profiles were measured with ImageJ and a Fourier Transformation was performed with Matlab. We determined the cluster velocities in fission yeast rings as follows. The rings were transformed to lines (Fig. 3g,h) by a polar transformation (ImageJ) and represented as kymographs. In these kymographs, the cluster can be traced as lines. If the cluster motion could be followed over at least three successive images, we measured their velocities by taking the slopes of their movement. Cluster lifetime and travelling length was also extracted from the kymographs. For better representation, we smoothed images of mammalian cells with ImageJ. For the rings in Figs 2a,c and 3g,h, and Supplementary Movie 4, we doubled the pixel and then smoothed the image. In Fig. 5b, we normalized the stack histogram.

Statistical analysis. All error bars indicate the s.d. of the mean. For the comparison of cluster velocities in fission yeast cells in Fig. 3j, we considered ring diameters that were equal and larger than 1.5 μm. The statistical significance was tested with one-way analysis of variance and accepted at $P<0.01$ and $P<0.05$. For the comparison of the myosin cluster in mammalian cells in drug-treated and control cells (Supplementary Fig. 5g), we took measurements on rings in the diameter range of 9–12 μm. The statistical significance was tested with Mann–Whitney test and accepted at $P<0.01$ and $P<0.05$.

Data availabilty. All relevant data are available from the authors.

References

1. Rappaport, R. *Cytokinesis in Animal Cells* (Cambridge Univ. Press, 1996).
2. Schroeder, T. E. *Molecules and Cell Movement* 305–334 (Raven Press, 1975).
3. Eggert, U. S., Mitchison, T. J. & Field, C. M. Animal cytokinesis: from parts list to mechanisms. *Annu. Rev. Biochem.* **75,** 543–566 (2006).

4. Carvalho, A., Desai, A. & Oegema, K. Structural memory in the contractile ring makes the duration of cytokinesis independent of cell size. *Cell* **137,** 926–937 (2009).
5. Schroeder, T. E. The contractile ring. II. Determining its brief existence, volumetric changes, and vital role in cleaving Arbacia eggs. *J. Cell Biol.* **53,** 419–434 (1972).
6. Selman, G. G. & Perry, M. M. Ultrastructural changes in the surface layers of the newt's egg in relation to the mechanism of its cleavage. *J. Cell. Sci.* **6,** 207–227 (1970).
7. Mabuchi, I., Tsukita, S., Tsukita, S. & Sawai, T. Cleavage furrow isolated from newt eggs: contraction, organization of the actin filaments, and protein components of the furrow. *Proc. Natl Acad. Sci. USA* **85,** 5966–5970 (1988).
8. Maupin, P. & Pollard, T. D. Arrangement of actin filaments and myosin-like filaments in the contractile ring and of actin-like filaments in the mitotic spindle of dividing HeLa cells. *J. Ultrastruct. Mol. Struct. Res.* **94,** 92–103 (1986).
9. Pelham, Jr R. J. & Chang, F. Role of actin polymerization and actin cables in actin-patch movement in Schizosaccharomyces pombe. *Nat. Cell Biol.* **3,** 235–244 (2001).
10. Pelham, R. J. & Chang, F. Actin dynamics in the contractile ring during cytokinesis in fission yeast. *Nature* **419,** 82–86 (2002).
11. Wu, J. Q., Kuhn, J. R., Kovar, D. R. & Pollard, T. D. Spatial and temporal pathway for assembly and constriction of the contractile ring in fission yeast cytokinesis. *Dev. Cell* **5,** 723–734 (2003).
12. Kamasaki, T., Osumi, M. & Mabuchi, I. Three-dimensional arrangement of F-actin in the contractile ring of fission yeast. *J. Cell Biol.* **178,** 765–771 (2007).
13. Mishra, M. *et al.* In vitro contraction of cytokinetic ring depends on myosin II but not on actin dynamics. *Nat. Cell Biol.* **15,** 853–859 (2013).
14. Stachowiak, M. R. *et al.* Mechanism of cytokinetic contractile ring constriction in fission yeast. *Dev. Cell* **29,** 547–561 (2014).
15. Wu, J. Q. & Pollard, T. D. Counting cytokinesis proteins globally and locally in fission yeast. *Science* **310,** 310–314 (2005).
16. Pollard, T. D. Mechanics of cytokinesis in eukaryotes. *Curr. Opin. Cell Biol.* **22,** 50–56 (2010).
17. Huxley, A. F. & Niedergerke, R. Structural changes in muscle during contraction; interference microscopy of living muscle fibres. *Nature* **173,** 971–973 (1954).
18. Huxley, H. & Hanson, J. Changes in the cross-striations of muscle during contraction and stretch and their structural interpretation. *Nature* **173,** 973–976 (1954).
19. Pollard, T. D. & Wu, J. Q. Understanding cytokinesis: lessons from fission yeast. *Nat. Rev. Mol. Cell Biol.* **11,** 149–155 (2010).
20. Biron, D., Alvarez-Lacalle, E., Tlusty, T. & Moses, E. Molecular model of the contractile ring. *Phys. Rev. Lett.* **95,** 098102 (2005).
21. Zumdieck, A., Kruse, K., Bringmann, H., Hyman, A. A. & Julicher, F. Stress generation and filament turnover during actin ring constriction. *PLoS ONE* **2,** e696 (2007).
22. Shlomovitz, R. & Gov, N. S. Physical model of contractile ring initiation in dividing cells. *Biophys. J.* **94,** 1155–1168 (2008).
23. Turlier, H., Audoly, B., Prost, J. & Joanny, J. F. Furrow constriction in animal cell cytokinesis. *Biophys. J.* **106,** 114–123 (2014).
24. Riveline, D. & Buguin, A. Devices and methods for observing the cell division. WO/2010/092116 (2009).
25. Wollrab, V. & Riveline, D. Devices and methods for observing eukaryotic cells without cell wall. WO/2013/135809 (2012).
26. Riveline, D. Methods for observing cells with cell wall or invertebrate embryos with oblong eggshell. WO/2013/144302 (2012).
27. Vavylonis, D., Wu, J. Q., Hao, S., O'Shaughnessy, B. & Pollard, T. D. Assembly mechanism of the contractile ring for cytokinesis by fission yeast. *Science* **319,** 97–100 (2008).
28. Watanabe, S. *et al.* mDia2 induces the actin scaffold for the contractile ring and stabilizes its position during cytokinesis in NIH 3T3 cells. *Mol. Biol. Cell* **19,** 2328–2338 (2008).
29. Kruse, K. & Julicher, F. Self-organization and mechanical properties of active filament bundles. *Phys. Rev. E Stat. Nonlin. Soft Matter Phys.* **67,** 051913 (2003).
30. Kruse, K. & Julicher, F. Actively contracting bundles of polar filaments. *Phys. Rev. Lett.* **85,** 1778–1781 (2000).
31. Reymann, A. C. *et al.* Actin network architecture can determine myosin motor activity. *Science* **336,** 1310–1314 (2012).
32. Gowrishankar, K. *et al.* Active remodeling of cortical actin regulates spatiotemporal organization of cell surface molecules. *Cell* **149,** 1353–1367 (2012).
33. Luo, W. *et al.* Analysis of the local organization and dynamics of cellular actin networks. *J. Cell Biol.* **202,** 1057–1073 (2013).
34. Mayer, M., Depken, M., Bois, J. S., Julicher, F. & Grill, S. W. Anisotropies in cortical tension reveal the physical basis of polarizing cortical flows. *Nature* **467,** 617–621 (2010).
35. Roh-Johnson, M. *et al.* Triggering a cell shape change by exploiting preexisting actomyosin contractions. *Science* **335,** 1232–1235 (2012).
36. Rauzi, M., Lenne, P. F. & Lecuit, T. Planar polarized actomyosin contractile flows control epithelial junction remodelling. *Nature* **468,** 1110–1114 (2010).
37. Robbins, E. & Marcus, P. I. Mitotically synchronized mammalian cells: a simple method for obtaining large populations. *Science* **144,** 1152–1153 (1964).
38. Comelles, J. *et al.* Cells as active particles in asymmetric potentials: motility under external gradients. *Biophys. J.* **107,** 1513–1522 (2014).
39. Caballero, D., Voituriez, R. & Riveline, D. Protrusion fluctuations direct cell motion. *Biophys. J.* **107,** 34–42 (2014).
40. Tang, J., Erikson, R. L. & Liu, X. Checkpoint kinase 1 (Chk1) is required for mitotic progression through negative regulation of polo-like kinase 1 (Plk1). *Proc. Natl Acad. Sci. USA* **103,** 11964–11969 (2006).

Acknowledgements

We thank P. Nurse, F. Nédélec, M.-F. Carlier, A. Ott, J. Comelles and the Riveline Lab for discussions and help, and we are grateful to X. Le Goff, A.-C. Reymann and U. Schwarz for critical reading of the manuscript. We thank J. Comelles for providing the scheme in Figs 4 and 6. We acknowledge the technical support from M. Marchand (Rockefeller), B. Rhoades and M. Skvarla (Cornell Ithaca), M. Koch and P. Kessler (Imaging Platform, IGBMC). We thank A. Hyman, J.Q. Wu, M. Balasubramanian, M. Lord, J. Moseley, P. Perez and T. Pollard for sharing strains. This study was performed in part for D.R. in a sabbatical stay at the Rockefeller University. It involved work at the Cornell NanoScale Facility, a member of the National Nanotechnology Infrastructure Network, which is supported by the National Science Foundation (Grant ECS-0335765), and in Femto (Besançon, France). This study with the reference ANR-10-LABX-0030-INRT has been also supported by a French state fund through the Agence Nationale de la Recherche under the frame programme Investissements d'Avenir labelled ANR-10-IDEX-0002-02. R.T. is an IGBMC International PhD Programme fellow supported by LabEx INRT funds. D.R. acknowledges support from CNRS (ATIP), ciFRC Strasbourg, the University of Strasbourg, Labex IGBMC, Fondation pour la Recherche Médicale and Foundation Cino del Duca. V.W. acknowledges support from UFA/DFH. K.K. was supported by Deutsche Forschungsgemeinschaft through SFB 1027.

Author contributions

D.R. initiated and coordinated the study, and developed the set-up for fission yeast. K.K. designed the theory. V.W., R.T. and D.R. performed the experiments; V.W. for mammalian cells, and R.T. and D.R. for fission yeast. A.W. and K.K. developed and analysed the model. All authors analysed and discussed the data. D.R. and K.K. wrote the manuscript with inputs from all authors.

Additional information

Supplementary Information accompanies this paper at http://www.nature.com/naturecommunications

Competing financial interests: The authors declare no competing financial interests.

Reprints and permission information is available online at http://npg.nature.com/reprintsandpermissions/

How to cite this article: Wollrab, V. *et al.* Still and rotating myosin clusters determine cytokinetic ring constriction. *Nat. Commun.* 7:11860 doi: 10.1038/ncomms11860 (2016).

Supplementary Figures

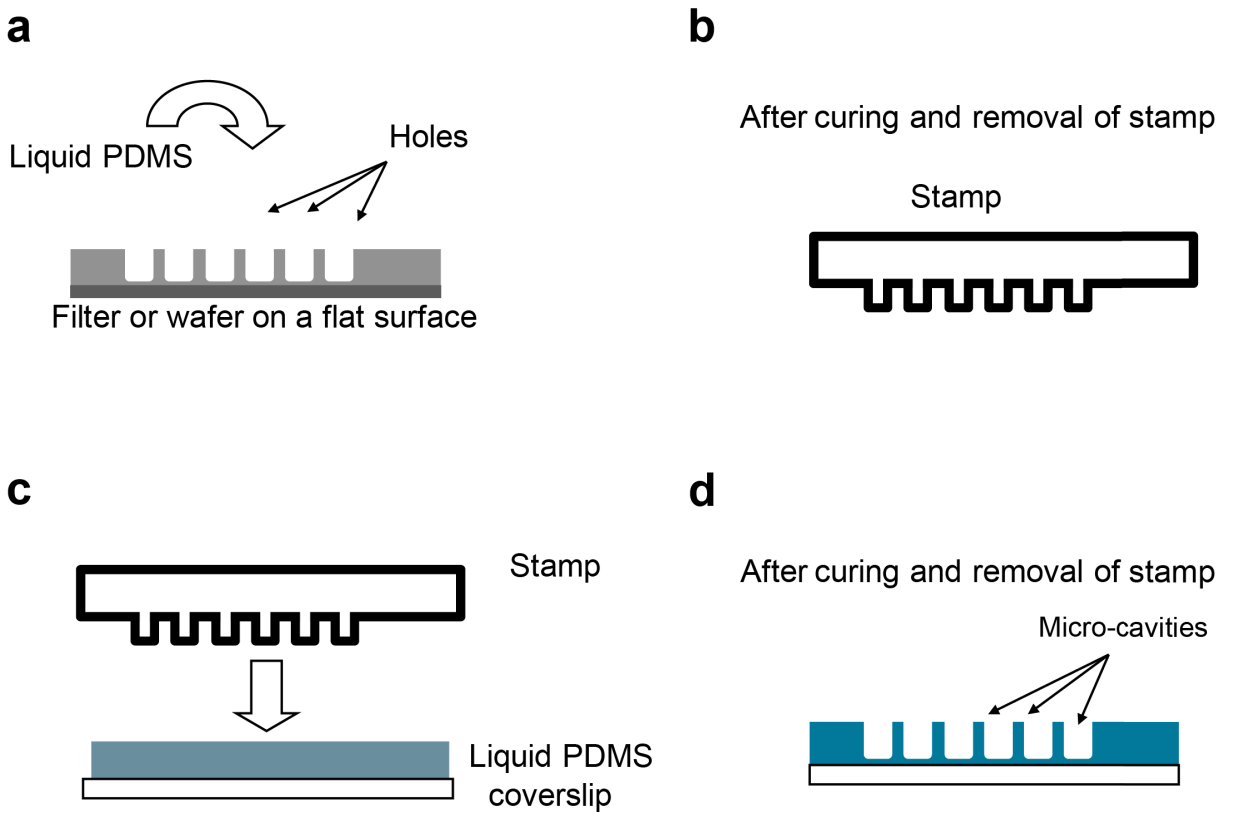

Supplementary Figure 1. Microfabrication of micro-cavities
a, Liquid PDMS is poured on the microstructured surface (filter or wafer).
b, The PDMS is degased for 30 min, cured for 4h at 65°C. The stamp is cut out and can easily be removed from the surface. **c,** Liquid PDMS is spin coated on plasma activated a glass coverslip (#0). The stamp is silanized and carefully put on the PDMS. **d,** The PDMS is kept for about 1h at room temperature to let gently air bubbles escape from the liquid PDMS. It is then cured for 4 h at 65°C. The stamp is very carefully removed[1].

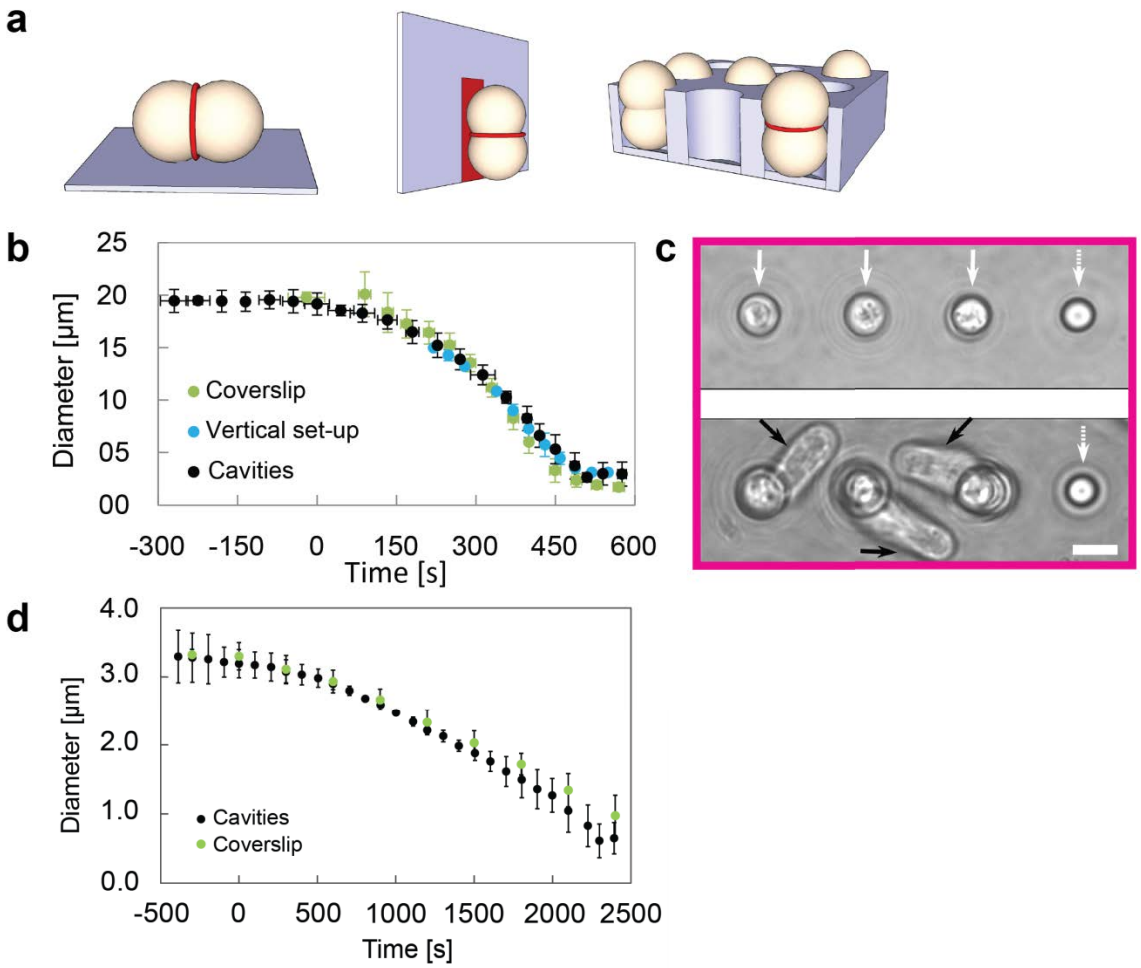

Supplementary Figure 2. Comparison of micro-cavities with standard surfaces

a, Schematic representation of the three set-ups and their comparison. Coverslip: Cell division on untreated glass coverslips, Vertical set-up: Cell division on vertically oriented glass coverslips. The coverslips are patterned with fibronectin lines, Cavities: Cells division in micro-cavities. **b**, Constriction behavior of HeLa cells on coverslips (green), in the vertical setup (blue) and in micro-cavities (black). Error bars indicate the standard deviation, coverslips: N = 12, vertical setup: N = 6, micro-cavities: N = 18. **c**, Fission yeast cells grow normally in wells, white arrows show cavities filled with cells and black arrows show sister cells after ~ 10 h of growth and division (compare top and bottom panels). The dashed arrow points at an empty well[1]. Scale bar, 4 µm. **d,** Constriction behavior of fission yeast cells on coverslips (green) and in micro-cavities (black). Error bars indicate the standard deviation, coverslips: N = 12, micro-cavities: N = 29.

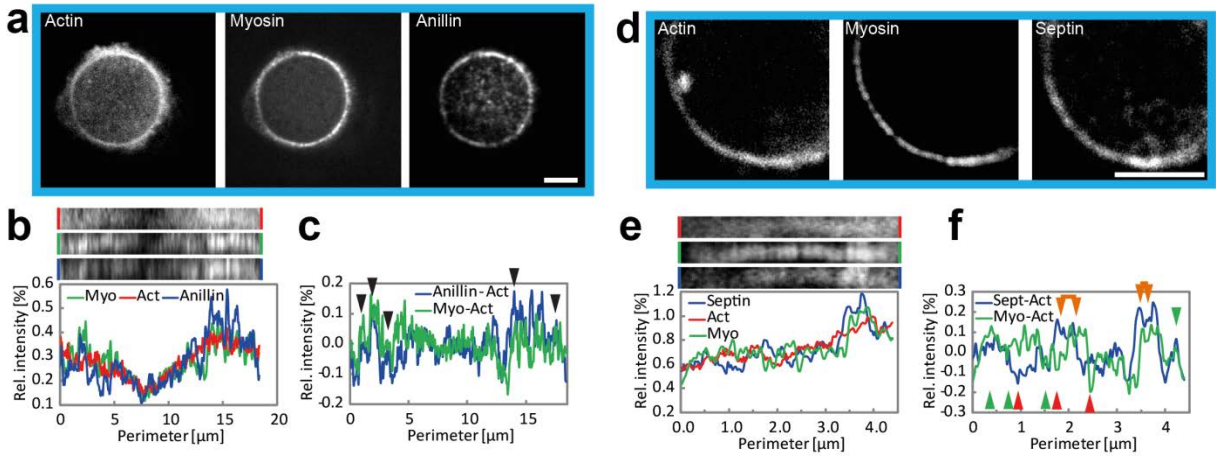

Supplementary Figure 3. Anillin and septin in the cytokinetic ring of mammalian cells

a, HeLa cells expressing LifeAct-mCherry and myosin-GFP stained for anillin. As myosin, anillin shows clusters distribution. Smoothen with ImageJ, scale bar 5 µm. **b**, Polar transformation of the rings and the corresponding intensity spectra. The intensities are normalized by their total intensity. Anillin and myosin profiles show peaks whereas actin spectrum is rather flat. **c**, Anillin and myosin spectra are subtracted by the actin signal, to flatten the profiles. Anillin and myosin show colocalization in some parts (arrows). **d**, HeLa cells expressing LifeAct-mCherry and myosin-GFP stained for septin7. Septin profile reveals clusters. Smoothen with ImageJ, scale bar 5 µm. **e**, Polar transformation of the indicated part of the rings and the corresponding intensity spectra. The intensities are normalized by their total intensity. Septin and myosin show peaks whereas the actin spectrum is rather flat. **f**, Septin and myosin spectra subtracted by the actin signal. Arrows indicate where profiles show colocalization (green), anti-correlation (red) and a shift (orange).

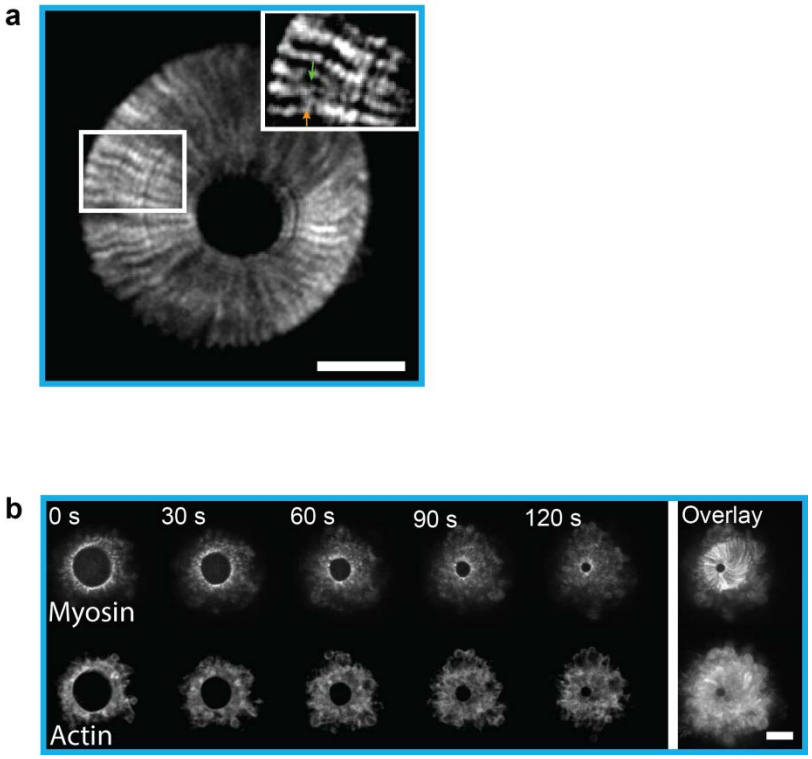

Supplementary Figure 4. Movements of myosin clusters in mammalian cells
a-b, Characteristics of clusters during ring closure. **a,** Overlay of rings in myosin. The clusters undergo fusion. The inset shows cluster fusion (indicated by arrows). Scale bar, 5 μm. **b,** Time lapse series of ring closure in actin and myosin. The overlay of the time series shows the rotation of the patterns/radial path of the clusters during constriction. Scale bar, 5 μm.

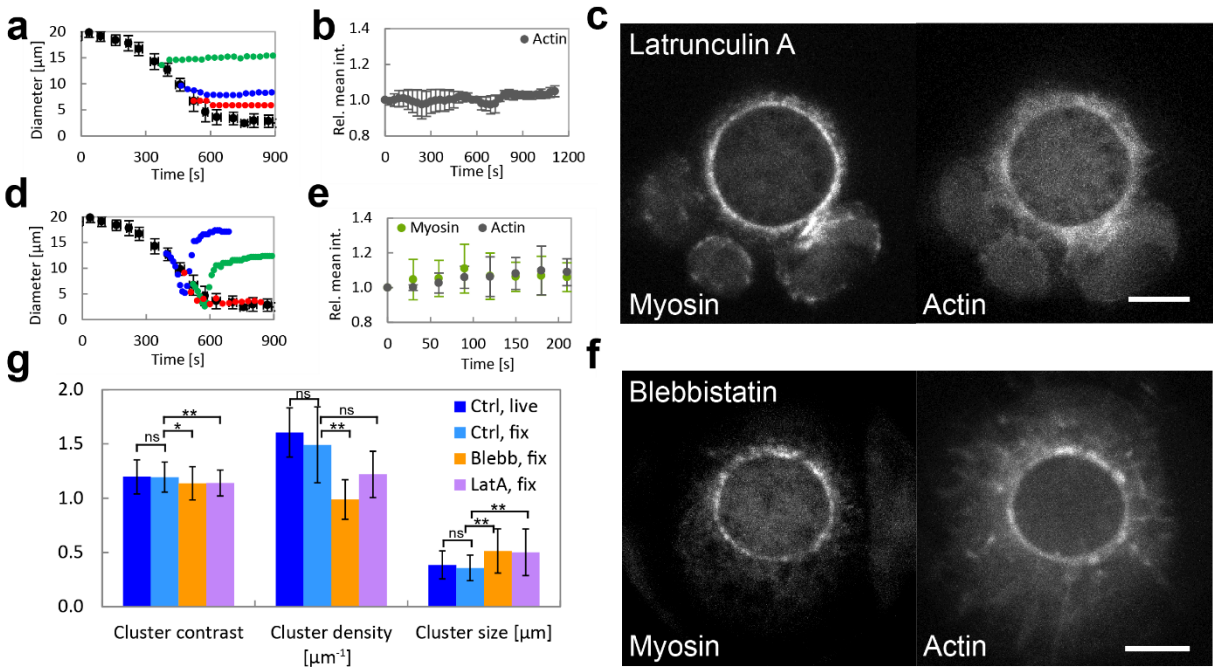

Supplementary Figure 5. Effects of cytoskeleton drugs on the cytokinetic ring in mammalian cells

a, The constriction behaviors of three representative rings in the presence of 100 µM blebbistatin (in black without blebbistatin). Ring closure is stalled upon blebbistatin addition.

b, After incubation with 100 µM blebbistatin the mean intensity of actin remains constant. Error bars indicate the standard deviation, N = 6. **c,f,** Cells fixed after incubation with c) latrunculin A (1.5 µM, 3 min) and f) blebbistatin (100 µM, 15 min). Scale bars 5 µm.

d, Three representative constriction behavior after incubation with 1.5 µM latrunculin A: the ring continues to constrict in some cases (red); and opens in others (blue and green). In all cases the constriction speed is faster after addition of the drug. **e,** With 1.5 µM latrunculin A, myosin and actin concentrations remain constant. Error bars indicate the standard deviation, N = 6. **g**, Mean value of cluster contrast, density and size for cells treated with drugs and fixed and untreated cells (Ctrl, live and fixed). Mean value for rings in the diameter range from 9 µm to 12 µm (Number of rings: N(Ctrl, live) = 16, N(Ctrl, fix) = 8, N(Lat A) = 9, N(Blebb) = 7, number of measurements of cluster contrast and cluster size: between 88 and 211 per conditions, number of measurements of cluster density: between 8 and 16 per condition). Mann-Whitney test was performed, ns not significantly different ($P>0.05$), * significantly different ($P<0.05$), ** significantly different ($P<0.01$). Error bars indicate the standard deviation.

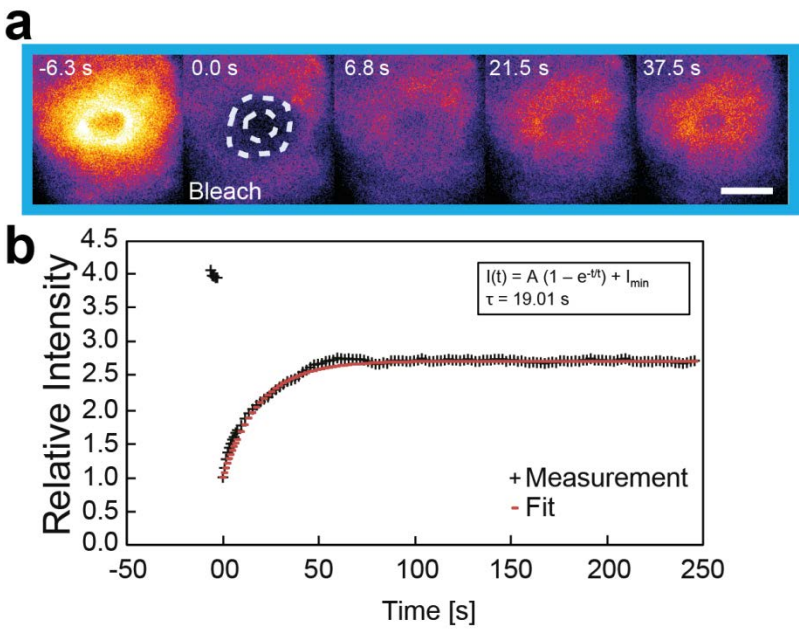

Supplementary Figure 6. Myosin FRAP in mammalian ring

a, FRAP experiment on myosin in the rings of HeLa cells. The entire ring is bleached. Scale bars 5 µm. **b**, The recovery is not complete. Its half time is ~20 s.

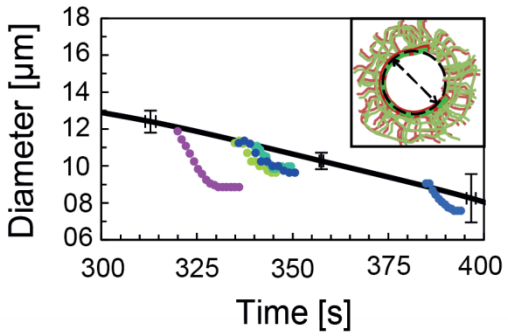

Supplementary Figure 7. Constriction behaviors after ablation of the cytokinetic ring in mammalian cells

Constriction behaviors after ablation of the cytokinetic ring in mammalian cells. The cut rings were fitted with a circle and their diameter measured as a function of time. The individual curves were aligned to the constriction curve of intact rings (Fig. 1e). The cut rings constrict faster than control rings.

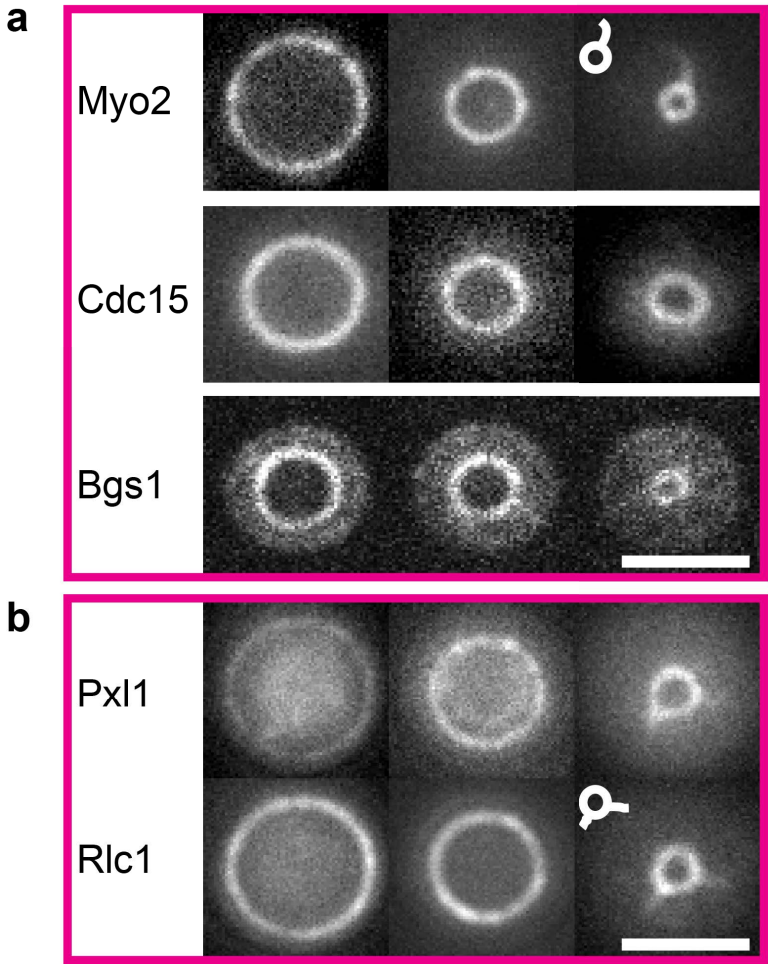

Supplementary Figure 8. Other cytokinetic ring proteins in fission yeast

a–b, Different cytokinetic proteins of fission yeast ring. **a**, Cells labeled with Myo2, Cdc15 and Bgs1. **b**, Pxl1 and Rlc1 on the same ring (top/bottom panels). Note the arms depicted in white. Scale bar, 2 μm.

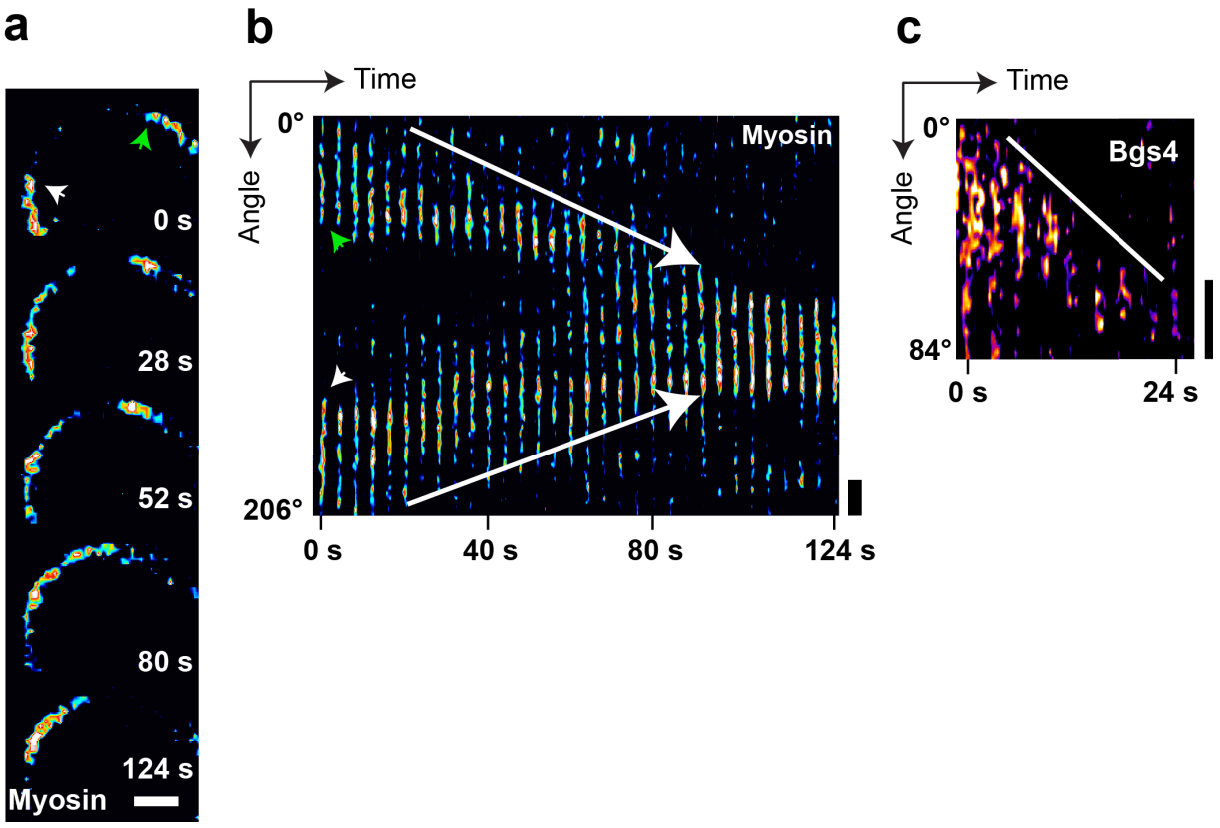

Supplementary Figure 9. Cluster rotations in fission yeast

a-b, Myosin clusters motion in fission yeast (a) and its kymograph after polar transformation (b). Small arrows point to the same clusters in (a) and in (b) at time 0 s, and large arrows in (b) indicate their rotations.

c, Rotation of a Bgs4 cluster. Scale bars, 2 μm.

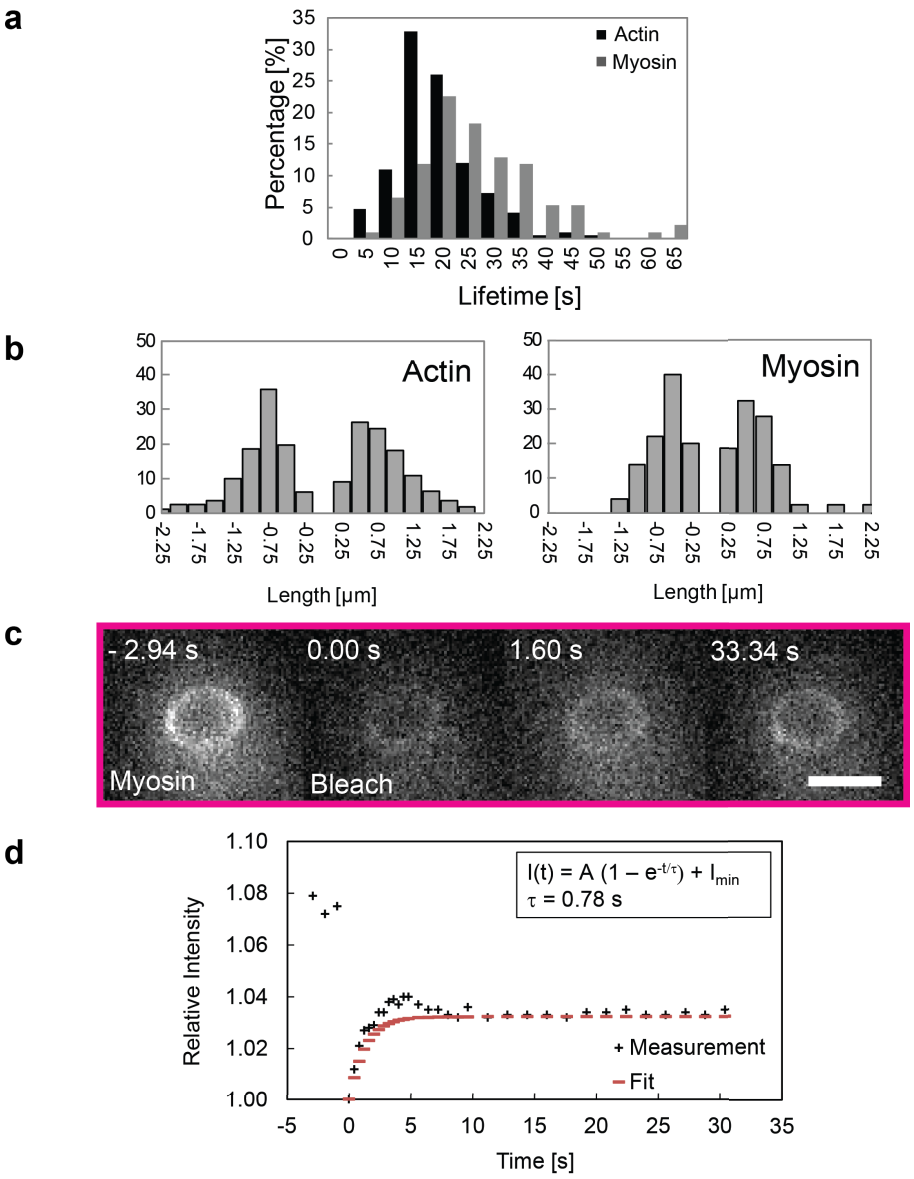

Supplementary Figure 10. Cluster characteristics and myosin FRAP in fission yeast

a–b, Cluster characteristics of fission yeast ring constriction. **a**, Histogram for lifetime of clusters. The mean lifetime is 16.4 s (s.d. = 7.7 s, n= 192) for actin and 24.1 s (s.d. = 11.6 s, n= 93) for myosin. **b,** Distance of cluster movement for cluster rotating clockwise and counterclockwise. The mean distance for all actin cluster is 0.72 µm (s.d. = 0.41 µm, n = 192) and 0.52 µm (s.d. = 0.34 µm, n = 93) for myosin cluster. **c–d,** FRAP experiment on myosin in the fission yeast cytokinetic ring. **c**, The entire ring is bleached, and partially recovers. Scale bar, 2 µm. **d,** The half time of recovery is ~1s.

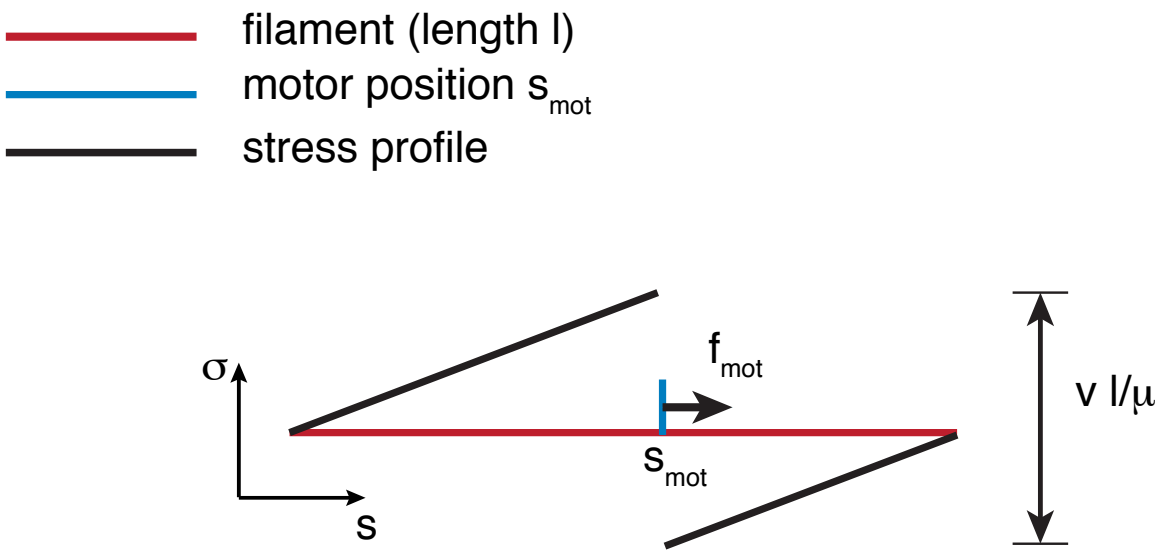

Supplementary Figure 11. Illustration of the stress distribution along a stiff slender rod

The rod is of length ℓ (the filament, red) that is drawn by a motor force f_{mot} at s_{mot} into the direction of the arrow. The filament velocity is v, its mobility μ. The black line indicates the stress profile that results from the applied force and the filament friction with the environment.

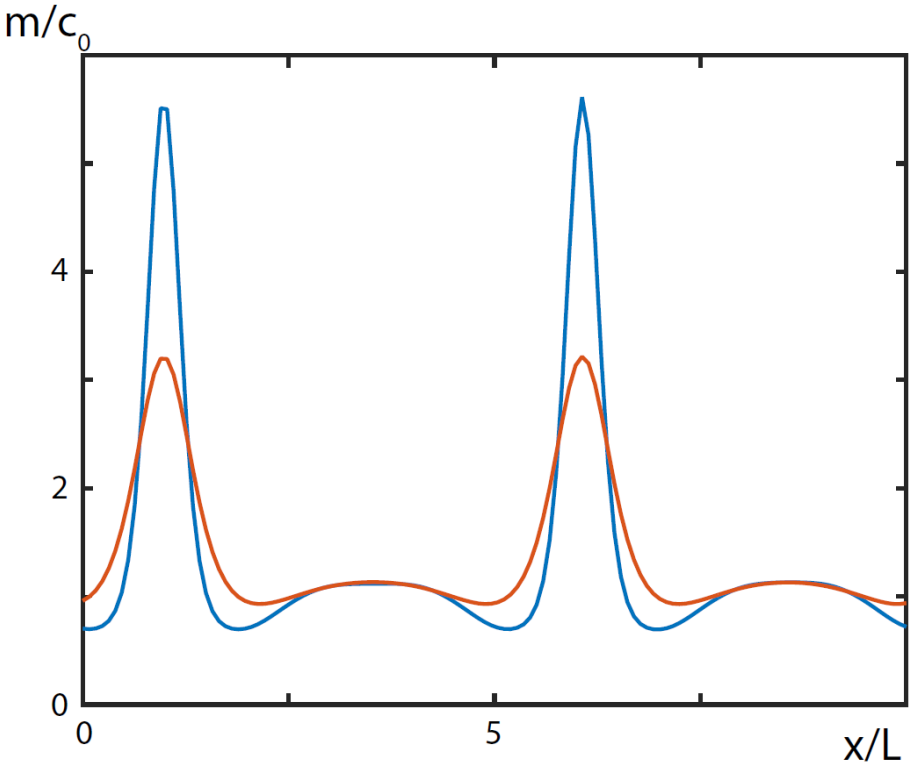

Supplementary Figure 12. Motor distribution m for two values of the motor activity α

Blue: $\alpha = 4\ell\omega_d$, orange: $\alpha = 2.5\ell\omega_d$ mimicking the effect of adding blebbistatin. Other parameters: perimeter $L = 10\ell$, $\beta = 0.1\ell\omega_d$, $\omega_d = 0.2$, $\omega_c = 1$, $v = 2.5\ell\omega_d c_0$, $D = \ell^2\omega_d c_0$. The total filament number was $\int dx\{2c_{bp}(x) + c^+(x) + c^-(x)\} = 2Lc_0$.

Supplementary Table

Supplementary Table 1: Strain genotypes, markers and sources.

Strain	Genotype	Fluorescent markers	Source / Reference
DR 2	pxl1::kanMX6 leu1+::GFPpxl1+ rlc1-mCherry::natR	Rlc1-mCherry myosin II regulatory light chain GFP-Pxl1 paxillin-like protein	This study
JW 1110	h^+ kanMX6-Pmyo2-mYFP-myo2 ade6-M210 leu1-32 ura4-D18	Myo2-YFP myosin II heavy chain	Wu and Pollard, 2005
PPG 5054	h^+ pxl1::kanMX6 leu1+::GFPpxl1+ leu1-32 ura4-D18	GFP-Pxl1 paxillin-like protein Pxl1	Pinar et al., 2008
JW 977	h^+ cdc15-mYFP-kanMX6 ade6-M210 leu1-32 ura4-D18	Cdc15-YFP membrane-cytoskeletal interactions, F-BAR domains	Wu and Pollard, 2005
519	h^- bgs1Δ::ura4+ P_{bgs1}+::GFP-bgs1+:leu1+ leu1-32 ura4-D18 his3- Δ1	GFP-Bgs1 1,3-beta-glucan synthase catalytic subunit Bgs1	Cortes et al., 2002
561	h^- bgs4Δ::ura4+ P_{bgs4}+::GFP-bgs4+:leu1+ leu1-32 ura4-D18 his3-Δ1	GFP-Bgs4 1,3-beta-glucan synthase catalytic subunit Bgs4	Pilar Pérez
JW1348	h^+ nmt41-GFP-CHD (rng2)-$leu1^+$ rlc1-mCherry-natMX6 ade6-M210 leu1-32 ura4-D18	Rlc1-mCherry myosin II regulatory light chain CHD-GFP calponin homology domain	Vavylonis et al., 2008
JW1349	h^+ nmt41-GFP-CHD (rng2)-leu1+ rlc1-tdTomato natMX6 ade6-M210 leu1-32 ura4-D18	Rlc1-tdTomato myosin II regulatory light chain CHD-GFP calponin homology domain	Vavylonis et al., 2008
JM207	h^+ rlc1-mCherry::natR ade-leu- ura-	Rlc1-mCherry myosin II regulatory light chain	James B. Moseley
PN 4461	h^- cps1-191 rlc1-GFP::KanR	Rlc1-mCherry myosin II regulatory light chain	Nurse lab. collection

Supplementary Note 1

MEAN-FIELD MODEL FOR THE DYNAMICS OF ACTIN FILAMENTS IN THE CONTRACTILE RING

In the following, we will give the mathematical details of the physical model used in the main text.

Model definition

With our theory, we try to capture essential features of the ring dynamics, such as, filament polarity, rules of interaction between filaments through molecular motors. Consequently, the final equations of motion describe the behavior of contractile rings independently of many details of the molecular interaction rules. Still, in the following, we will evoke a specific image to introduce the dynamic equations.

Consider a ring of perimeter L of actin filaments such that the filaments align with the ring perimeter. We denote the co-ordinate along the ring perimeter by x and describe the distribution of (polar) actin filaments along x by the densities c^+ for filaments with their plus-end pointing clockwise and c^- for filaments of the opposite orientation. Two filaments of opposite orientation can join their plus-ends forming a bipolar filament (Fig. 4a, (i)). Indirect evidence for such a process is given by the fusion of nodes observed in fission yeast[2]. While we refrain from suggesting an explicit molecular mechanism, such bipolar filaments may be formed by motor clusters linking the filaments. Also actin nucleating proteins of the formin family could be involved (Figs. 2c and 3b). The distribution of bipolar filaments is denoted by c_{bp} and gives the density of their centers. Bipolar filaments form at rate $\omega_c c^+ c^-$, bipolar filaments can split into two filaments of opposite orientations at rate ω_d (Fig. 4a, (i)).

Actin filaments continuously turn over. In general, they assemble at the barbed end by addition of actin monomers and disassemble at the pointed end by actin monomer removal or severing. Assembly and disassembly can be captured by effective rates. These rates depend on the state of the ends: Capping proteins can inhibit or promote assembly and disassembly. In a minimal model of the ring dynamics, we refrain from giving a detailed account of filament assembly and disassembly. Instead we assume that all filaments have a fixed length that is equal to the average filament length ℓ. Bipolar filaments thus have a length of 2ℓ and the total actin density at a point x is $\int_0^\ell d\xi \left(c^+(x+\xi) + c_{bp}(x+\xi) + c^-(x-\xi) + c_{bp}(x-\xi)\right)$. As a crude account of filament turnover, we will assume that filaments assemble and disassemble at the two ends at the same

rate. This leads to an apparent motion of the polar filaments at velocity $\pm v_{to}$.

Let us now turn to the filament dynamics induced by molecular motors. They can induce relative sliding between actin filaments. The corresponding velocities are α between filaments of the same orientations (Fig. 4a, (ii)) and β for filaments of opposite orientations (Fig. 4a, (iii)). We use these parameters to quantify the strength of the motor-mediated filament- filament interactions. We assume that motors are located at the filaments' plus-ends, such that $c^+ + c^- + c_{bp}$ is the distribution of motors. Finally, fluctuations are accounted for by diffusion terms with an effective diffusion constant D. The corresponding dynamic equations read:

$$\begin{aligned}\partial_t c^+(x) = {} & D\partial_x^2 c^+(x) - \partial_x \alpha \int_0^\ell d\xi \left(c^+(x+\xi) - c^+(x-\xi)\right) c^+(x) \\ & - \partial_x \alpha \int_0^\ell d\xi \, c_{bp}(x+\xi) c^+(x) + \partial_x \beta \int_0^\ell d\xi \left(c^-(x-\xi) + c_{bp}(x-\xi)\right) c^+(x) \\ & - \partial_x v_{to} c^+(x) - \omega_c c^+(x) c^-(x) + \omega_d c_{bp}(x)\end{aligned}$$

$$\begin{aligned}\partial_t c^-(x) = {} & D\partial_x^2 c^-(x) - \partial_x \alpha \int_0^\ell d\xi \left(c^-(x+\xi) - c^-(x-\xi)\right) c^-(x) \\ & + \partial_x \alpha \int_0^\ell d\xi \, c_{bp}(x-\xi) c^-(x) - \partial_x \beta \int_0^\ell d\xi \left(c^+(x+\xi) + c_{bp}(x+\xi)\right) c^-(x) \\ & + \partial_x v_{to} c^-(x) - \omega_c c^+(x) c^-(x) + \omega_d c_{bp}(x)\end{aligned}$$

$$\begin{aligned}\partial_t c_{bp}(x) = {} & D\partial_x^2 c_{bp}(x) - \partial_x \alpha \int_0^\ell d\xi \left(c_{bp}(x+\xi) - c_{bp}(x-\xi)\right) c_{bp}(x) \\ & - \partial_x \alpha \int_0^\ell d\xi \left(c^-(x+\xi) - c^+(x-\xi)\right) c_{bp}(x) \\ & - \partial_x \beta \int_0^\ell d\xi \left(c^+(x+\xi) - c^-(x-\xi)\right) c_{bp}(x) + \omega_c c^+(x) c^-(x) - \omega_d c_{bp}(x)\end{aligned}$$

To assist the reader, let us state explicitly the difference of this model to the one discussed in Ref.[3], where the framework used here was developed. The present model extends the former work by including the presence of bipolar filaments and processes of their assembly and disassembly. Furthermore, in the original formulation[3], filament assembly and disassembly were neglected. Here, we include it in an effective way, by adding the treadmilling currents. That treadmilling is an important part of the actin assembly dynamics was shown, for example, in Ref.[4].

For numerical solution of the dynamic equations, we used a first-order upwind scheme with adaptive time stepping. For the calculation, we have used dimensionless parameters, where time

has been scaled by $(\omega_c c_0)^{-1}$, length by ℓ, and the filament densities by c_0, where $c_0 L$ is the number of plus- and of minus-filaments. Consequently, v_{to} is scaled by $\ell\omega_c c_0$, α and β by $\ell\omega_c$, and D by $\ell^2\omega_c c_0$.

Mechanism of the instability

First note that the interaction of two bipolar filaments with each other tends to align their centers. For a homogenous ring of bipolar filaments, the force on each bipolar filament cancels out. As soon as there is a perturbation, locally imbalances are present that will lead to an accumulation of bipolar filaments, possibly at different positions along the ring, unless diffusion is dominating and smoothing the perturbations. What is the typical distance one can expect between two clusters of bipolar filaments? A bipolar filament can interact with all bipolar filaments that are a distance ℓ away. These bipolar filaments extend a distance 2ℓ from the original filament's center, which suggests that the typical distance between two clusters is about 4ℓ. This is indeed the typical distance we observe after clusters have developed starting from a random perturbation of the homogenous state. The typical distance is also affected by the system size (the ring perimeter). For $L = 10\ell$, which we use in the main text, only two clusters are seen. Note that the distances between clusters changes on long time scales, which presumably eventually leads to a single remaining cluster for systems of any size. However, this coarsening process takes place on such long time scales that it is irrelevant for the dynamics of contractile rings and not further discussed here.

Calculation of the stress in the bundle

The stress in the bundle is defined as the sum of the stresses in the individual filaments[3]. Stresses in a filament are generated by motors that pull on the filaments and by friction with the surrounding medium. Explicitly, force balance on a single filament gives

$$\partial_s \sigma = \frac{1}{\mu} v + f_{mot}.$$

In this expression, s is the co-ordinate along the filament, σ the stress in the filament, μ a mobility, v the filament's velocity, and f_{mot} the force density exerted by motors on the filament. Only the effects of motors cross-linking two filaments are accounted for. The stress along a filament is thus piece-wise linear in s with slope v/μ, where $v = \pm\alpha$ or $v = \pm\beta$ depending on the orientation and the relative position of the partner filament, the motor is connected to. If there is no motor at a filament end, then the stress vanishes at this point, and the stress jumps by an amount $|v|\ell/\mu$ at the positions s_{mot}, where motors are bound to the filament, see Fig. S11. The

total stress profile along the bundle is then obtained by summing the stress profiles along all filaments in the bundle. Since the expressions are quite involved, we refrain from giving them here explicitly.

Behavior after addition of blebbistatin

To capture the effect of the myosin inhibitor blebbistatin in our model, we reduced the motor activity α, compared to a case leading to a stationary state that corresponds to the pattern in mammalian rings. For stationary states, the myosin clusters subsequently broadened, see Fig. S12. This qualitatively agrees with the behavior observed in mammalian rings, see Fig. 2d in the main text. Similar results have been obtained when instead of α the values of ℓ and v_{to} were reduced to mimic the effects of latrunculin A.

Supplementary Methods

Analysis of rings

For mammalian cells, we measured the total and mean fluorescence intensities by tracing the ring contour with ImageJ. The total and mean intensity were normalized by the total and mean intensity of the cells at the onset of division (t = 0 s). The normalized values were averaged and the standard deviation is given by the error bars (Fig. 1 f, g). With intensities extracted from live samples, we measured the bleaching rate of the cytoplasmic pool of fluorescent proteins, as a good indicator for bleaching since the recovery times for FRAP at the ring were within seconds. The results yielded minor corrections for intensity measurements, within 10%. In addition, fixed samples gave the same measures as live samples, showing that corrections for photobleaching were not needed.

Fission yeast rings can be fitted by a circle. Therefore, we measured the intensities by measuring the intensity in circles of the dimensions of the outer ring diameter and the inner ring diameter with ImageJ. The subtraction of these two values gave the total fluorescence intensity of the ring. By dividing the total intensity by the area of the ring (which is the area of the outer circle minus the inner circle), we calculated the mean intensity. Since the variations in intensity measures between individual cells are small in fission yeast cells, we took snapshots of individual cells and assigned time points to the rings as a function of their diameter. The averaged intensity curve was then normalized with respect to the intensity value of 3.1 μm. For intensity measurements of rings before constriction where the diameter is constant we analyzed timelapse movies. We normalized the intensity with respect to the intensity at a diameter of 3.1 μm. Measurements on snapshots and timelapses are in agreement and they are plotted in Fig. 1 i, j (timelapse data until 250 s, then data from fixed cells).The standard deviation is given by the error bars (Fig. 1 i, j).

Microfabrication

Polydimethylsiloxane (PDMS) was mixed with its curing agent (Sylgard 184, Dow Corning) in a 10:1 ratio, and the solution allowed to degas for 30 min. A porous membrane filter (pore diameter 5.0 μm, shiny face up, Millipore Isopore, TMTP01300) was placed at the bottom of a

Petri dish and the sticky side of Scotch tape was applied to the top of the filter[1]. The tape with the filter was attached to a double sided tape attached to a Petri dish with the filter side exposed to the air, the PDMS poured onto the filters (non-shiny face up), and the mixture allowed to cure overnight, followed by 4 h curing at 65°C before the stamp was peeled off.

Alternatively the stamp can be fabricated by means of microfabrication (Supplementary Fig. 1) We used regular arrays of microcavities surfaces prepared using standard lithographic methods on silicon wafers[5]. Circular patterns on a mask can be transferred to a Si-Wafer. The surface will contain holes of the size of the wells. PDMS is mixed with curing agent (10:1) and poured on the wafer. Air bubbles are removed by degassing for 30 min. After 4 h at 65°C the PDMS will be cured and the stamp can carefully be cut out and peeled of the wafer.

The stamp was exposed to a plasma cleaning for 1 min (Harrick Plasma, PDC-32G, high setting power), followed by a 10 min exposure to Chlorotrimethylsilane 97% (Sigma-Aldrich, C72854, TMCS) vapor or by the deposition of an anti-adhesive layer (Sigma-Aldrich, SL2 Sigmacote).

The liquid degassed PDMS mixture was spread on a glass coverslip #0 (25 mm in diameter, Fisherbrand) with a Pasteur pipette[5,6], after its cleaning with a 1 min exposure in the plasma cleaner. The silanized stamp was then placed onto the PDMS coated coverslip, allowed to cure at room temperature overnight, followed by four hours curing at 65°C. The stamp was separated from the coverslips, generating the well pattern on the upper layer of the 30 μm thick elastomer, using the coverslip as the sealed bottom of the chamber. The overall thickness of the sample allowed objectives with small working distances and high numerical apertures to be used.

We modified the protocol for larger cavities for mammalian cells. The PDMS stamps were activated with a plasma cleaner and silanized with TMCS as described above. Liquid PDMS was spin-coated on the molds at 1500 rpm for 30 s. The PDMS was cured for at least 2 h at 65°C. For plasma binding of the cured PDMS layer to a coverslip (#0), both – the PDMS stamp and the coverslip – were plasma activated. The thin PDMS layer was then pressed on the coverslip. The pressure was maintained for several seconds. After about 30 min the PDMS stamp was unpeeled and the thin PDMS layer containing the microcavities was plasma bound to the coverslip.

Supplementary References

1 Riveline, D. & Buguin, A. Devices and methods for observing the cell division. WO/2010/092116 (2009).

2 Vavylonis, D., Wu, J. Q., Hao, S., O'Shaughnessy, B. & Pollard, T. D. Assembly mechanism of the contractile ring for cytokinesis by fission yeast. *Science* **319**, 97-100 (2008).

3 Kruse, K. & Julicher, F. Self-organization and mechanical properties of active filament bundles. *Phys Rev E Stat Nonlin Soft Matter Phys* **67**, 051913 (2003).

4 Erlenkamper, C. & Kruse, K. Treadmilling and length distributions of active polar filaments. *J Chem Phys* **139**, 164907 (2013).

5 Balaban, N. Q. *et al.* Force and focal adhesion assembly: a close relationship studied using elastic micropatterned substrates. *Nat Cell Biol* **3**, 466-472 (2001).

6 Riveline, D. *et al.* Focal contacts as mechanosensors: externally applied local mechanical force induces growth of focal contacts by an mDia1-dependent and ROCK-independent mechanism. *J Cell Biol* **153**, 1175-1186 (2001).

Bioarchitecture 4:4-5, 1–5; September 1, 2014; © 2014 Taylor & Francis Group, LLC

Synthetic polyamines: new compounds specific to actin dynamics for mammalian cell and fission yeast

Daniel Riveline[1,2,*], Raghavan Thiagarajan[1,2], Jean-Marie Lehn[3], and Marie-France Carlier[4]

[1]Laboratory of Cell Physics; ISIS/IGBMC; Université de Strasbourg and CNRS (UMR 7006); Strasbourg, France; [2]Development and Stem Cells Program; IGBMC; CNRS (UMR 7104); INSERM (U964); Université de Strasbourg; Illkirch, France; [3]Laboratoire de Chimie Supramoléculaire; ISIS; Université de Strasbourg and CNRS (UMR 7006); Strasbourg, France; [4]Dynamique du Cytosquelette; Laboratoire d'Enzymologie et Biochimie Structurales UPR 3082 CNRS; Gif-sur-Yvette, France

Keywords: actin cytoskeleton, cytokinetic ring, fission yeast, lamellipodia, mammalian cells, synthetic polyamine

Abbreviations: ADF, Actin depolymerizing factor; BPA, Branched polyamines; EMM5S, Edinburgh Minimal Media with 5 Supplements; F-actin, Filamentous actin; GFP, Green fluorescent protein; MPA, Macrocyclic polyamines; N-WASP, neuronal Wiskott-Aldrich syndrome protein; Rlc1, Regulatory light chain 1; ROCK, Rho-associated protein kinase.

Actin is a major actor in the determination of cell shape. On the one hand, site-directed assembly/disassembly cycles of actin filaments drive protrusive force leading to lamellipodia and filopodia dynamics. Force produced by actin similarly contributes in membrane scission in endocytosis or Golgi remodeling. On the other hand, cellular processes like adhesion, immune synapse, cortex dynamics or cytokinesis are achieved by combining acto-myosin contractility and actin assembly in a complex and not fully understood manner. New chemical compounds are therefore needed to disentangle acto-myosin and actin dynamics. We have found that synthetic, cell permeant, short polyamines are promising new actin regulators in this context. They generate growth and stabilization of lamellipodia within minutes by slowing down the actin assembly/disassembly cycle and facilitating nucleation. We now report that these polyamines also slow down cytokinetic ring closure in fission yeast. This shows that these synthetic compounds are active also in yeasts, and these experiments specifically highlight that actin depolymerization is involved in the ring closure. Thus, synthetic polyamines appear to be potentially powerful agents in a quantitative approach to the role of actin in complex processes in cell biology, developmental biology and potentially cancer research.

Acto-Myosin and Actin Dynamics as Key Players of Cell Dynamics

Cells and tissues change their shapes through 2 basic molecular mechanisms. Myosin motors interact with actin filaments and they can by themselves generate forces in a variety of phenomena, ranging from muscle contraction and stress fibers dynamics to intracellular transport processes. On the other hand, actin cycles of polymerization and depolymerization are also dictating morphogenesis events in the absence of myosin, like in the dynamics of membrane protrusions with filopodia and lamellipodia in mammalian cells. In these examples, each machinery can sustain forces and deformations in the absence of the other machinery. Indeed, it was shown experimentally [1,2] and theoretically [3,4] that both acto-myosin interactions and actin dynamics alone can generate stresses and strains.

However both force-producing machineries are often coupled in cells and tissues, and it is difficult to discriminate the specific contribution of each in the global process. For example, in the cytokinetic ring, bundles of actin and myosins are organized in a ring which undergoes closure. It was suggested that actin polymerization was a key player in these processes by experiments with mutants in actin dynamics leading to a delay in the ring closure of fission yeast.[5] On the other hand, experiments with spheroplasts - rings in cellular fragments extracted from fission yeasts - showed that myosin was mainly piloting the closure through its interactions with actin filaments.[6] Similar results were obtained in actin rings assembled *in vitro*.[7]

The interplay between the above force-producing machineries actually seems to be effective in most motile and morphogenetic processes. Cell migration requires a balance between actin-based protrusion and acto-myosin-driven contractility.[8] Adherens junctions maturation was reported to involve an interplay between acto-myosin forces at the junctions together with actin polymerization in the neighboring cell.[9,10] In the highly spatially organized podosome structures, the dynamics of protrusive cores and adhesive rings is coordinated by acto-myosin.[11] In developmental biology too, both machineries were demonstrated to be acting in concert. For example, cell division in Drosophila involves the action of myosin under the control of ROCK as well as actin

*Correspondence to: Daniel Riveline; Email: riveline@unistra.fr
Submitted: 07/29/2014; Revised: 09/09/2014; Accepted: 09/09/2014
http://dx.doi.org/10.4161/19490992.2014.965111

polymerization for keeping the tissue integrity between neighboring cells.[12]

A potential way to understand the molecular basis of these phenomena is to consider that both machineries cooperate. The acto-myosin could be pulling cellular structures which in turn will allow the insertion of actin monomers in a new regime of polymerization/depolymerization cycles. In support of this view, applying a pulling force to formin-initiated filaments in processive elongation increases their growth rate.[13] Similarly, growth of focal contacts results from the force applied by contractile stress fibers on focal adhesions, and the elongation of focal contacts requires the polymerization of actin.[14] In such a framework, there is a need for new specific tools to evaluate the contributions of each actor in the process.

Limited Set of Chemical Agents Acting on Actin

A limited set of agents are available (see **Table 1**), and they often lead to the disassembly of cellular structures. For example, Latrunculin A sequesters monomeric actin, causing disassembly of all actin meshworks in protrusive lamellipodia and contractile structures. Cytochalasins, as well as a large number of macrolides derived from marine organisms [15-17] generally strongly cap the barbed ends of actin filaments and often also sever filaments and trigger the disassembly of cellular structures. These agents are widely used to demonstrate that actin is involved in the process of interest, and they are complementary to transfection or genetic approaches which target a fraction of cells within tissues. Less brutal force tools, however, are required to gain mechanistic insight into the exact role of acto-myosin contractility or actin assembly in a global process.

Synthetic Polyamines as New Agents with Broad Application

We observed that addition of synthetic polyamines to cell culture medium promotes the growth of lamellipodia in cells within a few minutes.[18] Their direct and specific effect on actin was demonstrated by *in vivo* experiments with inhibitors and *in vitro* actin polymerization assays. We have shown that the compounds slow down filament elongation at barbed ends specifically, but do not affect pointed end growth. They also slow down filament disassembly in a concentration-dependent manner, and facilitate nucleation in the presence of capping protein.

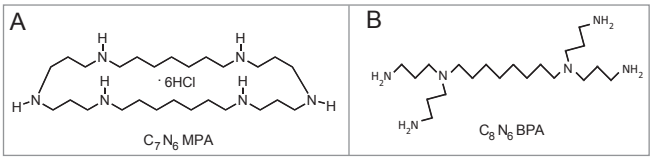

Figure 1. The compounds C_7N_6 MPA (**A**) and C_8N_6 BPA (**B**). The cyclic and branched polyamines have similar effects even though their topologies are different.

The Compounds, their Structures, and the Active Groups

Macrocyclic polyamines had been shown to greatly enhance actin polymerization *in vitro*.[19] Based on these structures, noncyclic branched polyamines were designed and synthesized for exploration of their effect on actin.[18,20] Both cyclic and branched polyamines of different sizes affected actin assembly similarly with affinities that depended on their size. Here we present 2 compounds that proved the most efficient ones in our study: (i) macrocyclic polyamines C_7N_6 MPA (MPAs), presenting 2 dipropylene triamine subunits linked by 2 aliphatic 7-carbon chains (**Fig. 1A**), and (ii) acyclic branched polyamines C_8N_6 BPA (BPAs), 2 dipropylene triamine groups connected through the central nitrogen by an octamethylene chain (**Fig. 1B**). In spite of their distinct topologies, MPAs and BPAs display identical effects on actin *in vitro* and *in vivo*, which suggests that it is essentially the distance between amine groups which play an important role in their activities.

Growth of Lamellipodia: *De Novo* Extension with Formation of Focal Contacts

We observed that following rapid entry of the compounds into the cell, lamellipodia were growing within 10 minutes in a nonpolarized fashion, from various regions at the edge of the cells (see **Fig. 2** and **Movie 1**). We show here the local growth of lamellipodia observed with actin-GFP transfected cells (**Movie 1**). They were *bona fide* lamellipodia, in a sense that focal contacts were associated with the growing protrusions (**Fig. 2C**). Other experiments in the presence of inhibitors of the Rho pathway and actin polymerization showed that actin was the main target of MPAs/BPAs.[18]

Table 1. Standard compounds targeted to the actin cytoskeleton and their effects. For more details, see associated references in [18].

Compounds	Effects
Synthetic Polyamines	slow down F-actin turn-over at the barbed end and facilitate F-actin nucleation
Cytochalasin D	inhibits actin polymerisation by binding filament barbed end at low concentration (<0 .1 μM) and promotes depolymerisation at high concentration (>1 μM)
Jasplakinolide	binds and stabilises F-actin and blocks filament disassembly
Latrunculin A/B	sequester monomeric actin and promote actin depolymerisation
CK666	inhibits Arp2/3
SMIFH2	inhibits formins
Wiskostatin	inhibits N-WASP

Correlations between *In Vivo* and *In Vitro* Effects of Synthetic Polyamines

We gained insight into the mechanism by studying the dynamics of actin polymerisation in various conditions *in vitro*. We showed that the compounds slowed down barbed end assembly specifically and had no effect on pointed end growth. They also slow down filament disassembly and greatly depress the effect of ADF. Consistently in a reconstituted motility assays, N-WASP coated beads move more slowly. The slower turn-over of actin filaments in the motility assay suggested that *in vivo* lamellipodial actin networks should also turn-over more slowly in the presence of polyamines, which was confirmed by measuring retrograde flow in cells.[18]

Finally, we demonstrated that actin nucleation was facilitated *in vitro* in the presence of capping proteins. So the molecular picture *in vivo* combines 2 effects: the stabilization of the lamellipodia over time together with the facilitated growth of the actin network at the cell border. Note that the absence of filopodia is consistent with the known facilitation, by capping protein, of dendritic branched filament arrays present in lamellipodia versus formin-initiated filament bundles present in filopodia, both *in vivo*[21] and *in vitro*.[22]

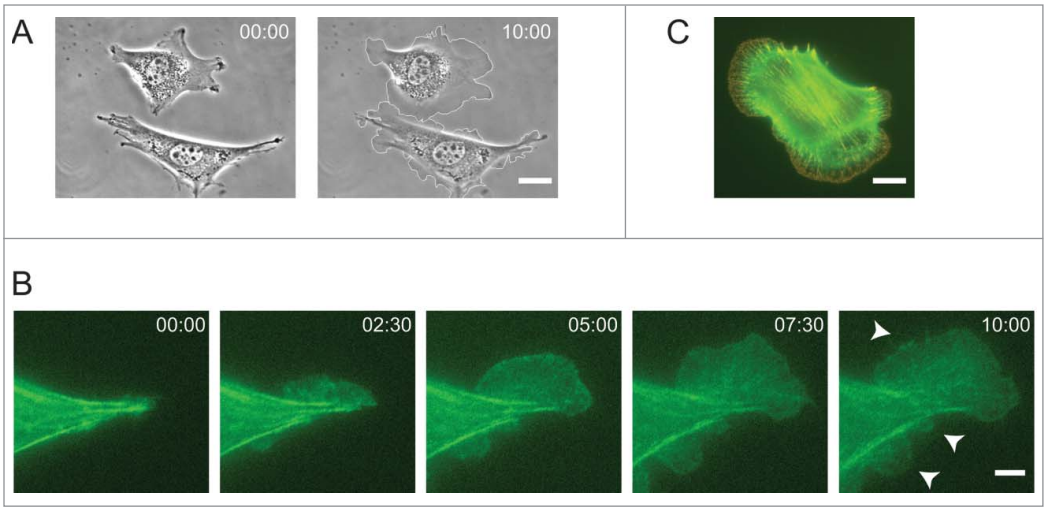

Figure 2. Synthetic polyamines promote growth of lamellipodia. (**A**) Promoted growth of lamellipodia in NIH3T3 cells; scale bar 30μm; (**B**) Dynamics of the growth visualized with actin-GFP in NIH3T3 cells, after addition of 300 μM C_7N_6 MPA (see also **Movie 1** and ref.[18]); time in minutes; arrows indicate new lamellipodia; scale bar 5μm. (**C**) Focal contacts are associated with new lamellipodia (actin in green and paxillin in red); scale bar 20μm.

Synthetic Polyamines Slow Down Cytokinetic Ring Closure

We tested whether MPAs and BPAs would similarly affect actin dynamics in another eukaryotic cell. We selected fission yeast as a powerful genetic system. In addition, we focused on cytokinetic ring closure, because it was suggested that actin dynamics could play a role in the velocity of closure.[5]

We observed the ring with a strain expressing myosin II regulatory light chain Rlc1-tdTomato. We measured the change in diameter as a function of time during the ring closure (see **Fig. 3** and **Movie 2**). We observed that ring closure was slowed down on average by 50% in the presence of 300μM C_7N_6 MPA, and by 20% and 40% in the presence of 100μM and 300μM C_8N_6

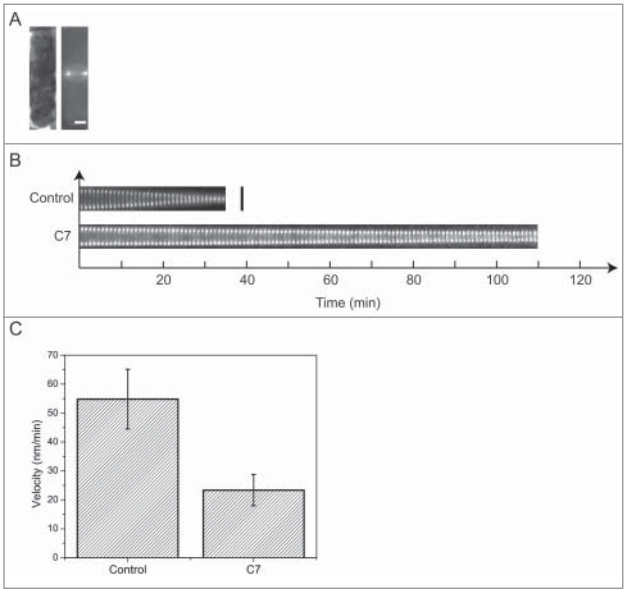

Figure 3. Synthetic polyamines delay the closure of the cytokinetic ring in fission yeast. (**A**) Fission yeast at cytokinesis, (left) phase contrast, (right) the ring visualized with Rlc1-tdTomato, scale bar 2μm; (**B**) Montage of dynamics of the ring diameter during closure for control cells and in the presence of C_7N_6 MPA; images were equalized in their contrast; scale bar 4μm. (**C**) Mean velocities for control rings (66 cells) and in the presence of 300 μM C_7N_6 MPA (76 cells). The error bars represent the standard deviation of the mean. $P \leq 0.01$ by Student's t-test. See also **Movie 2**.

Movie 1 Growth of lamellipodia promoted by C_7N_6 MPA in a NIH3T3 cell transfected with actin-GFP, time in mm:ss, scale bar 5μm.

BPA respectively (data not shown). This result is consistent with former experiments with mutants in which actin filament turnover was slowed down during cytokinesis.[5]

Future experiments with mutants in actin polymerization will probe the specific mechanisms that lead to the slowed closure and the relative contributions of actin filament disassembly and acto-myosin contractility at different steps of ring closure. A possible interpretation consistent with *in vitro* data is that MPA and BPA slow down the ADF-induced depolymerization that has been proposed to take place during ring closure, accounting for the decrease in amount of F-actin, at least in budding yeast.[23] Here we can speculate about a potential origin - knowing that MPA/BPAs have no effects on acto-myosin activities: these compounds could be binding actin filaments within the cytokinetic ring, slowing down depolymerization and treadmilling, thus slowing down the decrease in ring diameter. The facilitated nucleation might also generate new filaments within the closing ring, thereby impeding the reduction in amount and diameter.

New Compounds for the Study of Actin

We have shown that MPA and BPA can be good probes targeting the actin cytoskeleton in mammalian cells and in fission yeast. We explored the *de novo* growth of lamellipodia and the contraction of the cytokinetic ring. We anticipate that other cellular processes could be studied as well, such as endocytosis, transport mediated by actin polymerization, dynamics of the actin cytoskeleton through nodes, cell motility. In addition, other model organisms could be probed as well, such as budding yeast or developing embryos. Synthetic polyamines, by altering specific steps in shape changes of developing embryos, could provide insight into the underlying molecular and physical mechanisms.

Application in Cancer: Reduced Motility and Delayed Division

Actin is involved in a variety of phenomena, and a potential application in medicine could be cancer. Indeed, actin plays a key role in motility and in cell division: we propose that BPAs/MPAs would lead to a decrease in cell motility (see our paper[18] for the decreased migration in Boyden chamber) and to a delay in the proliferation rate. Also, it was recently shown that BPAs have a strong inhibitory effect on the transformation of cancer-associated fibroblasts into myofibroblasts, a key step in tumor progression.[24] Anti-actin compounds have failed so far as anti-cancer agents, because of the poor discrimination between actin in cancer cells and in healthy cells.[25] Hence, careful experiments on the small animal will be needed to evaluate the cytotoxicity of the BPAs/MPAs and their potential specific effects on tumors.

Movie 2 Closure of the cytokinetic ring in fission yeast visualized with Rlc1-tdTomato, time in mm:ss, comparison between control (left), and in the presence of C_7N_6 MPA (right). The frames were equalized in their contrast. Time in mm:ss, scale bar 2μm.

Methods

The MPAs and BPAs were synthesized in the Lehn Lab. C_8N_6 BPA can now be purchased from Tebu and Calbiochem. For mammalian cells (**Fig. 2B**), NIH3T3 cells were transfected with actin-GFP with Exgen using the manufacturer protocol (Euromedex). The other examples for mammalian cells (NIH3T3 cells) are presented in the original publication. For fission yeast experiments, cells were grown in standard exponential conditions.[26] Cells were deposited on coverslips coated with lectin,[27] and experiments were conducted in minimal medium EMM5S at 25°C in a temperature controlled environment. Rings were captured with a ×60 objective 1.45 N.A. mounted on an inverted CKX41 microscope (Olympus) equipped with a cooled couple-charge device camera (C4742–96–12G04; Hamamatsu). Each experimental condition was performed at least for 5 biological repeats. Rings were selected for their 'large' diameters (2.5μm-3μm) at the beginning of closure, and each ring was acquired every 60s with a 100ms or 200ms time exposure. Measurements were performed with ImageJ, and the evolution of diameter and measurements for velocities were done with Excel.

Disclosure of Potential Conflicts of Interest

No potential conflicts of interest were disclosed.

Acknowledgments

We acknowledge I Nedeva, M Toguchi and D Caballero, G Koripelly, for collaborations, E Pencréach (Hôpital Hautepierre, France) for fruitful discussions, J-Q Wu (Ohio State University, USA) for the fission yeast strain.

Funding

DR Lab is supported by funding from the CNRS, Fondation FRC and Université de Strasbourg. MFC acknowledges support from ERC advanced grant 249982 et EU FP7 241548.

Supplemental Materials

Supplemental data for this article can be accessed on the publisher's website.

References

1. Loisel TP, Boujemaa R, Pantaloni D, Carlier MF. Reconstitution of actin-based motility of Listeria and Shigella using pure proteins. Nature 1999; 401:613-6; PMID:10524632; http://dx.doi.org/10.1038/44183
2. Takiguchi K. Heavy meromyosin induces sliding movements between antiparallel actin filaments. J Biochem 1991; 109:520-7; PMID:1869506
3. Kruse K, Julicher F. Actively contracting bundles of polar filaments. Phys Rev Lett 2000; 85:1778-81; PMID:10970612; http://dx.doi.org/10.1103/PhysRevLett.85.1778
4. Zumdieck A, Kruse K, Bringmann H, Hyman AA, Julicher F. Stress generation and filament turnover during actin ring constriction. PLoS One 2007; 2:e696-6; PMID:17684545; http://dx.doi.org/10.1371/journal.pone.0000696
5. Pelham RJ, Chang F. Actin dynamics in the contractile ring during cytokinesis in fission yeast. Nature 2002; 419:82-6; PMID:12214236; http://dx.doi.org/10.1038/nature00999
6. Mishra M, Kashiwazaki J, Takagi T, Srinivasan R, Huang Y, Balasubramanian MK, Mabuchi I. In vitro contraction of cytokinetic ring depends on myosin II but not on actin dynamics. Nat Cell Biol 2013; 15:853-9; PMID:23770677; http://dx.doi.org/10.1038/ncb2781
7. Reymann AC, Boujemaa-Paterski R, Martiel JL, Guerin C, Cao W, Chin HF, De La Cruz EM, Théry M, Blanchoin L. Actin network architecture can determine myosin motor activity. Science 2012; 336:1310-4; PMID:22679097; http://dx.doi.org/10.1126/science.1221708
8. Bergert M, Chandradoss SD, Desai RA, Paluch E. Cell mechanics control rapid transitions between blebs and lamellipodia during migration. Proc Natl Acad Sci USA 2012; 109:14434-9; PMID:22786929; http://dx.doi.org/10.1073/pnas.1207968109
9. Brevier J, Montero D, Svitkina T, Riveline D. The asymmetric self-assembly mechanism of adherens junctions: a cellular push-pull unit. Phys Biol 2008; 5:016005-10; PMID:18379019; http://dx.doi.org/10.1088/1478-3975/5/1/016005
10. Brevier J, Vallade M, Riveline D. Force-extension relationship of cell-cell contacts. Phys Rev Lett 2007; 98:268101-4; PMID:17678130; http://dx.doi.org/10.1103/PhysRevLett.98.268101
11. van den Dries K, Meddens MB, de Keijzer S, Shekhar S, Subramaniam V, Figdor CG, Cambi A. Interplay between myosin IIA-mediated contractility and actin network integrity orchestrates podosome composition and oscillations. Nat Commun 2013; 4:1412-13; PMID:23361003; http://dx.doi.org/10.1038/ncomms2402
12. Herszterg S, Leibfried A, Bosveld F, Martin C, Bellaiche Y. Interplay between the dividing cell and its neighbors regulates adherens junction formation during cytokinesis in epithelial tissue. Dev Cell 2013; 24:256-70; PMID:23410940; http://dx.doi.org/10.1016/j.devcel.2012.11.019
13. Jegou A, Carlier MF, Romet-Lemonne G. Formin mDia1 senses and generates mechanical forces on actin filaments. Nat Commun 2013; 4:1883-7; PMID:23695677; http://dx.doi.org/10.1038/ncomms2888
14. Riveline D, Zamir E, Balaban NQ, Schwarz US, Ishizaki T, Narumiya S, Kam Z, Geiger B, Bershadsky AD. Focal contacts as mechanosensors: externally applied local mechanical force induces growth of focal contacts by an mDia1-dependent and ROCK-independent mechanism. J Cell Biol 2001; 153:1175-86; PMID:11402062; http://dx.doi.org/10.1083/jcb.153.6.1175
15. Bubb MR, Spector I, Bershadsky AD, Korn ED. Swinholide A is a microfilament disrupting marine toxin that stabilizes actin dimers and severs actin filaments. J Biol Chem 1995; 270:3463-6; PMID:7876075; http://dx.doi.org/10.1074/jbc.270.8.3463
16. Yeung KS, Paterson I. Actin-binding marine macrolides: total synthesis and biological importance. Angew Chem Int Ed Engl 2002; 41:4632-53; PMID:12481316; http://dx.doi.org/10.1002/anie.200290057
17. Klenchin VA, King R, Tanaka J, Marriott G, Rayment I. Structural basis of swinholide A binding to actin. Chem Biol 2005; 12:287-91; PMID:15797212; http://dx.doi.org/10.1016/j.chembiol.2005.02.011
18. Nedeva I, Koripelly G, Caballero D, Chieze L, Guichard B, Romain B, Pencreach E, Lehn J-M, Carlier M-F, Riveline D. Synthetic polyamines promote rapid lamellipodial growth by regulating actin dynamics. Nat Commun 2013; 4:2165-11; PMID:23893126; http://dx.doi.org/10.1038/ncomms3165
19. Oriol-Audit C, Hosseini MW, Lehn J-M. 'Superpolyamines'. Eur J Biochem 1985; 151:557-9; PMID:4029147; http://dx.doi.org/10.1111/j.1432-1033.1985.tb09139.x
20. Carlier M-F, Koripelly G, Nedeva I, Lehn JM, Riveline D. Universite de Strasbourg, Centre National de la Recherche Scientifique, Branched or macrocyclic polyamines and uses thereof. France patent application FR WO/2014/029888. 2014.
21. Mejillano MR, Kojima S, Applewhite DA, Gertler FB, Svitkina TM, Borisy GG. Lamellipodial versus filopodial mode of the actin nanomachinery: pivotal role of the filament barbed end. Cell 2004; 118:363-73; PMID:15294161; http://dx.doi.org/10.1016/j.cell.2004.07.019
22. Wiesner S, Helfer E, Didry D, Ducouret G, Lafuma F, Carlier MF, Pantaloni D. A biomimetic motility assay provides insight into the mechanism of actin-based motility. J Cell Biol 2003; 160:387-98; PMID:12551957; http://dx.doi.org/10.1083/jcb.200207148
23. Mendes Pinto I, Rubinstein B, Kucharavy A, Unruh JR, Li R. Actin depolymerization drives actomyosin ring contraction during budding yeast cytokinesis. Dev Cell 2012; 22:1247-60; PMID:22698284; http://dx.doi.org/10.1016/j.devcel.2012.04.015
24. Mifkova A, Kodet O, Szabo P, Kucera J, Dvorankova B, Andre S, Koripelly G, Gabius HJ, Lehn J-M, Smetana K. Synthetic Polyamine BPA-C8 Inhibits TGF-beta1-Mediated Conversion of Human Dermal Fibroblast to Myofibroblasts and Establishment of Galectin-1-Rich Extracellular Matrix in Vitro. Chembiochem 2014; 15:1465-70; PMID:24867251; http://dx.doi.org/10.1002/cbic.201402087
25. Stehn JR, Haass NK, Bonello T, Desouza M, Kottyan G, Treutlein H, Zeng J, Nascimento PRBB, Sequeira VB, Butler TL, et al. A novel class of anticancer compounds targets the actin cytoskeleton in tumor cells. Cancer Res 2013; 73:5169-82; PMID:23946473; http://dx.doi.org/10.1158/0008-5472.CAN-12-4501
26. Moreno S, Klar A, Nurse P. Molecular genetic analysis of fission yeast Schizosaccharomyces pombe. Methods Enzymol 1991; 194:795-823; PMID:2005825; http://dx.doi.org/10.1016/0076-6879(91)94059-L
27. Riveline D, Nurse P. 'Injecting' yeast. Nat Methods 2009; 6:513-4; PMID:19503081; http://dx.doi.org/10.1038/nmeth.1335

Raghavan THIAGARAJAN

Collective effects in living matter: from cytokinetic rings to epithelial monolayers

Résumé

L'émergence de comportements collectifs cellulaires n'est pas bien comprise. Nous l'abordons dans deux systèmes biologiques. A l'échelle du micromètre lors de la constriction de l'anneau cytokinétique, nous montrons que des complexes d'acto-myosine s'auto-organisent sous forme d'agrégats dans la levure à fission et dans la cellule de mammifères. Ces auto-organisations découlent de règles d'interactions communes mais pour des fonctions distinctes, le transport et la génération de stress respectivement. A l'échelle de 100 micromètres, nous observons des pulsations corrélées de cellules épithéliales. Nous montrons les rôles du frottement avec la surface, et le couplage entre l'aire cellulaire, sa hauteur et sa contractilité. Nous présentons aussi deux études, des polyamines synthétiques pour étudier la polymérisation d'actine in vivo, puis l'inversion de sens dans la migration - la ratchetaxie. Cette thèse illustre l'importance des phénomènes physiques dans la dynamique cellulaire.

Abstract

The emergence of collective behavior from the interaction of individual units is not clear. In this thesis, we address this question in two different systems at different scales. At the micrometer scale during cytokinetic ring constriction, we show that acto-myosin self-organizes into rotating and static clusters in fission yeast and mammalian cells. These self-organizations arise from common interaction rules, but to serve distinct functions, transport and stress generation respectively. At 100 micrometers scale, we report correlated pulsations of cells in an epithelial monolayer. We show the key roles of substrate friction, and the tight coupling between cell area, cell height and contractility. We also present two other studies: synthetic polyamines for studying actin polymerization *in vivo*, and direction reversal in single cell migration during ratchetaxis. Altogether, this PhD illustrates the importance of physical phenomena in cellular dynamics.